LA-11582-T
Thesis

UC-414
Issued: May 1989

LA--11582-T

DE89 011400

Coincidence Measurements of the $(\pi^+,\pi^0 p)$ Reaction in the Δ-Resonance Region

Steinar Høibråten*

*Graduate Research Assistant at Los Alamos.
Nuclear Physics Department, University of Colorado,
Campus Box 446, Boulder, CO 80309-0446.

Los Alamos National Laboratory
Los Alamos, New Mexico 87545

COINCIDENCE MEASUREMENTS OF THE $(\pi^+, \pi^0 p)$ REACTION IN THE Δ-RESONANCE REGION

by

STEINAR HØIBRÅTEN

Submitted to the Department of Physics on January 31, 1989
in partial fulfillment of the requirements for the degree of
Doctor of Philosophy

Abstract

This thesis describes an experimental study of the $(\pi^+, \pi^0 p)$ reaction at incident energy $T_{\pi^+} = 165$ MeV. The measurements were taken at the Clinton P. Anderson Meson Physics Facility (LAMPF) in Los Alamos, New Mexico. This work is part of the first experiment to detect neutral pions and protons in coincidence in kinematically complete measurements. The reaction was studied on ^{16}O (using water targets) at several pion angles: $\theta_{\pi^0} = 70°$, 80°, 110°, and 130°. At $\theta_{\pi^0} = 110°$ measurements were also made on ^{56}Fe, ^{120}Sn, and ^{208}Pb. The neutral pions were detected with the LAMPF π^0 spectrometer, while the protons were detected in a vertical array of plastic-scintillator ΔE–E telescopes, each spanning 8.5 msr.

Energy spectra of the differential cross sections $d^4\sigma/dE_{\pi^0}\, dE_p\, d\Omega_{\pi^0}\, d\Omega_p$ were obtained for each proton telescope and subsequently integrated over proton and pion energy and proton angle. The characteristics of these spectra are consistent with a quasi-free description of the $(\pi^+, \pi^0 p)$ reaction. The angular dependence of $d\sigma/d\Omega_{\pi^0}(\theta_{\pi^0})$ for $^{16}\mathrm{O}(\pi^+, \pi^0 p)$ was found to be in accordance with that of the cross section for the corresponding free reaction at backward π^0 angles. For the $^{16}\mathrm{O}(\pi^+, \pi^0 p)$ reaction, events in which a p-shell nucleon had been removed were identified. The p-shell events were found to constitute only $40 - 50\%$ of the total cross section for quasi-free one-nucleon removal. The $(\pi^+, \pi^0 p)$ cross section at $\theta_{\pi^0} = 110°$ proved to be almost the same for all target nuclei, possibly slightly decreasing as a function of A.

The $d^3\sigma/dE_{\pi^0}\, d\Omega_{\pi^0}\, d\Omega_p$ cross section spectra for $^{16}\mathrm{O}(\pi^+, \pi^0 p)$ were compared to Δ–hole model calculations done by Takaki and Thies. The calculations underestimate the cross section at the conjugate quasi-free angle by about $30 - 55\%$. However, they are in fair agreement with our results at the only other proton angle for which such calculations were available.

Results from a simultaneous study of the (π^+, π^0) reaction are also included in this thesis. The quasi-free part of the $^{16}\mathrm{O}(\pi^+, \pi^0 p)$ cross section was found to account for

about $30-40\%$ of the integrated cross section $d\sigma/d\Omega_{\pi^0}$ for the $^{16}O(\pi^+,\pi^0)$ reaction A study of the angular dependence of $d\sigma/d\Omega_{\pi^0}(\theta_{\pi^0})$ for the $^{16}O(\pi^+,\pi^0)$ reaction indicated that this was in agreement with the angular dependence of the corresponding free cross section at backward π^0 angles. It was found that the A-dependence of $d\sigma/d\Omega_{\pi^0}$ for the (π^+,π^0) reaction can be described by A^α where $\alpha = 0.41 \pm 0.06$.

Thesis Supervisor: Dr. Robert P. Redwine
Associate Professor of Physics

Acknowledgements

Work on pion coincidence experiments has dominated my research activities during most of my time at M.I.T. This work has over the years introduced me to a number of interesting and helpful collaborators, and I hope I have been able to retain at least part of the many good examples these people have set.

At M.I.T., my foremost thanks go, of course, to Bob Redwine, who has been my advisor since 1984. In between his many commitments, he has always found time to address the many problems I have raised. Moreover, I appreciate the relative independence in which I have been allowed to pursue my tasks. I also want to thank my first advisor here, June Matthews, whom it has always been a pleasure to interact with. She introduced me to Los Alamos and LAMPF in my first year at M.I.T., and I have been hooked ever since both on the nice working conditions at the lab and on its beautiful surroundings in northern New Mexico.

Several people in addition to Bob have made a sizable impact on my thesis project. It began with Shalev Gilad during the planning and preparations in 1983. Shalev first introduced me to the upcoming experiment not long after our first meeting at Albuquerque airport where he spotted someone with an "M.I.T." backpack and came over to chat. Thanks for the drink, Shalev! During the data taking phase of the experiment, the many night shifts I shared with the hard-working and thorough Eli Piasetzky taught me much about how to run experiments. It was also a pleasure to work with the other MP-4 physicists and the LAMPF support staff. The many other students in Los Alamos (Mark Bachman, Bill Burger, Ed Kinney, Mohini Rawool, Sayed Rokni, and others) contributed greatly to making both working and spare hours very enjoyable.

The data analysis involved an interesting visit to PSI (then SIN) in 1985 to reanalyze $^{16}O(\pi^{\pm},\pi^{\pm}p)$ data, and I want to thank Gary Kyle and Quentin Ingram for their

helpful and friendly assistance there during a difficult time of my life. Many thanks also to the skillful night guard at SIN who successfully traced me at 1 a.m. in the morning after receiving a phone call in a language he did not know.

This work would have been less complete if it had not been for the kindness of the same Gary Kyle, who let me use unpublished $(\pi^{\pm}, \pi^{\pm}p)$ data for comparison to $(\pi^{+}, \pi^{0}p)$ results, and Takashi Takaki, who provided me with theoretical Δ–hole model cross section estimates made for this experiment.

At M.I.T., I have on numerous occasions benefited from the helpful support of the staff of the Laboratory for Nuclear Science. In particular, I want to thank Jean Hudson, who has always in a very friendly way taken good care of my confusing travel plans, sometimes on rather short notice. I have also benefited a lot both professionally and personally from working with and sharing the company of my many office mates and the other members of our research group; I have had many fruitful encounters over the years with in particular Betsy Beise, Karen Dow, Eric Kronenberg, Long Don Phạm, Larry Weinstein, and Kevin Wilson. Long has also contributed greatly to keeping me physically fit during these years.

In writing this thesis, several people have been helpful with suggestions and proof reading. Two of these went particularly far out of their way in their efforts to make this work presentable: our post-doc, Gerard van der Steenhoven, whose numerous comments and suggestions have been very useful in my work, and my wife, Jennifer, whose tireless and persistent efforts in making my English clear and correct have meant a lot to the readability of the finished product.

And last, but definitely not least, I want to express my gratitude towards my parents and my wife for the support they have always given me in the many aspects of my life. This thesis is dedicated to them.

To my mother
and the memory of my father

and

To Jennifer

Table of Contents

List of Figures

Chapter 1

Chapter 2

Chapter 3

Chapter 4

List of Tables

Chapter 2

Chapter 3

Chapter 4

Chapter 5

Appendix E

Chapter 1

Background and Motivation

This thesis presents the experimental work and the corresponding data analysis associated with a series of coincidence measurements of the $(\pi^+, \pi^0 p)$ reaction at a beam energy of $T_{\pi^+} = 165$ MeV. The results of this work can be grouped into three separate studies: The main part of the project is a detailed study of the $^{16}O(\pi^+, \pi^0 p)$ reaction at several π^0 (and proton) angles. A second set of coincidence data constitute a study of the A-dependence of the $(\pi^+, \pi^0 p)$ reaction. The latter data were taken at $\theta_{\pi^0} = 110°$, and consist of measurements on ^{16}O, ^{56}Fe, ^{120}Sn, and ^{208}Pb. The third study is a series of single arm (π^+, π^0) measurements. These measurements were made along with all the coincidence measurements mentioned above. Since the (π^+, π^0) data could be taken with very little additional effort, and they allow for interesting comparisons to previous data as well as our coincidence results, it was decided to carry out these measurements as well even though studying this reaction was not part of the initial motivation for our experiment.

The present chapter is an introduction to our work. It gives an overview of relevant experiments and presents some aspects of the current theoretical basis for modeling pion–nucleus reactions. Chapter 2 contains a description of the experimental apparatus and the work done at the Clinton P. Anderson Meson Physics Facility (LAMPF) in Los Alamos, New Mexico. The results of the data analysis, which was done in full

at M.I.T., are presented in the two subsequent chapters. Chapter 3 contains the preparatory analysis to establish detector calibrations and various parameter values necessary for the full data analysis, while the results of the $(\pi^+,\pi^0 p)$ and (π^+,π^0) measurements are presented in Chapter 4. The impact of our work is discussed in Chapter 5 where our results are compared to other measurements and to theoretical predictions.

Some of our results were presented at the Third Conference on the Intersections Between Particle and Nuclear Physics in 1988.[1]

1.1 Pion Physics

This section provides the reader with some background information about pion physics. It consists of a general presentation followed by a more specialized discussion of certain topics of particular relevance to our experiment.

1.1.1 General Overview

The pion is today known as a pseudoscalar (spin 0, negative intrinsic parity), isovector (isospin 1) meson. The three members of the isospin triplet, π^+, π^0, and π^-, have charges +1, 0, and −1, respectively; their masses are $m_{\pi^+} = m_{\pi^-} = 139.6$ MeV and $m_{\pi^0} = 135.0$ MeV, and their mean lifetimes are $\tau_{\pi^+} = \tau_{\pi^-} = 26$ ns and $\tau_{\pi^0} = 84$ as (cf. Ref. 2).

The existence of pions was first predicted by Hideki Yukawa in a paper published in 1935.[3] Based on the known short range of the nuclear force, he presented a theory in which the carriers (the "massive quanta"[3]) of this force were spin-less particles with a mass about 200 times the electron mass (that is, approximately 100 MeV). A detailed historical review of the development of this theory is given in Ref. 4.

After initially having been confused with the muon, the charged pions were finally identified in cosmic-ray events in 1947.[5–7] The existence of the neutral pion was established in 1949 by observations of the decay $\pi^0 \rightarrow \gamma\gamma$, first in accelerator measurements[8] and

later confirmed by cosmic-ray observations.[9] The π^0 became the first particle to be discovered by use of a particle accelerator. This discovery took place at the 184-inch synchrocyclotron at Berkeley, California.

In later theories of the strong nuclear force, which is responsible for binding the individual nucleons together in nuclei, the pion has been taken as the lightest of several mesons mediating this force. The pion is the most well-known meson, and, because of its low mass, one-pion-exchange alone provides a good description of the long range part ($r > 3$ fm) of the nuclear force.[10]

The use of pion beams to probe nuclear properties is more recent. Pions are produced in abundance in most nuclear interactions provided that the available energy is higher than the pion mass. It was not until the mid-1960's, however, that the accelerator technology made high intensity proton beams possible. The typical beam current went from 1 μA to 100 μA, enough to produce rather intense secondary pion beams when hitting a target. This led to the construction of the "meson factories": LAMPF, the Paul Scherrer Institute (PSI) (formerly the Swiss Institute for Nuclear Research (SIN)) in Villigen, Switzerland, and TRIUMF (the Tri-University Meson Facility) in Vancouver, British Columbia, Canada. LAMPF, which has the highest proton beam intensity and energy, produced its first beam in June, 1972.[11,12]

An important reason for the interest in the use of pions as nuclear probes is the fact that they interact strongly. Thus pions also interact with neutrons, which cannot easily be studied using electrons or other leptonic probes. Pion beams have been employed to explore not only questions of nuclear reactions and nuclear structure, but also the details of reaction mechanisms and propagation/absorption of pions in the nuclei. Isospin is a conserved quantum number in strong interactions. The fact that the pion has isospin 1, and therefore can couple to many isospin states, makes it a particularly powerful probe of the isospin character of nuclear reactions. This is especially important in the energy region of the Δ-resonance where the coupling between pions and nucleons is very sensitive to the isospin channel. (The Δ-resonance is a strong and broad baryon resonance centered at $E_\Delta = 1232$ MeV total π–N center-of-momentum energy, corresponding to a pion of approximately $180-190$ MeV hitting a stationary nucleon. This resonance is discussed further in the subsection immediately following this one.)

Other important aspects of the pion probes are their zero spin (pions do not affect the spin of the system being studied), their relatively small size (the root-mean-square charge radius[13] is 0.65 fm), and also that they (at least the charged ones) are easily detected and easily distinguished from other particles. A more comprehensive discussion of the use of pion beams can be found in Ref. 11.

With the advent of the quark picture in the 1970's, a new description of the nuclear force and the pion was developed. Baryons, for example protons and neutrons, are composed of three quarks, while mesons, for example pions, are composed of one quark and one antiquark. The nuclear force is mediated by gluons that hold the various quarks together. The particles mentioned are all composed of a combination of up (u) and down (d) quarks: $p = uud$, $n = udd$, $\pi^+ = u\bar{d}$, $\pi^0 = (u\bar{u} - d\bar{d})/\sqrt{2}$, $\pi^- = \bar{u}d$. The quark description is mainly relevant to high-energy measurements, however. At energies where the pion wavelength is comparable to the nucleon size or larger, the quark structure cannot be resolved, and hence the nucleon-meson description should be equivalent to the quark-gluon description. (This equivalence is still a somewhat open question in nuclear physics, but so far there has been no sign of quark degrees of freedom at low energies.) At our beam energy, 165 MeV, the pion wavelength (taken as $\frac{\hbar}{p}$) is over 0.7 fm, thus indicating that the meson exchange picture should provide a satisfactory description in our case.

1.1.2 The Δ-Resonance

The Δ-resonance is observed in pion–nucleon scattering as a very prominent "bump" of width approximately 115 MeV (FWHM) centered near $T_\pi = 180$ MeV. This is illustrated in Fig. 1.1 which shows total cross sections for π^+p and π^-p scattering (by charge (isospin) symmetry the situation is the same for π^-n and π^+n scattering, respectively). The first experimental suggestions of the Δ-resonance were observed as early as $1951 - 52$, a discovery eased by the very large cross sections.[17–18] This resonance is known more precisely as the $\Delta(1232)$ because it is centered around a total energy of $E_\Delta = 1232$ MeV. It is the lowest and most pronounced excited state of the nucleon. It is also often referred to as the $\Delta(3,3)$-resonance, where the 3's indicate its isospin ($T_\Delta = \frac{3}{2}$) and spin ($J_\Delta = \frac{3}{2}$). Many other pion–nucleon resonances, with

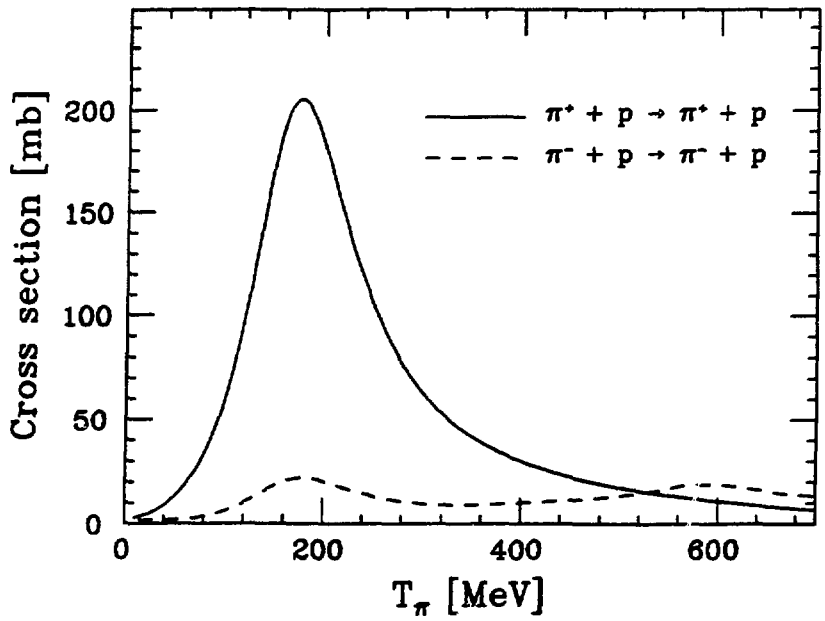

Figure 1.1. *π–N elastic scattering.* The figure shows the total cross sections for π^+p and π^-p elastic scattering. The $\Delta(1232)$-resonance is the prominent "bump" centered near $T_{\pi^+} = 180$ MeV in both cases. The cross sections are from Arndt phase shift calculations.[14–16] Due to charge symmetry, the situation for π^-n and π^+n scattering will be the same as shown here for π^+.

isospin either $\frac{3}{2}$ (Δ's) or $\frac{1}{2}$ (N's) are known, but they are separated from the $\Delta(1232)$ by several hundred MeV, and they are not as strong as this resonance.

Two features of Fig. 1.1 should be noted: First, the π–N cross sections are generally quite large. They are of the same order as the geometrical cross section of the particles. Pion scattering on a complex nucleus will therefore mainly probe the surface of the nucleus; the pions are generally not able to get past the surface nucleons without interacting. (The mean free path, calculated as $\frac{1}{\rho\sigma}$ where ρ is the density of nuclear matter (0.17 fm^{-3}, cf. Ref. 10) and σ is the cross section from Fig. 1.1, is less than 1 fm.) Second, in the Δ-resonance region there is a pronounced difference between the cross sections for π^+p and π^-n on the one hand and π^+n and π^-p on the other. This means that by choosing either π^+ or π^- as the probe, one can perform a selective study of respectively the proton or the neutron (surface) distribution in the target nucleus.

The ratio between the cross sections at the Δ-resonance energy can be understood quite well by just considering the isospin channels involved. In the cross section ratio

$$R^{+-} \equiv \frac{\sigma(\pi^+ p \to \pi^+ p)}{\sigma(\pi^- p \to \pi^- p)}, \tag{1.1}$$

only two states appear: $|\pi^+ p\rangle$ and $|\pi^- p\rangle$. Except for the isospin structure, these states are identical. In general, one may express a π–N system by an expansion in its isospin components:

$$|\pi N\rangle = |\psi\rangle \sum_T \langle T T_3 | T_\pi T_{\pi 3} T_N T_{N3}\rangle | T T_3\rangle \Big|_{T_3 = T_{\pi 3} + T_{N3}}. \tag{1.2}$$

Here, T and T_3 denotes the total πN isospin and its third component, respectively, and $|\psi\rangle$ symbolizes the common part of all πN couplings (the spatial and spin variables). The sum is over all values T consistent with the fixed value of T_3. The coefficients $\langle T T_3 | T_\pi T_{\pi 3} T_N T_{N3}\rangle$ are Clebsch-Gordan coefficients (see any quantum mechanics textbook). Using standard values for these coefficients (which may be found in Ref. 2), we get for the two states appearing in Eq. (1.1):

$$|\pi^+ p\rangle = |\psi\rangle \, |\tfrac{3}{2}\, \tfrac{3}{2}\rangle \tag{1.3}$$

$$|\pi^- p\rangle = |\psi\rangle \left\{ \sqrt{\tfrac{1}{3}}\, |\tfrac{3}{2}\, -\tfrac{1}{2}\rangle - \sqrt{\tfrac{2}{3}}\, |\tfrac{1}{2}\, -\tfrac{1}{2}\rangle \right\}, \tag{1.4}$$

where the isospin eigenvectors are denoted by the total isospin (T) and its third component (T_3), respectively.

Furthermore, because the Δ-resonance has isospin $\frac{3}{2}$ (and isospin is conserved in strong interactions), only the $T = \frac{3}{2}$ part of the above states can contribute to the scattering cross sections in the Δ-resonance region. (This assumes that the Δ-resonance is the dominating reaction mechanism in this region as suggested by the cross sections in Fig. 1.1.) In the Δ-resonance region we therefore have

$$R_\Delta^{+-} = \frac{|\langle \pi^+ p | \pi^+ p\rangle_\Delta|^2}{|\langle \pi^- p | \pi^- p\rangle_\Delta|^2} \tag{1.5}$$

$$= \frac{|\langle\psi|\psi\rangle|^2 \, |\langle \tfrac{3}{2}\, \tfrac{3}{2} | \tfrac{3}{2}\, \tfrac{3}{2}\rangle|^2}{|\langle\psi|\psi\rangle|^2 \, |\sqrt{\tfrac{1}{3}\cdot\tfrac{1}{3}}\langle \tfrac{3}{2}\, -\tfrac{1}{2} | \tfrac{3}{2}\, -\tfrac{1}{2}\rangle|^2} \tag{1.6}$$

$$= 9, \tag{1.7}$$

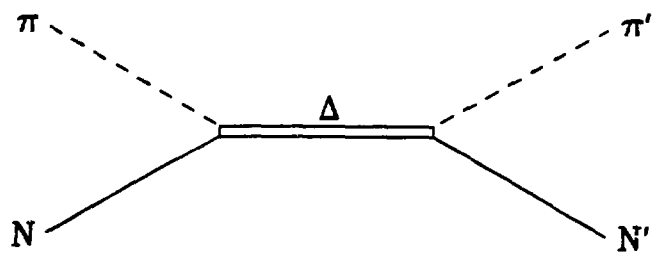

Figure 1.2. The Δ-resonance. This is a short-lived (10^{-23} s) pion–nucleon resonance which usually decays back to a pion and a nucleon. There are four possible charge states: Δ^{++}, Δ^{+}, Δ^{0}, and Δ^{-}.

which is in good agreement with the cross sections shown in Fig. 1.1. The ratio between the two curves in the figure is $R_{\Delta}^{+-} = 9.3$ at 180 MeV.

The Δ-resonance is usually illustrated schematically as shown in Fig. 1.2: a pion and a nucleon combine to form a resonance which shortly thereafter decays to a pion and a nucleon again. The Δ(1232) has one more decay mode; it decays to a nucleon and a photon with a branching ratio of 0.6%.[2] The Δ has four charge states, Δ^{++}, Δ^{+}, Δ^{0}, and Δ^{-}, corresponding to the various pion–nucleon combinations possible. The Δ^{+} and the Δ^{0} can both decay into two possible combinations of a pion and a nucleon (for example, $\Delta^{+} \rightarrow \pi^{+}n$ and $\Delta^{+} \rightarrow \pi^{0}p$). This allows for charge exchange through the Δ-resonance; that is, the charge of the decay pion is not the same as the charge of the pion that initiated the resonance.

The strong interaction is responsible for the decay of the Δ. Its lifetime must therefore be on the order of 10^{-23} s.[19] This lifetime may be affected somewhat inside a nucleus by, on the one hand, Pauli blocking of final states (which would lead to a longer lifetime) and, on the other hand, the dynamics of the process (which could open more decay channels and hence shorten the lifetime). In any case, the Δ may typically propagate a distance inside the nucleus of up to about the length of the inter-nucleon distance before decaying. The concept of Δ propagation and interactions of the Δ with other nucleons is essential to some of the theoretical work in the field, particularly to the "Δ–hole model", the predictions of which were an important part of the motivation for our measurements. We will expand more on this in the theory section later in this chapter.

1.1.3 Pion Single Charge Exchange and Nucleon Removal

By pion single charge exchange (SCX) reactions we generally mean pion interactions where the charge of the ejected pion has changed by -1 or $+1$ with respect to the charge of the incident pion. Since one cannot produce a beam of π^0's, the only SCX reactions that can be observed are

$$\pi^+ + n \rightarrow \pi^0 + p \tag{1.8}$$

and

$$\pi^- + p \rightarrow \pi^0 + n. \tag{1.9}$$

Of course, one is not restricted to studying these reactions only on free nucleons. Indeed, by doing SCX on complex nuclei, one might hope to learn something about the influence of the nuclear environment on the SCX reaction mechanism.

This thesis is a discussion of the $(\pi^+, \pi^0 p)$ and (π^+, π^0) reactions at $T_{\pi^0} = 165$ MeV. Both of these reactions are SCX reactions as described by Eq. (1.8). Because our measurements take place near the center of the Δ-resonance region, where the cross sections are overwhelmingly dominated by this resonance, the elementary SCX process must be the Δ-resonance as illustrated in Fig. 1.2 with incident π^+ and n and outgoing π^0 and p.

We can then compare expected SCX cross sections in the Δ-resonance region to the charged pion scattering cross sections discussed in Sec. 1.1.2 following the same isospin coupling scheme that led to Eq. (1.7) in that section. For the π^+ SCX reaction described in Eq. (1.8), we need to expand the following states:

$$|\pi^+ n\rangle = |\psi\rangle \left\{ \sqrt{\tfrac{1}{3}} \, |\tfrac{3}{2}\,\tfrac{1}{2}\rangle + \sqrt{\tfrac{2}{3}} \, |\tfrac{1}{2}\,\tfrac{1}{2}\rangle \right\}, \tag{1.10}$$

$$|\pi^0 p\rangle = |\psi\rangle \left\{ \sqrt{\tfrac{2}{3}} \, |\tfrac{3}{2}\,\tfrac{1}{2}\rangle - \sqrt{\tfrac{1}{3}} \, |\tfrac{1}{2}\,\tfrac{1}{2}\rangle \right\}. \tag{1.11}$$

This leads to a ratio

$$R_{\Delta}^{+0} = \left. \frac{\sigma(\pi^+ p \rightarrow \pi^+ p)}{\sigma(\pi^+ n \rightarrow \pi^0 p)} \right|_{\Delta} \tag{1.12}$$

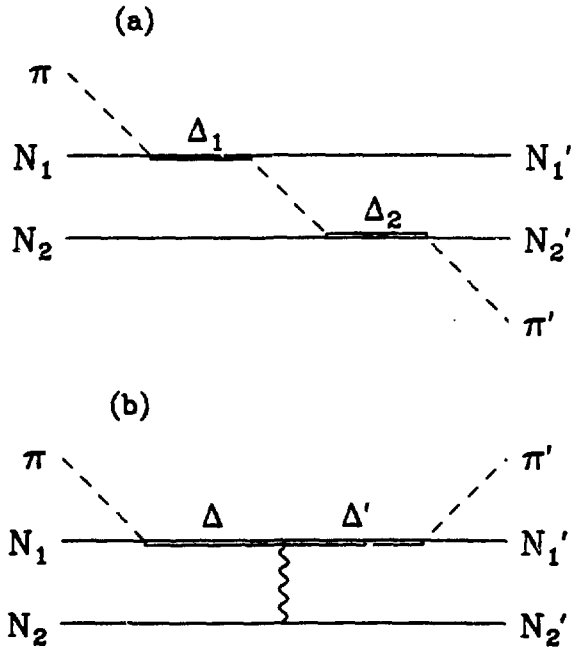

Figure 1.3. Possible second-order $(\pi,\pi' N)$ processes. These are processes that require participation of two nucleons in the nucleus. (a) shows interaction through one-pion-exchange, and (b) assumes an effective Δ–N interaction. Various combinations of specific pion and nucleon charge states are possible (depending on which $(\pi,\pi' N)$ process one is studying).

$$= \frac{|\langle \pi^+ p | \pi^+ p \rangle_\Delta|^2}{|\langle \pi^0 p | \pi^+ n \rangle_\Delta|^2} \tag{1.13}$$

$$= \frac{|\langle \psi|\psi\rangle|^2 \, |\langle \frac{3}{2}\,\frac{3}{2} | \frac{3}{2}\,\frac{3}{2}\rangle|^2}{|\langle \psi|\psi\rangle|^2 \, |\sqrt{\frac{2}{3}\cdot\frac{1}{3}}\langle \frac{3}{2}\,\frac{1}{2} | \frac{3}{2}\,\frac{1}{2}\rangle|^2} \tag{1.14}$$

$$= 4.5\,, \tag{1.15}$$

which is in rather close agreement with the measured free cross sections; from Arndt phase shift calculations[14–16] we get an experimental ratio of $R_\Delta^{+0} = 4.2$ at 180 MeV.

The $(\pi^+, \pi^0 p)$ reaction is a nucleon removal process. In addition to the first-order process described above and illustrated in Fig. 1.2, a number of second-order processes (involving another nucleon in the nucleus) are possible. Two examples are shown schematically in Fig. 1.3. The figure distinguishes between two types of second-order processes: one is a one-pion-exchange to excite the other participating nucleon, the

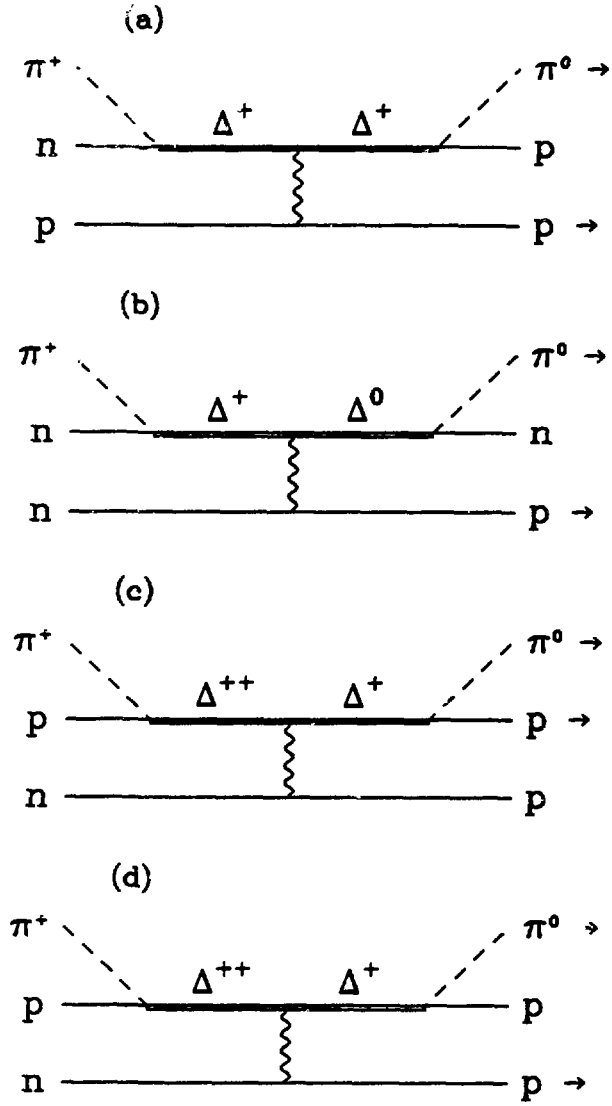

Figure 1.4. Δ–N interaction processes for $(\pi^+, \pi^0 p)$. All processes indicated in Fig. 1.3b for the $(\pi^+, \pi^0 p)$ reaction are shown explicitly. The arrows behind some of the final-state particles indicate those which are detected in the coincidence measurements. The process in (a) is similar to the first-order process in Fig. 1.2 except that another proton is knocked out by the Δ. (b) is the same with a charge exchange involved. (c) and (d) are identical except for the detection of a different proton.

other assumes an effective interaction between the Δ and the second nucleon. More details about this interaction are given in our discussion of current theoretical descriptions later in this chapter. The various Δ–N interaction processes of Fig. 1.3b that apply to $(\pi^+,\pi^0 p)$ are shown in detail in Fig. 1.4. The particles which are detected are indicated in each case.

1.1.4 Quasi-free Interactions

The concept of quasi-free interactions is central to our work. The term "free" interaction refers to an interaction taking place on a free nucleon. The term "quasi-free" is used similarly to describe interactions of particles with nuclei, and implies that the particle (in our case the beam pion) interacts with only one of the nucleons in the nucleus, leaving the remaining nucleons as "spectators".

The Δ-resonance as sketched in Fig. 1.2 involves, of course, only one nucleon. This does not necessarily mean that the $(\pi^+,\pi^0 p)$ and (π^+,π^0) reactions are predominantly quasi-free, however, because there could be other reaction mechanisms as well which might involve more than just one nucleon, or the higher-order Δ-resonance processes (cf. Fig. 1.4) might dominate.

To determine whether an interaction is quasi-free, one must compare the measured energy spectra and/or angular distributions to predictions from two-body kinematics. A signature of quasi-free processes is that they in general involve rather broad correlations between the kinematic variables. This broadening is due to the motion of the interacting nucleon inside the nucleus (Fermi broadening). Most recent $(\pi,\pi' N)$ and (π,π') measurements in the Δ-resonance region support the hypothesis that these reactions are indeed predominantly quasi-free in this region, particularly for the case of scattering to backward pion angles.[20–22]

1.2 Previous Experimental Work

This section contains a discussion of earlier experimental work leading up to our study of the $(\pi^+,\pi^0 p)$ and (π^+,π^0) reactions. Measurements have been made on these

reactions for several decades, but it was not until the employment of the LAMPF π^0 spectrometer in 1978 that one could obtain high-statistics high-resolution π^0 data (a few MeV in energy and a few degrees in angle). Details of the earlier work are found in review articles by Koltun[23] from 1969 and Alster and Warszawski[24] from 1979.

There are two subsections below. In the first subsection we present at some length the historical development of the $(\pi, \pi' N)$ measurements with respect to experimental techniques and questions addressed. This is followed by a subsection on recent inclusive $(\pi^{\pm}, \pi^0)$ measurements relevant to our own single arm (π^+, π^0) study.

1.2.1 $(\pi, \pi' N)$ Measurements

A paper on interactions of pions with ^{4}He in a diffusion cloud chamber was published by Kozodaev *et al.*[25] in 1960. Single nucleon removal cross sections were measured for a number of processes on ^{4}He: $(\pi^-, \pi^- n)$, $(\pi^-, \pi^- p)$, $(\pi^+, \pi^+ p)$, $(\pi^+, \pi^+ n)$, and $(\pi^+, \pi^0 p)$, with beam energies $T_{\pi^+} = (273 \pm 7)$ MeV and $T_{\pi^-} = (330 \pm 6)$ MeV. These appear to be the earliest documented $(\pi, \pi' N)$ measurements. The statistics were rather poor, however; only 35 $(\pi^+, \pi^0 p)$ events were observed.

The earliest nucleon removal measurements in the Δ-resonance region known to the author are described in a study of the $^{12}\mathrm{C}(\pi^-, \pi^- n)^{11}\mathrm{C}$ reaction by Reeder and Markowitz[26] from 1963. Like most other early experiments,[27–29] this study was limited to measuring only the excitation function (the angle integrated cross section as a function of beam energy). The reactions to specific nuclei had to be identified by radiochemical means, and the absolute cross sections were calculated from the activity of these residual nuclei. These cross sections would include processes leading to several of the low-lying excited states of the residual nucleus. The $\Delta(1232)$ is clearly observed in the data of Reeder and Markowitz, who made their measurements at a number of energies ranging from 53 MeV to 1610 MeV. They found a value of (68 ± 6) mb for the $^{12}\mathrm{C}(\pi^-, \pi^- n)^{11}\mathrm{C}$ cross section at $T_{\pi^-} = (179 \pm 10)$ MeV.

$(\pi^+, \pi^0 p)$ cross sections are included in results obtained in π^+-induced activity measurements,[28,29] but they cannot be separated from the $(\pi^+, \pi^+ n)$ cross sections because both reactions produce the same residual nucleus. Chivers *et al.*[29] were the

first to study ^{16}O (using a water target). At $T_{\pi^+} = 180$ MeV they measured the $^{16}O(\pi^+, \pi^+n + \pi^0p)^{15}O$ cross section to be (41 ± 4) mb. They also measured the similar cross sections for $^{14}N \rightarrow {}^{13}N$ and $^{12}C \rightarrow {}^{11}C$ as (56 ± 6) mb and (75 ± 4) mb, respectively, thus finding that within this limited range of nuclei, the cross section for $(\pi^+, \pi^+n + \pi^0p)$ may even decrease as the nuclear mass increases.

Chivers *et al.* also calculated the ratio

$$R'_\Delta \equiv \frac{\sigma(\pi^-, \pi^-n)}{\sigma(\pi^+, \pi^+n + \pi^0p)} \tag{1.16}$$

for the three targets, and found in all cases a value close to 1.0. From simple isospin arguments (cf. Sec. 1.1.2 and 1.1.3) one would expect $R'_\Delta = \frac{9}{1+2} = 3$. This discrepancy could not be explained, but it was interpreted as an indication that the reaction process must be more complicated than just simple quasi-free scattering only.[29,30] A better understanding of this ratio has been an important motivation for many later experiments and theoretical considerations.

Some other experimental techniques were employed in measurements around 1970. The first study of the reaction kinematics was presented by Aganyants *et al.*[31] in 1968. Using spark chambers, they measured the momentum of both the π^- and the proton in the reaction $^{12}C(\pi^-, \pi^-p)^{11}B$ at a beam kinetic energy of $T_{\pi^-} = 910$ MeV, that is, far above the $\Delta(1232)$-resonance. Shortly after this experiment, Gismatullin and Ostroumov[32] studied the (π^+, π^+p) process at $T_{\pi^+} = 117$ MeV using nuclear emulsions. This method "yields detailed information about all the charged particles and with good angular resolution",[32] but it does not allow a well-defined target; their results express the sum of scattering off all the light nuclei in the emulsion (C, O, and N). They include differential cross sections $(d\sigma/d\Omega)$ in the π^+p center-of-momentum system.

Bellotti *et al.*[33] published the first pure (π^+, π^0p) results obtained in the Δ-resonance region in 1973. They studied the $^{12}C(\pi^+, \pi^+p)^{11}B$ and $^{12}C(\pi^+, \pi^0p)^{11}C$ reactions at $T_{\pi^+} = 160$ MeV by means of a propane bubble chamber. In the (π^+, π^+p) analysis the events were completely reconstructed kinematically. The resulting missing energy (the difference between incident kinetic energy and the sum of the energies of the outgoing π^+ and proton) is shown in Fig. 1.5a. We can identify protons removed from each of

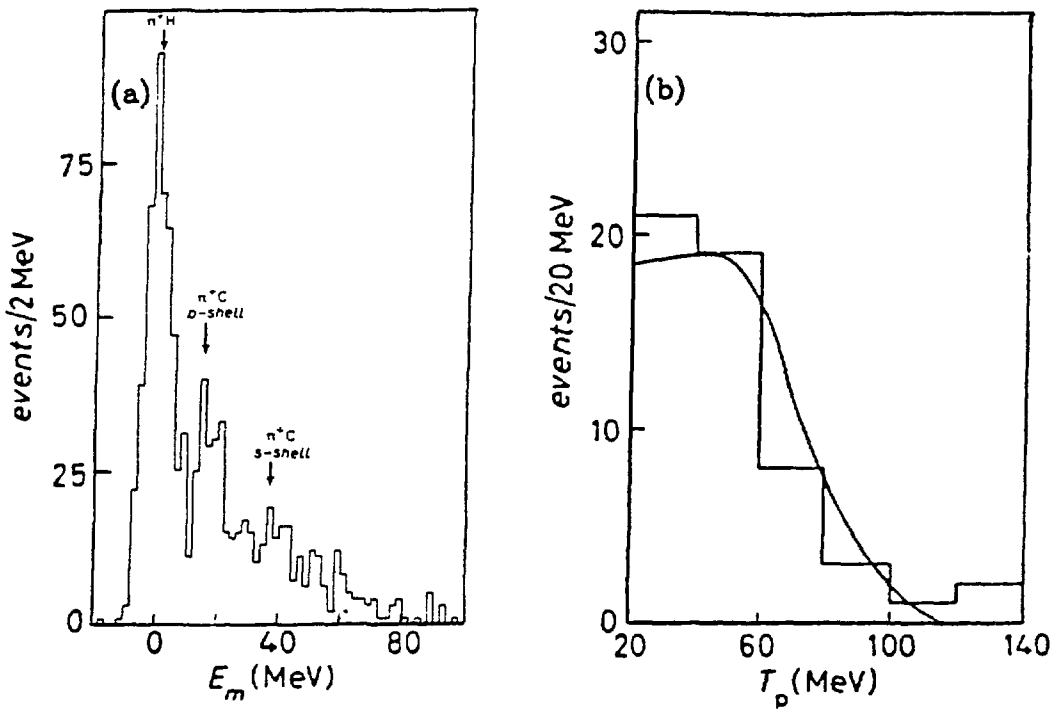

Figure 1.5. Results from Bellotti *et al.* for ^{12}C at 160 MeV. (a) shows the missing energy $(T_{\pi+} - T_{\pi+'} - T_p)$ for $^{12}C(\pi^+, \pi^{+'}p)^{11}B$. p-shell and s-shell events can be identified. The peak at zero is from scattering off the hydrogen in the propane bubble chamber. (b) shows the distribution of the kinetic energy of the ejected proton in $^{12}C(\pi^+, \pi^0 p)^{11}C$. This is the first pure study of the $(\pi^+, \pi^0 p)$ reaction in the Δ-resonance region. The graphs are from Ref. 33.

the two nuclear shells (1p and 1s). The energy resolution is approximately 10 MeV (FWHM). Bellotti *et al.* quote the ratio between the number of p-shell and s-shell events to be 1.5 ± 0.2 (^{12}C has four p-shell and two s-shell protons), and they estimate the total $^{12}C(\pi^+, \pi^+ p)^{11}B$ cross section to be (66 ± 10) mb, which is in agreement with the $^{12}C(\pi^-, \pi^- n)^{11}C$ cross section mentioned above from the measurements of Reeder and Markowitz[26]. The π^0 decay photons from the charge exchange events were detected by their creation of electron-positron pairs in the bubble chamber. However, since the radiation length of propane is rather large (around 110 cm), only a few two-photon events were detected, and a full kinematical analysis could not be done. The energy distribution of the ejected proton from the $(\pi^+, \pi^0 p)$ reaction is shown in Fig. 1.5b. The total $^{12}C(\pi^+, \pi^0 p)^{11}C$ cross section was measured to be $(18 \pm$

3) mb, which appears somewhat low compared to the result of Chivers *et al.*[29] The latter measurement was made a little closer to the peak of the Δ-resonance, however, and it included a contribution from the $(\pi^+, \pi^+ n)$ process, which from simple isospin arguments (Secs. 1.1.2 and 1.1.3) can be assumed to contribute about half as much as the $(\pi^+, \pi^0 p)$ process.

The method of nuclear activity measurements to determine excitation functions has also been used with the intense pion beams of the meson factories. The main improvement from the earlier measurements is the improved statistical accuracy associated with the higher pion fluxes. As an example we mention a thorough study of the $^{12}C(\pi^{\pm}, \pi N)^{11}C$ cross sections between 40 MeV and 600 MeV performed by Dropesky *et al.*[34] in the mid to late 1970's. These cross section values form the basis for the absolute calibration of the pion beam fluxes in our experiment (we will return to this in the chapter on Preparatory Analysis). For $^{12}C(\pi^-, \pi^- n)^{11}C$ at 180 MeV Dropesky *et al.* determined the cross section to be (70.0 ± 2.0) mb, which is in good agreement with the result (68 ± 6) mb of Reeder and Markowitz.[26] For $^{12}C(\pi^+, \pi^+ n + \pi^0 p)^{11}C$ at the same energy, Dropesky *et al.* measured (44.0 ± 1.5) mb. This is in rather poor agreement with the value (75 ± 4) mb determined by Chivers *et al.*,[29] and Dropesky *et al.* assumed the discrepancy to be a result of an underestimated proton contamination of the π^+ beam used by Chivers *et al.* Both collaborations agree on the π^- measurements, however, so the cross section ratios R'_Δ must differ. Dropesky *et al.* obtained the value $R'_\Delta = 1.59 \pm 0.07$ at 180 MeV, still lower than theoretical estimates assuming a mainly quasi-free model of the reaction mechanism.

Experiments relying on nuclear activity measurements always contain ambiguities as to which processes and final states one is truly observing. Morris *et al.*[35] avoided the latter uncertainty in their 1977 results. While all previous activity measurements had included several low-lying states of the residual nuclei, Morris *et al.* chose target nuclei (^{7}Li, ^{9}Be, ^{12}C, ^{13}C, and ^{16}O) such that specific states in the residual nuclei could be sorted out by detecting decay γ-rays. Two states in ^{6}Li and two states in ^{12}C were investigated with both π^+ and π^-. R'_Δ was calculated separately for each of these states (at beam energies near 180 MeV) yielding values from 0.85 ± 0.10 to 2.0 ± 0.2. Attempting to explain these values, Morris *et al.* discuss some possible reaction mechanisms based on quasi-free interactions, but they are all eventually rejected. The

cross section ratios obtained from this and other activity measurements remained unexplained by theory.

A new category of experiments was started in the late 1970's: true coincidence measurements with proper identification of both ejected particles. One could then distinguish between the $(\pi^+, \pi^+ n)$ and $(\pi^+, \pi^0 p)$ processes. This, in combination with good resolution particle detectors, makes possible well-defined measurements of the ratio R_Δ^{+-}, which from the simple isospin coupling arguments are expected to be 9 (cf. Eq. (1.7)).

The first measurements of this kind were reported by Swenson *et al.*[36] in 1978. The beam energy was 255 MeV, and both the pion and proton detectors (two telescope arms consisting of several plastic scintillators and, for the proton arm, delay-line wire chambers) were positioned at forward angles. At this energy the ratio between the free cross sections[14–16] is about 7.7, while Swenson *et al.* measured ratios (between differential cross sections) of 7.0 ± 0.7 for ^{27}Al and only 4.5 ± 0.5 for ^{208}Pb. Ziock *et al.*[37] performed a similar experiment on ^{12}C at 180 MeV. They centered the pion arm (a magnetic spectrometer) at 100° and 110° and the proton arm (a four-element Si-Ge telescope) at 30° (on the opposite side of the beam) and found $R_\Delta^{+-} = 5.5 \pm 1.0$ and $R_\Delta^{+-} = 5.2 \pm 0.5$, respectively. However, these ratios were strongly dependent on the excitation energy of the residual nucleus (the above values are averages); for low excitation energies (below 9.75 MeV) the ratios were around 14, and for high energies (above 9.75 MeV) they were about 3.

In a survey experiment involving good angular resolution and rather poor energy resolution, Piasetzky *et al.*[20] obtained results for the $(\pi^+, \pi^+ p)$ and $(\pi^-, \pi^- p)$ reactions on ^{12}C, ^{56}Fe, and ^{209}Bi at 245 MeV. The pions were detected in three plastic-scintillator telescopes (10° apart) positioned to cover scattering angles from 70° to 140°. The coincident nucleons were detected by a total of 20 plastic scintillators arranged in two layers and covering an angular range of approximately ±50° in the horizontal (scattering) plane and ±20° in the vertical plane. During the measurements, the array was centered around the angle corresponding to free π–N scattering. Piasetzky *et al.* found that the angular distribution of their data could be fitted by a sum of two gaussians: one narrow gaussian (about 30° FWHM) corresponding to the quasi-free nucleon removal process and one broad gaussian presumably representing the effects

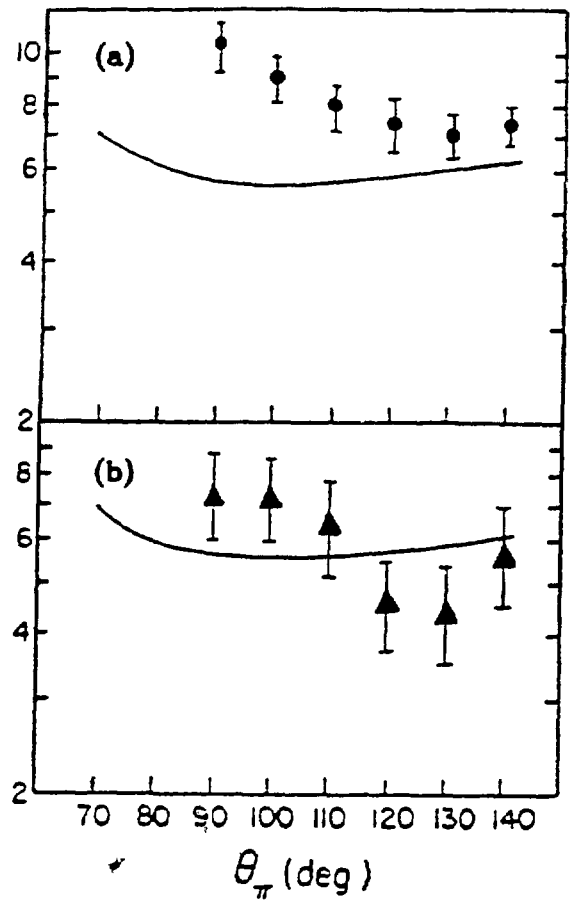

Figure 1.6. The ratio R_Δ^{+-} for ^{12}C at 245 MeV. The results are from Piasetzky *et al.*[20], and only the quasi-free part of the $(\pi^\pm, \pi^\pm p)$ cross sections is included. (a) shows the ratios between the peak values of the $d^2\sigma/d\Omega_\pi\, d\Omega_p$ cross sections, while (b) presents ratios taken after integration over all proton angles, that is, between $d\sigma/d\Omega_\pi$ for the two reactions. The solid curve in both cases is the ratio between the free π^+p and π^-p cross sections.

of pion multiple scattering and nucleon final state interactions. This allowed observation of the pure, direct quasi-free process. They concluded that this process is most pronounced in light nuclei and at backward pion scattering angles. Comparison to inclusive (π, π') cross sections indicated that approximately 30%, 20%, and 15% of the inclusive, inelastic scattering cross sections for C, Fe, and Bi, respectively, are accounted for by the quasi-free nucleon removal process. The integrated cross sections $d\sigma/d\Omega_\pi$ for (π^+, π^+p) were found to increase with A more slowly than inclusive (π, π') cross sections. No (π^-, π^-p) measurements were made on Fe and Bi. The results

for the ratio R_{Δ}^{+-} (for the quasi-free part of the cross sections) for ^{12}C are shown in Fig. 1.6. We note that the agreement with the ratio between the free cross sections now is good at the level of $d\sigma/d\Omega_{\pi}$. However, we still see significant deviations when the ratios are calculated between the peak values of the $d^2\sigma/d\Omega_{\pi}\, d\Omega_p$ cross sections.

In a similar experiment at 165 MeV (using the same apparatus and targets), Piasetzky *et al.*[38] studied the (π^+,π^+p) and (π^-,π^-n) reactions at backward pion angles (120°, 130°, and 140°). The general features of their results are similar to what was found earlier at 245 MeV. However, while the (π^+,π^+p) cross section was increasing slowly with A at 245 MeV, it was found to be approximately constant or possibly slowly decreasing at the lower energy. At 165 MeV the quasi-free nucleon removal process was accounting for 30%, 15%, and 8% of the inclusive, inelastic cross sections for C, Fe, and Bi, respectively (when averaged over the three pion angles). A comparison of the cross sections of the (π^+,π^+p) and (π^-,π^-n) reactions, which from the isospin symmetry should be equal, shows that while they are roughly the same for ^{12}C, π^- scattering off neutrons is increasingly dominating for the heavier nuclei; if the (π^-,π^-n) to (π^+,π^+p) cross section ratio is normalized to 1 for C, it becomes 1.5 for Fe and 3.3 for Bi. This is probably caused by different neutron and proton distributions at the surface of these nuclei (pions mainly probe the nuclear surface, cf. Sec. 1.1.2). Similar effects can also be seen in a comparison of (π^+,π^+p), (π^-,π^-p). and (π^-,π^-n) on ^{16}O and ^{18}O by the same collaboration.[39] The two isotopes were studied in the form of water and liquid $H_2{}^{18}O$, respectively.

Another set of measurements of the $(\pi^{\pm},\pi^{\pm}p)$ reactions on ^{16}O from water targets has been made by Kyle *et al.* This was done at two beam energies: 240 MeV[40] and 163 MeV.[41] The pions were detected in a magnetic spectrometer and the protons in three plastic-scintillator telescopes positioned near the conjugate proton angle for free πp scattering. The proton array spanned approximately 50° both horizontally and vertically. Some of the resulting excitation energy spectra at 240 MeV are shown in Fig. 1.7a. We note the improved resolution compared to the earlier ^{12}C results of Bellotti *et al.* (cf. Fig. 1.5). Kyle *et al.* can identify the two p-shell levels in oxygen ($1p_{\frac{1}{2}}$ and $1p_{\frac{3}{2}}$). The ratio of the areas of the two peaks appears to reflect fairly well the number of protons in each level (two and four, respectively). Fig. 1.7b show ratios R_{Δ}^{+-} for differential cross sections $d^3\sigma/dE_{\pi}\, d\Omega_{\pi}\, d\Omega_p$ for events where the residual ^{15}N

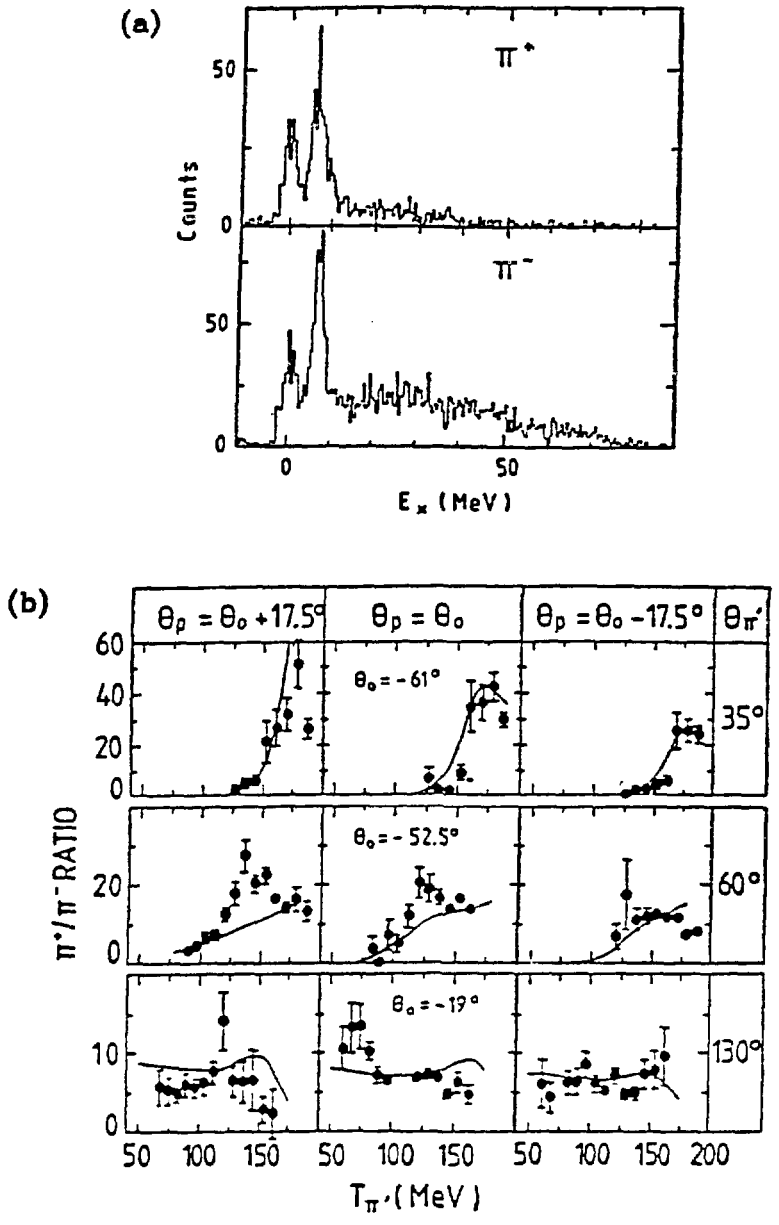

Figure 1.7. Results from Kyle *et al.* for ^{16}O at 240 MeV. (a) shows excitation energy spectra for the residual ^{15}N nucleus in $^{16}O(\pi^{\pm},\pi^{\pm}p)^{15}N$. The ground state (removal of a $p_{\frac{1}{2}}$ proton) and the $p_{\frac{3}{2}}$ hole state are identified as the two prominent peaks at zero and at approximately 6.5 MeV. The spectra were obtained with $\theta_\pi = 60°$ and $\theta_p = 35°$. (b) shows cross section ratios R_Δ^{+-} between differential cross sections $d^3\sigma/dE_\pi\, d\Omega_\pi\, d\Omega_p$ for $p_{\frac{1}{2}}$ proton removal. The three proton angles given for each pion angle correspond to the center of the three proton telescopes used. Both illustrations are from Ref. 40.

was left in its ground state ($1p_{\frac{1}{2}}$ proton removal). For the forward pion angles there are quite dramatic deviations from the free ratio of approximately 9. We also note that the new ratios depend rather strongly on the energy of the scattered pion.

Particularly striking about the measurements of Kyle *et al.* was that they detected ratios significantly *larger* than the ratio of the free cross sections (up to several times this value, cf. Eq. (1.7) and Fig. 1.7b). This excludes explanations based on initial state interactions (pion SCX) or finial state interactions (nucleon SCX) because these will tend to *decrease* the value of R_{Δ}^{+-}:

(a) The free $\pi^+ p$ cross section is essentially geometrical (cf. Sec. 1.1.2), so it cannot be increased very much by additional mechanisms inside the nucleus. Modifications of this cross section can therefore only contribute to a decrease of R_{Δ}^{+-}.

(b) All pion SCX events ($\pi^- + p \rightarrow \pi^0 + n$) are lost to the free cross section, but inside the nucleus the π^0 can go on to another SCX process with a neutron (the inverse of the first SCX) and thereby increase the nuclear $\pi^- p$ cross section above the free one. This will reduce the value of R_{Δ}^{+-}.

(c) In the nucleus there will be many $\pi^- n$ interactions. Applying charge symmetry to Eq. (1.7) indicates that this happens nine times as often (modified by the ratio of neutrons to protons) as the $\pi^- p$ interaction that we are studying. Occasionally the scattered neutron will interact with a proton through $p(n,p)n$, and this will again lead to an increased nuclear $\pi^- p$ cross section relative to the free one. This process will therefore also reduce R_{Δ}^{+-}.

The experiment of Kyle *et al.* therefore indicated a need to include new physical arguments in the discussion. The solid curves in Fig. 1.7b are a response to this. They show calculations done in the framework of the Δ–hole model (which we will elaborate more on in the theory section below). Kyle *et al.* conclude that their ratios must be a clear manifestation of Δ–nucleus interactions.

Faucett *et al.*[42] have complemented the work of Piasetzky *et al.*[20] by detailed and kinematically complete measurements of the $^{12}C(\pi^{\pm}, \pi^{\pm}p)$ reactions at $T_{\pi} = 220$ MeV. They used a magnetic spectrometer for pion detection and four plastic-scintillator telescopes for proton detection. Their results confirm the quasi-free picture of the $(\pi, \pi' N)$ reactions as established by Piasetzky *et al.*

For completeness, the paper by Gilad *et al.*[43] on the $^{16}O(\pi^+, \pi^0 p)$ reaction at $T_{\pi^+} =$ 245 MeV should also be mentioned here. This work presents the first kinematically

complete coincidence measurements of the $(\pi^+, \pi^0 p)$ reaction. It was formally part of the same LAMPF experiment as the work described in this thesis, and the same apparatus (the LAMPF π^0 spectrometer and an array of eight plastic-scintillator proton telescopes) was used. The water targets were of the same design as those used by Kyle *et al.*,[40] and this experiment investigating the SCX channel was seen as an extension of their work. Because of its close connection to our own work, we will postpone the presentation of the results of Gilad *et al.* until the very last section of this chapter.

1.2.2 $(\pi^\pm, \pi^0)$ Measurements

Much work has been done over the years studying details particular to the various (π, π') reactions. These reactions have also been used as tools for investigating other nuclear physics questions. This subsection is limited to discussing the $(\pi^\pm, \pi^0)$ reactions, and only to the extent that the work is relevant to our measurements.

The first pion SCX measurements were presented by Fermi *et al.*[44] in 1952. By detection of the two π^0 decay photons from the neutral pion in the reaction $\pi^- + p \rightarrow \pi^0 + n$, they measured a cross section of (20 ± 5) mb for this process at $T_{\pi^-} = 118$ MeV. The first observations of the (π^+, π^0) process were reported by Roberts, Spry, and Tinlot at a conference later the same year.[45] The energy of the incident pions was $T_{\pi^+} = 34$ MeV. Only a few two-photon π^0 events were observed.

Before the construction of the LAMPF π^0 spectrometer, there appear to have been only two "modern" studies of pion SCX in nuclei in which the π^0's were detected directly by coincidence measurements of their two decay photons. The first, by Hilscher *et al.*[46] in 1970, was a measurement of (π^-, π^0) on ^{12}C, ^{27}Al, ^{63}Cu, and ^{208}Pb at $T_{\pi^0} = 70$ MeV. The second experiment was a study several years later by Bowles *et al.*[47] of $(\pi^\pm, \pi^0)$ on ^{9}Be, ^{12}C, ^{16}O, ^{58}Ni, and ^{208}Pb at 50 MeV and 100 MeV. Both experiments used one NaI detector and one Pb-glass detector to measure the energy of the two photons. Hilscher *et al.* measured total cross sections only, while Bowles *et al.* could move the detectors to correspond to different π^0 angles, and obtained angular resolution good enough to present differential cross sections $d^2\sigma/dE_{\pi^0}\, d\Omega_{\pi^0}$. Since the energy of the incident pions in both experiments was considerably lower than the 165 MeV used in our experiment, we will not be able to compare directly to the

results of these experiments. We note that Bowles *et al.* found their data qualitatively consistent with the picture of SCX reactions as mainly quasi-free interactions with a small component of multistep reactions. They observed the A-dependence of their (π^+,π^0) measurements to be approximately $A^{-0.4}$ when scaling cross section per neutron (approximately equivalent to $A^{0.6}$ for the nuclear cross sections). Hilscher *et al.* present their (π^-,π^0) results similarly as cross section per proton. This appears to fall off faster than the above $A^{-0.4}$.

The only existing pion SCX measurements directly comparable to our own were made by Ashery *et al.*[48,22] They used the LAMPF π^0 spectrometer and investigated the (π^+,π^0) and/or (π^-,π^0) reactions on ^{12}C, ^{14}C, ^{16}O, ^{18}O, ^{58}Ni, ^{120}Sn, and ^{208}Pb at 160 MeV. Only a few of their setups (almost) coincide with ours, and the measured energy spectra of the cross sections $d^2\sigma/dE_{\pi^0}\,d\Omega_{\pi^0}$ for these cases are shown in Fig. 1.8a. Fig. 1.8b shows the angular distribution of $d\sigma/d\Omega_{\pi^0}$ (after integration over all π^0 energies) for ^{16}O(π^+,π^0). The curve is the free SCX cross section normalized to the data at back angles. We see from this comparison that the quasi-free description does not provide a good qualitative explanation of the process at more forward angles. Ashery *et al.* observed an A-dependence of $A^{0.48}$ for the (π^+,π^0) cross sections. The large uncertainties taken into account, this is still in fair agreement with the value $A^{0.6}$ found by Bowles *et al.*

1.3 Theoretical Calculations (The Δ–hole Model)

Reactions involving hadrons in the nucleus are well known to be difficult to describe quantitatively. There are too many particles involved to permit an exact description of the dynamics in single-particle coordinates, and there are too few particles to permit use of statistical-mechanics tools. This also makes it difficult to extract information that may lead to better descriptions from the experimental data available, even though most experiments are designed such that as few parameters as possible influence the results (for example, by scattering to known states, quasi-free measurements, single particle removal, *etc.*).

The isospin conservation arguments leading to Eqs. (1.7) and (1.15) were applied immediately at the discovery of the Δ-resonance.[18] In Sec. 1.2.1 we reviewed some

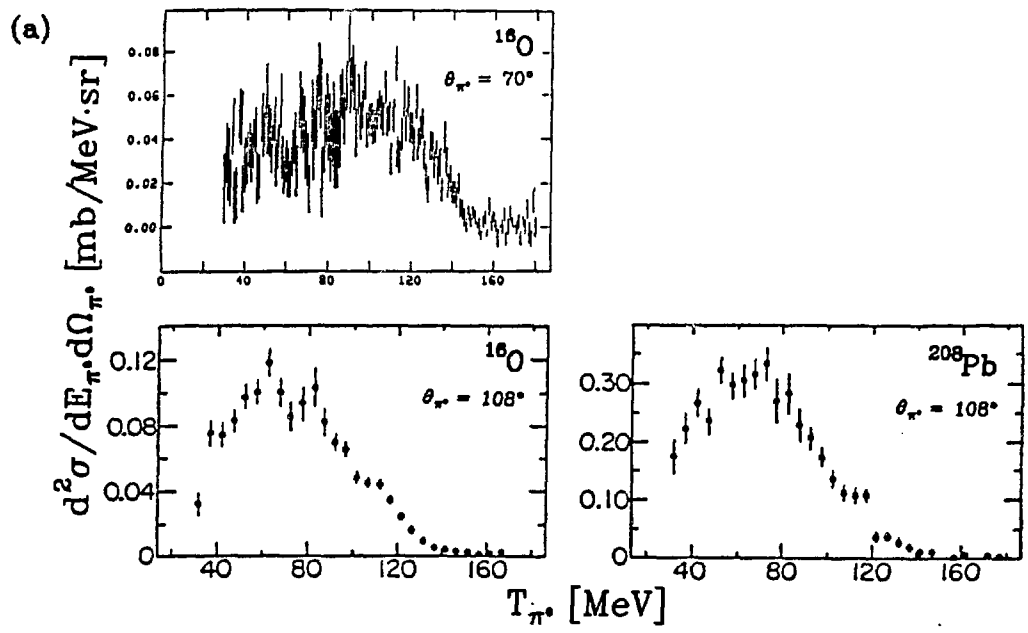

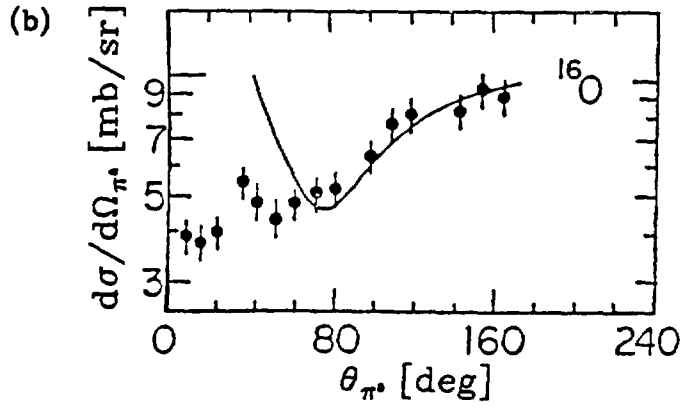

Figure 1.3. Results from Ashery *et al.* at 160 MeV. (a) shows cross sections $d^2\sigma/dE_{\pi^0}\,d\Omega_{\pi^0}$ as a function of the π^0 energy for the (π^+, π^0) reaction. The $\theta_{\pi^0} = 70°$ spectrum is from Ref. 49, and the spectra for $\theta_{\pi^0} = 108°$ are from Ref. 22. (b) shows integrated cross sections $d\sigma/d\Omega_{\pi^0}$ for ^{16}O as a function of θ_{π^0}. The solid curve is the free pion SCX cross section normalized to the measured cross sections at back angles. The normalization factor is 2.0. The illustration is from Ref. 22. All angles are laboratory angles.

of the discussions (and confusion) about these cross section ratios over the years. Many reaction mechanisms have been proposed within the framework of the impulse approximation to explain the observed ratios and cross sections; for details, see Ref. 50 and references therein. The most successful theoretical calculations today are based on the Δ–hole model, which was introduced by Kisslinger and Wang[51] in 1973. Their initial approach has since been further expanded on by a number of other researchers (see Ref. 52 and references therein).

The Δ–hole model, as applied today, involves a combination of microscopic and phenomenological tools. The Δ is treated as an explicit degree of freedom and is allowed to propagate within the nuclear medium. It faces competition between decay, absorption ($\Delta N \rightarrow NN$), and Δ–N scattering. The modern, full Δ–hole model approach, as well as that of the simpler version known as "modified DWIA", is outlined in some detail below. Our presentation is strongly influenced by a recent article by Takaki and Thies.[52]

The Δ–hole model has so far been able to treat elastic pion–nucleus scattering (in the one particle–one hole space) without unjustified technical approximations. More complicated channels (many particle–many hole) have been treated phenomenologically by adding a "spreading potential" to the Δ self-energy. This includes pion absorption which is known to be important in nuclei.[53] Recently, attempts have been made to go beyond this description by explicitly adding reaction mechanisms that cannot be included in the spreading potential. This was triggered by the experimental measurements of cross sections ratios discussed earlier (cf. Sec. 1.2.1). Deviations from the free cross section ratios for $T = 0$ nuclei (for example ^{12}C and ^{16}O) indicate that there must be some reaction mechanism(s) not accounted for by distorted wave impulse approximation (DWIA) calculations irrespective of the details of the Δ–nucleus potential.[52] In the first attempts along these lines, Hirata, Lenz, and Thies[54] pointed out that in a strong potential the Δ may excite the nucleus through a Δ–N collision. By analogy with the $\pi^+ d \rightarrow pp$ reaction, they assumed this Δ–N interaction to be dominated by the $^5S_2(T_{\Delta N} = 1)$ channel. This work forms the basis for the quantitative $(\pi, \pi' N)$ cross section calculations done by Takaki and Thies.[52]

The mathematical framework is developed by modifying the isobar model for free π–N

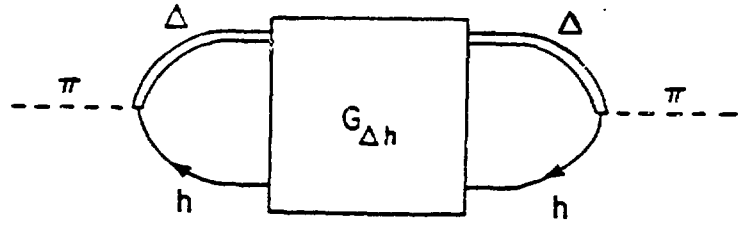

Figure 1.9. The elastic pion–nucleus amplitude in the Δ–hole model. The figure is from Ref. 52.

scattering, in which the scattering amplitude is given as

$$t_{\pi N} = F \frac{1}{D(E)} F^{\dagger}, \tag{1.17}$$

where the F's are vertex functions for the $\pi\Delta N$ coupling, and $D(E)$ represents the inverse Δ propagator in free space. E is the total energy of the π–N system in the center-of-momentum (c.m.) frame. All quantities can be determined from the π–N phase shift in the $P33$ channel.

The amplitude in Eq. (1.17) is defined in the π–N c.m. frame. In the nuclear medium we have instead

$$T_{\pi A} = \sum_{i=1}^{A} F_i \frac{1}{D(E - T_{\Delta})} F_i^{\dagger}. \tag{1.18}$$

The sum is over all nucleons. T_{Δ} is the kinetic energy of the Δ (Fermi motion), and $E - T_{\Delta}$ is the total πN c.m. energy. To include all medium effects of the Δ in the nucleus, we exchange the free space Δ propagator with a general Δ–hole propagator $G_{\Delta h}$. Assuming the same general form as before, but allowing all nucleons to take part in the scattering, we then have

$$T_{\pi A} = \sum_{ij} F_i G_{\Delta h} F_j^{\dagger}. \tag{1.19}$$

This is sketched in Fig. 1.9.

The Δ–hole propagator $G_{\Delta h}$ is considered in the Δ–nucleus space. The explicit form of this operator is derived by starting with the free Δ propagator and adding medium

corrections to this propagator step by step. Traditionally, the full Δ–hole propagator in the Δ–hole model is written as

$$G_{\Delta h}^{-1} = D(E - H_\Delta) - W_p - W_\pi - V_{sp}\,. \tag{1.20}$$

H_Δ accounts for the Fermi motion, the shell model potential V_B, and the hole energy H_{A-1}:

$$H_\Delta = T_\Delta + V_B + H_{A-1}\,. \tag{1.21}$$

The remaining terms in the Δ–hole propagator of Eq. (1.20) are additions to the free propagator. W_p is called the "Fock term". The free Δ propagator allows the Δ to decay into Pauli-violating states. The Fock term subtracts this contribution:

$$W_p = -\sum_i F_i^\dagger G_\pi P_V F_i\,, \tag{1.22}$$

where G_π is the free pion Green's function and P_V is the projection operator onto Pauli-violating states. W_π accounts for coherent multiple scattering of the pion, which is very important in the Δ-resonance region. This rescattering operator corresponds to one-pion exchange. It is included as a Δ–hole interaction:

$$W_\pi = \sum_{i \neq j} F_i^\dagger G_\pi P_0 F_j\,, \tag{1.23}$$

where P_0 is the projection operator onto the nuclear ground state. The last term, the spreading potential V_{sp}, is the only term involving phenomenological parameters. It accounts for the coupling to many particle–many hole states. It has been proven very important; without it, the calculated pion–nucleus scattering cross sections become significantly overestimated. It contains two complex strength parameters: one for a nuclear density term and one for a spin-orbit term. The imaginary components turn out to be large. This may be a manifestation of a strong coupling to the pion absorption channel.

The next level of sophistication is to attempt to describe the spreading potential in a manner that better reflects its physical origin. This is the Δ–N interaction of Hirata,

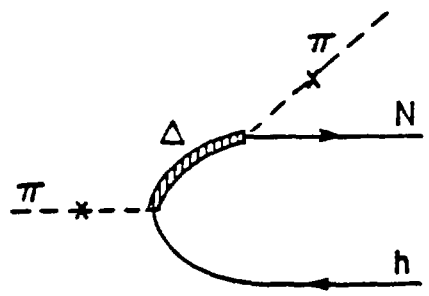

Figure 1.10. Diagram for modified DWIA. The crosses indicate distorted pion wave functions, and the hatching indicate the Δ–hole propagator. Self-energies are inserted into each particle line. The figure is from Ref. 52.

Lenz, and Thies.[54] They assume the spreading potential to arise from an effective two-body Δ–N interaction $\tilde{t}_{\Delta N}$. The general Δ–N interaction $\tau_{\Delta N}$ is then defined as

$$\tau_{\Delta N} = W_\pi + \tilde{t}_{\Delta N} \tag{1.24}$$

$$= v_{\Delta N} + v_{\Delta N} G Q \tau_{\Delta N} \tag{1.25}$$

In Eq. (1.25), G is the free Δ–N Green's function, and Q is the projection operator onto the many particle–many hole states ("Q space"). The terms in Eq. (1.24) correspond to the second-order processes shown earlier in Fig. 1.3, and the potential $v_{\Delta N}$ includes both one-pion-exchange and pion absorption. Eq. (1.25) leads to the modern form of the Δ–hole propagator. It consists of a one-body operator $D(E - H_\Delta) - W_p$ and a two-body operator $\tau_{\Delta N}$:

$$G^{-1}_{\Delta h} = D(E - H_\Delta) - W_p - \tau_{\Delta N} \,. \tag{1.26}$$

Let us now go back to the elementary π–N interaction as shown in Fig. 1.2. The matrix element for such a first-order transition between the ground state $|0\rangle$ and a particle-hole state $|ph\rangle$ is illustrated in Fig. 1.10. Self-energies are inserted into each particle line. This is known as "modified DWIA". One uses a distorted pion wave function calculated within the Δ–hole model and a proton wave function calculated from a phenomenological optical potential. The Δ–hole propagator used is

$$\hat{G}^{-1}_{\Delta h} = D(E - H_\Delta) - W_p - \tilde{t}_{\Delta N} \,. \tag{1.27}$$

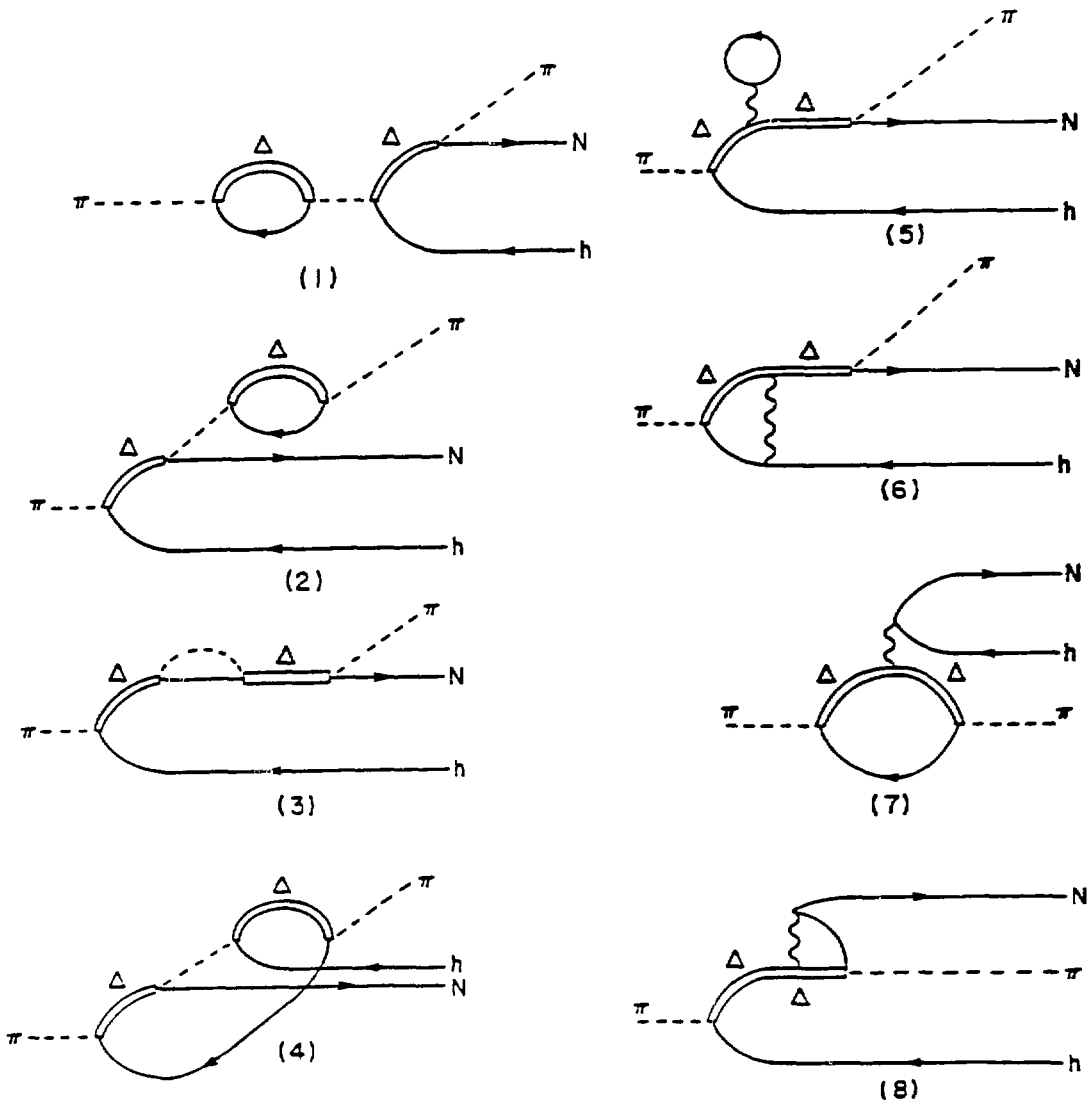

Figure 1.11. Diagrams for second order processes in the framework of the Δ–hole model. These processes are induced by one-pion-exchange $(1-4)$ or the effective Δ–N interaction $(5-8)$. The figure is from Ref. 52.

The self-energies of pion and Δ are determined from elastic scattering. Except for this use of elastic scattering results and the phenomenological optical potential mentioned above, there are no free parameters in the modified DWIA approach. More details are given in Ref. 52.

The modified DWIA, which has been successful in reproducing (π, π') cross sections,[55]

does not do well with the cross section ratios R_Δ^{+-} and R_Δ^{+0}. They come out to be the same as for free π–N scattering,[52] so no new information is gained. It is therefore necessary to include second-order terms as indicated for the full Δ–hole model (cf. Eq. (1.24)). Nuclear transitions corresponding to the processes of Fig. 1.3 are shown in Fig. 1.11. Diagrams $(1-3)$, (5), and (6) correspond to self-energies of pion or delta and are hence already included in the modified DWIA. Takaki and Thies considered diagrams (7) ("direct term") and (8) ("exchange term") in their Δ–hole model calculations of the $(\pi, \pi' N)$ reactions. Diagram (4) has the same isospin structure as diagram (7) and is not included in their work.[52]

The relative importance of the possible Δ–N isospin channels is also discussed in Ref. 52. The isospin vectors of a Δ and a nucleon can couple to $T_{\Delta N} = 1$ or $T_{\Delta N} = 2$. Takaki and Thies show that the $T_{\Delta N} = 2$ channel affects all $(\pi, \pi' N)$ cross sections with the same factor. Deviations from the free isospin ratios can therefore only be generated through the $T_{\Delta N} = 1$ channel, so they limited their calculations to this channel only. (Note that also the $T_{\Delta N} = 2$ channel may lead to deviations from the free ratio, but only in the presence of a $T_{\Delta N} = 1$ component.) The $T_{\Delta N} = 1$ channel is generally assumed to be the dominating channel.[52] Because of this dominance of the ${}^5S_2(T_{\Delta N} = 1)$ channel, Takaki and Thies describe the effective Δ–N interaction by the zero-range expression

$$\tilde{t}_{\Delta N} = C_{21}\delta(\vec{r}_\Delta - \vec{r}_N) P_{S_{\Delta N}=2} P_{T_{\Delta N}=1}\,, \tag{1.28}$$

where $P_{S_{\Delta N}=2}$ and $P_{T_{\Delta N}=1}$ are spin and isospin projection operators, respectively.

As mentioned above, the spreading potential is believed to be closely related to pion absorption. Since this potential is represented by the two-body effective interaction $\tilde{t}_{\Delta N}$, we note that only two-nucleon absorption ($\Delta N \rightarrow NN$) is included in the calculations.

Takaki and Thies did modified DWIA calculations as well as Δ–hole model calculations with the direct and the exchange terms included. The reactions and the kinematics were chosen to match the experimental data of Kyle *et al.*[40] and Gilad *et al.*[43] The technical details of the calculations are given in Ref. 52. The calculations included the non-resonant π–N interaction and the π and Δ Coulomb interaction in the pion wave

functions and the transition operator (in addition to the resonant term). Harmonic oscillator wave functions were used for the bound nucleons, and the spectroscopic factor N_α was assumed to be 1.0 (which means a pure single-particle transition).

We will only discuss the results which apply to the data of Kyle *et al.* here. The $^{16}O(\pi^+,\pi^0 p)$ results are deferred to the last section of this chapter where the measurements of Gilad *et al.* are presented. Takaki and Thies[52] found that the modified DWIA calculations generally describe the $(\pi^+,\pi^+ p)$ data for p-shell nucleon removal well. For larger excitation energies of the residual nucleus (the "continuum"), the agreement is rather poor (the calculations clearly underestimate the cross sections). Their calculations in this region only included s-shell removal, however, so this supports the view that other processes (namely, multi-particle emission) might be relatively more important there. In the $(\pi^-,\pi^- p)$ case the modified DWIA leads to more serious discrepancies between data and theory, and hence the ratios R_Δ^{+-} cannot be understood within the DWIA framework.

The inclusion of the Δ–N interaction is technically complicated. Takaki and Thies therefore restricted their calculations to a rather simple form of the interaction.[52] Some qualitative features were pointed out earlier by Hirata, Lenz, and Thies:[54] The Δ–N interaction (through the $^5S_2(T_{\Delta N}=1)$ channel) is most important for the $(\pi^-,\pi^- p)$ reaction. The effect on the $(\pi^+,\pi^+ p)$ reaction is only one ninth of this, and the effect on the charge exchange process $(\pi^+,\pi^0 p)$ is one third (but with opposite sign). The conclusions of Hirata, Lenz, and Thies were that $(\pi^+,\pi^+ p)$ is basically quasi-free, that for $(\pi^-,\pi^- p)$ the first- and second-order terms interfere destructively to reduce the estimated cross section, and that for $(\pi^+,\pi^0 p)$ one should expect an enhanced cross section estimate. Takaki and Thies[52] confirmed this in their calculations. The $(\pi^+,\pi^+ p)$ cross sections were left essentially unchanged, while the $(\pi^-,\pi^- p)$ cross sections were reduced. They also obtained a better qualitative description of the $(\pi^-,\pi^- p)$ data. However, being restricted to one fixed value (derived from the spreading potential) of the strength parameter C_{21} of Eq. (1.28) at all scattering angles, made it impossible to reproduce all cross section ratios correctly. Takaki and Thies point out that if one assumes that other effects besides two-body pion absorption are part of the spreading potential, then there is no reason to fix C_{21}. Indeed, by varying this parameter to fit the $(\pi^-,\pi^- p)$ data as well as the cross section ratio R_Δ^{+-} independently for each

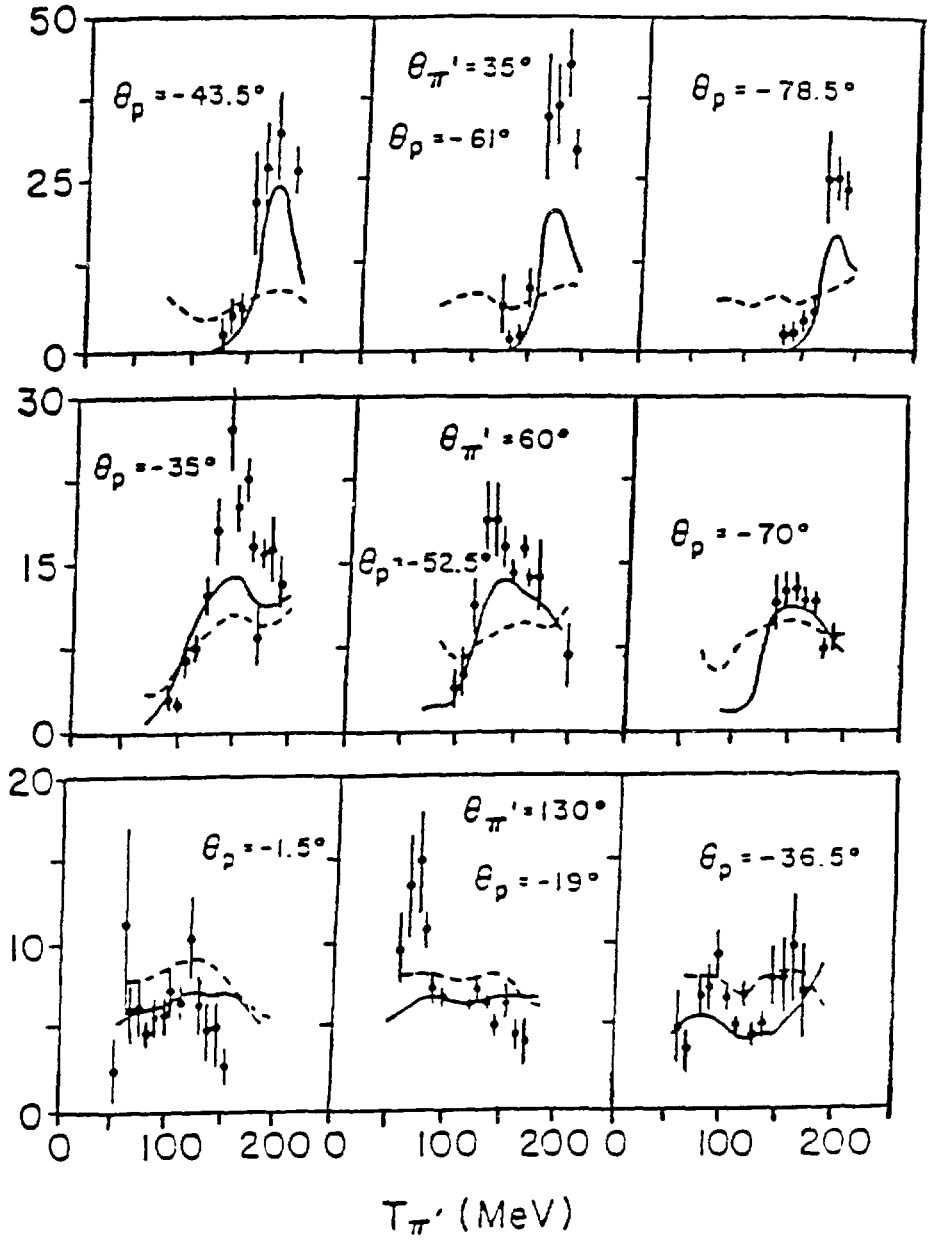

Figure 1.12. Δ–hole model ratios R_Δ^{+-} for $p_{\frac{1}{2}}$ proton removal on ^{16}O. The calculations were made for differential cross sections $d^3\sigma/dE_\pi\, d\Omega_\pi\, d\Omega_p$. The data are the same as those shown in Fig. 1.7b (there are small discrepancies because they result from an independent, and more preliminary, analysis[56]). The solid curves result from calculations including the Δ–N interaction; the dashed curves are from modified DWIA calculations. The figure is from Ref. 52.

scattering angle, they obtained a good qualitative description of the ratios. This is illustrated in Fig. 1.12 which shows R_{Δ}^{+-} both for the modified DWIA calculations and the calculations including the Δ–N interaction.

1.4 Our Experiment

After this review of previous experimental and theoretical work, the natural question to ask is: What should be the next step in the process of understanding the $(\pi, \pi' N)$ reactions? Before addressing this question, it may be useful to summarize where the earlier research (cf. Secs. 1.2 and 1.3) has brought us:

1. The $(\pi^{\pm}, \pi^{\pm} p)$ reactions, as well as the (π, π') reactions, are predominantly quasi-free in the Δ-resonance region.[20–22]
2. Survey measurements have shown that the ratios between integrated cross sections $d\sigma/d\Omega_{\pi}$ for the $(\pi^{+}, \pi^{+} p)$ and $(\pi^{-}, \pi^{-} p)$ reactions in the Δ-resonance region roughly agree with the ratios between the free $\pi^{+} p$ and $\pi^{-} p$ cross sections.[20]
3. On a more detailed level ($d^2\sigma/d\Omega_{\pi}\, d\Omega_{p}$ and $d^3\sigma/dE_{\pi}\, d\Omega_{\pi}\, d\Omega_{p}$), deviations from the free cross section ratios are sometimes very large, and the experimental ratios clearly depend on scattering angle and particle energy.[20,40]
4. The cross sections of the $(\pi^{\pm}, \pi^{\pm} p)$ reactions have been found to increase with A more slowly than those of the inclusive (π, π') reactions. The A-dependence of the (π^{+}, π^{0}) reaction is roughly $A^{0.5}$ at 160 MeV.[29,47,20,22]
5. First-order Δ–hole model calculations using a phenomenological "spreading potential" (modified DWIA) are in agreement with inclusive (π, π') data.[55,52]
6. The cross section ratios in (2.) cannot be understood theoretically within the framework of (modified) DWIA calculations.[52]
7. Δ–hole model calculations including second-order Δ–N interactions appear promising when compared to $(\pi^{\pm}, \pi^{\pm} p)$ measurements, but an understanding of the origin of the phenomenological parameters involved is still lacking. It is necessary to determine some of the parameter values by fitting to experimental data.[54,52]
8. Using the Δ–hole model parameters that were determined from the $(\pi^{\pm}, \pi^{\pm} p)$ experiments, one can make predictions for the single-charge-exchange reaction $(\pi^{+}, \pi^{0} p)$.[52]

The above list clearly indicates the desirability of obtaining $(\pi^{+}, \pi^{0} p)$ data. Kinematically complete measurements for this reaction are interesting in themselves (Is the

reaction quasi-free? What is the angular dependence? What is the A-dependence?) and also as a comparison to the $(\pi^{\pm},\pi^{\pm}p)$ data. Cross section ratios involving this reaction should reveal whether the general descriptions of $(\pi,\pi'N)$ reaction mechanisms are also valid for the SCX reaction. By comparison to the predictions of Takaki and Thies based on the Δ–hole model, one can provide a test of this model and hopefully extract more information about the relative importance of various reaction mechanisms and isospin channels.

A proposal to study the $^{16}O(\pi^{+},\pi^{0}p)$ reaction under conditions similar to those chosen by Kyle *et al.* for their measurements of the $^{16}O(\pi^{\pm},\pi^{\pm}p)$ reaction[40] was accepted at LAMPF. The experiment ran in two separate parts: one study at $T_{\pi^+} = 245$ MeV and one at $T_{\pi^+} = 165$ MeV. (Kyle *et al.* used 240 MeV and 163 MeV.) This work covers the full study at $T_{\pi^+} = 165$ MeV, which includes measurements of the $^{16}O(\pi^{+},\pi^{0}p)$ and $^{16}O(\pi^{+},\pi^{0})$ reactions at four π^0 angles from 70° to 130° as well as a study of the A-dependence of these reactions on four targets from oxygen to lead at $\theta_{\pi^0} = 110°$. The measurements at $T_{\pi^+} = 245$ MeV were made first, and a partial analysis of these data has been published by Gilad *et al.*[43] We end this chapter with a short review of their results. The $T_{\pi^+} = 165$ MeV data were taken before the published analysis of the $T_{\pi^+} = 245$ MeV data had been completed.

Gilad *et al.*[43] presented the first kinematically complete coincidence measurements of the $(\pi^{+},\pi^{0}p)$ reaction. These were obtained by use of the LAMPF π^0 spectrometer and an array of eight plastic-scintillator telescopes (the same apparatus that will be described in detail later in this work). All measurements were done on ^{16}O using water targets. Their partial analysis only includes data from two of these proton telescopes, both in the scattering plane: one at the conjugate free proton angle for $\pi^{+}+n \rightarrow \pi^{0}+p$, and one 17° further away from the beam. Two of the π^0 angles (60° and 130°) coincide with pion scattering angles used by Kyle *et al.*[40] For these angles Gilad *et al.* present cross section ratios R_{Δ}^{+0} (cf. Eq. (1.12)). These are ratios of differential cross sections $(d^3\sigma/dE_{\pi}\,d\Omega_{\pi}\,d\Omega_{p})$ of $^{16}O(\pi^{+},\pi^{+}p)$ to $^{16}O(\pi^{+},\pi^{0}p)$ for p-shell nucleon removal. The ratios are shown in Fig. 1.13. We note that at the forward π^0 angle R_{Δ}^{+0} is clearly smaller than the free ratio, in qualitative agreement with the predictions of the Δ–hole model (inclusion of the Δ–N interaction should increase the $(\pi^{+},\pi^{0}p)$ cross section estimates while not affecting the $(\pi^{+},\pi^{+}p)$ estimates very much[54]). At 130° the ratio

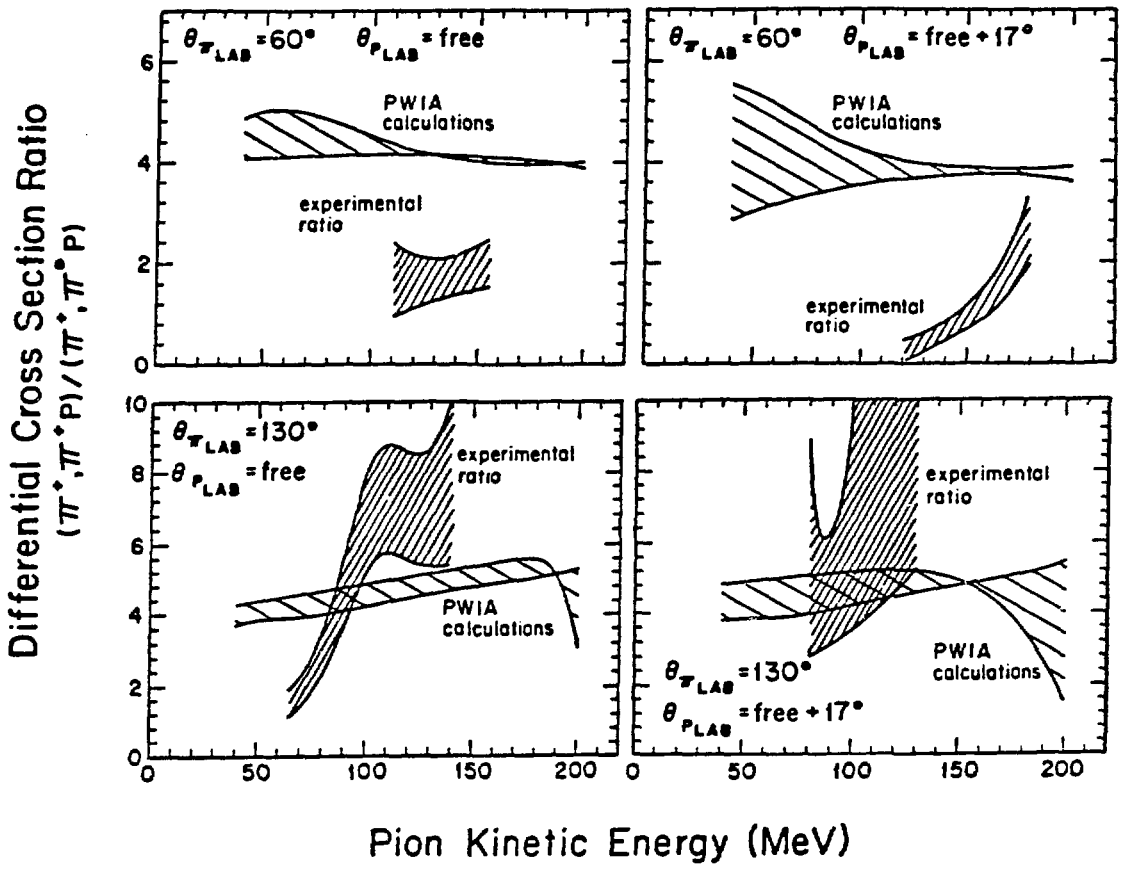

Figure 1.13. Cross-section ratios of $^{16}O(\pi^+,\pi^+p)$ to $^{16}O(\pi^+,\pi^0p)$. The (π^+,π^+p) measurements were made at 240 MeV at PSI (formerly SIN) while the (π^+,π^0p) measurements were made at 245 MeV at LAMPF. Only nucleon removal from the two p-shell levels is included in the cross sections. The column to the left is for protons ejected at the conjugate free angle, while the column to the right is for those hitting the proton telescope that was positioned 17° further away from the beam. The π^0 angle is indicated in each case. The figure is from Ref. 43.

is close to the free one, as was seen also in the measurements of Kyle *et al.* and the calculations of Takaki and Thies (cf. Fig. 1.12).

Fig. 1.14 shows the $d^3\sigma/dE_{\pi^0}\,d\Omega_{\pi^0}\,d\Omega_p$ cross section spectra obtained by Gilad *et al.* using the proton telescope at the conjugate free angle. Spectra for all π^0 angles are included. Also included for each spectrum are the results of the calculations of Takaki and Thies.[52] The calculations that include the Δ–N interaction were done

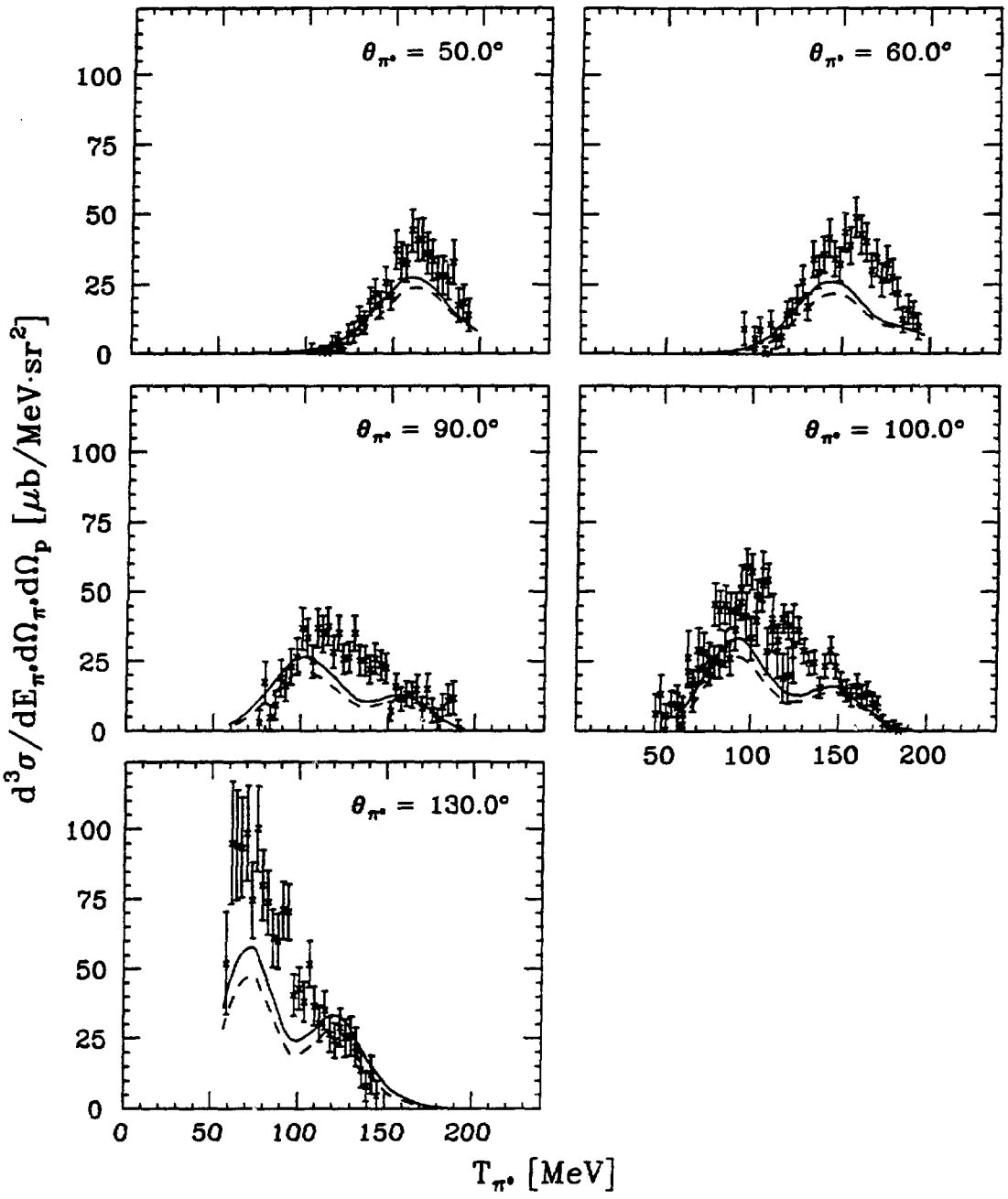

Figure 1.14. $d^3\sigma/dE_{\pi^0}\,d\Omega_{\pi^0}\,d\Omega_p$ at $T_{\pi^+} = 245$ MeV as a function of π^0energy. All π^0 angles investigated by Gilad *et al.* are shown. A normalization uncertainty of 18% is not included in the spectra. The dashed curves are from modified DWIA calculations, while the solid curves represent Δ–hole model calculations including the Δ–N interaction (cf. Ref. 52). The spectra are identical to those presented in Ref. 43.

with parameters determined from fitting the $(\pi^-, \pi^- p)$ data at $\theta_\pi = 35°$. We see that while these calculations change the cross section estimates from the modified DWIA in the right direction, the quantitative agreement between experiment and theory is still rather poor.

Chapter 2

Experimental Apparatus and Data Acquisition

The experimental work that forms the basis for this thesis took place at the Clinton P. Anderson Meson Physics Facility (LAMPF) in Los Alamos, New Mexico, in the fall of 1984. It was the second, and final, part of LAMPF experiment number 776 ("Study of the $^{16}O(\pi^+,\pi^0 p)$ Reaction"). In our work the reaction was studied at a pion beam energy of 165 MeV. The first part of experiment 776 took place in December 1983 – January 1984 and used a pion beam of 245 MeV.[43]

This chapter contains descriptions of the apparatus used: beams, targets, and particle detectors. Two main detector systems were used, the LAMPF π^0 spectrometer and an array of proton detectors. The latter was designed especially for experiment 776 and is described in detail. The last sections of this chapter are devoted to the data acquisition system, including electronics, triggers, and the data acquisition software.

2.1 Pion Beams

Fig. 2.1a shows an overview of LAMPF at the time of this experiment. The heart of the facility is a linear accelerator capable of delivering up to 1 mA (average) of protons

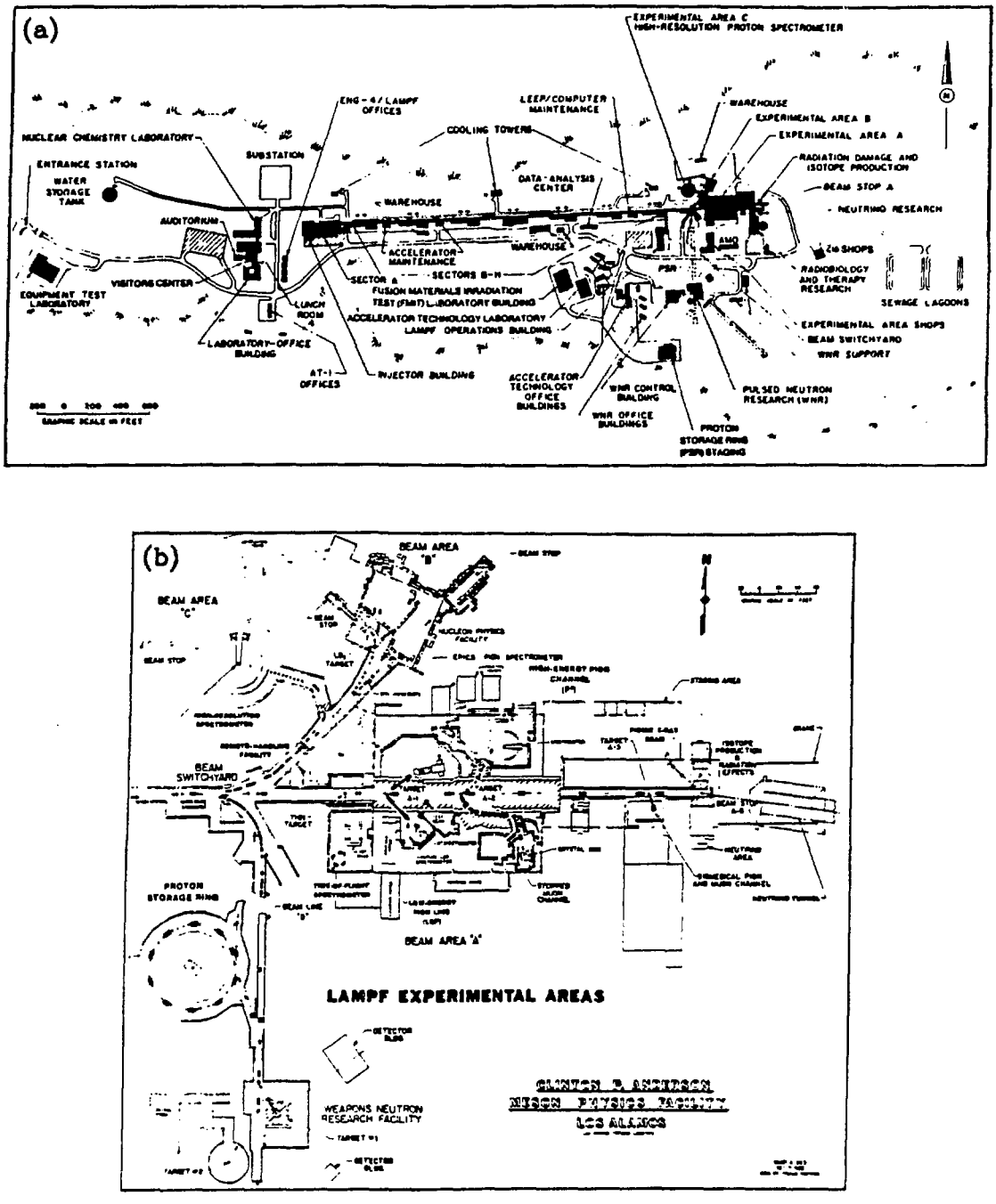

Figure 2.1. The Clinton P. Anderson Meson Physics Facility (LAMPF). (a) shows the layout of the complete facility as of October 1984, while (b) is a close-up of the experimental areas showing the various beam lines. Our experiment took place at the Low Energy Pion channel in Area A. Both sketches are from Ref. 57.

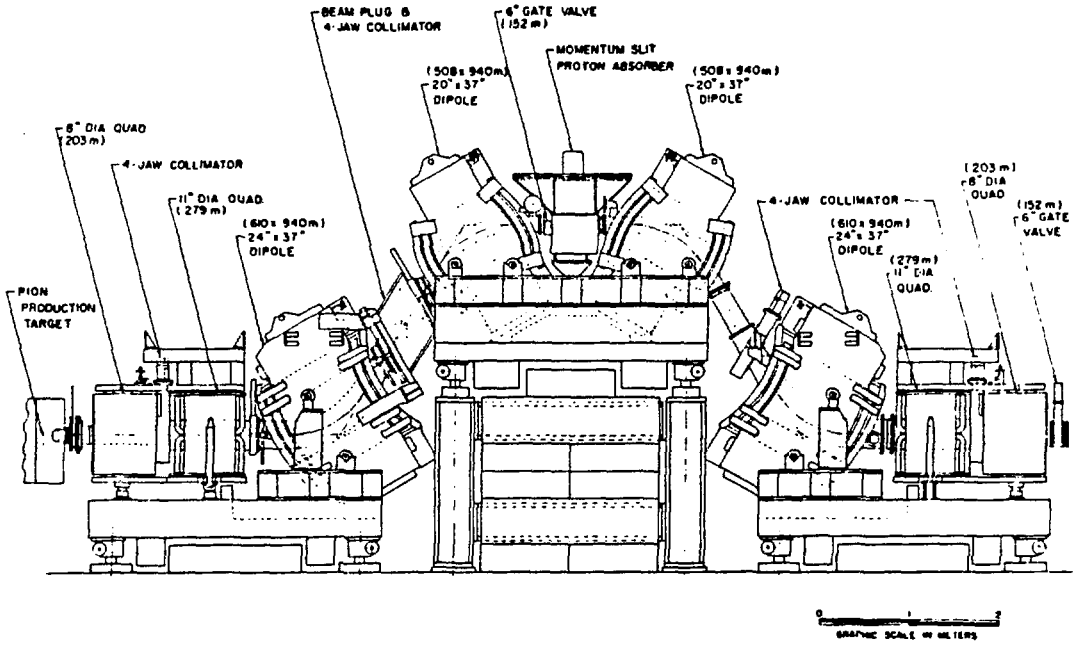

Figure 2.2. Side view of the Low Energy Pion channel. The illustration is from Ref. 58.

at up to 800 MeV kinetic energy. The beam is pulsed with 120 bursts per second. The duty factor of the beam can be varied. To optimize the signal-to-background ratio in a coincidence experiment it is desirable to have as large a duty factor as possible. (The rate of coincidence events is proportional to the average current, while the rate of background events in all detectors during a beam pulse is proportional to the square of the peak current.) The duty factor was set beyond our control. It was about 6.2% during most of the measurements, but it went as high as around 9.3% for part of the experiment. Fig. 2.1a indicates the various experimental areas at LAMPF. Some use the proton beam directly; others use secondary beams produced at several carbon targets in the main beam (see Fig. 2.1b). More details about LAMPF can be found in Ref. 57.

Our experiment took place at the Low Energy Pion channel (LEP) in Area A (cf. Refs. 57 and 58). The channel is designed with a short flight path to make it possible to utilize low energy pion beams (the range is approximately from 10 MeV to 300 MeV kinetic energy). The minimum channel length is 14 m from the A–1 production target

to the user's target. The length was 18 m in our experiment (at our main beam energy of 165 MeV about 70% of the initial pions would then decay before reaching the target). Fig. 2.2 gives a layout view of the LEP beam channel. It consists of two entrance and two exit quadrupole magnets and four bending (dipole) magnets. The bending takes place in a vertical plane, and each bend is 60° with a radius of curvature of 1 m. Beams of positive pions are contaminated by a large number of protons (about 5 protons per π^+ at 50 MeV (Ref. 57)). These protons have the same momentum as the beam pions. Their kinetic energy is therefore much lower than that of the pions. The protons can then be removed from the beam by inserting an absorber near the center of the channel (cf. Fig. 2.2). Going through the polyethylene absorber will affect the momentum of the protons more than that of the pions. LEP can be used for both positive and negative pion beams. Because of the lower cross section for production of negative pions, the flux of a negative pion beam will be about one quarter of the flux for the corresponding positive pion beam.[57] The momentum bite ($\frac{\Delta p}{p}$) can be adjusted by a momentum slit at the center of the channel. The smallest value one can achieve is about 0.05%. Our experiment did not require such high resolution, and we generally opened these momentum jaws to get as high a beam flux as the particle detectors could tolerate (typical values for $\frac{\Delta p}{p}$ were from 0.4% to 1.0%, corresponding to a flux of up to about $1 \cdot 10^7$ pions per second).

During data acquisition the beam flux was monitored by a toroid loop around the primary proton beam. This gives a measure of the total charge in this beam during a run, and it is therefore also a measure of the total amount of beam delivered in the secondary beam channels (assuming the secondary channel settings are not changed). Absolute calibration of the toroid readings was achieved by special "activation runs" that usually were performed twice every time the LEP beam channel was retuned (for a new energy). In such runs a thin plastic scintillator disc, with diameter large enough to include the full beam spot, is placed at the target position. Irradiating this disc causes production of ^{11}C nuclei by $^{12}\mathrm{C}(\pi^{\pm}, X)^{11}\mathrm{C}$, and by measuring the activity of the radioactive ^{11}C nuclei, one can determine the absolute flux of incident pions and hence obtain a calibration of the beam toroid. The discs were typically irradiated for 5 minutes. The method is described in detail in Appendix A.

We used a number of different beam tunes to acquire the data presented in this work.

The $(\pi^+, \pi^0 p)$ coincidence data were taken with 165 MeV π^+ beams of various momentum bites; in addition, measurements to determine the π^0 spectrometer conversion efficiency and the thickness of our targets were made with π^- beams at several energies between 77.0 MeV and 186.0 MeV.

2.2 Targets and Detectors

This section contains descriptions of all experimental apparatus inside the LEP "cave" (the area exposed to the beam), that is, the targets and the particle detectors. The last subsection discusses the assembly of these parts into the setups used for data acquisition.

2.2.1 Targets

A number of targets were used during the experiment. Oxygen for the study of the $^{16}O(\pi^+, \pi^0 p)$ reaction was provided by water targets of different thicknesses. Water targets were chosen because they are much easier to handle than targets made of liquid oxygen. Furthermore, the hydrogen "contamination" is of no concern to the $^{16}O(\pi^+, \pi^0 p)$ study since the $(\pi^+, \pi^0 p)$ reaction cannot take place on a single proton. The water targets were made at PSI (formerly SIN). Each target consisted of a thin aluminum frame with a window of size 100 mm (vertical) times 300 mm. The window was covered on both sides with 50 μm Mylar,[59] so that the thickness of the water target was determined by the thickness of the aluminum frame. We had three frame sizes which were designed to give full water targets of thickness 5 mm, 9 mm, and 12 mm, respectively. In addition we made a 3 mm target by squeezing water out of a spare 5 mm target.

Establishing the exact thickness of each water target was difficult because the weight of the water inside the targets made the Mylar windows bulge. Two methods of measuring the target thicknesses were considered: (1) using a gamma source and measure the loss due to photon attenuation in the targets, or (2) using the π^0 spectrometer to measure known cross sections and deduce the thicknesses from that information. The second

option was provided for by doing single arm measurements of the reaction $H(\pi^-, \pi^0)$ (using the hydrogen in the water) on all the water targets. This was normally done either just before or just after the coincidence measurements on the same target.

Immediately upon the conclusion of the experiment, we made some attempts to measure the thicknesses with a radioactive source by measuring the attenuation of 356 keV photons from ^{133}Ba. However, we found it more difficult than expected to get consistent results this way; the measurements appeared quite sensitive to changes in collimation, for example. Two other factors also encouraged using the π^0 spectrometer measurements instead. When similar targets were used before at PSI, it was found that significant amounts of water were lost by diffusion through the Mylar. The targets shrank by typically 0.1 mm per week.[60] In our case, the dry New Mexico air could possibly make this even worse. Hence, it was desirable to obtain the thickness of any target at about the same time as the real measurements with this target were performed. The second reason is that by using the π^0 spectrometer, the cross section measurements will implicitly also include the π^0 spectrometer efficiency, and one avoids the extra uncertainty caused by performing separate efficiency measurements. We therefore decided to rely on the π^0 spectrometer measurements to establish the target thicknesses. The analysis of these measurements is discussed in detail in the chapter on Preparatory Analysis.

Empty frames (including the Mylar windows) were used throughout the experiment to obtain information about the background (non-target-related events).

The experiment also required several other targets. For the A-dependence study of the $(\pi^+, \pi^0 p)$ and (π^+, π^0) reactions we used targets made of natural Fe, Sn, and Pb in addition to the water targets. Independent measurements of the π^0 spectrometer conversion efficiency required a polyethylene (CH_2) target and a carbon target. Finally, part of the proton detector calibration measurements were made on a deuterium target (in the form of CD_2). The physical parameters for all these targets are given in Table 2.1.

2.2.2 The π^0 Spectrometer

The neutral pions were detected using the LAMPF π^0 spectrometer, which by the

Table 2.1. List of all targets used in the experiment. The thicknesses listed for the water targets are the nominal (design) values; the actual values were determined in the off-line analysis (next chapter). The other targets were measured mechanically, and the uncertainty of these measurements is insignificant compared to other experimental uncertainties.

target	description	thickness [mm]	thickness [g/cm^2]
"3 mm"	3 mm water target for ^{16}O	3*	0.30*
"5 mm"	5 mm water target for ^{16}O	5*	0.50*
"9 mm"	9 mm water target for ^{16}O	9*	0.90*
"12 mm"	12 mm water target for ^{16}O	12*	1.20*
^{56}Fe	natural iron	1.17	0.902
^{120}Sn	natural tin	2.05	1.61
^{208}Pb	natural lead	1.02	1.160
CH_2	polyethylene	6.35	0.551
C	sheets of graphite powder	2.82	0.289
CD_2	deuterated polyethylene	4.06	0.428

* *nominal* value

time of our experiment was a well established instrument. Only a brief overview of this spectrometer is given here. Further details can be found in Refs. 61 and 62.

The π^0 is a short-lived particle. Its mean lifetime at rest is 84 as (Ref. 2). At the energies of this experiment it will therefore typically decay after moving only a few tens of nanometers, so for our purposes the decay can be considered instantaneous. The dominant decay mode is $\pi^0 \rightarrow \gamma\gamma$ with a branching ratio of 98.8%.[2] The π^0 spectrometer is designed to measure the energy and direction of these two decay photons. One can then deduce the energy and momentum of the original π^0.

Fig. 2.3 illustrates the principle of π^0 detection by showing the active elements of the LAMPF π^0 spectrometer. The two photons are detected independently in the two spectrometer "arms". There are three steps involved in each photon measurement: first, the photon must be made to convert into charged particles whose properties can be measured; second, its direction of motion must be determined; third, its total energy must be measured. Each π^0 spectrometer arm has three sets of Pb-glass converters and multi-wire proportional chambers (MWPC's) for the first two tasks. In a converter a photon converts to an electron-positron pair, which in turn may interact further and

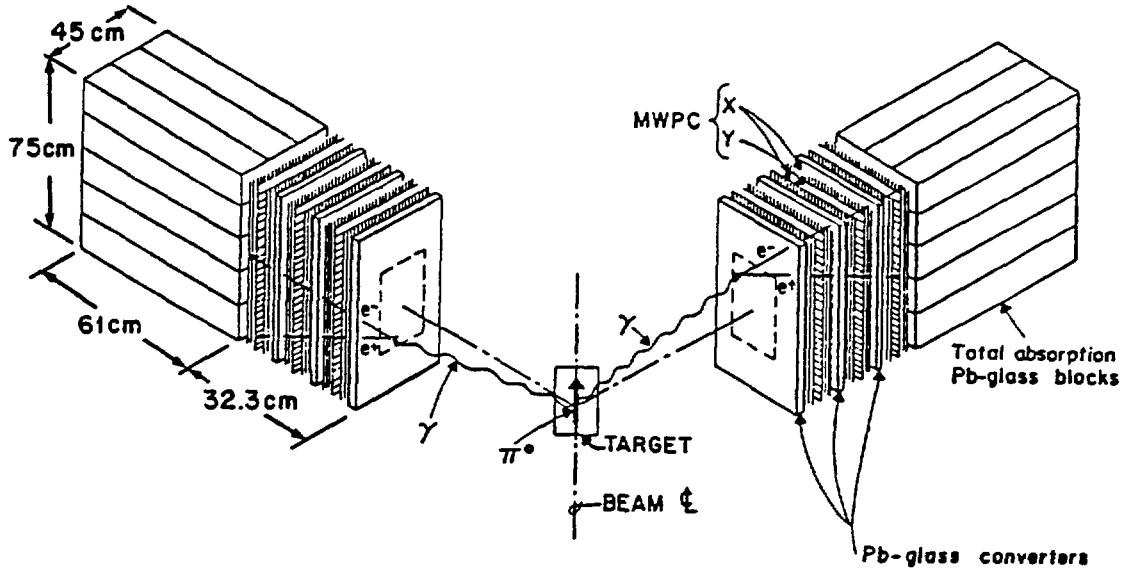

Figure 2.3. Schematic diagram of the LAMPF π^0 spectrometer. Each spectrometer arm detects one of the two π^0 decay photons. There is some flexibility in choosing both the angle between the spectrometer arms (the spectrometer opening angle) and the distance from the target to each arm. The figure is from Ref. 61.

lead to showers of charged particles. The MWPC's register the coordinates of these particles so that one can deduce the point of conversion and hence the direction of motion of the photon from the target. Each converter is followed by three MWPC's. Two of them measure the coordinate "x" in the plane of the spectrometer opening angle (with 2 mm resolution), while the third measures the coordinate "y" perpendicular to this (with 4 mm resolution). The probability for conversion of a given photon in a given converter[61] is about 30%. With three converters in each arm, the probability of successful conversion of both decay photons becomes approximately 40%. The converters are active, that is, they are connected to photo-multiplier tubes so that the energy loss can be measured. The showers of charged particles are finally stopped in an array of 15 Pb-glass blocks where the remaining photon energy is measured. For discussions of the detailed design criteria, see Ref. 61 and references therein.

The limiting factor when setting the beam flux as high as possible for a measurement is often the count rate of the detectors in the π^0 spectrometer. In addition to the converters and total-absorption blocks already mentioned, each conversion system (converter

plus three MWPC's) in each spectrometer arm is followed by a thin (3 mm) plastic scintillator whose signal is used for trigger purposes. A similar plastic scintillator is also placed in front of each arm to serve as a veto against incoming charged particles. As a rule of thumb, the count rate in all of these elements should be kept around or below $1 \cdot 10^6$ per second.

Using information about the conversion points and the energies of both decay photons, one can calculate the actual ejection angle for each measured π^0. Knowing this angle on an event-by-event basis permits angular binning of the results (tailored to the needs of the individual experiments) within the fairly wide range of angles covered by the physical size of the π^0 spectrometer arms (cf. Fig. 2.3) (the exact angular acceptance depends on the setup geometry chosen).

The LAMPF π^0 spectrometer can be used in two configurations, known as "one-post" and "two-post". In the one-post configuration both spectrometer arms are mounted on the same support (post), and the spectrometer opening angle η_{π^0} (the angle between the directions from the target to the center of each arm) is in a (vertical) plane normal to the scattering plane. In the two-post configuration each arm is supported independently, and η_{π^0} is in the scattering plane.

The energy of the π^0 is given not only by the total energy of the two photons as measured in the Pb-glass counters, but also by the angle between the two photons. Since the π^0 spectrometer measures both quantities, there is in principle a redundancy of information available. The opening angle can be measured more precisely than the energies, and it is shown in Ref. 62 that the total π^0 energy E_{π^0} is best determined from the expression

$$E_{\pi^0}^2 = \frac{2m_{\pi^0}^2}{(1-\cos\eta)(1-X^2)}\,, \tag{2.1}$$

where $m_{\pi^0} = 134.973$ MeV (Ref. 2) is the π^0 rest mass, η is the laboratory opening angle between the two decay photons, and X depends on the measured photon energies:

$$X = \frac{E_{\gamma_1} - E_{\gamma_2}}{E_{\gamma_1} + E_{\gamma_2}} \tag{2.2}$$

The expression in Eq. (2.1) is best for small X, in which case the energy resolution depends almost entirely upon the measurement of the opening angle η. In the analysis of π^0 spectrometer data one therefore normally imposes a maximum limit on the

absolute value of X. The specific value chosen will depend on the resolution requirements of the experiment. Our case will be discussed in more detail in the chapter on Preliminary Analysis.

2.2.3 The Proton Arm

The detectors for the protons ejected in the $(\pi^+, \pi^0 p)$ reaction were designed especially for this experiment. One goal of the experiment was to study the angular distribution of these protons. To achieve this, a proton arm consisting of an array of eight independent ΔE–E telescopes was constructed.

The main advantage of the ΔE–E concept is that it provides particle identification. A high energy proton will leave little energy in the thin ΔE detector and a large amount in the E (stopping) detector; a low energy proton will leave somewhat more in the ΔE detector and not have very much left for the E detector. Other particles with other masses (in our case, particularly pions) will share their energy differently between the detectors. Therefore, in a plot of the loss in the ΔE detector versus the loss in the E detector, each kind of particle will form a separate band that can be used for identifying the respective particles. This will be discussed further in connection with the data analysis.

The design of each telescope is shown in Fig. 2.4. The ΔE detector is a 0.3 cm thick plastic scintillator (BC–408), and the E detector is a 20.3 cm thick block of the same material capable of stopping protons with kinetic energies up to about 175 MeV. The telescope design ensures that the solid angle spanned by each telescope is defined by the ΔE detector; any particle originating at the target and passing through this detector will not escape through the side of the E detector. All detectors are connected to 2″ photomultiplier tubes (EMI 9813B).

The ΔE and E detectors in each telescope are wrapped independently. They are both covered by one layer of aluminum foil followed by one layer of plastic tape. In addition, the E detectors are painted white (underneath the wrapping) to improve the uniformity of the collection of scintillation light. A small light-emitting diode (LED)[63] is built

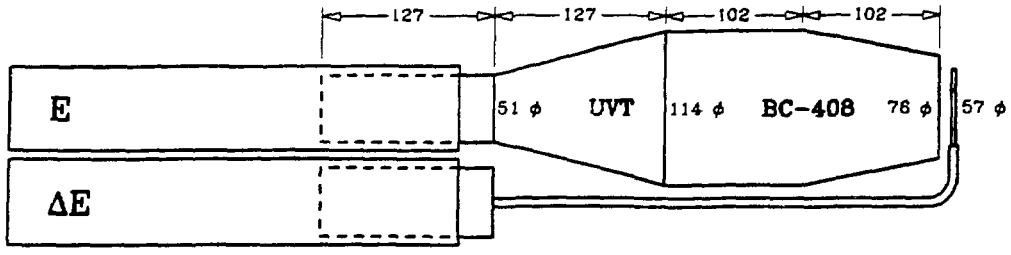

Figure 2.4. Proton telescope. The figure shows a cut through the center of the detectors. The ΔE detector is a circular, 3.2 mm thick, piece of plastic scintillator material (BC–408) connected to a UVT light guide of cross section 6.4 mm × 51 mm and a standard LAMPF 2″ photomultiplier (PM) tube (EMI 9813B) and base. The E detector is made of the same materials. It has a circular cross section and is wide enough to prevent protons that enter through the ΔE detector from escaping through its side. Protons with kinetic energies up to approximately 175 MeV will stop inside the scintillator material. The PM tubes and bases are not shown in the figure. The large structures to the left carrying the labels "E" and "ΔE" are metal cylinders protecting the PM tubes. In addition, the tubes are shielded by μ-metal cylinders inside these external cylinders. The two detectors are mounted on the same small aluminum frame to allow them to be moved as one unit. All measures in the figure are in mm.

into each E detector to make available a stable source of light signals for monitoring drifts in the detector system.

The configuration of the proton arm is normally as shown in Fig. 2.5. The eight telescopes are attached to an aluminum support structure that can be tethered to the same pivot post as the π^0 spectrometer, and that is free to rotate around the pivot point. Seven of the telescopes are placed 17° apart in a vertical array, thus spanning ±51° about the central telescope (referred to as telescope 4), which is placed in the scattering plane. The remaining telescope (telescope 8) (not shown in the figure) is placed in the scattering plane 17° away from the central proton angle. The complete assembly can be rotated 90° or 180° from the position shown. In the first case one gets a large horizontal (in-plane) detector array with only telescope 8 being out-of-plane (above the plane). The latter case just has telescope 8 on the other side of the seven-telescope array. Telescope 4 is at the central angle in all configurations.

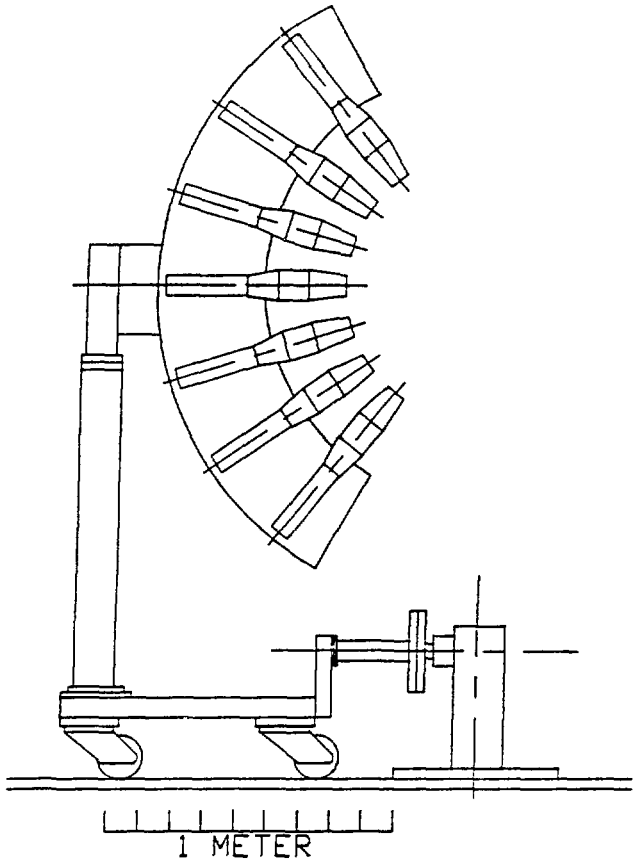

Figure 2.5. The proton arm. The figure shows its normal configuration with the main array vertical. The telescopes are placed 17° apart, with the central telescope (telescope 4) being in the (horizontal) scattering plane. The eighth telescope is not shown. It is mounted 17° away from telescope 4 in the horizontal plane. The whole assembly can be rotated about the center of telescope 4; the rotation must be either 90° (making a horizontal array) or 180°. The proton arm and the π^0 spectrometer are tethered to the same pivot post, and the proton arm can easily be moved around this pivot.

2.2.4 Other Detectors

Some of the proton telescope calibration measurements (using the reaction $\pi^+ + d \rightarrow 2p$) required coincidences between the proton in the telescope to be calibrated and a conjugate proton. We had two detectors for conjugate protons, allowing calibration measurements for two telescopes to be made simultaneously. Each of these detectors consisted of two thin plastic scintillators, about 10 cm × 10 cm in area, mounted about 3 cm apart, one behind the other. We used scintillators that were already available

in the laboratory, so the thickness varied a little. However, since the only use of these detectors was to tag coincidence particles, the exact thickness is of little concern to this experiment. The conjugate proton detectors were generally placed as far away from the target as possible to minimize their solid angle.

2.2.5 Setups

A sketch of the floor layout of the LEP cave is shown in Fig. 2.6. The pivot for the particle detectors is quite far from the back wall to allow a wide range of possible detector angles. The magnets on the floor (two steering magnets and two quadrupole magnets) were added to the beam channel to focus the beam at this new pivot point four meters downstream of the standard LEP pivot. Based on images on photographic film exposed to the beam, we estimate that the size of the beam spot at our pivot was approximately 1.5 cm × 1.5 cm (square) for the 165 MeV π^+ beam. The spots for the various π^- beams had the same width, but were clearly not as high (typically $0.5 - 1.0$ cm).

Both the π^0 spectrometer and the proton arm were tethered to a post at the pivot. The π^0 spectrometer was used in its one-post configuration, and its distance from the pivot could be varied (cf. Sec. 2.2.2). The proton arm was always mounted such that the distance from the target to the front of any telescope (the ΔE detector) was 55 cm, thus giving each telescope a solid angle of 8.46 msr. The target in use was mounted in a slit on top of the pivot post. This slit could be set at any angle (within $\pm 0.25°$) with respect to the beam.

A Monte Carlo code (PIANG[62]) that calculates the effects of the setup geometry on π^0 measurements was developed in parallel with the construction of the π^0 spectrometer. A special version of this code that also included the proton variables was developed for our coincidence measurements.[64] This allowed us to estimate the resolution of the excitation energy of the residual ^{15}O nucleus for a number of possible setups, and thus optimize the running conditions for the actual measurements.

The protons detected in $^{16}\mathrm{O}(\pi^+, \pi^0 p)$ measurements must originate from one of the neutron shells in ^{16}O. One goal of the experiment is to identify nucleons removed from

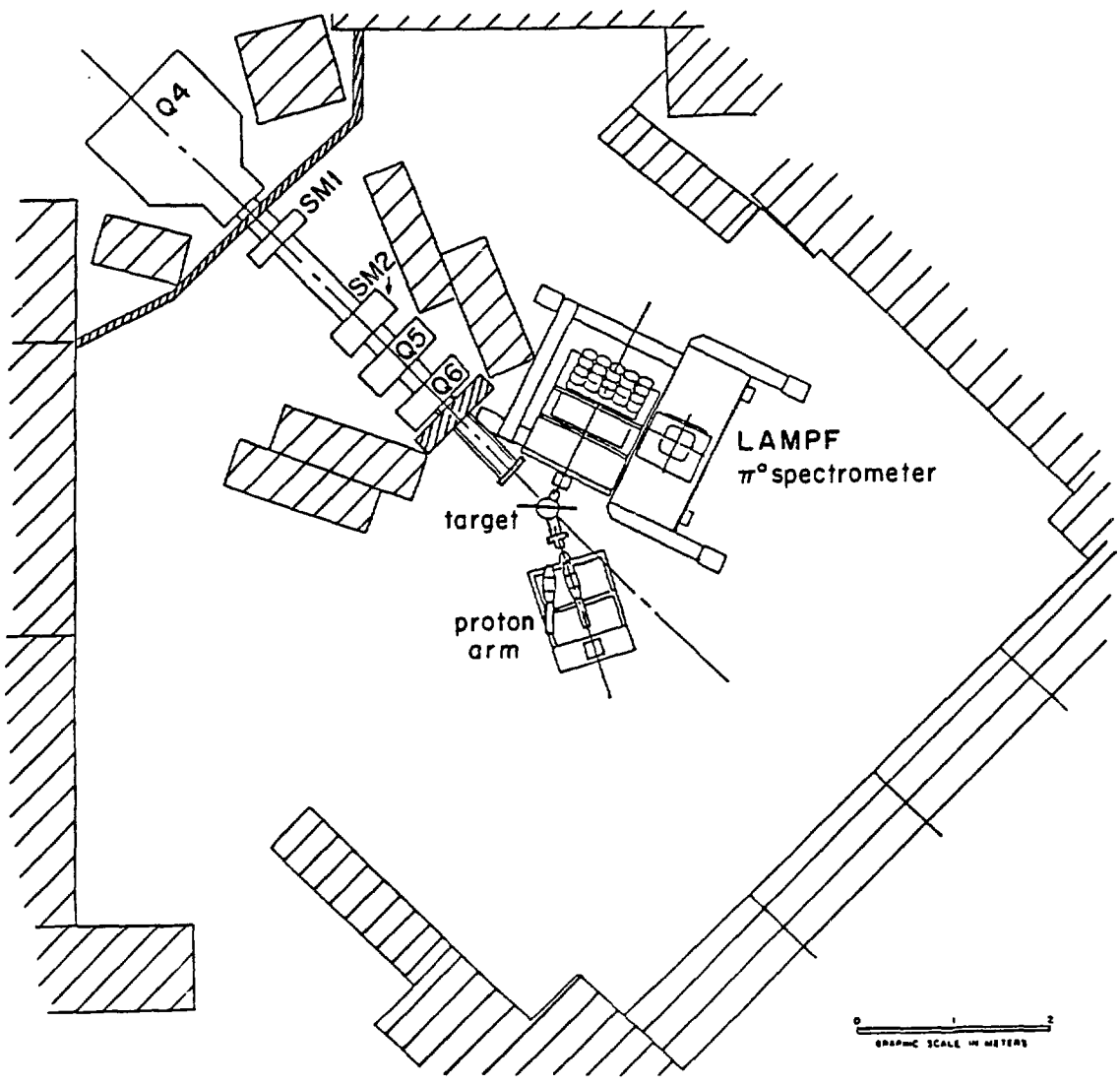

Figure 2.6. Floor layout of the LEP cave. The figure shows the extension of the channel with its magnets, the target, the particle detectors, and the main shielding. Q4 is the last quadrupole magnet in the standard beam channel (cf. Fig. 2.2), Q5 and Q6 were installed to provide focusing at our pivot. SM1 and SM2 are steering magnets. The shielding is indicated by the hatched areas. The most densely hatched areas indicate lead shielding; the remaining shielding was provided by concrete blocks. The most downstream part of the beam pipe (after Q6) was made of lead. The configuration shown corresponds to the setup for $\theta_{\pi^0} = 110.0°$.

one of the two p-shell neutron levels ($1p_{\frac{1}{2}}$ and $1p_{\frac{3}{2}}$). The ^{15}O nucleus is then left in its ground state or in a weakly excited state. This goal provides a lower limit to the acceptable resolution in the excitation energy of the residual nucleus. We did not expect to resolve the two p-shell levels, which are separated by approximately 6.2 MeV (cf. Ref. 65), but we had to be able to distinguish between overall p-shell removal and any other (most importantly, s-shell removal) processes.

We obtained some guidance in determining the necessary resolution from previous pion- and electron-induced nucleon removal experiments.[40,66] Some results from these measurements are shown in Fig. 2.7. Kyle *et al.* measured the excitation energy of the residual ^{15}N nucleus in $^{16}O(\pi^{\pm},\pi^{\pm}p)^{15}N$ under conditions similar to ours (cf. Figs. 1.7a and 2.7).[40] Good resolution $^{16}O(e,e'p)^{15}N$ measurements have determined that the $1s_{\frac{1}{2}}$-hole state in ^{15}N is centered at an excitation energy of approximately 28 MeV with a width of about 24 MeV (FWHM).[69] The situation for neutron removal leading to ^{15}O was expected to be similar to what had been observed for proton removal leading to ^{15}N. We concluded that we wanted a resolution in the calculated excitation energy of 10 MeV (FWHM) or better. (At the time of this experiment preliminary results were available from our earlier 245 MeV measurements of the $^{16}O(\pi^{+},\pi^{0}p)$ reaction. These results did not contradict the resolution requirements mentioned here.)

The ultimate criterion in selecting the setup parameters was therefore that the event rate should be as high as possible while maintaining resolution in the excitation energy no worse than 10 MeV (FWHM). In other words, the π^0 spectrometer solid angle should be made as large as possible within this resolution requirement. Our special version of the program PIANG[64] was used extensively to find how this could best be done.

We studied the $(\pi^{+},\pi^{0}p)$ and (π^{+},π^{0}) reactions at four different π^0 angles: 70.0°, 80.0°, 110.0°, and 129.7°. The largest angle was limited by the space available for the π^0 spectrometer in the LEP cave, and $\theta_{\pi^0} = 70°$ was the smallest angle where the PIANG results indicated that we could obtain satisfactory energy resolution while maintaining a satisfactory counting rate.

The opening angle (η_{π^0}) of the π^0 spectrometer determines the π^0 energy which is optimal for detection with the spectrometer. For each π^0 angle chosen, this opening

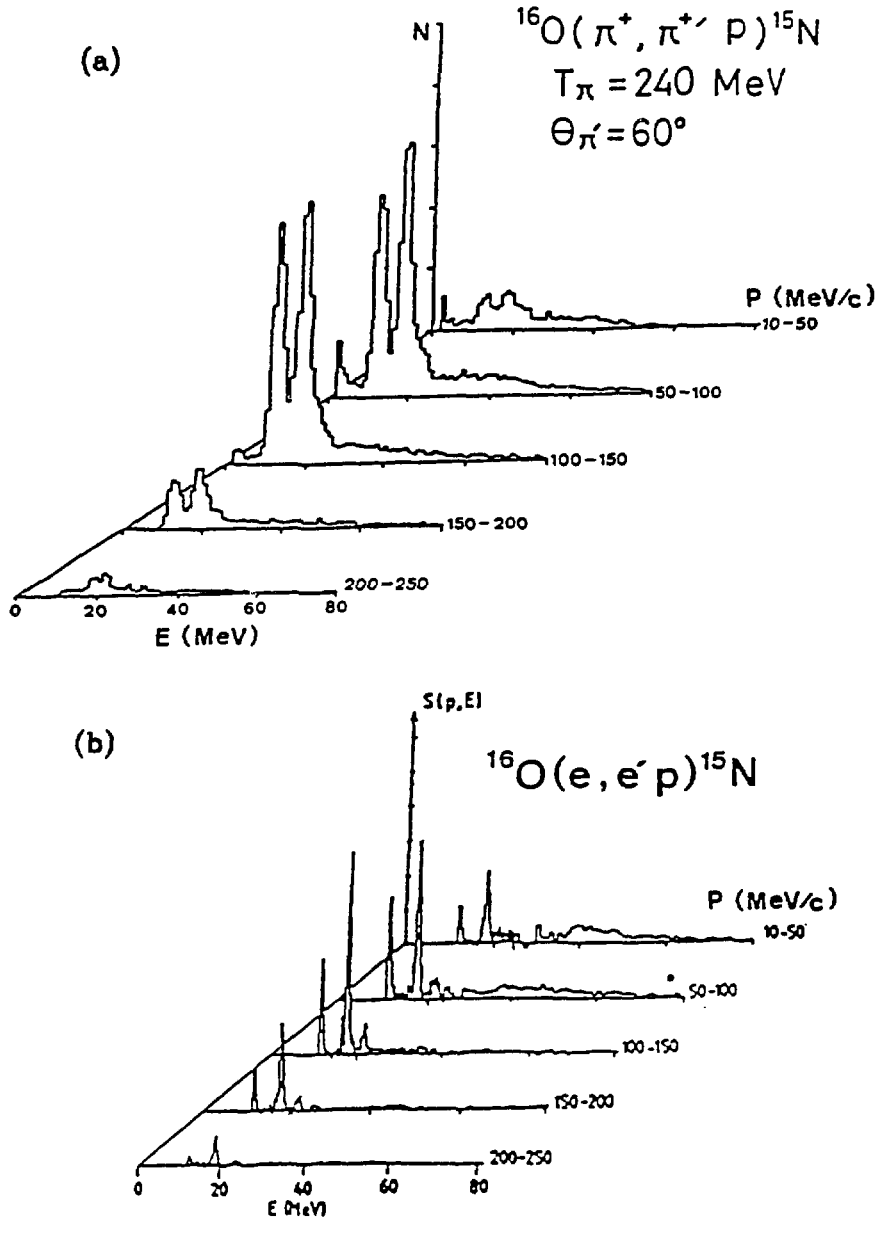

Figure 2.7. Comparison of pion- and electron-induced nucleon removal data. (a) shows pion results obtained by Kyle *et al.* The two peaks are the p-shell levels in ^{15}N. These data are also shown in Fig. 1.7a. (b) shows corresponding electron scattering data presented in Ref. 67. The figure is from Ref. 68.

Table 2.2. Physical setup parameters. The parameters listed are the π^0 angle θ_{π^0}, the π^0 spectrometer opening angle η_{π^0} and the corresponding optimal π^0 kinetic energy T_{π^0}, the distance from the target to the π^0 spectrometer r_{π^0}, the target angle θ_t (the angle between the beam and a normal to the target on the downstream side), the nominal target thickness $t_t^{\rm nom}$, and the proton angle θ_p. Positive angles indicate beam right, and negative angles indicate beam left. The proton arm and the π^0 spectrometer swapped sides for the measurement at $\theta_{\pi^0} = 70°$ to make better use of the space available.

θ_{π^0} [deg]	η_{π^0} / T_{π^0} [deg] / [MeV]	r_{π^0} [cm]	θ_t [deg]	$t_t^{\rm nom}$ [mm]	θ_p [deg]
70.0	73.73 / 90.0	60.0	−52.0	3	−47.6
−80.0	73.73 / 90.0	50.0	50.0	5	42.3
−110.0	81.40 / 72.0	50.0	55.0	9	27.9
−129.7	84.90 / 65.0	60.0	35.0	12	19.45

angle was set to match approximately the expected central π^0 energy at that π^0 angle. The central energy was estimated by running the two-body kinematics program KINREL[70] for the free reaction $\pi^+ + n \rightarrow \pi^0 + p$. The opening angles actually used deviate a little from those calculated strictly from the reaction kinematics because the general shape of the π^0 spectrometer energy acceptance was also taken into account in the optimization. (The energy acceptance will be discussed more thoroughly in the chapter on Preliminary Analysis. It is typically quite sharply peaked at the optimal energy, and it falls off more steeply towards lower energies than higher energies.)

The choices of target angle (θ_t), target thickness (t_t), and distance from the target to the π^0 spectrometer (r_{π^0}) were also made based on the Monte Carlo simulations.

For each π^0 angle the proton arm was positioned such that the central telescope was at the proton angle of the corresponding free process $\pi^+ + n \rightarrow \pi^0 + p$; that is, this telescope was positioned to observe the peak of the quasi-free contribution to the $^{16}O(\pi^+, \pi^0 p)$ reaction. This angle is usually referred to as the "conjugate quasi-free angle" (conjugate to the π^0 angle).

The values of the physical setup parameters for all our measurements are listed in Table 2.2.

2.3 Data Acquisition Electronics

The data acquisition electronics was placed inside the LEP counting house adjacent to the LEP cave (just outside the left shielding wall shown in Fig. 2.6). The signals from the detectors were led to the counting house through 30.5 m long 50 Ω RG–58 coaxial cables. Data acquisition electronics serves two purposes: to create triggers to activate data acquisition when a "good" event occurs, and to collect the necessary data and pass these on to the data acquisition computer when such an event has taken place.

The electronics for our experiment was divided into two main parts: one for the π^0 spectrometer and one for the proton arm. The π^0 spectrometer electronics was left as close as possible to its standard configuration, which is described in detail elsewhere.[62] The discussion below concerns only the proton arm electronics and the modifications of the π^0 spectrometer electronics necessary for coincidence measurements.

2.3.1 Triggers

The requirements for a "good" event depend upon the kind of measurements being made. In any given run only one kind of detector event was wanted. Instead of having a system ready for any kind of event at any time, we therefore adjusted the trigger electronics between runs whenever necessary to accommodate another kind of event. The different event types were:

1. Single protons. This is for calibration of the proton telescopes when these are exposed directly to beam protons.
2. Stabilization signals. This is for runs where the LED's in the E detectors are turned on (cf. Sec. 2.2.3).
3. Tagged protons. This is for runs where the signal in a proton telescope is required to be in coincidence with a signal from another proton detector (cf. Sec. 2.2.4). Tagged protons are used for some of the calibration measurements of the proton telescopes.
4. Single π^0's. This is for single arm ($\pi^\pm, \pi^0$) measurements.

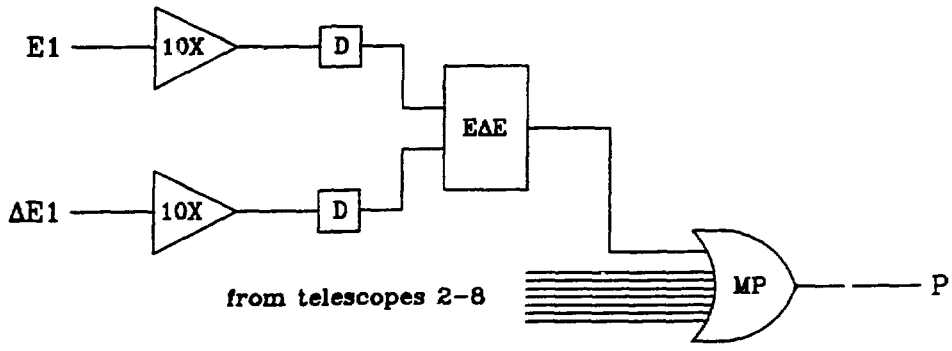

Figure 2.8. Proton trigger electronics. The input signals are unprocessed detector pulses from the cave. The boxes labeled "D" are discriminators. The logic unit "EΔE" was always set to give an OR of the input signals. The gate "MP" is known as the "Master OR" for the proton arm. Its output signal P identifies a proton event to the rest of the system.

5. $\pi^0 p$ coincidences. This is for the main part of our study.

The trigger electronics for the proton telescopes is shown in Fig. 2.8. The analog signals from the detectors were first amplified and discriminated (to get well-defined logical pulses). Then the two signals from each telescope were fed to a logic unit that could be set to require either an AND (both signals present) or an OR (at least one signal present) of these signals. In the AND state many unwanted background events, in which only one of the two detectors is hit, are eliminated. The data rate (and the background level) during the experiment was low enough, however, that even in the OR state the acceptable beam flux in the coincidence measurements was still limited by the π^0 spectrometer (cf. Sec. 2.2.2). We therefore kept this logic unit in its OR state during all data acquisition. The trigger signals from each telescope were subsequently combined in a Master OR for the proton arm. This signal (P) identified a proton event to the rest of the system.

The proton stabilization measurements had to be done with beam in the cave. In this case, we could therefore not use the standard proton arm trigger signal P because we wanted a trigger only when the detected signal was due to a pulse from the LED's. The LED's in all the telescopes were connected to the same pulse generator and therefore fired at the same time. The stabilization event trigger (STAB) was formed by requiring a coincidence between the signal from this pulse generator and a signal from

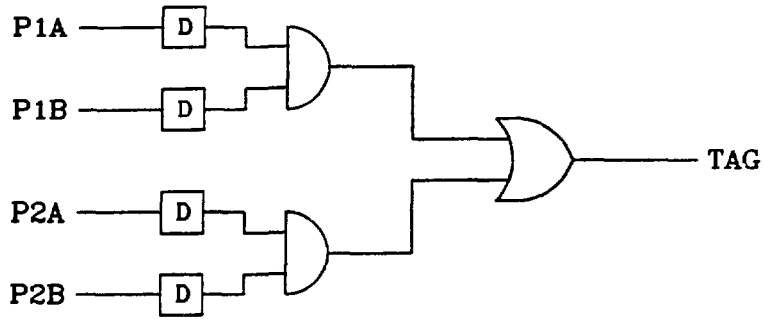

Figure 2.9. Trigger electronics for proton "tags". The input signals are from the individual scintillators in the two conjugate proton detectors. These detectors are described in Sec. 2.2.4.

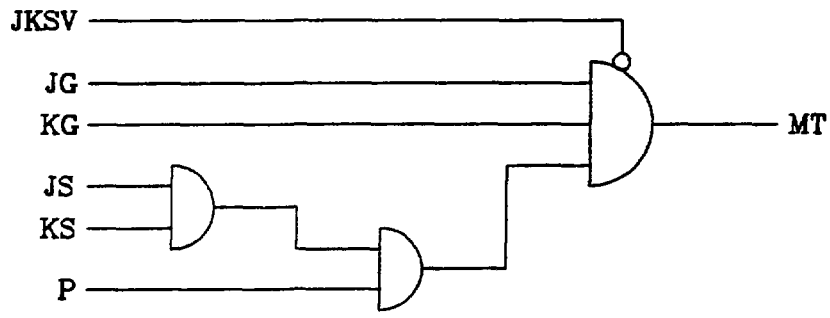

Figure 2.10. The $\pi^0 p$ coincidence event trigger. The signals involved are explained in the text.

detector E4. (Any of the detector signals could have been chosen.)

The "tag" for calibration protons was based on signals from the conjugate proton detectors (cf. Sec. 2.2.4). In these measurements two proton telescopes were calibrated in the same run, and we needed tags whenever either of these was hit by "good" protons. Fig. 2.9 shows how this signal (TAG) was formed as an OR between the two detectors, each of which requiring a coincidence between its two scintillators. (Since the information about which conjugate detector was hit is lost, this method for proton tagging cannot be used for high event rates. This was of no concern in our case, however.)

The general requirement for a π^0 event is that in each π^0 spectrometer arm there

must be signals from one or more of the conversion system scintillators, as well as from one or more of the Pb-glass elements (the converters and the total-absorption blocks). It is also required that neither of the veto counters fire (cf. Sec. 2.2.2). In the electronics this is implemented by first forming independent signals JS and KS, for the combination of the scintillators in each arm, and JG and KG, for the signals from the glass elements. (The two arms of the π^0 spectrometer are traditionally referred to as the "J arm" and the "K arm".) The scintillator signals are AND'ed to form JKS, and then an overall AND of JG, KG, and JKS is made. This last AND is vetoed by the signals from the veto counters (JKSV). Fig. 2.10 shows our $\pi^0 p$ coincidence trigger. This consisted of the standard π^0 trigger just described plus the proton signal P. The proton signal was removed in runs where single arm π^0's were measured. The signals were timed such that the overall coincidence timing was determined by the π^0.

The actual event trigger for all the different running modes described above was taken from a Master Gate. The combination of signals leading to this Master Trigger (MT) was different for each running mode. Fig. 2.11 illustrates how the various combinations were obtained. As shown, changing running mode involved changing the status of two logic units: JKSP, where the proton related signals were combined with the π^0 spectrometer scintillator signals, and the Master Gate, where the output from JKSP was combined with the signals from the Pb-glass elements of the π^0 spectrometer.

In addition to the logic shown, the complete system was arranged such that MT could not occur unless (a) there was a run going, (b) the beam was on (not between beam bursts), and (c) the computer was not busy.

2.3.2 Data Acquisition

The data acquisition electronics collected the event information through several different input devices: scalers, input registers, ADC's, and TDC's. Scalers operate independently of event triggers. Each scaler counts the number of input pulses it receives during the full run. Scalers can be set up to accept input pulses only under certain conditions. In our experiment most scalers required that the beam was on, but we also had some of them set up to count only when the beam was off (that is, between beam pulses). The other devices were read separately every time a Master

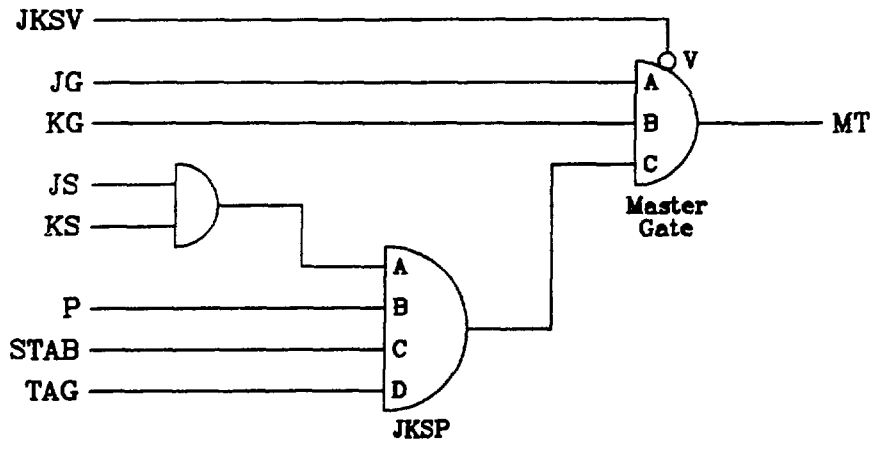

mode	inputs enabled	
	JKSP	Master Gate
Single p	B	C
Stabilization	C	C
Tagged p	B,D	C
Single π^o	A	A,B,C,V
π^op	A,B	A,B,C,V

Figure 2.11. The Master Trigger. The logic shown covers all the running modes used in the experiment. Changing mode involved changing the status of two AND gates as listed in the table. All signals are discussed in the text. The Master Trigger (MT) is the signal that identifies a "good" event.

Trigger (MT) occurred. An input register (pattern unit) indicates which (if any) of its inputs received a pulse during the event. An ADC (Analog to Digital Converter) produces a number proportional to the total charge of the input signal. This signal will therefore also be proportional to the energy deposited in a given detector. The input registers and the ADC's were gated by MT. In this way they were open to receive information only during the short time when good information (according to the trigger) was available. The duration of the gates was 55 ns for the input registers and 80 ns for the ADC's. These gates had to be carefully timed with the input signals. TDC's (Time to Digital Converters) are used to obtain timing information (time-of-flight) in an experiment. They receive a common start (by MT in our case), and each TDC is

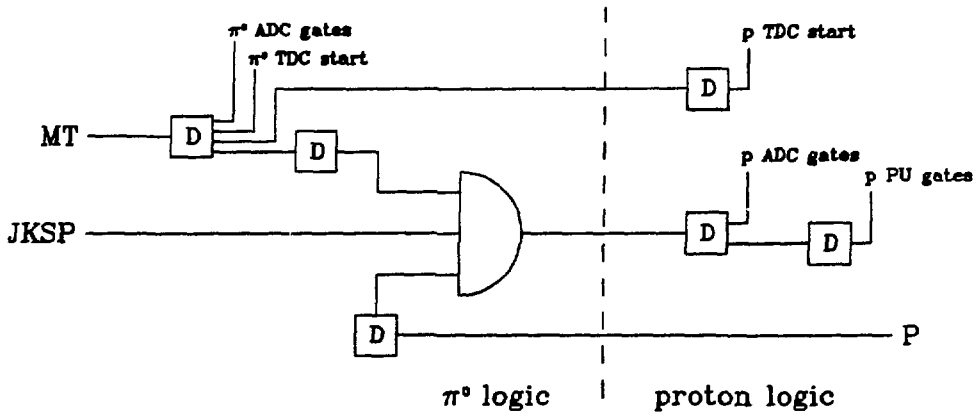

Figure 2.12. Gates and TDC starts for the data acquisition. This involves both the $\pi^0$and the proton parts of the electronics. The physical separation between the two groups of electronics was about 2 m. "PU gates" is the gate signal for the input registers (Pattern Units). MT also provides the trigger signal to the LAMPF Trigger Module activating computer readout of the event information.

stopped individually whenever a logic pulse arrives at its input. A logic diagram of the gate electronics is shown in Fig. 2.12. The reason for explicitly including the proton Master OR signal P was to make sure that the timing of the gates for the proton electronics was the same in *all* running modes ("re-timing").

Fig. 2.13 shows the full proton arm electronics. It consisted of the trigger logic already shown in Fig. 2.8 and electronics to process the event information. A detailed description of the electronics for the π^0 spectrometer can be found in Ref. 62.

Two special circuits were set up to estimate the occurrence of certain unwanted events. Fig. 2.14a shows the setup of a counter for accidental $\pi^0 p$ coincidences. This circuit was a close copy of the Master Trigger (cf. Fig. 2.11), but the proton signal had been delayed by 65 ns. The output could therefore not be set by true coincidence events; instead it provided a measure for the probability of a random charged particle to cause a coincidence Master Trigger.

The purpose of the circuit in Fig. 2.14b was to detect events with pile-up, that is, events where an ADC value represents the energy deposited by more than one particle. This occurs when two pulses arrive at the ADC within the same ADC gate. They will then be added (at least partially) together. The performance of such a circuit depends

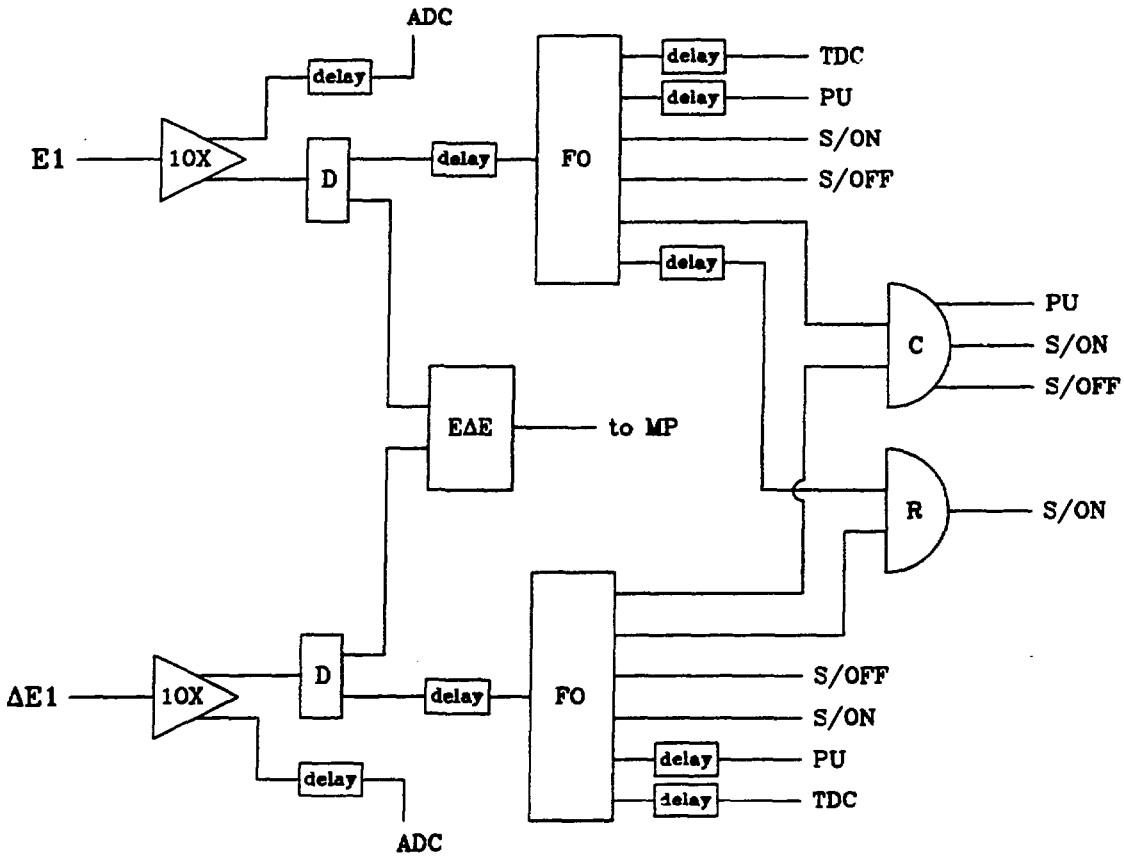

Figure 2.13. The proton arm electronics. The figure shows only the electronics pertaining to telescope 1. The same circuits are repeated for the remaining seven telescopes. Some of the symbols are explained in connection with Fig. 2.8. FO indicates a logic fan-out, C is the gate for true $E \cdot \Delta E$ coincidences, and R is the gate for random $E \cdot \Delta E$ coincidences (the E signal here is delayed relative to ΔE). Other symbols used are PU for Pattern Unit (input register), S/ON for Scaler requiring beam on, and S/OFF for Scaler requiring beam off.

critically on the timing of the delays and the pulse lengths. The total width of the pile-up gate was the same as the ordinary proton ADC gate. The discriminated proton ADC gate signal was a very short pulse (around 10 ns). At the AND gate this pulse would normally coincide with the central (zero) area of the pile-up gate, keeping the output pile-up flag low. If, on the other hand, a pulse arrived shortly before or shortly after the pulse that triggered the event (that is, within the pile-up gate), the pile-up flag was set. This flag was read for every event by an input register, and it was also

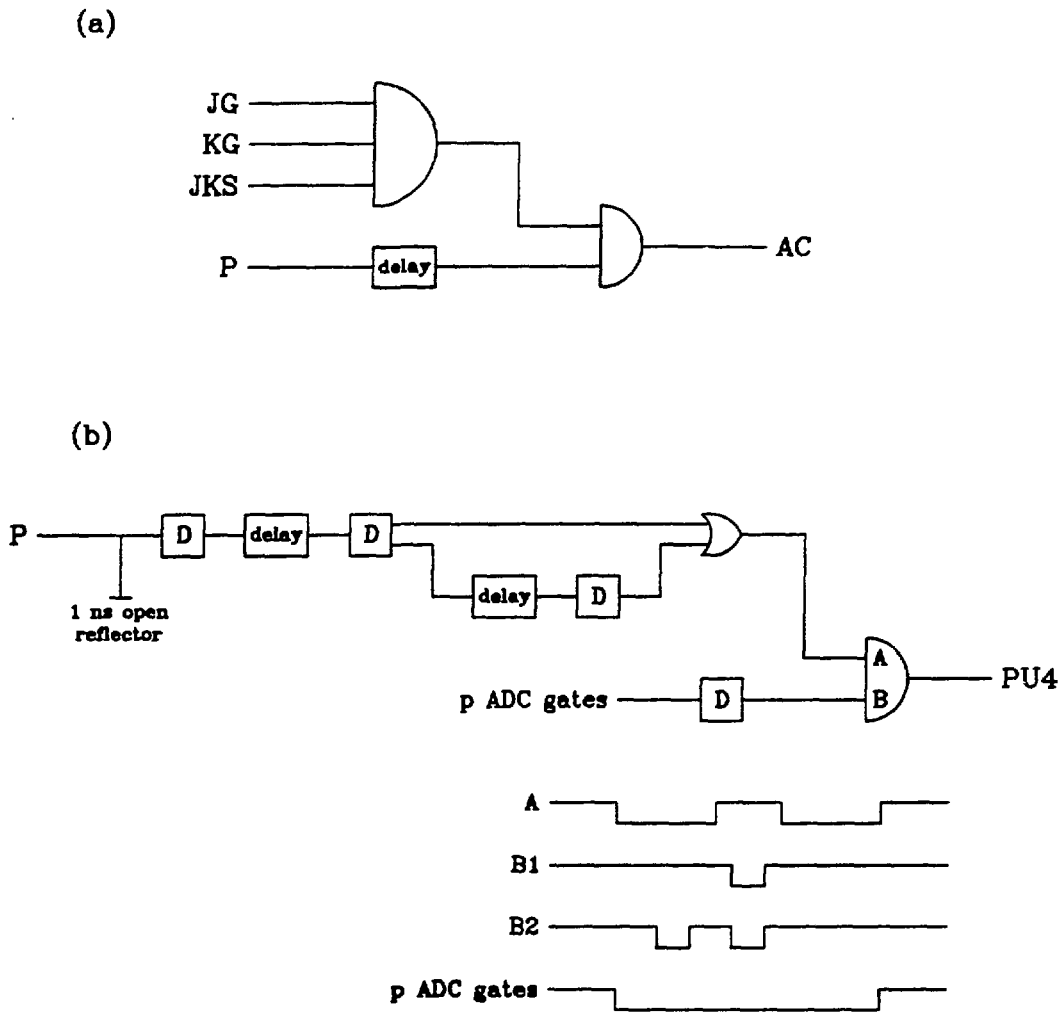

Figure 2.14. Special electronics for accidental events. (a) shows a counter for accidental coincidences. This is a close copy of the circuit generating the Master Trigger (Fig. 2.11), but in this case the proton signal is delayed by 65 ns. The output AC is connected to a scaler. (b) is a circuit to detect pile-up. The pile-up flag PU4 applies only to events where proton telescope 4 (the central telescope) has been hit; no similar flags were set up for the other telescopes. The pulse patterns below the logic diagram show the various important signals. "A" is the pile-up gate as it arrives at the AND gate in the diagram. "B1" and "B2" are possible patterns of the discriminated "p ADC gates" signal. In the case of B1, PU4 will not be set; B2 is an example of pile-up, and PU4 will be set in this case. The standard proton ADC gate signal is shown at the bottom for comparison. The total length of the pile-up gate should match this.

counted by a scaler. In principle, the use of an input register permits a rejection of events with pile-up. It was not used in this way, however, because we only had a pile-up flag for proton telescope 4. The method could therefore not be applied consistently to all data, and the main use of the pile-up flag was as a diagnostic tool and as a qualitative indication of the importance of pile-up.

The Master Trigger signal was also used to activate computer readout of the data in the input registers, ADC's, and TDC's. In order to leave the π^0 electronics and software undisturbed as much as possible, we treated the coincidence events as separate π^0 and proton events, thus requiring two trigger signals for these events. These triggers were sensed by a LAMPF Trigger Module[71] which, like the other input devices mentioned above, is made in CAMAC electronics.[72] When a trigger module receives a trigger, it activates a computer code for that particular event. This code runs in a special-purpose data acquisition computer, the MBD (a Bi-Ra Microprogrammable Branch Driver). It reads the information relevant to the particular event from the various input devices and puts this in a large buffer for later processing and taping by the experiment control computer, in our case a PDP–11/44.

2.4 Data Acquisition Software

Our data acquisition software worked within the framework of the "Q" system.[73] Q was originally developed at LAMPF, and it is used both for data acquisition and the later replay analysis of the data. Below is a short overview of this system and our implementation of it. More details about our analyzer can be found in Appendix B.

Only parts of the analyzer code are activated by Q when a given event takes place. The code running on the MBD is segmented such that when the Trigger Module indicates that a certain event has taken place in the laboratory, only that part of the code which is identified with this event will be run. The MBD code is written in QAL (Q Acquisition Language). This programming language is somewhere between a typical high-level and a typical assembly language in style. A more complete description of the QAL language can be found in Ref. 71. The QAL command repertoire is dominated by commands for communication with CAMAC electronics. When a given event is

triggered (either by an input pulse to the Trigger Module or by software), the QAL instructions for that event will normally result in a number of data words being passed on from CAMAC to a buffer in the MBD. When this buffer is full (typically after a few events), its contents are passed further on from the MBD to the experiment control computer for analysis. Separate events were defined for each of the two particles to be detected, as well as for reading information from the scalers and for various "book-keeping" tasks required for the operation of the π^0 spectrometer. The detailed event structure of our code is discussed in Appendix B.

The data acquisition is controlled from the experiment control computer. This is where the user gives his commands, for example to start and end runs, and the bulk of the software runs here. The software can be divided into several categories:

1. The main analyzer.
2. The dynamic parameter array.
3. The test system.
4. The histogramming system.
5. Independent analyzer tasks.

The main analyzer consists of user-written Fortran code tailored to the needs of the experiment. When a data buffer is received from the MBD, the event data it contains may or may not be processed by the main analyzer depending upon the process status of the respective events and upon the availability of computer time. The process status of an event can be either "must process", "may process", or "no process". A "may process" event is processed only if computer time is available at the time, while a "must process" event will be held until it can be processed. The main analyzer has a separate subroutine to analyze each event. The relevant subroutine is automatically called by the Q system whenever an event is to be processed. Our analyzer consisted of the standard π^0 spectrometer code plus new code to handle processing of data from the proton arm. Some small modifications had to be made to the π^0 event code to make π^0 information available to the coincidence kinematics calculations done in the proton event code. (The timing of the event triggers was set up such that the π^0 event was always processed before the proton event.) The π^0 and the proton events were both "must process" events, but only events in which the π^0 results indicated that both decay photons had converted properly in the spectrometer arms (cf. Sec. 2.2.2) were taped for later replay analysis.

The dynamic parameter array is a section of computer memory that may be accessed by any of the analyzer routines. Its purpose is to pass results from one program to another (for instance from the π^0 event code to the coincidence calculations), and to provide a way for the user to easily enter and change various parameters and flags. The array can be accessed on-line during a run to inspect or change the parameter values. For a more in-depth presentation of the dynamic parameter array, as well as other Q features described below, the reader is referred to the Q manuals.[73]

To determine whether an event is "good", it is usually necessary to impose certain requirements on the data. This is handled by the test system, which is a software package operating independently of the main analyzer (but under its control). The requirements are formulated in a standardized way as a number of tests operating on parameter values or on results of previous tests. Different groups of tests can be executed individually from the appropriate subroutines in the main analyzer. The test results can be used directly in the main analyzer as requirements in the analysis, but they are used mostly in connection with the histogramming system. The histogramming system permits on-line display of preliminary results. This is another independent software package running under the control of the main analyzer. The histograms are defined by simple standard commands, and for each histogram one may require that only events in which certain tests have been passed are to be included. On-line we had a number of tests and histograms defined to assist in monitoring the experiment and the apparatus as well as to display our preliminary results. As was the case for the main analyzer, we had to merge an already existing π^0 system with the added requirements of the proton arm. Only the QAL code and the tests that determine whether an event should be taped are crucial to the data acquisition, however, since everything else can be modified in the replay data analysis.

The last category, independent analyzer tasks, covers all programs that are run independently of the main analyzer. These programs may still have access to the dynamic parameter array and other Q features by being linked to the Q system. Examples of programs in this category are the routines that are run automatically at the beginning and at the end of each run, a program that sets up the software parameters to match the run mode (cf. Sec. 2.3.1), and programs that produce run summaries after each run.

Chapter 3

Preparatory Analysis

This chapter is devoted to the determination of various parameters, calibration constants, and uncertainties necessary for the full data analysis presented in the next chapter. This includes studying the performance of the π^0 spectrometer and the proton detectors, determining the flux of the incident beams, quantifying losses in the targets, and establishing the thickness of the water targets. Special runs were necessary to determine some of these parameters, and the full analysis of these is presented in this chapter.

The software for the data replay system was very similar to the data acquisition software. See Appendix B for details. The major difference was that data were retrieved from tape instead of being read from CAMAC electronics. All data replay and analysis were done using the Laboratory for Nuclear Science computers at M.I.T.

3.1 Beam Calibration and Monitoring

All measured cross sections depend directly on the number of incident pions. A good determination of this is therefore essential to the analysis. The total charge of primary

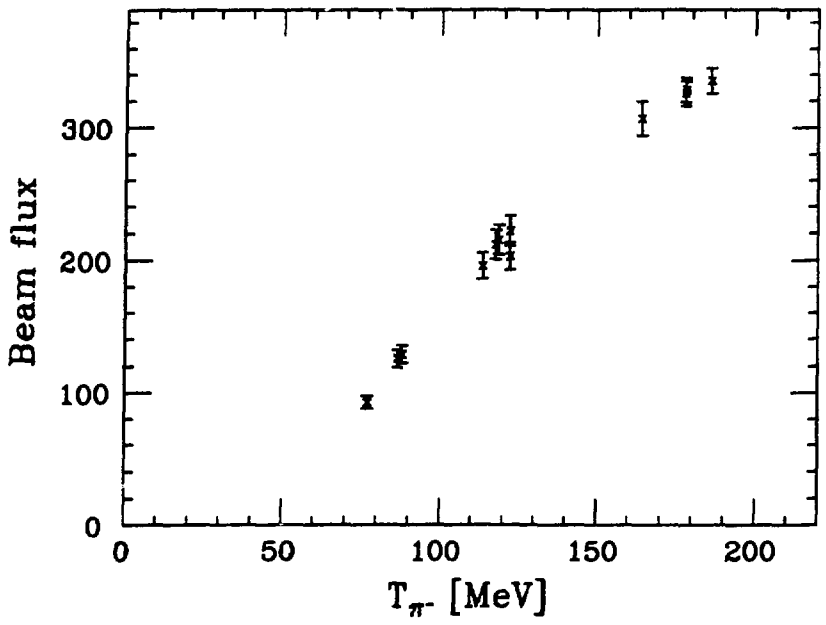

Figure 3.1. Calculated flux for all setups using negative pion beams. The vertical axis shows the flux in number of pions per toroid count. The values have been normalized to 1% momentum bite ($\frac{\Delta p}{p}$) for the channel. In the measurements the momentum bite varied between 0.6% and 3%.

beam delivered in each run was monitored by a toroid loop around this beam, and absolute calibration of the toroid measurements for the various settings of the LEP beam channel was obtained by special "activation runs" as described in Sec. 2.1 and Appendix A.

The first step in the off-line analysis was to process the ^{11}C activation data to obtain good toroid calibrations for all our measurements. The dominating contribution to the uncertainty in this calibration is the $3-5\%$ uncertainty in the cross sections for the $^{12}C(\pi^{\pm},X)^{11}C$ reaction.[34] The uncertainty caused by fitting to the β-decay is negligible (each fit is based on tens of thousands of counts). Comparing several measurements done under the same conditions, we also found that the reproducibility of the results was very good, well inside the cross section uncertainties. The uncertainties used with the final beam calibration results are therefore based solely on the above mentioned cross section uncertainties.

Negative pion beams of various energies were used during the experiment. The calibra-

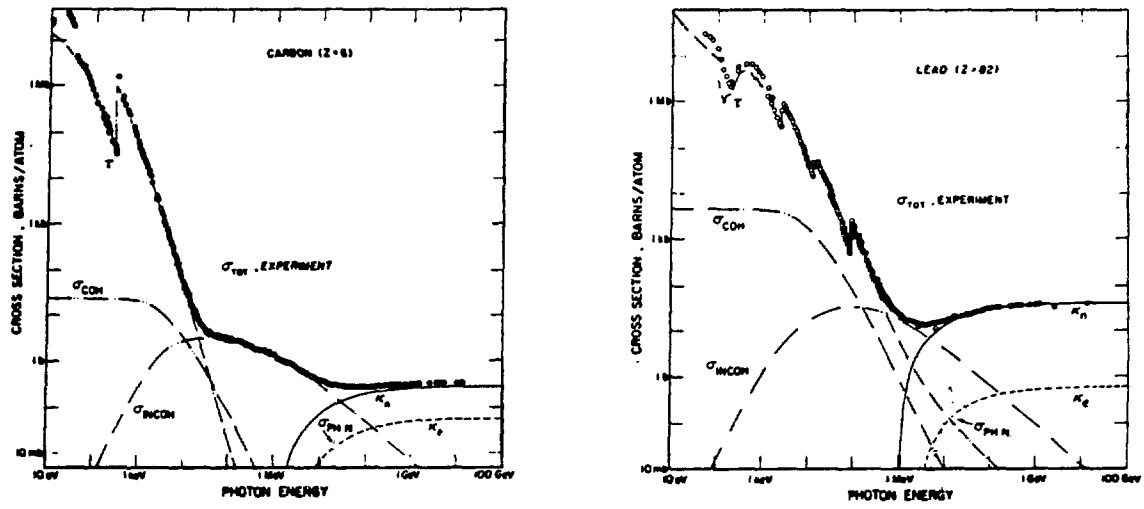

Figure 3.2. Total cross sections for photon interactions. The cross sections are presented as a function of energy in carbon and lead, showing the contributions of the different processes:

τ = Atomic photo-effect
σ_{COH} = Coherent (Rayleigh) scattering
σ_{INCOH} = Incoherent (Compton) scattering
κ_{n} = Pair production, nuclear field
κ_{e} = Pair production, electron field
$\sigma_{\mathrm{PH.N.}}$ = Photonuclear absorption

The figure is from Ref. 76. It is based on data from Ref. 74.

tion results for these are plotted in Fig. 3.1. This shows that the various calibrations and channel settings are quite consistent. With the channel settings used during the experiment these beams had a flux of approximately $2-5\cdot10^6$ π^-'s per second, while the positive pion beams (all at 165 MeV) typically had about $1\cdot10^7$ pions per second.

3.2 Photon Attenuation Losses in the Targets

Since the operation of the π^0 spectrometer is based on detecting the two decay photons from the almost immediate decay $\pi^0 \rightarrow \gamma\gamma$ (cf. Sec. 2.2.2), we need to know possible effects that may disturb the photons on their way to the spectrometer.

The various processes that can lead to a loss of photons are illustrated in Fig. 3.2. For very low energy photons (up to approximately 1 MeV) the atomic photo-effect (where

the photon is absorbed and an electron is ejected) is the most important process. For higher energy photons (up to $10 - 100$ MeV) scattering takes over. This includes both coherent (Rayleigh) scattering, where the atom is left in its ground state, and incoherent (Compton) scattering, where the photon scatters off the atomic electrons. Since the spectrometer solid angle is very small (typically $1-10$ msr), we can to a good approximation treat any scattered photon as lost. At high energies pair production is the main process, and above approximately 100 MeV it accounts for almost all of the photon cross section. Fig. 3.2 also shows a small contribution from photonuclear absorption, but this never becomes very significant.

The photons encountered in this experiment are all roughly in the range $50-200$ MeV. Photon mass attenuation coefficients μ/ρ have been calculated for all elements in this energy region by Hubbell, Gimm, and Øverbø.[75] Here μ is the (energy dependent) photon attenuation coefficient per unit length, and ρ is the density of the material. Corresponding coefficients for composite media can be calculated by[75]

$$\left(\frac{\mu}{\rho}\right)_{\text{comp}} = \sum_i w_i \left(\frac{\mu}{\rho}\right)_i \tag{3.1}$$

where the sum is over all elements, and w_i is the relative density of the i^{th} element in this medium.

There will be photon attenuation losses both in the various targets and in the air between the target and the π^0 spectrometer. The loss in the air is to a very good approximation the same for all targets (all targets are very thin compared to the distance to the spectrometer). This loss can therefore be considered included in the π^0 spectrometer conversion efficiency, which is determined experimentally, and we need to calculate photon attenuation losses in the targets only.

The fraction of photons that survive through a distance d of target material is given by $e^{-\mu d}$. To detect a π^0, two photons must make it to the spectrometer. Assuming that they both travel the same distance d inside the target, the fraction of the π^0's which can be detect ⊥ is then $e^{-2\mu d}$.

The orientation of the target relative to the π^0 spectrometer is sketched in Fig. 3.3. We see from Fig. 3.3a that photons created at the point z_{π^0} inside the target will have

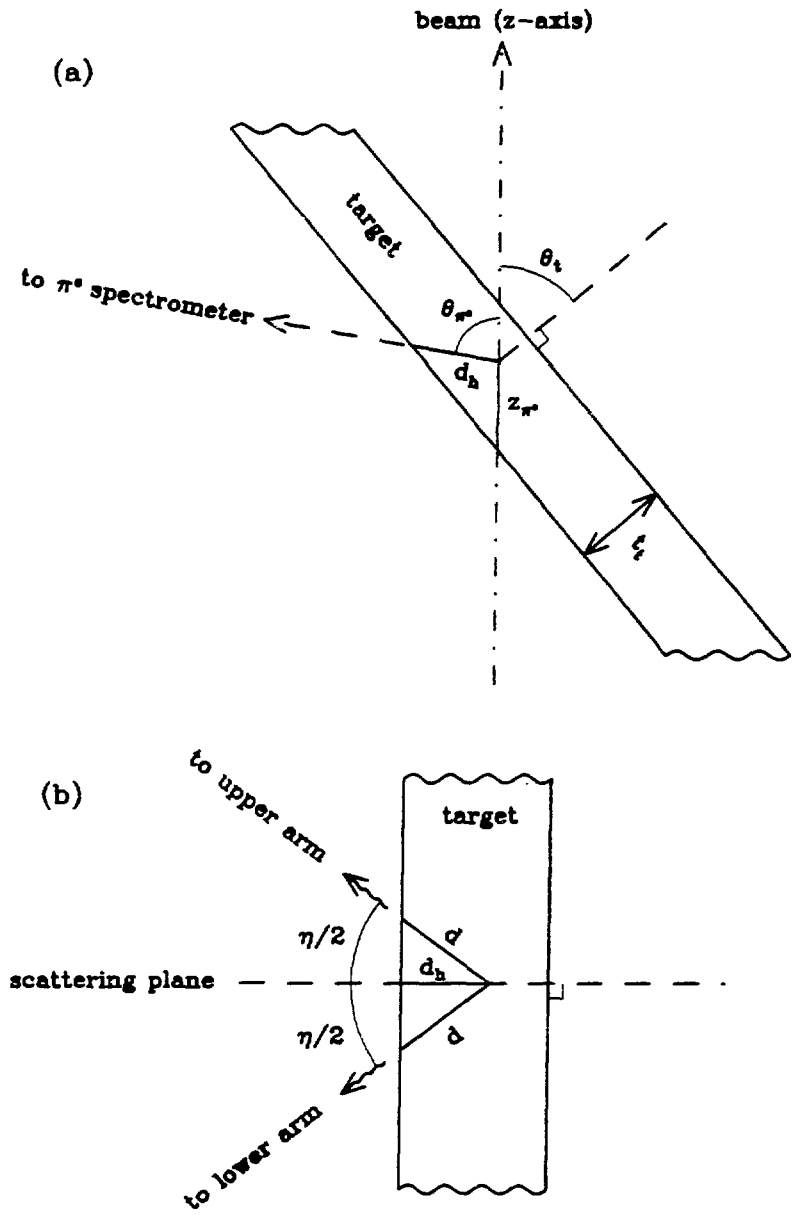

Figure 3.3. Target geometry. (a) shows the target as seen from above, and it defines the geometrical parameters involved: the π^0 scattering angle θ_{π^0}, the target angle θ_t, and the target thickness t_t. For all setups, $\frac{\pi}{2} < \theta_{\pi^0} + \theta_t < \frac{3\pi}{2}$. z_{π^0} is the distance from where the beam enters the target to the point of interaction, and d_h is the projection in the horizontal plane of the distance d the photons travel inside the target. (b) shows a vertical cut through the trajectory from the interaction point to the spectrometer. The opening angle η between the two photons is (approximately) bisected by the scattering plane because of the symmetry of the π^0 spectrometer.

to move a distance

$$d_h(z_{\pi^0}) = z_{\pi^0} \frac{\cos\theta_t}{\cos(\pi - \theta_{\pi^0} - \theta_t)} \tag{3.2}$$

in the horizontal (scattering) plane to get out of the target. Here θ_{π^0} is the angle of the π^0 spectrometer, and θ_t is the target angle (defined as the direction of the downstream target normal with respect to the z-axis, cf. Fig. 3.3a). In Eq. (3.2) both angles are treated as positive when the target angle and the spectrometer angle are on opposite sides of the 0° line (as they always were, cf. Table 2.2). The two photons from the π^0 decay are detected by detector arms positioned symmetrically about the scattering plane. This limits detection to π^0's where the laboratory opening angle η between the decay photons is (approximately) bisected by the scattering plane. The distance covered by each photon (Fig. 3.3b) then becomes

$$d(z_{\pi^0}) = \frac{d_h(z_{\pi^0})}{\cos\frac{\eta}{2}} = z_{\pi^0} \frac{\cos\theta_t}{\cos\frac{\eta}{2}\cos(\pi - \theta_{\pi^0} - \theta_t)}. \tag{3.3}$$

The fraction $f_\mu(z_{\pi^0})$ of π^0's generated at z_{π^0} that may be detected outside the target is thus

$$f_\mu(z_{\pi^0}) = \exp\left(-2\mu d(z_{\pi^0})\right) = \exp\left(-\frac{2\mu z_{\pi^0}\cos\theta_t}{\cos\frac{\eta}{2}\cos(\pi - \theta_{\pi^0} - \theta_t)}\right). \tag{3.4}$$

Since only a very small fraction of the beam pions actually interact with the target nucleons, the probability for creation of π^0's is approximately the same all along the beam path through the target. The correction for the photon attenuation can therefore be applied as a simple average over all possible positions $0 < z_{\pi^0} < \frac{t_t}{\cos\theta_t}$, where t_t is the target thickness:

$$\begin{aligned} f_\mu &\equiv \frac{\cos\theta_t}{t_t} \int_0^{\frac{t_t}{\cos\theta_t}} dz_{\pi^0}\, f_\mu(z_{\pi^0}) \\ &= \frac{\cos\frac{\eta}{2}\cos(\pi - \theta_{\pi^0} - \theta_t)}{2\mu t_t} \left(1 - \exp\left(-\frac{2\mu t_t}{\cos\frac{\eta}{2}\cos(\pi - \theta_{\pi^0} - \theta_t)}\right)\right). \end{aligned} \tag{3.5}$$

The quantity f_μ from Eq. (3.5) expresses the π^0 transparency, or the total fraction of produced π^0's (of a given energy) that may be detected outside of a target of given

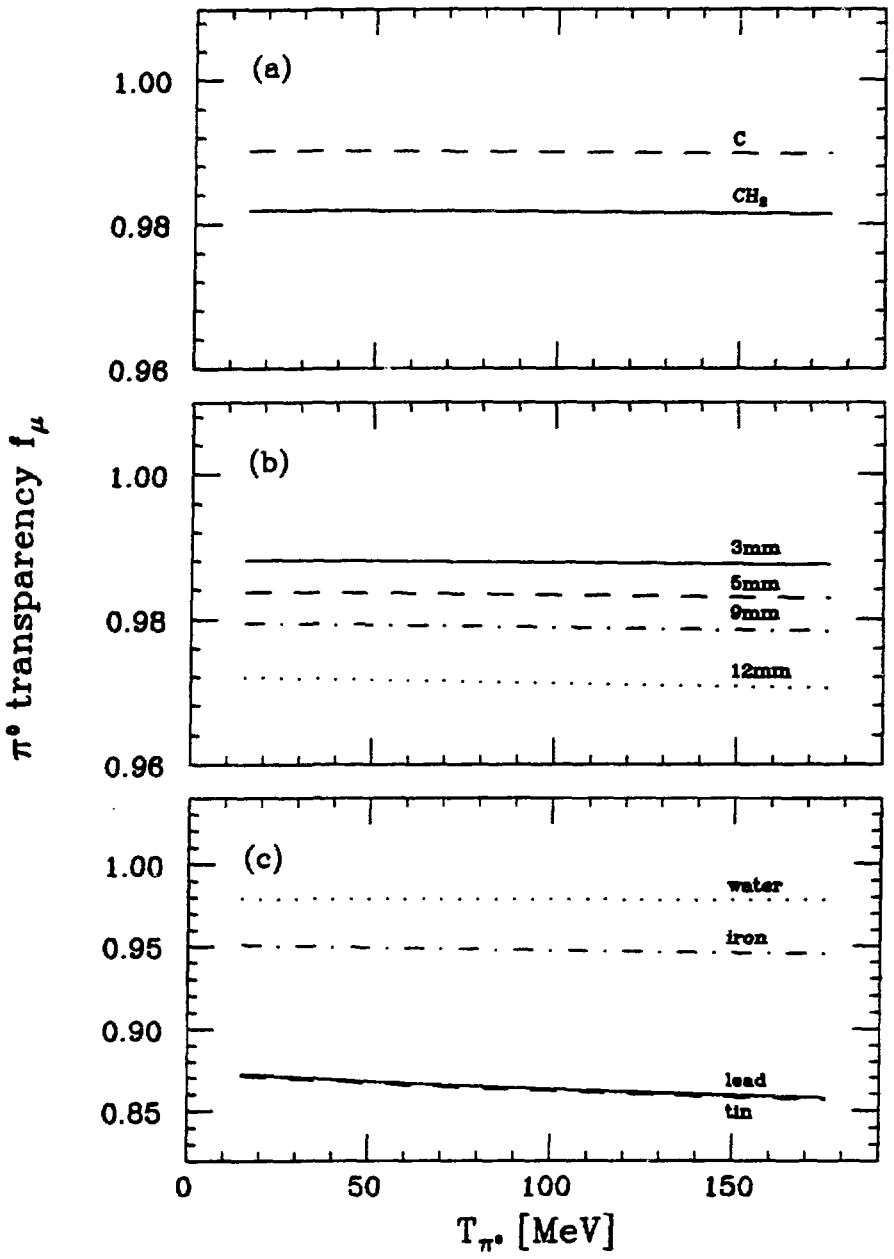

Figure 3.4. π^0 transparency in the various targets. The quantity f_μ shown here is the fraction of the π^0's that may be detected outside of a given target. (a) shows the worst cases for the CH_2 and C targets that are used for studies of the π^0 spectrometer efficiency, (b) shows the four water targets used in the main part of the experiment, assuming their nominal thicknesses of 3 mm, 5 mm, 9 mm, and 12 mm, and (c) shows the targets used in the *A*-dependence study: lead, tin, iron, and water (9 mm). All targets are described in Table 2.1.

thickness and density. Strictly speaking, in the derivation we also required these pions to decay into two photons that are symmetric about the scattering plane, and that both have the same energy in the laboratory. These conditions are sufficiently satisfied by the symmetric positioning of the π^0 spectrometer arms. f_μ is energy-dependent since the photon attenuation coefficient μ depends on the photon energy. If $N(T_{\pi^0})$ is the number of pions measured in a certain energy bin around T_{π^0}, the photon attenuation loss correction is applied by

$$N(T_{\pi^0}) \rightarrow \frac{N(T_{\pi^0})}{f_\mu(T_{\pi^0})}. \tag{3.6}$$

Photon mass attenuation coefficients are taken from Ref. 74, and when necessary (for CH_2 and H_2O) they are combined using Eq. (3.1). The final transparencies f_μ are plotted in Fig. 3.4. We see that for the water targets and the CH_2 and C targets the correction is quite small (up to about 3%). For the heavier targets used in the *A*-dependence study, however, this correction proves to be rather important (around $12-15\%$), and here it is also somewhat more energy-dependent.

In most cases the correction to the data due to photon attenuation is so small that whatever reasonable uncertainty one might assign to it will be negligible compared to other sources of uncertainty in the analysis. The two most important contributions to the uncertainty of the photon attenuation correction are the distance actually traveled by the photons inside the target and the thickness of the target. The latter is only significant for the water targets, but since the calculated cross sections depend critically on this thickness, the uncertainty in the thickness will enter more dramatically in those calculations. One may therefore ignore this uncertainty here. The distance traveled inside the target cannot be known precisely on an event-to-event basis since there is no way of knowing where a specific event actually took place. This was taken into account by the averaging process that lead to Eq. (3.5). It is also reflected in the general data analysis as a loss of resolution in energy and angle. Again, because the effect of the photon attenuation correction on the whole is rather small, it was decided to ignore this contribution to the total uncertainty.

3.3 The π^0 Spectrometer

The π^0 spectrometer is a rather complicated detector system (cf. Sec. 2.2.2). It has

been used successfully in many experiments since 1978, and its operation now mainly requires establishing and monitoring a number of system parameters. This is discussed in the subsections below.

3.3.1 Stabilization

Each spectrometer arm contains 30 Pb-glass elements with photomultiplier tubes connected to ADC's for signal readout. The determination of the π^0 energy is based partly on these signal values (cf. Eq. (2.1)). The initial calibration is done by exposing each element to various electron beams of known energies. Linear fits are then made to the detected signals, yielding the relative gains of all the detector elements.[61] Calibrations like these are rather cumbersome, and they are seldom performed. Our experiment uses calibration data obtained in 1982.[77]

The parameters of the detector system (pedestals and gains) tend to drift with time. The gains of the photomultiplier tube systems were monitored using signals from small plastic scintillators containing radioactive ^{207}Bi (Refs. 61 and 78). Each Pb-glass element had one such scintillator attached to it. The drift with time of these signals thus determined the drift of the gain of each individual photomultiplier tube system. The signals from the ^{207}Bi-scintillator systems, as well as all ADC pedestal positions, were sampled and analyzed on-line (cf. Appendix B), and the appropriate software parameters were adjusted when necessary.

The updated pedestal and gain values calculated during data acquisition were put on tape and were therefore also available to the replay analyzer.

3.3.2 Spectrometer Acceptance

The energy of the ejected π^0 is reflected in the laboratory opening angle between its two decay photons (cf. Eq. (2.1)). The opening angle of the π^0 spectrometer is normally set so that it corresponds to the most probable π^0 energy to be measured. Because the spectrometer spans a non-zero solid angle, a range of other energies will also be detected. However, the larger the deviation from the optimal energy, the smaller the

probability that both decay photons hit the spectrometer arms. The acceptance of the spectrometer is therefore strongly energy-dependent.

The energy acceptance is a function of the geometry of the setup. This can be simulated on a computer using the program PIANG[62] (see also Sec. 2.2). For a given π^0 kinetic energy, this program performs a Monte Carlo calculation of the corresponding effective π^0 spectrometer solid angle $\Delta\Omega_{MC}$. PIANG also calculates the statistical uncertainty of this solid angle. We always ran the program long enough to ensure that this would not contribute significantly to the total uncertainty of the analysis. The uncertainty in $\Delta\Omega_{MC}$ was usually kept at $1 - 1.5\%$.

The value of a software cut defining the maximum asymmetry allowed between the energy of the two detected photons is also included in the Monte Carlo calculations. This is done through a restriction on the parameter

$$X = \frac{E_{\gamma_1} - E_{\gamma_2}}{E_{\gamma_1} + E_{\gamma_2}} \tag{3.7}$$

that was introduced in Eq. (2.1). As implied by that equation, the energy resolution of the spectrometer depends on X; the larger values of X one allows, the poorer the resolution. The effect of this maximum $|X|$ (known as XCUT) on our data was taken into consideration in the feasibility simulations we performed before data acquisition started. It was reconsidered (with only minor changes) as part of the replay process. The value finally used for XCUT was 0.25 for all setups.

The π^0 spectrometer covers a large range of scattering angles. The exact range where one can obtain reliable data depends on the distance from the target to the spectrometer. In the setups we used, the spectrometer could detect π^0's up to $18.8^\circ - 20.5^\circ$ away from the nominal π^0 angle in the scattering plane and up to $11.7^\circ - 12.7^\circ$ vertical to this plane. These ranges are taken into account in the simulations done by PIANG. This program allows for defining angular bins similarly to the way it is done in the data analysis. We concentrated on two cases: one considering events only from a narrow π^0 angular bin spanning $\pm 4^\circ$ around the central scattering angle (for good resolution), and one accepting events from a wide bin spanning $\pm 12^\circ$ (for better statistics and comparisons with previous work[43]).

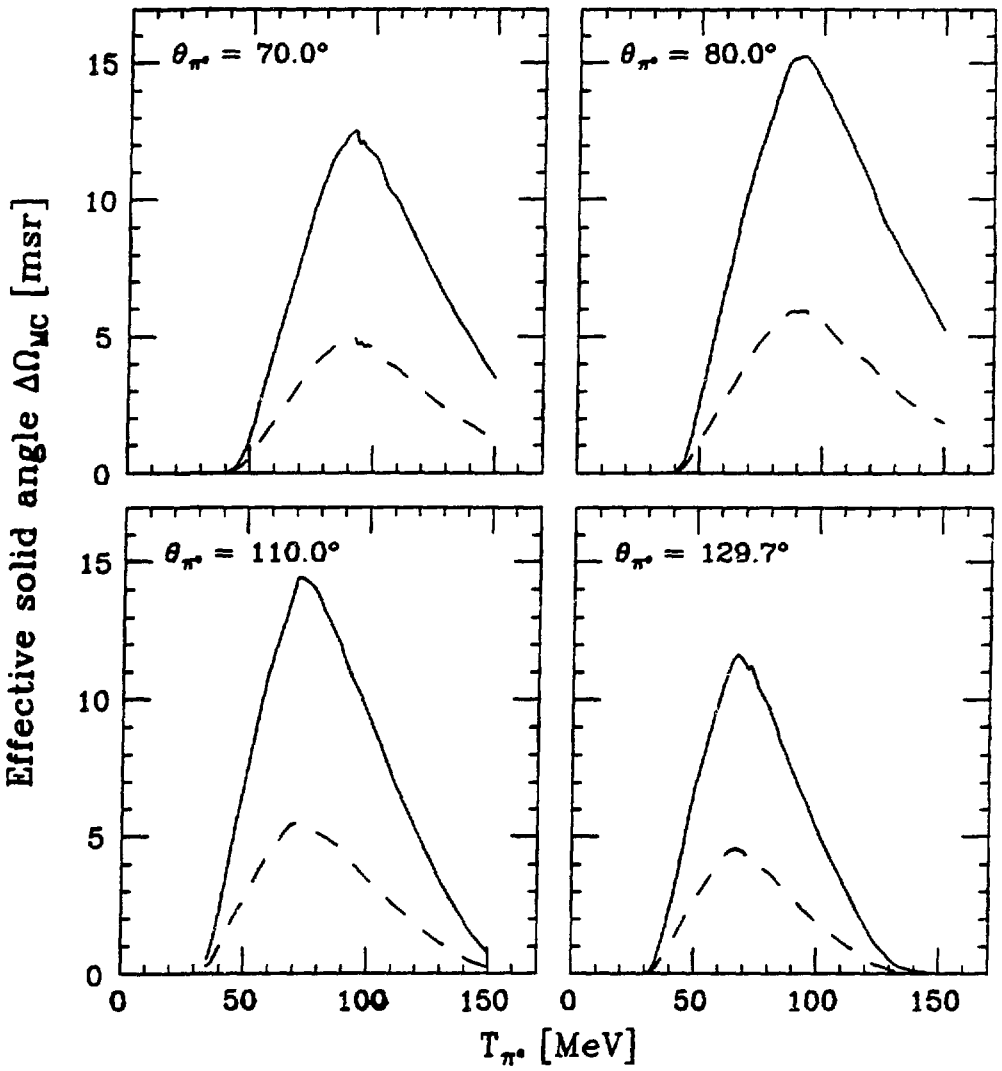

Figure 3.5. Calculated π^0 spectrometer energy acceptance for all setups. The solid curves are calculations for a π^0 spectrometer angular acceptance of $\pm 12°$ around the nominal π^0 angle and the dashed curves are for an angular acceptance of $\pm 4°$. All calculations shown here assume water targets, and parameter values for the target actually used for each setup have been applied. The plots show the effective solid angle covered by the spectrometer as a function of the kinetic energy of the ejected π^0's. Each curve is drawn through more than 20 calculated points, each of which has a statistical uncertainty of about 1% for the larger angular acceptance and about 1.5% for the smaller. The relative uncertainties are larger towards either end of all the curves. All calculations assumed a value 0.25 of the parameter XCUT. The calculated acceptances are larger at $\theta_{\pi^0} = 80.0°$ and $\theta_{\pi^0} = 110.0°$ mainly because the distance from the target to the spectrometer was shorter here than in the other setups.

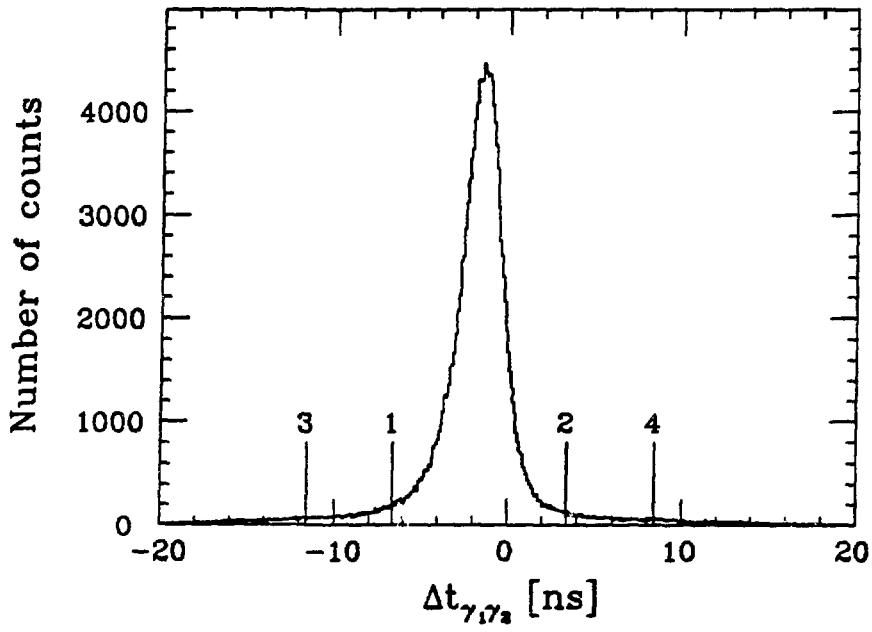

Figure 3.6. Relative timing between the two photons detected by the π^0 spectrometer. The zero of the horizontal scale is arbitrary; it depends on the hardware (cables, *etc.*) used. In this example the π^0 spectrometer was at 110°, but the picture is very similar for all setups. The numbered lines indicate the regions used in the data analysis. "Good" events are limited to the region between lines 1 and 2, while the events that fall between 3 and 1 and between 2 and 4 are used to estimate the contribution of accidental coincidences in the final results. The coincidence peak shown has a width of 3.3 ns (FWHM).

In our experiment the π^0 spectrometer was positioned at four different scattering angles. It was therefore necessary to run PIANG with four different sets of geometrical parameters to determine all of the acceptance values needed in the analysis. The final energy acceptance curves are shown in Fig. 3.5. The results shown assume water targets. There is a small dependence on target material and target thickness, so in the analysis of our A-dependence data similar calculations were repeated for each target.

3.3.3 Timing

Detection of a π^0 is really a coincidence measurement where a "simultaneous" detection of two photons is required. We try to distinguish real coincidences from accidental ones (where one or both spectrometer arms is activated by other, random particles)

by studying the timing between the two signals. Fig. 3.6 shows how most events have a well defined relative timing. In our data these coincidence peaks were typically about 3 ns wide (FWHM).

The information from the relative timing is used for two purposes: to eliminate accidental coincidences from further analysis, and to estimate the contribution of such accidental events actually included in the final analysis. The first goal is achieved by requiring that all "good" events have a relative timing that is within the coincidence peak. This is indicated by the lines labeled 1 and 2 in Fig. 3.6. If this timing cut is made very tight, many good π^0's will be removed along with the accidentals. However, since most of the accidentals that happen to be within the cut will fail some of the other tests that are required for making a positive π^0 identification, one can in general make the cut rather loose. The events that fall between lines 3 and 1 on the left hand side of the peak and between lines 2 and 4 on the right hand side are used to provide an estimate of accidental events in the final analysis. These events are tested further just like the good events. The number of events surviving all the tests is then assumed to be representative for the number of unwanted events between lines 1 and 2 that also survived. In the data analysis it was decided to limit good events to ± 5 ns around the coincidence peak and to use another 5 ns on either side to provide the estimate of accidental coincidences.

3.3.4 Wire Chambers

As mentioned earlier, the π^0 spectrometer contains a total of 18 wire chambers (cf. Fig. 2.3). They are necessary to determine the opening angle between the two coincident photons, and also to establish in which converter a given photon converted to the detected electron-positron pair. These wire chambers generally have a quite high efficiency (about 99% each). The total wire chamber efficiency due to all chambers is therefore typically around 80%. It is important to know this value precisely since it is used to scale all final results. Determining these efficiencies turned out to be more complicated than anticipated.

There is an established algorithm for calculating wire chamber efficiencies. Each spectrometer arm is considered separately. As Fig. 2.3 shows, the wire chambers are placed

in groups. Each arm has three groups (corresponding to the three converter planes), each group consisting of three chambers. The individual efficiency of chamber k in group g of arm i is defined as

$$\epsilon_{wc}^{igk} \equiv \frac{N^{ig}}{N^{igk}} \tag{3.8}$$

where N^{ig} is the total number of events having hits in ***all three*** chambers in group g of arm i, and N^{igk} is the total number of events where ***both other*** chambers of the group were hit (with or without a corresponding hit in chamber k). ϵ_{wc}^{igk} therefore expresses the ratio between the number of detected good wire chamber events and the maximum number of such events possible. The efficiency ϵ_{wc}^{ig} of each group is calculated as the product of the three individual wire chamber efficiencies.

In combining the three group efficiencies we follow the same philosophy. An event is considered "good" if the photon converts properly into an electron-positron pair in one of the converters. The definition of proper conversion is that in each arm the first wire chamber group with two or more chambers hit must have hits in all three chambers. Only events satisfying this requirement are saved on tape for replay analysis. Denoting the number of events where proper conversion took place in group g of arm i by C^{ig}, we can then express the ratio between detected good events in arm i and the number of such events that would have been detected by a perfect wire chamber system as

$$\epsilon_{wc}^{i} = \sum_{g=1}^{3} C^{ig} \Big/ \sum_{g=1}^{3} \frac{C^{ig}}{\epsilon_{wc}^{ig}}. \tag{3.9}$$

Finally, the total π^0 spectrometer wire chamber efficiency is the product of the efficiencies of the two arms:

$$\epsilon_{wc} = \prod_{i=1}^{2} \epsilon_{wc}^{i}. \tag{3.10}$$

When an event has resulted in proper conversion of both photons, the wire chamber information is used to determine the points of conversion and from that the opening angle between the two photons. In each group of wire chambers there are two chambers that measure the coordinate "x" in the plane of the opening angle of the π^0 spectrometer and one that measures "y" perpendicular to this. The conversion quite often results in several charged prongs, which in turn lead to multiple hits in the

wire chamber. The algorithm for determining the point of conversion is to take the average y of all prongs as the (less important) final y-value, and to use the x-information to find the most forward directed prong and trace this back to an imaginary "conversion plane" located at a depth (from the front face of the converter) equivalent to 5/6 of the converter thickness. This is discussed in more detail in Ref. 61.

Since only events with proper conversion have been taped, the wire chamber efficiency cannot be recalculated as part of the replay analysis. Therefore one has conventionally used the on-line wire chamber efficiency, as expressed by Eq. (3.10), as the total correction due to deficiencies in the wire chambers and their readout system. That was also our initial approach in the replay analysis of the $(\pi^+, \pi^0 p)$ data. However, analysis results calculated in this way fluctuated much more than expected.

A careful study of all factors involved in the replay analysis revealed that a large number of events were failed by the routine that uses the wire chamber information to determine the point of conversion. This tracing routine is set up to ignore (fail) events in which any individual wire chamber has more than five hits. The corresponding inefficiency is not included in the wire chamber efficiency calculations described above.

Occasionally wire chambers have "hot wires", that is, wires that appear to fire too often. This can be caused by a defect in the wire chamber itself, or, more commonly, by problems with the wire chamber readout electronics. Examples of such hot wires are shown in Fig. 3.7. The standard way of accounting for hot wires is to inspect the hit pattern in all wire chambers regularly and maintain a list of wires to be ignored by the computer. Thus these hot wires do not confuse the analysis, but they lead to a lower efficiency since real hits on these wires are also ignored. The π^0 spectrometer standard software is set up to monitor up to nine hot wires per wire chamber. The on-line list of hot wires is used automatically in the replay analysis (cf. the description of Event 19 in Appendix B).

Looking at the wire chamber information for the events that had been taped, we found that in many cases they contained a number of "hot" and "warm" wires that were not accounted for in the list of hot wires, often because the list was already filled up for the wire chamber in question. In developing an improved and consistent way of analyzing the data, we therefore focused on factors that could reduce the influence of all these

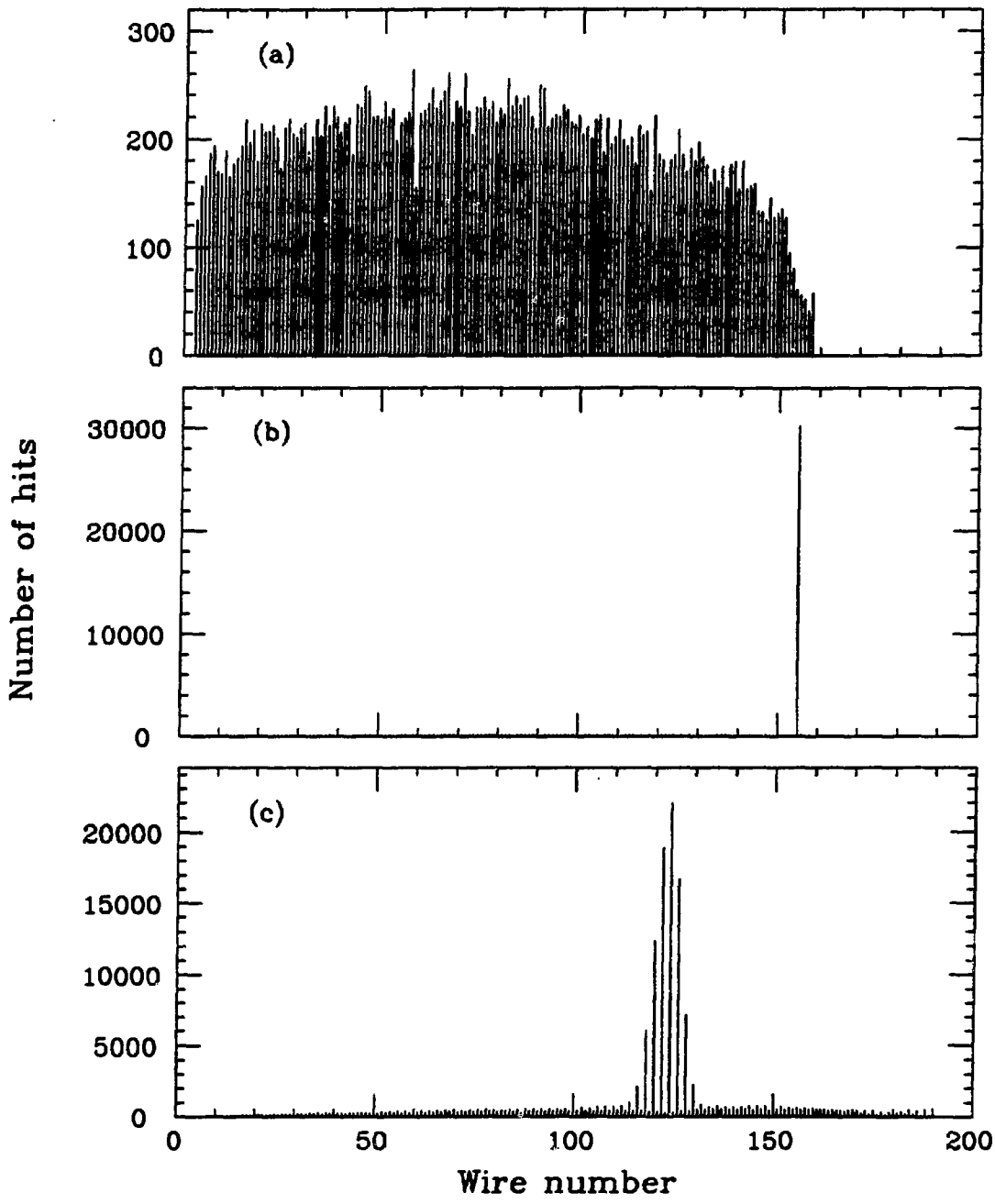

Figure 3.7. Examples of wire chamber hit patterns. (a) shows a normal hit distribution; it is fairly structureless, and all wires are hit almost equally often, (b) is a case with one hot wire, and (c) shows a case where problems with the readout electronics have made every second wire in a large section stand out, creating an artificial peak. All examples are taken from the same run (number 248).

hot wires: the maximum acceptable number of hits for conversion was changed, and the list of hot wires was extended.

The immediate consequence of limiting the number of hits allowed in a chamber is that if this maximum number is exceeded, that chamber will be considered not to have fired at all. This influences the determination of the conversion plane which, as already mentioned, is determined by requiring that all three wire chambers in that particular group must have fired, while at most one of the chambers in the preceding group is allowed to have fired. Testing the wire chamber information on the number of hits in each chamber is done as part of the initial screening of the event data. During data acquisition the maximum number of hits allowed was 21, that is, any wire chamber with more than 21 hits was assumed not to have been hit at all. Trying several smaller values for this maximum limit, we found that even if that led to a larger number of events failing the formal conversion criterion, the net number of events that would pass all further tests in the analyzer was higher. This was probably because the amount of "confusing" information was now reduced. The improvement achieved was around $2-3$ percentage points in the total efficiency. We finally decided to allow a maximum number of six hits in any wire chamber in the replay analysis.

An additional list of hot wires was created to allow for more wires to be ignored by the analyzer. Up to nine more wires for each chamber could be removed in this way. The improvement in the total efficiency was up to $7-8$ percentage points when all wires firing more than $3-4$ times as often as their neighboring wires were excluded from the analysis. This demonstrated a clear need for ignoring the hot wires. We decided to do a special initial replay of all runs with π^0 data to establish consistent and complete hot wire lists.

The total on-line wire chamber efficiency (Eq. (3.10)) is not affected by the replay analysis because the events that did not convert properly, and hence made the efficiency less than perfect, were never put on tape. With the same software parameters as used on-line any replay efficiency calculation must yield 100% efficiency. However, with the new value of the maximum number of hits allowed and with the extended lists of hot wires, some additional events now failed the conversion tests in replay. To determine the effect of this, it was necessary also to calculate a replay wire chamber efficiency according to Eq. (3.10).

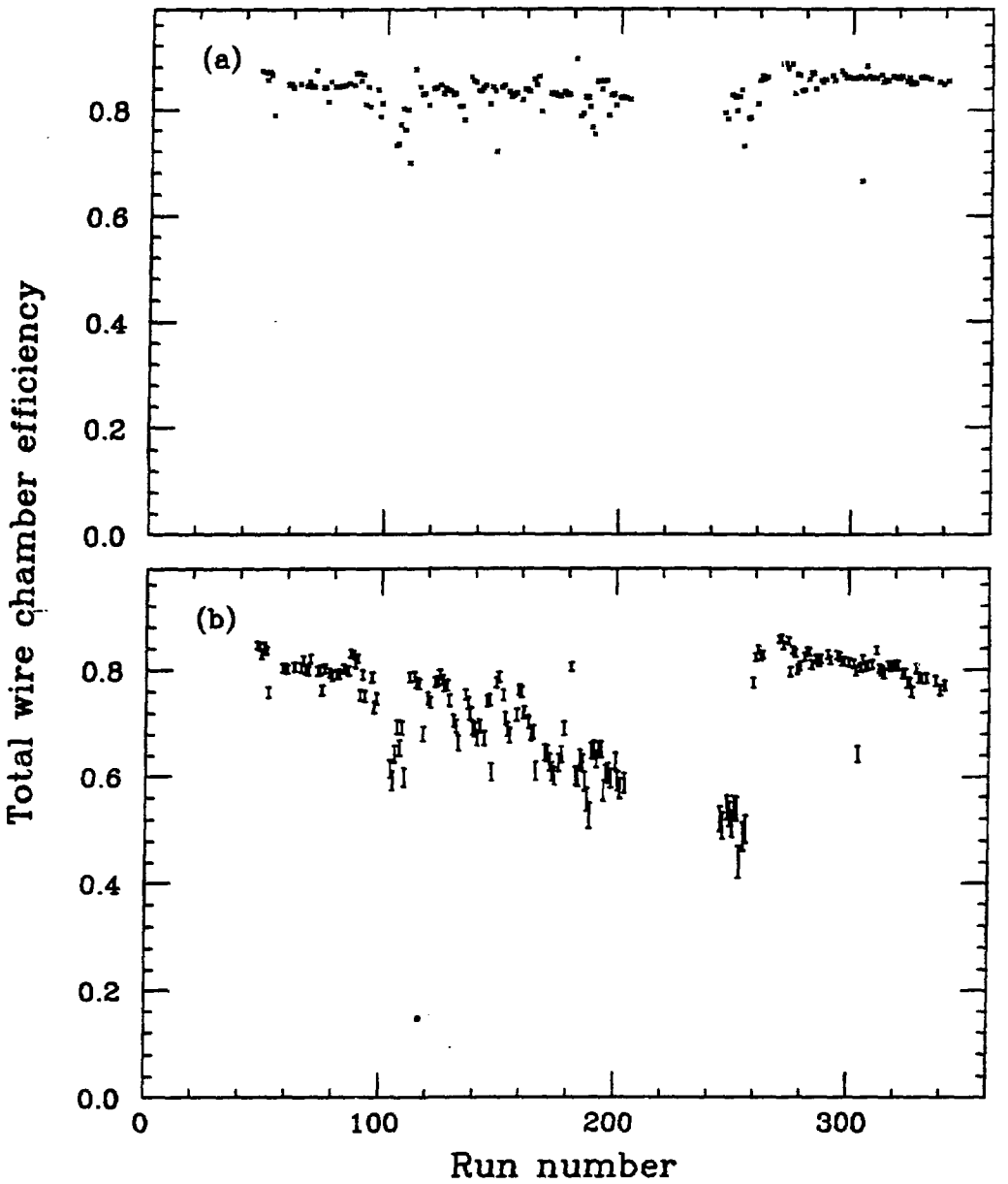

Figure 3.8. Total wire chamber efficiencies as a function of run number. The figure shows the development of this parameter over time. In (a) the on-line values are displayed. They appear fairly constant, and they are mostly in the 80 – 90% range. (b) shows the final values used in the data analysis. These are in most cases considerably worse than the standard values of (a), and there is a clear trend of decreased efficiency over time. The indicated uncertainties are explained in the text. The dramatic improvement after run 256 was due to repair work on a power supply for the wire chamber readout electronics.

Finally, one must catch the remaining, and previously unaccounted for, events that are failed by the tracing routine (which is run at a later stage in the analysis and only if the conversion tests are passed). This routine rejects events where any individual wire chamber is left with more than five hits (after removal of hits on wires listed as hot). We took these failed events into account by introducing a "tracing efficiency" $\epsilon_{\rm tr}$ defined by

$$\epsilon_{\rm tr} \equiv \frac{N_{\rm tot} - F_{\rm c}}{N_{\rm tot} - F_{\rm c} + F_{\rm tr}} \tag{3.11}$$

where $N_{\rm tot}$ is the total number of events that were put on tape, $F_{\rm c}$ is the number of events that failed the convergence test in replay, and $F_{\rm tr}$ is the number of events failed by the tracing routine because of too many wire chamber hits.

The total wire chamber efficiency must be the product of these independent efficiencies:

$$\epsilon_{\rm wc} = \epsilon_{\rm wc}^{\text{on-line}} \cdot \epsilon_{\rm wc}^{\text{off-line}} \cdot \epsilon_{\rm tr}. \tag{3.12}$$

The on-line and off-line efficiencies referred to here are both calculated by the method that led to Eq. (3.10), the former during data acquisition and the latter during data replay. In the final data analysis the total wire chamber efficiency was calculated individually for each run using Eq. (3.12). Fig. 3.8 shows these final efficiencies together with the on-line values that were used initially. A dramatic improvement of the efficiency is seen after run 256. At this point a faulty power supply for the PCOS II readout electronics was repaired. (It had been delivering power at 4.92 V instead of the nominal (5.35 ± 0.10) V.)

One also needs an estimate of the uncertainty in the wire chamber efficiency calculations. This uncertainty had to be assigned based on the experience acquired during all the testing described above. Generally, it seemed that the uncertainty was rather small when the efficiency was good, but that it could become significant when the efficiency was poorer. In the end, we applied the following parabolic function to describe the uncertainty:

$$\Delta\epsilon_{\rm wc} = a\,(1 - \epsilon_{\rm wc})^2 + b \tag{3.13}$$

where a and b are constants determined by the conditions $\Delta\epsilon_{\rm wc}(\epsilon_{\rm wc} = 100\%) = 0.5\%$ and $\Delta\epsilon_{\rm wc}(\epsilon_{\rm wc} = 50\%) = 2.5\%$. (This formula would be incorrect for very low efficiencies because then the efficiency would again be more accurately determined. This consideration has no relevance to our data, however.)

3.3.5 Conversion Efficiency

We have already discussed the efficiency of the π^0 spectrometer wire chamber system (Sec. 3.3.4). Its performance tends to vary significantly during an experiment, and the efficiency has to be determined on a run-to-run basis. Detection is also limited by the energy and angular acceptances of the spectrometer (Sec. 3.3.2). This subsection contains a discussion of the efficiency of the photon conversion in the spectrometer arms. This quantity is measured in special runs during the experiment, and any inefficiencies not treated explicitly in the subsections above (for example attenuation of the photons in the air and in the spectrometer parts or scintillators not being 100% efficient) will all automatically become part of this experimental "conversion efficiency".

This subsection is split into two parts: the first part gives a general description of the π^0 spectrometer conversion efficiency, while the second part presents our efficiency measurements.

3.3.5.1 General

Each spectrometer arm has three converter planes (cf. Fig. 2.3), but a large fraction of the photons still go through all of them without converting. The π^0 spectrometer was designed to optimize the number of conversions while keeping at a minimum undesirable effects such as multiple scattering, absorption of the charged particles, and many charged prongs.[62,61] The chosen configuration with relatively thin converters was arrived at after extensive Monte Carlo simulations of the above effects.

Empirically, it has been found that the conversion efficiency of a photon of energy E_γ in one converter plane can be expressed as[79,80]

$$\epsilon_{cp} = 0.28 + 0.1 \cdot \log\left(\frac{E_\gamma}{100\,\mathrm{MeV}}\right). \tag{3.14}$$

That is, ϵ_{cp} is almost independent of the photon energy. Since the π^0 spectrometer requires two photons of nearly the same energy for π^0 detection, one can use

$$E_\gamma = \frac{1}{2}\left(T_{\pi^0} + m_{\pi^0}\right) \tag{3.15}$$

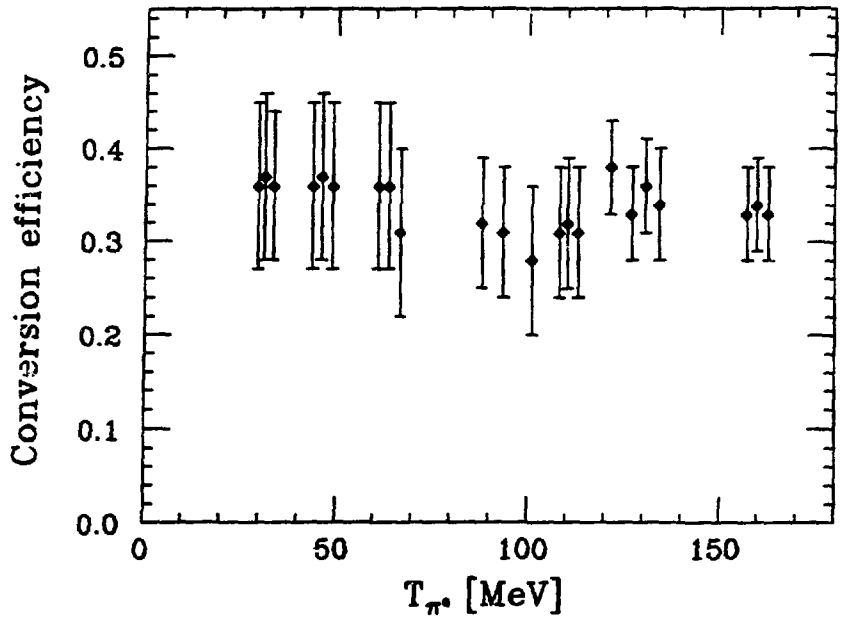

Figure 3.9. π^0 spectrometer conversion efficiency. The efficiency is plotted as a function of the kinetic energy of the π^0. From Ref. 22.

in Eq. (3.14). The total π^0 spectrometer conversion efficiency is

$$\epsilon_c = \left[1 - (1 - \epsilon_{cp})^3\right]^2 . \tag{3.16}$$

For a 100 MeV π^0 the above formulas lead to a total conversion efficiency of approximately 41%.

Experimentally the "conversion efficiency" is defined as

$$\epsilon_c^{\rm exp} \equiv \frac{\Delta\Omega_{\pi^0}}{\Delta\Omega_{\rm MC}} , \tag{3.17}$$

where $\Delta\Omega_{\pi^0}$ is the π^0 spectrometer solid angle determined from the experiment, and $\Delta\Omega_{\rm MC}$ is the corresponding solid angle calculated by PIANG as described in Sec. 3.3.2. One experimental study of the π^0 spectrometer conversion efficiency has been published by Ashery *et al.*[22] The results of their measurements are shown in Fig. 3.9. As expected from Eq. (3.14), there is no strong energy dependence in their data. This confirms that the Monte Carlo simulation PIANG indeed catches all the geometric (energy-dependent) effects. All the measured efficiencies are lower than the 41% conversion efficiency calculated from Eq. (3.16). This may be seen as a manifestation

of other inefficiencies not included in the calculation. In any case, because they are independent of energy, they may be considered accounted for when one measures the conversion efficiency using Eq. (3.17). Ref. 79 provides a thorough treatment of the various factors influencing the efficiency.

3.3.5.2 Our Measurements

We measured the π^0 spectrometer conversion efficiency for all four setups used in the experiment. It was measured at three different π^0 energies for each setup. These energies were chosen with reference to the energy acceptance curves in Fig. 3.5. One measurement was done at the energy corresponding to the peak of each curve, and two more were made at the energies corresponding to 50% of this acceptance. This provided a total of 12 independent measurements.

The general idea is that one can use a measurement of a known cross section on a known target to deduce the conversion efficiency. We chose the reaction

$$\pi^- + p \rightarrow \pi^0 + n.$$

Measurements were made using a polyethylene (CH_2) target of 0.551 g/cm^2 to provide essentially free protons and a carbon target of 0.289 g/cm^2 for background subtractions.

A complicating factor was the large angular acceptance of the π^0 spectrometer, which caused a kinematic broadening of the measured spectra. To reduce this broadening, a kinematic correction $\Delta T_{\pi^0}(\theta - \theta_{\pi^0})$ was applied to the measured kinetic energy of π^0's detected at angles θ not equal to the nominal π^0 angle θ_{π^0}:

$$T_{\pi^0}(\theta) \rightarrow T_{\pi^0}(\theta) - \Delta T_{\pi^0}(\theta - \theta_{\pi^0}), \tag{3.18}$$

where

$$\Delta T_{\pi^0}(\theta - \theta_{\pi^0}) = \frac{dT_{\pi^0}}{d\theta} \cdot (\theta - \theta_{\pi^0}) + \frac{1}{2} \frac{d^2T_{\pi^0}}{d\theta^2} \cdot (\theta - \theta_{\pi^0})^2. \tag{3.19}$$

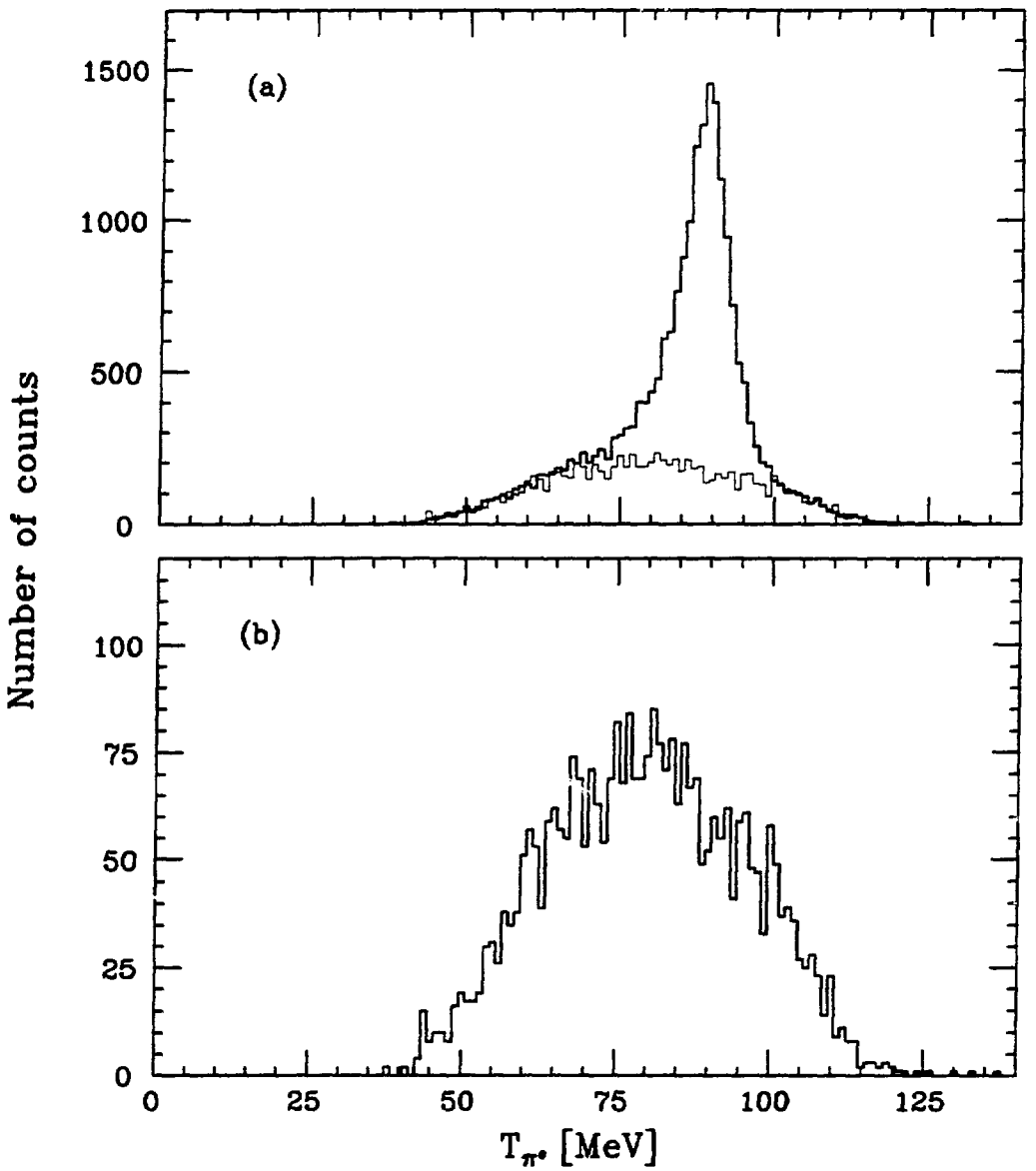

Figure 3.10. Examples of (π^-, π^0) measurements. (a) is with a polyethylene (CH_2) target and (b) with a carbon target. In both cases the π^0 angle was $\theta_{\pi^0} = 80°$ with an angular acceptance of $\theta_{\pi^0} \pm 12°$, and the incident beam energy was 122.0 MeV. The energy of the ejected π^0's was 90.0 MeV, corresponding to the peak of the acceptance curve at this setup. The horizontal axis is the kinetic energy of the detected π^0's, and the vertical axis shows the uncorrected number of counts for each 1 MeV energy bin. The fine drawn curve in (a) shows the carbon data from (b) scaled by the target densities and the amounts of beam used. The data shown have been adjusted for the kinematic broadening due to the large angular acceptance of the π^0 spectrometer.

The derivatives were found from two-body kinematics calculations by running the program KINREL.[70] Since the only cross sections calculated in our analysis were based on the total number of detected π^0's, our results were not affected by the kinematic correction, but the correction was still useful for our viewing and interpreting the data, and it was applied in all replay analysis of the conversion efficiency runs. An example of π^0 energy spectra from these measurements is given in Fig. 3.10.

Experimental cross sections were obtained for each target separately using the formula

$$\left(\frac{d\sigma}{d\Omega_{\pi^0}}\right)^{\exp} = \frac{N'_{\pi^0}}{N'_{\pi^-}\frac{n_t}{\cos\theta_t}\Delta\Omega_{\rm MC}}. \tag{3.20}$$

In this expression N'_{π^0} is the "real" number of π^0's detected; it is the total number of particles properly identified as good π^0's after corrections for accidental coincidences in the spectrometer (see Sec. 3.3.3) and photon attenuation losses in the target (Sec. 3.2) have been applied. The fraction of accidental coincidences was typically $1.5-2.0\%$. Photon attenuation losses are less than 2% (cf. Fig. 3.4a). N'_{π^-} is the effective number of beam pions incident on the target:

$$N'_{\pi^-} = \sum_i N^i_{\pi^-} \cdot \epsilon^i_{\rm live} \cdot \epsilon^i_{\rm wc} \tag{3.21}$$

where the summation is over all runs included in the measurement. $N^i_{\pi^-}$ is the total number of incident pions in run i as determined by the calibration procedure described in Sec. 3.1, $\epsilon^i_{\rm live}$ is the "livetime" (the fraction of the total amount of beam delivered in run i that could be utilized by our data acquisition system), and $\epsilon^i_{\rm wc}$ is the total wire chamber efficiency according to Eq. (3.12) for this run. The livetime was typically $50-80\%$ during the runs of the conversion efficiency study. The remaining parameters in Eq. (3.20) are the density n_t of target "molecules" (CH_2 or C) per unit area, the target angle θ_t, and the spectrometer solid angle $\Delta\Omega_{\rm MC}$ as calculated by PIANG for the target in use.

Traditionally, one has calculated $\Delta\Omega_{\rm MC}$ at the π^0 energy that corresponds to the kinematics for the nominal π^0 angle. However, because we are studying events in angular bins up to $\pm 12°$around this nominal central angle, the energy range of the π^0's we are using is rather large. In the example shown in Fig. 3.11a, the difference in

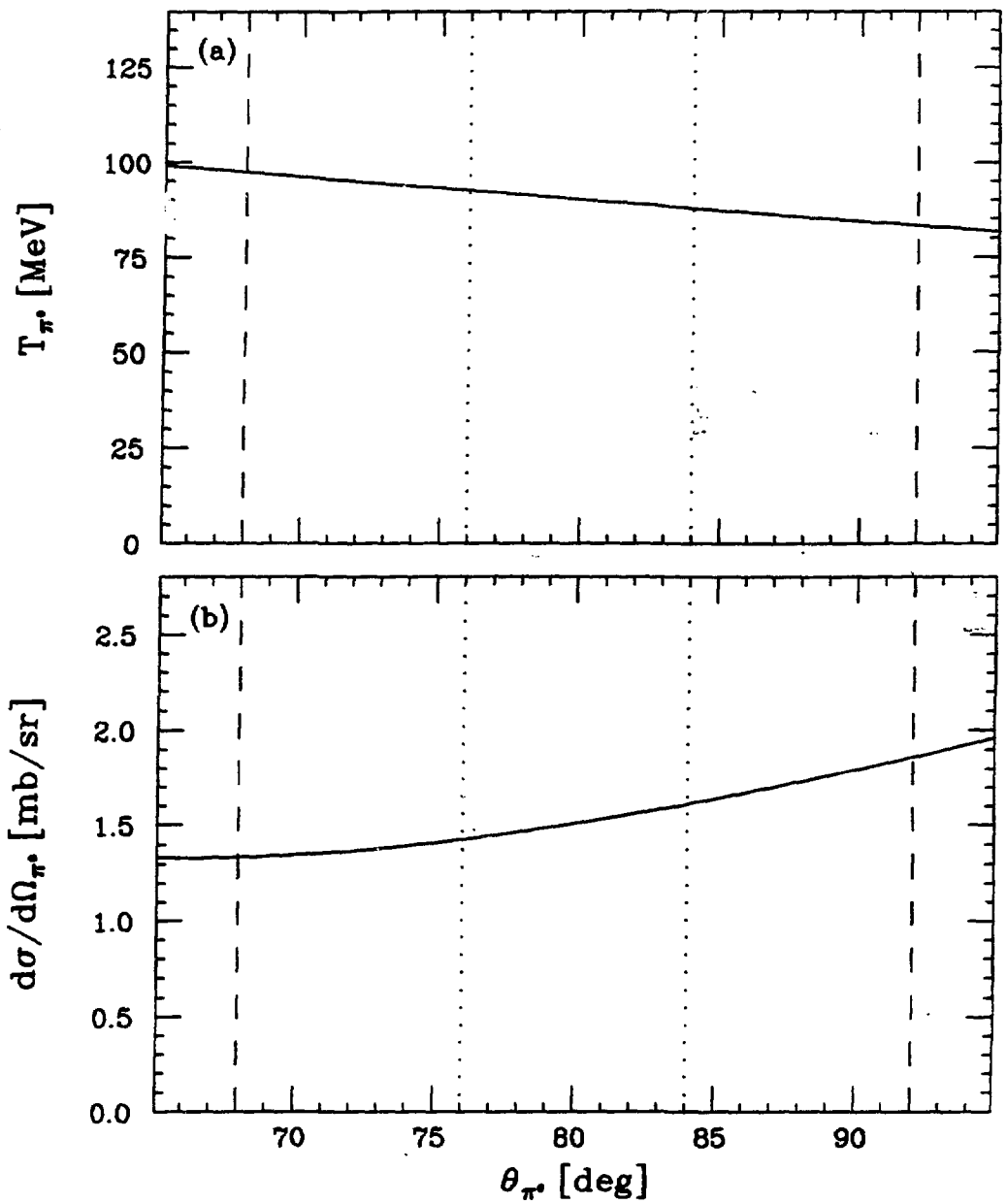

Figure 3.11. Angular distributions for $H(\pi^-, \pi^0)$. (a) shows the π^0 kinetic energy and (b) shows the differential cross section. The calculations are for an incident beam energy of 122.0 MeV, which was used for one of the three measurements done at 80°. The vertical lines show the extent of the π^0 spectrometer angular bins used in the analysis; the dotted lines indicate the smaller bin (76°−84°), and the dashed lines indicate the larger bin (68°−92°). The kinetic energies were calculated using the program KINREL,[70] the cross sections using SAID.[16]

energy over the spectrometer angular acceptance is approximately 15 MeV. Looking at the π^0 spectrometer energy acceptance curves calculated for water targets in Fig. 3.5, we see that applying the acceptance for the central energy to all detected π^0's cannot be justified. This would be particularly inaccurate for the measurements done at the energies corresponding to the peak of each acceptance curve; under such circumstances the acceptance for π^0's of all other energies detected will be lower than the central value assumed in the calculations.

We decided to calculate $\Delta\Omega_{MC}$ by splitting the large angular bins into a number of sub-bins with a width of 2°. PIANG was then run for each of these bins with a π^0 energy corresponding to the central value for each bin. Because the differential cross section for (π^-,π^0) varies with the π^0 angle (see Fig 3.11b), the individual 2° bin acceptances had to be weighted with the appropriate cross section values when the results for the sub-bins were added together. The values obtained for $\Delta\Omega_{MC}$ in this way were on the average 1.8% smaller than the "traditional" values for the ±12° angular bin for the measurements done at the peak of the acceptance curves, and 1.2% smaller for the measurements done at the 50% level of the acceptance curves.

The differential cross sections used to weigh the acceptances were calculated using the program SAID[14] which calculates pion-nucleon cross sections by partial-wave analysis.[15] Our calculation was based on an updated version[16] of the partial-wave solution described in Ref. 15.

The cross section for $H(\pi^-,\pi^0)$can be calculated from the measurements on CH_2 and C:

$$\left(\frac{d\sigma}{d\Omega_{\pi^0}}\right)_H^{exp} = \frac{1}{2}\left[\left(\frac{d\sigma}{d\Omega_{\pi^0}}\right)_{CH_2}^{exp} - \left(\frac{d\sigma}{d\Omega_{\pi^0}}\right)_C^{exp}\right]. \tag{3.22}$$

To calculate the experimental conversion efficiencies, differential cross sections measured according to Eq. (3.22) had to be compared to established values for these cross sections. We used the program SAID to obtain these values. The ratio

$$\epsilon_c^{exp} = \left(\frac{d\sigma}{d\Omega_{\pi^0}}\right)_H^{exp} \Big/ \left\langle\frac{d\sigma}{d\Omega_{\pi^0}}\right\rangle_H^{SAID}, \tag{3.23}$$

where the superscript SAID indicates cross sections obtained from the program SAID, is equivalent to the definition of the experimental conversion efficiency in Eq. (3.17).

Table 3.1. Measurements of the experimental conversion efficiency. All results are for the larger π^0 angular acceptance bin ($\theta_{\pi^0} \pm 12°$). (a) lists the measured differential cross section. (b) contains quantities derived from these. The superscript SAID indicates cross sections calculated by the program SAID. These cross sections are averaged over the angular acceptance.

(a)

θ_{π^0} [deg]	T_{π^-} [MeV]	T_{π^0} [MeV]	$\left(\frac{d\sigma}{d\Omega_{\pi^0}}\right)^{exp}_{CH_2}$ [mb/sr]	$\left(\frac{d\sigma}{d\Omega_{\pi^0}}\right)^{exp}_{C}$ [mb/sr]
70.0	88.0	71.6	0.69 ± 0.04	0.28 ± 0.02
70.0	113.5	90.1	1.31 ± 0.07	0.59 ± 0.04
70.0	164.0	125.1	3.90 ± 0.17	1.88 ± 0.09
80.0	88.0	67.3	0.90 ± 0.05	0.38 ± 0.03
80.0	122.0	90.0	1.89 ± 0.10	0.76 ± 0.04
80.0	178.0	125.1	3.82 ± 0.13	2.07 ± 0.08
110.0	77 0	50.1	1.44 ± 0.08	0.55 ± 0.03
110.0	117.5	71.9	2.61 ± 0.15	1.02 ± 0.08
110.0	186.0	104.9	4.84 ± 0.16	2.50 ± 0.10
129.7	86.5	50.0	2.23 ± 0.13	0.98 ± 0.07
129.7	118.5	65.1	3.16 ± 0.18	1.18 ± 0.07
129.7	178.0	90.2	5.34 ± 0.20	2.42 ± 0.11

(b)

θ_{π^0} [deg]	T_{π^-} [MeV]	T_{π^0} [MeV]	$\left(\frac{d\sigma}{d\Omega_{\pi^0}}\right)^{exp}_{H}$ [mb/sr]	$\left\langle\frac{d\sigma}{d\Omega_{\pi^0}}\right\rangle^{SAID}_{H}$ [mb/sr]	ϵ_C^{exp}
70.0	88.0	71.6	0.20 ± 0.01	0.63 ± 0.01	0.325 ± 0.022
70.0	113.5	90.1	0.36 ± 0.03	1.15 ± 0.02	0.314 ± 0.023
70.0	164.0	125.1	1.01 ± 0.06	2.46 ± 0.02	0.411 ± 0.024
80.0	88.0	67.3	0.26 ± 0.02	0.80 ± 0.01	0.328 ± 0.024
80.0	122.0	90.0	0.56 ± 0.03	1.53 ± 0.02	0.366 ± 0.022
80.0	178.0	125.1	0.88 ± 0.05	2.29 ± 0.01	0.384 ± 0.021
110.0	77.0	50.1	0.44 ± 0.03	1.19 ± 0.02	0.372 ± 0.023
110.0	117.5	71.9	0.79 ± 0.06	2.32 ± 0.02	0.342 ± 0.027
110.0	186.0	104.9	1.17 ± 0.06	2.80 ± 0.01	0.417 ± 0.021
129.7	86.5	50.0	0.63 ± 0.05	1.74 ± 0.02	0.361 ± 0.031
129.7	118.5	65.1	0.99 ± 0.06	2.90 ± 0.03	0.340 ± 0.022
129.7	178.0	90.2	1.46 ± 0.09	3.67 ± 0.02	0.398 ± 0.023

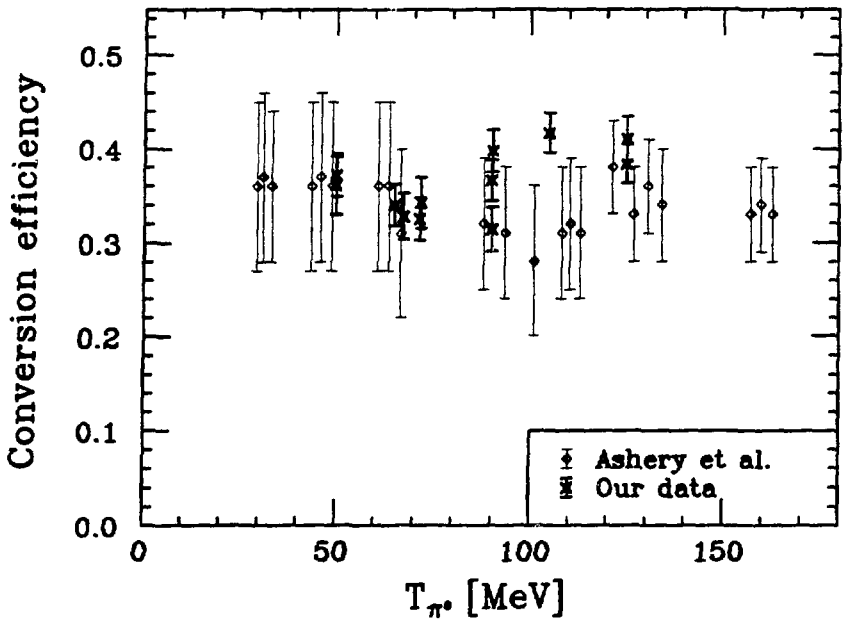

Figure 3.12. Comparison of experimental conversion efficiencies. The values of Ashery *et al.* are from Ref. 22. Our data include all π^0's in the largest π^0 angular bin considered. Efficiencies calculated from other angular bins do not differ much from the values shown in the figure.

The angle brackets indicate that the calculated cross section has been averaged over the appropriate π^0 spectrometer angular bin used (weighted by the acceptance of each 2° sub-bin). This averaging is necessary because the differential cross section varies considerably over the accepted angular ranges, as shown in Fig. 3.11b. All our measured cross sections and the resulting experimental conversion efficiencies based on data from the larger π^0 angular bin ($\theta_{\pi^0} \pm 12°$) are presented in Table 3.1. Conversion efficiencies were also calculated based on data from the smaller angular bin ($\theta_{\pi^0} \pm 4°$). The agreement with the larger bin is fairly good, but the statistical uncertainty is necessarily somewhat larger since the number of π^0's considered is smaller. Fig. 3.12 shows that our conversion efficiencies are in close agreement with the values found by Ashery *et al.* Our data show a slight increase of the efficiency with energy, however, while their measurements indicate that the efficiency is a flat or possibly decreasing function of the energy. One may note that the formulas in Eqs. (3.14) – (3.16) predict a slow increase in efficiency as the energy increases. Between $T_{\pi^0} = 50$ MeV and $T_{\pi^0} = 125$ MeV this predicted increase amounts to about 7.5%, which seems to be

reasonably well represented by our data.

The detailed algorithm for our analysis is given in Appendix C.

3.4 Thickness of Water Targets

To calculate a properly normalized cross section, one must know the precise thickness of the target. This was easily established for our solid targets, but rather complicated to measure for the water targets. We used four such targets during the experiment. They were designed to be 3 mm, 5 mm, 9 mm, and 12 mm thick, respectively. As described in Sec. 2.2.1, these targets consisted of two large, thin Mylar[59] windows mounted on a metal frame. The weight of the water made the Mylar windows bulge, and this bulging made it difficult to establish the correct thickness of the target at the position where the beam went through it.

Our method of establishing the target thicknesses is similar to the method described in Sec. 3.3.5.2 of measuring the π^0 spectrometer conversion efficiencies (cf. Sec. 2.2.1). We used the same reaction, $H(\pi^-,\pi^0)$, but this time the hydrogen was provided by water molecules (H_2O). Measurements were made at the same beam energies as those used for the conversion efficiency measurements. They were made twice for each target; one measurement was always made at the energy corresponding to the largest spectrometer acceptance, and the other was made at one of the two other energies used for efficiency measurements.

Combining Eqs. (3.20) and (3.23), we can write

$$\left(\frac{d\sigma}{d\Omega_{\pi^0}}\right)^{\mathrm{SAID}}_{\mathrm{H}} = \frac{N'_{\pi^0}}{N'_{\pi^-}\,\frac{n_t(\mathrm{H})}{\cos\theta_t}\,\epsilon_c^{\mathrm{exp}}\,\Delta\Omega_{\mathrm{MC}}}. \tag{3.24}$$

Provided N'_{π^0} can be properly established as the yield of π^0's from the hydrogen nuclei, this expression may be used to calculate the density $n_t(\mathrm{H})$ of hydrogen nuclei if the appropriate conversion efficiency $\epsilon_c^{\mathrm{exp}}$ is applied, or it may be used to calculate the product $n_t(\mathrm{H})\cdot\epsilon_c^{\mathrm{exp}}$. To find the density $n_t(\mathrm{O})$ of oxygen nuclei, which is what we eventually need in the analysis, $n_t(\mathrm{H})$ deduced from Eq. (3.24) must be divided by 2 (because there are twice as many hydrogen nuclei as oxygen nuclei in water).

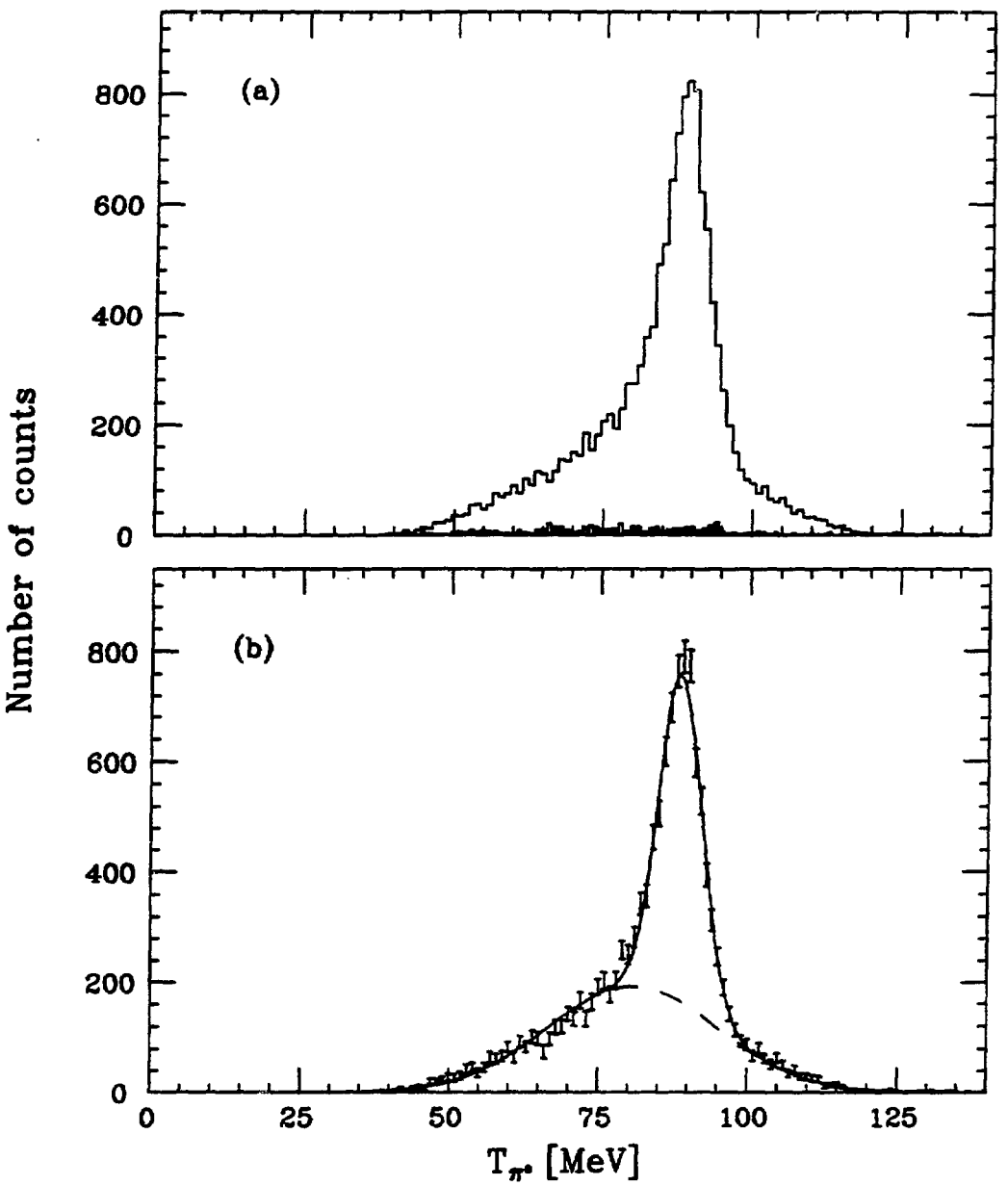

Figure 3.13. Example of π^0 energy spectra from target thickness measurements. All data shown were taken with a 122.0 MeV incident π^- beam. The π^0 angle was $\theta_{\pi^0} = 80°$, and the angular acceptance was $\theta_{\pi^0} \pm 12°$. (a) shows the raw data for the full target (histogram) with the empty target data, scaled by the amounts of beam used, overlayed (bargraph). In this example 4.3% of the full target data can be accounted for by the data obtained from the empty target. (b) shows a two-gaussian fit to the same data after bin-by-bin subtraction of the empty target data. The contribution from $H(\pi^-, \pi^0)$ is identified as the area of the narrower of the two gaussians.

Table 3.2. Measured thicknesses of the water targets. All results are for the larger π^0 angular acceptance bin ($\theta_{\pi^0} \pm 12°$). t_t^{nom} is the nominal (design) value of the thickness, and t_t is the corresponding measured value. $n_t(O)$ is the density of oxygen nuclei.

θ_{π^0} [deg]	T_{π^-} [MeV]	T_{π^0} [MeV]	t_t^{nom} [mm]	t_t [mm]	$n_t(O) \cdot \epsilon_c^{exp}$ [10^{-6} mb^{-1}]
70.0	88.0	71.6	3	3.5 ± 0.4	3.8 ± 0.4
70.0	113.5	90.1	3	3.1 ± 0.3	3.3 ± 0.2
80.0	122.0	90.0	5	5.3 ± 0.4	6.4 ± 0.4
80.0	178.0	125.1	5	6.5 ± 0.5	8.3 ± 0.4
110.0	117.5	71.9	9	5.5 ± 0.6	6.3 ± 0.5
110.0	186.0	104.9	9	6.1 ± 0.4	8.4 ± 0.4
129.7	118.5	65.1	12	9.0 ± 0.8	10.1 ± 0.7
129.7	178.0	90.2	12	9.2 ± 0.7	12.1 ± 0.5

All quantities in Eq. (3.24) with the exception of N'_{π^0} were determined as explained before in Sec. 3.3.5.2. Data were taken both with full and empty targets so that background contributions could be subtracted. In all replay analysis the kinematic correction described earlier (Eq. (3.19)) was applied. Fig. 3.13a shows an example of raw energy spectra. The contribution from the empty target was relatively small (approximately 11.9%, 4.5%, 3.4%, and 2.5% for the $\pm 12°$ angular acceptance bin around $\theta_{\pi^0} = 70.0°$, 80.0°, 110.0°, and 129.7°, respectively). Corrections were made for accidental coincidences (typically $1.5-2.5\%$, cf. Sec. 3.3.3) before the empty target data were subtracted from the full target data. This subtraction was done bin by bin for each 1 MeV π^0 energy bin. We did not have an O target to facilitate subtraction of the contribution from the oxygen nuclei in the water. Instead the yield from the hydrogen had to be determined by fitting to the full H_2O spectra. We decided to fit a sum of two gaussians to the data. An example is shown in Fig. 3.13b. (All curve fitting in this work was done using the program MINUIT[81] which allows fitting to almost any mathematical function.) After being corrected for photon attenuation losses in the target (cf. Fig. 3.4b), the area of the narrower gaussian is taken to be the proper π^0 yield N'_{π^0} from hydrogen.

Table 3.3. Final water target thicknesses.

Nominal thickness [mm]	3	5	9	12
Measured thickness [mm]	3.24 ± 0.25	5.85 ± 0.32	5.90 ± 0.33	9.07 ± 0.51

The absolute target thickness t_t is related to $n_t(\mathrm{O})$ by

$$t_t = n_t(\mathrm{O}) \cdot \frac{A_w}{N_A \, \rho_w}, \tag{3.25}$$

where A_w is the molecular weight of water, ρ_w is its density, and N_A is the Avogadro constant.

The results of our target thickness measurements are listed in Table 3.2. We see that the thicknesses of the thicker targets deviate significantly from the nominal design values of 9 mm and 12 mm. (One reason for the deviation for the 9 mm target could be that the original Mylar windows had been replaced at LAMPF; the new windows may have a different tension.) The results shown are all based on data from the larger angular bin used in the analysis ($\theta_{\pi^0} \pm 12°$). Results from the smaller bin ($\theta_{\pi^0} \pm 4°$) are in good agreement with the listed values.

We used the average of the two thickness values t_t calculated for each target for the $\pm 12°$ angular bin as our "official" target thicknesses. The final numbers are listed in Table 3.3. The agreement between the two values for the density $\times$ efficiency product ($n_t(\mathrm{O}) \cdot \epsilon_c^{\mathrm{exp}}$) for each target is poorer than the agreement between the thicknesses (see Table 3.2), as was to be expected since the conversion efficiency had been found to vary with pion kinetic energy (cf. Table 3.1). This product is used more often in the analysis than the absolute thickness. We did not find it justified to average the various values of the density $\times$ efficiency product. Instead we used the values measured under conditions as similar as possible to those found during the real data runs, that is, we used the values obtained at π^0 energies corresponding to the peak in each π^0 spectrometer energy acceptance curve (Fig. 3.5).

The detailed algorithm for our analysis is given in Appendix C.

3.5 The Proton Arm

The proton arm is the other major detector system used in the experiment. It was made especially for this experiment, and its design is described in detail in Sec. 2.2.3. It consists of plastic scintillators attached to photomultiplier tubes. This is considered to be a highly efficient way of proton detection,[82] and we will assume in the analysis that the detectors were indeed 100% efficient.

The subsections below discuss the problems of detector stabilization, particle identification, and absolute energy calibration. At the end there is a discussion of the resolution obtained with the proton detector system.

3.5.1 Stabilization

The eight E detectors (the main detectors stopping the protons, cf. Fig. 2.4) have light-emitting diodes (LED's) built into them. By regularly firing these LED's during the experiment, one can in principle monitor any changes and drifts in the detector system. If some of the LED data sampled should change over time, the corresponding part of the system must have changed as well, and appropriate corrections can be applied in software.

In light of this we regularly made special runs in which the LED's were turned on while ordinary data taking was disabled. By the end of the experiment more than 40 such runs had been carried out. Each run was quite quick, about 10 minutes of data-taking, but we soon learned that there were instabilities connected to the warming up of the LED's, and that more consistent data were obtained if the LED's were given $10 - 15$ minutes to warm up before data were taken. In most of the runs the system appeared to work very well, and sharply defined LED energy peaks were found. A typical example is shown in Fig. 3.14.

There were some problems, however. While most runs showed narrow, well-defined peaks, the positions of these peaks seemed to drift rather strongly from run to run, particularly for detectors E5 and E7. Detector E7 also several times showed up with two peaks in the same run. This led us to believe that we could not trust the stability

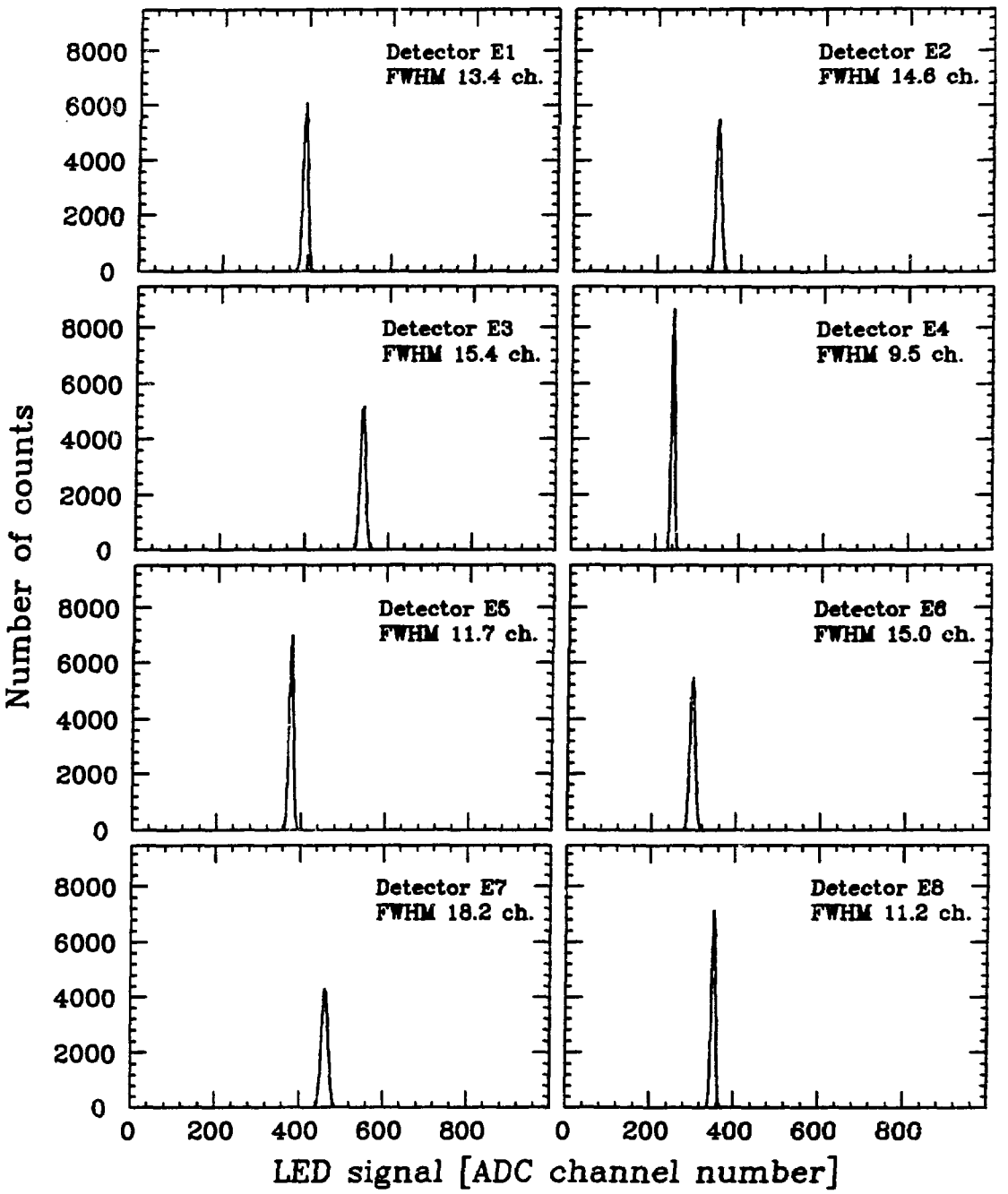

Figure 3.14. LED data for all E detectors as measured in run 162. The horizontal axis shows the ADC channel numbers where the signals were detected. We used 1024 channel ADC's. The peak positions are (as in most runs) very well defined. The widths vary somewhat, reflecting accidental differences in the detector hardware, but all peaks are quite narrow.

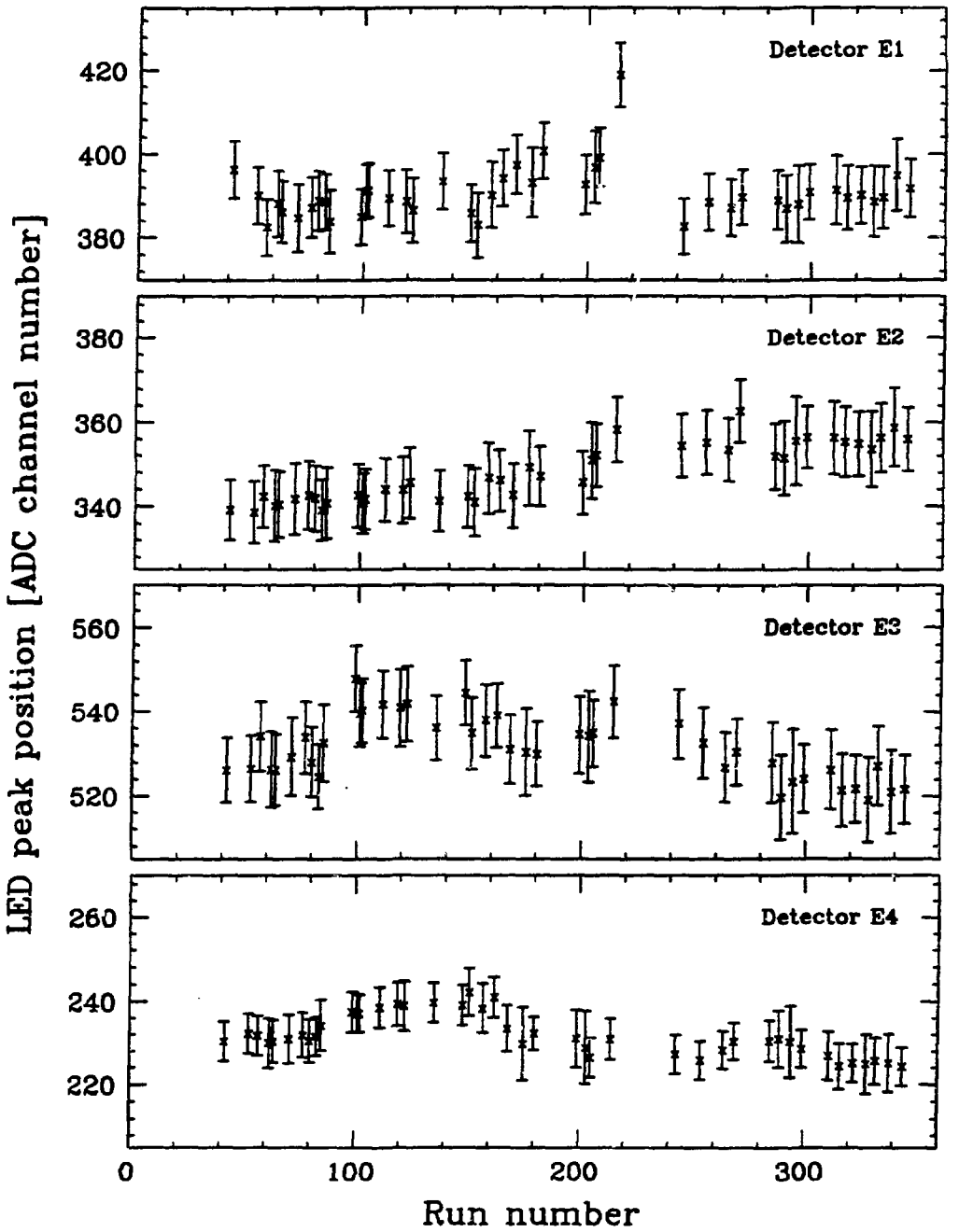

Figure 3.15. Compiled results of all LED runs for proton detectors E1 – E4. The vertical axis shows the ADC channel of the peak position. The indicated width is the FWHM of the peak, not the uncertainty in the peak position. The statistical uncertainty in the peak positions were typically very small, considerably less than one channel.

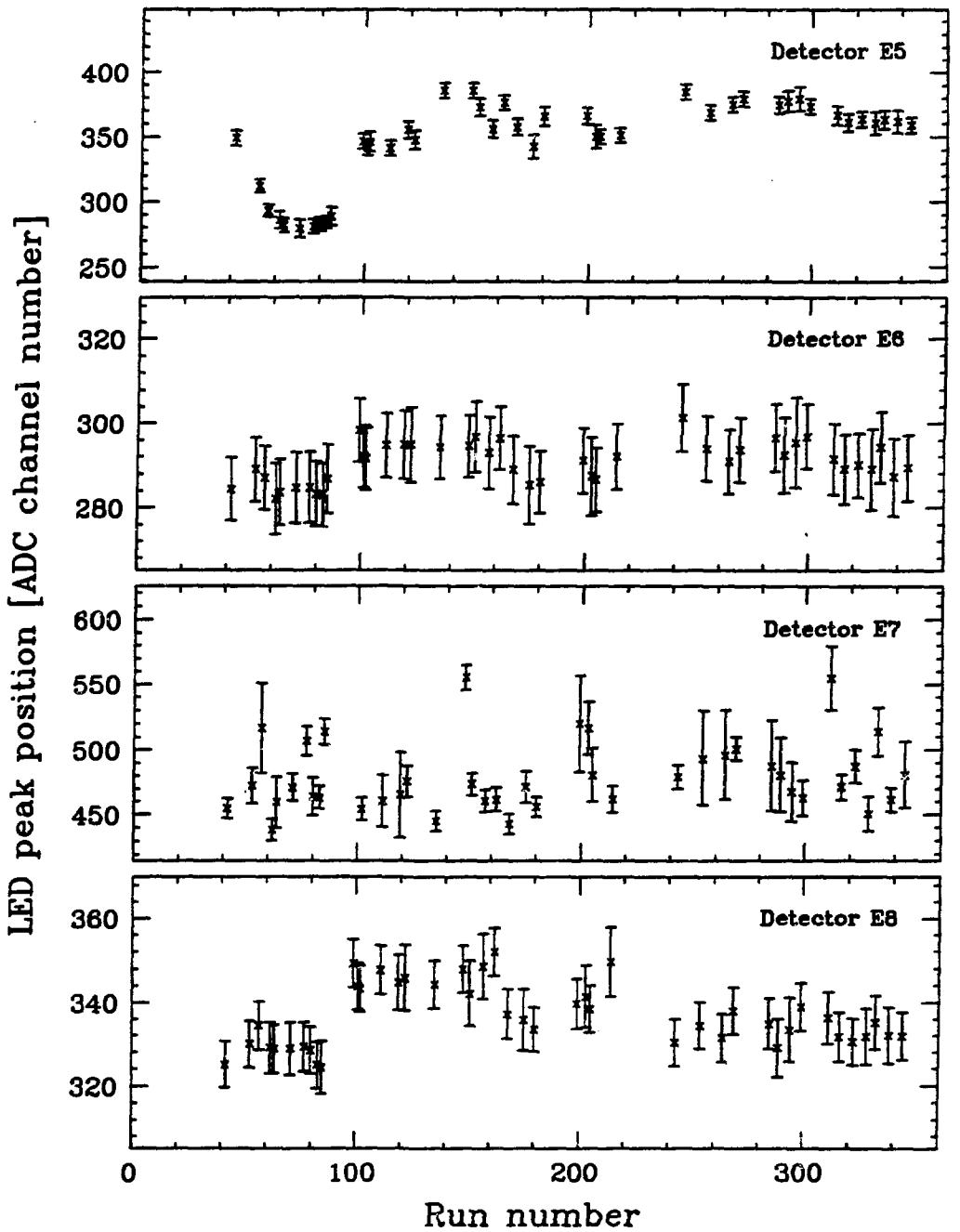

Figure 3.16. Compiled results of all LED runs for proton detectors E5 – E8. The vertical axis shows the ADC channel of the peak position. The indicated width is the FWHM of the peak, not the uncertainty in the peak position. The statistical uncertainty in the peak positions were typically very small, considerably less than one channel.

of the LED system, at least not any more than we could trust the stability of the detector system the LED's were supposed to monitor.

All the results from the LED runs are collected in Figs. 3.15 – 3.16. The large widths of some of the detector E7 data points are due to the double peaks. Note that the vertical scale showing the ADC channel number of the peak position is more compressed for detectors E5 and E7. It is the opinion of the author that these plots can be taken as indicators of the overall performance of the proton detectors during the experiment, but that using their information for actual run-by-run software corrections of the energy calibration is not feasible.

The LED's proved to be useful during the experiment as a qualitative check of the proton detector system. If something was seriously wrong with a detector, or if a connection was broken, it would show up immediately in the next LED run.

In future experiments one should consider improving the LED stabilization scheme. Two related methods have been used successfully by other experimenters. The first involves placing light sensitive diodes near each LED. These photodiodes are generally more stable than LED's, and they are used to monitor the light output from the LED's. The signals from the photodiodes can then be used to normalize the LED data, either in the off-line analysis[83] or actively on-line by adjusting the light output from each LED.[84]

The other method involves sending the same light signal to several or all detectors through optical fibers. At the same time this light signal is monitored by a reference detector which also receives signals from a radioactive source. Again schemes have been developed for both off-line[85] and on-line corrections.[86] Clearly, one could also use combinations of these ideas. Even a passive system where the same light signal is sent through fibers to all detectors without a special monitor would be possible, since then any drifts observed due to the light signal should appear similarly in all detectors, while real drifts of the detector gains would occur with no correlation between the detectors.

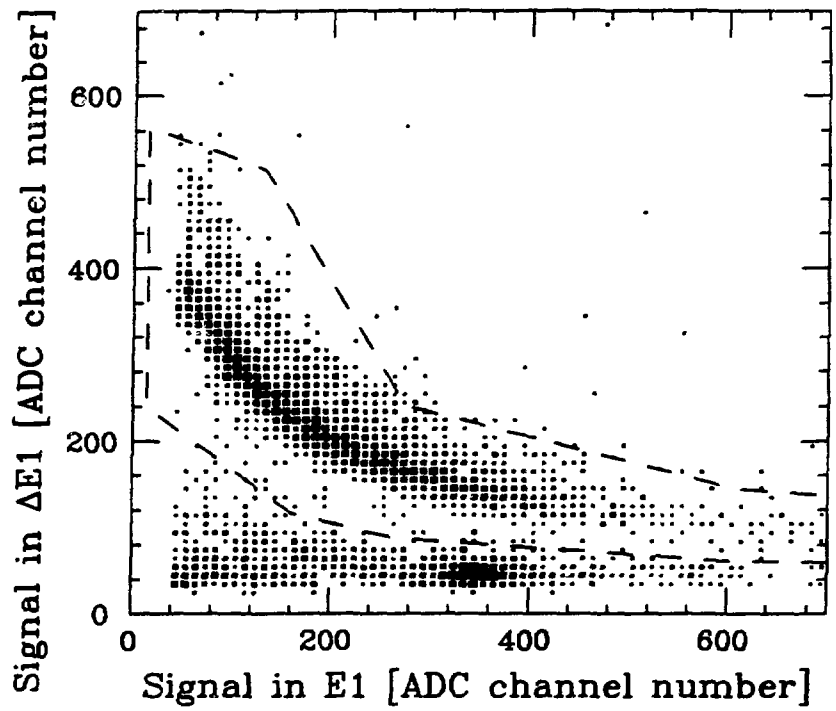

Figure 3.17. Proton band. The plot shows the energy deposited in a ΔE detector versus the energy deposited in the corresponding E detector. The protons fall into a clearly distinguishable band in the plot. The energies in the plot are all presented in the form of raw ADC signals. This example is for telescope 1. The proton angle was $\theta_p = 27.9°$. The particles below the proton band are mainly pions. The dashed line shows the proton identification cut applied in the data analysis. Only events inside this box were accepted as protons.

3.5.2 Particle Identification

As explained in Sec. 2.2.3, the main purpose of the ΔE–E configuration of the proton telescopes is to enable reliable proton identification. In a plot of the loss in the ΔE detector versus the loss in the E detector, the protons will form a separate band. An example of this is shown in Fig. 3.17.

In the data analysis we required that a "good" proton event should have its (E,ΔE) point within certain limits put around the proton band of the telescope in question. These limits were applied in software as two broken lines of up to five segments each. This is also illustrated in Fig. 3.17. Since no two detectors can be built exactly alike,

the limits had to be established separately for each proton telescope. Once established, these limits should ideally stay completely fixed for the duration of the experiment. However, because the photomultiplier tube gains and other system parameters might drift over time, we still checked the band positions separately for each of the four setups (the four π^0 angles used in the experiment); with the exception of telescope 5 there were only very small variations.

The band position observed in telescope 5 varied significantly even from run to run. It seemed to slide up and down along the ΔE-axis, indicating that detector ΔE5 may have been rather unstable. It never did, however, slide so far down that it got into the upper part of the pion region below. The solution to the problem of proton identification was therefore just to make sure that the proton band limits were wide enough to include all positions of the proton band for a given setup.

The proton band was easily recognized for all detectors in all setups. We therefore consider our proton identification to be quite reliable. The uncertainty in the particle identification enters as a direct uncertainty in the final cross sections. The number of particles in the areas around the boundaries of the proton bands suggest an uncertainty of about $1-2\%$ in the number of protons. We made the bands slightly wide. In this way a few pions and other particles may have been included, but we did not lose many protons, and most of the other particles would eventually fail some of the other requirements in the analysis anyway. We found 1% to be an appropriate estimate of the uncertainty due to the proton identification process.

3.5.3 Energy Calibration

One cannot perform meaningful calculations of the reaction kinematics unless all detectors are properly calibrated, that is, unless one knows the relationship between detected ADC channels and absolute energy units. We exposed each telescope to protons of well-known energies to map out this relationship. A polynomial could then be fitted to the calibration points found in this way to give an analytical expression valid for all energies.

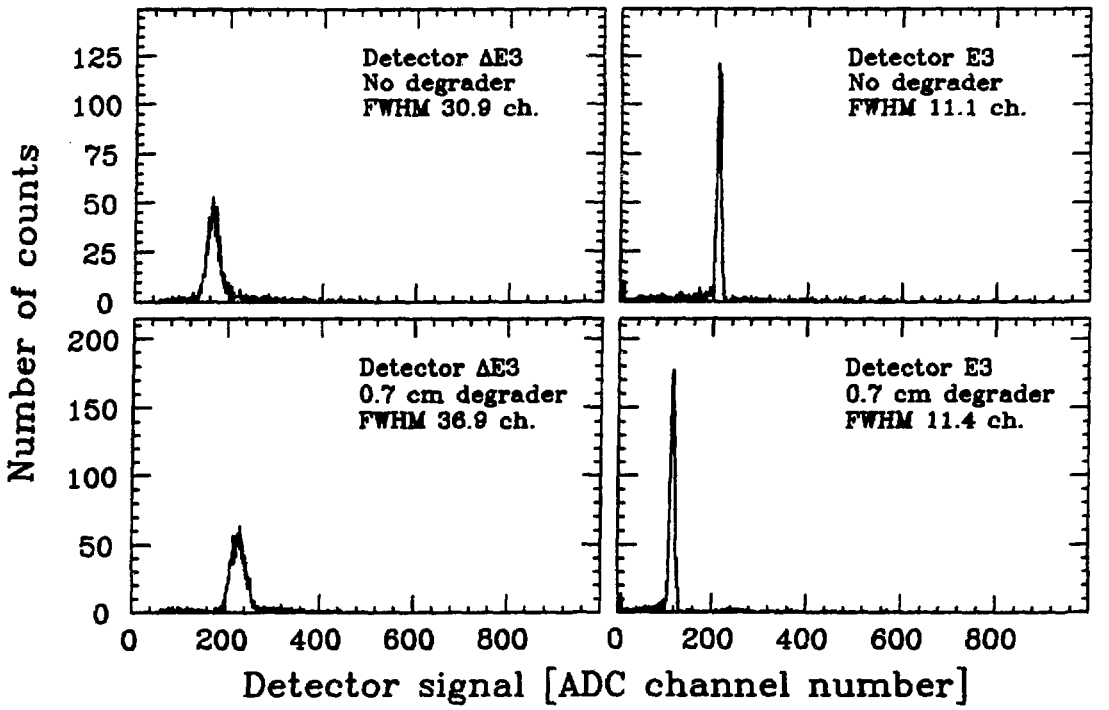

Figure 3.18. Raw energy spectra obtained by telescope 3 using direct beam protons. The channel was tuned for 230.0 MeV pion kinetic energy, corresponding to a proton energy of 60.5 MeV. The upper spectra are taken without a degrader (energies deposited are 3.7 MeV in ΔE3 and 55.2 MeV in E3), the lower spectra are taken with a 0.7 cm Al degrader (5.0 MeV in ΔE3, 35.5 MeV in E3). The contributions to the spectra from other particles have been suppressed by requiring the (E,ΔE) points to be within the "proton band" (cf. Fig. 3.17).

We used three methods of obtaining protons of known energies:

$$(i) \qquad \text{Direct beam protons,}$$

$$(ii) \qquad \pi^+ + d \rightarrow 2p,$$

and

$$(iii) \qquad \pi^+ + p \rightarrow \pi^+ + p.$$

Method (i) is the easiest. The π^+ beam in LEP is accompanied by a substantial number of protons.[57] These protons are normally removed by inserting absorbers in the beam channel. For our calibration runs we simply did not insert these absorbers.

Table 3.4. Proton detector calibration points. The table lists all energies used for calibration measurements. The columns labeled "ΔE" and "E" show the energies deposited in these detectors for the various beams. The methods (*i*) – (*iii*) are explained in detail in the text.

method	T_{π^+} [MeV]	T_p [MeV]	degrader [cm Al]	ΔE [MeV]	E [MeV]
(*i*)	230.0	60.5	—	3.7	55.2
(*i*)	230.0	60.5	0.7	5.0	35.5
(*i*)	130.0	27.9	—	8.0	16.6
(*ii*)	130.0	140.5	—	1.9	136.8
(*ii*)	130.0	140.5	3.3	2.6	90.5
(*ii*)	130.0	123.8	—	2.1	119.6
(*ii*)	130.0	123.8	3.6	3.5	59.3
(*iii*)	130.0	40.1	—	6.1	26.9

The protons coming through the beam channel must have the same momentum as the pions the channel is tuned for. Since protons are much heavier than pions, they are therefore limited to fairly low kinetic energies. This method was used at two different beam energies. In addition, a 0.7 cm thick piece of aluminum (a degrader) was used at the higher beam energy to give a third proton energy. For details see Table 3.4, which lists all the calibration measurements. Typical examples of the data obtained by method (i) are shown in Fig. 3.18.

With method (*ii*) we obtained calibration data for two telescopes simultaneously. The proton telescopes were mounted 17° apart from each other on the proton arm (cf. Sec. 2.2.3). We positioned the proton arm such that the two telescopes to be studied were at $\theta_p = 71°$ and $\theta_p = 88°$. These telescopes were required to fire in coincidence with "paddle" detectors (cf. Sec. 2.2.4) positioned (on the other side of the beam) at −83.5° and −66.8°, respectively. The second set of detectors was only used to give a signal indicating that a particle (the other proton) had passed through. They were placed as far away from the target as possible to minimize their solid angle. The incident pion beam energy was 130.0 MeV. The target deuterons were provided by a 4.1 mm thick CD_2 target. This setup was used with and without aluminum degraders. See Table 3.4 for details. Some typical energy spectra are shown in Fig. 3.19.

Method (*iii*) was used only once to get an additional low-energy calibration point for

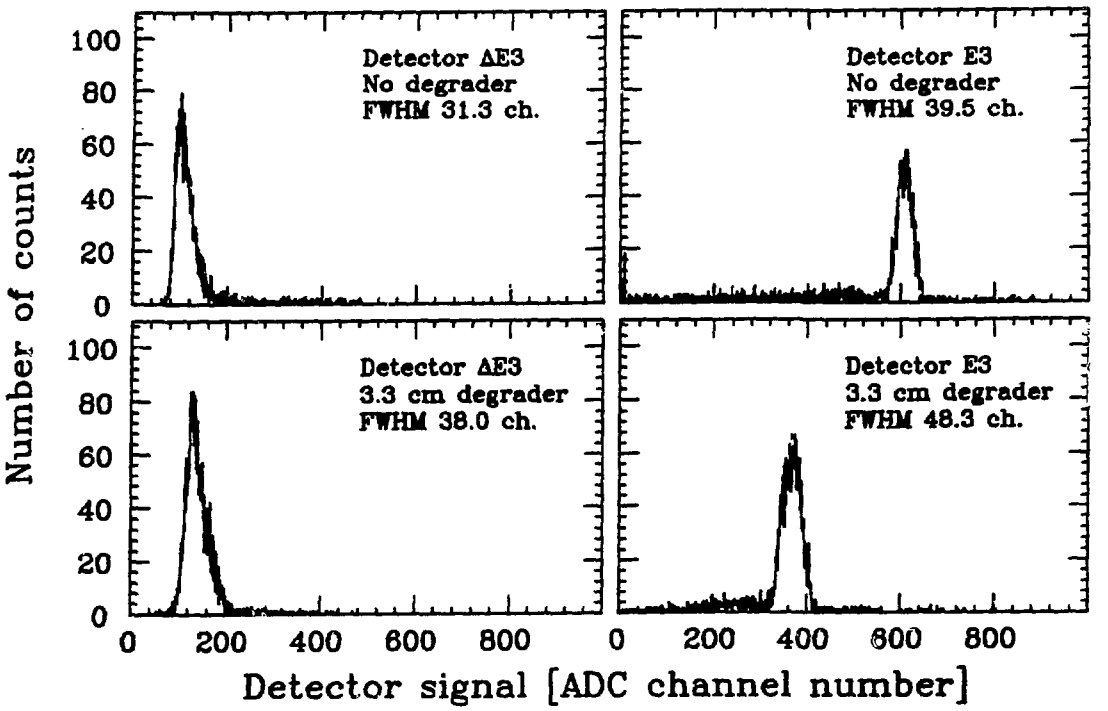

Figure 3.19. Raw energy spectra obtained by telescope 3 using the reaction $\pi^+ + d \rightarrow 2p$. The incident beam energy was 130.0 MeV, and the proton angle was 71.0°, corresponding to a proton energy of 140.5 MeV. The upper spectra were taken without a degrader (energies deposited are 1.9 MeV in ΔE3 and 136.8 MeV in E3), and the lower spectra were taken with a 3.3 cm Al degrader (2.6 MeV in ΔE3, 90.5 MeV in E3). The contributions to the spectra from other particles have been suppressed by requiring the (E,ΔE) points to be within the "proton band" (cf. Fig. 3.17).

telescope 4. (The high voltage for this telescope had been changed after all method (*i*) calibration measurements were completed.) We used a 6.4 mm thick polyethylene (CH_2) target and the same incident beam as for method (*ii*). We took our calibration data with the proton telescope at $\theta_p = 40.8°$ requiring a coincidence with the scintillator array at $-83.5°$ (for the scattered pion).

One additional calibration point was obtained by observing the signal from each ADC when the attached detector did not have a particle going through it. Such "pedestal" values can be adjusted on the ADC's. They were typically set around channel 10. (Since the information read from an ADC is a channel number between 0 and 1023, it is important that the pedestals also are non-negative. There is no direct way to

measure a negative pedestal position.)

Table 3.4 lists both the nominal proton energy for each calibration measurement (calculated by momentum matching for method (*i*) and by KINREL[70] for methods (*ii*) and (*iii*)), and the energies deposited in each detector. The latter values were established by calculating the energy loss in all the various media the protons go through (target, air, aluminum, tape, plastic scintillator). Energy is lost principally via interactions with the electrons of the media, and the loss per unit path length (the stopping power) can be calculated by the Bethe-Bloch formula (see for instance Ref. 76):

$$\frac{dE}{dx} \approx D\,\rho\,\frac{Z}{A}\frac{1}{\beta^2}\left[\ln\left(\frac{2m_e c^2}{I}\right) - \ln\left(\frac{1}{\beta^2} - 1\right) - \beta^2\right]. \tag{3.26}$$

In this equation D is a constant depending only on elementary physical quantities ($D = 0.3070\ \mathrm{MeV\,cm^2/g}$), ρ is the mass density of the medium, Z and A are its charge and mass numbers, β is the speed of the proton (relative to c, the speed of light), and m_e is the electron mass. I is a phenomenological constant for each element (ionization potential) and may be estimated to within 10% by

$$I \approx 16\,\mathrm{eV} \cdot Z^{0.9} \tag{3.27}$$

The protons mostly go through composite media; tape is treated as CH_2, plastic scintillators as $CH_{1.1}$, and air as $(N_2)_4O_2$. The stopping power of such media are taken to be

$$\left(\frac{dE}{dx}\right)_{\mathrm{comp}} = \rho \sum_i \frac{w_i}{\rho_i}\left(\frac{dE}{dx}\right)_i \tag{3.28}$$

where w_i is the partial density of element i in the medium, ρ_i is the mass density of this element used in calculating its stopping power in Eq. (3.26), and ρ is the mass density of the composite medium.

The energy calculations also take the target into account. It is assumed that the protons originate from the center of the target, and a loss of energy is calculated accordingly. To show the importance of the various losses, Table 3.5 lists how the energy is distributed in the telescopes for the calibration points obtained by methods (*ii*) and (*iii*). We see that a significant amount of energy is deposited outside of the active detectors (ΔE and E), particularly by low energy protons.

Table 3.5. Distribution of the proton energy in the telescopes. For each of the proton energies obtained by methods (*ii*) and (*iii*) this table lists the losses in the targets (CD_2 for method (*ii*), CH_2 for (*iii*)), the air, the degrader (3.3 cm for $T_p = 140.5$ MeV, 3.6 cm for $T_p = 123.8$ MeV), and the three layers of tape and aluminum foil around the detectors.

T_p [MeV]	target [MeV]	air [MeV]	degrader [MeV]	tape [MeV]	foil [MeV]	ΔE [MeV]	E [MeV]
140.5	1.2	0.3	—	0.3	0.1	1.9	136.8
140.5	1.2	0.3	45.5	0.4	0.1	2.6	90.5
123.8	1.4	0.4	—	0.3	0.1	2.1	119.6
123.8	1.4	0.3	58.7	0.6	0.1	3.5	59.3
40.1	5.0	1.0	—	1.0	0.2	6.1	26.9

The photomultiplier tube gains were fairly linear over the proton energies encountered in the experiment. We therefore decided to fit a second order polynomial to the calibration data, accounting for the ADC pedestals as raw data offsets. The proton kinetic energy observed in detector i (i goes from 1 to 16, 8 E detectors and 8 ΔE detectors) is then

$$(T_p)_i = a_i \left(T_i^{\text{raw}} - p_i\right) + b_i \left(T_i^{\text{raw}} - p_i\right)^2 , \tag{3.29}$$

where T_i^{raw} is the raw channel number read from the ADC. The other parameters, including the pedestal value p_i, are all determined by fitting Eq. (3.29) to the calibration data.

The statistical uncertainties in the calibration data are negligible. There are some uncertainties in the energy calculations. When making fits to the E detector data we assumed an uncertainty of 2.0 MeV in the calculated energies $(T_p)_i$, and we also assigned an uncertainty of 1.0 MeV to the pedestal points (at zero energy) to allow for some more flexibility in the fits. In fitting to the ΔE detector data we instead assumed uncertainties of 0.14 MeV and 0.07 MeV, respectively. As an illustration, the calibration points and the resulting fits for telescope 6 are shown in Fig. 3.20. Table 3.6 lists the calibration parameters for all detectors. The table clearly verifies our assumption that all photomultiplier tube gains were predominantly linear; all fits are strongly dominated by the first order term.

During the particle identification process described in Sec. 3.5.2 we had found that telescope 5 was unstable. This manifested itself in the calibration data as well. We

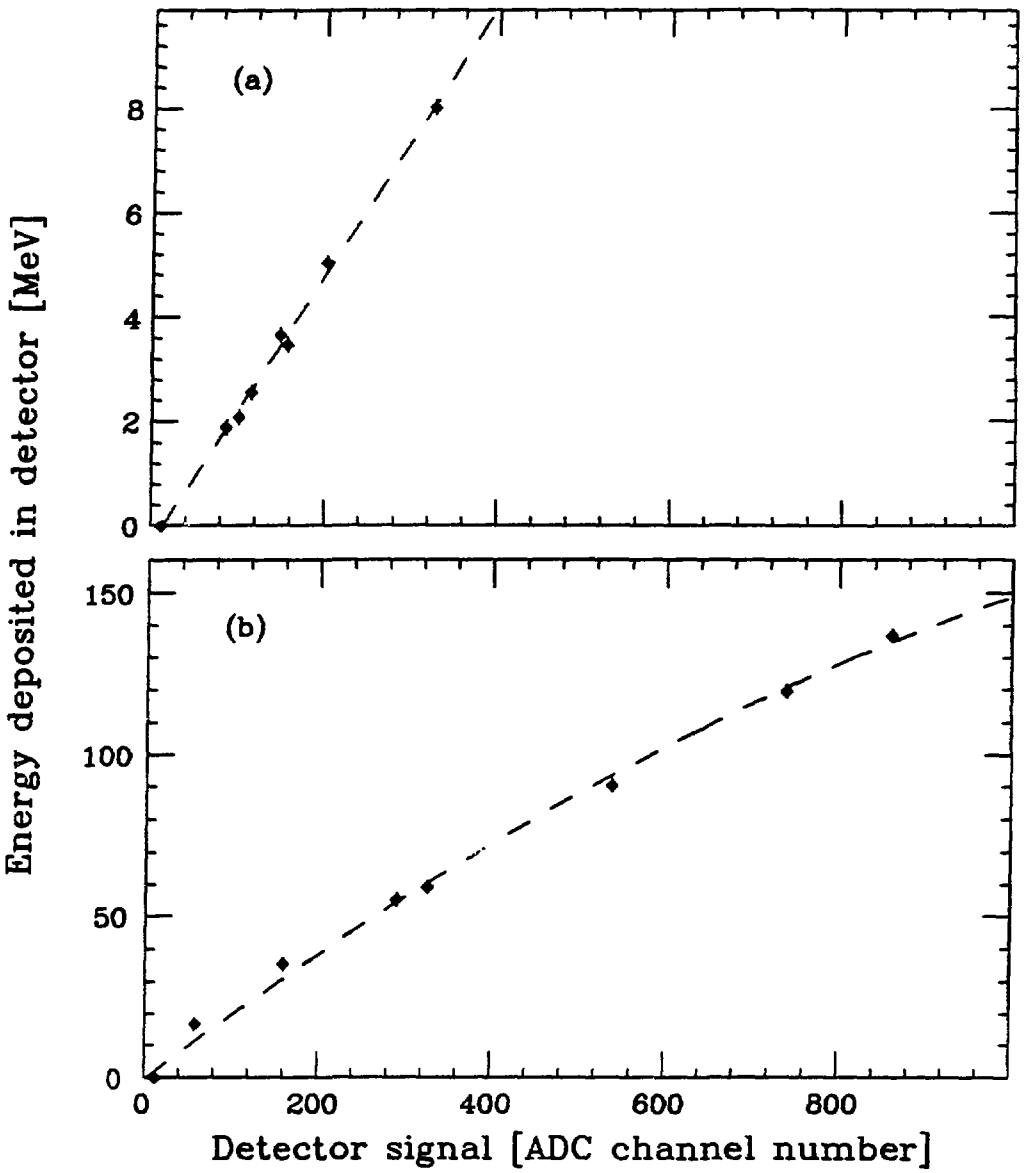

Figure 3.20. Calibration curves for telescope 6. (a) shows all calibration data and the resulting fit for detector ΔE6. (b) contains the same information for detector E6. The two points in (a) that seem to be in reverse order (at 3.5 MeV and 3.7 MeV) appear in this way for all the ΔE detectors. They are based on two different calibration methods, and the discrepancy can be taken as an indication of the uncertainty in calculating the energy losses for the various methods. The fit for detector ΔE6 was made assuming uncertainties of ±0.14 MeV for all data points except the pedestals which were assigned an uncertainty of ±0.07 MeV; for detector E6 the uncertainties assumed were ±2.0 MeV and ±1.0 MeV, respectively.

Table 3.6. Calibration parameters for all detectors. The energy observed in a given detector is calculated as $T_p = a\,(T^{\rm raw} - p) + b\,(T^{\rm raw} - p)^2$, where $T^{\rm raw}$ is the raw signal from its ADC. Detector ΔE5 could not be calibrated, and the energy loss was instead calculated on an event-by-event basis (see the text).

detector	a [MeV/channel]	b [10^{-4} MeV/channel^2]	p [channel]
E1	0.248 ± 0.009	-0.81 ± 0.14	10.9 ± 3.7
E2	0.217 ± 0.007	-0.61 ± 0.10	10.3 ± 4.3
E3	0.298 ± 0.010	-1.24 ± 0.18	1.2 ± 3.1
E4	0.381 ± 0.017	-1.04 ± 0.46	13.9 ± 2.5
E5	0.313 ± 0.011	-1.23 ± 0.21	6.7 ± 3.0
E6	0.205 ± 0.007	-0.55 ± 0.09	2.9 ± 4.6
E7	0.241 ± 0.010	-0.68 ± 0.16	2.5 ± 4.0
E8	0.322 ± 0.011	-1.32 ± 0.23	5.7 ± 2.9
ΔE1	0.023 ± 0.001	0.06 ± 0.04	12.3 ± 3.0
ΔE2	0.023 ± 0.001	0.02 ± 0.03	20.6 ± 3.0
ΔE3	0.022 ± 0.001	0.02 ± 0.03	14.3 ± 3.0
ΔE4	0.019 ± 0.001	-0.01 ± 0.02	4.5 ± 3.6
ΔE5	—	—	—
ΔE6	0.025 ± 0.001	0.01 ± 0.04	13.7 ± 2.6
ΔE7	0.025 ± 0.001	0.04 ± 0.04	8.2 ± 2.7
ΔE8	0.028 ± 0.002	0.06 ± 0.06	9.8 ± 2.5

found that detector E5 appeared to be working properly, while detector ΔE5 was unreliable. We therefore decided to calculate the energy loss in ΔE5 on an event-by-event basis using the Bethe-Bloch formula (Eq. (3.26)), following the same approach as described for the energy loss calculations earlier in this section. The resulting energy spectra for this detector appear quite similar to the spectra from the other ΔE detectors; hence we do not anticipate any significantly increased uncertainties due to these calculated energies.

The software package for curve-fitting (MINUIT[81]) provides a full covariance matrix for the fitted parameters. Using this, one can estimate the total statistical uncertainty in the measured proton energies due to the energy calibration. A detailed description of how to make such estimates is given in Appendix D. The calibration uncertainty is energy-dependent. For the 8 E detectors at 70 MeV it varies from 1.6% to 2.0% with an average of 1.7%, at 50 MeV the average is 2.1%, and at 100 MeV it is 1.1%.

Table 3.7. Proton detector energy resolutions derived from the LED data in Fig. 3.14. Resolution here is defined as the FWHM of the energy peaks. The calculations were performed using calibration data from Table 3.6.

Detector	E1	E2	E3	E4	E5	E6	E7	E8
LED peak energy [MeV]	83.2	66.0	124.4	81.1	98.9	55.4	96.3	95.7
Resolution [MeV]	2.5	2.6	2.5	3.2	2.6	2.6	3.2	2.6
Resolution [%]	3.0	3.9	2.0	3.9	2.6	4.7	3.4	2.7

The relative uncertainty for the ΔE detectors is similar; at 3.5 MeV, which is a typical energy deposited in these detectors, the uncertainty averages 1.9%. The energy deposited in the ΔE detectors is rather small, however, and the energy uncertainties in these detectors do not contribute much to the overall uncertainty. The total energy calibration uncertainty for a proton leaving the target with 75 MeV kinetic energy averages about 1.6%.

3.5.4 Resolution

This subsection contains a discussion of factors that affect the resolution of the proton detectors. In this experiment it is important to achieve satisfactory resolution particularly in the energy measurements. We are also interested in angular distributions, but the requirements on angular resolution are shown to be rather loose.

3.5.4.1 Energy Resolution

The best measure of the basic energy resolution of the detectors is the width of the peaks in energy spectra obtained with monoenergetic particles, that is, with direct beam protons or, equivalently, with the LED's.

Table 3.7 lists the resolutions derived from the LED data shown in Fig. 3.14 using the calibration parameters in Table 3.6. Resolution here is defined as the FWHM of the peak in the spectrum. Doing the same calculation for the beam proton spectra for E3 shown in Fig. 3.18, we find a resolution of 4.8% (2.7 MeV) at 56.8 MeV (no degrader) and 9.4% (3.1 MeV) at 32.8 MeV (0.7 cm Al degrader). These values are consistent

Table 3.8. Energy uncertainty due to non-zero target thickness. The table lists the range of real proton kinetic energies possible for estimated proton energies T_p = 40 and 80 MeV. These ranges are due to the non-zero thickness of the targets. The table lists all targets used for $(\pi^+,\pi^0 p)$ measurements, and the calculations have been performed using setup parameters from these measurements. The ranges are in MeV. The numbers in parenthesis are the relative uncertainties assigned to T_p (in percent) because of the target thicknesses. ϕ_p is the proton angle in a plane normal to the scattering plane. $\phi_p = 0°$ for the central telescope and 51° for the extreme out-of-plane telescopes.

target	$T_p = 40$ MeV		$T_p = 80$ MeV	
	$\phi_p = 0°$	$\phi_p = 51°$	$\phi_p = 0°$	$\phi_p = 51°$
3 mm	37.5 – 42.4 (4.2)	36.0 – 43.7 (6.6)	78.6 – 81.4 (1.2)	77.7 – 82.2 (1.9)
5 mm	35.4 – 44.3 (7.6)	32.4 – 46.6 (12.1)	77.4 – 82.5 (2.2)	75.8 – 84.0 (3.5)
9 mm	34.8 – 44.8 (8.5)	31.3 – 47.4 (13.6)	77.1 – 82.8 (2.5)	75.3 – 84.5 (3.9)
12 mm	32.3 – 46.6 (12.1)	27.0 – 50.2 (19.4)	75.8 – 84.0 (3.5)	73.3 – 86.3 (5.5)
Fe	34.5 – 44.9 (8.9)	31.0 – 47.7 (14.1)	76.9 – 83.0 (2.6)	75.0 – 84.8 (4.2)
Sn	32.7 – 46.4 (11.7)	27.7 – 49.9 (18.7)	75.8 – 84.0 (3.5)	73.3 – 86.3 (5.5)
Pb	35.2 – 44.4 (7.8)	32.2 – 46.8 (12.4)	77.2 – 82.7 (2.3)	75.5 – 84.3 (3.7)

with the data in Table 3.7. The relative energy resolution of the ΔE detectors is not very good, but the absolute resolution is rather small (on the order of 0.5 MeV), so these detectors do not have much influence on the overall resolution. We conclude that the energy resolution of our proton telescopes is about 3 MeV at the energies of interest. This corresponds to a relative resolution of 2.5 – 6%.

3.5.4.2 Target Thickness Effects on Energy Calculations

In the analysis it is assumed that the detected protons originate from the center of the target. In reality, a given proton has equal probability to originate from any point along the beam path through the target. This implies that in each event the estimated energy may be off by as much as the energy lost by a proton going through half of the target.

The range of possible true initial kinetic energies corresponding to a given nominal detected energy T_p can be calculated using the Bethe-Bloch formula (Eq. (3.26)). Some

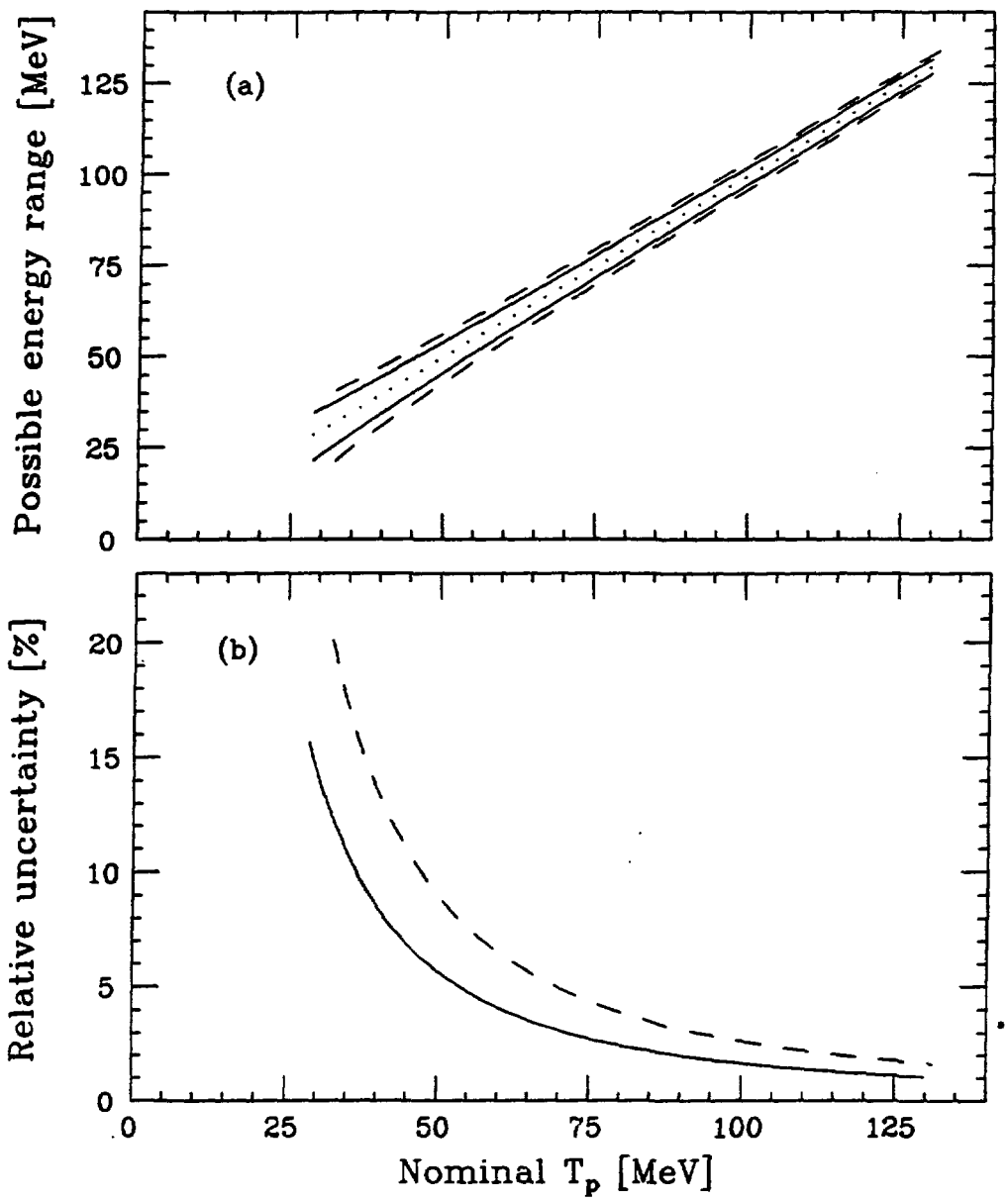

Figure 3.21. Uncertainty in the calculated proton energies T_p for the "9 mm" target. (a) shows the range of possible energies for all values of T_p. The solid curves limit the range for the central telescope; the dashed curves are for the extreme out-of-plane telescopes positioned $\phi_p = 51°$ away from the scattering plane. The dotted line indicates the nominal energy T_p. (b) shows the energy dependence of the relative uncertainty for the same telescopes. The low energy end of each curve indicates the lowest energy that can be detected by that telescope, that is, the energy of a proton that just barely makes it through to the E detector.

results for all $(\pi^+, \pi^0 p)$ targets are presented in Table 3.8. We performed the calculations both for the central telescope (telescope 4) and for the extreme out-of-plane telescopes (telescopes 1 and 7, which were 51° away from the scattering plane). The energy dependence of the range of possible proton energies is illustrated in Fig. 3.21a for the "9 mm" water target. We see that while the effect of the target thickness is almost negligible at high energies, it becomes quite serious at low energies.

In a normal distribution approximately 68.3% of all events are within one standard deviation of the center. We used this as a requirement in estimating a "standard" uncertainty due to the non-zero target thicknesses. Results for the "9 mm" target for both the central and the extreme out-of-plane telescopes are shown in Fig. 3.21b. Fig. 3.22 shows this proton energy uncertainty for the central telescope for all targets as a function of the calculated energy. The low energy end of each curve marks the lowest energy that the analyzer software will assign to any detected proton when a given target is used.

3.5.4.3 Angular Resolution

The angular resolution of the proton arm is not particularly important to the $(\pi^+, \pi^0 p)$ measurements because the pions are collected in rather wide angular bins (8° or 24°, cf. Sec. 3.3.2) by the π^0 spectrometer.

The solid angle spanned by each proton telescope is determined by the size of the ΔE detectors (cf. Sec. 2.2.3). These detectors are circular, and in the setups used they provided an opening angle of approximately 3.0° around the central line through each telescope. The corresponding solid angle is then $\Delta\Omega_p = 8.46$ msr for each telescope. Looking at possible uncertainties in the dimensions defining the solid angle, we estimated the uncertainty in $\Delta\Omega_p$ to be 0.25 msr.

The positioning of the proton arm as well as the mounting of each telescope on this arm was done carefully. The deviations from the nominal angles should be less than 0.5° both for the central proton angle and for the out-of-plane angle. Any possible effects of this small uncertainty are ignored in this work.

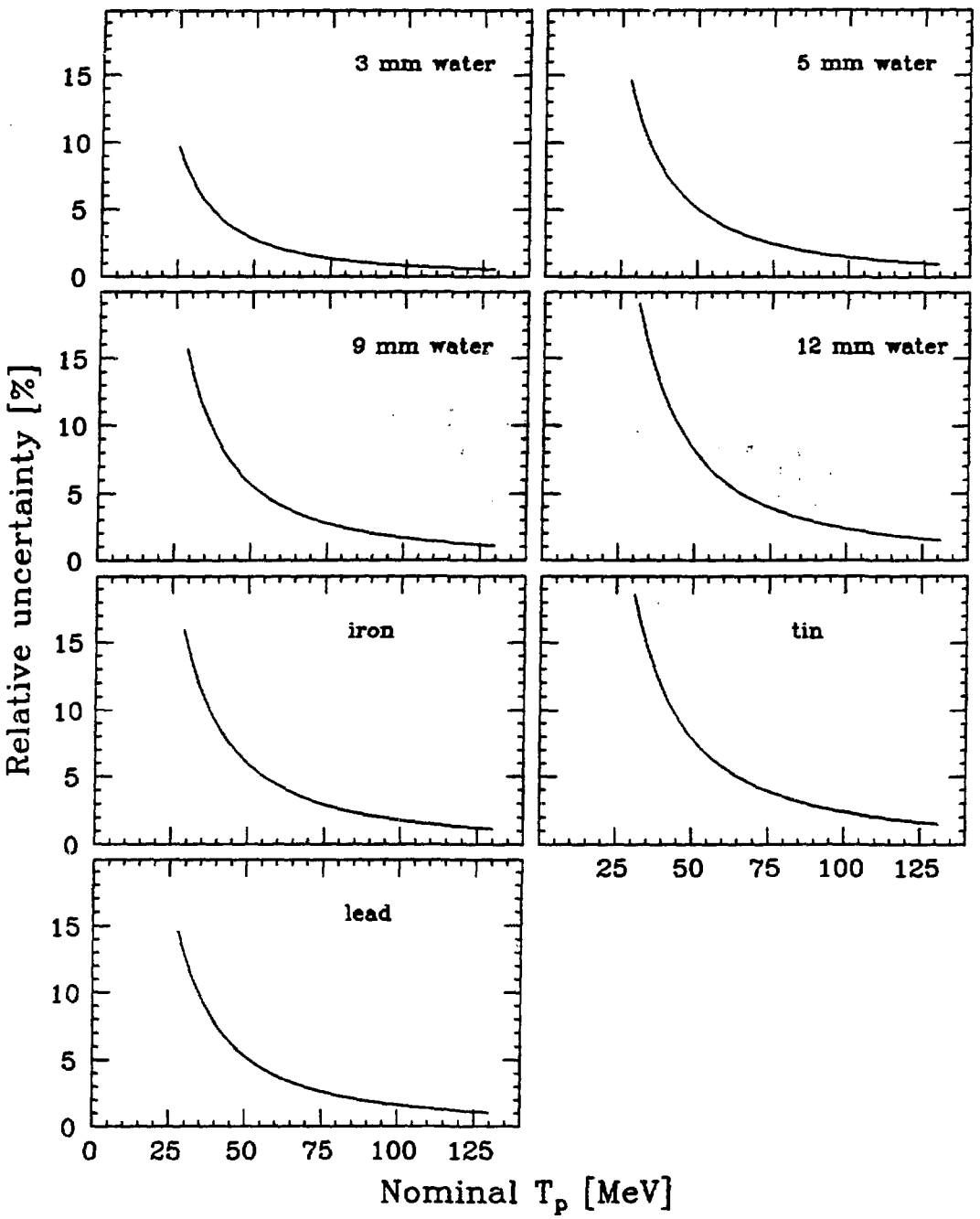

Figure 3.22. Energy uncertainty due to non-zero target thickness. The figure shows the relative uncertainty in the calculated proton kinetic energy T_p due to the non-zero target thickness for all targets used for $(\pi^+, \pi^0 p)$ measurements. The calculations have been performed using setup parameters from these measurements, and they apply to protons detected by the central telescope.

Chapter 4

Experimental Results

This chapter presents the main results of the experiment. Most of the preparations were dealt with in the previous chapter, but some concerns that are essential only to parts of the data are instead treated in the relevant sections of this chapter. The chapter is split into three sections. The first is a presentation of our $(\pi^+, \pi^0 p)$ coincidence measurements on oxygen, discussing the angular dependence of the reaction; the second is a study of the A-dependence of the same reaction, comparing our measurements on several targets (oxygen, iron, tin, and lead); and the third is a presentation of our single arm (π^+, π^0) measurements. The current chapter includes all data analysis based on our own experimental work. Comparisons to theory and to the results of other experiments are deferred to the chapter immediately following this.

Experimental results that are presented only in the form of energy spectra in this chapter can be found tabulated in Appendix E.

4.1 Coincidence Measurements of the $^{16}O(\pi^+, \pi^0 p)$ Reaction

The main purpose of our experiment was to study the $^{16}O(\pi^+, \pi^0 p)$ reaction. This section is therefore rather extensive. The first few subsections below discuss factors important to the analysis of the coincidence data. The last three subsections contain our

final experimental cross sections at different levels of integration: $d^3\sigma/dE_{\pi^0}\, d\Omega_{\pi^0}\, d\Omega_p$, $d^2\sigma/d\Omega_{\pi^0}\, d\Omega_p$, and $d\sigma/d\Omega_{\pi^0}$, respectively.

All coincidence data were analyzed using the larger π^0 angular bin ($\theta_{\pi^0} \pm 12°$) to minimize the rather large statistical uncertainties.

4.1.1 Monte Carlo Simulations of Quasi-Free Removal Processes

To better understand the effects of the presumed quasi-free nature of our coincidence measurements, we wrote a Monte Carlo code to simulate quasi-free nucleon removal processes. These calculations provide insight into expected energy spectra and angular distributions, but one should note that they mainly include the *kinematical* effects; the deeper-lying nuclear physics is only included through various empirical parameter values used in the calculations.

In our simulations an incident pion with $T_{\pi^+} = 165$ MeV collides with a neutron in random motion. The neutron motion is sampled according to empirical momentum distributions for p-shell or s-shell nucleons. (We used data for $1p_{\frac{3}{2}}$ and $1s_{\frac{1}{2}}$ protons in ^{12}C from Ref. 87.) After the collision we let the π^0 move in a direction chosen randomly within a cone around the nominal direction to the π^0 spectrometer. (The solid angle spanned by the cone was kept the same size as the corresponding π^0 spectrometer solid angle calculated by PIANG (cf. Sec. 3.3.2).) It is then a standard two-body kinematics problem to solve for the momenta of the π^0 and the proton and for the direction of the proton. In these calculations the momentum of the target neutron is not included in the conserved energy ($E_n = m_n$). This is done to account for "off-shell" effects, that is, the fact that the standard expression $E^2 = m^2 + p^2$ is not generally valid for bound nucleons. (The data presented in Fig. 2.7 indicate that energy and momentum for a nucleon in a nucleus are almost independent of each other.) We account for the binding energies and the excitation level of the residual nucleus by subtracting this energy from the neutron energy E_n and thus removing it from the total energy available to the $\pi^0 p$ system. An event is considered "good" if the kinetic energy of both the proton and the π^0 is high enough to allow detection of these particles (the limits used were 20 MeV for the proton and 30 MeV for the π^0). Depending on the

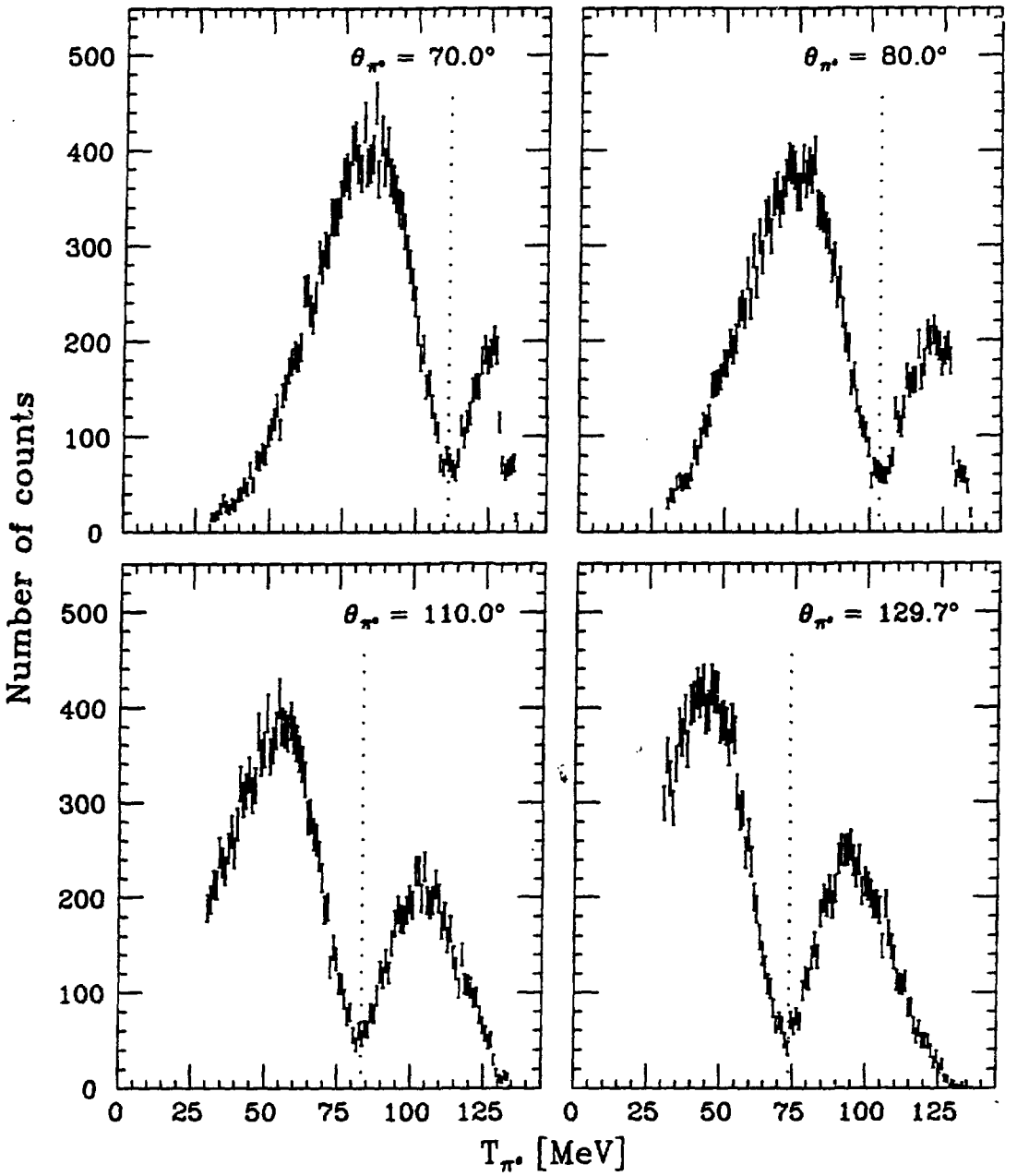

Figure 4.1. Monte Carlo simulations of $d^3\sigma/dE_{\pi^0}\, d\Omega_{\pi^0}\, d\Omega_p$ for p-shell removal. The figure shows cross section spectra for $^{16}O(\pi^+, \pi^0 p)^{15}O$ as a function of T_{π^0} based on calculations including only the reaction kinematics and the momentum distribution of p-shell nucleons (see the text). The π^0 angle is indicated in each plot. The dotted line marks the quasi-free energy for each setup. In all calculations the proton was required to hit the central proton telescope.

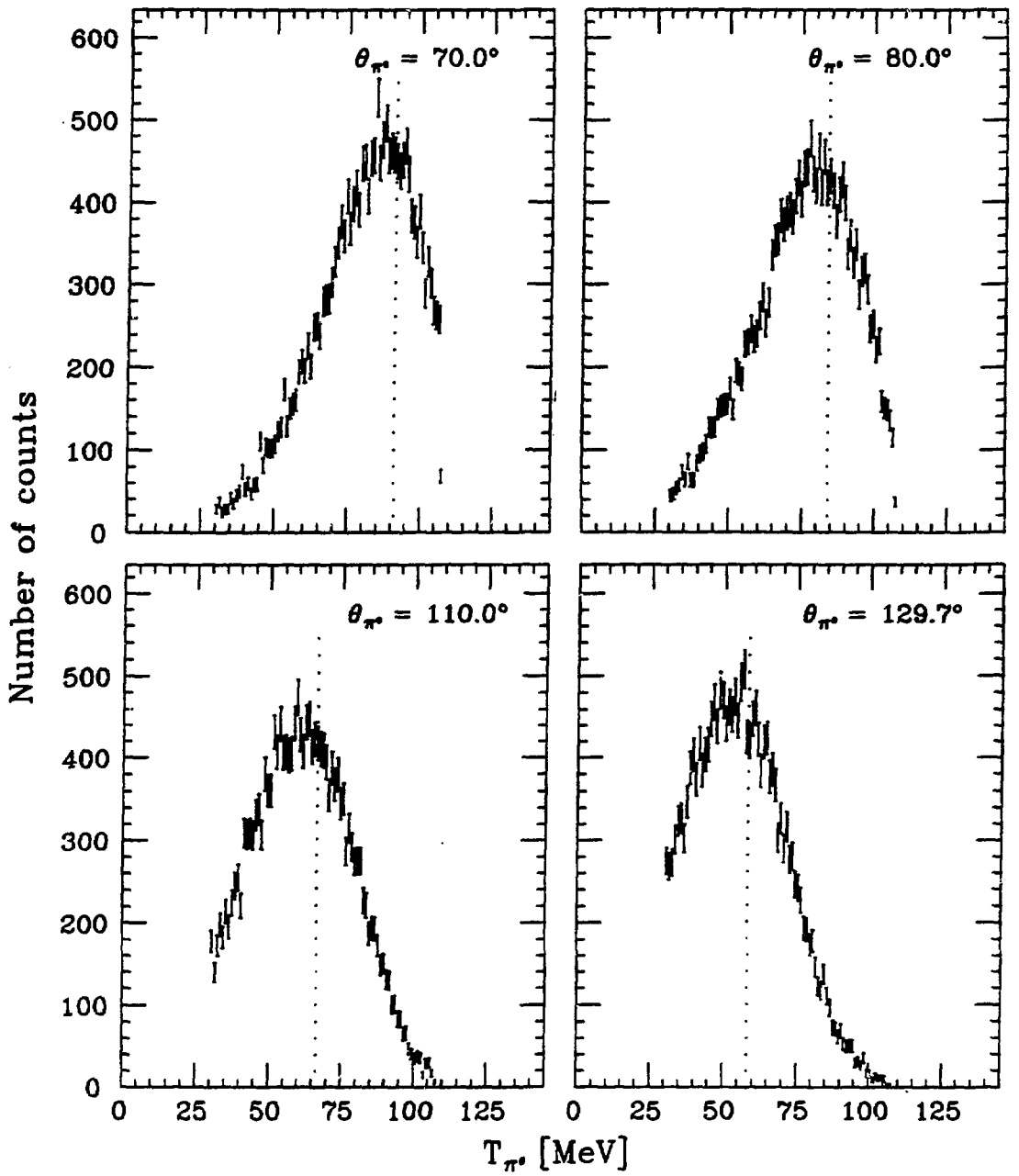

Figure 4.2. Monte Carlo simulations of $d^3\sigma/dE_{\pi^0}\,d\Omega_{\pi^0}\,d\Omega_p$ for s-shell removal. The figure shows cross section spectra for $^{16}O(\pi^+,\pi^0 p)^{15}O$ as a function of T_{π^0} based on calculations including only the reaction kinematics and the momentum distribution of s-shell nucleons (see the text). The π^0 angle is indicated in each plot. The dotted line marks the quasi-free energy for each setup. In all calculations the proton was required to hit the central proton telescope.

details of the situation being simulated, further limitations may be put on the direction of the ejected proton.

We performed such Monte Carlo calculations for all setups. The resulting π^0 energy spectra (representing $d^3\sigma/dE_{\pi^0}\,d\Omega_{\pi^0}\,d\Omega_p$) are shown in Fig. 4.1 for p-shell nucleon removal and in Fig. 4.2 for s-shell removal. In both cases the ejected proton was required to hit an area of the same size and at the same position as the central proton telescope. In the p-shell calculations the excitation level of the residual ^{15}O nucleus was randomly chosen to correspond to either $p_{\frac{1}{2}}$ removal (ground state) or $p_{\frac{3}{2}}$ removal (6.176 MeV, cf. Ref. 65) according to the number of nucleons in these states in the ^{16}O nucleus (two and four, respectively). Our s-shell calculations should only be taken as a rather qualitative indication of what s-shell momentum distributions lead to. In these calculations the residual nucleus was always left at the same level (at 27.7 MeV, which is the peak of the $s_{\frac{1}{2}}$-hole state), while s-shell nucleon removal in reality involves a quite broad and irregular state of excitation.[69]

The quasi-free energy is indicated in all spectra in Figs. 4.1 and 4.2. This is the π^0 kinetic energy corresponding to an event where the incident π^+ hits a target nucleon at rest. All p-shell spectra show a characteristic dip around this energy caused by the low probability of finding p-shell nucleons almost at rest (cf. Ref. 66). We also note that in all spectra the lower energy part (with respect to the π^0 quasi-free energy) appears to be kinematically favored.

To obtain information about the angular distribution of the quasi-free process, we performed some calculations where the proton was allowed to hit anywhere within a vertical (out-of-plane) band spanning $\pm 3^\circ$ about the quasi-free proton angle. This corresponds to the angular width of the proton telescopes. Figs. 4.3 and 4.4 show the resulting out-of-plane angular distributions for p-shell removal and s-shell removal, respectively. The "p-shell dip" discussed above now manifests itself as a lack of cross section near the central angle. Both figures indicate that the quasi-free angular distribution gets narrower as the π^0 angle is increased. The FWHM's of the p-shell angular distributions (extracted by simply measuring the widths at half of the peak value) are approximately 57°, 54°, 47°, and 45° for the four setups in increasing order of θ_{π^0}. The corresponding numbers for the s-shell distributions are 39°, 36°, 32°, and 31°, respectively. This narrowing can be understood qualitatively by the fact that as

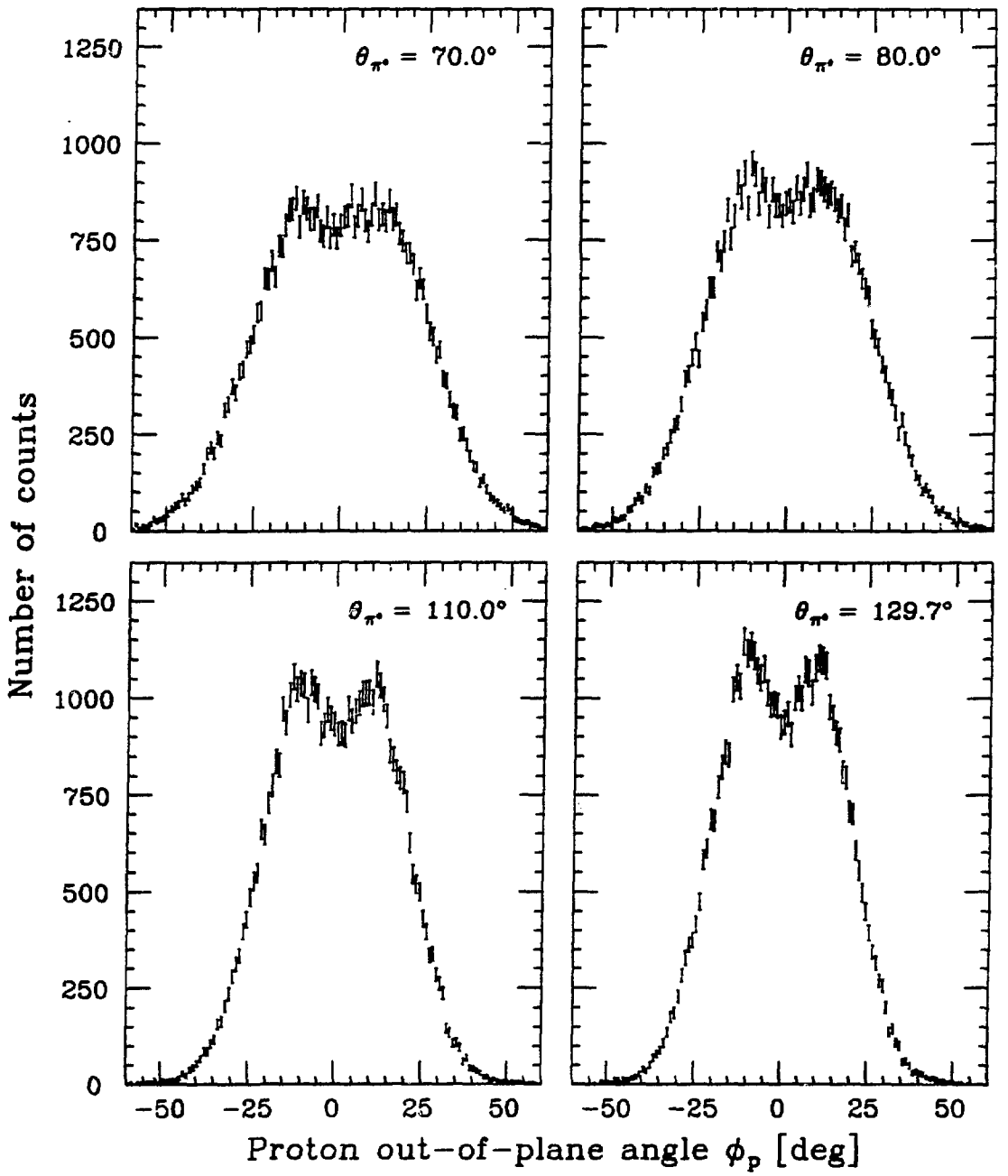

Figure 4.3. Monte Carlo simulations of $d^2\sigma/d\Omega_{\pi^0}\, d\Omega_p$ for p-shell removal. The figure shows cross section spectra for $^{16}O(\pi^+,\pi^0 p)^{15}O$ as a function of the proton out-of-plane angle ϕ_p based on calculations including only the reaction kinematics and the momentum distribution of p-shell nucleons (see the text). The π^0 angle is indicated in each plot. The proton was required to hit a vertical band spanning $\pm 3°$ about the nominal proton angle.

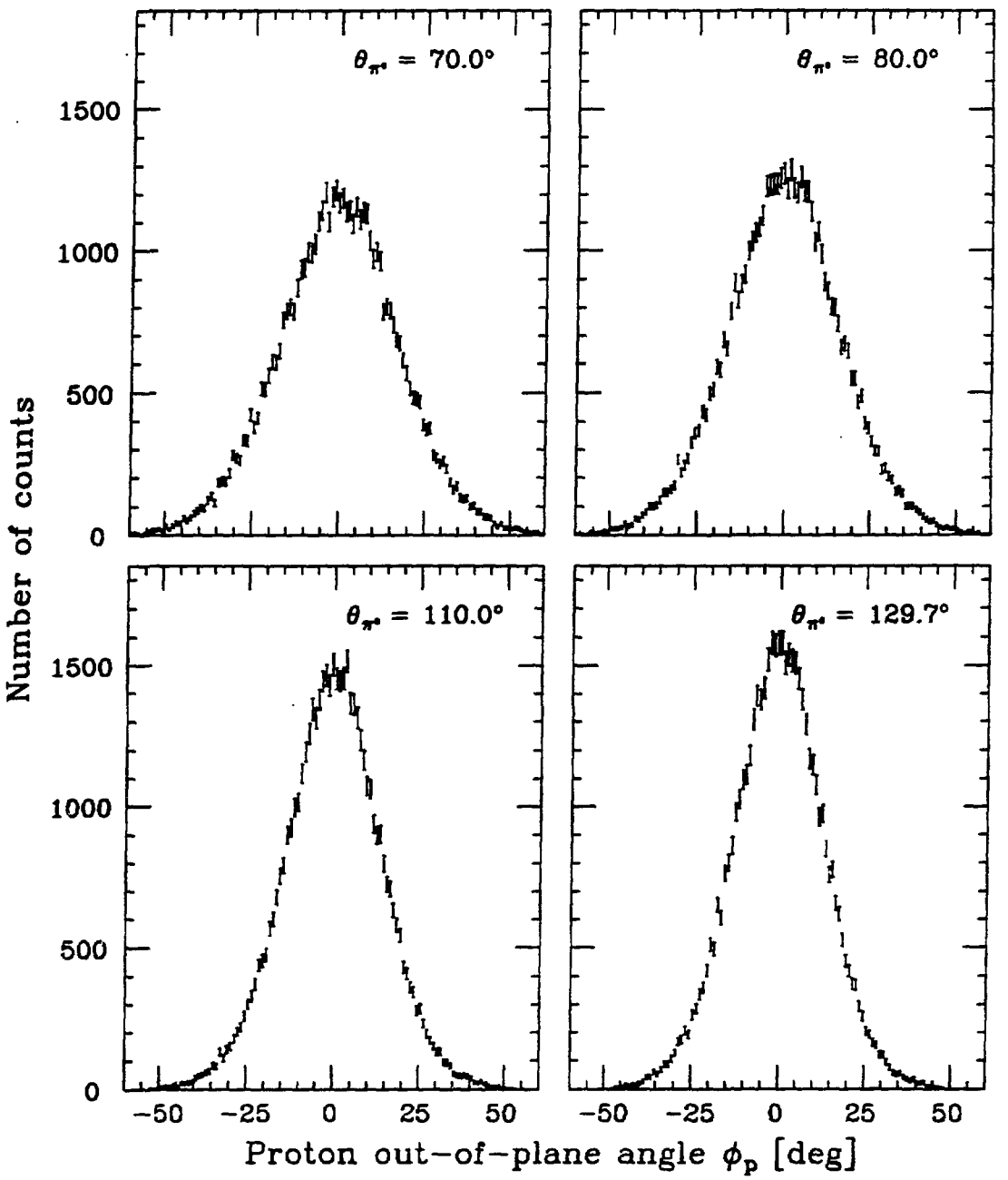

Figure 4.4. Monte Carlo simulations of $d^2\sigma/d\Omega_{\pi^0}\, d\Omega_p$ for s-shell removal. The figure shows cross section spectra for $^{16}O(\pi^+, \pi^0 p)^{15}O$ as a function of the proton out-of-plane angle ϕ_p based on calculations including only the reaction kinematics and the momentum distribution of s-shell nucleons (see the text). The π^0 angle is indicated in each plot. The proton was required to hit a vertical band spanning $\pm 3°$ about the nominal proton angle.

the π^0 angle is increased, the fraction of the total energy in the $\pi^0 p$ system available to the proton increases while the π^0 energy decreases (cf. Figs. 4.1 and 4.2). The out-of-plane angle is essentially a measure of the momentum of the interacting target neutron. A proton moving towards more forward angles (and hence having a relatively high energy) must be less sensitive to a given neutron out-of-plane momentum than one moving towards more backward angles (having a relatively low energy).

4.1.2 Timing

In Sec. 3.3.3 we discussed some implications of the coincidence detection of the two photons from the π^0 decay process. In the present section we are concerned about coincidences between π^0's and protons. Experimentally we are thus requiring a triple $\gamma\gamma p$ coincidence. Obviously such a requirement reduces the number of accidental events (that is, accidental coincidences) significantly.

We used the timing information in the $\pi^0 p$ measurements in much the same way as described in Sec. 3.3.3 for the $\gamma\gamma$ coincidences. In this case we studied distributions of the difference between the time-of-flight of the proton and that of one of the two photons detected. An example of this is shown in Fig. 4.5. We see a well-defined coincidence peak with some accidental coincidences on both sides. In the analysis we restricted "good events" to be those where the difference in time-of-flight was less than 3.5 ns away from the center of the timing peak (markers 1 and 2 in the figure). In many cases this was a slightly wider range than was strictly necessary, but we wanted to keep any loss of good coincidence events from the tails of the peaks as small as possible. (π^0 events lost because of tight restrictions on the $\gamma\gamma$ coincidences were corrected for by the π^0 spectrometer efficiency measurements (cf. Sec. 3.3.5), but no similar efficiency corrections could be made for the $\pi^0 p$ system.) The coincidence peak shown in Fig. 4.5 has a small bump near marker 2. This feature was observed in other timing histograms as well, but we did not feel justified in breaking the general algorithm for the timing cuts just to include these events. The effect of the added events would be small in any case.

Events where the coincidence timing was outside the "good" range of ± 3.5 ns around the peak position were assumed to be accidental coincidences. We see from the figure

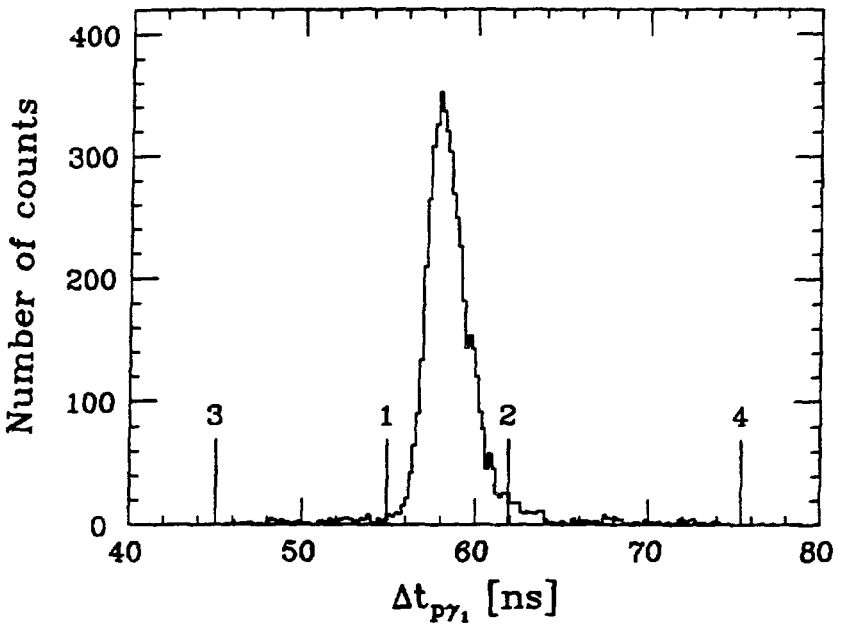

Figure 4.5. Relative timing between the proton and the π^0. The timing of the π^0 is represented by the timing of one of the photons detected by the π^0 spectrometer (always the same spectrometer arm). The zero of the horizontal scale is arbitrary; it depends on the hardware (cables, *etc.*) used. In this example the π^0 spectrometer was at 110°, and the proton was detected in telescope 4, but the picture is similar for all telescopes in all setups. The numbered lines indicate the regions used in the data analysis. "Good" events are limited to the region between markers 1 and 2, while the events that fall between 3 and 1 and between 2 and 4 are used to estimate the contribution of accidental coincidences in the "good" region (see the text for the exact algorithm). The coincidence peak shown has a width of 2.6 ns (FWHM).

that these events are spread out fairly evenly over a roughly 30 ns wide region. This region corresponds to the duration of the hardware coincidence gate, which was made this wide to allow accurate measurements of the contribution from such accidental coincidences. The range studied in the analysis is indicated by markers 3 and 4 in Fig. 4.5. The positions of markers 1 and 2 were set by hand for each proton telescope in each setup by establishing the "good" timing range as described above. The range considered for calculating the contribution from accidental coincidences (markers 3 and 4) was determined by the computer during the analysis according to the following algorithm:

1. Go 8 ns to either side from the center of the peak.
2. Go further out in each direction until a region of at least 1.2 ns containing no

events is found.

3. Position markers 3 and 4 such that 0.6 ns of each of these empty regions are included in the calculations.
4. Use the full range between markers 3 and 1 and between markers 2 and 4 for the calculations except for the first 0.6 ns immediately outside markers 1 and 2 (to avoid possibly including the ends of the tails of the peak).

In general, the ranges determined by this algorithm reflected the 30 ns coincidence gate reasonably well.

In the analysis the accidental events were assumed to be spread out evenly over the full duration of the coincidence gate. A careful study of the timing histograms (for example Fig. 4.5) reveals that the accidental events are somewhat clustered; there is an increased occurrence of such events approximately every 5 ns. We believe this effect is due to the microstructure of the LAMPF beams (primary beams are delivered in bursts of 0.25 ns every 5 ns (cf. Ref. 57)). The effect is small, however, and the fraction of accidental events is small as well, so we ignored this substructure in the analysis.

Analyzing the $\pi^0 p$ measurements on water targets, we found an average contribution of $(1.4 \pm 0.3)\%$ accidental coincidences in each data set obtained with proton telescopes 3, 4, 5, and 8 (that is, near the quasi-free angle). For the extreme out-of-plane telescopes, where the event rate was considerably lower, accidental coincidences amounted to typically $5 - 7\%$ of the events detected within the "good" timing range.

Pile-up in the detectors is another timing-related effect (cf. Sec. 2.3.2). One cannot completely eliminate pile-up in an experiment, but by keeping the rate of hits in the detectors sufficiently low (by reducing the beam flux), one can minimize the influence of this effect. Looking at the ΔE–E plots (see for example Fig. 3.17), we see very few events above the proton band; this is one indication that the number of pile-up events in our experiment was low. As described in Sec. 2.3.2 we had set up an electronic circuit to estimate the occurrence of pile-up. Comparison of this pile-up counter to a counter for accidental coincidences (also described in Sec. 2.3.2) indicates that in our experiment pile-up occurred much less frequently than accidental coincidences. It is therefore ignored in the analysis.

4.1.3 p-Shell Separation

An important goal in the $^{16}O(\pi^+,\pi^0 p)$ measurements was to identify nucleons removed from one of the two p-shell neutron levels ($1p_{\frac{1}{2}}$ and $1p_{\frac{3}{2}}$). In Sec. 2.2 we determined that this requires a resolution of 10 MeV (FWHM) or better in the calculated excitation energy of the residual ^{15}O nucleus. This section discusses the p-shell identification process in the data analysis.

In the experiment we measured directly both energy and direction (that is, the full four-momentum vector) for both the π^0 and the proton. Assuming that the target ^{16}O nucleus is at rest, we can then calculate the total energy E_r and the momentum $\vec{p}_r$ of the residual ^{15}O nucleus:

$$\vec{p}_r = \vec{p}_{\pi^+} - \vec{p}_{\pi^0} - \vec{p}_p \tag{4.1}$$

$$E_r = E_{\pi^+} + m_t - E_{\pi^0} - E_p \tag{4.2}$$

where the index π^+ refers to the incident pion (that is, $\vec{p}_{\pi^+} = p_{\pi^+}\hat{e}_z$), and $m_t = 14895.20$ MeV is the target mass.[65]

Using energy and momentum from Eqs. (4.1) and (4.2), one can calculate the excitation energy E_{ex} of the residual nucleus from

$$E_r = \sqrt{p_r^2 + (m_r + E_{ex})^2}. \tag{4.3}$$

We used $m_r = 13971.29$ MeV for the ^{15}O mass[65] in our calculations. E_{ex} is sometimes referred to as "missing mass"; we prefer to use the more precise term "excitation energy" in this context.

The excitation energy was calculated according to Eq. (4.3) event-by-event. Resulting spectra from all water target measurements are shown in Fig. 4.6. These spectra include only events in which the proton was detected in the central telescope, and they have been corrected for the acceptance of the π^0 spectrometer (cf. Sec. 3.3.2). (This correction was made by first considering the spectra as functions of both excitation energy and π^0 energy, and then applying the correction to each histogram bin as a function of π^0 energy before summing over all π^0 energies.) All spectra shown, as well

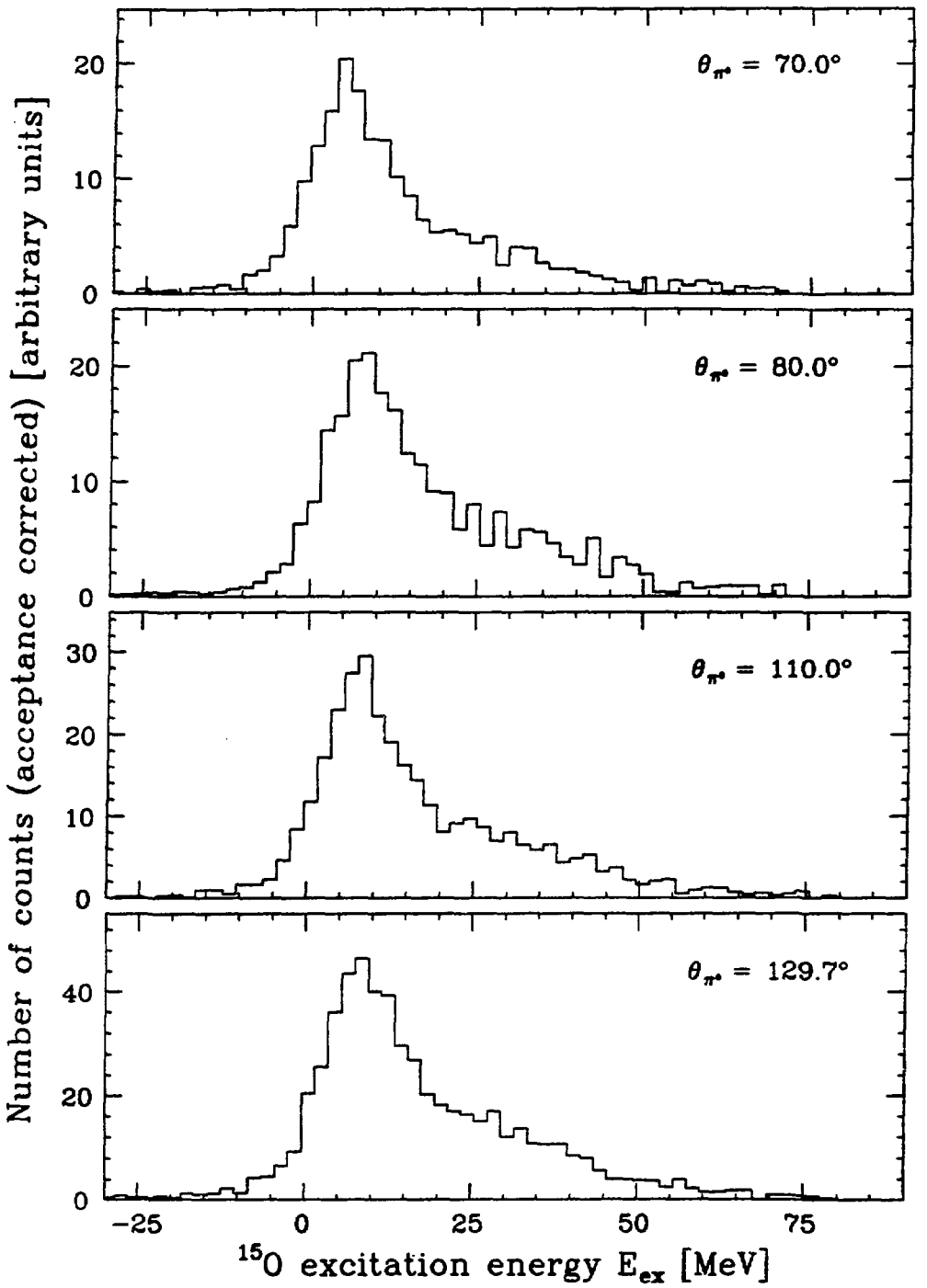

Figure 4.6. Excitation energy spectra for the residual ^{15}O nucleus. Only events in which the proton was detected in the central telescope are included. The spectra have been corrected for the acceptance of the π^0 spectrometer (cf. Sec. 3.3.2). They are tabulated in Appendix E.

Table 4.1. Analysis of excitation energy spectra. The values were extracted by fitting the function $f_{ex}(E_{ex})$ (see the text) to the measured spectra of Fig. 4.6. The table lists the central energies of the presumed $p_{\frac{1}{2}}$ state and the "s-shell" state. The latter is a quite broad state, and it includes everything except the two p-shell states. The table also lists the widths of these states. For the ground state this width can be taken as a measure of the experimental resolution. The resolutions predicted from running PIANG are given for comparison. All uncertainties in the table are purely statistical.

θ_{π^0}	ground state ($1p_{\frac{1}{2}}$)		"s-shell"		pred. resolution
[deg]	E_{ex} [MeV]	FWHM [MeV]	E_{ex} [MeV]	FWHM [MeV]	FWHM [MeV]
70.0	0.6 ± 0.3	10.2 ± 0.7	17.8 ± 0.9	34.5 ± 1.2	10.7
80.0	3.6 ± 0.3	10.4 ± 0.7	21.6 ± 0.7	36.1 ± 1.0	11.0
110.0	3.2 ± 0.2	10.7 ± 0.6	24.6 ± 0.7	37.1 ± 0.9	10.2
129.7	4.1 ± 0.2	10.1 ± 0.5	22.8 ± 0.5	38.2 ± 0.7	9.4

as the spectra involving the other proton telescopes (except for the extreme out-of-plane ones), have a well-defined, but somewhat wide, peak at energies corresponding to p-shell removal. However, isolating the p-shell contribution based on these spectra necessarily involves a significant uncertainty.

We used the excitation energy spectra in Fig. 4.6 to calculate the resolution of each p-shell peak. Since these peaks consist of two nuclear states that are too close to be resolved by our detector system, we fitted a rather special function f_{ex} to the energy spectra:

$$f_{ex}(E_{ex}) = 2c_1 \exp\left(-\frac{(E_{ex}-c_2)^2}{2c_3^2}\right) + 4c_1 \exp\left(-\frac{(E_{ex}-E_{ex}^{nom}(p_{\frac{3}{2}})-c_2)^2}{2c_3^2}\right) + c_4 \exp\left(-\frac{(E_{ex}-c_5)^2}{2c_6^2}\right). \quad (4.4)$$

The values of the coefficients c_i in Eq. (4.4) are determined by the fitting. The first two exponentials describe the two p-shell states; the parameter $E_{ex}^{nom}(p_{\frac{3}{2}}) = 6.176$ MeV is the nominal excitation energy of the $p_{\frac{3}{2}}$ state.[65] The coefficients 2 and 4 in front of these exponentials represent the relative number of protons being removed from the two states (cf. Fig. 1.7a). The third exponential describes s-shell removal plus any other possible processes. Results from fitting to all the excitation energy spectra shown in Fig. 4.6 are listed in Table 4.1. The natural width of the p-shell states is

small (cf. Refs. 40 and 67), and their experimental width is therefore essentially a measure of the energy resolution of our detector system. We see from the table that this resolution was indeed close to the 10 MeV (FWHM) we wanted to achieve. The results are also in good agreement with the values predicted by PIANG. This supports our assumption that PIANG provides a reliable description of the π^0 spectrometer. The table also lists the central energies of the ground state and the "s-shell" state. The values for the ground state are not consistent with zero. There is also a clear difference between the measured energy levels for $\theta_{\pi^0} = 70°$ and the values from the other setups. This may be interpreted as an indication of the energy calibration uncertainties in our measurements. The experimental parameters for the "s-shell" state do not match the $1s_{\frac{1}{2}}$-hole parameters quoted earlier (peak at 28 MeV, width 24 MeV). The measured peak positions were significantly lower, and the widths significantly larger. This is probably due to the influence of other processes in addition to s-shell nucleon removal.

An equivalent way of viewing the energy sharing in the reaction is to consider the measured yield Y as a function of both π^0 energy and proton energy. By yield we here mean the raw number of counts corrected for the π^0 spectrometer acceptance. This quantity is roughly proportional to the experimental cross sections $d^4\sigma/dE_{\pi^0}\,dE_p\,d\Omega_{\pi^0}\,d\Omega_p$. A plot of $Y(T_{\pi^0}, T_p)$ is shown in Fig. 4.7. In such a plot events that leave the residual nucleus in the same state of excitation should all be along the same straight line

$$T_{\pi^0} + T_p = C_{\mathrm{ex}}\,, \tag{4.5}$$

where C_{ex} is a constant reflecting the excitation state of the ^{15}O nucleus. The plot in Fig. 4.7 shows a clear band near the highest values of C_{ex}, that is, in the region where a maximum of energy is available to be shared between the π^0 and the proton. This region corresponds to the p-shell peaks in Fig. 4.6. Plots of $Y(T_{\pi^0}, T_p)$ therefore provide an alternative way of extracting the p-shell events.

We decided to follow the latter approach in our determination of p-shell cuts for the data analysis. Using excitation energy spectra like those in Fig. 4.6 may seem more intuitive, but we preferred the $Y(T_{\pi^0}, T_p)$ plots because they provide a more direct view of the energy sharing in the process. Furthermore, this method does not require a second pass replay of the data in order to extract p-shell cross sections as a function of π^0 energy (after determining a limit for the excitation energy, we would have needed

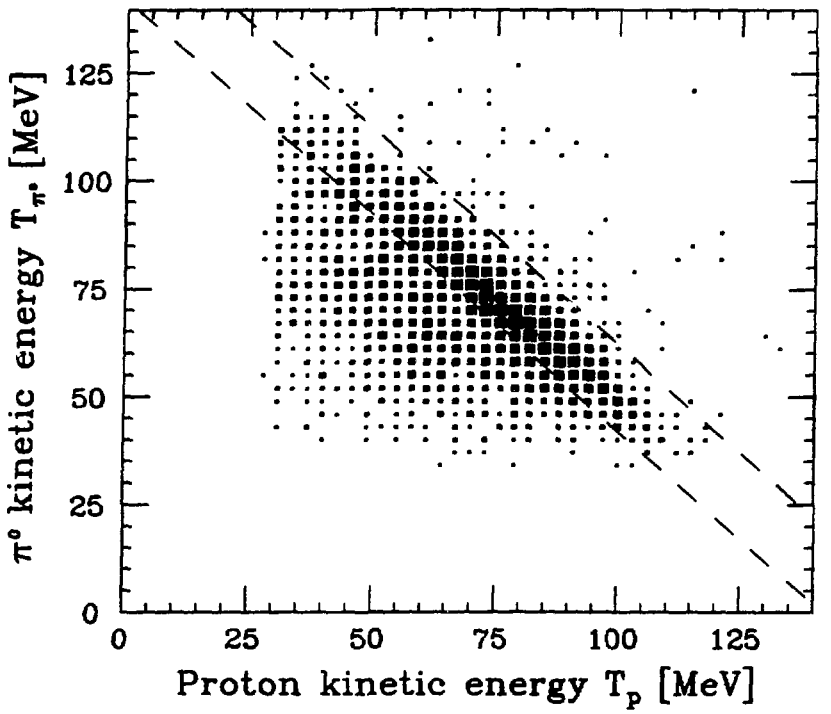

Figure 4.7. p-shell band. The figure shows the experimental yield (number of counts corrected for the energy acceptance of the π^0 spectrometer) as a function of the π^0 energy T_{π^0} and the proton energy T_p. The band near the highest values of $(T_{\pi^0} + T_p)$ corresponds to the p-shell peaks in Fig. 4.6. The dashed lines indicate our final p-shell cut (each border line square is taken to be fully on the same side of the line as its center is). The data shown are for the central proton telescope and the larger π^0 spectrometer angular bin $(\theta_{\pi^0} \pm 12°)$ with $\theta_{\pi^0} = 110.0°$.

to replay again with such a cut imposed on each event; using $Y(T_{\pi^0}, T_p)$, cross sections could be extracted from the same histograms that were used in determining the p-shell cuts). The uncertainty in making the cuts is substantial, and in our judgment similar, for both methods.

As indicated by the dashed lines in Fig. 4.7, we limited our "p-shell" by cuts both below and above the band. Determining these lines is equivalent to determining two values of C_{ex} in Eq. (4.5). To get an estimate of what values to expect for C_{ex} we can rewrite Eq. (4.2) as

$$T_{\pi^0} + T_p = T_{\pi^+} + Q - T_r - E_{ex}\,, \tag{4.6}$$

where

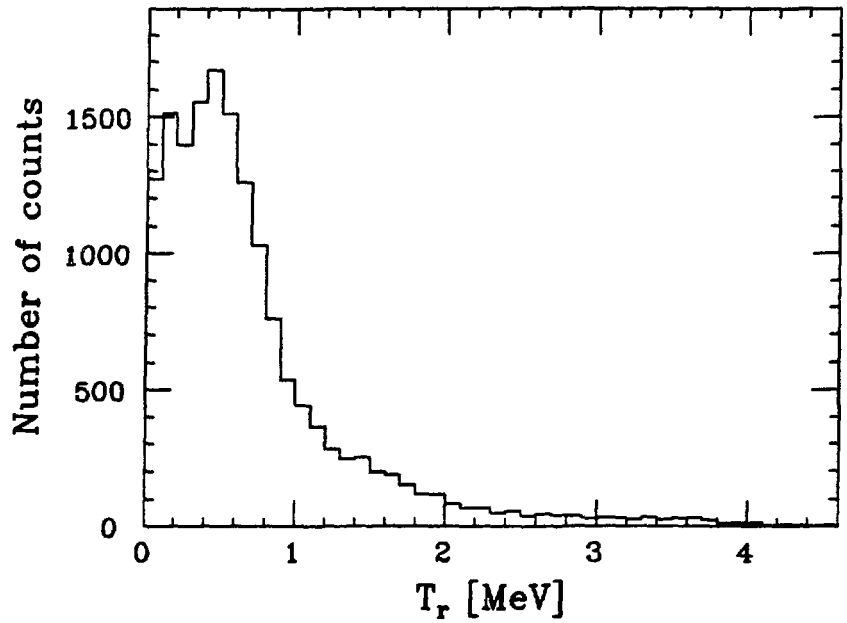

Figure 4.8. Kinetic energy of the residual nucleus. The figure shows the distribution of the kinetic energy T_r of the residual ^{15}O nucleus in the $^{16}O(\pi^+,\pi^0 p)^{15}O$ reaction at $T_{\pi^+} = 165$ MeV and $\theta_{\pi^0} = 110.0°$. All p-shell protons hitting any of the eight proton telescopes are included, and the distribution does indeed display a p-shell structure (cf. Ref. 66).

$$Q = m_{\pi^+} + m_t - m_{\pi^0} - m_p - m_r = -9.8\,\text{MeV}\,, \tag{4.7}$$

and T_r is the kinetic energy of the residual nucleus (which is of the order of 1 MeV or less, cf. Fig. 4.8). The incident pions always had $T_{\pi^+} = 165$ MeV. The ground state of the residual ^{15}O nucleus should therefore correspond to approximately $C_{ex} = 154$ MeV and the $p_{\frac{3}{2}}$ state to $C_{ex} = 148$ MeV.

s-shell nucleons have a momentum distribution peaking at zero momentum while p-shell nucleons have a low probability of being nearly at rest (cf. Ref. 67). One would therefore expect the p-shell cross section spectra to have a dip around the quasi-free energy (the energy obtained when the incident π^+ hits a nucleon at rest). This effect is quite pronounced in our Monte Carlo simulations of the $^{16}O(\pi^+,\pi^0 p)$ process (see Figs. 4.1 and 4.2). We tried a number of different excitation energy cuts in our data to look for the shell-dependent structures predicted by the Monte Carlo calculations. Some of these results are shown in Fig. 4.9. We found it difficult to draw clear conclusions about the p-shell based on the observed shapes of the various spectra.

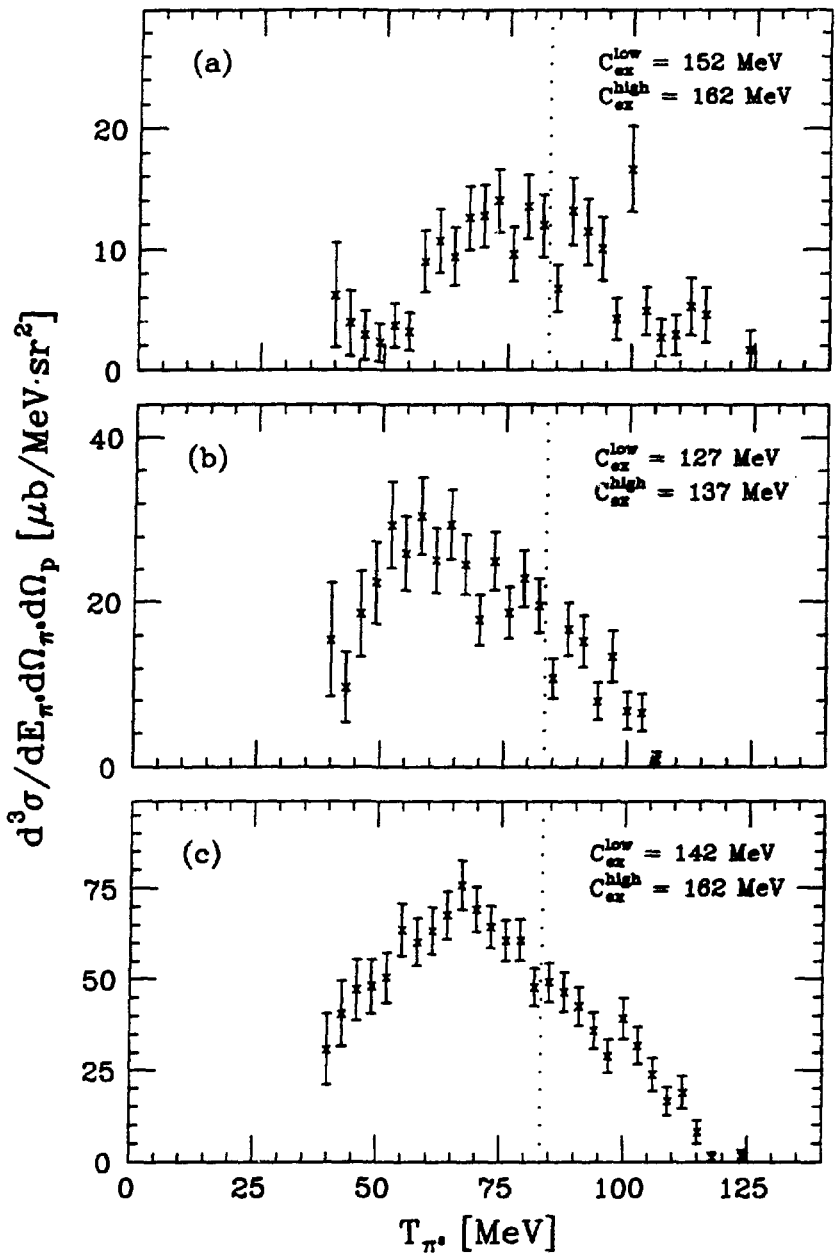

Figure 4.9. Comparison of p-shell cuts. The $d^3\sigma/dE_{\pi^0}\,d\Omega_{\pi^0}\,d\Omega_p$ cross section spectra shown are for $^{16}O(\pi^+,\pi^0 p)$, and they result from the p-shell cuts indicated. The cuts in (a) and (b) are very narrow to try to capture the characteristics of (a) the p-shell and (b) the "s-shell" (far away from the p-shell states). (c) shows the spectrum as calculated from the final p-shell cut. The dotted line indicates the quasi-free energy. All spectra are for the central proton telescope and the larger π^0 spectrometer angular bin ($\theta_{\pi^0} \pm 12°$) with $\theta_{\pi^0} = 110.0°$.

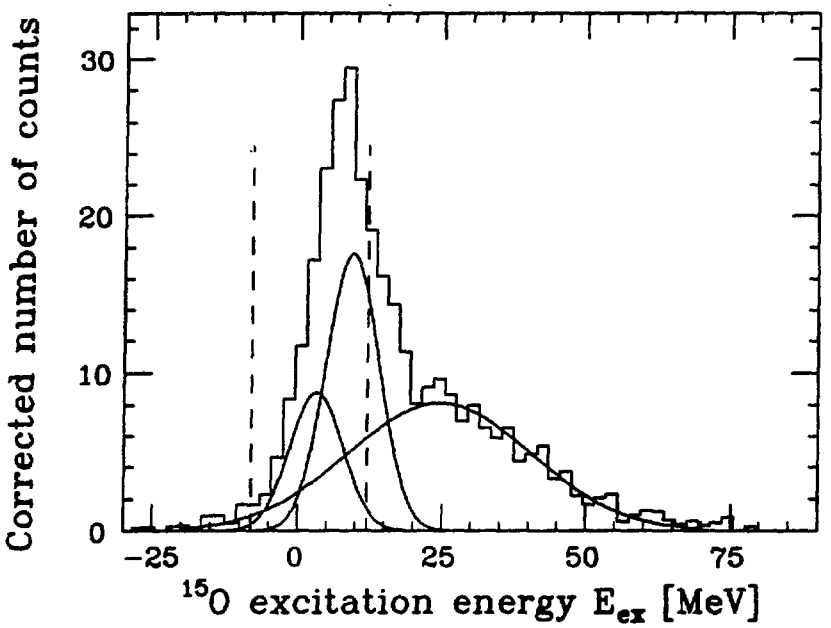

Figure 4.10. Excitation energy spectrum with p-shell cut. The spectrum shown is for $\theta_{\pi^0} = 110.0°$ (cf. Fig. 4.6), and the parameters for the fits shown are listed in Table 4.1. The three solid curves represent, from left to right, the two p-shell states and the "s-shell" state, respectively. The dashed lines indicate the p-shell cut used in the analysis.

We arrived at the final p-shell cut shown in Fig. 4.9c and in Fig. 4.7 by comparing both the shapes and the absolute sizes of the test spectra. This cut corresponds to the values $C_{ex}^{low} = 142$ MeV and $C_{ex}^{high} = 162$ MeV of the constant C_{ex} in Eq. (4.5) (which in turn corresponds to excitation energies of approximately 12 MeV and −8 MeV, respectively). This cut is compared to an excitation energy spectrum in Fig. 4.10. Also shown in the figure are the fits listed in Table 4.1. We clearly cannot make a very clean separation between p-shell and s-shell. All spectra shown in the figures are based on data from the larger π^0 spectrometer angular bin ($\theta_{\pi^0} \pm 12°$). The situation is similar for the narrower bin ($\theta_{\pi^0} \pm 4°$).

Ideally, the above discussion and the values for C_{ex} apply to all spectra based on all proton telescopes in all setups. We found two exceptions: at $\theta_{\pi^0} = 70.0°$ and $\theta_{\pi^0} = 80.0°$ the band was a few MeV lower for proton telescope 5. In Sec. 3.5.3 we found it necessary to use calculated values for the energy deposited in detector ΔE5. The discrepancy in the band position was probably due to these calculated values.

Table 4.2. Uncertainty due to the p-shell cut. The table lists the changes in the summed $d^3\sigma/dE_{\pi^0}\,d\Omega_{\pi^0}\,d\Omega_p$ spectra resulting from moving the lower line in the p-shell cut one histogram bin (3 MeV) up and one bin down from the nominal cut ($C_{ex}^{low} = 142$ MeV, $C_{ex}^{high} = 162$ MeV). For each setup the results apply to the cross sections measured using the central proton telescope and the larger π^0 spectrometer angular bin ($\theta_{\pi^0} \pm 12°$). The calculated cross sections are not very sensitive to the position of the upper line.

θ_{π^0} [deg]	$C_{ex}^{low} = 139$ MeV, $C_{ex}^{high} = 162$ MeV [%]	$C_{ex}^{low} = 145$ MeV, $C_{ex}^{high} = 162$ MeV [%]
70.0	+11.5	−15.0
80.0	+14.8	−21.1
110.0	+13.2	−19.7
129.7	+16.1	−22.1

To get an estimate of the uncertainty caused by the p-shell cut, we moved the lower cut one histogram bin (3 MeV) up and one bin down and looked at the changes in the summed $d^3\sigma/dE_{\pi^0}\,d\Omega_{\pi^0}\,d\Omega_p$ spectra (summing all the data and thus getting a rough measure of $d^2\sigma/d\Omega_{\pi^0}\,d\Omega_p$). The results are listed in Table 4.2. The average change is 16.7%. The uncertainty in the upper cut is small. In a normal distribution 68.3% of the events are within one standard deviation of the center. Using this factor conservatively here we estimate the total systematic uncertainty due to the p-shell cut to be ±12%.

4.1.4 Proton Interaction Losses in the E Detectors

When a proton passes through a material it will undergo nuclear interactions. Some of these interactions are inelastic, leading to a loss of energy that in general is impossible to detect. The importance of such losses and appropriate corrections for them have been considered by several authors. A thorough, but now slightly old, review is given by Measday and Richard-Serre.[88] The effect is not large enough to be of concern for the thin ΔE detectors. However, high energy protons may lose a significant fraction of their energy in stopping detectors like the E detectors.

The immediate effect of the energy loss is that a given event will be found at too low an energy in a proton energy spectrum, or, equivalently, that the calculated ^{15}O

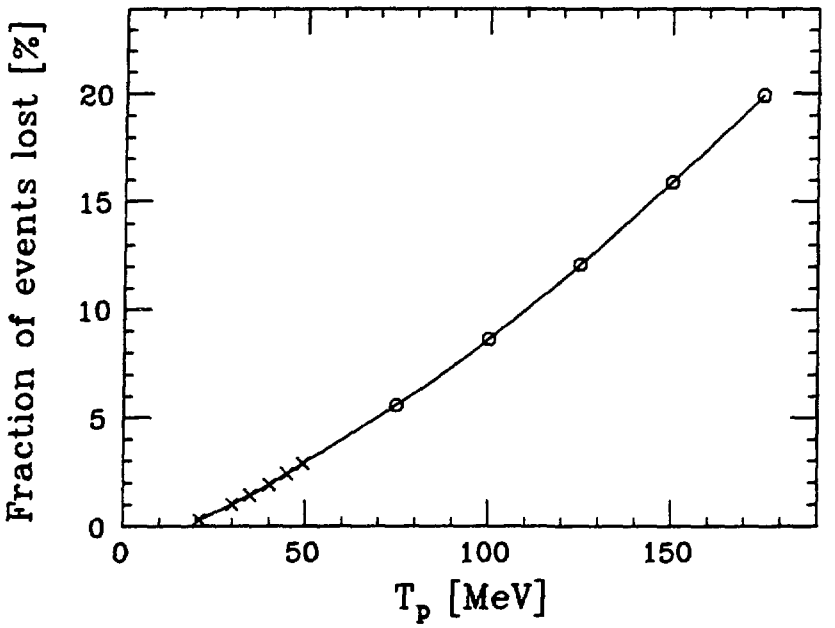

Figure 4.11. Proton interaction losses. The figure shows the fraction of events lost from the p-shell peak due to proton interaction losses in the E detectors. The low energy values (crosses) are from Ref. 89 and the high energy values (circles) from Ref. 88. The curve shows the interpolated values used in the analysis. When making corrections for proton interaction losses, we assigned a 10% relative uncertainty to the quoted numbers. The range of proton energies measured in our experiment was from about 25 MeV to about 110 MeV.

excitation energy will be too high. In the analysis we immediately sum over detected proton energies to get pion energy spectra of $d^3\sigma/dE_{\pi^0}\, d\Omega_{\pi^0}\, d\Omega_p$. Proton interaction loss effects therefore only affect situations where this sum does not include all detected protons, that is, when we are looking only at the p-shell. In this case some fraction of the true p-shell events will be assigned too much excitation energy and therefore will be lost to the analysis.

Values for the fractional loss of events lost from the p-shell peak were published in the paper by Measday and Richard-Serre.[88] In the analysis we used these values in addition to some more recent low energy values calculated by Sourkes *et al.* (Ref. 89). This is illustrated in Fig. 4.11. The calculated values apply to events lost from a band limited by cuts 7 – 10 MeV below the peak, and are all assigned a 5% relative uncertainty.[88,89] In our experiment the situation was quite similar, but with a some-

Table 4.3. Empty target contributions. The table lists the contribution of empty target data in the full target data (including the empty target background) for all p-shell measurements. The numbers shown are averages over proton telescopes 3, 4, 5, and 8. The more extreme out-of-plane detectors are not included because of the low number of empty target events detected there.

θ_{π^0} [deg]	70.0	80.0	110.0	129.7
Empty target contribution [%]	15.3 ± 4.5	7.3 ± 1.4	4.5 ± 1.1	3.8 ± 1.0

what wider and less well-defined cut (cf. Sec. 4.1.3). We therefore decided to use the same values in the analysis of our p-shell data, but assigned a relative uncertainty of 10% to the correction.

4.1.5 Empty Target Subtraction

The background consists not only of the accidental coincidence events discussed in Sec. 4.1.2, but also of true $\pi^0 p$ coincidence events due to the $(\pi^+, \pi^0 p)$ reaction taking place in the Mylar[59] target windows and in the air.

In addition to our water target runs we also collected data using an empty target (an empty frame with Mylar windows). In the analysis these empty target results are subtracted from the full water target results to account for the unwanted real coincidence events. Our guideline in deciding how much beam time to spend on the empty target measurements was to minimize the total experimental uncertainty given a fixed total time available. Denoting (effective) beam time for full and empty target by t_f and t_e, respectively, one then gets

$$t_e = t_f \sqrt{\frac{r_e}{r_f}}, \tag{4.8}$$

where r_f and r_e are the respective event rates. The reasoning leading to Eq. (4.8) is presented in Appendix F.

In the analysis full target data and empty target data were subject to the same cuts on timing and p-shell identification. We generally did not have enough empty target data to permit a bin-by-bin subtraction of this contribution. We consider it reasonable,

however, to assume that these events are distributed in approximately the same way as the "good" coincidence events. (The distribution of empty target events compared to that of full target events in our data supports this assumption, but the statistics are low.) We therefore summed (separately) the total contributions of both full and empty target data, calculated the fractional contribution of empty target data in the full target data, and subtracted this fraction from each histogram bin. Table 4.3 lists the average empty target contributions to the p-shell data for all setups. It is evident from the table that this contribution is significantly angle-dependent, decreasing as the π^0 angle increases. All details about handling of uncertainties are given in Appendix C which contains a complete description of the algorithm for calculating coincidence cross sections.

For one of the setups ($\theta_{\pi^0} = 80.0°$) we also collected data with no target at all in the beam. These data were analyzed in the same manner as the full target and the empty target data. The energy spectra obtained were hard to compare because of low statistics in both the empty target and the no target measurements. Instead we summed the cross sections for the central proton detector over all pion and proton energies (not just the p-shell) to get a rough estimate of $d^2\sigma/d\Omega_{\pi^0}\, d\Omega_p$. The results ($2594 \pm 218$, 162 ± 31, and 217 ± 132 μb/sr^2, for full target, empty target, and no target, respectively) indicate that the number of background events coming from the Mylar was low. Comparing the amounts of material, one finds that the Mylar windows (100 μm) are equivalent to 10.8 cm of air. We therefore conclude that the contribution of unwanted real coincidence events essentially consists of events from a rather large volume of air, and hence that the importance of events coming from the Mylar windows is relatively low.

4.1.6 Experimental Cross Sections $d^3\sigma/dE_{\pi^0}\, d\Omega_{\pi^0}\, d\Omega_p$

This subsection contains all the various $d^3\sigma/dE_{\pi^0}\, d\Omega_{\pi^0}\, d\Omega_p$ cross sections we measured. The data replay presented the cross section information in the form shown in Fig. 4.7. After making p-shell cuts as described in Sec. 4.1.3, we immediately summed over all proton energies included in each p-shell band. No attempt was made to account for the tail of low proton energies that could not be detected. However,

since the total energy of proton and pion is approximately constant for all p-shell events, this discrepancy must manifest itself also as missing high energy π^0's, and it can be dealt with later as such. Below is a short description of how we arrived at the $d^3\sigma/dE_{\pi^0}\,d\Omega_{\pi^0}\,d\Omega_p$ spectra. This is followed by a complete presentation of these spectra. All cross sections shown in this subsection are calculated using data from the larger π^0 spectrometer angular bin ($\theta_{\pi^0} \pm 12°$). See Appendix C for a complete description of the software for calculating coincidence cross sections. The appendix also describes how we accounted for the various uncertainties.

Full target and empty target measurements were first corrected independently for π^0 spectrometer acceptance (Sec. 3.3.2) and accidental coincidences (Sec. 4.1.2). Then the p-shell cut (Sec. 4.1.3) was applied and the remaining data corrected for proton interaction losses (Sec. 4.1.4) before being summed over all proton energies. At this point we thus had two unnormalized cross section spectra (full target and empty target) as functions of the π^0 kinetic energy T_{π^0}. The next step was to scale the data by the amounts of beam used (Sec. 3.1) and by the wire chamber efficiencies (Sec. 3.3.4). This made it possible to subtract the empty target contribution from the full target results (Sec. 4.1.5). The resulting spectrum of only "good" coincidence events was then normalized to absolute cross section units by the appropriate density × efficiency product (Sec. 3.4) and finally corrected for photon attenuation losses in the target (Sec. 3.2).

Fig. 4.12 shows $d^3\sigma/dE_{\pi^0}\,d\Omega_{\pi^0}\,d\Omega_p$ spectra as a function of T_{π^0} calculated according to the above procedure for the central proton telescope in all setups. The dotted line in each spectrum indicates the quasi-free energy where we would expect to see a dip in the cross section due to the p-shell momentum distribution (cf. Fig. 4.1). The data do not display much of this p-shell signature. The spectra are plotted on the same scale. We see that the cross section is significantly larger at the backward π^0 angles than at the more forward angles.

We also looked at the complete data set without making the p-shell cut and at what was left outside the p-shell cut (the "s-shell", also known as the "continuum"). The precise definitions of these cuts are that the p-shell is limited by lines having $C_{\rm ex}^{\rm low} = 142$ MeV and $C_{\rm ex}^{\rm high} = 162$ MeV (cf. Sec. 4.1.3, particularly Eq. (4.5)), the complete set includes everything between $C_{\rm ex} = 0$ and $C_{\rm ex}^{\rm high}$, and the "s-shell" is limited by $C_{\rm ex} = 0$ and

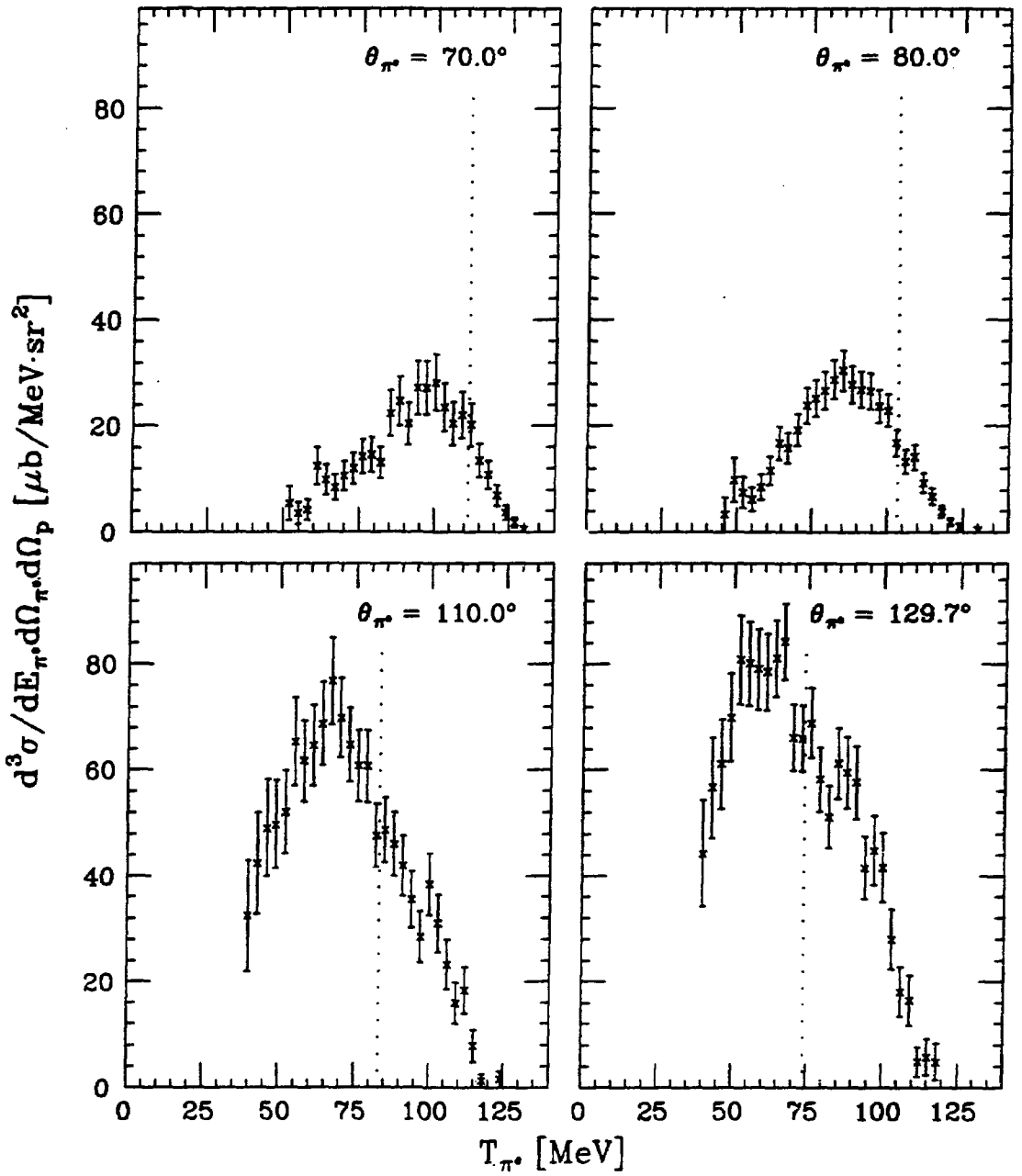

Figure 4.12. $d^3\sigma/dE_{\pi^0}\,d\Omega_{\pi^0}\,d\Omega_p$ spectra for the $^{16}O(\pi^+,\pi^0 p)$ reaction for all setups. The data shown were collected using the central proton telescope (in the scattering plane), and only the p-shell band is included. The dotted line indicates the quasi-free energy. There is a 15% normalization uncertainty in addition to the uncertainties shown in the figure.

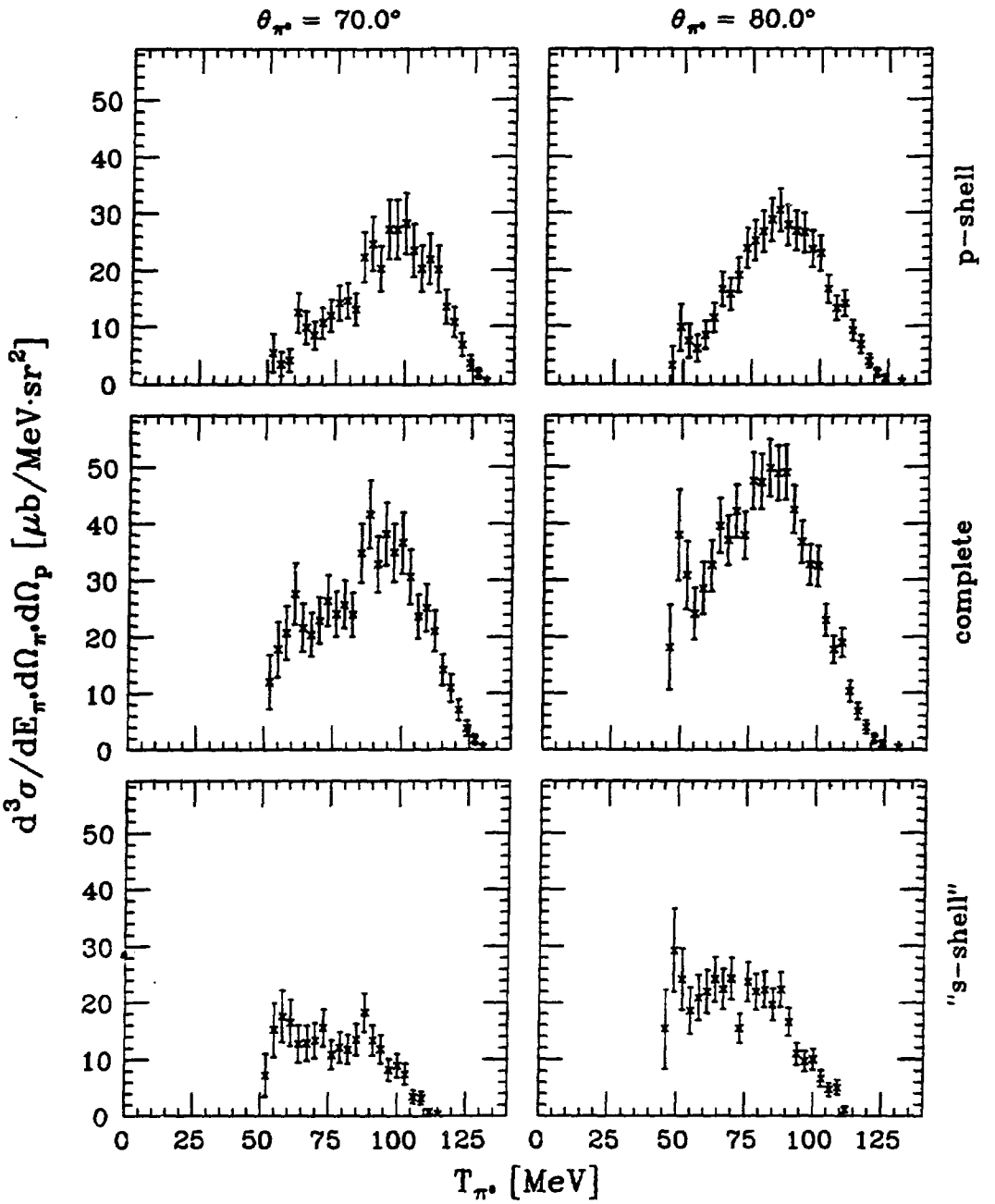

Figure 4.13. $d^3\sigma/dE_{\pi^0}\,d\Omega_{\pi^0}\,d\Omega_p$ spectra with different excitation energy cuts. In all cases the proton was detected in the central telescope. This figure shows the situation for the forward π^0 angles. The various energy cuts and π^0 angles are indicated in the figure. The normalization uncertainty (9% and 8% for the complete spectra at 70.0° and 80.0°, respectively, and 15% for the remaining spectra) is not included.

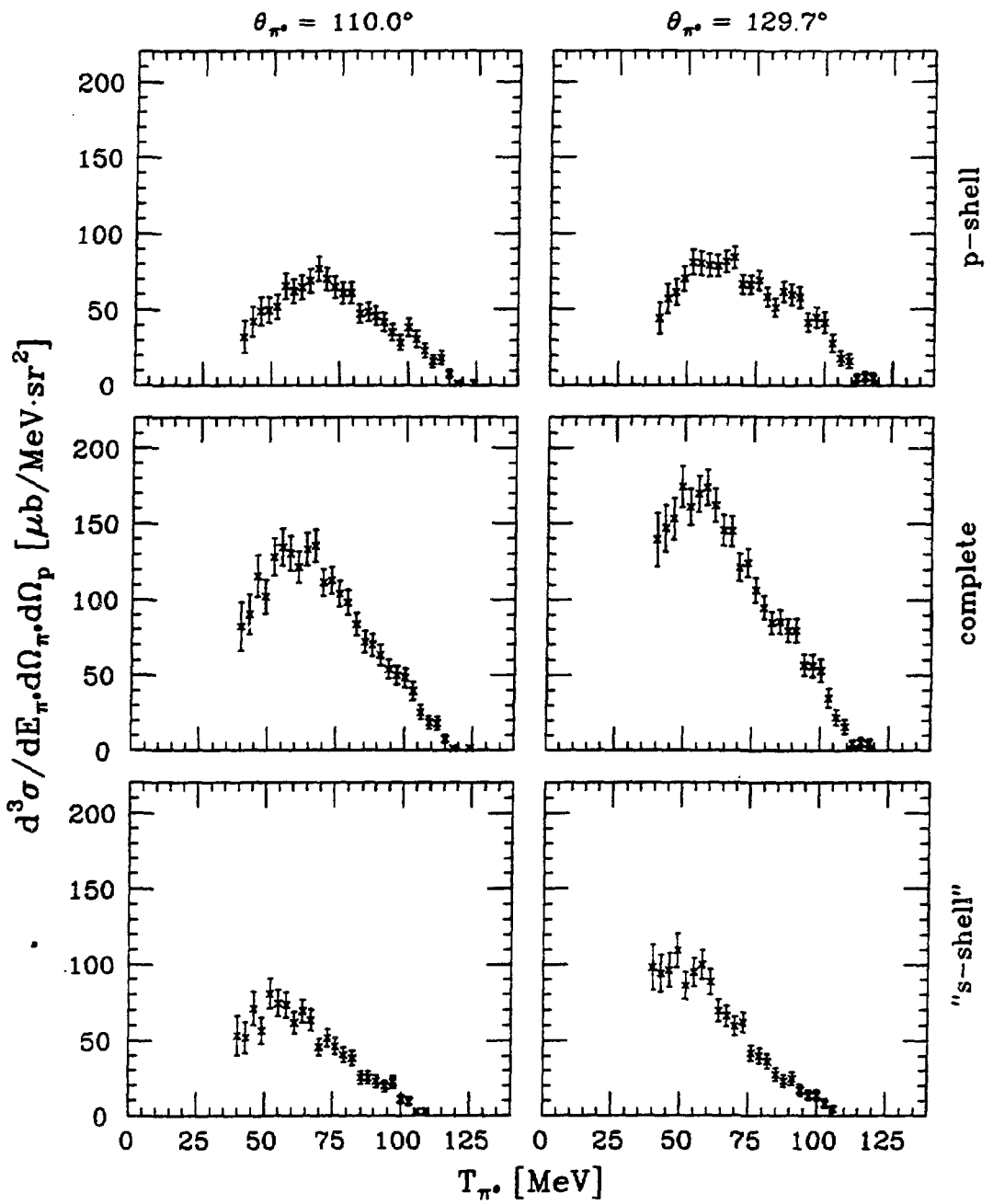

Figure 4.14. $d^3\sigma/dE_{\pi^0}\,d\Omega_{\pi^0}\,d\Omega_p$ spectra with different excitation energy cuts. In all cases the proton was detected in the central telescope. This figure shows the situation for the backward π^0 angles. The various energy cuts and π^0 angles are indicated in the figure. The normalization uncertainty (9% and 8% for the complete spectra at 110.0° and 129.7°, respectively, and 15% for the remaining spectra) is not included.

C_{ex}^{low}. Figs. 4.13 – 4.14 compare these different cuts in the data set. We see that the total coincidence cross section $d^3\sigma/dE_{\pi^0}\, d\Omega_{\pi^0}\, d\Omega_p$ is split roughly evenly between p-shell and "s-shell". The p-shell cross sections appear to favor higher π^0 energies somewhat more than the "s-shell" cross sections do. This was to be expected since the "s-shell" data necessarily involve a higher excitation level of the residual nucleus.

So far only spectra involving the central (scattering plane) proton telescope have been presented. We also analyzed the data from the other telescopes. For completeness $d^3\sigma/dE_{\pi^0}\, d\Omega_{\pi^0}\, d\Omega_p$ spectra for all telescopes are reproduced in Figs. 4.15 – 4.26. For each setup three kinds of spectra are shown: p-shell, complete data set, and "s-shell" (defined as above). The arrangement of the spectra in each figure reflects the arrangement of the telescopes in the proton arm. The lower three spectra were obtained by the telescopes below the scattering plane; then follow the central telescope and the telescopes above the scattering plane. The spectrum to the side of the vertical array is for telescope 8, which was positioned in the scattering plane at a larger scattering angle than the main array. The laboratory angle between each telescope was 17° (cf. Sec. 2.2.3). We see that all results are quite symmetric about the scattering plane. The position of the p-shell peak appears to shift towards higher π^0 energies as the out-of-plane angle increases. This is to be expected since the proton angle with respect to the beam increases with the out-of-plane angle. Kinematically, increasing the out-of-plane angle would therefore favor lower energy protons or, equivalently, higher energy pions. The statistics in the extreme out-of-plane spectra are too low to permit discussion of spectral features, but these spectra still provide important information about the absolute size of the cross sections at these angles.

4.1.7 Experimental Cross Sections $d^2\sigma/d\Omega_{\pi^0}\, d\Omega_p$

To obtain better information about the angular dependences of the measured cross sections we integrated the $d^3\sigma/dE_{\pi^0}\, d\Omega_{\pi^0}\, d\Omega_p$ cross sections presented in Sec. 4.1.6 over all energies. Several methods of integration were considered. The easiest would have been to sum the energy spectra bin by bin, but this method could not account for the missing parts of the spectra (some tails are lost because the energy acceptances of the π^0 spectrometer and the proton arm discriminated against certain energy ranges,

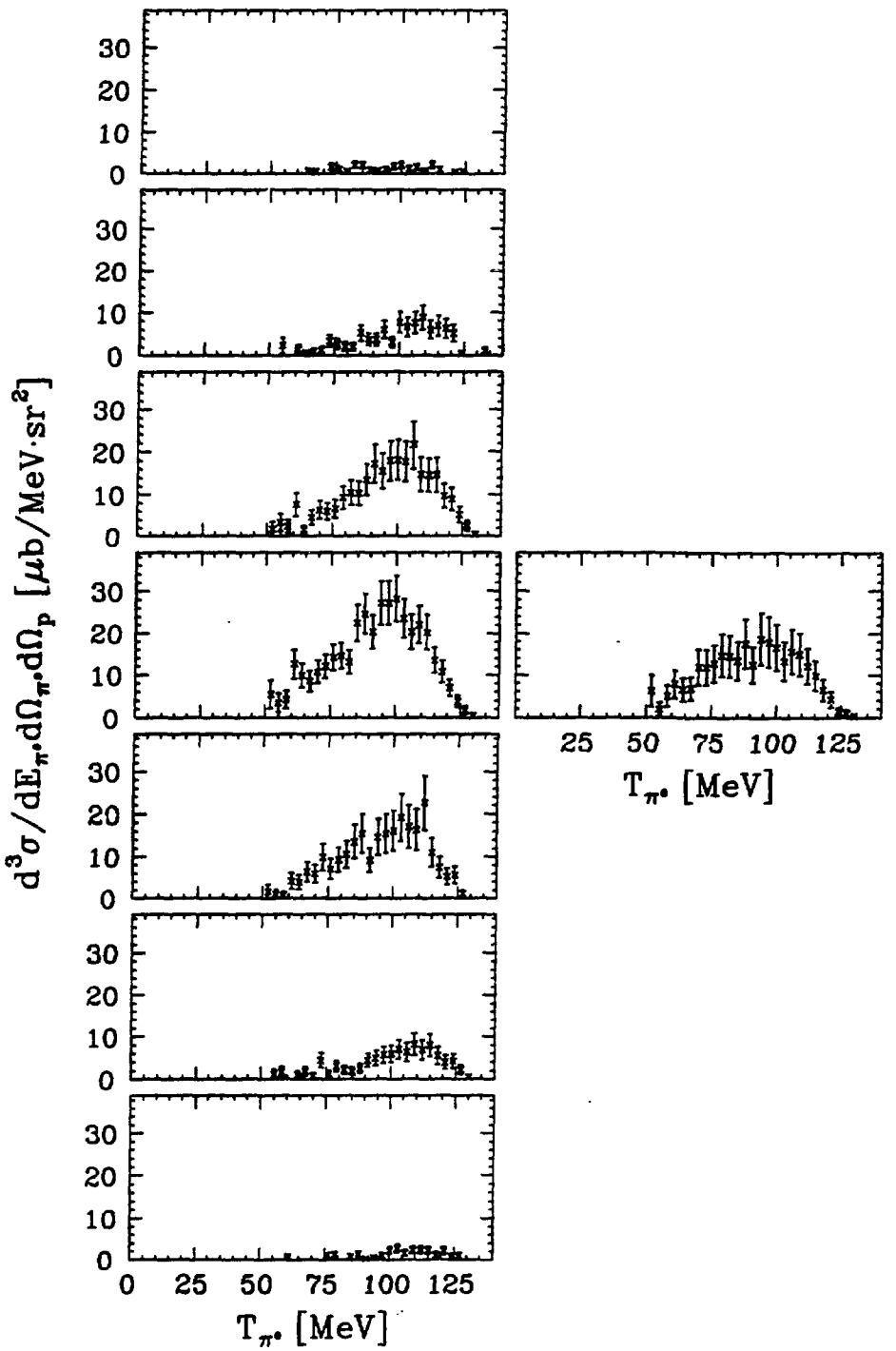

Figure 4.15. $d^3\sigma/dE_{\pi^0}\, d\Omega_{\pi^0}\, d\Omega_p$ p-shell spectra for all detectors at $\theta_{\pi^0} = 70.0°$. The normalization uncertainty (15%) is not included in the figure. The spectra are tabulated in Appendix E.

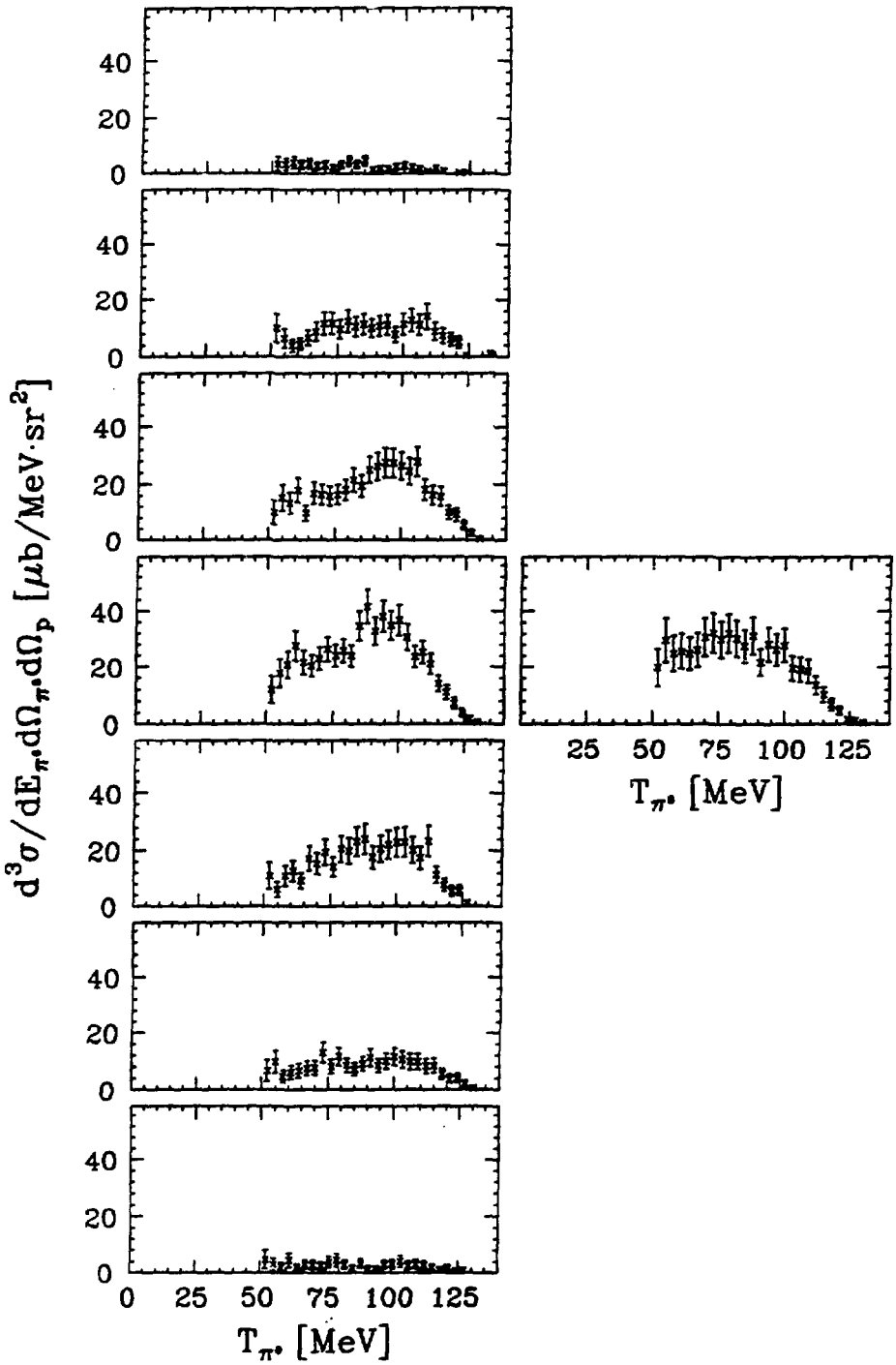

Figure 4.16. Complete $d^3\sigma/dE_{\pi^0}\,d\Omega_{\pi^0}\,d\Omega_p$ spectra for all detectors at $\theta_{\pi^0} = 70.0°$. The normalization uncertainty (9%) is not included in the figure. The spectra are tabulated in Appendix E.

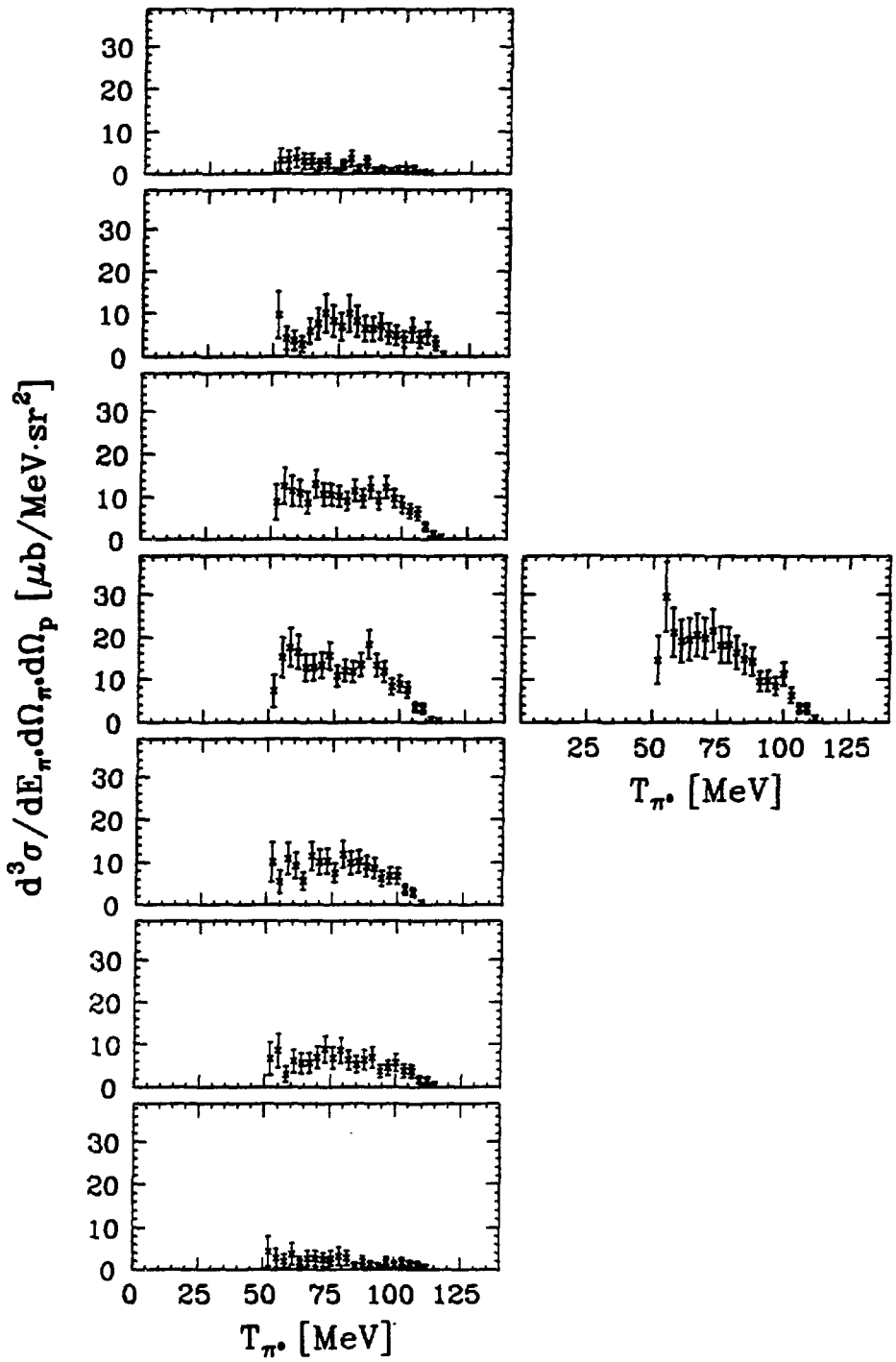

Figure 4.17. $d^3\sigma/dE_{\pi^0}\,d\Omega_{\pi^0}\,d\Omega_p$ "s-shell" spectra for all detectors at $\theta_{\pi^0} = 70.0°$. The normalization uncertainty (15%) is not included in the figure. The spectra are tabulated in Appendix E.

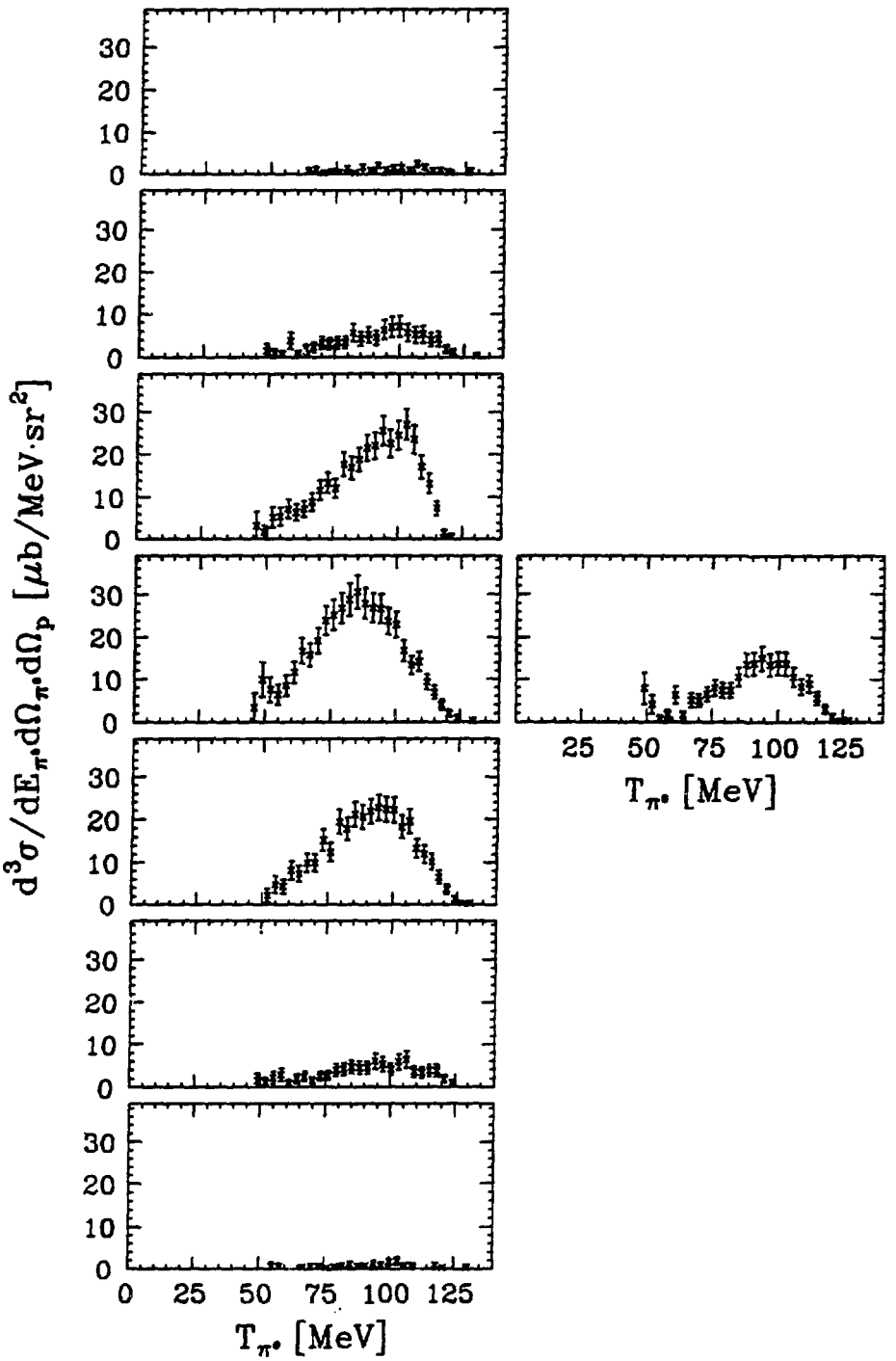

Figure 4.18. $d^3\sigma/dE_{\pi^0}\, d\Omega_{\pi^0}\, d\Omega_p$ p-shell spectra for all detectors at $\theta_{\pi^0} = 80.0°$. The normalization uncertainty (15%) is not included in the figure. The spectra are tabulated in Appendix E.

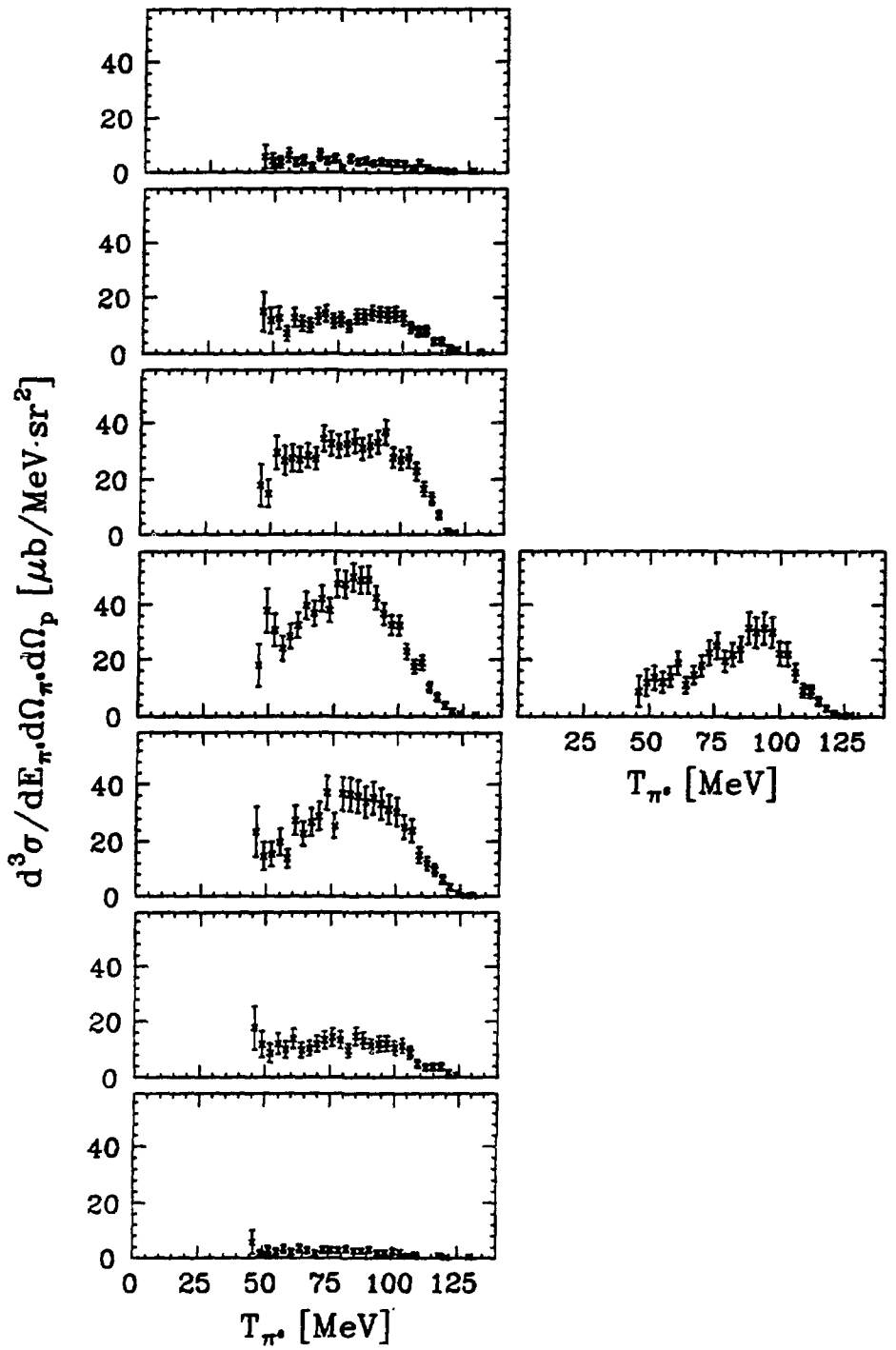

Figure 4.19. Complete $d^3\sigma/dE_{\pi^0}\,d\Omega_{\pi^0}\,d\Omega_p$ spectra for all detectors at $\theta_{\pi^0} = 80.0°$. The normalization uncertainty (8%) is not included in the figure. The spectra are tabulated in Appendix E.

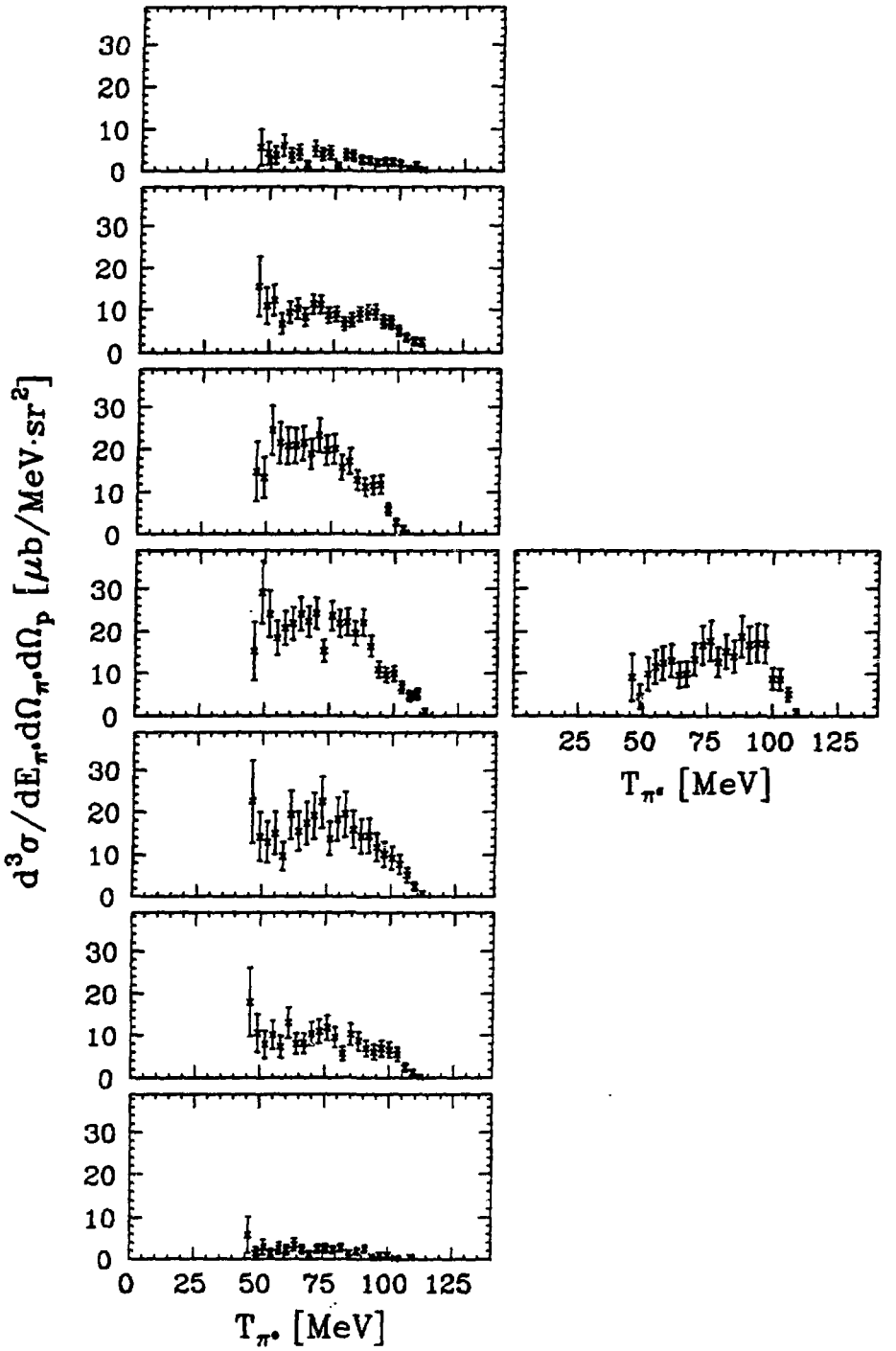

Figure 4.20. $d^3\sigma/dE_{\pi^0}\,d\Omega_{\pi^0}\,d\Omega_p$ "s-shell" spectra for all detectors at $\theta_{\pi^0} = 80.0°$. The normalization uncertainty (15%) is not included in the figure. The spectra are tabulated in Appendix E.

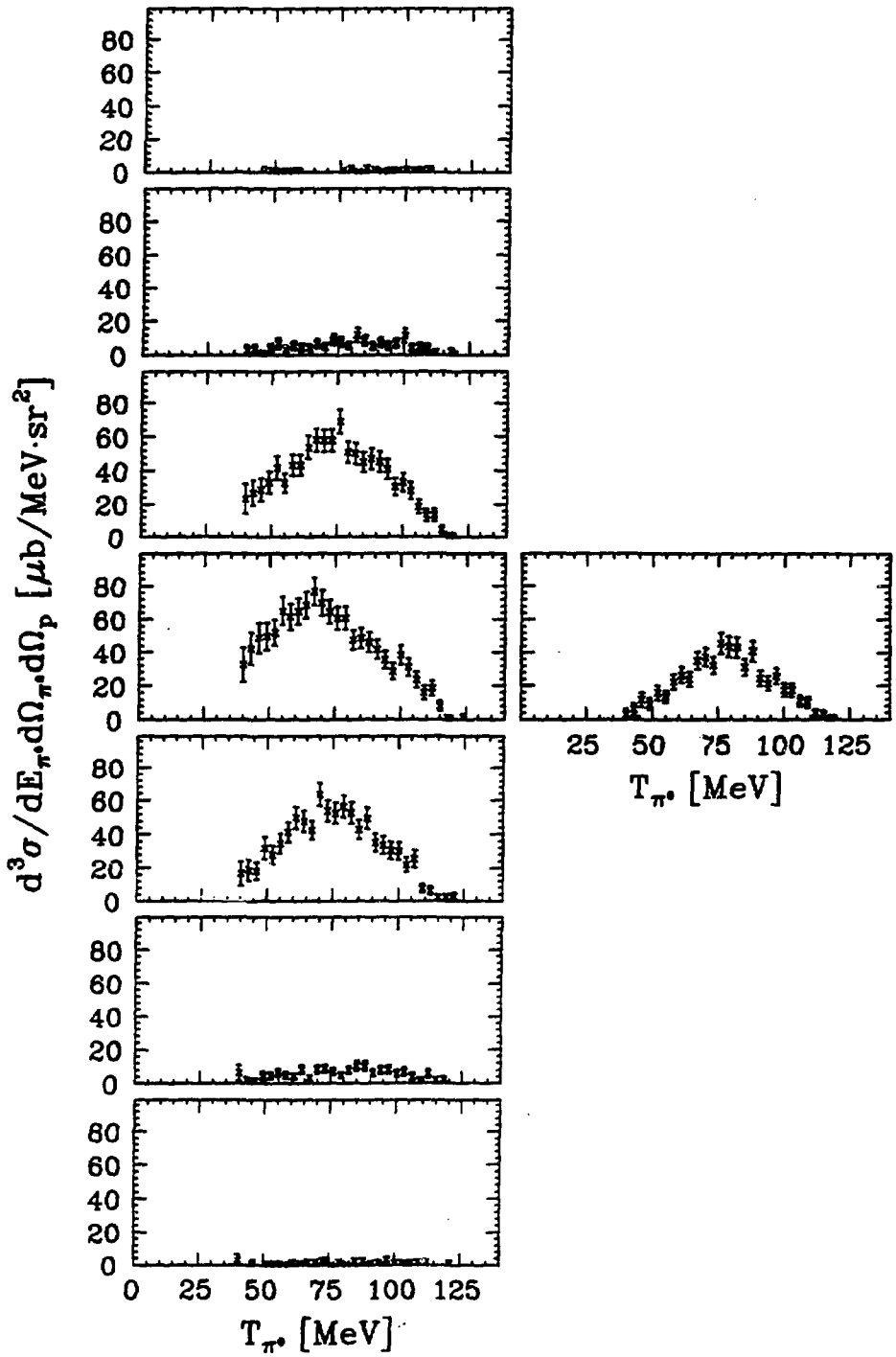

Figure 4.21. $d^3\sigma/dE_{\pi^0}\, d\Omega_{\pi^0}\, d\Omega_p$ p-shell spectra for all detectors at $\theta_{\pi^0} = 110.0°$. The normalization uncertainty (15%) is not included in the figure. The spectra are tabulated in Appendix E.

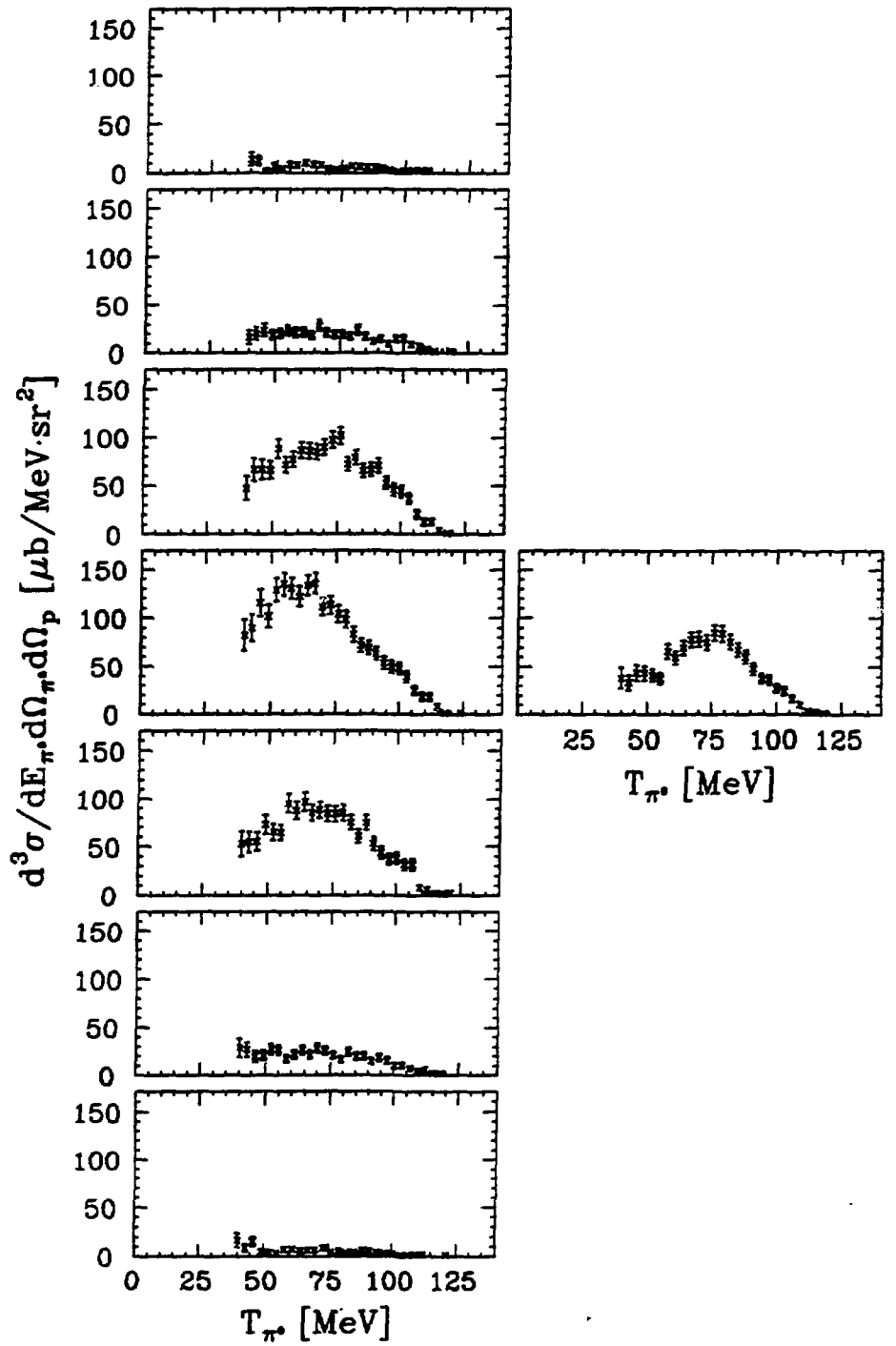

Figure 4.22. Complete $d^3\sigma/dE_{\pi^o}\,d\Omega_{\pi^o}\,d\Omega_p$ spectra for all detectors at $\theta_{\pi^o} = 110.0°$. The normalization uncertainty (9%) is not included in the figure. The spectra are tabulated in Appendix E.

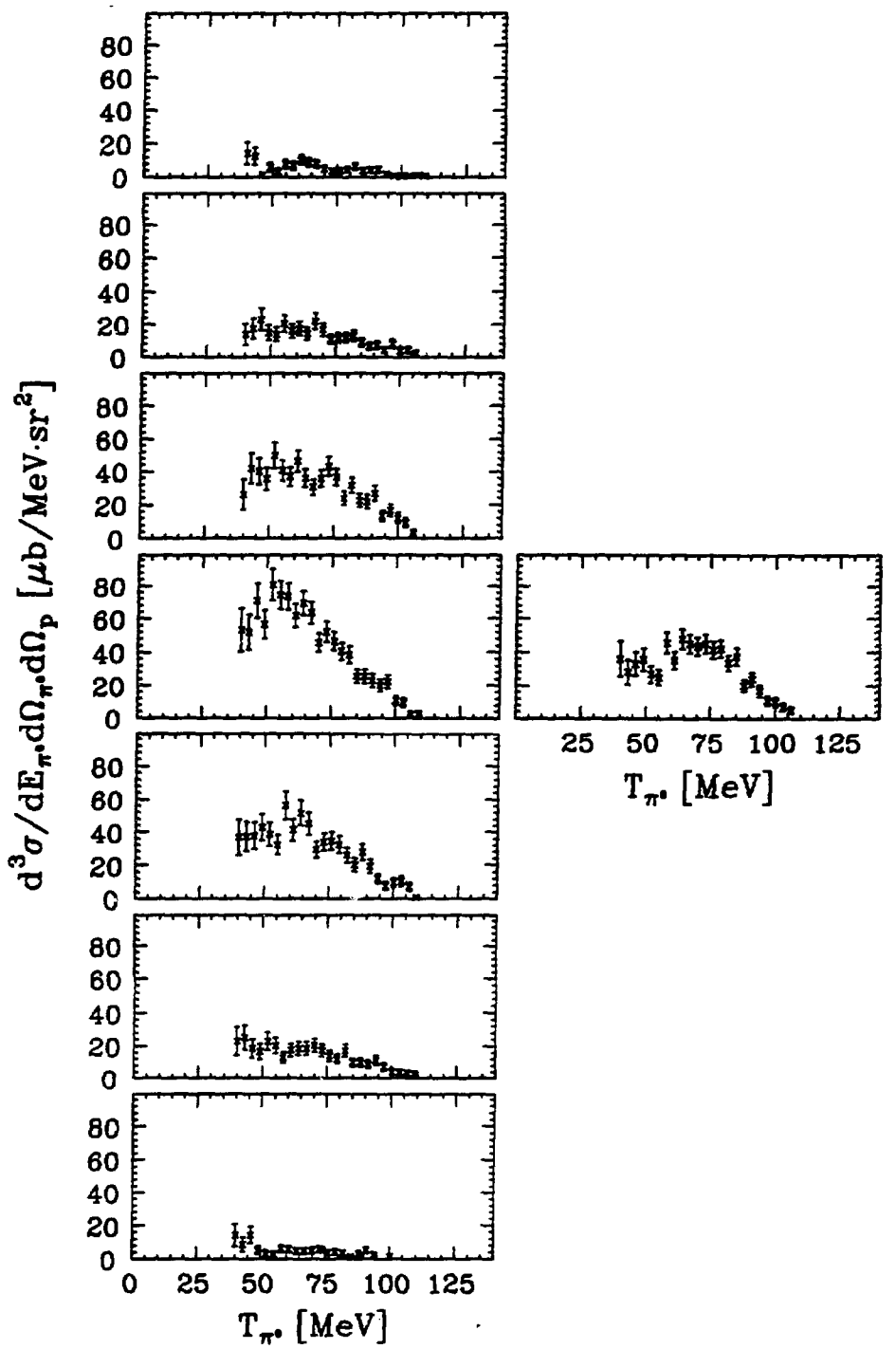

Figure 4.23. $d^3\sigma/dE_{\pi^o}\,d\Omega_{\pi^o}\,d\Omega_p$ "s-shell" spectra for all detectors at $\theta_{\pi^o} = 110.0°$. The normalization uncertainty (15%) is not included in the figure. The spectra are tabulated in Appendix E.

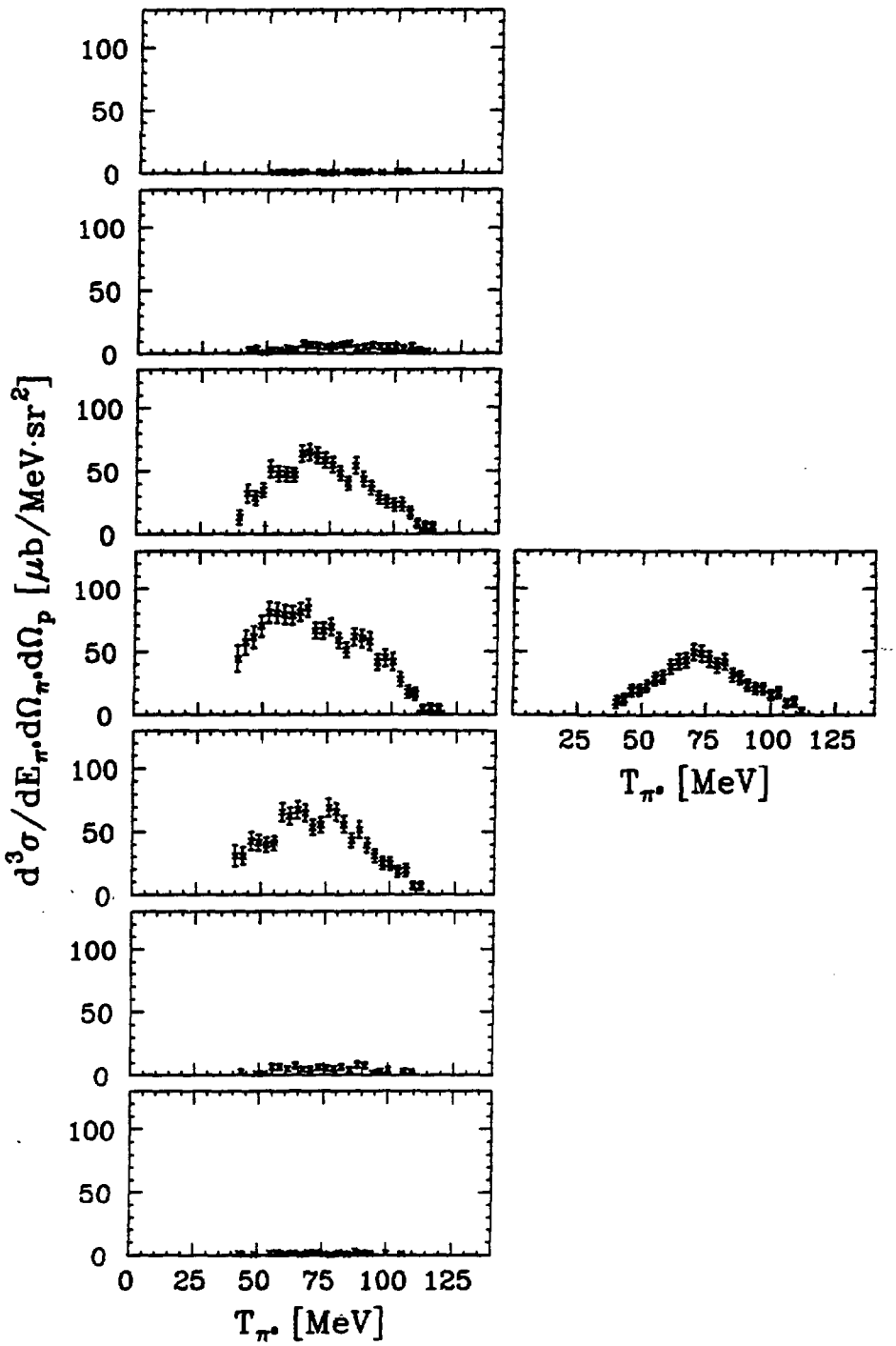

Figure 4.24. $d^3\sigma/dE_{\pi^0}\, d\Omega_{\pi^0}\, d\Omega_p$ p-shell spectra for all detectors at $\theta_{\pi^0} = 129.7°$. The normalization uncertainty (15%) is not included in the figure. The spectra are tabulated in Appendix E.

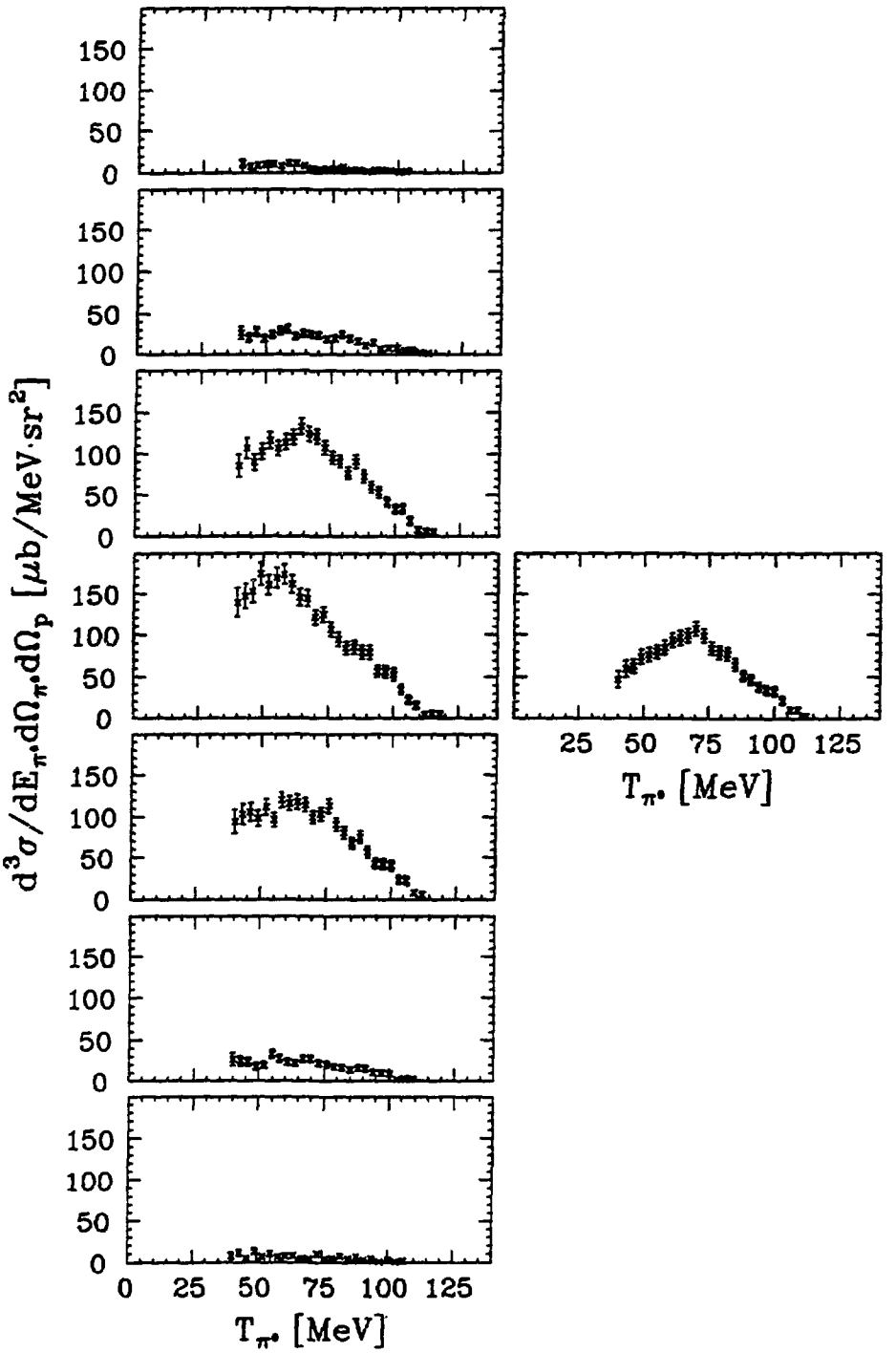

Figure 4.25. Complete $d^3\sigma/dE_{\pi^0}\,d\Omega_{\pi^0}\,d\Omega_p$ spectra for all detectors at $\theta_{\pi^0} = 129.7°$. The normalization uncertainty (8%) is not included in the figure. The spectra are tabulated in Appendix E.

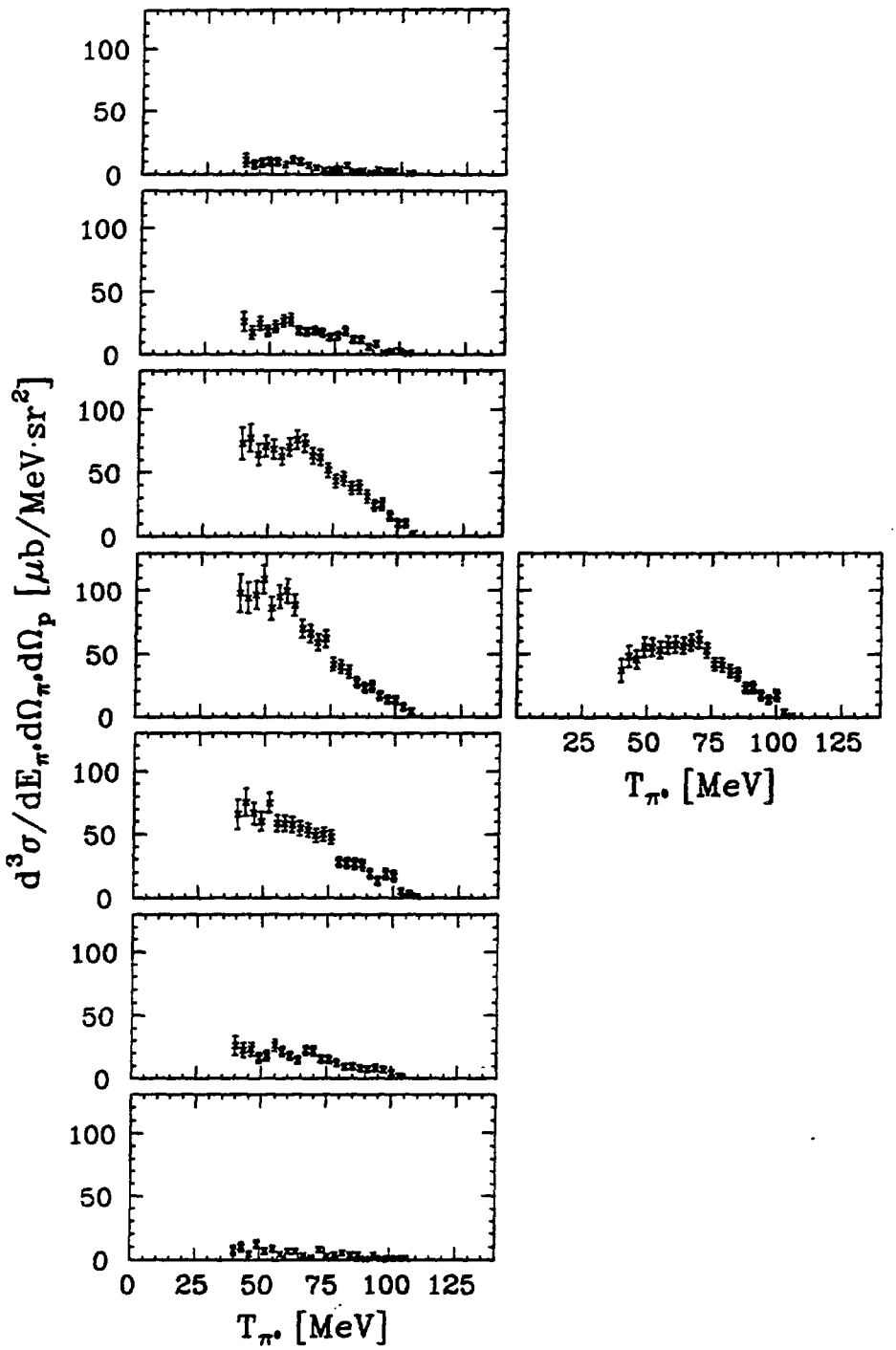

Figure 4.26. $d^3\sigma/dE_{\pi^0}\,d\Omega_{\pi^0}\,d\Omega_p$ "s-shell" spectra for all detectors at $\theta_{\pi^0} = 129.7°$. The normalization uncertainty (15%) is not included in the figure. The spectra are tabulated in Appendix E.

cf. Secs. 3.3.2 and 3.5.4.2). It was therefore necessary to fit a mathematical function to the data. We found that either an asymmetric gaussian,

$$\frac{d^3\sigma}{dE_{\pi^0}\,d\Omega_{\pi^0}\,d\Omega_p}(T_{\pi^0}) = c_1 \exp\left(-\frac{(T_{\pi^0}-c_2)^2}{2c_3^2}\right)\cdot\theta(c_2-T_{\pi^0}) + c_1\exp\left(-\frac{(T_{\pi^0}-c_2)^2}{2\,(c_3-c_4)^2}\right)\cdot\theta(T_{\pi^0}-c_2)\,, \qquad (4.9)$$

or a sum of two gaussians,

$$\frac{d^3\sigma}{dE_{\pi^0}\,d\Omega_{\pi^0}\,d\Omega_p}(T_{\pi^0}) = c_1\exp\left(-\frac{(T_{\pi^0}-c_2)^2}{2c_3^2}\right) + c_4\exp\left(-\frac{(T_{\pi^0}-c_5)^2}{2c_3^2}\right), \qquad (4.10)$$

was best suited for the purpose. In the above equations the c_i's are coefficients to be determined by the fitting process, and $\theta(x)$ is the unit step function:

$$\theta(x) = \begin{cases} 0 & \text{if } x<0; \\ \frac{1}{2} & \text{if } x=0; \\ 1 & \text{if } x>0. \end{cases} \qquad (4.11)$$

The two-gaussian function was initially chosen because the p-shell cross section spectra are thought of as composed of two similar peaks if the quasi-free energy is somewhere central in the spectrum (cf. Fig. 4.1). Note that both peaks are given the same width. In cases where most of the detected p-shell energy spectrum is on one side of the quasi-free energy, or where no p-shell cut was made, the one-peak, asymmetric gaussian was assumed to provide an adequate description of the data. The asymmetry was loosely restricted by $|c_4| < 50$ MeV. Our experience from the actual fitting is that the asymmetric gaussian is not as flexible in use as the sum of two gaussians, and we ended up using the sum of two gaussians for all complete (no p-shell cut) spectra as well as for the p-shell spectra taken at $\theta_{\pi^0} = 110.0°$ and $\theta_{\pi^0} = 129.7°$.

The fits for the central proton telescope are shown in Figs. 4.27 and 4.28. Due to the low statistics of the spectra for the extreme out-of-plane telescopes, fitting to these is a more uncertain process, but the integrated areas of all fits should still provide fair estimates of the integrated cross sections $d^2\sigma/d\Omega_{\pi^0}\,d\Omega_p$. All our integrated cross sections are listed in Table 4.4.

The data in Table 4.4 show the angular distribution of the $^{16}O(\pi^+,\pi^0 p)$ cross sections. This is illustrated in Figs. 4.29 and 4.30, where we have plotted the data for telescopes

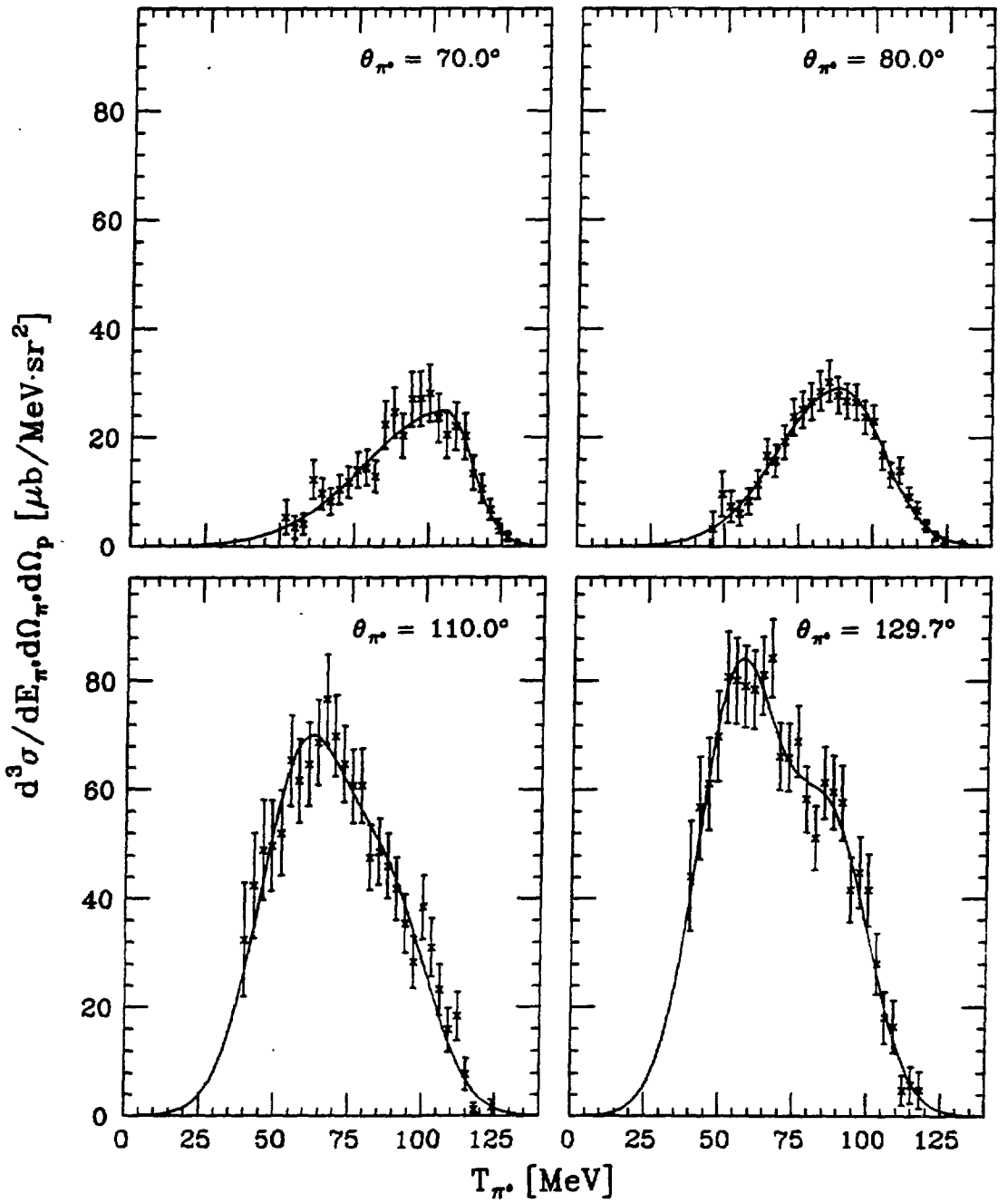

Figure 4.27. Fits to p-shell $d^3\sigma/dE_{\pi^0}\,d\Omega_{\pi^0}\,d\Omega_p$ energy spectra. The spectra are for the $^{16}O(\pi^+,\pi^0 p)$ reaction, and they are all obtained using the central proton telescope. The fits for the two forward π^0 angles are asymmetric gaussians, while a sum of two gaussians was used for the backward angles. The spectra are the same as those shown in Fig. 4.12. The normalization uncertainty (15%) is not included in the figure.

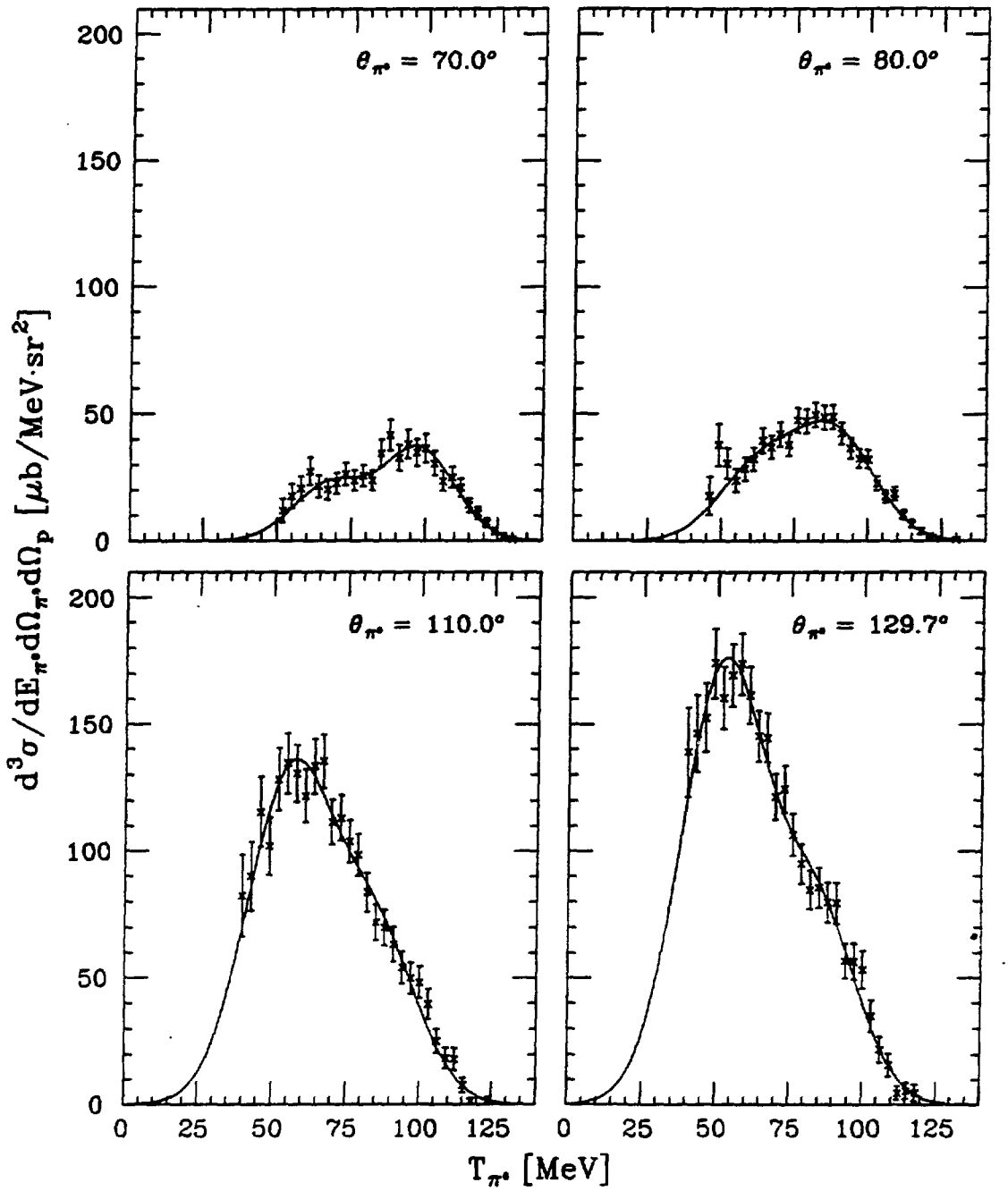

Figure 4.28. Fits to complete $d^3\sigma/dE_{\pi^0}\,d\Omega_{\pi^0}\,d\Omega_p$ energy spectra. The spectra are for the $^{16}O(\pi^+,\pi^0 p)$ reaction, and they are all obtained using the central proton telescope. All fits were made with a sum of two gaussians. The normalization uncertainty (9% for $\theta_{\pi^0} = 70.0°$ and $\theta_{\pi^0} = 110.0°$ and 8% for the other setups) is not included in the figure.

Table 4.4. Integrated cross sections $d^2\sigma/d\Omega_{\pi^0}\,d\Omega_p$. (a) lists all p-shell cross sections, and (b) lists the cross sections obtained when the ejected nucleon is not restricted to the p-shell only. The normalization uncertainty comes in addition to the uncertainties quoted in the table. This is 15% for all setups in (a). In (b) it is 9% for $\theta_{\pi^0} = 70.0°$ and $\theta_{\pi^0} = 110.0°$ and 8% for the other setups.

(a)

telescope	$\frac{d^2\sigma}{d\Omega_{\pi^0}\,d\Omega_p}$ for $^{16}O(\pi^+,\pi^0 p_{\text{p-shell}})$ $\left[\frac{\text{mb}}{\text{sr}^2}\right]$			
	$\theta_{\pi^0} = 70.0°$	$\theta_{\pi^0} = 80.0°$	$\theta_{\pi^0} = 110.0°$	$\theta_{\pi^0} = 129.7°$
1	0.07 ± 0.01	0.05 ± 0.01	0.10 ± 0.02	0.09 ± 0.02
2	0.26 ± 0.02	0.26 ± 0.02	0.44 ± 0.04	0.29 ± 0.03
3	0.76 ± 0.05	1.00 ± 0.04	2.70 ± 0.10	3.19 ± 0.10
4	1.14 ± 0.06	1.30 ± 0.05	3.70 ± 0.14	4.46 ± 0.15
5	0.71 ± 0.05	1.03 ± 0.04	3.05 ± 0.13	2.99 ± 0.10
6	0.26 ± 0.02	0.27 ± 0.02	0.42 ± 0.08	0.32 ± 0.03
7	0.08 ± 0.01	0.06 ± 0.01	0.10 ± 0.02	0.04 ± 0.01
8	0.80 ± 0.06	0.53 ± 0.03	1.71 ± 0.07	2.09 ± 0.14

(b)

telescope	$\frac{d^2\sigma}{d\Omega_{\pi^0}\,d\Omega_p}$ for $^{16}O(\pi^+,\pi^0 p)$ $\left[\frac{\text{mb}}{\text{sr}^2}\right]$			
	$\theta_{\pi^0} = 70.0°$	$\theta_{\pi^0} = 80.0°$	$\theta_{\pi^0} = 110.0°$	$\theta_{\pi^0} = 129.7°$
1	0.17 ± 0.02	0.15 ± 0.02	0.39 ± 0.05	0.38 ± 0.05
2	0.60 ± 0.04	0.80 ± 0.05	1.50 ± 0.09	1.33 ± 0.08
3	1.34 ± 0.06	1.83 ± 0.08	4.82 ± 0.22	6.39 ± 0.19
4	1.79 ± 0.07	2.40 ± 0.07	6.89 ± 0.22	8.78 ± 0.28
5	1.17 ± 0.07	1.90 ± 0.07	5.17 ± 0.22	6.50 ± 0.18
6	0.61 ± 0.04	0.80 ± 0.04	1.33 ± 0.09	1.38 ± 0.08
7	0.18 ± 0.03	0.25 ± 0.03	0.40 ± 0.08	0.42 ± 0.04
8	1.77 ± 0.13	1.35 ± 0.07	3.89 ± 0.14	4.88 ± 0.14

1−7 as a function of the out-of-plane angle ϕ_p. The cross sections are clearly symmetric about the scattering plane. The solid curves in the figures are fits to the data.

In their study of the $(\pi^\pm,\pi^\pm p)$ reactions,[20] Piasetzky *et al.* found it appropriate to fit a sum of two gaussians to the angular distribution, one narrow gaussian associated with the quasi-free pion-nucleon process and one broad gaussian to account for other processes. In our case we only had seven points to fit to; we therefore decided to use

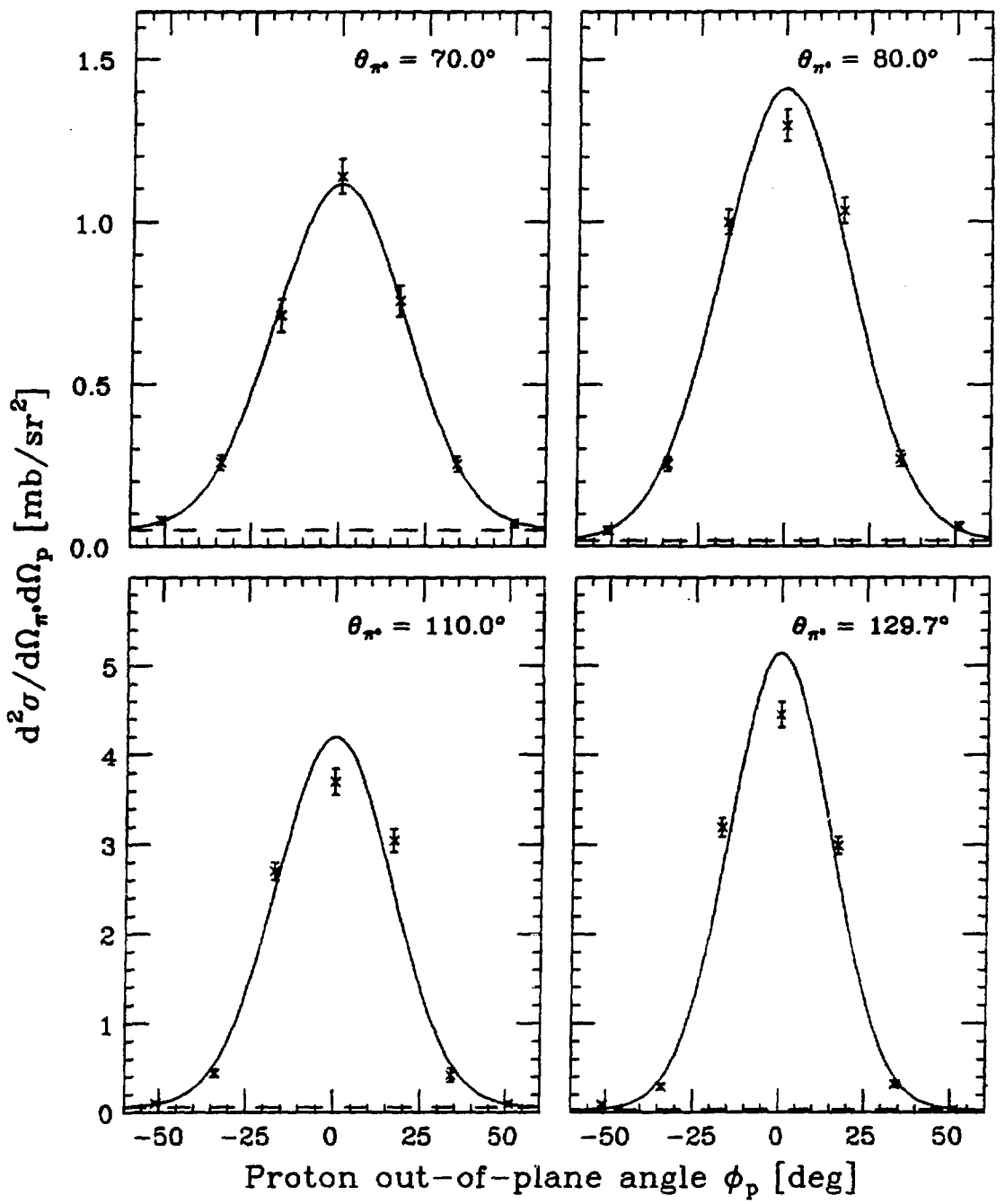

Figure 4.29. p-shell cross sections $d^2\sigma/d\Omega_{\pi^o}\,d\Omega_p$ for $^{16}O(\pi^+,\pi^0 p)$ for all setups. The data are from Table 4.4a (telescopes 1 – 7). The normalization uncertainty (15%) is not included in the figure. The solid curves are gaussian fits to the data (added to a constant background (dashes)).

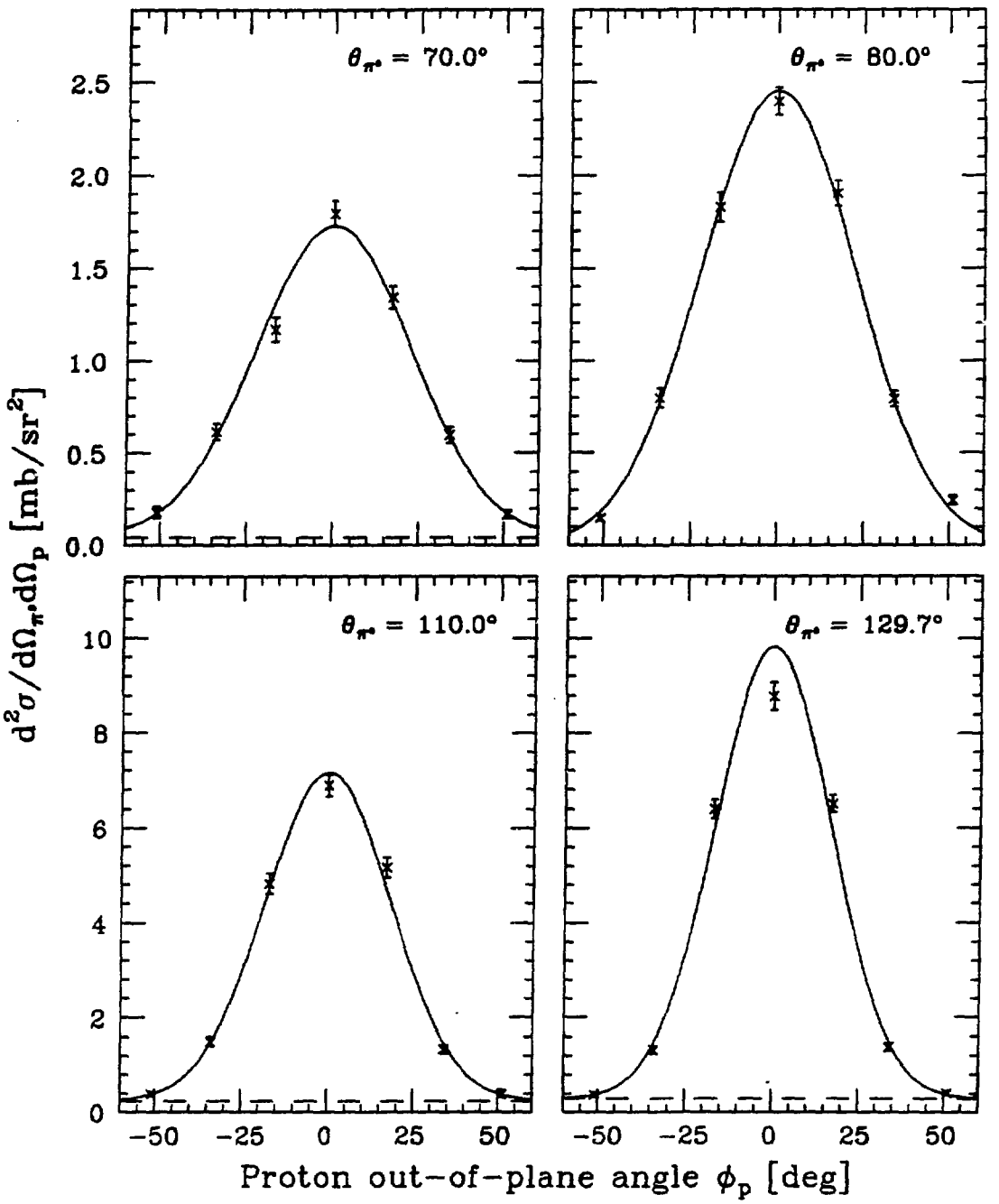

Figure 4.30. Complete cross section $d^2\sigma/d\Omega_{\pi^0}\,d\Omega_p$ for $^{16}O(\pi^+,\pi^0 p)$ for all setups. The data are from Table 4.4b (telescopes 1 – 7). The normalization uncertainty (9% for $\theta_{\pi^0} = 70.0°$ and $\theta_{\pi^0} = 110.0°$ and 8% for the other setups) is not included in the figure. The solid curves are gaussian fits to the data (added to a constant background (dashes)).

Table 4.5. Fit parameters for $d^2\sigma/d\Omega_{\pi^0}\,d\Omega_p$. The parameters listed results from fitting to the distribution of $d^2\sigma/d\Omega_{\pi^0}\,d\Omega_p$ as a function of the proton out-of-plane angle ϕ_p (see the text). (a) lists the results for the p-shell cross sections shown in Fig. 4.29, and (b) lists the results for the complete cross sections shown in Fig. 4.30. "amplitude" in the table means the amplitude of the gaussian contribution to the fit.

(a)

θ_{π^0} [deg]	amplitude [mb/sr^2]	FWHM [deg]	background [mb/sr^2]
70.0	1.06 ± 0.04	44.1 ± 1.7	0.05 ± 0.01
80.0	1.39 ± 0.04	44.2 ± 1.1	0.02 ± 0.01
110.0	4.14 ± 0.11	38.8 ± 0.8	0.06 ± 0.02
129.7	5.12 ± 0.12	34.8 ± 0.5	0.03 ± 0.01

(b)

θ_{π^0} [deg]	amplitude [mb/sr^2]	FWHM [deg]	background [mb/sr^2]
70.0	1.69 ± 0.05	53.2 ± 2.8	0.04 ± 0.05
80.0	2.45 ± 0.05	52.8 ± 0.8	0.00 ± 0.02
110.0	6.91 ± 0.18	43.1 ± 1.0	0.24 ± 0.06
129.7	9.52 ± 0.21	39.2 ± 0.6	0.29 ± 0.04

a single gaussian centered at $\phi_p = 0$ added to an angle-independent background:

$$\frac{d^2\sigma}{d\Omega_{\pi^0}\,d\Omega_p}(\phi_p) = c_1 \exp\left(-\frac{\phi_p^2}{2c_2^2}\right) + c_3\,, \tag{4.12}$$

where the c_i's are the coefficients varied in the fitting process. The background (c_3) was required to be non-negative. The fit results are listed in Table 4.5. We see from Fig. 4.30 that the angular distribution is described well by a gaussian function when no p-shell cut is imposed on the data. The p-shell data shown in Fig. 4.29, however, appear to be either too wide near the peak or too low at the peak for the gaussian fit. This is in qualitative agreement with the predictions of our Monte Carlo simulations as shown in Figs. 4.3 and 4.4. In all cases the background is small compared to the gaussian part of the cross section; the p-shell data have practically no background at all (cf. Table 4.5).

Table 4.6. Integrated cross sections $d\sigma/d\Omega_{\pi^0}$. The second uncertainty term is the normalization uncertainty. The normalization is independent for each setup. The numbers in parentheses are the total (combined) uncertainties.

θ_{π^0} [deg]	$\frac{d\sigma}{d\Omega_{\pi^0}}$ $\left[\frac{\text{mb}}{\text{sr}}\right]$	
	$^{16}\text{O}(\pi^+,\pi^0 p_{\text{p-shell}})$	$^{16}\text{O}(\pi^+,\pi^0 p)$
70.0	$0.71 \pm 0.05 \pm 0.11$ (0.12)	$1.65 \pm 0.19 \pm 0.15$ (0.24)
80.0	$0.94 \pm 0.05 \pm 0.14$ (0.15)	$2.36 \pm 0.18 \pm 0.19$ (0.26)
110.0	$2.15 \pm 0.08 \pm 0.33$ (0.34)	$4.43 \pm 0.20 \pm 0.41$ (0.46)
129.7	$2.14 \pm 0.05 \pm 0.31$ (0.32)	$5.04 \pm 0.14 \pm 0.42$ (0.45)

4.1.8 Experimental Cross Sections $d\sigma/d\Omega_{\pi^0}$

Piasetzky *et al.* found in their study[20] of the $(\pi^\pm,\pi^\pm p)$ reaction at 245 MeV that the spatial distribution of the quasi-free process is symmetric in all dimensions about the quasi-free angle. (Their data were presented in the laboratory frame.) We therefore estimate the cross section $d\sigma/d\Omega_{\pi^0}$ of the quasi-free part of the $^{16}\text{O}(\pi^+,\pi^0 p)$ reaction by assuming spatial symmetry around the quasi-free angle of the fits made in Sec. 4.1.7.

Assuming the quasi-free process to be described by the gaussian part of Eq. (4.12), we then get

$$\begin{aligned}
\frac{d\sigma}{d\Omega_{\pi^0}} &= \int_{4\pi} d\Omega_p \left.\frac{d^2\sigma}{d\Omega_{\pi^0}\, d\Omega_p}\right|_{\text{quasi-free}} \\
&= 2\pi c_1 \int_0^\pi d\vartheta \, \sin\vartheta \, \exp\left(-\frac{\vartheta^2}{2c_2^2}\right) \\
&\approx 2\pi c_1 \int_0^\infty d\vartheta \, \sin\vartheta \, \exp\left(-\frac{\vartheta^2}{2c_2^2}\right) \\
&= 2\pi c_1 c_2^2 \left[1 + \sum_{k=1}^{\infty} (-1)^k \frac{c_2^{2k}}{(2k+1)!!}\right] . \qquad (4.13)
\end{aligned}$$

This is a rapidly converging series. The first term alone is what one gets by simply rotating the gaussian function about the central axis. The change in $d\sigma/d\Omega_{\pi^0}$ when adding the third term in the sum was always less than 0.1%.

Our values for $d\sigma/d\Omega_{\pi^0}$ are tabulated as a function of the π^0 angle θ_{π^0} in Table 4.6. The normalization uncertainty is also given in the table. This should be included in any further processing of the data because each setup has it own independent normalization.

4.2 *A*-Dependence of the $(\pi^+, \pi^0 p)$ Reaction

At $\theta_{\pi^0} = 110.0°$ we collected data for a study of the *A*-dependence of the $(\pi^+, \pi^0 p)$ reaction. In addition to the measurements on oxygen presented in Sec. 4.1, we measured the reaction on three other targets: iron, tin, and lead. These targets are described in Table 2.1.

Our results are presented in two subsections below. The first contains the basic $d^3\sigma/dE_{\pi^0}\, d\Omega_{\pi^0}\, d\Omega_p$ cross sections for all targets and proton telescopes, and the second presents the integrated cross sections $d^2\sigma/d\Omega_{\pi^0}\, d\Omega_p$ and $d\sigma/d\Omega_{\pi^0}$.

4.2.1 Experimental Cross Sections $d^3\sigma/dE_{\pi^0}\, d\Omega_{\pi^0}\, d\Omega_p$

All *A*-dependence data were analyzed as described for the oxygen data in Sec. 4.1. We did not attempt to identify specific nuclear shells; all values of the excitation energy parameter C_{ex} up to $C_{ex}^{high} = 162$ MeV were allowed. In Sec. 4.1.5 we found that most real background events in the water target measurements originated in the air, not in the Mylar target windows. We therefore decided to subtract the data obtained with an empty water target also from all iron, tin, and lead data.

Our results for $d^3\sigma/dE_{\pi^0}\, d\Omega_{\pi^0}\, d\Omega_p$ for the central proton detector for the four targets studied at $\theta_{\pi^0} = 110.0°$ are shown in Fig. 4.31. The cross sections are remarkably similar in magnitude. The complete set of cross section spectra for all proton telescopes for the iron, tin, and lead targets are presented in Figs. 4.32–4.34. The corresponding information for oxygen is found in Fig. 4.22.

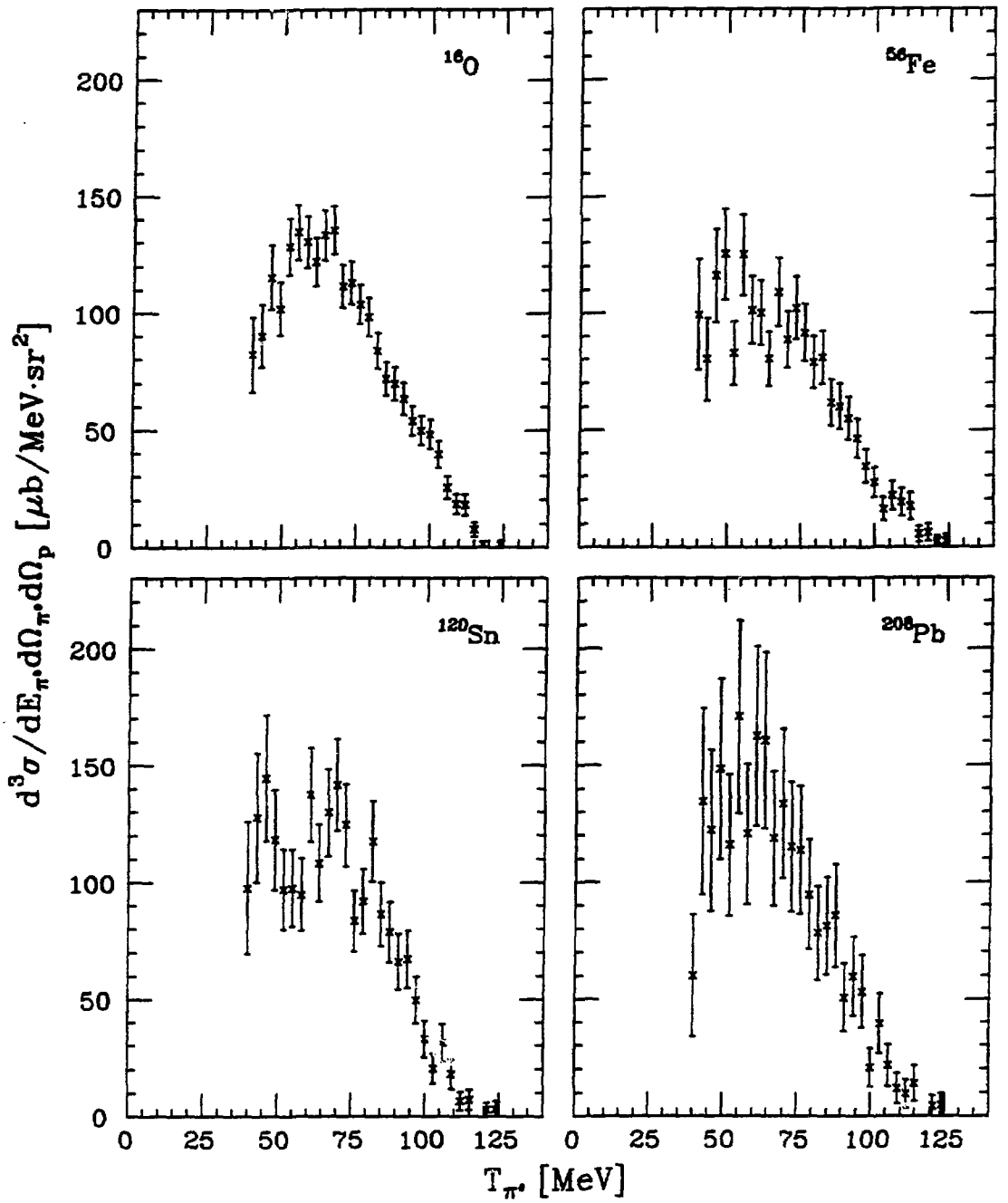

Figure 4.31. $d^3\sigma/dE_{\pi^0}\,d\Omega_{\pi^0}\,d\Omega_p$ spectra for the $(\pi^+,\pi^0 p)$ reaction on various targets. All data are for $\theta_{\pi^0} = 110.0°$, and they were collected using the central proton telescope. The target used is indicated in each plot. The normalization uncertainty comes in addition to the uncertainties shown in the figure. This is 9% for oxygen and 10% for the other targets.

Table 4.7. Integrated cross sections $d^2\sigma/d\Omega_{\pi^0}\, d\Omega_p$ for all targets. The measurements were done at $\theta_{\pi^0} = 110.0°$ with a beam energy of $T_{\pi^+} = 165$ MeV. The normalization uncertainty comes in addition to the uncertainties quoted in the table. This is 9% for the oxygen data and 10% for data from the other targets.

telescope	$\frac{d^2\sigma}{d\Omega_{\pi^0}\, d\Omega_p}$ for $(\pi^+,\pi^0 p)$ $\left[\frac{\mathrm{mb}}{\mathrm{sr}^2}\right]$			
	^{16}O	^{56}Fe	^{120}Sn	^{208}Pb
1	0.39 ± 0.05	0.49 ± 0.06	0.60 ± 0.11	0.72 ± 0.15
2	1.50 ± 0.09	1.42 ± 0.12	1.93 ± 0.23	1.83 ± 0.23
3	4.82 ± 0.22	3.85 ± 0.20	4.18 ± 0.31	4.33 ± 0.39
4	6.89 ± 0.22	6.06 ± 0.31	6.89 ± 0.36	7.51 ± 0.59
5	5.17 ± 0.22	3.91 ± 0.22	4.56 ± 0.27	4.29 ± 0.36
6	1.33 ± 0.09	1.28 ± 0.15	1.45 ± 0.17	1.50 ± 0.24
7	0.40 ± 0.08	0.51 ± 0.06	0.79 ± 0.10	0.94 ± 0.14
8	3.89 ± 0.14	3.14 ± 0.15	3.85 ± 0.23	4.25 ± 0.39

4.2.2 Experimental Cross Sections $d^2\sigma/d\Omega_{\pi^0}\, d\Omega_p$ and $d\sigma/d\Omega_{\pi^0}$

The same integration procedures as outlined in Secs. 4.1.7 and 4.1.8 for the oxygen data were applied to the data from the other targets; a sum of two gaussians (Eq. (4.10)) was fitted to each spectrum, and a gaussian on a constant background (Eq. (4.12)) was fitted to the out-of-plane angular distribution to obtain the cross sections $d\sigma/d\Omega_{\pi^0}$ for the quasi-free contribution to the $(\pi^+,\pi^0 p)$ reaction (Eq. (4.13)).

The integrated cross sections $d^3\sigma/dE_{\pi^0}\, d\Omega_{\pi^0}\, d\Omega_p$ are all presented in Table 4.7. The table also lists the relevant results for the oxygen target from Table 4.4. The fits to the out-of-plane angular distributions are shown in Fig. 4.35. Again one notes that there is very little difference between the different nuclei. Also note that the background appears to get larger with A, indicating that the relative importance of non-quasi-free processes (multiple scattering, final state interactions) increases with the complexity of the nuclei. The fit parameters and the resulting cross sections $d\sigma/d\Omega_{\pi^0}$ are all listed in Table 4.8.

4.3 Single Arm Measurements of the (π^+,π^0) Reaction

The single arm measurements presented in this section were taken between the coin-

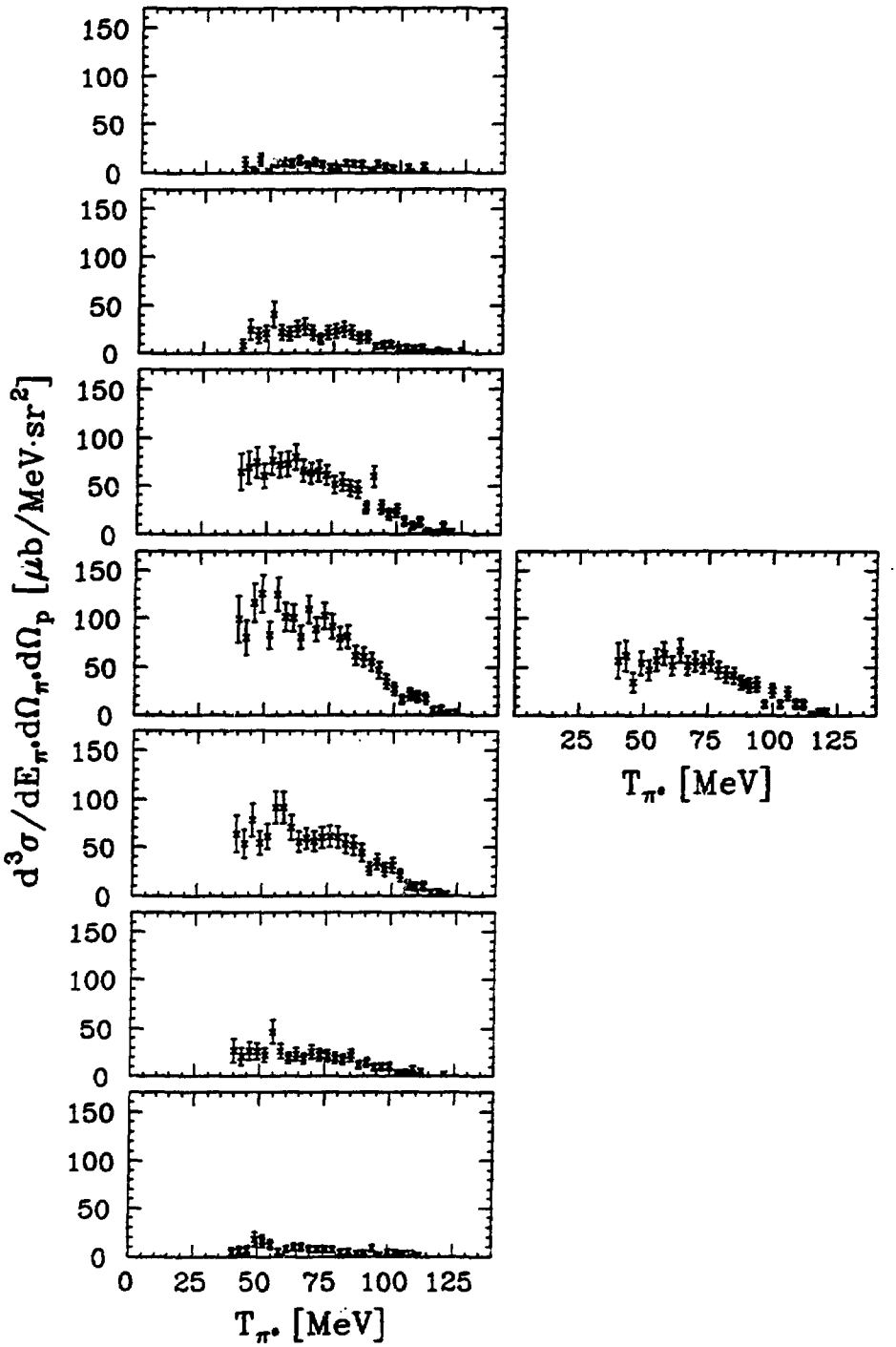

Figure 4.32. $d^3\sigma/dE_{\pi^0}\,d\Omega_{\pi^0}\,d\Omega_p$ spectra obtained with the iron target for all detectors. The π^0 angle was $\theta_{\pi^0} = 110.0°$. The normalization uncertainty (10%) is not included in the figure. See Appendix E for listing.

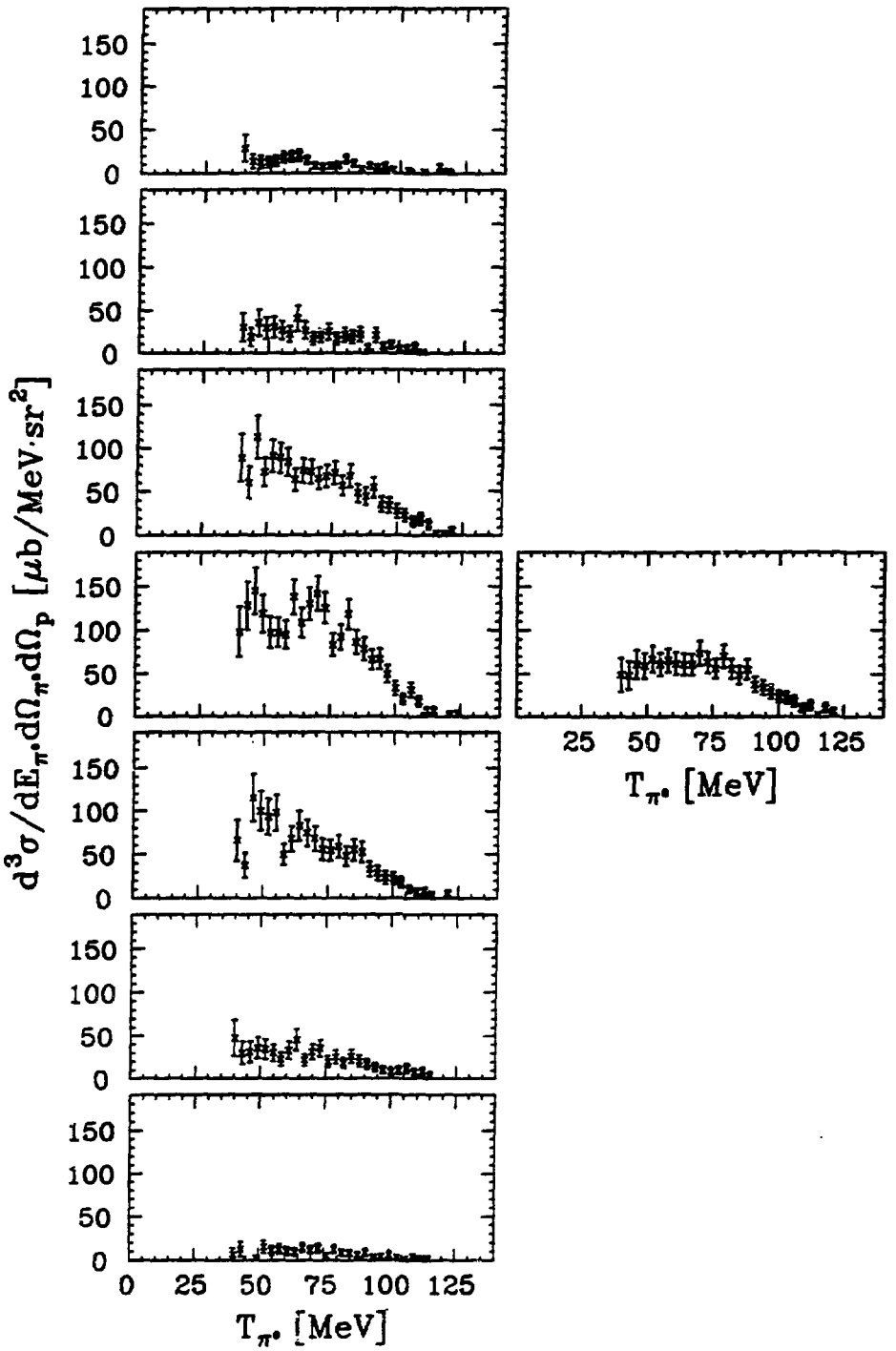

Figure 4.33. $d^3\sigma/dE_{\pi^0}\,d\Omega_{\pi^0}\,d\Omega_p$ spectra obtained with the tin target for all detectors. The π^0 angle was $\theta_{\pi^0} = 110.0°$. The normalization uncertainty (10%) is not included in the figure. See Appendix E for listing.

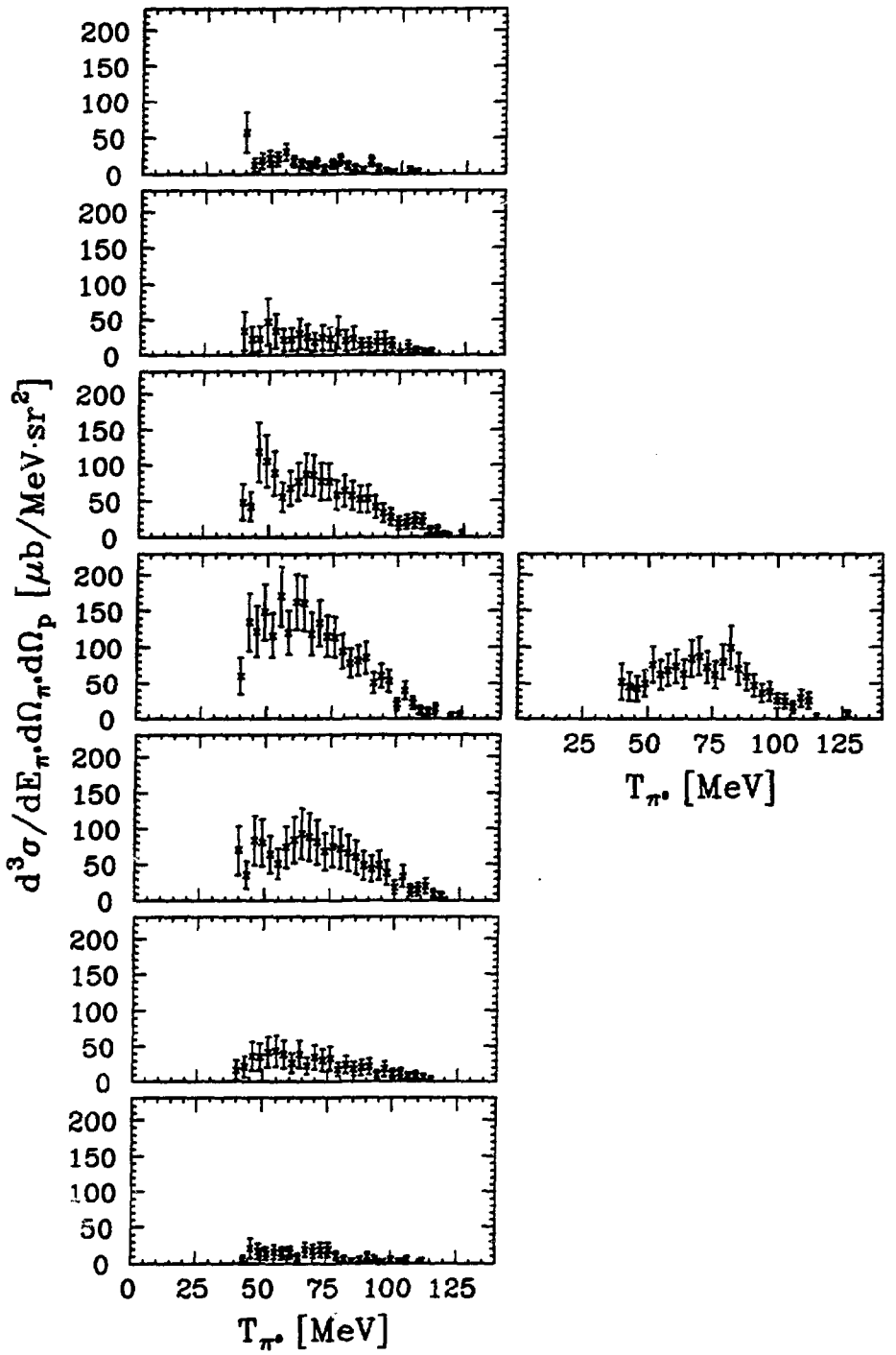

Figure 4.34. $d^3\sigma/dE_{\pi^0}\,d\Omega_{\pi^0}\,d\Omega_p$ spectra obtained with the lead target for all detectors. The π^0 angle was $\theta_{\pi^0} = 110.0°$. The normalization uncertainty (10%) is not included in the figure. See Appendix E for listing.

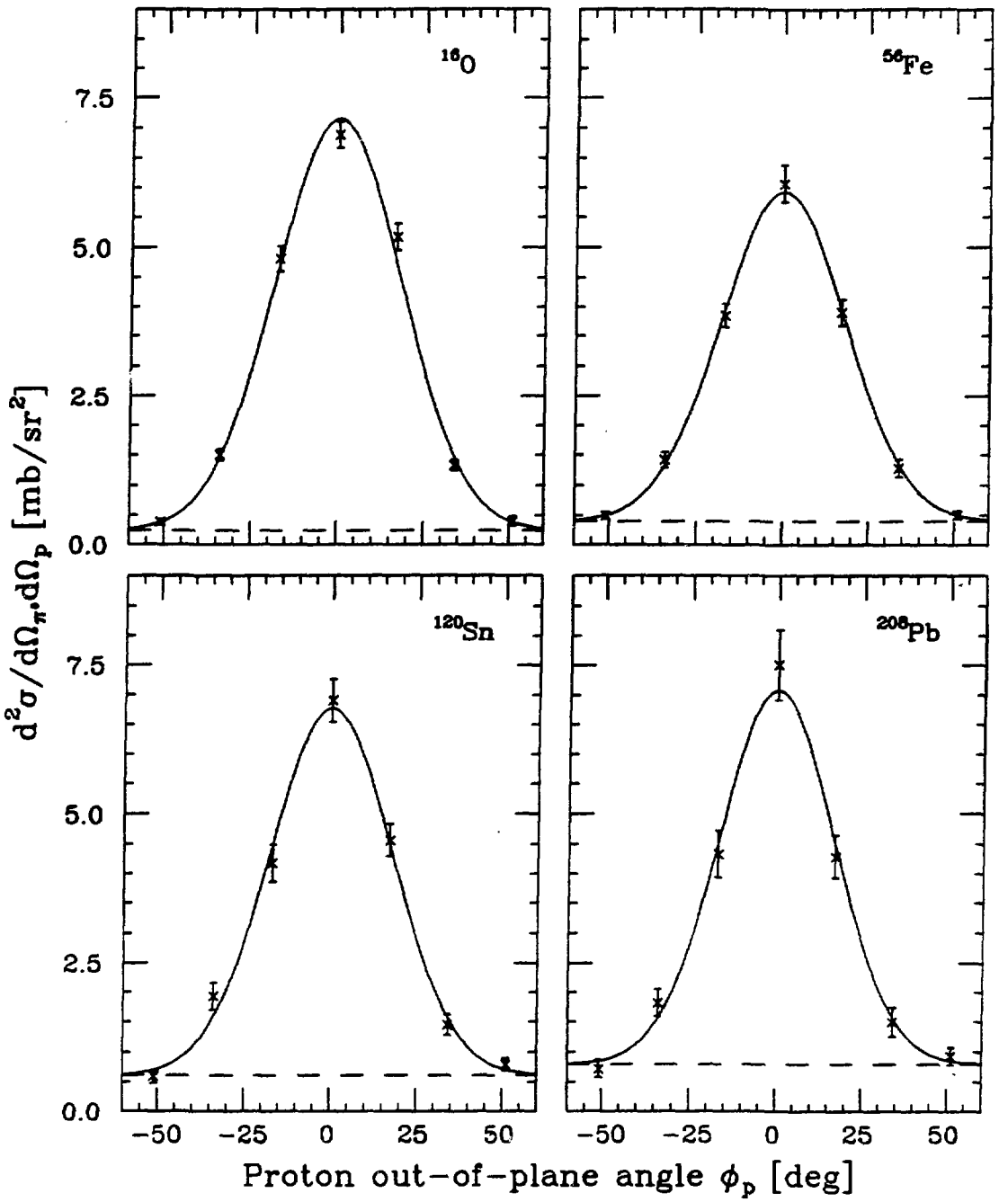

Figure 4.35. $d^2\sigma/d\Omega_{\pi^0}\, d\Omega_p$ for the $(\pi^+, \pi^0 p)$ reaction on various targets. The data are from Table 4.7 (telescopes $1-7$). The target used is indicated in each plot. The normalization uncertainty (9% for the oxygen data and 10% for data from the other targets) is not included in the figure. The solid curves are gaussian fits to the data (added to a constant background (dashes)).

Table 4.8. Integrated cross sections $d\sigma/d\Omega_{\pi^0}$. The fit parameters and the resulting cross section values were obtained by fitting to the distribution of $d^2\sigma/d\Omega_{\pi^0}\,d\Omega_p$ as a function of the proton out-of-plane angle ϕ_p (cf. Fig. 4.35). "Amplitude" in the table means the amplitude of the gaussian contribution to the fit. The second uncertainty term given for the integrated cross sections is the normalization uncertainty. The numbers in parentheses are the total (combined) uncertainties.

target	amplitude [mb/sr^2]	FWHM [deg]	background [mb/sr^2]	$\frac{d\sigma}{d\Omega_{\pi^0}}$ [mb/sr]
^{16}O	6.91 ± 0.18	43.1 ± 1.0	0.24 ± 0.06	$4.43 \pm 0.20 \pm 0.41$ (0.46)
^{56}Fe	5.52 ± 0.23	42.5 ± 1.8	0.40 ± 0.06	$3.44 \pm 0.24 \pm 0.33$ (0.41)
^{120}Sn	6.16 ± 0.29	41.7 ± 2.2	0.61 ± 0.10	$3.69 \pm 0.35 \pm 0.35$ (0.50)
^{208}Pb	6.28 ± 0.47	39.0 ± 2.9	0.80 ± 0.12	$3.30 \pm 0.40 \pm 0.32$ (0.51)

cidence runs. The event rate was much higher than the rate for coincidence events; typically around two hours of beam time was spent on each target in each setup. The (π^+,π^0) reaction was measured for all setups and all targets used for coincidence measurements. In all cases the beam energy was $T_{\pi^+} = 165$ MeV.

The analysis of the single arm data was similar to the analysis of π^0 data that was done to find the π^0 spectrometer conversion efficiency (Sec. 3.3.5.2) and the thicknesses of the water targets (Sec. 3.4). The most important difference was that in the analysis of the (π^+,π^0) process we were in each case measuring an energy spectrum, not just one well-defined peak.

This section is divided into two subsections. The first is a presentation of our directly measured cross sections $d^2\sigma/dE_{\pi^0}\,d\Omega_{\pi^0}$ for all setups and targets. This subsection also includes a discussion of the integration of these cross sections to $d\sigma/d\Omega_{\pi^0}$, which can be compared to the $(\pi^+,\pi^0 p)$ results from Secs 4.1 and 4.2. The second subsection is a special study of the angular distribution of $d\sigma/d\Omega_{\pi^0}$ for $^{16}\mathrm{O}(\pi^+,\pi^0)$.

All $d^2\sigma/dE_{\pi^0}\,d\Omega_{\pi^0}$ cross section spectra shown in this section are tabulated in Appendix E.

4.3.1 Experimental Cross Sections $d^2\sigma/dE_{\pi^0}\,d\Omega_{\pi^0}$ and $d\sigma/d\Omega_{\pi^0}$

All cross sections presented in this subsection are based on data from the larger π^0 spec-

trometer angular bin ($\theta_{\pi^0} \pm 12°$). Background measurements were done using empty water targets. No measurements were made without any target at all, so the empty target results were also used to correct the data from the solid targets (cf. Sec. 4.1.5). Full target and empty target data were corrected independently for accidental events (Sec. 3.3.3) and the π^0 spectrometer energy acceptance (Sec. 3.3.2). The spectrum resulting after subtraction of the empty target contribution was finally corrected for photon attenuation losses in the target (Sec. 3.2). Appendix C contains a complete description of the software used to calculate the π^0 energy spectra of $d^2\sigma/dE_{\pi^0}\, d\Omega_{\pi^0}$.

Our $d^2\sigma/dE_{\pi^0}\, d\Omega_{\pi^0}$ cross section spectra for the $^{16}O(\pi^+,\pi^0)$ reaction are shown in Fig. 4.36. We observe a clear difference in magnitude between the spectra for forward π^0 angles and those for backward angles, similar to what was seen for the coincidence spectra in Fig. 4.12. The A-dependence of the (π^+,π^0) reaction is illustrated in Fig. 4.37. Here we see a clear increase in the cross section with A, unlike the almost A-independent $(\pi^+,\pi^0 p)$ cross sections presented in Sec. 4.2.

The $d^2\sigma/dE_{\pi^0}\, d\Omega_{\pi^0}$ cross sections were integrated over all π^0 energies by fitting a sum of two gaussians (Eq. (4.10)) to the spectra in Figs. 4.36 and 4.37. The results are listed in Table 4.9. The trends that were noticed above for $d^2\sigma/dE_{\pi^0}\, d\Omega_{\pi^0}$ are also seen in the integrated cross sections.

4.3.2 Angular Distribution of the $^{16}O(\pi^+,\pi^0)$ Cross Section

The measurements on oxygen were made with the π^0 spectrometer in four different positions. This is quoted as four different π^0 angles in Sec. 4.3.1. The results shown in that section (Fig. 4.36) were obtained using the larger of the π^0 spectrometer angular bins discussed so far ($\theta_{\pi^0} \pm 12°$). For the purpose of producing a more detailed angular distribution (at the cost of increased statistical uncertainty), we divided this large bin into three sub-bins, each spanning 8°: $\theta^s_{\pi^0} - 12°$ to $\theta^s_{\pi^0} - 4°$, $\theta^s_{\pi^0} \pm 4°$ (identical to the "smaller bin" mentioned earlier in this work), and $\theta^s_{\pi^0} + 4°$ to $\theta^s_{\pi^0} + 12°$. In this notation $\theta^s_{\pi^0}$ is the central π^0 spectrometer angle. The π^0 angle θ_{π^0} assigned to each bin is now in general different from this central angle $\theta^s_{\pi^0}$, and we can present data at 12 angles instead of the previous four.

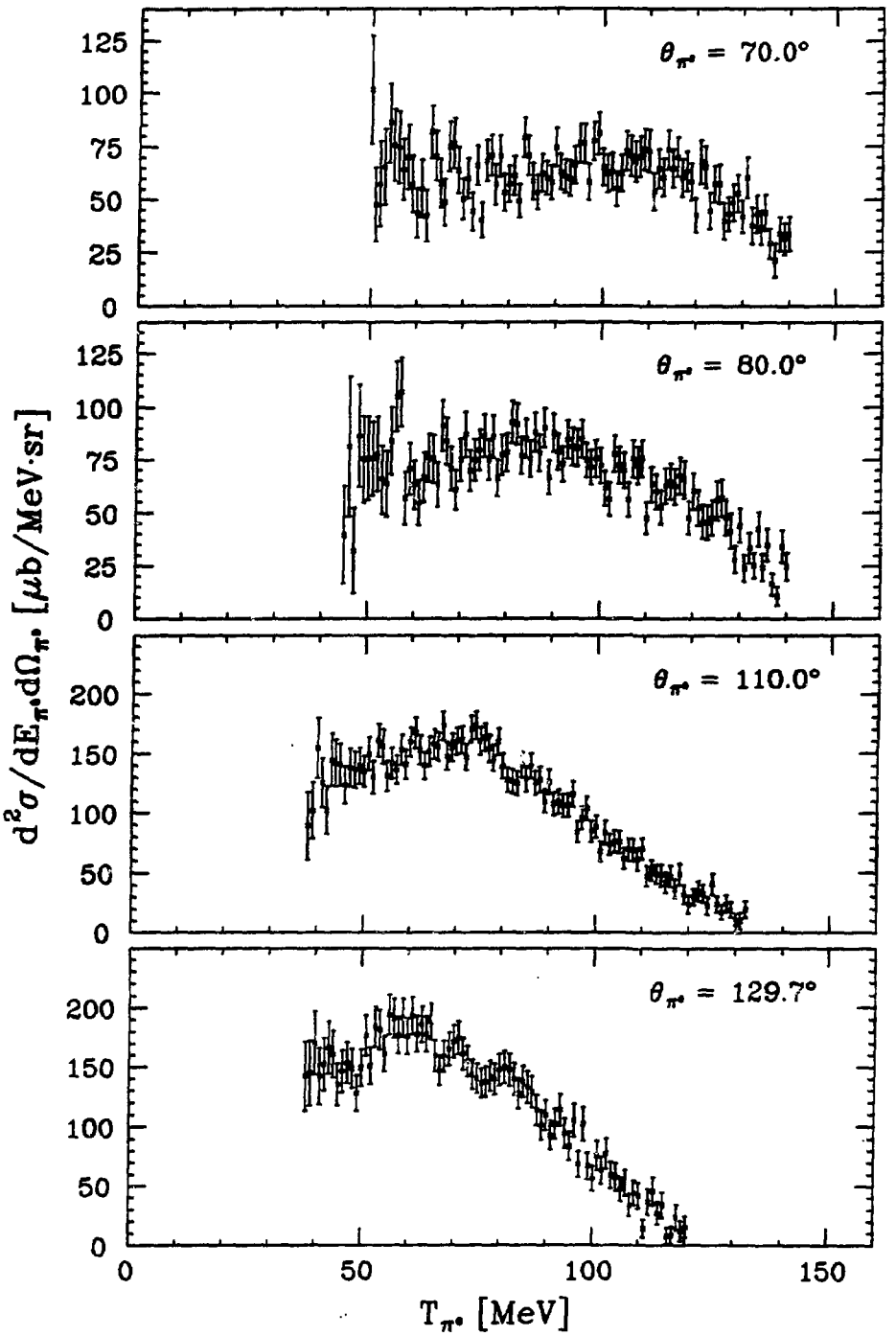

Figure 4.36. $d^2\sigma/dE_{\pi^0}\,d\Omega_{\pi^0}$ for the reaction $^{16}O(\pi^+,\pi^0)$ The π^0 angle is indicated next to each spectrum. The normalization uncertainty is not included in the figure. It is 9%, 8%, 9%, and 8%, respectively, for the four setups.

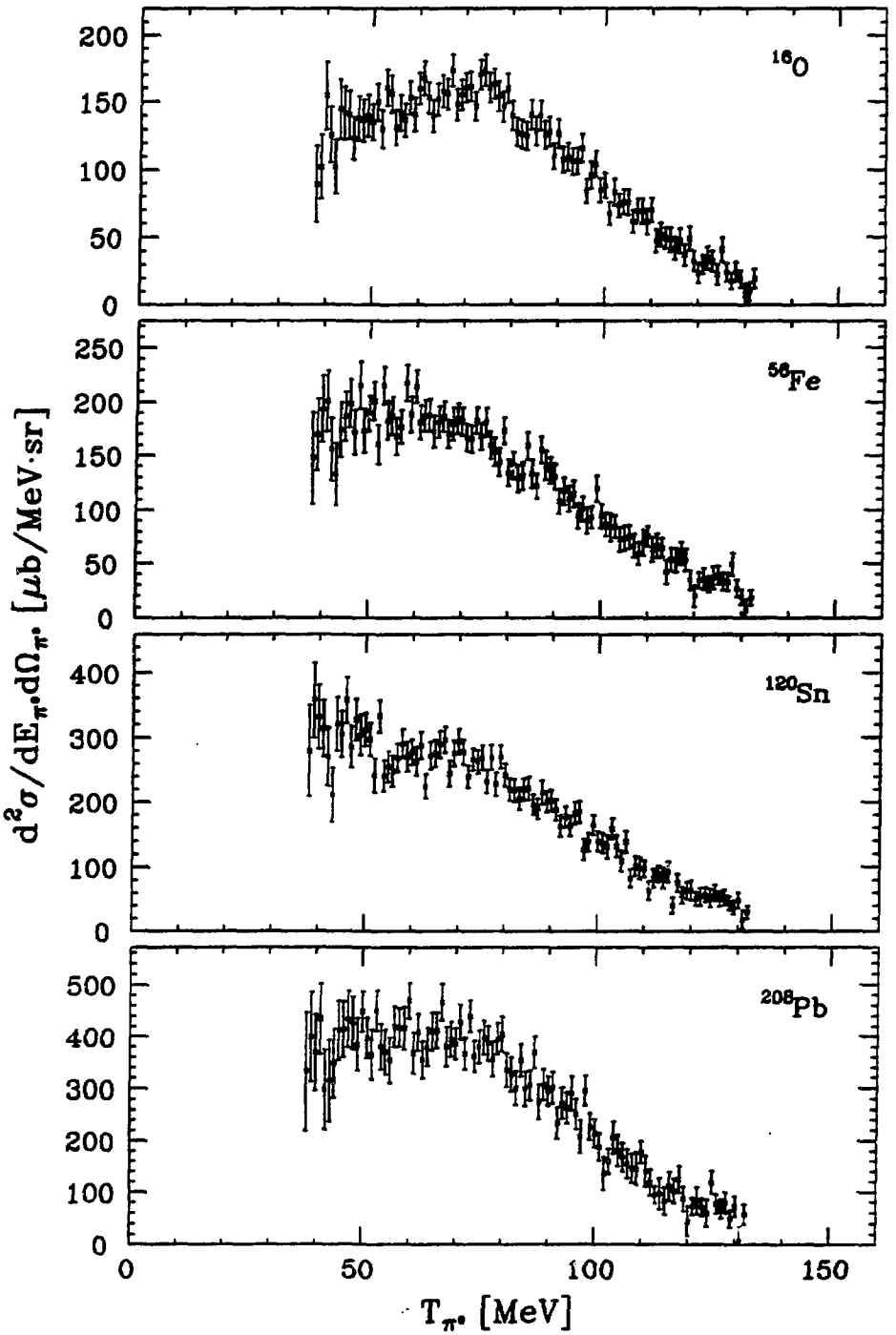

Figure 4.37. $d^2\sigma/dE_{\pi^0}\,d\Omega_{\pi^0}$ for the (π^+,π^0) reaction for all targets. The measurements were made at $\theta_{\pi^0} = 110.0°$. The target used is indicated next to each spectrum. The normalization uncertainty is not included in the figure. It is 9% for all targets.

Table 4.9. Integrated cross sections $d\sigma/d\Omega_{\pi^0}$ for the (π^+,π^0) reaction. The second uncertainty term given is the normalization uncertainty. The numbers in parentheses are the total (combined) uncertainties.

target	θ_{π^0} [deg]	$\frac{d\sigma}{d\Omega_{\pi^0}}$ [mb/sr]
^{16}O	70.0	$6.18 \pm 0.18 \pm 0.54$ (0.57)
^{16}O	80.0	$6.92 \pm 0.23 \pm 0.52$ (0.57)
^{16}O	110.0	$11.19 \pm 0.25 \pm 0.99$ (1.02)
^{16}O	129.7	$11.58 \pm 0.26 \pm 0.93$ (0.96)
^{16}O	110.0	$11.19 \pm 0.25 \pm 0.99$ (1.02)
^{56}Fe	110.0	$13.70 \pm 0.35 \pm 1.25$ (1.30)
^{120}Sn	110.0	$22.27 \pm 0.69 \pm 2.03$ (2.14)
^{208}Pb	110.0	$32.26 \pm 1.22 \pm 2.90$ (3.15)

Data from the three sub-bins were analyzed as outlined for the single-arm data presented in Sec. 4.3.1. Appropriate values for the density × efficiency product were calculated from the (π^-,π^0) measurements as described before in Sec. 3.4. We also ran more Monte Carlo simulations (PIANG[62]) to establish the π^0 spectrometer energy acceptance curves for the new angular bins (cf. Sec. 3.3.2).

The resulting energy spectra of $d^2\sigma/dE_{\pi^0}\,d\Omega_{\pi^0}$ are shown in Figs. 4.38 – 4.40. The π^0 angle indicated next to each spectrum is the central angle of the spectrometer bin used. (For more careful, high-statistics analysis one should instead use an average angle weighted by the spectrometer acceptance.) The spectra for the most forward angles do not exhibit much structure, but there is a clear trend throughout all spectra of a peak moving towards lower energies as the scattering angle increases. This is in qualitative agreement with the behavior of the corresponding free process $\pi^+ + n \rightarrow \pi^0 + p$, for which the π^0 energy is 135 MeV at 62.0°, 113 MeV at 88.0°, and 84 MeV at 137.7°. As before, we see that the cross sections generally increase with the π^0 angle, with the forward angles having clearly lower cross sections than the backward angles.

The energy spectra were integrated over all π^0 energies by fitting a sum of two gaussians (Eq. (4.10)) to the data. The calculated values of $d\sigma/d\Omega_{\pi^0}$ are listed in Table 4.10. They are also plotted in Fig. 4.41. The uncertainties indicated in the figure include the normalization uncertainty. Comparing to the values calculated using the larger angular bin (Table 4.9), one finds that the results for the 8° bins are in close agreement with the

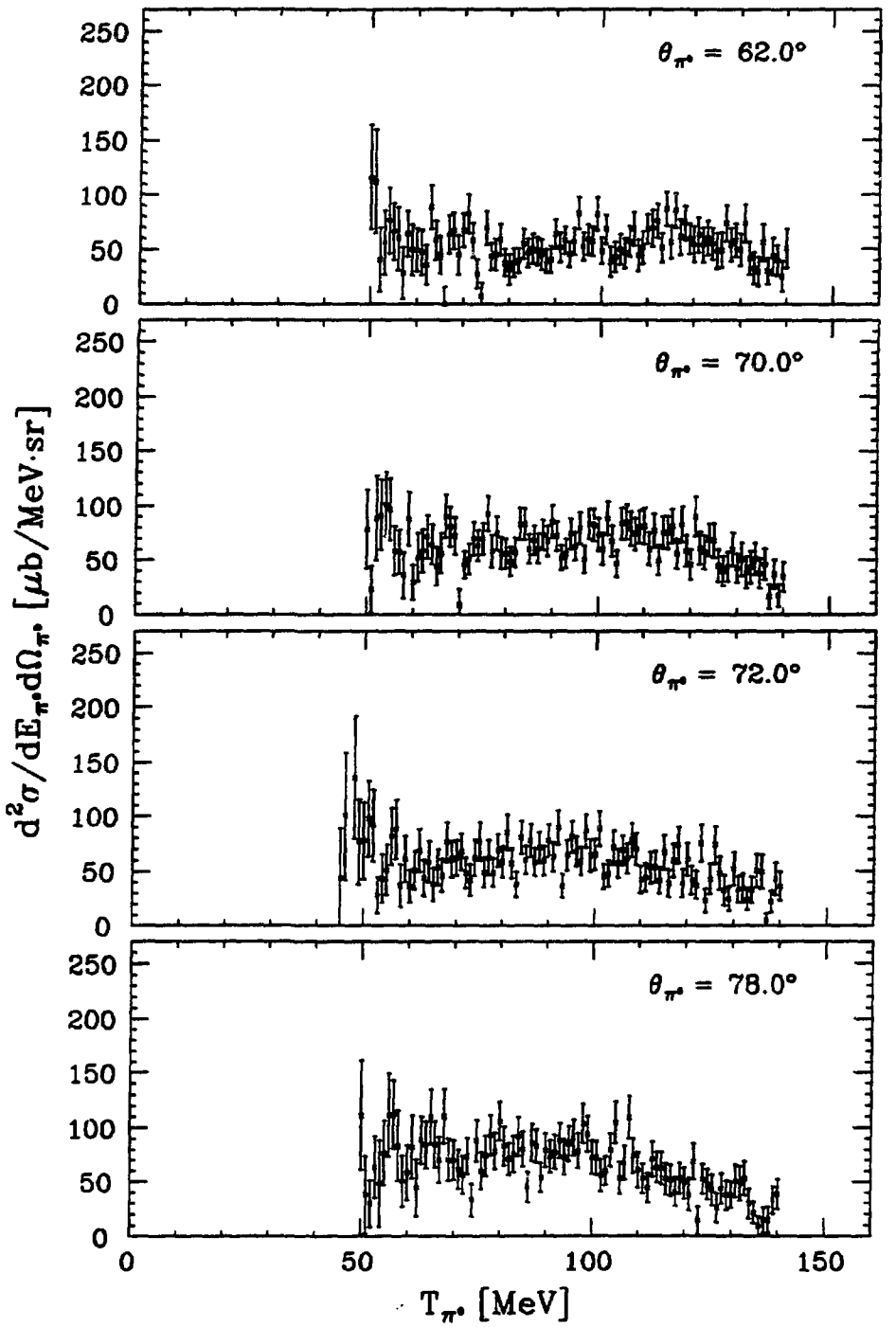

Figure 4.38. Narrow bin single arm cross sections. The figure shows $d^2\sigma/dE_{\pi^0}\,d\Omega_{\pi^0}$ for $^{16}O(\pi^+,\pi^0)$ using data from 8° angular bins (see the text) centered at the indicated π^0 angles. The spectra shown have an additional normalization uncertainty of 11%, 11%, 9%, and 11%, respectively.

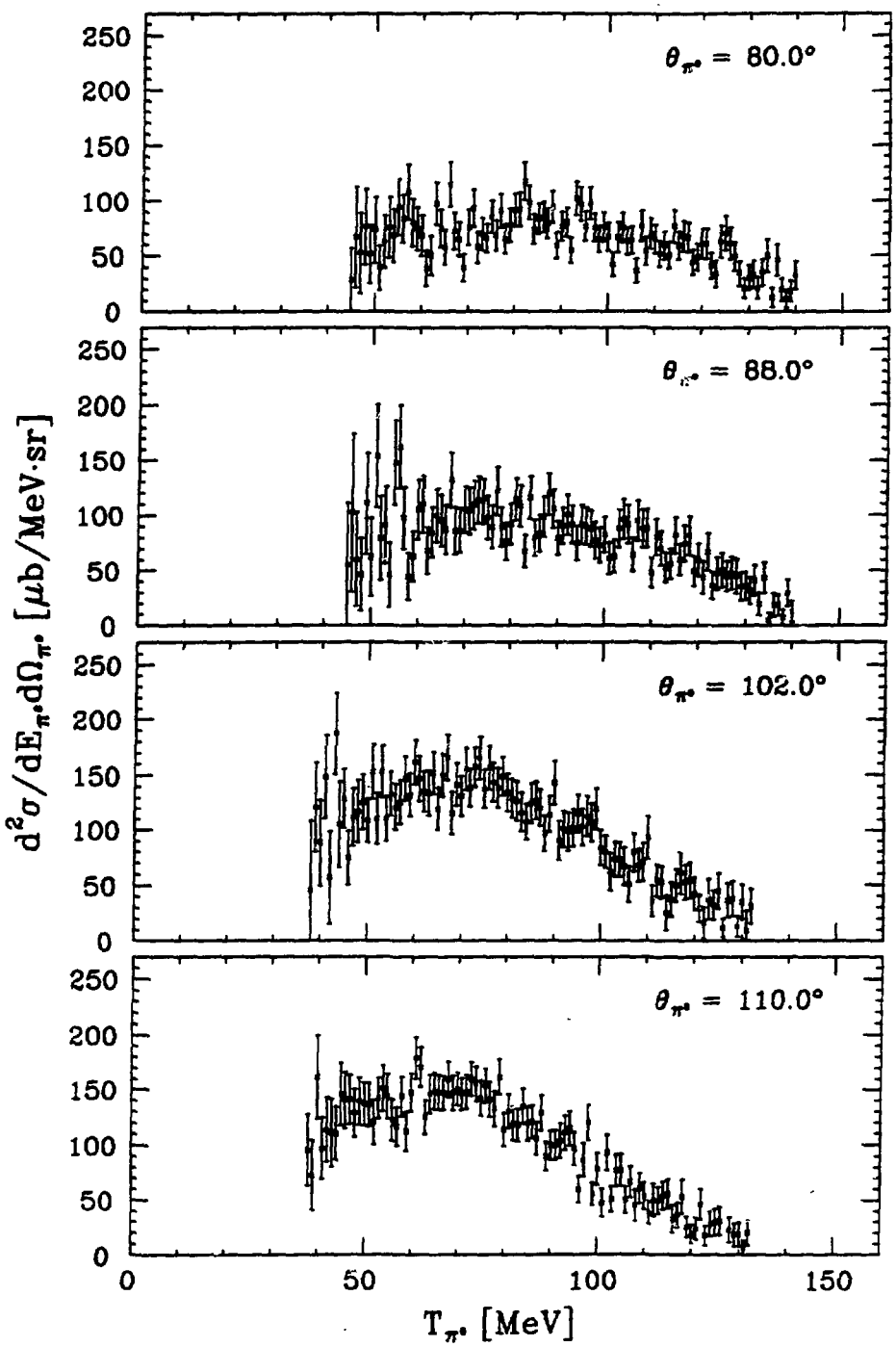

Figure 4.39. Narrow bin single arm cross sections. The figure shows $d^2\sigma/dE_{\pi^0}\,d\Omega_{\pi^0}$ for $^{16}O(\pi^+,\pi^0)$ using data from 8° angular bins (see the text) centered at the indicated π^0 angles. The spectra shown have an additional normalization uncertainty of 8%, 9%, 11%, and 10%, respectively.

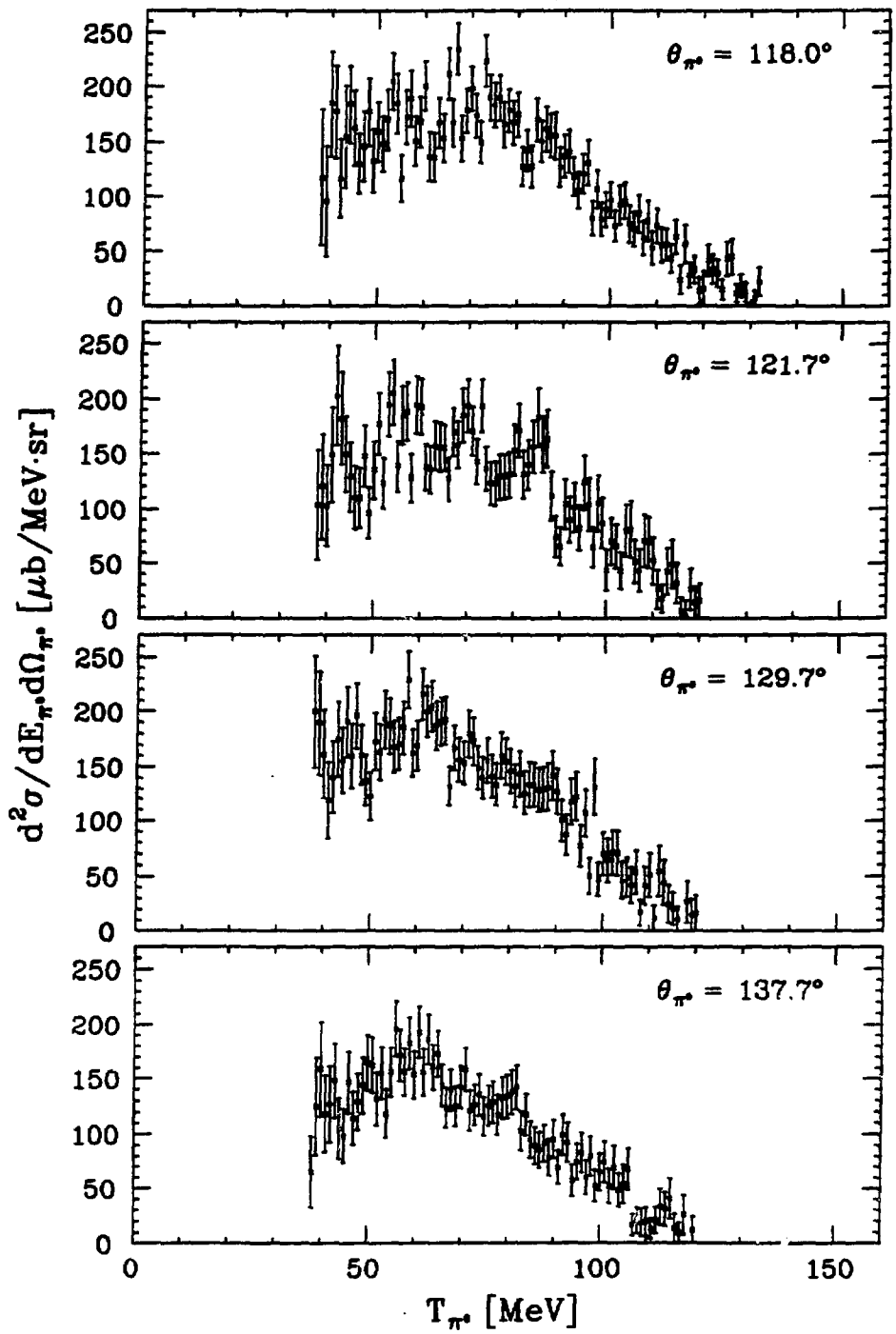

Figure 4.40. *Narrow bin single arm cross sections.* The figure shows $d^2\sigma/dE_{\pi^0}\,d\Omega_{\pi^0}$ for $^{16}O(\pi^+,\pi^0)$ using data from 8° angular bins (see the text) centered at the indicated π^0 angles. The spectra shown have an additional normalization uncertainty of 11%, 9%, 9%, and 9%, respectively.

Table 4.10. $d\sigma/d\Omega_{\pi^0}$ for $^{16}O(\pi^+,\pi^0)$ using narrow angular bins. All results are for the 8° angular bins described in the text. The beam energy was $T_{\pi^+} = 165$ MeV. The π^0 angle θ_{π^0} given in the table is the central angle of each bin. The second uncertainty term given is the normalization uncertainty, and the numbers in parentheses are the total (combined) uncertainties.

θ_{π^0} [deg]	$\frac{d\sigma}{d\Omega_{\pi^0}}$ [mb/sr]
62.0	$5.54 \pm 0.31 \pm 0.63$ (0.70)
70.0	$6.22 \pm 0.30 \pm 0.67$ (0.74)
72.0	$5.55 \pm 0.26 \pm 0.48$ (0.55)
78.0	$6.45 \pm 0.31 \pm 0.72$ (0.79)
80.0	$6.52 \pm 0.32 \pm 0.54$ (0.62)
88.0	$7.50 \pm 0.31 \pm 0.65$ (0.72)
102.0	$10.63 \pm 0.44 \pm 1.18$ (1.26)
110.0	$10.57 \pm 0.43 \pm 1.05$ (1.13)
118.0	$12.28 \pm 0.42 \pm 1.35$ (1.42)
121.7	$10.90 \pm 0.61 \pm 1.01$ (1.18)
129.7	$11.74 \pm 0.54 \pm 1.09$ (1.22)
137.7	$9.36 \pm 0.41 \pm 0.87$ (0.96)

results for the 24° bin (confirming our earlier observations that the π^0 spectrometer produces quite reliable results even when it spans a very wide angle, cf. Secs. 3.3.5.2 and 3.4).

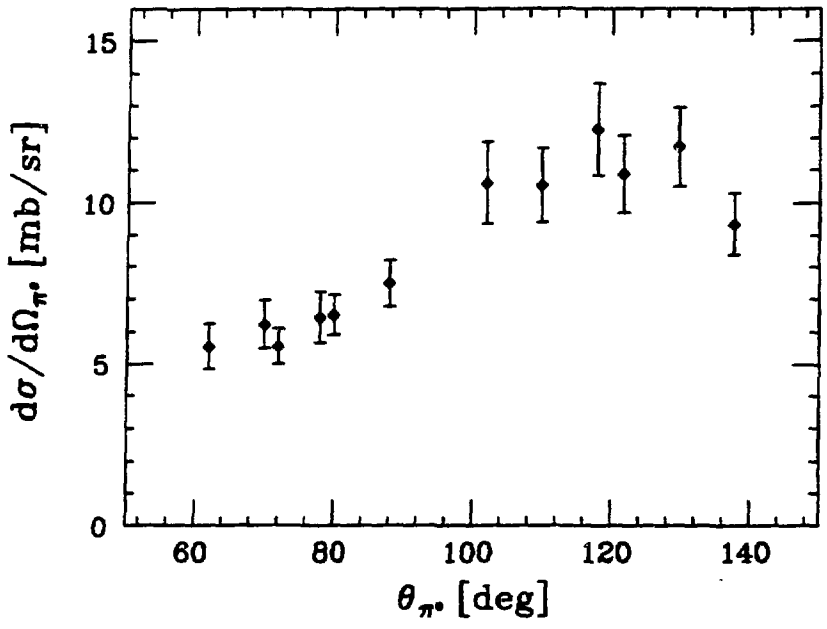

Figure 4.41. Integrated cross sections $d\sigma/d\Omega_{\pi^0}$ as a function of the π^0 angle θ_{π^0}. The results shown are for the $^{16}O(\pi^+,\pi^0)$ reaction at T_{π^+} = 165 MeV (cf. Table 4.10). The indicated uncertainties include the normalization uncertainty.

Chapter 5

Discussion and Conclusions

In this chapter we discuss and summarize the results of our experiment. This includes comparison of the results to earlier measurements as well as to theoretical predictions of the Δ–hole model (cf. Chapter 1). The first three sections of this chapter each address one of the three main topics of our study: the $^{16}O(\pi^+,\pi^0 p)$ reaction, the A-dependence of the $(\pi^+,\pi^0 p)$ reaction, and the (π^+,π^0) reaction. At the end is a short summary of our findings and conclusions.

5.1 Coincidence Measurements of the $^{16}O(\pi^+,\pi^0 p)$ Reaction

We begin this section by discussing the general features of our data. This is followed by several subsections containing comparisons to other results and to theoretical calculations.

5.1.1 Our Measurements

As mentioned in Sec. 1.4, one purpose of our measurements was to find out if the $^{16}O(\pi^+,\pi^0 p)$ reaction indeed is predominantly quasi-free, as one might expect from measurements of similar reactions (cf. Sec. 1.1.4). This question is best illuminated by comparing the measured proton out-of-plane angular distributions illustrated in Figs. 4.29 and 4.30 with the results of our Monte Carlo simulations shown in Figs. 4.3 (p-shell nucleon removal) and 4.4 (s-shell nucleon removal). Qualitatively, the agreement between data and simulations is good, especially when we consider the fact that our p-shell results most likely include a significant contribution from processes other than single p-shell nucleon removal. The fits shown in Fig. 4.10 indicate an "s-shell" contamination of 20% in the region of the p-shell cut, for instance. Such an s-shell contribution may explain why the p-shell structure manifests itself in our data only as a slightly reduced cross section at $\phi_p = 0°$ (compared to the gaussian fit) instead of a clear dip (see Fig. 4.29). Also other, more complicated, processes may be affecting these cross sections, but the resolution of our data does not permit a detailed, quantitative study of this aspect.

Fig. 5.1 shows a comparison between the experimental results and those of the simulations after scaling the latter to the data. The scaling is a least-squares fit to the data points. However, because of its sensitivity to other processes than single p-shell nucleon removal, the measurement at the central proton telescope was ignored in the fitting process. The flat background indicated in Fig. 4.29 was subtracted from the data before the fitting was done and later added to the scaled Monte Carlo results. The close agreement clearly shows that the gaussian part of the cross section has its origin in quasi-free processes.

Another, not so firm, indication of the importance of quasi-free reaction mechanisms for $^{16}O(\pi^+,\pi^0 p)$ p-shell nucleon removal is the qualitative similarity between the simulated and the measured $d^3\sigma/dE_{\pi^0}\, d\Omega_{\pi^0}\, d\Omega_p$ cross section spectra (Figs. 4.1 and 4.12, respectively). As could be expected from the discussion above, the p-shell structure is not very pronounced in the experimental results. (Our data also suffer a lack of structure because of the large angle spanned by the π^0 spectrometer; we include π^0's collected within $\pm 12°$ of the central π^0 angle. The Monte Carlo simulations account for the full size of the π^0 spectrometer solid angle, but this is assumed to constitute a

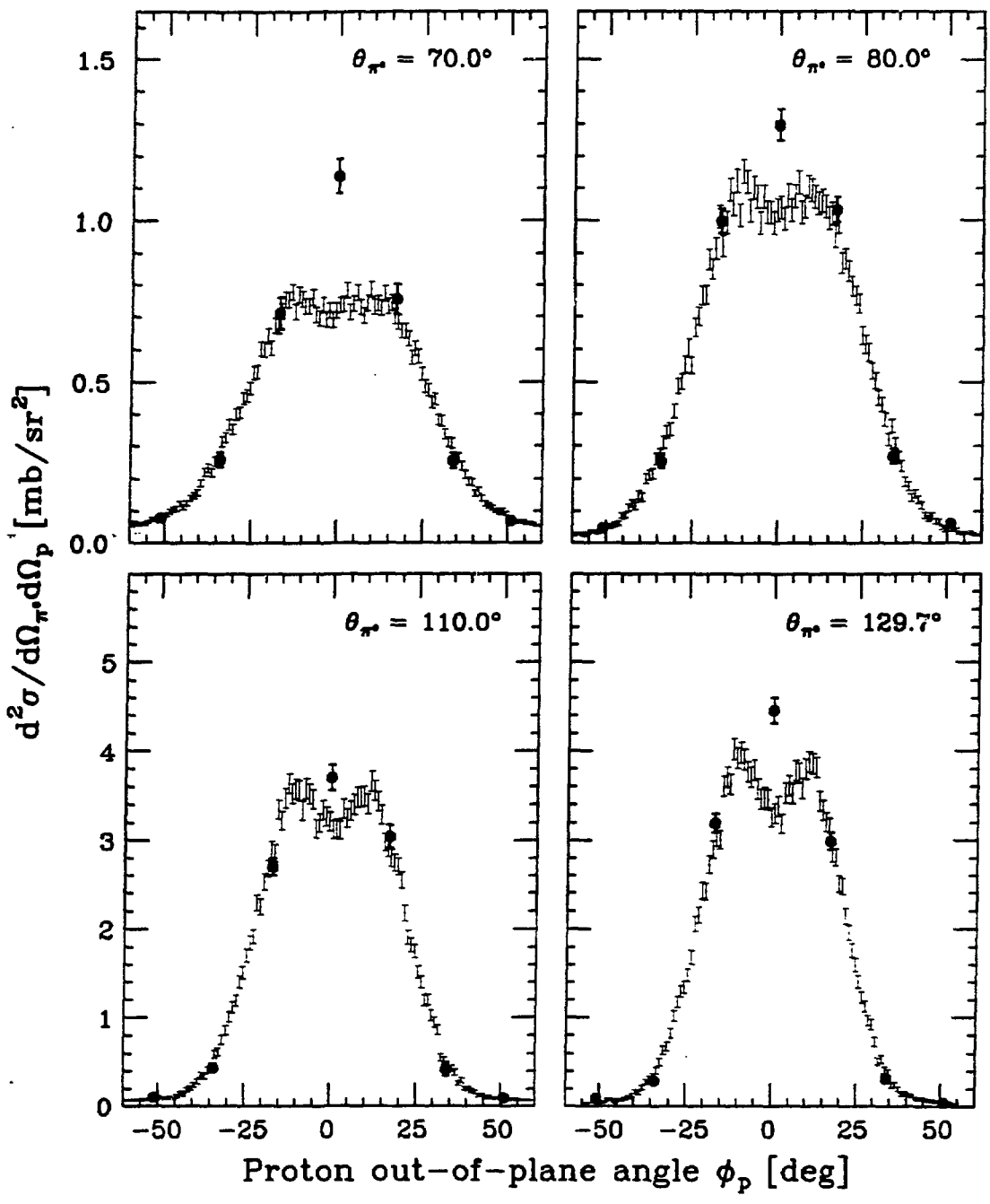

Figure 5.1. Comparison of angular distributions to Monte Carlo simulations. The experimental results (filled circles) are from Fig. 4.29 and the simulations from Fig. 4.3. The measurements at the quasi-free angle (the central proton telescope) were ignored in the process of fitting the calculated distributions to the data (see the text).

cone centered around the nominal π^0 angle, cf. Sec. 4.1.1, while in reality the angular acceptance of the π^0 spectrometer is a more complicated (essentially triangular according to the Monte Carlo program PIANG[62,64]) function of θ_{π^0} over the full range of the angular bin.)

Using our data, it is difficult to estimate the fraction of the $^{16}O(\pi^+,\pi^0 p)$ cross section that can be assigned to the quasi-free SCX process. A careful assessment would require a more well-determined angular distribution, in particular a better determination of the background. One could then for instance use the approach of Piasetzky *et al.*[20] and fit the angular data to a sum of two gaussians, where the wider one is taken to represent the non-quasi-free part of the cross section. To get a rough estimate based on our data, we may assume that the flat background used in the fits to the angular distributions in Sec. 4.1.7 (cf. Table 4.5) extends throughout all directions. We then find that the quasi-free part of the integrated cross sections $d\sigma/d\Omega_{\pi^0}$ in the case of p-shell nucleon removal (Table 4.6) accounts for 53%, 79%, 74%, and 85% of the total (quasi-free plus non-quasi-free) cross section at π^0 angles 70.0°, 80.0°, 110.0°, and 129.7°, respectively. The uncertainty in these values is substantial, but we may at least conclude that our data show a *dominance* of a quasi-free reaction mechanism in the $^{16}O(\pi^+,\pi^0 p)$ reaction for p-shell nucleon removal. Moreover, the quasi-free contribution appears to increase somewhat with the π^0 angle.

The question of the angular dependence of the $^{16}O(\pi^+,\pi^0 p)$ reaction was also raised in Sec. 1.4. The $d^3\sigma/dE_{\pi^0}\,d\Omega_{\pi^0}\,d\Omega_p$ cross section spectra shown in Figs. 4.13 and 4.14 indicated a clear difference between forward and backward π^0 angles. Fig. 5.2 shows the quasi-free part of the integrated cross sections $d\sigma/d\Omega_{\pi^0}$ for the $^{16}O(\pi^+,\pi^0 p)$ reaction, both for the case of a p-shell cut on the removed nucleon and the case of no such cut (cf. Table 4.6). Also shown is the free $\pi^+ + n \rightarrow \pi^0 + p$ cross section,[14–16] which has been scaled to go through the data point at 129.7° for both sets of data. Our results indicate a qualitative agreement between the angular distribution of the $^{16}O(\pi^+,\pi^0 p)$ cross section and that of the corresponding free reaction at backward π^0 angles. However, our most forward measurement, at $\theta_{\pi^0} = 70°$, yields a significantly suppressed cross section compared to the free reaction. This is very similar to the angular distribution of the $(\pi^+,\pi^+ p)$ reaction as observed by Piasetzsky *et al.* on C, Bi, and Pb at $T_{\pi^+} = 245$ MeV.[20] We also note that their scaling factors for best

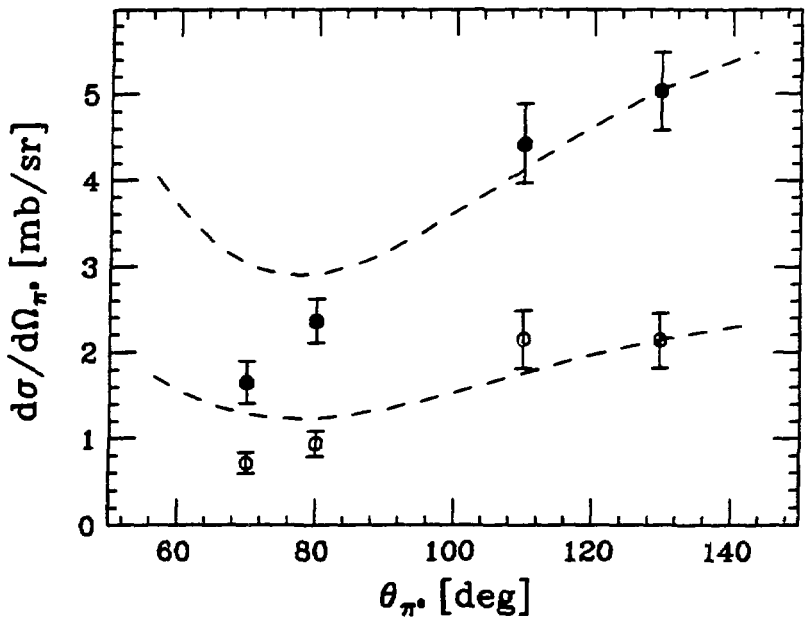

Figure 5.2. Integrated cross sections $d\sigma/d\Omega_{\pi^0}$ for the $^{16}O(\pi^+,\pi^0 p)$ reaction. The figure shows our results when all ejected protons are accepted (filled circles), and when only p-shell protons are included (open circles). The data are from Table 4.6, and the normalization uncertainty is included. The dashed curves both represent the free πN single-charge-exchange cross section.[14–16] They have been scaled (by 1.26 and 0.54, respectively) to go through the data points at $\theta_{\pi^0} = 129.7°$.

agreement with the free cross sections were 0.9, 1.36, and 1.89, respectively, for the three targets, compared to 1.26 in our case. Qualitatively, the behavior of the angular distribution is not surprising. Because of the large πN cross sections, pions mostly interact with nucleons near the back surface of the nuclei. Hence a pion ejected in a forward direction has to travel a sizable distance through the remaining part of the nucleus before it can escape. This enhances the influence of final state interactions, which in turn will reduce the cross section. On the other hand, a pion ejected from the back surface in a backward direction has essentially a clear path to the detector. For the $(\pi^+,\pi^0 p)$ reaction, the situation is somewhat complicated by the ejected proton which also has to make its way through the nucleus. Its mean free path in a nucleus is much larger than that of the pion, however, and the proton angle does not vary as much as the π^0 angle (from 47.6° to 19.45° for our measurements, cf. Table 2.2); we therefore do not expect proton final state interactions to be of importance to the general shape

Table 5.1. Comparison of p-shell to complete cross sections $d\sigma/d\Omega_{\pi^0}$ for $(\pi^+, \pi^0 p)$. The indices on the cross sections are cp for p-shell coincidence events and c for the complete $\pi^0 p$ coincidence cross section (cf. Table 4.6, and Fig. 5.2). The uncertainty estimates include the normalization uncertainty.

θ_{π^0} [deg]	$\left(\frac{d\sigma}{d\Omega_{\pi^0}}\right)_{cp} / \left(\frac{d\sigma}{d\Omega_{\pi^0}}\right)_{c}$ [%]
70.0	43 ± 10
80.0	40 ± 8
110.0	49 ± 9
129.7	42 ± 7

of the angular distribution. One may note that the binding energy which the removed proton must overcome to escape the nucleus is high for ^{16}O, about 15.7 MeV. This may contribute to the relative suppression of the cross section at forward π^0 angles because the average proton energy is lower there than at backward angles.

Our data permit us to estimate the fraction of p-shell nucleon removal events in the total one-nucleon removal cross section. Using $d\sigma/d\Omega_{\pi^0}$ data (for the quasi-free part of the cross sections) from Table 4.6, we obtained the results presented in Table 5.1. We note that the fraction of p-shell removal events in the $^{16}O(\pi^+, \pi^0 p)$ reaction is roughly the same for all π^0 angles, about 40 – 50% (see also Fig. 5.2). In the simple quasi-free picture this fraction is surprisingly small, since ^{16}O has six p-shell neutrons out of a total of eight neutrons. This indicates that even if the cross sections show a quasi-free behavior, other processes, more complicated than single-particle nucleon removal, must also be of importance.

5.1.2 Comparison to the $^{16}O(\pi^+, \pi^0 p)$ Measurements of Gilad *et al.*

As mentioned in Chapter 1, the measurements of Gilad *et al.*[43] were formally part of the same experiment as the measurements described in this thesis, and the experimental apparatus used was the same. Their measurements were made at T_{π^+} = 245 MeV, so this comparison will provide information about the energy dependence of the $^{16}O(\pi^+, \pi^0 p)$ reaction. We note that while our measurements were made near the peak of the Δ-resonance, those of Gilad *et al.* were made at an energy where the

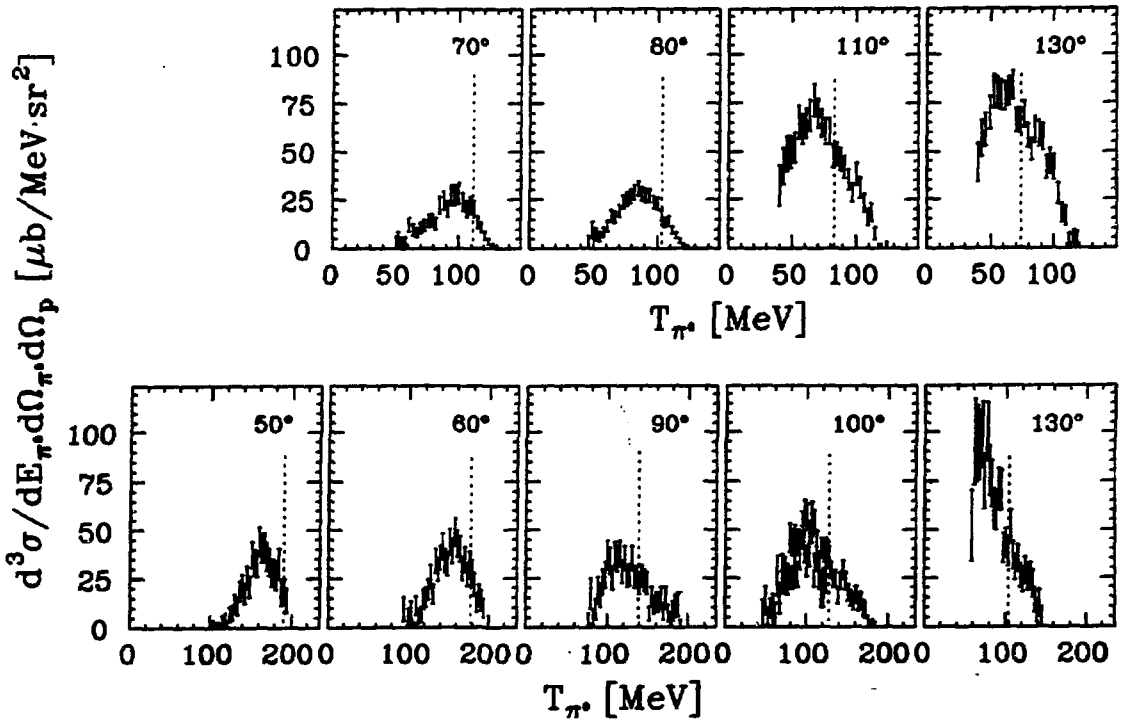

Figure 5.3. Comparison to $d^3\sigma/dE_{\pi^0}\,d\Omega_{\pi^0}\,d\Omega_p$ spectra of Gilad *et al.* The upper spectra are our 165 MeV results (cf. Fig. 4.12), and the lower spectra are 245 MeV results from Gilad *et al.* (cf. Fig. 1.14). The π^0 angle is indicated in each case, and the dotted lines mark the quasi-free energy. All results are for the central proton telescope, and only p-shell nucleon removal events are included.

importance of this resonance is significantly reduced (even if it still dominates the πN cross section, cf. Fig. 1.1).

The data of Gilad *et al.* have only been partially analyzed, and we are presently limited to comparing $d^3\sigma/dE_{\pi^0}\,d\Omega_{\pi^0}\,d\Omega_p$ cross sections only. The cross section energy spectra of Gilad *et al.* for the central proton telescope (at the quasi-free angle) are compared to our results in Fig. 5.3 (larger versions of these spectra are found in Figs. 1.14 and 4.12). We see that the general shapes of the spectra and the positions of the peaks relative to the positions of the quasi-free energy markers are quite similar. The cross sections at $T_{\pi^+} = 245$ MeV appear to be somewhat larger than those at 165 MeV, especially for the forward angles which can be reached by an ejected π^0 only if this travels through a large part of the nucleus in which it originated before escaping (cf.

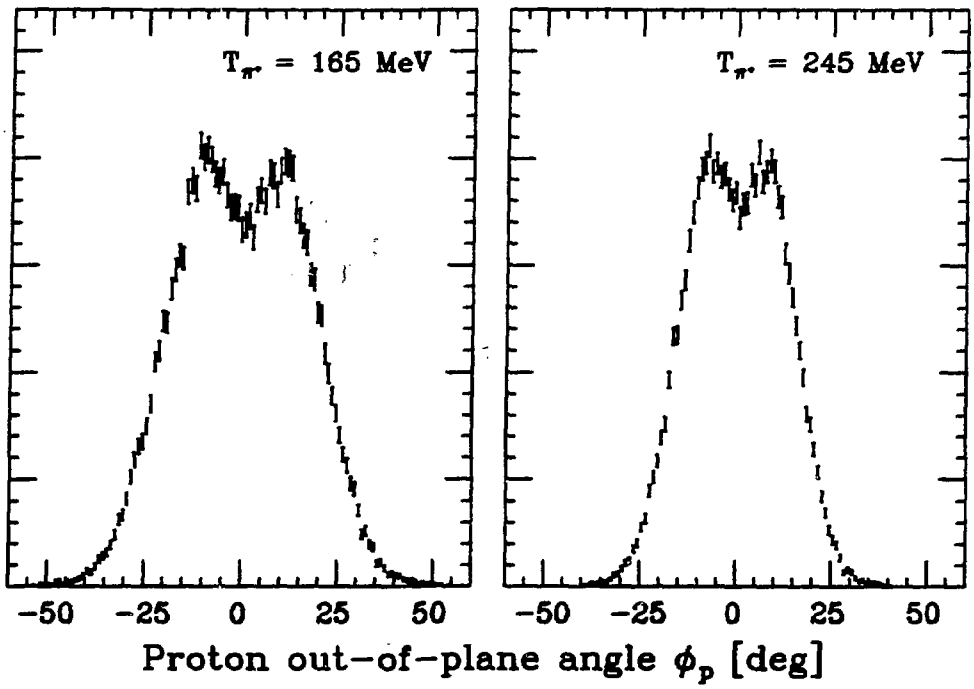

Figure 5.4. Quasi-free angular distributions for $\theta_{\pi^0} = 130°$. The results are from Monte Carlo simulations for p-shell nucleon removal as described in Sec. 4.1.1. The distribution for $T_{\pi^+} = 165$ MeV is also shown in Fig. 4.3.

Sec. 5.1.1). Several (competing) effects contribute to the observed energy dependency: (1) the free $\pi^+ n$ cross section is lower at 245 MeV than at 165 MeV, since the latter energy is close to the peak of the Δ-resonance (cf. Fig. 1.1); (2) at the higher beam energy the ejected π^0's typically have an energy close to the peak of the Δ-resonance and will therefore experience more final state interactions than π^0's ejected in reactions induced at the lower beam energy; (3) final state interactions of the ejected proton become less important as the energy increases (cf. Ref. 90); (4) the higher the energy is, the more final states are generally available (increased phase space). (1) and (2) reduce the cross section at the higher energy, whereas (3) and (4) increase it.

Furthermore, when comparing the cross sections one should keep in mind that the angular distribution of the quasi-free process is considerably narrower at the higher energy. Therefore an increased cross section observed in telescope 4 does not necessarily mean that the integrated cross section is any larger. This is illustrated in Fig. 5.4 which shows the results of a Monte Carlo simulation of the process for $\theta_{\pi^0} = 130°$ at

$T_{\pi^+} = 245$ MeV compared to the earlier result for the same angle at $T_{\pi^+} = 165$ MeV (cf. Fig. 4.3). Gilad *et al.* do not have analyzed results for the out-of-plane telescopes, which would be necessary in order to make a meaningful comparison of the integrated cross sections.

The only π^0 angle investigated by both Gilad *et al.* and us, is $\theta_{\pi^0} = 130°$. All data sets of Gilad *et al.* at this angle are compared to our corresponding measurements in Fig. 5.5. The most striking feature is the very low cross section observed for telescope 8 at $T_{\pi^+} = 245$ MeV, a clear indication of the narrower angular distribution at this energy. Telescope 8 is positioned symmetrically to telescopes 3 and 5 (cf. Sec. 2.2.3). Based on Fig. 5.4 we would then expect the difference between telescopes 4 and 8 at 245 MeV to amount to a factor of $3 - 4$. This is supported by similar Monte Carlo calculations of the angular distribution in the scattering plane which indicate that the cross section in telescope 8 should be about 90% of that in telescopes 3 or 5. The factor suggested by Fig. 5.5 is even larger than estimated, however, about $8 - 12$.

5.1.3 Comparison to the $^{16}O(\pi^{\pm},\pi^{\pm}p)$ Measurements of Kyle *et al.*

The measurements of Kyle *et al.*[40] constitute the only set of $^{16}O(\pi^{\pm},\pi^{\pm}p)$ data suitable for direct comparison to our work as well as to that of Gilad *et al.* In our measurements, an array of relatively small proton telescopes was used, whereas each proton telescope in the experiment of Kyle *et al.* spanned a very large solid angle. This made it desirable to reanalyze their data in a manner corresponding to our setup.

Kyle *et al.* used three proton telescopes, each spanning 15° horizontally and 50° vertically. These were placed 17.5° apart centered around the quasi-free angle.[40] As seen in Fig. 5.6, our proton telescopes 3, 4, 5, and 8 fall within the range of their telescopes. Kyle *et al.* had additional proton position information available from two multi-wire proportional chambers placed in front of their plastic-scintillator telescopes. This made it possible to impose cuts on their data corresponding to the solid angles spanned by our proton telescopes (cf. Fig. 5.6). The angular acceptance of the magnetic spectrometer used by Kyle *et al.* to detect the charged pions (15 msr, cf. Ref. 68) was approximately the same as that of the LAMPF π^0 spectrometer (cf. Fig. 3.5).

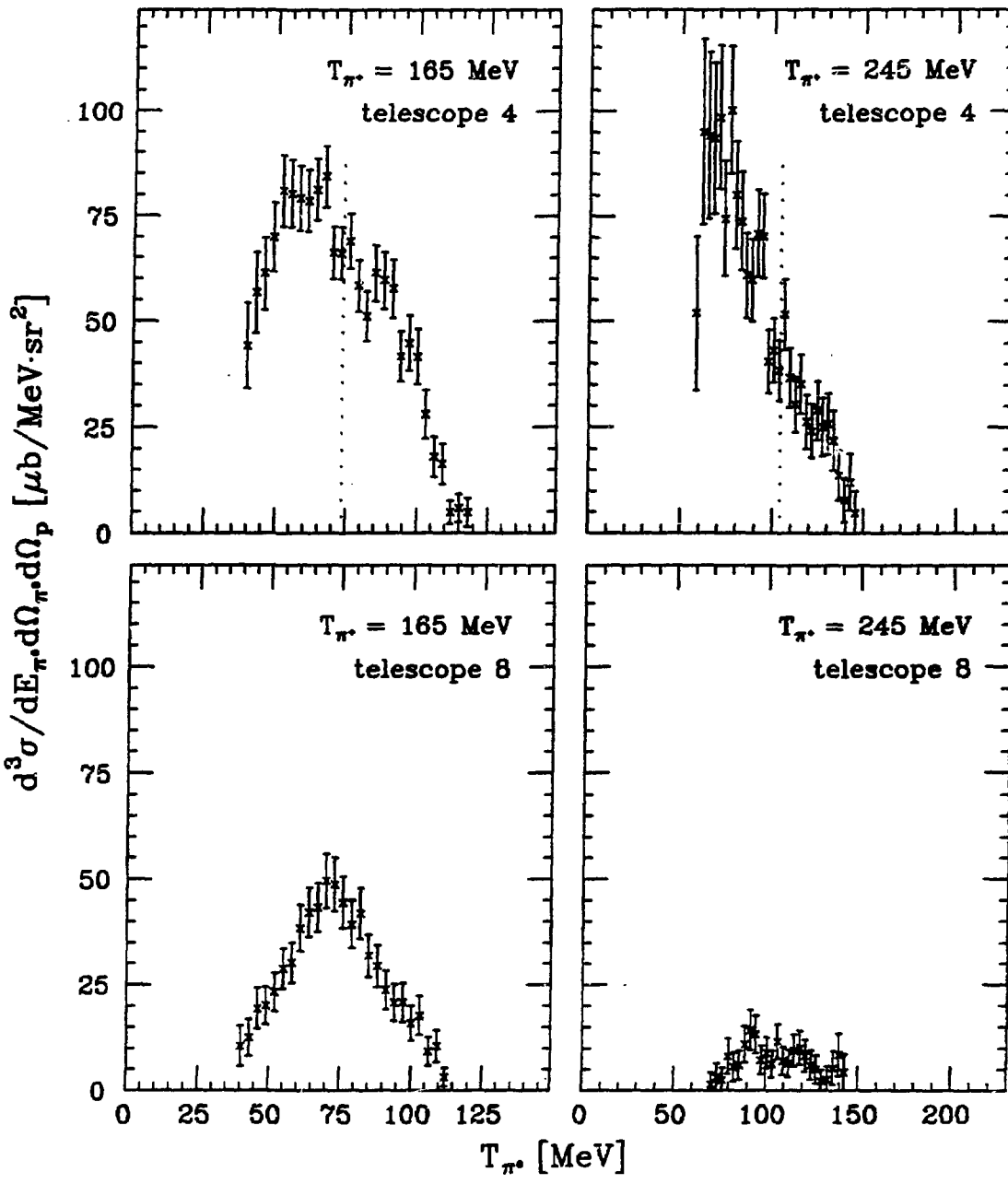

Figure 5.5. Comparison of $^{16}O(\pi^+,\pi^0 p)$ cross section spectra at θ_{π^0} = 130°. This figure compares our 165 MeV data obtained with telescope 4 (the central proton telescope) and telescope 8 (in the scattering plane 17° further away from the beam than the central telescope) to the 245 MeV data of Gilad *et al.*[43,91] obtained with the same telescopes. The normalization uncertainty is not included. The dotted lines indicate the quasi-free energy. Only p-shell nucleon removal events are included in the spectra.

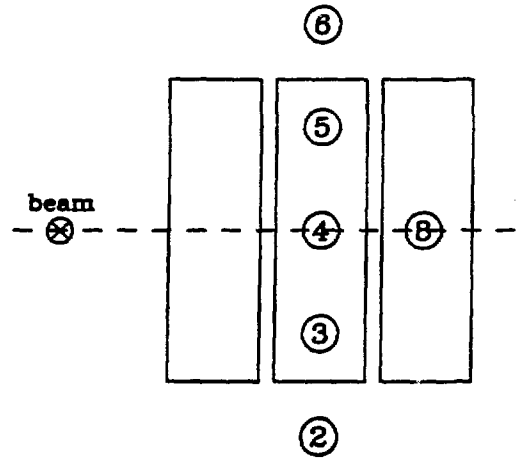

Figure 5.6. Proton detector solid angles. The figure sketches the angular extent of the proton telescopes used by Kyle *et al.* (large rectangles) compared to that of our telescopes (circles). The horizontal axis is the proton in-plane angle, and the vertical axis is the out-of-plane angle. The numbers refer to the numbering of our telescopes. The dashed line indicates the position of the scattering plane. Each telescope used by Kyle *et al.* spans 15° horizontally and 50° vertically (see the text). The symbol to the left of the proton telescopes shows the position of the beam relative to the telescopes. Our telescope 8 was always positioned farther away from the beam than the central telescope.

The $^{16}O(\pi^{\pm},\pi^{\pm}p)$ data of Kyle *et al.*[40,41] were reanalyzed with proton-angle cuts corresponding to our telescopes 3, 4, 5, and 8.[92] This analysis covered all setups that could be used for comparison to both our data (pion angles 80° and 134° at $T_{\pi^{\pm}} = 163$ MeV) and those of Gilad *et al.* (60° and 130° at $T_{\pi^{\pm}} = 240$ MeV). To ensure the best possible exclusion of events from elastic $\pi^{\pm}p$ scattering off the hydrogen in the water targets, it was necessary to do a complete reanalysis starting with the tapes of raw data. The analysis was done using a CDC computer at the ETH (Eidgenössische Technische Hochschule) in Zürich. Because the proton solid angle was significantly reduced in the reanalysis compared to the original size (cf. Fig. 5.6), the statistics of the resulting cross section spectra are not as high as one might desire.

Cross section spectra from this reanalysis of the data of Kyle *et al.* were used by Gilad *et al.* to calculate the cross section ratios R_{Δ}^{+0} shown in Fig. 1.13.

$^{16}O(\pi,\pi'p)$ cross section spectra for p-shell nucleon removal obtained under similar

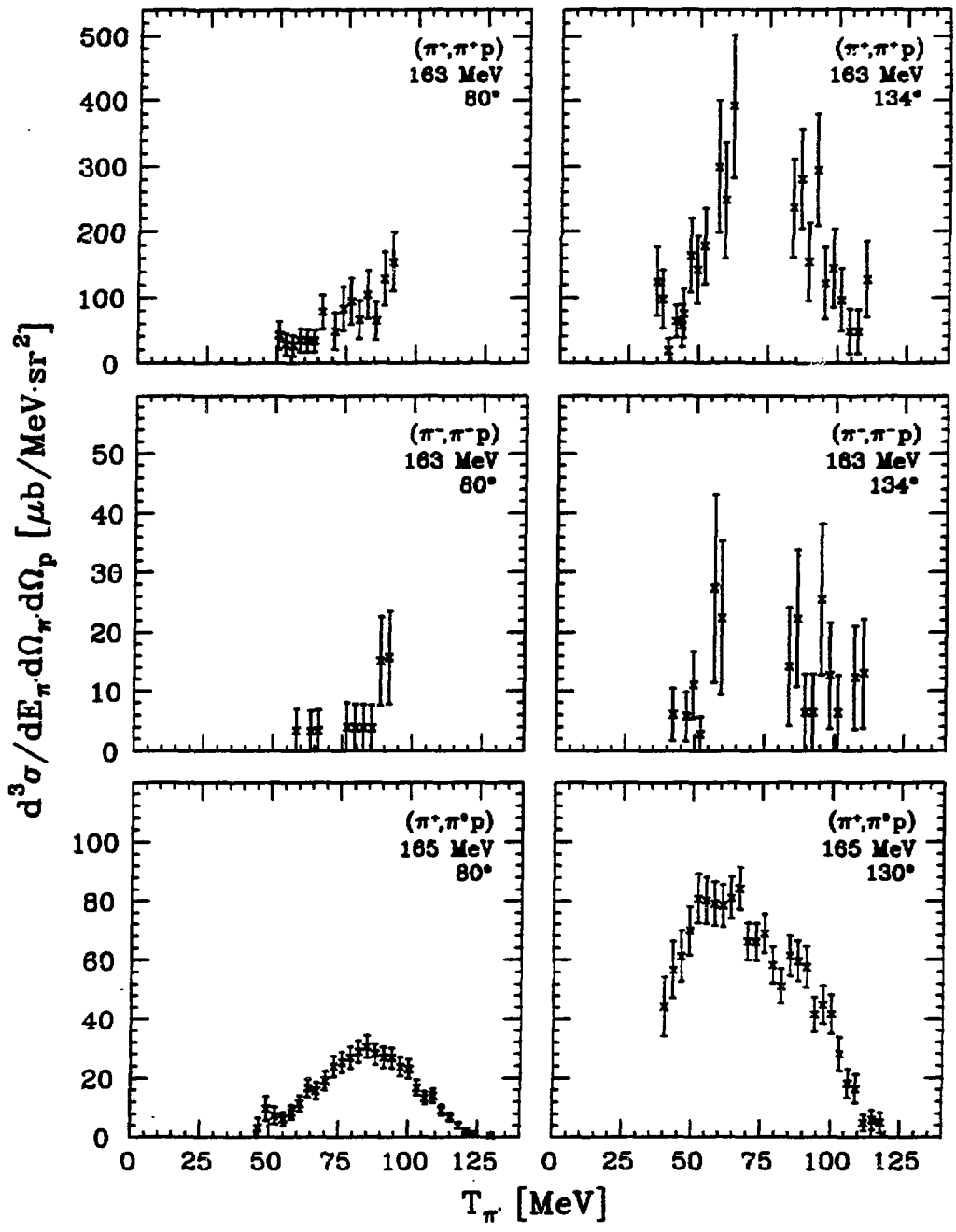

Figure 5.7. Comparison to $^{16}O(\pi^{\pm},\pi^{\pm}p)$ results for telescope 4 data. The figure compares our $^{16}O(\pi^{+},\pi^{0}p)$ measurements (third row) to the re-analyzed charged-pion measurements of Kyle *et al.*[40,92] (upper two rows). Information about the beam energy and the pion angle is given next to each spectrum. The vertical axes are scaled by the isospin ratios 9 : 1 : 2 (top to bottom).

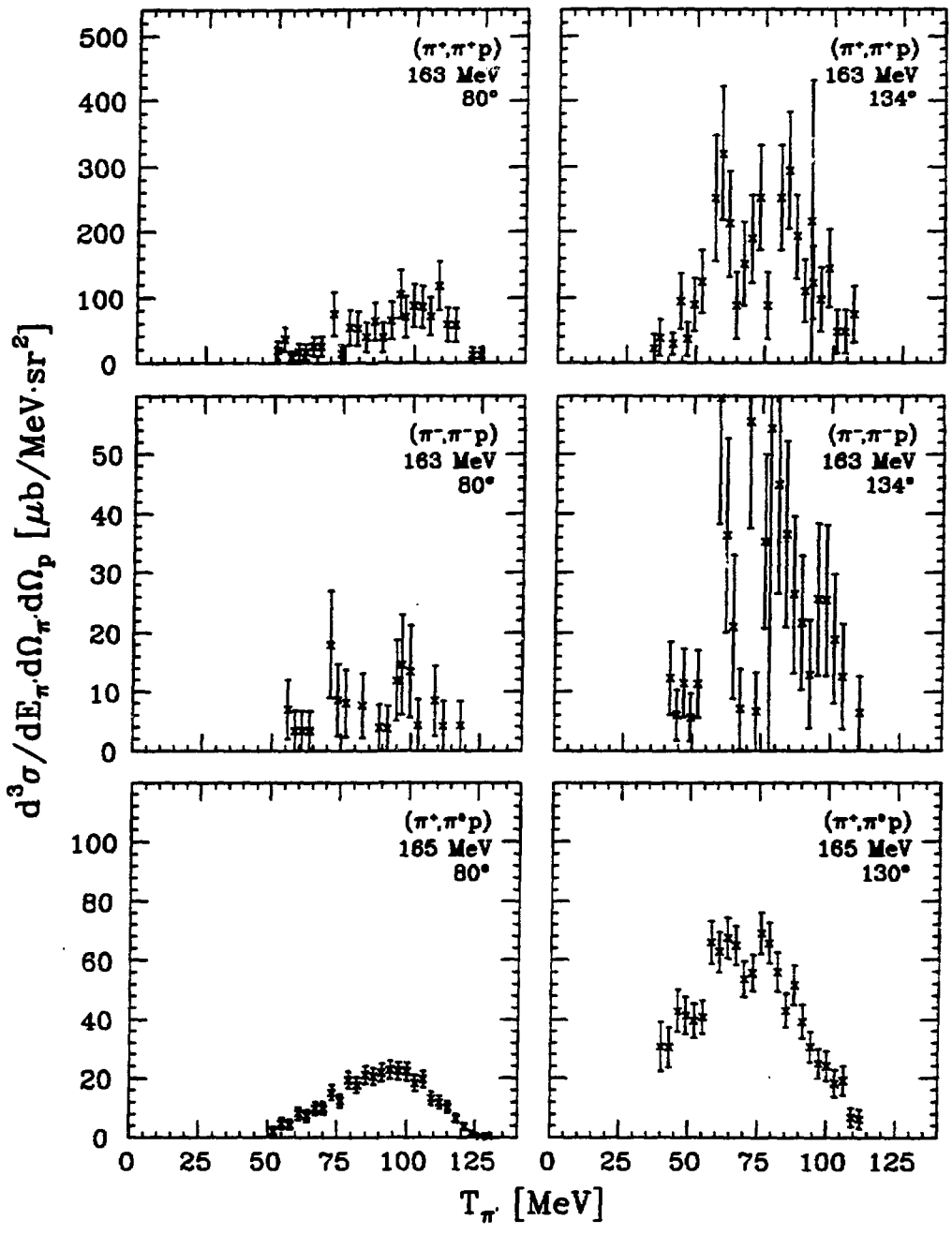

Figure 5.8. Comparison to $^{16}O(\pi^{\pm},\pi^{\pm}p)$ results for telescope 3 data. The figure compares our $^{16}O(\pi^{+},\pi^{0}p)$ measurements (third row) to the re-analyzed charged-pion measurements of Kyle *et al.*[40,92] (upper two rows). Information about the beam energy and the pion angle is given next to each spectrum. The vertical axes are scaled by the isospin ratios 9:1:2 (top to bottom).

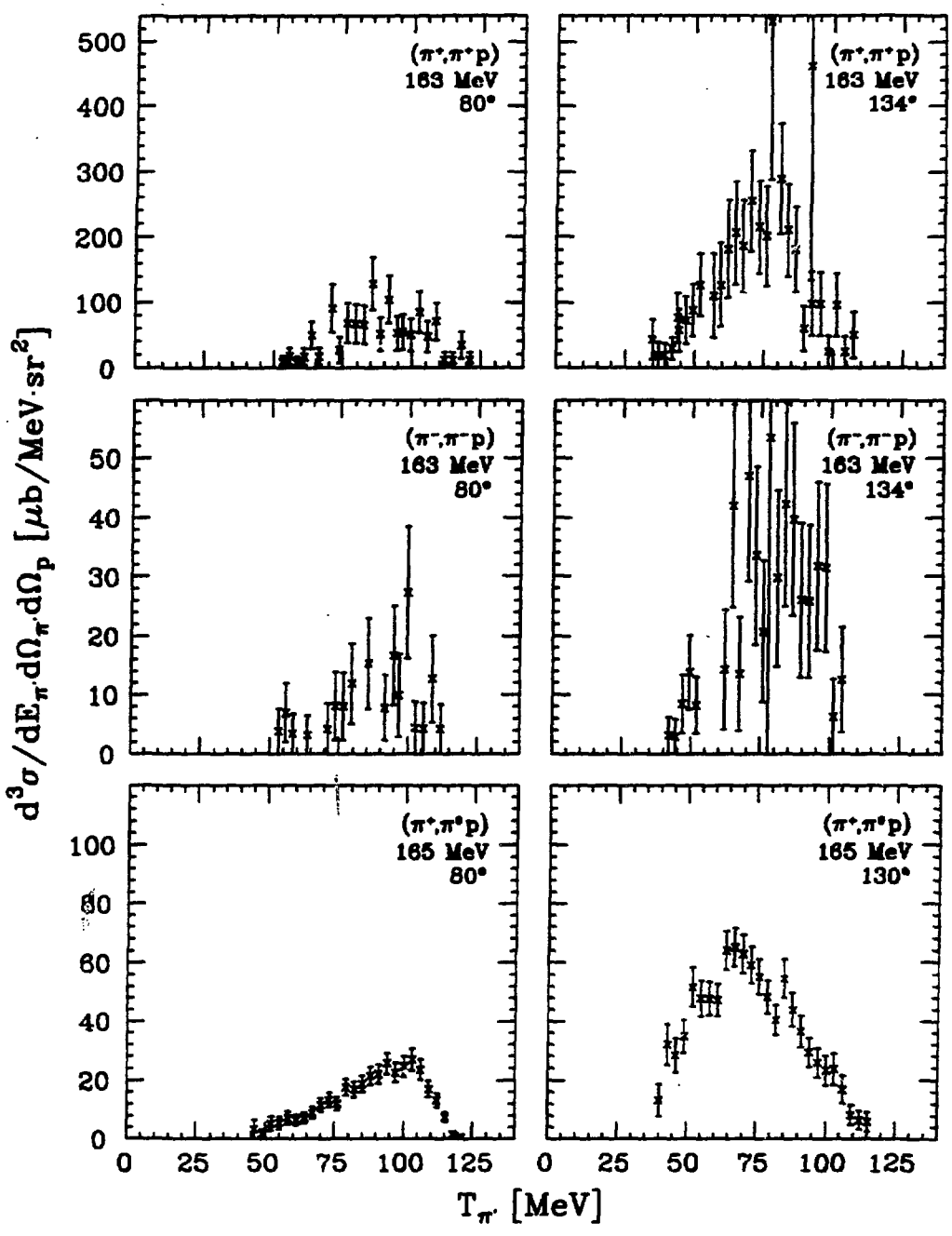

Figure 5.9. Comparison to $^{16}O(\pi^{\pm},\pi^{\pm}p)$ results for telescope 5 data. The figure compares our $^{16}O(\pi^{+},\pi^{0}p)$ measurements (third row) to the re-analyzed charged-pion measurements of Kyle *et al.*[40,92] (upper two rows). Information about the beam energy and the pion angle is given next to each spectrum. The vertical axes are scaled by the isospin ratios 9:1:2 (top to bottom).

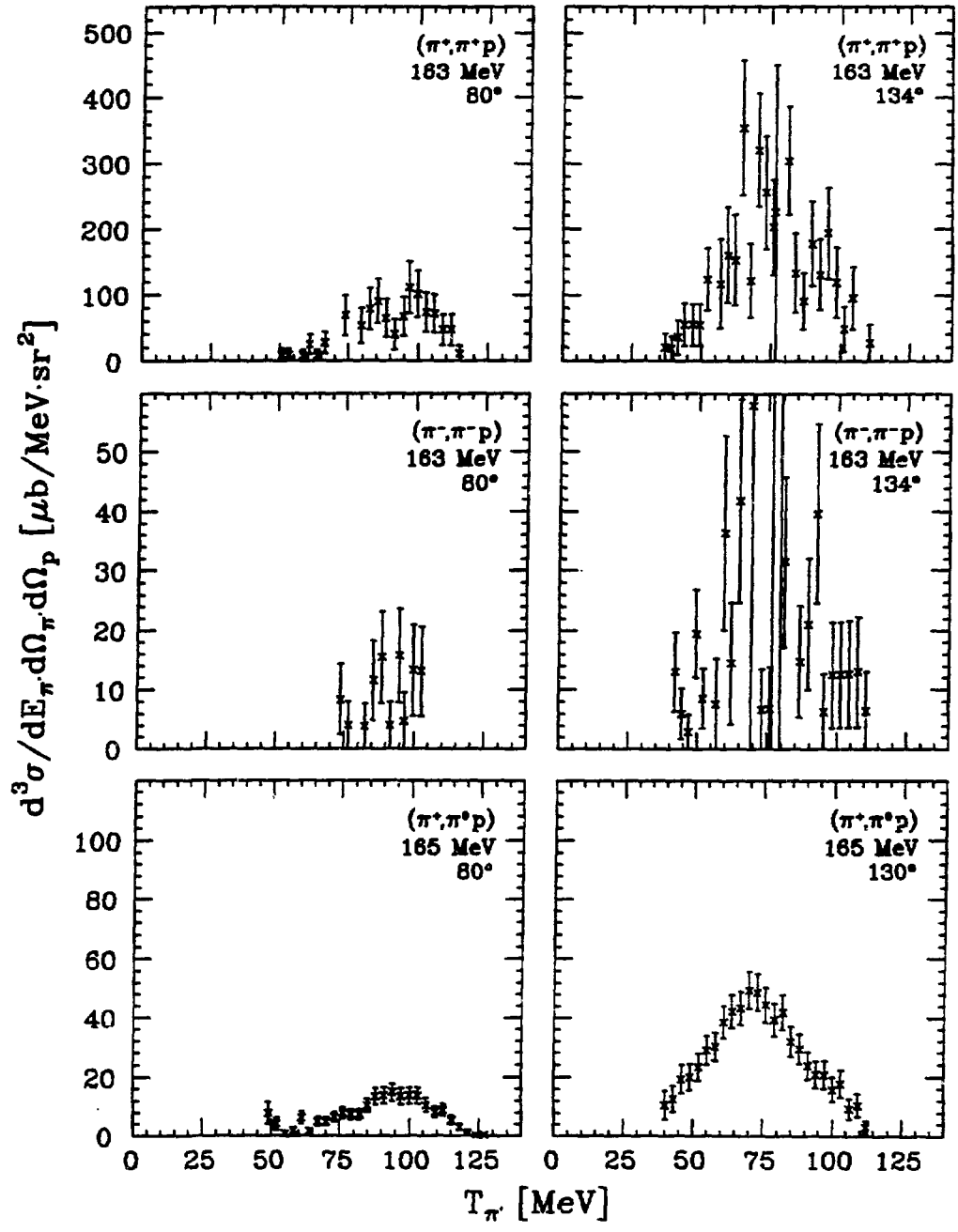

Figure 5.10. Comparison to $^{16}O(\pi^{\pm},\pi^{\pm}p)$ results for telescope 8 data. The figure compares our $^{16}O(\pi^{+},\pi^{0}p)$ measurements (third row) to the re-analyzed charged-pion measurements of Kyle *et al.*[40,92] (upper two rows). Information about the beam energy and the pion angle is given next to each spectrum. The vertical axes are scaled by the isospin ratios 9 : 1 : 2 (top to bottom).

Table 5.2. $d^2\sigma/d\Omega_{\pi^0}\,d\Omega_p$ for (π^+,π^+p) and (π^+,π^0p). The table compares our integrated cross sections from Table 4.4 (including the normalization uncertainty) to integrals of the (π^+,π^+p) cross sections of Kyle *et al.* shown in Figs. 5.7 – 5.10. The central pion angle in the backward scattering measurements of Kyle *et al.* was 134°. This was taken into account in calculating the free cross section ratios (between cross sections $d\sigma/d\Omega_{\pi^0}$).[14–16]

θ_{π^0} [deg]	telescope	$\frac{d^2\sigma}{d\Omega_{\pi^0}\,d\Omega_p}\ \left[\frac{\text{mb}}{\text{sr}^2}\right]$		R_Δ^{+0}
		(π^+,π^+p)	(π^+,π^0p)	
80	3	3.4 ± 0.4	1.00 ± 0.15	3.5 ± 0.6
80	4	5.3 ± 0.8	1.30 ± 0.19	4.1 ± 0.9
80	5	2.9 ± 0.3	1.03 ± 0.16	2.8 ± 0.5
80	8	2.9 ± 0.4	0.53 ± 0.08	5.5 ± 1.1
80	free	—	—	3.89 ± 0.03
130	3	8.6 ± 0.8	3.19 ± 0.48	2.7 ± 0.5
130	4	15.6 ± 2.0	4.46 ± 0.67	3.5 ± 0.7
130	5	9.0 ± 0.9	2.99 ± 0.45	3.0 ± 0.5
130	8	9.4 ± 0.9	2.09 ± 0.34	4.5 ± 0.8
130	free	—	—	3.93 ± 0.04

conditions by Kyle *et al.* and by us are shown in Figs. 5.7 – 5.10 for telescopes 4, 3, 5, and 8, respectively. In each figure the vertical axes are scaled 9 : 1 : 2, corresponding to the simple isospin ratios of Eqs. (1.7) and (1.15). That is, if this most naïve model is correct, all three spectra in each column should look the same.

Comparing our 130° spectra to those for charged-pion measurements, we note that the (π^+,π^+p) and (π^+,π^0p) spectra look roughly equal for all telescopes (that is, the ratio between them is roughly equal to the isospin ratio). This is in accordance with the observations of Gilad *et al.*, who found that the ratio R_Δ^{+0} of the (π^+,π^+p) to the (π^+,π^0p) cross section was about the same as the isospin ratio at $\theta_{\pi^0} = 130°$, and that it was clearly smaller than this ratio at $\theta_{\pi^0} = 60°$ (cf. Fig. 1.13). In our case the (π^+,π^+p) and (π^+,π^0p) spectra also appear similar at the more forward angle. We do not see any relative enhancement of the (π^+,π^0p) process at 80°. These observations are not necessarily in conflict, however, because 80° is not a very forward angle; we have noticed before (Fig. 5.2) that the behavior at 70° is significantly different from that at 80°, and the observation of Gilad *et al.* was made at an even more forward angle of 60°. Furthermore, the statistics are poor.

We have calculated ratios R_Δ^{+0} between the integrated cross sections $d^2\sigma/d\Omega_{\pi^0}\,d\Omega_p$ of the (π^+,π^+p) and (π^+,π^0p) spectra in Figs. 5.7 – 5.10. The integration of the (π^+,π^+p) spectra was done as described for our data in Sec. 4.1.6. The curve fitting was done by the author independently of Kyle *et al.* The results are listed in Table 5.2. The table also includes ratios of free cross sections $(d\sigma/d\Omega_{\pi^0})$.[14–16] These are somewhat lower than the simple isospin ratio of 4.5. Considering the large uncertainties of the calculated ratios, we can only conclude that they are not in obvious disagreement with the free ratios at either angle.

The statistics of the (π^-,π^-p) spectra are so low that we do not consider it feasible to perform any quantitative analysis involving these results. Qualitatively, they do not appear to contradict the conclusions drawn for R_Δ^{+0}; cross section ratios involving (π^-,π^-p) are not in obvious disagreement with the simple isospin ratios (nor with the free ratio R_Δ^{+-} which is 10.6 ± 0.2 at 80° and 11.6 ± 0.1 at 134°, cf. Refs. 14 – 16).

5.1.4 Comparison to Predictions of the Δ–Hole Model

Theoretical $(\pi,\pi'p)$ cross section calculations have been made within the framework of the Δ–hole model by Takaki and Thies[52] (cf. Sec. 1.3). In Fig. 1.14 we showed how these calculations compared to the $^{16}O(\pi^+,\pi^0p)$ results of Gilad *et al.* Such calculations have also been made for conditions corresponding to our experiment.[93]

Fig. 5.11 shows our telescope 4 (the central proton telescope) results for $^{16}O(\pi^+,\pi^0p)$ p-shell nucleon removal along with the calculations. The dashed curves result from "modified DWIA" calculations (cf. Fig. 1.10), while the solid curves include the Δ–N interaction of Eq. (1.28). The calculations assumed a point-like proton detector, while our proton telescopes each span about 8.5 msr (cf. Sec. 2.2.3). This may explain why the p-shell structure (the dip near the quasi-free energy, cf. Sec. 4.1.3) is more evident in the calculations than in the data. Moreover, we know from Fig. 4.10 that we have a significant contribution, perhaps as much as 20%, from other processes (mainly s-shell removal) within our p-shell cut. This will also tend to fill in the expected dip. However, Fig. 4.10 also indicates that while we include these unwanted contributions, we also lose a similar amount of p-shell events. The integrated cross sections should therefore not be influenced much by the ambiguities in the p-shell cut. We integrated

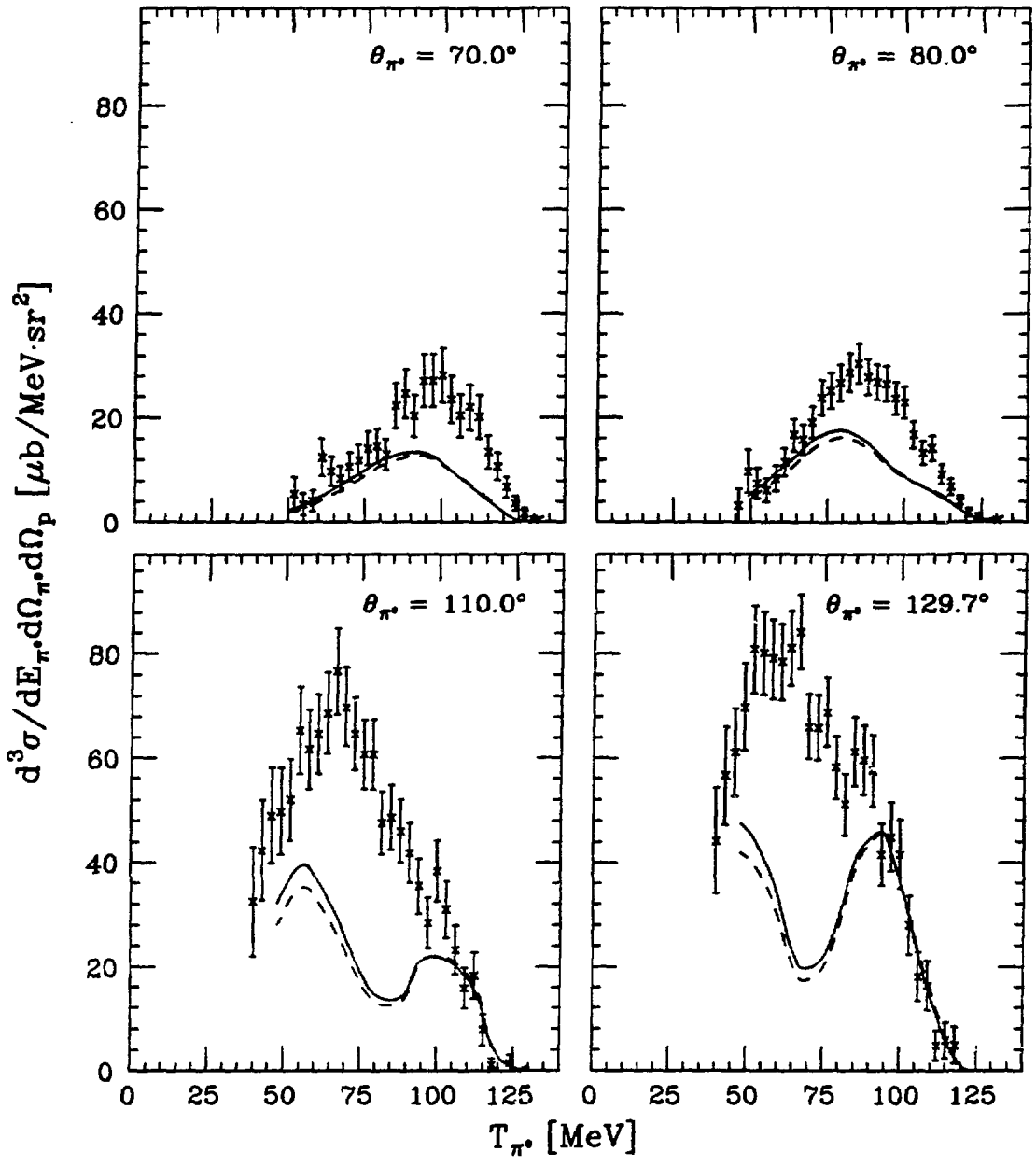

Figure 5.11. Δ–hole model calculations for telescope 4 at $T_{\pi^+} = 165$ MeV. The spectra show our results for $^{16}O(\pi^+, \pi^0 p)$ with p-shell nucleon removal, and they only include events where the central proton telescope (telescope 4) was hit. There is a 15% normalization uncertainty in addition to the uncertainties shown in the figure. (The same data were shown in Fig. 4.12.) The curves show theoretical calculations by Takaki and Thies.[52,93] The dashed curves are from modified DWIA calculations, while the solid curves represent Δ–hole model calculations including the Δ–N interaction.

the theoretical estimates (including the Δ–N interaction) as described for our data in Sec. 4.1.6 and compared the integrated cross section estimates to our values of $d\sigma/d\Omega_{\pi^0}$ from Table 4.4. We found that the Δ–hole model calculations account for 55%, 64%, 50%, and 54% of the integrated cross sections at pion angles 70.0°, 80.0°, 110.0°, and 129.7°, respectively. The calculations thus on the average underestimate the cross sections by more than 40%. (Because of our normalization uncertainty of 15%, this value may be up to about 10 percentage points larger or smaller.) The relative constancy of the fraction accounted for at the four π^0 angles indicates that the angular dependence is handled well in the calculations. We note that the inclusion of the Δ–N interaction terms (the "direct" term (7) and the "exchange" term (8) of Fig. 1.11) changed the cross section estimates in the correct direction, but by much too small an amount to reach agreement with the data. A similar situation was observed for the calculations pertaining to the measurements of Gilad *et al.*, but there the discrepancy between theory and data was a little smaller (30% according to Ref. 52) (see Fig. 1.14).

Calculations have also been made for telescope 8 (which was in the scattering plane 17° further away from the beam than telescope 4) for two of our setups.[93] These are shown in Fig. 5.12. Interestingly, with our 15% normalization uncertainty taken into account, the theoretical estimates now appear to be basically in agreement with our data. As in the case of telescope 4, we note that inclusion of the Δ–N interaction increases the cross section estimates. Unfortunately, no calculations have been done corresponding to the telescope 8 measurements of Gilad *et al.*. We are therefore unable to comment on the generality of the above observations for this telescope. Based on the comparisons in Figs. 5.11 and 5.12 alone, a possible conclusion is that the Δ–hole model calculations of Ref. 52 do not treat the angular correlation of the ejected particles correctly; our observations suggest that the calculated angular distribution may be too broad. It is also possible that the disagreement exists only at the central telescope (as appears to be the case for our simple Monte Carlo calculations shown in Fig. 5.1). Here, at the conjugate quasi-free angle, the experimental p-shell cross sections are most vulnerable to contributions from other processes (in particular s-shell nucleon removal) and final state interactions.

Returning to telescope 4, we conclude that there are serious discrepancies between the

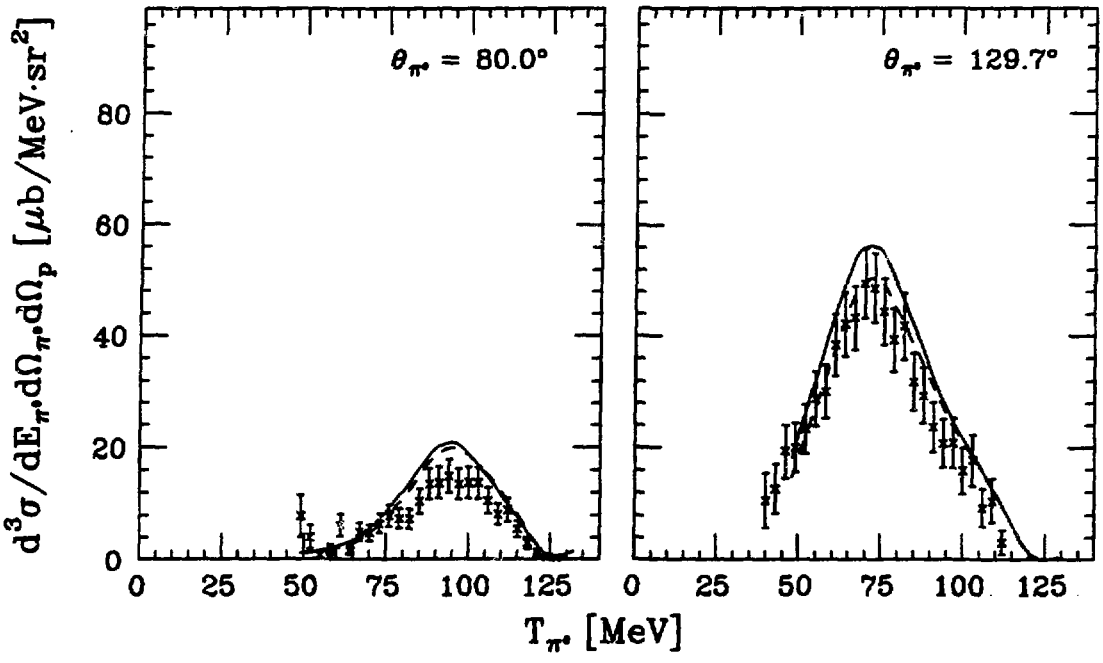

Figure 5.12. Δ–hole model calculations for telescope 8 at $T_{\pi^+} = 165$ MeV. The spectra show our results for $^{16}O(\pi^+,\pi^0 p)$ with p-shell nucleon removal, and they only include events where telescope 8 was hit. There is a 15% normalization uncertainty in addition to the uncertainties shown in the figure. The curves show theoretical calculations by Takaki and Thies.[52,93] The dashed curves are from modified DWIA calculations, while the solid curves represent Δ–hole model calculations including the Δ–N interaction.

calculated cross section estimates and the actual measured cross sections. There are two limitations in the calculations of Takaki and Thies[52] that may need to be investigated further in order to improve the theoretical estimates (cf. Sec. 1.3): First, they decided not to include the rearrangement process shown in diagram (4) of Fig. 1.11 in their calculations. The importance of this term is discussed in their paper.[52] They found that its contribution for $(\pi^+,\pi^0 p)$ is five times that for $(\pi^-,\pi^- p)$, and 15 times that for $(\pi^+,\pi^+ p)$. Inclusion of diagram (4) may therefore be important to the theoretical understanding of our data. Takaki and Thies estimate that including it may modify the calculated $^{16}O(\pi^+,\pi^0 p)$ cross sections by about $10-20\%$ at the quasi-free peak.[52] If so, a large discrepancy between theory and experiment still exists.

The second limitation in the calculations is the restriction to consider only the $T_{\Delta N} = 1$ channel for the Δ–N interaction. Takaki and Thies show that the possible $T_{\Delta N} =$

2 channel has the same effect on all $(\pi,\pi'p)$ reactions. The $T_{\Delta N} = 2$ component can therefore only contribute to deviations from the free cross section ratios in the presence of a $T_{\Delta N} = 1$ component. As mentioned in Sec. 1.3, $T_{\Delta N} = 1$ corresponds to two-nucleon absorption of pions. Recent experiments have shown that multi-nucleon absorption is also important,[53,94] and this might be related to the $T_{\Delta N} = 2$ channel.[52] The $T_{\Delta N} = 2$ channel may therefore be important to explaining our cross section spectra. Takaki and Thies note that diagram (4) is three times as important for the $T_{\Delta N} = 2$ component than it is for the $T_{\Delta N} = 1$ component.[52]

One should also keep in mind that the calculations of Takaki and Thies were done using the simple, one-parameter expression of Eq. (1.28) for the Δ–N interaction. In their work,[52] they express some caution about the present understanding of the strength parameter C_{21} of the interaction. Treating this as a constant for all cases may not be justified. A better physical description of the interaction strength is presently lacking, however.

5.2 A-Dependence of the (π^+,π^0p) Reaction

The essence of our A-dependence study of the (π^+,π^0p) reaction on ^{16}O, ^{56}Fe, ^{120}Sn, and ^{208}Pb at $\theta_{\pi^0} = 110.0°$ is that within the constraints of our experiment there is hardly any variation with A at all (cf. Figs. 4.31 – 4.35 and Table 4.8). If anything, there may be a slight decrease in cross section as the nuclear mass increases, and there may be another slight decrease in the width of the quasi-free angular distribution. The trend of constant or slowly decreasing cross sections with increasing A is in agreement with earlier observations made by Piasetzky *et al.*[38] for the (π^+,π^+p) reaction at the same beam energy (cf. Sec. 1.2.1). Our plots of integrated cross sections in Fig. 4.35 show that the background increases with the nuclear mass. This clearly indicates that processes such as multiple scattering and other final state interactions become increasingly important as the nuclei become more complex (as one would naturally expect).

Since pions mainly interact with the back surface of the target nuclei (see Sec. 1.1.2), and we were detecting the π^0's at a backward angle, the obvious first guess for the

A-dependence was that it should go as $A^{\frac{2}{3}}$. This argument ignores the role of the ejected proton (which interacts less strongly than the pion), and it proved not to be true. The deviation from the proportionality to $A^{\frac{2}{3}}$ is then most likely due to final state interactions disturbing the motion of the proton, which has to travel through a substantial part of the nucleus to get to the detector at $\theta_p = 29.7°$.

An intuitive way of accounting for proton final state interactions is to calculate the average distance d_p that a proton has to travel inside the different nuclei and estimate a corresponding reduction in the cross section from the factor $\exp(-\frac{d_p}{\lambda_p})$, where λ_p is the mean free path of a proton in nuclear matter. d_p can be estimated by considering a point-like pion hitting a spherical nucleus: The hit position of the incident pion on the back surface of the nucleus can be described by the coordinates x in the horizontal direction and y in the vertical direction. The origin is on the z-axis which goes through the center of the nucleus. We only have to consider proton paths parallel to the scattering plane. We will first look at a horizontal slice of the nucleus of radius r ($r < R$, where R is the nuclear radius). In studying the geometry, one finds that for a proton being ejected at an angle θ_p from the nuclear (back) surface a distance x away from the central trajectory, the distance to travel inside the nucleus is

$$d(x,y) = 2\sqrt{r(y)^2 - x^2}\,\cos\theta_p - 2x\,\sin\theta_p\,. \tag{5.1}$$

The radius r of the horizontal slice is related to the vertical coordinate y by $r(y)^2 = R^2 - y^2$. The average distance then becomes

$$d_p = \frac{1}{\pi R^2}\int_{-R}^{R} dy \int_{-r(y)}^{r(y)} dx\, d(x,y) \tag{5.2}$$

$$= \tfrac{4}{3} R \cos\theta_p\,. \tag{5.3}$$

In this model, the A-dependence of the cross sections should therefore be described by

$$\sigma(A) = \sigma_0\, A^{\frac{2}{3}} \exp\left(-\frac{4R(A)\cos\theta_p}{3\lambda_p}\right), \tag{5.4}$$

where σ_0 is the A-independent part of the cross section. For nuclei with A larger than approximately 20 (which we in this context take to include oxygen) the root-mean-square radius (of the charge density) can be expressed by[10]

$$R(A) = 0.82\, A^{\frac{1}{3}} + 0.58\,. \tag{5.5}$$

We fitted the expression of Eq. (5.4) to our cross section data of Table 4.8 by varying the parameters σ_0 and λ_p. This approach yielded the value (1.6 ± 0.2) fm for λ_p. On the other hand, recent studies[90,95] indicate that the value of the proton mean free path should be in the range $5 - 7$ fm. We also investigated the opposite approach: choose a physical value for λ_p, calculate relative cross sections from Eq. (5.4), and determine the A-dependence by fitting these calculated cross sections to $\sigma(A) = \sigma_0 A^{\alpha}$. Using $\lambda_p = 5.5$ fm, this approach led to $\alpha = 0.42$, that is, a clear increase in cross section with A. From the above we therefore have to conclude that the model described by Eq. (5.4) does not account properly for the A-dependence of the observed cross sections; there appear to be more losses of cross section in the $(\pi^+, \pi^0 p)$ process than can be accounted for by final state interactions of the proton alone. This could possibly be explained by final state interactions of the ejected pions. With a π^0 angle of 110°, a sizeable fraction of the pions will have to travel through some part of the nucleus from which they were ejected. Since pions interact very strongly with nucleons, a number of the ejected pions might be lost also at this backward π^0 angle.

Evidently, more careful, quantum mechanical calculations will be necessary in order to obtain a better description of the A-dependence of the $(\pi^+, \pi^0 p)$ process.

5.3 Single Arm Measurements of the (π^+, π^0) Reaction

In this section we discuss all our inclusive (π^+, π^0) measurements, which include both a study of the angular dependence of the $^{16}O(\pi^+, \pi^0)$ reaction and a study of the A-dependence of the (π^+, π^0) reaction. This section is divided into three parts: the first focuses on our measurements alone, including a comparison to our $(\pi^+, \pi^0 p)$ measurements, while the second contains a comparison to similar measurements made by Ashery *et al.*, and the third contains a comparison to (π^+, π^+) measurements made by Ingram *et al.*

5.3.1 Our Measurements

Our single arm $^{16}O(\pi^+, \pi^0)$ spectra presented in Fig. 4.36 (for the wide angular bin covering $\theta_{\pi^0} \pm 12°$) and Figs. 4.38 – 4.40 ($\theta_{\pi^0} \pm 4°$) display a clear difference in the

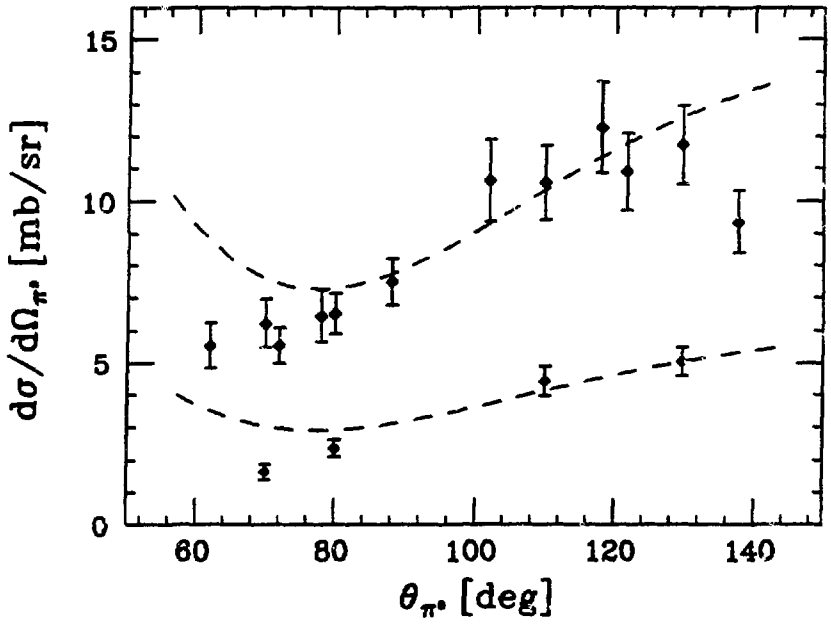

Figure 5.13. Integrated cross sections $d\sigma/d\Omega_{\pi^0}$ for the $^{16}O(\pi^+,\pi^0)$ reaction. The figure shows all our narrow-bin single arm results from Fig. 4.41 (filled diamonds) compared to the $^{16}O(\pi^+,\pi^0 p)$ results (including all ejected protons) from Fig. 5.2 (open diamonds). The normalization uncertainty is included in the figure. The dashed curves both represent the free πN single-charge-exchange cross section,[14–16] and they have been scaled by 3.16 and 1.26, respectively.

magnitude of the cross sections for forward π^0 angles compared to those for backward π^0 angles. The former are roughly a factor 2 smaller than the latter. We have earlier noticed similar behavior in the $(\pi^+,\pi^0 p)$ cross sections (cf. Sec. 5.1.1), and we note also here that part of the reduction for forward ejected pions may be due to the final state interactions (including absorption) that these pions experience while traveling through a substantial part of the nucleus. Some reduction may also be due to Pauli blocking of the interacting nucleon, which on the average has a lower energy for the more forward pion angles (cf. Sec. 5.1.1).

Fig. 5.13 shows a comparison of our narrow bin $^{16}O(\pi^+,\pi^0)$ integrated cross sections $d\sigma/d\Omega_{\pi^0}$ to the angular distribution of the cross section of the free $\pi^+ + n \rightarrow \pi^0 + p$ process.[14–16] The curve for the free cross sections has been scaled by 3.16 to match the measurements at the backward π^0 angles (the point at $\theta_{\pi^0} = 137.7°$ was not included in the fitting process). We observe that our results at backward π^0 angles are not

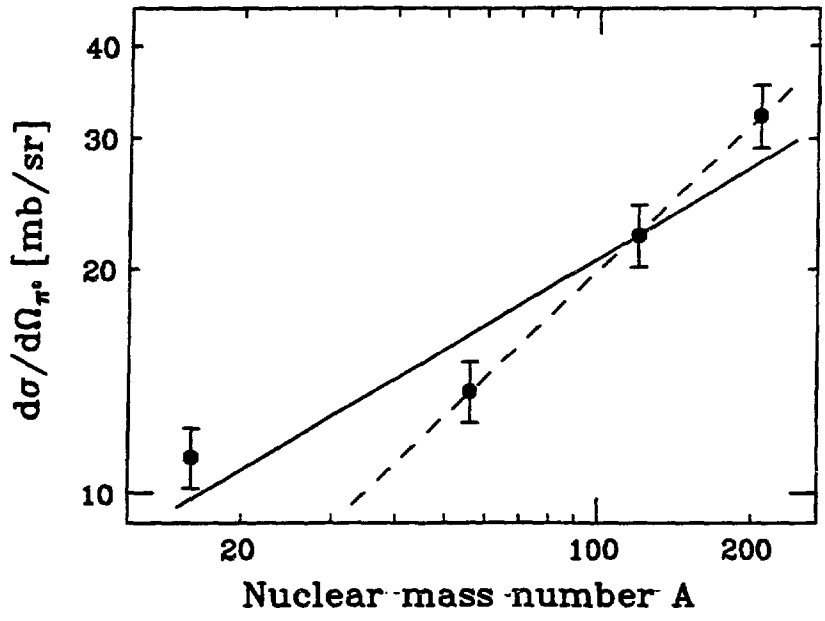

Figure 5.14. *A*-dependence of the (π^+, π^0) process at $T_{\pi^+} = 165$ MeV. The figure shows the results of our measurements on ^{16}O, ^{56}Fe, ^{120}Sn, and ^{208}Pb from Table 4.9. The normalization uncertainty is included. The lines are A^α fits to the data; the solid line is based on all four data points, while the dashed line results from a fit to the three heaviest nuclei only (see the text).

in disagreement with the (scaled) curve for the free process. This is very similar to what we observed for the $^{16}O(\pi^+, \pi^0 p)$ reaction in Fig. 5.2. Some of that information is included in Fig. 5.13 for direct comparison. Our results are in agreement with the hypothesis that backward pion scattering in the Δ-resonance region is essentially a quasi-free process. Moreover, from the scaling factors used in Fig. 5.13, we note that at backward angles the $^{16}O(\pi^+, \pi^0 p)$ reaction constitutes approximately 40% of the inclusive $^{16}O(\pi^+, \pi^0)$ cross section. More careful estimates of this fraction will be presented later.

The results of our *A*-dependence measurements of the (π^+, π^0) process were presented in Fig. 4.37 and Table 4.9. The $d^2\sigma/dE_{\pi^0}\, d\Omega_{\pi^0}$ spectra look rather similar for all targets, featuring a broad peak centered at approximately $T_{\pi^0} = 70$ MeV (the π^0 energy in the free process is 97.1 MeV, for $^{16}O(\pi^+, \pi^0 p)$ p-shell proton removal it is 83.3 MeV). Contrary to our observations for the coincidence measurements (Sec. 5.2), the single

Table 5.3. Comparison of $(\pi^+,\pi^0 p)$ cross sections to those of (π^+,π^0). The cross sections used for the calculations are $d\sigma/d\Omega_{\pi^0}$ from Tables 4.6, 4.8, and 4.9. Only the quasi-free part of the coincidence cross sections is included. The beam energy was $T_{\pi^+} = 165$ MeV for all measurements. The indices are *s* for single arm events, *c* for coincidence events, and *cp* for p-shell coincidence events. The values in the last column are also found in Table 5.1. The uncertainty estimates include the normalization uncertainty.

target	θ_{π^0} [deg]	$\left(\frac{d\sigma}{d\Omega_{\pi^0}}\right)_c \Big/ \left(\frac{d\sigma}{d\Omega_{\pi^0}}\right)_s$ [%]	$\left(\frac{d\sigma}{d\Omega_{\pi^0}}\right)_{cp} \Big/ \left(\frac{d\sigma}{d\Omega_{\pi^0}}\right)_s$ [%]	$\left(\frac{d\sigma}{d\Omega_{\pi^0}}\right)_{cp} \Big/ \left(\frac{d\sigma}{d\Omega_{\pi^0}}\right)_c$ [%]
^{16}O	70.0	27 ± 5	11 ± 2	43 ± 10
^{16}O	80.0	34 ± 5	14 ± 2	40 ± 8
^{16}O	110.0	40 ± 5	19 ± 4	49 ± 9
^{16}O	129.7	44 ± 5	18 ± 3	42 ± 7
^{16}O	110.0	40 ± 5	—	—
^{56}Fe	110.0	25 ± 4	—	—
^{120}Sn	110.0	17 ± 3	—	—
^{208}Pb	110.0	10 ± 2	—	—

arm cross sections clearly increase with A. Making a simple fit to our four data points, we found that the A-dependence of our measurements can be described by A^α where $\alpha = 0.41 \pm 0.06$. The data and the fit are shown in Fig. 5.14. To get a better estimate for the uncertainty in this number, we made a fit in which the data point for ^{16}O was ignored. That approach led to $\alpha = 0.65 \pm 0.11$. This fit is also shown in Fig. 5.14. As mentioned earlier (Sec. 5.1.3), in a simple quasi-free picture with very strongly interacting pions, one would expect the A-dependence to be just $A^{\frac{2}{3}}$. Our latter fit is actually consistent with this simple value, while our main result of $\alpha = 0.41 \pm 0.06$ is clearly lower than that. As lighter nuclei are not very well described by uniform spheres, one may speculate that the factor $A^{\frac{2}{3}}$ does not apply to such nuclei; however, more measurements on more nuclei are necessary before any firm conclusions can be drawn about this.

It is also of interest to compare the $(\pi^+,\pi^0 p)$ coincidence measurements to the inclusive (π^+,π^0) results. From the values of $d\sigma/d\Omega_{\pi^0}$ in Table 4.9 and the corresponding integrated cross sections for the $(\pi^+,\pi^0 p)$ process (Tables 4.6 and 4.8), we can obtain an estimate of the contribution of the quasi-free $(\pi^+,\pi^0 p)$ process in the total (π^+,π^0) cross section. These contributions are listed in Table 5.3. We note that the quasi-free

$(\pi^+,\pi^0 p)$ component of the (π^+,π^0) reaction appears to increase with the π^0 angle and to decrease with the nuclear mass. Both of these observations are in accordance with our earlier qualitative remarks: As the π^0 angle increases (in particular, as it goes from forward to backward), the path towards the π^0 spectrometer becomes more and more free of (nuclear) obstructions, and the importance of final state interactions decreases accordingly. This simple picture is supported by the observation that the relative effects on the p-shell cross sections are basically the same as on the complete ones. (The fraction of p-shell cross section in the complete cross section is approximately constant for all setups.) The *A*-dependence part of the table provides another illustration of the increasing importance of more complicated processes as the nuclei become more complex.

A similar comparison has been made by Piasetzky *et al.*[20,38] for the contribution of the $(\pi^+,\pi^+ p)$ reaction to the inclusive (π^+,π^+) cross section. They made their measurements at 165 MeV and 245 MeV incident energy on ^{12}C, ^{56}Fe, and ^{209}Bi, mostly at backward pion angles (cf. Sec. 1.2.1). At 165 MeV they found an average contribution of 30% for C, 15% for Fe, and 8% for Bi. Comparing these fractions to our results in Table 5.3, we see that their measurements are in qualitative agreement with ours, but that we in general found somewhat higher contributions from the single-nucleon removal process.

5.3.2 Comparison to the (π^+,π^0) Measurements of Ashery *et al.*

Several of the measurements of Ashery *et al.*[48,22] were made under conditions that corresponded closely to those of our experiment. Of particular interest to us are their measurements on ^{16}O at several angles (of which $\theta_{\pi^0} = 70°$ and $\theta_{\pi^0} = 108°$ overlap directly with two of our setups) and a measurement of ^{208}Pb(π^+,π^0) at $\theta_{\pi^0} = 108°$ (cf. Fig. 1.8). All the measurements of Ashery *et al.* were made at $T_{\pi^+} = 160$ MeV.

We first consider the $d^2\sigma/d\Omega_{\pi^0}\, d\Omega_p$ energy spectra. Fig. 5.15 shows results from both experiments. The spectra look similar, but in all cases our cross sections are clearly higher (by 30 – 50%) than the corresponding spectra of Ashery *et al.* The disagreement thus appears to be in the normalization of the cross sections. Considering the normalization uncertainty (9% for our data, 10% for those of Ashery *et al.*), it is

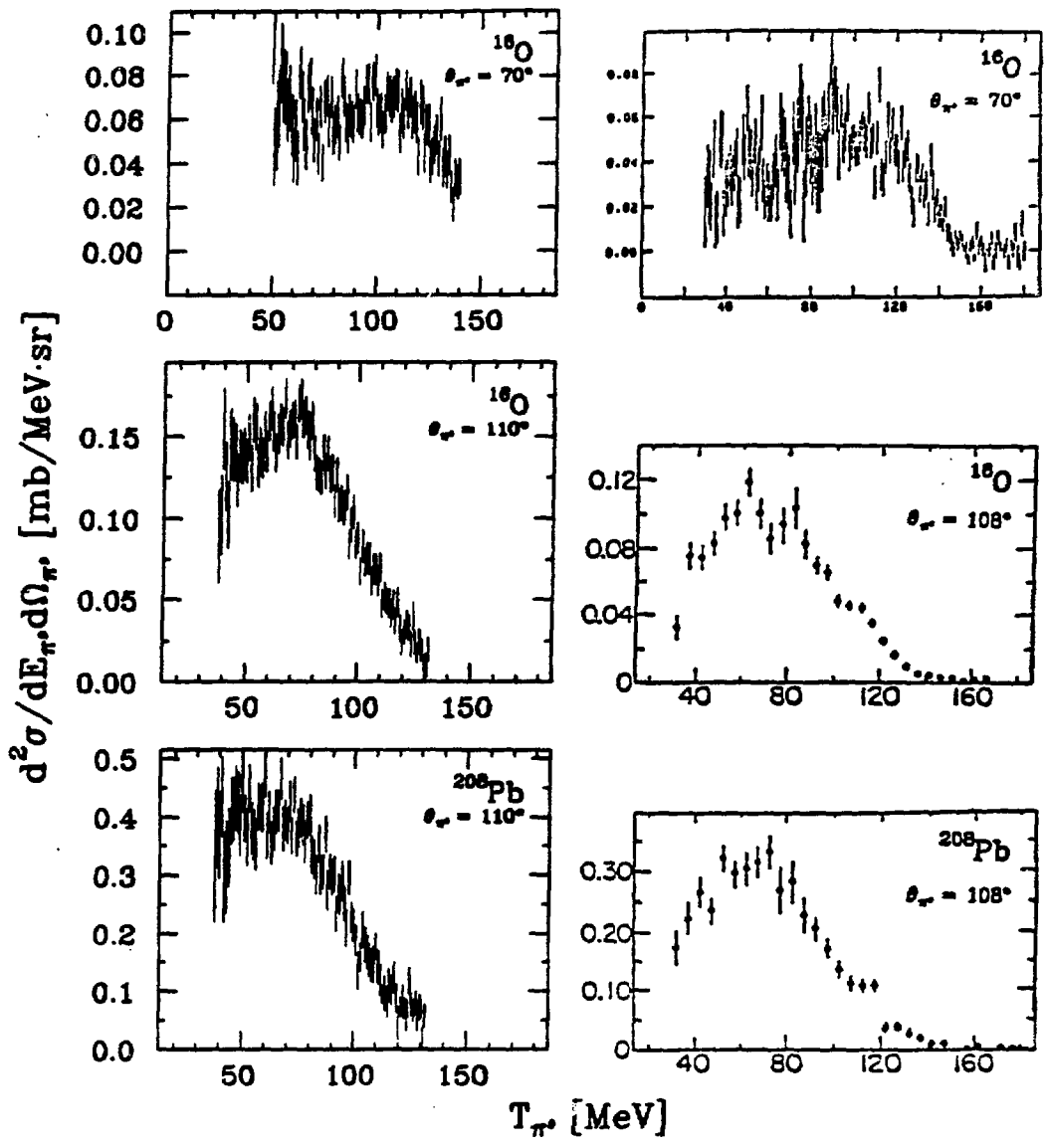

Figure 5.15. Comparison to cross section spectra of Ashery *et al.* The left hand column contains our results from Figs. 4.36 and 4.37 (not including a 9% normalization uncertainty), and the right hand column presents the corresponding measurements made by Ashery *et al.*[22,49] (not including a 10% normalization uncertainty). The π^0 spectrometer angular bin was 24° in our analysis and about 10° for Ashery *et al.*

possible that the cross sections at $\theta_{\pi^0} = 70°$ are in fair agreement with each other. The remaining measurements are in disagreement in any case, however. In Sec. 3.4, we discussed the complications involved in establishing the thickness of a water target.

Table 5.4. *A*-dependence of the scaling factor. This factor N_{eff} is the ratio of the measured cross section $d\sigma/d\Omega_{\pi^0}$ for the (π^+,π^0) reaction on a given nucleus at backward π^0 angles to the cross section of the free π^+n reaction. The values listed for Ashery *et al.* are from Ref. 22. The factors given for our data are each based on only one measurement, taken at $\theta_{\pi^0} = 110.0°$.

target	N_{eff} for (π^+,π^0)	
	Ashery *et al.*	Our data
^{12}C	1.6	—
^{14}C	2.7	—
^{16}O	2.0	3.4
^{18}O	2.8	—
^{56}Fe	—	4.2
^{58}Ni	4.0	—
^{120}Sn	—	6.8
^{208}Pb	6.6	9.9

Such thickness measurements could be a source of (some) normalization disagreement. Also, the data of Ashery *et al.* are not corrected for photon attenuation losses in the targets (cf. Sec. 3.2).[49] This correction is small for the water targets, but it is quite important for Pb; according to Fig. 3.4, about 13% of the π^0's could not be detected in our case. For as thick a Pb target as the one used by Ashery *et al.* (2.585 $\frac{g}{cm^2}$, cf. Ref. 22), expressing the π^0 transparency by Eq. (3.5) may be too simple. Nevertheless, for the purpose of illustrating the importance of photon attenuation, we applied this formula to their Pb target parameters. This led to an estimated π^0 transparency of only a little more than 40% assuming that their target was normal to the beam, or about 75% assuming an optimal target angle. In the latter case, correcting their data for photon attenuation losses would bring them into agreement with our data (cf. Fig. 5.15).

Comparing $d\sigma/d\Omega_{\pi^0}$ angular distributions for $^{16}O(\pi^+,\pi^0)$ (Figs. 1.8b and 5.13), we find that both collaborations agree on the general trend of the data. The measurements at back angles (from about $\theta_{\pi^0} = 80°$) follow the distribution of the free cross section, while the results at forward angles are suppressed relative to this (cf. our discussion in Sec. 5.3.1). With respect to the absolute size of the cross sections, we note the same disagreement as discussed for $d^2\sigma/dE_{\pi^0}\,d\Omega_{\pi^0}$ above. Our cross sections, especially for the backward π^0 angles, are generally higher than those of Ashery *et al.* A measure

for this disagreement is the scaling factor between the $^{16}O(\pi^+,\pi^0)$ cross sections at backward angles and the free cross sections. Table 5.4 lists this factor for all our 110° measurements as well as the scaling factors calculated by Ashery *et al.* from their (π^+,π^0) observations. The disagreements for ^{16}O and ^{208}Pb are again quite striking.

Ashery *et al.*[22] state the A-dependence of their total (π^+,π^0) cross sections (σ) to be A^α where $\alpha = 0.48$, but this would clearly change if their Pb data were corrected for photon attenuation losses as discussed above. Using our own fitting routine on their data, we find that α changes from 0.45 ± 0.05 to 0.56 ± 0.05 if the Pb cross section is adjusted for a π^0 transparency of 75%, or to 0.68 ± 0.06 if the Pb cross section is multiplied by a factor 2. Ignoring their Pb result altogether leads to $\alpha = 0.53 \pm 0.10$. Only the lowest value is in agreement with our result $\alpha = 0.41 \pm 0.06$ (calculated from $d\sigma/d\Omega_{\pi^0}$, cf. Sec. 5.3.1).

5.3.3 Comparison to the $^{16}O(\pi^+,\pi^+)$ Measurements of Ingram *et al.*

We now want to make a short comparison to charged-pion scattering. Ingram *et al.*[96] have made a series of $^{16}O(\pi^+,\pi^+)$ measurements using water targets, and Thies[55] has shown that these measurements are described well by modified DWIA calculations (cf. Sec. 1.3). Of interest to us here are some of the $T_{\pi^+} = 163$ MeV measurements of Ingram *et al.* Three angles were (almost) the same as ours: $\theta_{\pi^+} = 80°$, $\theta_{\pi^+} = 110°$, and $\theta_{\pi^+} = 134°$.

Fig 5.16 compares the relevant $d^2\sigma/dE_\pi\, d\Omega_\pi$ cross section spectra from both experiments. We note that the (π^+,π^+) cross sections are typically about a factor $2-3$ larger than those of the (π^+,π^0) reaction. This factor is smaller than one would expect from simple isospin coupling arguments (cf. Chapter 1) which suggests a ratio of $\frac{9+1}{2} = 5$ (the numerator includes both π^+p and π^+n scattering). We found above (Table 5.3) that quasi-free single nucleon removal accounts for typically about 40% of the single-arm inclusive cross section. There must therefore be significant contributions also from other reaction mechanisms, which could explain why the ratio of the (π^+,π^+) cross section to the (π^+,π^0) cross section is so poorly described by the simple isospin ratio.

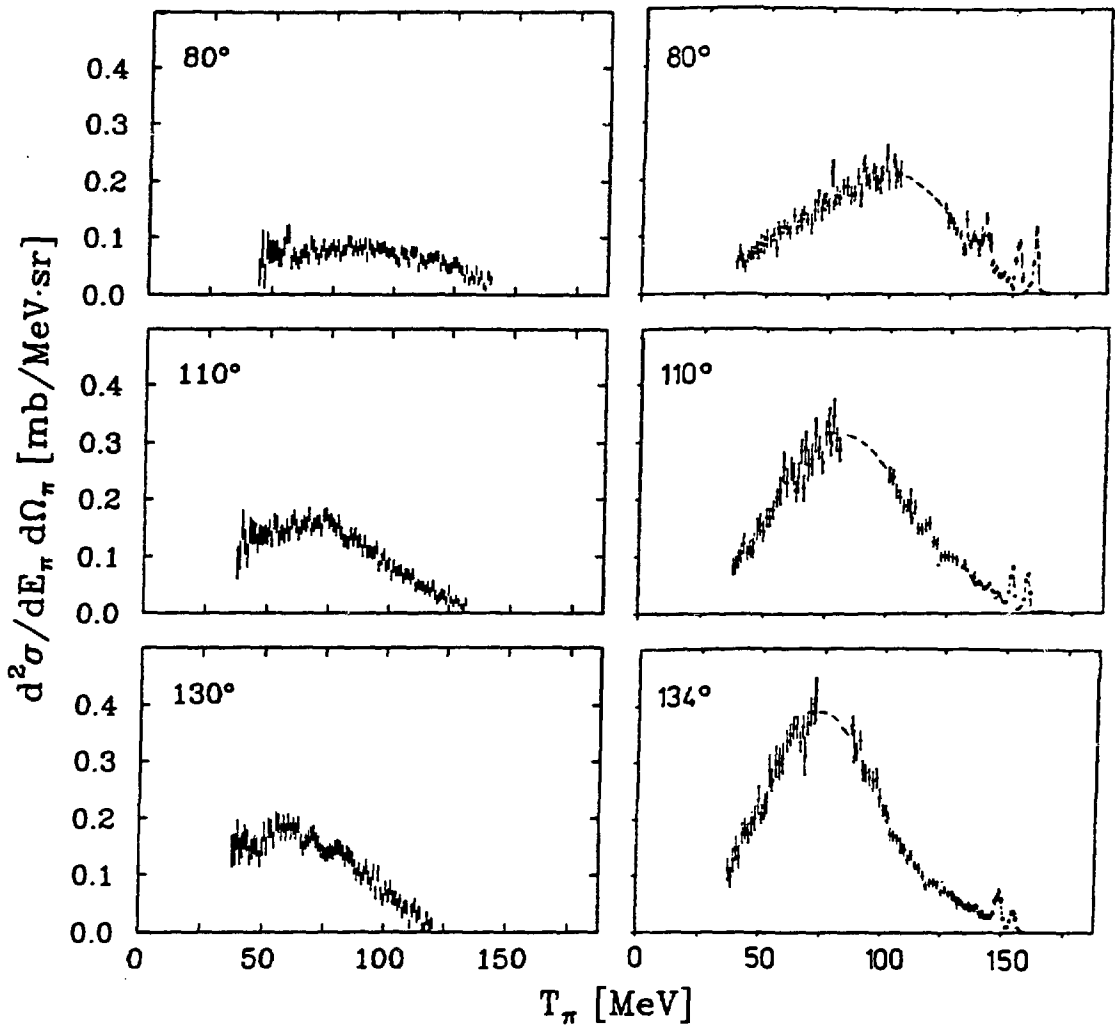

Figure 5.16. Comparison to $^{16}O(\pi^+,\pi^+)$ cross section spectra of Ingram *et al.* The left hand column contains our $^{16}O(\pi^+,\pi^0)$ results from Fig. 4.36 (not including an 8% normalization uncertainty), and the right hand column presents the corresponding $^{16}O(\pi^+,\pi^+)$ measurements made by Ingram *et al.*[96] (not including a 5% normalization uncertainty).

Comparing the shapes of the spectra in Fig 5.16, we see that the peaks are at a higher energy (about 10 MeV or so) in the π^+ spectra than in the corresponding π^0 spectra. This is the opposite effect of that expected for the single-particle interactions, since the SCX process then gains almost 6 MeV from the mass differences. This is another indication that more complicated processes also play an important role. The most striking feature in the comparison of the shapes is probably the low-energy part of the

spectra. The (π^+,π^0) spectra do not decrease as rapidly to the low-energy side of the peak as the (π^+,π^+) spectra do. This trend was also observed by Ashery *et al.* (cf. Ref. 22 and Fig. 5.15), and it is most likely yet another manifestation of the influence of multi-step processes.

5.4 Summary

The main purpose of our study was to investigate the $^{16}O(\pi^+,\pi^0p)$ reaction in the Δ-resonance region. Such information, in comparison with results from $^{16}O(\pi^\pm,\pi^\pm p)$ studies and theoretical calculations, will increase our understanding of pion–nucleus interaction mechanisms in general, and of the $(\pi,\pi'N)$ reactions in particular (cf. Sec. 1.4). The $^{16}O(\pi^+,\pi^0p)$ investigation is also interesting in itself because the LAMPF experiment consisting both of the measurements of Gilad *et al.* and of our own measurements constitute the first kinematically complete study of the (π^+,π^0p) reaction.

Our $^{16}O(\pi^+,\pi^0p)$ measurements. The shape of our $d^3\sigma/dE_{\pi^0}\,d\Omega_{\pi^0}\,d\Omega_p$ cross section energy spectra is described fairly well qualitatively by a simple Monte Carlo calculation based on two-body kinematics (Secs. 4.1.6 and 4.1.1). This indicates that the reaction is predominantly quasi-free. The cross section at forward π^0 angles is considerably lower (more than a factor 2) than those at backward angles (Fig. 4.12), even more so than expected from the angular dependence of the free π^+n cross section (Fig. 5.2). This discrepancy with respect to the free cross section may be due to final state interactions (including pion absorption) experienced by the forward ejected π^0's (Sec. 5.1.1). The proton out-of-plane angular distributions of the $d^2\sigma/d\Omega_{\pi^0}\,d\Omega_p$ cross sections for all angles closely follow the shape calculated by our two-body kinematics Monte Carlo program (Fig. 5.1). This again shows that the process is indeed predominantly quasi-free. We found that $40-50\%$ of the quasi-free π^0p coincidence events were due to p-shell proton removal (Table 5.1). This somewhat low value suggests that the non-p-shell-removal part of the cross sections may have a substantial contribution of apparently quasi-free events which in reality originate from more complicated processes.

Energy dependence of the $^{16}O(\pi^+,\pi^0 p)$ reaction. Data exist at $T_{\pi^+} = 165$ MeV (this work) and $T_{\pi^+} = 245$ MeV (Gilad *et al.*[43]). Spectra of differential cross sections $d^3\sigma/dE_{\pi^0}\, d\Omega_{\pi^0}\, d\Omega_p$ obtained with the proton telescope at the quasi-free angle look similar for the two energies, and they were also found to be of roughly the same magnitude (Sec. 5.1.2). As expected for two-body kinematics, the quasi-free angular correlation is substantially narrower at the higher energy (Fig. 5.5).

Comparison to $^{16}O(\pi^\pm,\pi^\pm p)$ measurements. Qualitatively, the energy spectra of Kyle *et al.*[40] of the $d^3\sigma/dE_{\pi^0}\, d\Omega_{\pi^0}\, d\Omega_p$ cross sections for $^{16}O(\pi^\pm,\pi^\pm p)$ look similar to our spectra when the ratios between the respective free cross sections are taken into account (Sec. 5.1.3). This is in accordance with earlier observations of cross section ratios in which dramatic deviations from the free ratios were observed only for more forward pion angles (Figs. 1.12 and 1.13), and it is further supported by our quantitative comparisons of the integrated cross sections $d^2\sigma/d\Omega_{\pi^0}\, d\Omega_p$ for $(\pi^+,\pi^+ p)$ and $(\pi^+,\pi^0 p)$ (Table 5.2).

Comparison to Δ–hole model calculations. Comparing our $d^3\sigma/dE_{\pi^0}\, d\Omega_{\pi^0}\, d\Omega_p$ cross section energy spectra for the central proton telescope to Δ–hole model calculations by Takaki and Thies,[52,93] we found that the calculations underestimated the cross sections by about 30–55% (including the normalization uncertainty) (Sec. 5.1.4). This discrepancy is similar to, but somewhat larger than, what was found for $T_{\pi^+} = 245$ MeV (about 30%, Fig. 1.14).[43,52] It is possible that inclusion of the $T_{\Delta N} = 2$ isospin channel and the rearrangement diagram (number (4) in Fig. 1.11) could bring the theoretical estimates closer to the experimental data. The calculations done for proton telescope 8 (which is in the scattering plane, but 17° further away from the beam than the central telescope) are in agreement with our data (Fig. 5.12), suggesting that the Δ–hole model calculations either do not estimate the width of the angular correlation correctly, or that these calculations do not describe the physics near the quasi-free angle properly (this is where the p-shell cross sections are most vulnerable to contributions from other processes and final state interactions).

In addition to our investigation of the $^{16}O(\pi^+,\pi^0 p)$ reaction, we also obtained data both on the A-dependence of the $(\pi^+,\pi^0 p)$ process and on the single-arm, inclusive (π^+,π^0) process. This is summarized below.

The A-dependence of the $(\pi^+,\pi^0 p)$ process. Our experimental cross sections are almost constant over the range from ^{16}O to ^{208}Pb (Tables 4.7 and 4.8). This is in agreement with an earlier study of the $(\pi^+,\pi^+ p)$ reaction (Piasetzky *et al.*[38]). The effects of proton final state interactions alone appear not to be sufficient to explain this weak A-dependence (Sec. 5.2).

The ^{16}O(π^+,π^0) reaction. We observed an angular dependence of this reaction similar to that of the ^{16}O$(\pi^+,\pi^0 p)$ reaction. The cross section $(d\sigma/d\Omega_{\pi^0})$ was suppressed relative to the free $\pi^+ n$ cross section at forward angles (Fig. 5.13). We found that about 30% of the cross section at our forward π^0 angles and about 40% at the backward angles were accounted for by the ^{16}O$(\pi^+,\pi^0 p)$ process. A comparison to similar measurements made by Ashery *et al.*[22] showed that while the shapes of the $d^2\sigma/dE_{\pi^0}\,d\Omega_{\pi^0}$ cross section energy spectra of the two experiments were in agreement, the normalization of the cross sections seems to differ (Sec. 5.3.2). At the most backward angle of the comparison $(\theta_{\pi^0} = 110°)$ our cross section is about 50% higher than that of Ashery *et al.*

The A-dependence of the (π^+,π^0) process. Our $d\sigma/d\Omega_{\pi^0}$ cross sections measured on ^{16}O, ^{56}Fe, ^{120}Sn, and ^{208}Pb at $\theta_{\pi^0} = 110°$ indicate an A-dependence of A^α where $\alpha = 0.41 \pm 0.06$. This value is essentially in agreement with measurements of Ashery *et al.*[22] (Sec. 5.3.2). (However, if their measurement on Pb is corrected for photon attenuation losses, which brings it in better agreement with ours, their new value of α will not be in agreement with ours.) The fraction of quasi-free $(\pi^+,\pi^0 p)$ cross section found in the respective (π^+,π^0) cross sections decreases with A from about 40% for ^{16}O to about 10% for ^{208}Pb (Table 5.3). This trend is in fair agreement with a similar study by Piasetzky *et al.*[20,38]

5.5 Outlook

We have now discussed at length the results and conclusions of our experiment. Here in the final section we would like to address some of the questions that remain unanswered, as well as new ones raised by our work.

We found that the ratios of cross sections $d^3\sigma/dE_{\pi^0}\,d\Omega_{\pi^0}\,d\Omega_p$ of the $^{16}O(\pi^+,\pi^+p)$ reaction to those of the $^{16}O(\pi^+,\pi^0p)$ reaction are equal to the ratios between the corresponding free cross sections (to within the rather large experimental uncertainties of the measurements) at π^0 angles of 80° and 130°. A lot of interesting physics might still be found at more forward π^0 angles, however, which we were unable to investigate due to constraints on our apparatus. It is at these more forward angles that final state interactions are most important and that the cross sections are seen to deviate the most from the behavior of the free cross sections. It is also here that Kyle *et al.*[40] found the most dramatic deviations from the free cross section ratios.

The angular correlation between the ejected particles was found to provide a clean identification of the quasi-free part of the cross sections. A better quantitative analysis of this correlation would require a more careful mapping of the proton out-of-plane distribution (more data points). More important than pursuing this, however, is to improve the measurements at the central, conjugate quasi-free proton angle (our telescope 4). This is where the effects of the nuclear p-shell momentum distribution are most striking; the p-shell contribution, which we were trying to isolate, is low while other, unwanted, contributions are at their maxima. These measurements are therefore the most challenging to theory, and it would be very desirable to improve the quality of the experimental data available (better statistics, better energy resolution). Construction of a new, higher-resolution π^0 spectrometer[97] would be one way of obtaining such an improvement.

At this point we are also in need of more theoretical calculations. A small, but quite important, task would be to extend the present Δ–hole model calculations to include our out-of-plane telescopes. This would immediately establish whether the problems faced by the model are manifested only in the more complicated spectra from the central telescope or if the general angular correlation is wrong. The single most important extension of the present level of Δ–hole model calculations would most likely be the inclusion of the $T_{\Delta N} = 2$ channel for the Δ–N coupling, which would correspond to accounting for pion absorption on more than two nucleons. Probably less dramatic, but perhaps physically more interesting, would be to obtain a better description of the Δ–N interaction and the variations in the strength parameter C_{21} used by Takaki and Thies.[52]

Thies has shown[55] that modified DWIA calculations describe the $^{16}O(\pi^+,\pi^+)$ reaction well. Similar calculations corresponding to our $^{16}(\pi^+,\pi^0)$ measurements would provide an interesting test of this theoretical framework.

Furthermore, we see a need for theoretical guidance in describing the A-dependence of both the $(\pi^+,\pi^0 p)$ process and the (π^+,π^0) process.

Measurements of the $^3He(\pi^\pm,\pi^0 p)$ reactions at $T_{\pi^\pm} = 245$ MeV were made at LAMPF recently in an attempt to shed more light on the Δ–N interaction.[98,99] The ^3He nucleus is simple and well understood, and it has twice as many protons (2) as neutrons (1). Since the elementary $(\pi^+,\pi^0 p)$ process takes place on a neutron, one expects a relative enhancement of the theoretically important second-order processes in ^3He compared to ^{16}O. The $^3He(\pi^-,\pi^0 p)$ reaction puts even more emphasis on second-order processes since it cannot take place at all on only one nucleon. Furthermore, the small number of nucleons in the ^3He nucleus greatly reduces the distortions due to initial and final state interactions compared to the situation for ^{16}O. The $(\pi^-,\pi^0 p)$ measurements may also provide some interesting comparisons to pion double charge exchange measurements. Data for both reactions are presently under analysis.

Another interesting approach in this field is to study the photon-induced nucleon removal reaction $(\gamma,\pi^- p)$. The electromagnetic coupling involved in the photoexcitation of the Δ is fairly well understood theoretically; in this reaction it is combined with propagation and subsequent decay of the Δ similar to the case of the previously studied pion-induced πp coincidence reactions. Measurements of the $^{16}O(\gamma,\pi^- p)$ reaction at $T_\gamma = 350$ MeV (which is near the peak of the Δ-resonance) have recently been made at the Bates Linear Accelerator Center in Middleton, Massachusetts.[100] If theoretical (Δ–hole model) calculations were made corresponding to these measurements, a comparison of the experimental data on the pion- and the photon-induced processes may increase our understanding of the relative importance of the various reaction mechanisms involving the Δ. Also, since photons do not interact as strongly with nucleons as pions do, the $(\gamma,\pi^- p)$ reaction should probe the whole nuclear volume instead of just the surface as in the case of the pion-induced reactions. This aspect may in itself lead to interesting comparisons to measurements of the pion-induced processes. The $^{16}O(\gamma,\pi^- p)$ data are presently under analysis.

The results and conclusions from the on-going analyses of the experiments mentioned above will, when they become available, be essential to the discussion about possible future πp coincidence experiments exploring the dynamics of the Δ. With the present status of experimental techniques and facilities, we see more of a need for further theoretical developments that can be tested against the data that already exists. This would most likely in turn call for experimental investigations of new aspects. Improvements of the experimental facilities beyond the present state-of-the-art (faster electronics, new spectrometers with better resolution and larger solid angles) would lead to much exciting experimental work, however. Many of the questions we have discussed throughout this work about cross section ratios and A-dependence, as well as questions related to multi-nucleon removal (such as pion absorption on more than two nucleons), could then be settled much more precisely.

Appendix A

Activation Measurements for Beam Calibration

This appendix describes the method of determining the absolute flux of the pion beams by measuring the ^{11}C activity of irradiated plastic scintillator discs.

In an "activation run" a thin plastic scintillator disc, with diameter large enough to include the full beam spot, is placed at the target position and is irradiated for a few minutes. The irradiation causes production of ^{11}C nuclei by $^{12}C(\pi^{\pm}, X)^{11}C$. These reactions have relatively large cross sections. ^{11}C β-decays with a half-life of 20.4 minutes[65] by

$$^{11}C \rightarrow e^{+} + \nu_e + {}^{11}B,$$

a decay that is well suited for measurements. Determining the ^{11}C activity is a routine procedure at LAMPF. This reveals the amount of ^{11}C produced. Combining this with known cross sections for the $^{12}C(\pi^{\pm}, X)^{11}C$ reaction[34] and the physical parameters of the actual disc used, one can then deduce the absolute flux of incident pions and hence obtain a calibration of the beam toroid.

Two factors can make the activation measurements less reliable. If the beam is contaminated with other particles, the pion-induced fraction of the measured ^{11}C activity will have to be estimated. The contamination of protons and neutrons is negligible, but the fraction of muons and electrons can be sizeable, especially at our lowest

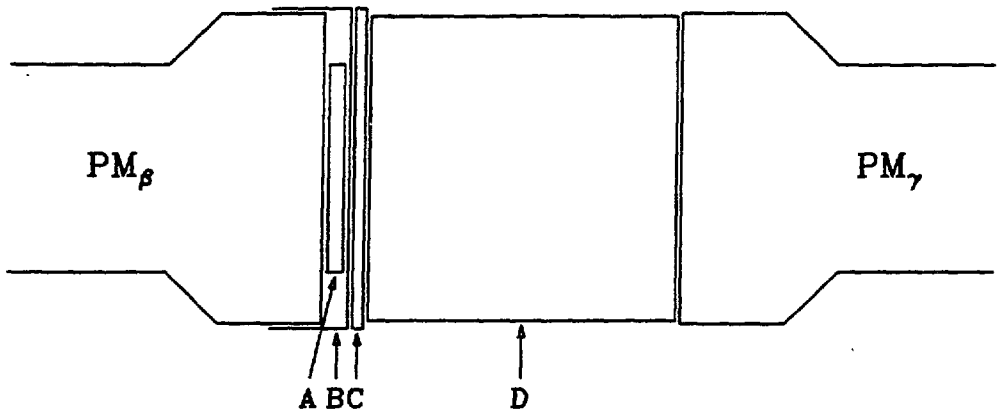

Figure A.1. Setup for ^{11}C activation measurements. A is the irradiated scintillator disc, B is a piece of aluminum foil serving as a reflector, C is a 1.6 mm thick copper plate to ensure that all positrons annihilate as close as possible to the scintillator disc, and D is a 75 mm thick × 75 mm diameter NaI(Tl) scintillator. The two devices labeled "PM" are photomultiplier tubes. PM$_\beta$ is used to count positron scintillation pulses and PM$_\gamma$ to count electron-positron annihilations. The latter detector system is set electronically to look only for 0.511 MeV photons. Cf. Ref. 34.

beam energies (0.4 e^- per π^- at 80 MeV).[57] The cross sections for $^{12}C(e^\pm, e^\pm n)^{11}C$ and $^{12}C(\mu^\pm, \mu^\pm n)^{11}C$ are quite small compared to those for the corresponding pion-induced reactions, however, and the total contribution from the lepton-induced reactions to the ^{11}C activity has been estimated to be less than 1% at our beam energies[34] (in most cases considerably less).

The second factor is a possible enhancement of the ^{11}C production due to the non-zero thickness of the scintillator discs, that is, production induced by secondary particles. Dropesky *et al.*[34] have found that this effect is negligible for our discs (which are approximately 1.5 – 3 mm thick).

The setup for the activation measurements is sketched in Fig. A.1. Since the irradiated disc itself is a scintillator, the escaping e^+ will induce a scintillator signal that can be detected by the photomultiplier tube next to the disc. The positron will annihilate with an electron inside the disc or in the thin copper plate next to it, producing two gamma-rays. One of these is detected by the other detector in the setup, an NaI(Tl) scintillator. This method permits determination of the ^{11}C disintegration

rate independently of the efficiencies of the two individual detectors by counting the number of detected positron scintillator pulses (N_β), the number of detected gamma-rays (N_γ), and the number of detected coincidences between the two ($N_{\beta\gamma}$). Denoting the various detector efficiencies by ϵ_i and the true number of ^{11}C decays by N_0, one must have

$$N_\beta = N_0 \epsilon_\beta \tag{A.1}$$

$$N_\gamma = N_0 \epsilon_\gamma \tag{A.2}$$

$$N_{\beta\gamma} = N_0 \epsilon_{\text{coinc.}} \approx N_0 \epsilon_\beta \epsilon_\gamma \tag{A.3}$$

and hence,

$$N_0 \approx \frac{N_\beta N_\gamma}{N_{\beta\gamma}} \tag{A.4}$$

In an activation measurement the above procedure is used to determine the number of ^{11}C decays in several two-minute intervals after the irradiation. By fitting to the β-decay one can then determine the amount of ^{11}C produced. The computational details of this fitting and the calculation of the corresponding beam flux are all built into the program ACT.[101]

Appendix B

Analyzer Software ("Q")

An overview of our use of the "Q" system for data acquisition and on-line analysis is given in Sec. 2.4. Q was also used for the replay data analysis. For operational details of the Q system the reader should consult the Q manuals.[73] This appendix presents the structure of our Q data analysis system.

B.1 Data Acquisition and On-line Analysis

In Sec. 2.3.1 five different running modes (triggers) were discussed (single protons, stabilization signals, tagged protons, single π^0's, and $\pi^0 p$ coincidences). "Single protons" and "tagged protons" involves the same kind of reading and processing of proton information. They are therefore handled by the same software. That leaves the following four software running modes:

1. **Single protons.** Single arm proton measurements (including tagged protons). This mode was only used for calibration purposes.
2. **Stabilization signals.** Data taken with the proton arm LED's to check for possible drifts in the proton detector system.
3. **Single π^0's.** Measurements of the $(\pi^{\pm}, \pi^0)$ process using the π^0 spectrometer.

4. $\pi^0 p$ coincidences. Use of both detector systems for $(\pi^+, \pi^0 p)$ measurements.

The appropriate software mode for each run was set up by the program DETMOD which is executed automatically as part of the beginning-of-run procedure. The program prompts the user for the desired mode and then sets up parameters and enables events accordingly.

The event structure was outlined briefly in Sec. 2.4. Below is a complete presentation of all user defined events in our analyzer. In addition, there are a few events defined and used by Q itself. They are the same in all Q systems. (See the Q manuals[73] for details.) In case of conflicting "simultaneous" events, Q gives the highest priority to the event with the highest event number. Unless explicitly mentioned, each event processor consists of a hardware communication (QAL) part running on the MBD to pass information to and from the CAMAC electronics and a corresponding subroutine (known as PROCn, where n is the event number) running on the experiment control computer to analyze the event data. Our data acquisition events were:

Event 4. (All modes.) Scaler event. This event was triggered automatically every 8 s (typically) to read and clear all scalers and to update the software arrays containing the accumulated scaler values.

Event 5. (Modes 3 and 4.) π^0 spectrometer stabilization event. This event is triggered by the signals from small plastic scintillators containing radioactive ^{207}Bi. Its purpose is to monitor any drifts in the gains of the 60 photomultiplier tube systems in the π^0 spectrometer. After a preset number of events (for example 100000 or 150000) has been accumulated, the data are analyzed to calculate new gain values. The stabilization energy spectra are written to tape as Event 17 and the new gain values as Event 18. (An Event 18 is put on tape also at the beginning of every run so that the replay analysis starts out with the correct gains.)

Event 6. (Modes 1 and 4.) Main proton event. This event reads and processes information from the proton detectors. In the case of coincidence measurements it also calculates the kinematics of the reaction (see Sec. 4.1.3 for more details).

Event 7. (Modes 3 and 4.) π^0 spectrometer pedestal event. This event is disabled most of the time, but gets enabled by the Event 22 processor regularly to collect pedestal data for the π^0 spectrometer ADC's (cf. the description of Event 22 below). This event is then the only π^0 spectrometer event being

enabled. After a preset number of events (for example 1000) has been accumulated, new pedestal values are calculated, Event 7 is disabled, and Events 5 and 9 are again enabled. The new pedestals are written to the output tape as Event 16 (the individual Event 7's are not taped).

Event 9. (Modes 3 and 4.) Main π^0 event. This event reads and processes π^0 information from the π^0 spectrometer. In mode 4 it is triggered before Event 6 so that information about the π^0 is available for the kinematics calculations done by the Event 6 processor.

Event 10. (Mode 2 only.) Proton stabilization event. This event reads raw ADC data for the proton detectors and prepares them for histogramming.

Event 22. (Modes 3 and 4.) Pedestal scheduling event. This event is triggered automatically throughout runs in which one wants the π^0 ADC pedestals monitored. The interval between triggering is set by a parameter in the dynamic parameter array, and could be for instance 30 or 60 minutes. There is no QAL code for this event; all processing is done on the control computer. The Event 22 processor enables Event 7 and disables the other π^0 spectrometer events (Events 5 and 9).

Event 23. (All modes.) Electronics initialization event. This event is triggered once at the beginning of every run. It clears and enables all the CAMAC electronics modules. All event processing is done on the MBD; there is no corresponding Fortran analyzer subroutine.

The above list mentions several groups of data being written to tape as separate events by some of the event processors. Two more groups of data are treated in this way: At the beginning of every run all the parameters in the dynamic parameter array are taped as Event 19, and at the end of every run all test counters (that is, the number of times each test was passed) are taped as Event 20.

B.2 Replay Analysis

From a software point of view, the difference between data acquisition and data replay is minimal, with the exception in the former case of a need for special software to monitor the apparatus. During data acquisition the data buffers fed to the analyzer come from the MBD; during data replay they are taken from a magnetic tape instead. The QAL code from the data acquisition software is therefore not used in replay. The data testing and histogramming packages of Q are used in the same way as during

data acquisition, but with modifications and extensions as one might find necessary. Also the Fortran event subroutines (PROC*n*) may be modified for the replay analysis.

We used the same analyzer modes in the replay analysis as described in Sec. B.1 for the data acquisition process. The event structure was slightly different, however. Below is a description of the events recognized by the replay analyzer:

Event 4. (All modes.) Scaler event. As described for data acquisition.

Event 6. (Modes 1 and 4.) Main proton event. As described for data acquisition.

Event 9. (Modes 3 and 4.) Main π^0 event. As described for data acquisition.

Event 10. (Mode 2 only.) Proton stabilization event. As described for data acquisition.

Event 16. (Modes 3 and 4.) π^0 spectrometer pedestal retrieval event. This event retrieves updated π^0 spectrometer ADC pedestal values that were written to tape by the data acquisition Event 7 processor whenever enough information for an update had been assembled. (Cf. Sec. B.1.)

Event 17. (Modes 3 and 4.) π^0 spectrometer stabilization data retrieval event. This event retrieves and checks the stabilization data for one of the π^0 spectrometer photomultiplier tube systems. It calculates the present gain value and compares this to the most recently used value to detect any drifts. A total of 60 Event 17's were written to tape at a time by the data acquisition Event 5 processor whenever enough information had been assembled. (Cf. Sec. B.1.)

Event 18. (Modes 3 and 4.) π^0 spectrometer gain retrieval event. This event retrieves updated values of the gains of all 60 π^0 spectrometer photomultiplier tube systems. These were written to tape at the beginning of every run as well as by the data acquisition Event 5 processor whenever enough information for an update had been assembled. (Cf. Sec. B.1.)

Event 19. (Modes 3 and 4.) Dynamic parameter array retrieval event. This event retrieves all parameter values for the dynamic parameter array. These were written to tape at the beginning of every run. Only the information about the π^0 spectrometer wire chambers ("hot wires") is actually used.

Event 20. (Modes 3 and 4.) Test counter event. This event obtains the values of all test counters at the end of the run and puts those values necessary for calculating the π^0 spectrometer wire chamber efficiencies into the dynamic parameter array. The test counters may be current values from the Q test package, or they may be retrieved from tape (the test counters were always written to tape at the end of every run).

The end results from the Q part of the analysis were a number of computer files containing histogram data (Figs. 4.5, 4.6, and 4.7 are examples of such saved histograms). The further analysis presented in Chapters 3 and 4 was done without the use of the Q system. Our own analyzing software read the Q results from the various histogram files and performed the necessary manipulations to obtain the final calculated quantities. More details about these calculations are presented in Appendix C.

Appendix C

Software Algorithms

This appendix describes in detail the algorithms of the most important software used besides the Q analyzer. These are four large Fortran programs that all start by retrieving Q histogram files. The programs are:

PI0EFF. This program calculates the experimental conversion efficiency of the LAMPF π^0 spectrometer.

THICKNFIT. This program calculates the thickness of water targets.

PISPEC. This program calculates differential cross section energy spectra for our coincidence measurements ($d^3\sigma/dE_{\pi^0}\, d\Omega_{\pi^0}\, d\Omega_p$ for $(\pi^+, \pi^0 p)$ as a function of T_{π^0}).

SSPEC. This program calculates differential cross section energy spectra for our single arm measurements ($d^2\sigma/dE_{\pi^0}\, d\Omega_{\pi^0}$ for (π^+, π^0) as a function of T_{π^0}).

There is one section devoted to each of these programs below. Emphasis is placed on the algorithms used in producing the final quantitative results. Further options (such as for making plots, saving Q histograms, and printing results) are not discussed here.

C.1 PI0EFF — π^0 Spectrometer Conversion Efficiency

PI0EFF is a program that calculates the LAMPF π^0 spectrometer conversion efficiency from Q histograms of π^0 energy spectra. The principles for this are discussed in Sec. 3.3.5.2.

The main histograms retrieved for these calculations are accumulated energy spectra (TPICT*n*, where *n* indicates the spectrometer angular bin) for both targets, CH2 and C. In order to subtract the contribution from accidental events we use similar energy spectra (TPIR*n*) based on events that did not satisfy the coincidence timing requirement (cf. Sec. 3.3.3). Only integrated cross sections are of interest for calculating the conversion efficiency. The number of "good" π^0 events for each target t is then

$$N'^{t}_{\pi^0} = \left(N^t - N^t_a\right) , \tag{C.1}$$

where N^t and N^t_a are the number of well-timed and accidental events, respectively. The corresponding statistical uncertainty is

$$\Delta N'^{t}_{\pi^0} = \sqrt{(\Delta N^t)^2 + (\Delta N^t_a)^2} , \tag{C.2}$$

where

$$\Delta N^t = \sqrt{N^t} \tag{C.3}$$

$$\Delta N^t_a = \max(\sqrt{N^t_a},\, N^t_a \cdot 0.15) . \tag{C.4}$$

The expression in Eq. (C.4) implies that we do not trust the estimate of accidental events to better than 15% even if the statistical uncertainty should be less.

The number of "good" events is next corrected for the photon attenuation losses in the target. Since we have a small spread in π^0 energy, this correction is done by calculating f_μ from Eq. (3.5) at the energy corresponding to the histogram bin with the most counts in TPICT*n*. Then

$$N'^{t}_{\pi^0} \rightarrow \frac{N'^{t}_{\pi^0}}{f_\mu} \tag{C.5}$$

$$\Delta N'^{t}_{\pi^0} \rightarrow \frac{\Delta N'^{t}_{\pi^0}}{f_\mu} . \tag{C.6}$$

For absolute normalization one needs information about the actual runs. Run information was kept in a special file, and it was available to programs such as PI0EFF through a subroutine which in response to a run number would return the toroid counts N_{tor} (adjusted for livetime of the electronics), the wire chamber efficiency ϵ_{wc} and the uncertainty of this $\Delta\epsilon_{wc}$ (from Eq. (3.13)), the momentum bite $\frac{\Delta p}{p}$ of the beam channel, the beam calibration C_{tp} (the number of pions per toroid count and $\frac{\Delta p}{p}$) and its uncertainty ΔC_{tp}, the beam energy, and the target name. This information is used to calculate the effective number of incident pions during a given measurement. For run i this number is

$$N'^{i}_{\pi^-} = C^i_{tp} N^i_{\rm tor} \left(\frac{\Delta p}{p}\right)^i \epsilon^i_{\rm wc} . \tag{C.7}$$

The total effective number of incident pions for a given target t in a given setup is then given by the expression in Eq. (C.7) summed over all runs i involved in the measurement:

$$N'^{t}_{\pi^-} = \sum_i N'^{i}_{\pi^-} . \tag{C.8}$$

The corresponding uncertainty is given by

$$(\Delta N'^{t}_{\pi^-})^2 = \left(N'^{t}_{\pi^-} \frac{\Delta C_{tp}}{C_{tp}}\right)^2 + \sum_i \left(N'^{i}_{\pi^-} \frac{\Delta \epsilon^i_{\rm wc}}{\epsilon^i_{\rm wc}}\right)^2 . \tag{C.9}$$

Note that the calibration uncertainty is not treated on a run-by-run basis. It is an overall uncertainty affecting each run in the same way.

The density of target nuclei n_t (per area) is also necessary for calculating cross sections. This is connected to the target thickness $(t\rho)_t$ (in g/cm^2) by

$$n_t = (t\rho)_t \frac{N_A}{A_t} , \tag{C.10}$$

where A_t is the molecular weight of the target material and N_A is the Avogadro constant.

With this information available, PI0EFF calculates cross sections individually for the two targets using Eq. (3.20):

$$\sigma^{\rm exp}_t \equiv \left(\frac{d\sigma}{d\Omega_{\pi^0}}\right)^{\rm exp}_t = \frac{N'^{t}_{\pi^0}}{N'^{t}_{\pi^-} \frac{n_t}{\cos\theta_t} \Delta\Omega^t_{\rm MC}} . \tag{C.11}$$

Here, θ_t is the target angle and $\Delta\Omega^t_{\rm MC}$ is the π^0 spectrometer solid angle as calculated by the Monte Carlo program PIANG.[62] Assuming that the uncertainty in the target thickness is negligible, the uncertainty in the cross section can be expressed by

$$\Delta\sigma_t^{\rm exp} = \sigma_t^{\rm exp}\sqrt{\left(\frac{\Delta N'^t_{\pi^0}}{N'^t_{\pi^0}}\right)^2 + \left(\frac{\Delta N'^t_{\pi^-}}{N'^t_{\pi^-}}\right)^2 + \left(\frac{\Delta(\Delta\Omega^t_{\rm MC})}{\Delta\Omega^t_{\rm MC}}\right)^2 + (\tan\theta_t\,\Delta\theta_t)^2}\,, \quad \text{(C.12)}$$

where the uncertainty in the target angle is taken as $\Delta\theta_t = 0.25°$.

The cross section for SCX on H is then found by combining the individual cross sections as indicated by Eq. (3.22):

$$\sigma_{\rm H}^{\rm exp} = \tfrac{1}{2}\left(\sigma_{\rm CH_2}^{\rm exp} - \sigma_{\rm C}^{\rm exp}\right)\,. \quad \text{(C.13)}$$

A subtle point in the corresponding uncertainty estimate is the treatment of the beam calibration uncertainty ΔC_{tp}. The same beam calibration was used for both targets. It is therefore not correct to include this uncertainty in a statistical combination of the uncertainties in Eq. (C.13); it must first be removed, then included again after the other contributions have been taken care of. Thus, defining

$$\Delta\sigma_t'^{\rm exp} = \sigma_t^{\rm exp}\sqrt{\left(\frac{\Delta\sigma_t^{\rm exp}}{\sigma_t^{\rm exp}}\right)^2 - \left(\frac{\Delta C_{tp}}{C_{tp}}\right)^2}\,, \quad \text{(C.14)}$$

one has

$$\Delta\sigma_{\rm H}^{\rm exp} = \sqrt{\left(\tfrac{1}{2}\Delta\sigma'^{\rm exp}_{\rm CH_2}\right)^2 + \left(\tfrac{1}{2}\Delta\sigma'^{\rm exp}_{\rm C}\right)^2 + \sigma_{\rm H}^{\rm exp}\left(\frac{\Delta C_{tp}}{C_{tp}}\right)^2}\,. \quad \text{(C.15)}$$

The experimental conversion efficiency is the ratio of the measured cross section to the "correct" cross section (free pion SCX is well known), as expressed by Eq. (3.23):

$$\epsilon_c^{\rm exp} = \frac{\sigma_{\rm H}^{\rm exp}}{\sigma_{\rm H}^{\rm SAID}}\,. \quad \text{(C.16)}$$

We calculated the correct cross sections using the program SAID.[14–16] These calculated cross sections were averaged over the π^0 spectrometer angular acceptance (see Sec. 3.3.5.2). The corresponding uncertainty is straightforward:

$$\Delta\epsilon_c^{\rm exp} = \epsilon_c^{\rm exp}\sqrt{\left(\frac{\Delta\sigma_{\rm H}^{\rm exp}}{\sigma_{\rm H}^{\rm exp}}\right)^2 + \left(\frac{\Delta\sigma_{\rm H}^{\rm SAID}}{\sigma_{\rm H}^{\rm SAID}}\right)^2}\,. \quad \text{(C.17)}$$

C.2 THICKNFIT — Thickness of Water Targets

THICKNFIT is a program that calculates the thickness of water targets. This is expressed both as an absolute thickness t_t and in the form of a density × efficiency product $n_t\epsilon_c^{\exp}$. Q histograms of π^0 energy spectra obtained in full and empty target runs constitute the input to the calculations. The method is discussed in Sec. 3.4.

A crucial point is to estimate the yield due to pion SCX on the hydrogen in the water. This is done by curve fitting to the experimental energy spectra. The Q histograms retrieved are the same as for the efficiency calculations described in Sec. C.1 (TPICTn and TPIRn). The statistics of the histograms for accidental events were generally too poor to allow a bin-by-bin subtraction of this contribution. Instead we calculated the overall fractional contribution from accidental events and subtracted this fraction from all histogram bins. This corresponds to assuming that the energy distribution of accidental events is the same as that of the "good" events. Denoting the initial number of counts at a certain π^0 energy T_{π^0} by $N^t_{\pi^0}(T_{\pi^0})$, one then has the following yield corrected for accidental events:

$$N'^t_{\pi^0}(T_{\pi^0}) = N^t_{\pi^0}(T_{\pi^0})\left(1 - \frac{N^t_a}{N^t}\right). \tag{C.18}$$

As in Sec. C.1, the energy-independent N^t's indicate number of counts summed over the whole π^0 energy spectrum. In the case of no accidental events detected at all, we assume $N^t_a = 0 \pm 1$. The uncertainties in the summed quantities then become

$$\Delta N^t = \sqrt{N^t} \tag{C.19}$$

$$\Delta N^t_a = \max(\sqrt{N^t_a},\, N^t_a \cdot 0.15,\, 1). \tag{C.20}$$

These uncertainties are not applied in the analysis until after the curve fitting has been done.

Information about the individual runs is read from a special file as described for PI0EFF in Sec. C.1. This information is first used to calculate a scaling factor to normalize the empty target data to the full target data. This factor f_s is the ratio between the amounts of beam used for full (f) and empty (e) target measurements,

respectively:

$$f_s = \frac{\sum_f N^i_{\rm tor}(\frac{\Delta p}{p})^i \epsilon^i_{\rm wc}}{\sum_e N^i_{\rm tor}(\frac{\Delta p}{p})^i \epsilon^i_{\rm wc}} \,. \tag{C.21}$$

The beam calibration was always the same for all runs at a given beam energy and is therefore not included in Eq. (C.21).

The net energy spectrum and its uncertainty are then given by

$$N'_{\pi^0}(T_{\pi^0}) = N'^f_{\pi^0}(T_{\pi^0}) - f_s\, N'^e_{\pi^0}(T_{\pi^0}) \tag{C.22}$$

$$\Delta N'_{\pi^0}(T_{\pi^0}) = \sqrt{N'^f_{\pi^0}(T_{\pi^0}) + f_s^2\, N'^e_{\pi^0}(T_{\pi^0})} \,. \tag{C.23}$$

To obtain the net yield from the hydrogen in the water, a function $f(T_{\pi^0})$ consisting of a sum of two gaussians is fitted to the net energy spectrum:

$$f(T_{\pi^0}) = c_1 \exp\left(-\frac{(T_{\pi^0}-c_2)^2}{2c_3^2}\right) + c_4 \exp\left(-\frac{(T_{\pi^0}-c_5)^2}{2c_6^2}\right) . \tag{C.24}$$

All six coefficients c_n are varied in the fitting, which is done by the routine MINUIT.[81] The yield N'_{π^0} from hydrogen (which for our purpose is the number of "good" events) is the area of the narrower of the two gaussians. The statistical uncertainty $\Delta N'^{\rm stat}_{\pi^0}$ in this estimate is calculated from the fit parameters as described in Appendix D. At this point the uncertainty due to the earlier subtraction of accidental events is included. This uncertainty can be expressed as

$$\Delta N_a = \sqrt{(\Delta N^f_{\rm tot})^2 + f_s^2\,(\Delta N^e_{\rm tot})^2} \,, \tag{C.25}$$

where

$$(\Delta N^t_{\rm tot})^2 = (\Delta N^t)^2 + (\Delta N^t_a)^2 \,. \tag{C.26}$$

The total uncertainty in the yield is therefore

$$\Delta N'_{\pi^0} = \sqrt{(\Delta N'^{\rm stat}_{\pi^0})^2 + (\Delta N_a)^2} \,. \tag{C.27}$$

The final values for the yield and its uncertainty are determined by correcting the values above for losses due to photon attenuation in the water targets. This is a

small correction (cf. Fig. 3.4). The π^0 transparency f_μ is calculated for the energy corresponding to the center of the narrow gaussian in the fit and then applied to all the data:

$$N'_{\pi^0} \rightarrow \frac{N'_{\pi^0}}{f_\mu} \tag{C.28}$$

$$\Delta N'_{\pi^0} \rightarrow \frac{\Delta N'_{\pi^0}}{f_\mu}\,. \tag{C.29}$$

The cross section of the pion SCX reaction can be expressed as (cf. Eq. (3.24)):

$$\sigma_{\rm H}^{\rm SAID} \equiv \left(\frac{d\sigma}{d\Omega_{\pi^0}}\right)_{\rm H}^{\rm SAID} = \frac{N'_{\pi^0}}{N'^{f}_{\pi^-}\,\frac{n_t({\rm H})}{\cos\theta_t}\,\epsilon_c^{\rm exp}\,\Delta\Omega_{\rm MC}}\,, \tag{C.30}$$

The various variables involved in this equation are described in Sec. C.1. The unknown quantity is the density of hydrogen nuclei in the target n_t(H), while the conversion efficiency $\epsilon_c^{\rm exp}$ is either taken from the efficiency analysis (cf. Sec. C.1) or solved for in Eq. (C.30) as part of the density × efficiency product.

In the first case we get

$$n_t({\rm H}) = \frac{N'_{\pi^0}\,\cos\theta_t}{N'^{f}_{\pi^-}\,\Delta\Omega_{\rm MC}\,\epsilon_c^{\rm exp}\,\sigma_{\rm H}^{\rm SAID}} \tag{C.31}$$

and

$$\left(\frac{\Delta n_t({\rm H})}{n_t({\rm H})}\right)^2 = \left(\frac{\Delta N'_{\pi^0}}{N'_{\pi^0}}\right)^2 + \left(\frac{\Delta N'^{f}_{\pi^-}}{N'^{f}_{\pi^-}}\right)^2 + \left(\frac{\Delta(\Delta\Omega_{\rm MC})}{\Delta\Omega_{\rm MC}}\right)^2 + \left(\frac{\Delta\epsilon_c^{\rm exp}}{\epsilon_c^{\rm exp}}\right)^2 + (\tan\theta_t\,\Delta\theta_t)^2\,. \tag{C.32}$$

Note that the uncertainty in the "correct" cross section $\sigma_{\rm H}^{\rm SAID}$ is not included in the above expression because this was already taken into account in the calculation of $\epsilon_c^{\rm exp}$ (cf. Eq. (C.17)). Because of the chemical composition of water (H_2O), the density of oxygen nuclei n_t(O) must be half of that for hydrogen nuclei. The absolute target thickness and its uncertainty are given by

$$t_t = n_t({\rm O}) \cdot \frac{A_w}{N_A\,\rho_w} \tag{C.33}$$

and

$$\Delta t_t = t_t \frac{\Delta n_t(\mathrm{H})}{n_t(\mathrm{H})} . \tag{C.34}$$

The subscript w indicates water.

In the other case we calculate a density × efficiency product:

$$n_t(\mathrm{O})\epsilon_c^{\mathrm{exp}} = \tfrac{1}{2} \frac{N'_{\pi^0} \cos\theta_t}{N'^f_{\pi^-} \Delta\Omega_{\mathrm{MC}} \sigma_{\mathrm{H}}^{\mathrm{SAID}}} \tag{C.35}$$

with an uncertainty given by

$$\left(\frac{\Delta(n_t(\mathrm{O})\epsilon_c^{\mathrm{exp}})}{n_t(\mathrm{O})\epsilon_c^{\mathrm{exp}}}\right)^2 = \left(\frac{\Delta N'_{\pi^0}}{N'_{\pi^0}}\right)^2 + \left(\frac{\Delta N'^f_{\pi^-}}{N'^f_{\pi^-}}\right)^2 + \left(\frac{\Delta(\Delta\Omega_{\mathrm{MC}})}{\Delta\Omega_{\mathrm{MC}}}\right)^2 + \left(\frac{\Delta\sigma_{\mathrm{H}}^{\mathrm{SAID}}}{\sigma_{\mathrm{H}}^{\mathrm{SAID}}}\right)^2 + (\tan\theta_t \Delta\theta_t)^2 . \tag{C.36}$$

C.3 PISPEC — $(\pi^+, \pi^0 p)$ Cross Section Energy Spectra

PISPEC is a program that generates $d^3\sigma/dE_{\pi^0}\, d\Omega_{\pi^0}\, d\Omega_p$ cross section energy spectra for the $(\pi^+, \pi^0 p)$ process from Q histograms of $\pi^0 p$ coincidence yields as a function of pion and proton kinetic energy. There are two kinds of data runs: for full target and empty target measurements, respectively, cf. Sec. C.2. The method is discussed in Sec. 4.1.

The input histograms for these calculations are PI0P*mn* (cf. Fig. 4.7) for the cross section data and coincidence timing histograms PTDC1*m* as shown in Fig. 4.5 for information about accidental coincidences. *m* indicates the proton telescope used, and *n* indicates the π^0 spectrometer angular bin used. The four histograms thus necessary for the analysis (two each for both full and empty target information) are retrieved in the beginning of the program. Relative statistical uncertainties (the inverse of the square root of the number of counts) are assigned to each histogram bin in the two-dimensional PI0P*mn* histograms before the yield is manipulated.

The first step is to account for the energy acceptance of the π^0 spectrometer. This is discussed in Sec. 3.3.2, and amounts to dividing the yield in each histogram bin by the spectrometer solid angle $\Delta\Omega_{MC}$ appropriate for the π^0 energy corresponding to this bin. The statistical uncertainty in this process, which is quite small, is stored for use later when the final π^0 energy spectrum is made.

The next step is to subtract the contributions from accidental coincidences. The algorithm to determine which part of the timing histogram corresponds to "good" events and which parts are suitable for estimating the contribution from accidentals is described in detail in Sec. 4.1.2. The subtraction was done as described for the thickness measurements in Sec. C.2, that is, we assumed that the accidental events were distributed as the "good" events. The fraction of accidentals for target t (where t is either f for "full" or e for "empty") can be expressed as

$$f_a^t = \frac{N_a^t}{N^t}\,\frac{x^t}{x_a^t}\,. \tag{C.37}$$

Here, the N^t's denote the total number of counts as defined in the sections above, and the x^t's are the widths of the (timing) regions considered for true and accidental contributions. We include only the N^t's in the uncertainty estimate, which when expressed as a relative uncertainty in the corrected data becomes

$$\delta_a^t = \frac{f_a^t}{1-f_a^t}\sqrt{\left(\frac{\Delta N_a^t}{N_a^t}\right)^2+\left(\frac{\Delta N^t}{N^t}\right)^2}\,, \tag{C.38}$$

where

$$\Delta N^t = \sqrt{N^t} \tag{C.39}$$

$$\Delta N_a^t = \max(\sqrt{N_a^t},\, N_a^t\cdot 0.15)\,. \tag{C.40}$$

The yield in all histogram bins are multiplied by $(1-f_a^t)$.

One is then ready to perform the p-shell cut if such a cut is desired. Values for C_{ex}^{low} and C_{ex}^{high} of the cut lines (cf. Eq. (4.5) and Fig. 4.7) must be given. The cutting is done by checking the position of the center of all histogram bins. A given bin passes the cut if its center is either in between the cut lines or exactly on one of them. The same

cut is applied to the corresponding full and empty target data. A relative uncertainty of $\delta_{\rm psh} = 0.12$ is assigned to cross sections that are cut on p-shell nucleon removal (cf. Sec. 4.1.3). This is applied later during the normalization of the cross sections.

Correction for proton interaction losses in the target is also optional. This correction only makes sense if a p-shell cut has been made since it describes a transfer of events to lower proton energy bins (in the case of no p-shell cut these events will still be included when one integrates over proton energy). More details about this correction are given in Sec. 4.1.4. We assigned a 10% uncertainty to the correction. This still does not amount to very much, however, because the correction itself is only on the order of a few percent (cf. Fig. 4.11). The resulting (energy-dependent) relative uncertainty $\delta^t_{\rm pint}(T_{\pi^0})$ in each cross section bin is calculated as an average over all the proton energies present for each π^0 energy in the two-dimensional (p-shell cut) yield histogram. This uncertainty is applied in the calculations later.

This concludes the manipulations that depend on proton energy. The data are still in the form of two-dimensional arrays $Y^t(T_{\pi^0}, T_p)$. The next step is therefore to integrate these arrays over the proton energies. This is done by a straightforward summation over all histogram bins representing this variable:

$$N'^t_{\pi^0}(T_{\pi^0}) = \sum_{T_p} Y^t(T_{\pi^0}, T_p)\,. \tag{C.41}$$

Each of the π^0 energy bins are assigned a statistical uncertainty based on the original number of counts in each raw data bin involved in the summation.

To prepare for the subtraction of the empty target data, we need run information for all runs included in the measurements. This is read from a file just as described in Sec. C.1, and the calculation of the effective number of incident pions $N'^t_{\pi^+}$ from this information is done in the same way as described in that section. As before, the scaling factor to account for the empty target data is the ratio between the effective number of pions in the two measurements:

$$f_s = \frac{N'^f_{\pi^+}}{N'^e_{\pi^+}}\,. \tag{C.42}$$

The yield from the empty target measurement was in general too low to permit a bin-by-bin subtraction of the empty target data. It was therefore necessary to do as described in Sec. C.2: assume that the distributions of empty and full target data are identical and simply subtract the same fractional contribution from each π^0 energy bin. This leaves a net yield $N'_{\pi^0}(T_{\pi^0})$.

At this point all the various uncertainties have to be included, too. This is more complicated, because several contributions (in addition to the statistical uncertainties already included) entering in different ways must be considered:

(a) The relative uncertainty from the π^0 spectrometer acceptance correction $\delta_{\pi^0}(T_{\pi^0})$ was calculated for each π^0 energy when this correction was made and can therefore be applied directly to the energy bins of $N'_{\pi^0}(T_{\pi^0})$.

(b) As mentioned, an uncertainty contribution was calculated (separately for full and empty target data) for each π^0 energy due to the corrections for proton interaction losses in the target. After the subtraction of the empty target data, the two uncertainty contributions are averaged:

$$\delta_{\text{pint}}(T_{\pi^0}) = \frac{N'^{f}_{\pi^0}(T_{\pi^0})\,\delta^{f}_{\text{pint}}(T_{\pi^0}) + N'^{e}_{\pi^0}(T_{\pi^0})\,\delta^{e}_{\text{pint}}(T_{\pi^0})}{N'^{f}_{\pi^0}(T_{\pi^0}) + N'^{e}_{\pi^0}(T_{\pi^0})}. \tag{C.43}$$

(c) We do not have any energy dependence information about the correction for accidental events. Therefore, we instead distribute the total uncertainty for each target over all non-zero energy bins such that each π^0 energy bin gets the same relative contribution, and in a way such that when these bins are later added, the total uncertainty will be properly included. This relative contribution is

$$\bar{\delta}^{t}_{a} = \delta^{t}_{a}\,\frac{\sum\limits_{T_{\pi^0}} N'^{t}_{\pi^0}(T_{\pi^0})}{\sqrt{\sum\limits_{T_{\pi^0}} \left(N'^{t}_{\pi^0}(T_{\pi^0})\right)^2}}. \tag{C.44}$$

(d) There is also an uncertainty associated with the subtraction of the empty target contribution. This subtraction was done as an overall correction. Again the uncertainty is distributed over all non-zero energy bins in a way such that when the corrected

spectrum is summed, the statistical uncertainty will correctly represent the uncertainty of the empty target contribution. One finds that this requirement leads to a relative uncertainty in each energy bin of

$$\delta_e = \frac{\sum\limits_{T_{\pi^0}} \left(\Delta N'^{f}_{\pi^0}(T_{\pi^0})\right)^2 + \sum\limits_{T_{\pi^0}} \left(\Delta N'^{\epsilon}_{\pi^0}(T_{\pi^0})\right)^2 - \sum\limits_{T_{\pi^0}} \left(\Delta N'_{\pi^0}(T_{\pi^0})\right)^2}{\sum\limits_{T_{\pi^0}} \left(N'_{\pi^0}(T_{\pi^0})\right)^2} . \tag{C.45}$$

The uncertainty terms in Eq. (C.45) are all calculated by multiplying the particular quantity by the corresponding initial relative uncertainty (that is, the relative uncertainty before subtraction of the empty target contribution).

The correction for photon attenuation losses in the target is applied as usual, but now separately for each π^0 energy bin because of the broad range and the slight energy dependence of the correction (cf. Fig. 3.4). That is,

$$N'_{\pi^0}(T_{\pi^0}) \rightarrow \frac{N'_{\pi^0}(T_{\pi^0})}{f_\mu(T_{\pi^0})} \tag{C.46}$$

$$\Delta N'_{\pi^0}(T_{\pi^0}) \rightarrow \frac{\Delta N'_{\pi^0}(T_{\pi^0})}{f_\mu(T_{\pi^0})} . \tag{C.47}$$

We are then left with the absolute normalization of the cross section spectrum. The cross section can be expressed as

$$\frac{d^3\sigma}{dE_{\pi^0}\, d\Omega_{\pi^0}\, d\Omega_p} = \frac{N'_{\pi^0}(T_{\pi^0})}{N'^{f}_{\pi^+}\, \Delta E_{\pi^0}\, \Delta\Omega_p\, \frac{n_t\, \epsilon_c^{\exp}}{\cos\theta_t}} . \tag{C.48}$$

The normalization coefficient for the yield is thus

$$C_{d^3\sigma} = \frac{\cos\theta_t}{N'^{f}_{\pi^+}\, \Delta E_{\pi^0}\, \Delta\Omega_p\, (n_t\, \epsilon_c^{\exp})} . \tag{C.49}$$

All quantities needed in Eq. (C.49) are known. ΔE_{π^0} is the bin size in the spectrum (3 MeV in our analysis), $\Delta\Omega_p$ is the solid angle of each proton telescope (which was (8.46 ± 0.25) msr), and the density $\times$ efficiency product is known from the target thickness analysis (Eq. (C.35)). (The π^0 spectrometer solid angle $\Delta\Omega_{MC}$ was included in $N'_{\pi^0}(T_{\pi^0})$ as part of the spectrometer acceptance correction.) In the corresponding

uncertainty we include the p-shell separation uncertainty $\delta_{\rm psh}$ (12%) mentioned earlier and a contribution $\delta_{\rm pid}$ due to the uncertainty of the proton identification (1%, cf. Sec. 3.5.2). Hence,

$$\left(\frac{\Delta C_{d^3\sigma}}{C_{d^3\sigma}}\right)^2 = \left(\frac{\Delta N'^f_{\pi^+}}{N'^f_{\pi^+}}\right)^2 + \left(\frac{\Delta(\Delta\Omega_p)}{\Delta\Omega_p}\right)^2 + \left(\frac{\Delta(n_t\,\epsilon_c^{\rm exp})}{n_t\,\epsilon_c^{\rm exp}}\right)^2 + (\tan\theta_t\,\Delta\theta_t)^2 + \delta^2_{\rm psh} + \delta^2_{\rm pid}\,. \tag{C.50}$$

C.4 SSPEC — (π^+, π^0) Cross Section Energy Spectra

SSPEC is a program that generates $d^2\sigma/dE_{\pi^0}\,d\Omega_{\pi^0}$ cross section energy spectra for the (π^+, π^0) process from Q histograms. There are again two kinds of data runs: for full target and empty target measurements, respectively. The method is discussed in Sec. 4.3.1. It is closely related to the other analyses presented in the preceding sections.

The correction for accidental events is applied as described for the analysis of coincidence data in Sec. C.3:

$$N'^t_{\pi^0}(T_{\pi^0}) = N^t_{\pi^0}(T_{\pi^0})\left(1 - \frac{N^t_a}{N^t}\right). \tag{C.51}$$

The relative uncertainty in the corrected data due to this correction is given by Eq. (C.38), which can be written as

$$\delta^t_a = \frac{N^t_a}{N^t - N^t_a}\sqrt{\left(\frac{\Delta N^t_a}{N^t_a}\right)^2 + \left(\frac{\Delta N^t}{N^t}\right)^2}, \tag{C.52}$$

where

$$\Delta N^t = \sqrt{N^t} \tag{C.53}$$

$$\Delta N^t_a = \max(\sqrt{N^t_a},\, N^t_a \cdot 0.15)\,. \tag{C.54}$$

This uncertainty is included as an average over all non-zero energy bins:

$$\left(\frac{\Delta N'^t_{\pi^0}(T_{\pi^0})}{N'^t_{\pi^0}(T_{\pi^0})}\right)^2 = \frac{1}{N^t_{\pi^0}(T_{\pi^0})} + (\bar{\delta}^t_a)^2\,, \tag{C.55}$$

where

$$\bar{\delta}_a^t = \delta_a^t \frac{\sum\limits_{T_{\pi^0}} N_{\pi^0}^t(T_{\pi^0})}{\sqrt{\sum\limits_{T_{\pi^0}} \left(N_{\pi^0}^t(T_{\pi^0})\right)^2}}. \tag{C.56}$$

The next step is to account for the π^0 spectrometer acceptance (its solid angle as a function of energy). This was done separately for each energy bin as described for the coincidence analysis in Sec. C.3 (see also Sec. 3.3.2).

The empty target data were normalized to the full target data by the ratio of beam pions involved in the measurements (as usual):

$$f_s = \frac{N'^f_{\pi^+}}{N'^e_{\pi^+}}. \tag{C.57}$$

The quantities $N'^t_{\pi^+}$ were determined as described earlier (see Sec. C.1). However, for the (π^+, π^0) measurements, the empty target contributions were large enough that the subtraction of these contributions could be done bin-by-bin:

$$N'_{\pi^0}(T_{\pi^0}) = N'^f_{\pi^0}(T_{\pi^0}) - f_s\, N'^e_{\pi^0}(T_{\pi^0}), \tag{C.58}$$

and, correspondingly,

$$\Delta N'_{\pi^0}(T_{\pi^0}) = \sqrt{\left(N'^f_{\pi^0}(T_{\pi^0})\right)^2 + \left(f_s\, N'^e_{\pi^0}(T_{\pi^0})\right)^2}. \tag{C.59}$$

The correction for photon attenuation losses in the target is applied as usual. This is again done separately for each π^0 energy bin because of the broad range and the slight energy dependence of the correction. That is,

$$N'_{\pi^0}(T_{\pi^0}) \rightarrow \frac{N'_{\pi^0}(T_{\pi^0})}{f_\mu(T_{\pi^0})} \tag{C.60}$$

$$\Delta N'_{\pi^0}(T_{\pi^0}) \rightarrow \frac{\Delta N'_{\pi^0}(T_{\pi^0})}{f_\mu(T_{\pi^0})}. \tag{C.61}$$

The overall normalization is also similar to what was described in Sec. C.3 and quite straightforward. The differential cross section is

$$\frac{d^2\sigma}{dE_{\pi^0}\, d\Omega_{\pi^0}} = \frac{N'_{\pi^0}(T_{\pi^0})}{N'^f_{\pi^+}\, \Delta E_{\pi^0}\, \frac{n_t\, \varepsilon_c^{exp}}{\cos\theta_t}}, \tag{C.62}$$

and the normalization coefficient is thus

$$C_{d^2\sigma} = \frac{\cos\theta_t}{N'^f_{\pi^+}\,\Delta E_{\pi^0}\,(n_t\,\epsilon_c^{\rm exp})}\,. \tag{C.63}$$

All quantities on the right hand side of Eq. (C.63) are known. In our single arm measurements the bin size in the spectra was $\Delta E_{\pi^0} = 1$ MeV. The density × efficiency product is known from the target thickness analysis (Eq. (C.35)). The corresponding uncertainty is also straightforward:

$$\left(\frac{\Delta C_{d^2\sigma}}{C_{d^2\sigma}}\right)^2 = \left(\frac{\Delta N'^f_{\pi^+}}{N'^f_{\pi^+}}\right)^2 + \left(\frac{\Delta(n_t\,\epsilon_c^{\rm exp})}{n_t\,\epsilon_c^{\rm exp}}\right)^2 + (\tan\theta_t\,\Delta\theta_t)^2\,. \tag{C.64}$$

Appendix D

Statistical Uncertainty of MINUIT Fits

All curve fitting in this work has been done using MINUIT,[81] a software package that originated at CERN. Our version is the 1971 CERN version modified for use on VAX computers at LAMPF in 1979. MINUIT allows a high degree of flexibility in the fitting; one can easily make fits to almost any functional shape. However, probably because MINUIT was written in the days when communication with computers mostly took place through punched cards, using the fitting routines can be somewhat awkward. For ordinary running of MINUIT we recommend using our program MINFIT which can easily be set up to fit any function to any set of data. The purpose of this appendix is to show how the information produced by MINUIT can be used to estimate the total statistical uncertainty of the fitted function, a topic which is not treated in the available documentation (Ref. 81).

Symbolically, the problem we face when making a curve fit is to determine the optimal values of the n parameters $\vec{c} = (c_1, \ldots, c_n)$ in the analytical function $y = f(x; \vec{c})$ based on a number of experimental data points (x_i, y_i). MINUIT calculates these optimal values $\vec{c} = \vec{c^o}$ by minimizing a user supplied function $g_{\chi^2}(f(x; \vec{c}))$, which usually is a function representing the χ^2 of the fit. The algorithm applied[102] is called "The Davidon Variable Matrix Algorithm", and it works by making successive approximations to the covariance matrix $\mathrm{Cov}(c_i, c_j)$ of the fit parameters.

RESULTS OF FULL MINOS ERROR ANALYSIS

Fit target thickness data to a two-peak gaussian

FCN VALUE	CALLS	TIME	EDM	INT.	EXT.	PARAMETER	VALUE	PARABOLIC ERROR	MINOS ERRORS POSITIVE	MINOS ERRORS NEGATIVE
7.52803332E+01	649	17.98	4.77E-06	1	1	Ab	6.26701E+01	6.27709E+00	6.29372E+00	-6.32628E+00
				2	2	xb	6.50146E+01	8.70273E-01	7.85145E-01	-1.05859E+00
				3	3	sb	8.57775E+00	3.64012E-01	3.59760E-01	-4.09033E-01
				4	4	Ap	1.97197E+02	1.01808E+01	1.03966E+01	-1.01139E+01
				5	5	xp	7.20233E+01	1.52377E-01	1.52072E-01	-1.52763E-01
				6	6	sp	3.30889E+00	1.92022E-01	2.00591E-01	-1.87172E-01

ERRORS CORRESPOND TO FUNCTION CHANGE OF 1.0000

INTERNAL COVARIANCE MATRIX

CORRELATION COEFFICIENTS

INT.	1	2	3	4	5
2	0.697				
3	-0.016	0.522			
4	-0.481	-0.538	-0.229		
5	0.331	-0.003	-0.336	-0.029	
6	-0.701	-0.669	-0.248	0.073	-0.228

	PARAMETER	GLOBAL CORRELATION COEFFICIENT
1	Ab	0.80803
2	xb	0.80371
3	sb	0.69180
4	Ap	0.58179
5	xp	0.25650
6	sp	0.74240

Figure D.1. MINUIT output. This is the format for presenting uncertainties when the MINOS command has been given. Similar formats are usually found several times in most output listings. What is of immediate use is the information in the columns "PARAMETER", "VALUE", and "PARABOLIC ERROR". The first column lists the symbolic names given to the fit parameters, the second contains the values of these parameters, and the third shows their estimated uncertainties. These uncertainty estimates are calculated from the covariance matrix (see the text). The two columns labeled "MINOS ERRORS" are more elaborate "true" estimates of the same uncertainties.[81] In most cases the various estimates are in reasonably close agreement.

Fig. D.1 shows an example of output from MINUIT. It lists the best parameter values found ($\vec{c^o}$) as well as various pieces of information based on the covariance matrix $\mathrm{Cov}(c_i^o, c_j^o)$. The "Parabolic Error" Δc_i^o for parameter c_i^o is an estimate of the uncertainty of the value of this parameter:

$$\Delta c_i^o = \sqrt{\mathrm{Var}(c_i^o)} = \sqrt{\mathrm{Cov}(c_i^o, c_i^o)}\,. \tag{D.1}$$

One must also know the correlation between the fit parameters to be able to estimate the total uncertainty in the fitted function. This information can be read from the

table below the heading "Internal Covariance Matrix Correlation Coefficients". The numbers in front of the rows and above the columns correspond to the labels i and j above (they are the parameter numbers used internally by MINUIT to identify the parameters). The remaining table entries are correlation coefficients $\rho(c_i^o, c_j^o)$ defined by

$$\rho(c_i^o, c_j^o) \equiv \frac{\mathrm{Cov}(c_i^o, c_j^o)}{\Delta c_i^o \, \Delta c_j^o} \tag{D.2}$$

$$= \frac{\mathrm{Cov}(c_i^o, c_j^o)}{\sqrt{\mathrm{Cov}(c_i^o, c_i^o)\,\mathrm{Cov}(c_j^o, c_j^o)}}. \tag{D.3}$$

The matrix of correlation coefficients is always symmetric. Therefore the elements above the diagonal are not printed. The diagonal elements are always trivially equal to one (cf. Eq. (D.3)) and are thus also unnecessary to print.

Using the above information one can calculate the uncertainty in the fitted function $f(x; \vec{c^o})$ at any given value of the free variable x:

$$(\Delta f)^2 = \sum_{i=1}^{n} \sum_{j=1}^{n} \frac{\partial f}{\partial c_i} \frac{\partial f}{\partial c_j} \, \mathrm{Cov}(c_i^o, c_j^o) \tag{D.4}$$

$$= \sum_{i=1}^{n} \sum_{j=1}^{n} \frac{\partial f}{\partial c_i} \frac{\partial f}{\partial c_j} \, \rho(c_i^o, c_j^o) \, \Delta c_i^o \, \Delta c_j^o \tag{D.5}$$

$$= \sum_{i=1}^{n} \left(\frac{\partial f}{\partial c_i} \right)^2 (\Delta c_i^o)^2 + 2 \sum_{i=1}^{n} \sum_{j=i+1}^{n} \frac{\partial f}{\partial c_i} \frac{\partial f}{\partial c_j} \, \rho(c_i^o, c_j^o) \, \Delta c_i^o \, \Delta c_j^o \tag{D.6}$$

When one is doing a lot of curve fitting, it is obviously desirable not to have to type in all the uncertainties and correlation coefficients required by Eq. (D.6). The MINUIT documentation[81] does not indicate any straightforward way of achieving this, that is, there is no documented way of passing the covariance matrix to the user-written routines. The available commands still offer one clumsy solution to the problem: use the MINUIT command PUNCH. This command was made to produce punched cards containing the parameter names and values and also the internal covariance matrix. With our version of MINUIT this information is just written to logical unit 7. An

```
Fit target thickness data to a two-peak gaussian                    18.070
         1        Ab6.2670E+016.2771E+00
         2        xb6.5015E+018.7027E-01
         3        sb8.5777E+003.6401E-01
         4        Ap1.9720E+021.0181E+01
         5        xp7.2023E+011.5238E-01
         6        sp3.3089E+001.9202E-01
COVARIANCE        6
 3.940E+01 3.805E+00-3.547E-02-3.076E+01 3.170E-01-8.451E-01 3.805E+00    18.070 1 1
 7.574E-01 1.652E-01-4.767E+00-3.514E-04-1.119E-01-3.547E-02 1.652E-01    18.070 1 2
 1.325E-01-8.497E-01-1.861E-02-1.734E-02-3.076E+01-4.767E+00-8.497E-01    18.070 1 3
 1.036E+02-4.538E-02 1.432E-01 3.170E-01-3.514E-04-1.861E-02-4.538E-02    18.070 1 4
 2.322E-02-6.671E-03-8.451E-01-1.119E-01-1.734E-02 1.432E-01-6.671E-03    18.070 1 5
 3.687E-02 0.000E+00 0.000E+00 0.000E+00 0.000E+00 0.000E+00 0.000E+00    18.070 1 6
```

Figure D.2. Example of PUNCH file format. This is identical to the input format originally required by MINUIT, so that the punched cards could be used directly as new input. The first line is a user comment. Then follow the fit parameters and their values (including uncertainties). Note that there is no room for minus signs here. The bottom part of the output is the complete covariance matrix in internal coordinates, listed with seven elements on each line in the order $\mathrm{Cov}(c_1, c_1)$, $\mathrm{Cov}(c_1, c_2)$, ..., $\mathrm{Cov}(c_n, c_n)$. Remaining room in the last line is filled with zeroes. The numbers appearing beyond position 70 in some of the lines can be ignored (their main purpose appear to be to assist the user if his card deck gets mixed up; the first number is the CPU time used so far by MINUIT).

example of a PUNCH output file is shown in Fig. D.2. The format of this file is not as "user friendly" as one might wish, but in principle it is trivial to write a routine that can read the fit information from the file.

A better way of getting access to many of the variables used by MINUIT, including the fit parameters and the covariance matrix, is to declare the Fortran common blocks containing the desired information also in the user routines. This information will then be available to the user as well. (A lack of documentation makes it necessary to search the MINUIT source code to obtain the structure of these common blocks.) The information found in the PUNCH file can be made accessible in user-written code by including the following program statements:

```
INTEGER*4  MAXEXT,NU,MAXINT,NPAR
REAL*8     U(30),XNAM(30),WERR(30),X(15),XT(15),DIRIN(15),V(15,15)
COMMON     /PAREXT/ U,XNAM,WERR,MAXEXT,NU
COMMON     /PARINT/ X,XT,DIRIN,MAXINT,NPAR
COMMON     /VARIAN/ V
```

The first common block contains the parameter values (U) and their uncertainties (WERR). The array XNAM stores the symbolic names of the variables. If an entry in this array is zero, the corresponding parameter is not defined. The remaining two common blocks are necessary for retrieving the internal covariance matrix. NPAR contains the number of variable parameters, and the covariance matrix itself is stored in the array V. Only elements V(1,1) up to V(NPAR,NPAR) are used. Note that the array elements of the variables in the common block PAREXT (U, XNAM, WERR) are referred to by their *external* parameter numbers, while the elements of the arrays in PARINT and VARIAN (V, *etc.*) are numbered by their *internal* parameter numbers (cf. the columns labeled "EXT." and "INT." in Fig. D.1).

The covariance matrix is given in MINUIT's internal coordinates. These differ from the external coordinates (the coordinates of the data) only when one or more of the fit parameters are restricted to vary within certain limits. The matrix elements can still be used for calculating correlation coefficients as described by Eq. (D.3), however. When applying Eq. (D.6) to estimate uncertainties it is then important that the values for the Δc_i^2's are taken from the array WERR, while the correlation coefficients must be calculated strictly from the covariance matrix.

The method of getting access to MINUIT variables through common blocks is relatively easy and painless to implement, and it provides full precision values of these variables. All calculations in MINUIT are done with double precision Fortran variables, so important information is sometimes lost when the correlation coefficients are taken from the output listings (giving only three significant digits) or calculated from PUNCH files (providing covariances with four significant digits).

Appendix E

Data Tables

This appendix contains a collection of tables of data that have been presented in Chapter 4 in the form of energy spectra. The three sections below are for excitation energy spectra, $d^3\sigma/dE_{\pi^0}\, d\Omega_{\pi^0}\, d\Omega_p$ spectra, and single arm $d^2\sigma/dE_{\pi^0}\, d\Omega_{\pi^0}$ spectra, respectively. The experimental uncertainties listed in the tables do not include the normalization uncertainty (which is approximately 10% in most cases and 15% for spectra including only p-shell nucleon removal events). For detailed information about this, see the corresponding figure captions in Chapter 4.

E.1 Excitation Energy Spectra

Excitation energy spectra are found only in Fig. 4.6. That figure presents the data as histograms with no assigned uncertainties. The table below also contains uncertainty estimates (based only on the number of counts in each histogram bin).

Table E.1. Data of Fig. 4.6. Excitation energy spectra.

E_{ex} [MeV]	Number of counts (acceptance corrected) [arbitrary units]			
	$\theta_{\pi^0} = 70.0°$	$\theta_{\pi^0} = 80.0°$	$\theta_{\pi^0} = 110.0°$	$\theta_{\pi^0} = 129.7°$
−29.5	0.1 ± 0.3	0.2 ± 0.4	—	0.5 ± 0.7
−27.5	—	0.2 ± 0.4	0.2 ± 0.5	0.9 ± 0.9
−25.5	0.4 ± 0.6	0.2 ± 0.5	0.2 ± 0.5	0.5 ± 0.7
−23.5	0.1 ± 0.3	0.4 ± 0.6	—	0.3 ± 0.6
−21.5	0.3 ± 0.5	0.3 ± 0.5	0.3 ± 0.5	0.7 ± 0.8
−19.5	—	0.5 ± 0.7	0.4 ± 0.6	0.4 ± 0.6
−17.5	0.5 ± 0.7	0.3 ± 0.6	0.1 ± 0.3	1.3 ± 1.1
−15.5	0.6 ± 0.8	0.2 ± 0.5	1.0 ± 1.0	1.0 ± 1.0
−13.5	0.8 ± 0.9	0.4 ± 0.6	1.0 ± 1.0	1.2 ± 1.1
−11.5	0.4 ± 0.6	0.6 ± 0.8	0.5 ± 0.7	2.2 ± 1.5
−9.5	1.6 ± 1.3	0.8 ± 0.9	1.6 ± 1.3	1.3 ± 1.2
−7.5	2.1 ± 1.4	1.2 ± 1.1	1.6 ± 1.3	4.3 ± 2.1
−5.5	3.3 ± 1.8	2.1 ± 1.4	2.3 ± 1.5	4.5 ± 2.1
−3.5	5.8 ± 2.4	2.7 ± 1.7	4.6 ± 2.2	6.6 ± 2.6
−1.5	9.8 ± 3.1	6.3 ± 2.5	8.4 ± 2.9	9.3 ± 3.0
0.5	12.9 ± 3.6	8.2 ± 2.9	11.7 ± 3.4	20.4 ± 4.5
2.5	15.9 ± 4.0	14.3 ± 3.8	17.2 ± 4.1	25.6 ± 5.1
4.5	20.5 ± 4.5	15.6 ± 4.0	23.0 ± 4.8	36.0 ± 6.0
6.5	17.7 ± 4.2	20.4 ± 4.5	27.4 ± 5.2	43.5 ± 6.6
8.5	13.5 ± 3.7	21.1 ± 4.6	29.4 ± 5.4	46.5 ± 6.8
10.5	13.5 ± 3.7	17.7 ± 4.2	22.3 ± 4.7	40.0 ± 6.3
12.5	10.2 ± 3.2	16.1 ± 4.0	19.1 ± 4.4	39.3 ± 6.3
14.5	8.4 ± 2.9	12.3 ± 3.5	16.2 ± 4.0	29.6 ± 5.4
16.5	6.4 ± 2.5	11.4 ± 3.4	14.3 ± 3.8	26.9 ± 5.2
18.5	5.4 ± 2.3	9.2 ± 3.0	11.3 ± 3.4	20.2 ± 4.5
20.5	5.5 ± 2.3	9.0 ± 3.0	8.1 ± 2.8	18.2 ± 4.3
22.5	5.2 ± 2.3	5.8 ± 2.4	9.1 ± 3.0	17.0 ± 4.1
24.5	4.4 ± 2.1	8.0 ± 2.8	9.7 ± 3.1	16.4 ± 4.0
26.5	5.0 ± 2.2	4.4 ± 2.1	8.6 ± 2.9	15.0 ± 3.9
28.5	2.5 ± 1.6	7.3 ± 2.7	7.0 ± 2.6	17.0 ± 4.1
30.5	4.1 ± 2.0	4.2 ± 2.1	8.0 ± 2.8	12.0 ± 3.5
32.5	4.0 ± 2.0	5.8 ± 2.4	6.5 ± 2.6	13.6 ± 3.7
34.5	2.7 ± 1.6	5.5 ± 2.4	5.9 ± 2.4	10.7 ± 3.3
36.5	2.2 ± 1.5	4.6 ± 2.1	6.5 ± 2.6	10.6 ± 3.3
38.5	2.2 ± 1.5	3.4 ± 1.8	4.4 ± 2.1	10.6 ± 3.3
40.5	1.9 ± 1.4	2.7 ± 1.6	4.9 ± 2.2	8.4 ± 2.9
42.5	1.6 ± 1.3	5.0 ± 2.2	5.4 ± 2.3	8.0 ± 2.8
44.5	1.2 ± 1.1	1.6 ± 1.3	3.3 ± 1.8	5.6 ± 2.4
46.5	1.0 ± 1.0	3.3 ± 1.8	3.7 ± 1.9	3.9 ± 2.0
48.5	0.3 ± 0.6	2.7 ± 1.6	2.2 ± 1.5	4.0 ± 2.0
50.5	1.4 ± 1.2	1.8 ± 1.4	1.7 ± 1.3	3.7 ± 1.9
52.5	0.1 ± 0.3	0.4 ± 0.6	2.1 ± 1.4	3.6 ± 1.9
54.5	1.1 ± 1.1	0.3 ± 0.6	2.3 ± 1.5	2.5 ± 1.6
56.5	0.7 ± 0.8	1.2 ± 1.1	0.6 ± 0.8	3.9 ± 2.0
58.5	1.1 ± 1.1	0.7 ± 0.8	1.0 ± 1.0	2.2 ± 1.5
60.5	0.9 ± 0.9	0.8 ± 0.9	1.3 ± 1.1	1.5 ± 1.2
62.5	0.3 ± 0.5	0.9 ± 1.0	1.2 ± 1.1	1.6 ± 1.3
64.5	0.6 ± 0.8	0.9 ± 1.0	0.7 ± 0.8	1.8 ± 1.3
66.5	0.5 ± 0.7	0.9 ± 1.0	0.4 ± 0.6	1.8 ± 1.3
68.5	0.6 ± 0.7	0.2 ± 0.5	0.6 ± 0.8	0.1 ± 0.4
70.5	0.3 ± 0.5	1.0 ± 1.0	0.3 ± 0.6	1.1 ± 1.0
72.5	—	—	0.5 ± 0.7	0.9 ± 0.9
74.5	—	—	0.9 ± 0.9	0.8 ± 0.9
76.5	—	—	—	0.7 ± 0.8
78.5	—	—	0.3 ± 0.5	0.3 ± 0.5

Table E.2. Data of Fig. 4.15. p-shell cut for O at $\theta_{\pi^0} = 70.0°$.

T_{π^0} [MeV]	$\frac{d^3\sigma}{dE_{\pi^0}\, d\Omega_{\pi^0}\, d\Omega_p}$ $\left[\frac{\mu b}{\text{MeV sr}^2}\right]$							
	telescope 7	telescope 6	telescope 5	telescope 4	telescope 3	telescope 2	telescope 1	telescope 8
52	—	—	1.6 ± 1.7	5.5 ± 3.3	1.7 ± 1.8	—	—	6.2 ± 3.7
55	—	1.2 ± 1.2	1.1 ± 1.1	3.5 ± 2.1	3.4 ± 2.1	2.4 ± 1.8	—	2.0 ± 1.6
58	—	1.7 ± 1.3	0.8 ± 0.8	4.2 ± 2.0	2.4 ± 1.5	—	—	5.0 ± 2.5
61	0.7 ± 0.7	—	4.2 ± 1.9	12.5 ± 3.5	7.6 ± 2.8	1.3 ± 1.0	—	7.9 ± 3.3
64	—	1.1 ± 0.8	4.0 ± 1.8	9.9 ± 2.8	1.6 ± 1.0	0.6 ± 0.6	0.6 ± 0.6	6.6 ± 2.7
67	—	1.9 ± 1.1	6.4 ± 2.3	8.5 ± 2.4	4.5 ± 1.8	1.0 ± 0.7	0.5 ± 0.5	6.8 ± 2.7
70	—	0.8 ± 0.6	5.9 ± 2.1	10.7 ± 2.7	6.3 ± 2.1	1.3 ± 0.8	—	11.9 ± 4.3
73	—	4.5 ± 1.7	9.8 ± 3.1	12.0 ± 2.9	6.0 ± 2.0	3.4 ± 1.4	1.6 ± 0.8	11.8 ± 4.2
76	1.1 ± 0.6	1.4 ± 0.8	7.1 ± 2.4	14.2 ± 3.2	6.7 ± 2.1	2.7 ± 1.2	1.1 ± 0.6	12.7 ± 4.5
79	1.3 ± 0.7	3.1 ± 1.3	9.3 ± 2.9	14.6 ± 3.2	9.3 ± 2.7	2.2 ± 1.0	0.7 ± 0.5	14.8 ± 5.1
82	—	2.3 ± 1.0	10.6 ± 3.2	13.1 ± 2.9	10.5 ± 2.9	2.0 ± 0.9	2.2 ± 0.8	14.5 ± 5.0
85	0.9 ± 0.5	1.9 ± 0.9	13.5 ± 4.0	22.3 ± 4.4	10.2 ± 2.8	5.2 ± 1.8	2.1 ± 0.8	13.4 ± 4.6
88	1.4 ± 0.6	2.7 ± 1.1	15.4 ± 4.5	24.6 ± 4.7	13.5 ± 3.6	3.7 ± 1.4	0.9 ± 0.5	17.5 ± 5.9
91	0.3 ± 0.3	4.5 ± 1.5	9.2 ± 2.8	20.4 ± 4.0	17.3 ± 4.4	3.8 ± 1.4	0.8 ± 0.5	12.5 ± 4.3
94	0.5 ± 0.4	5.0 ± 1.7	14.6 ± 4.2	27.2 ± 5.1	15.6 ± 4.1	6.1 ± 2.0	1.1 ± 0.6	18.7 ± 6.3
97	1.1 ± 0.6	5.6 ± 1.9	15.4 ± 4.4	27.2 ± 5.1	17.8 ± 4.6	3.0 ± 1.2	1.7 ± 0.7	17.9 ± 6.0
100	2.3 ± 0.8	6.0 ± 2.0	16.1 ± 4.7	28.2 ± 5.3	18.2 ± 4.7	7.7 ± 2.5	2.1 ± 0.8	16.6 ± 5.6
103	2.7 ± 0.9	7.0 ± 2.3	19.2 ± 5.5	23.5 ± 4.6	17.7 ± 4.6	6.7 ± 2.2	1.3 ± 0.6	13.3 ± 4.6
106	1.6 ± 0.7	6.4 ± 2.1	17.1 ± 4.9	20.3 ± 4.1	21.6 ± 5.5	7.6 ± 2.5	1.6 ± 0.7	15.7 ± 5.3
109	2.3 ± 0.9	8.1 ± 2.6	16.3 ± 4.8	22.0 ± 4.4	14.7 ± 4.0	8.8 ± 2.8	0.7 ± 0.5	14.9 ± 5.1
112	2.4 ± 0.9	6.9 ± 2.3	22.6 ± 6.4	20.2 ± 4.1	14.5 ± 3.9	6.0 ± 2.1	2.1 ± 0.9	12.1 ± 4.2
115	2.2 ± 0.9	8.0 ± 2.6	11.0 ± 3.4	13.5 ± 3.1	14.7 ± 4.0	7.0 ± 2.4	1.1 ± 0.6	9.8 ± 3.5
118	1.2 ± 0.7	5.5 ± 2.0	7.5 ± 2.5	10.8 ± 2.6	9.7 ± 2.9	6.3 ± 2.2	—	6.5 ± 2.5
121	2.1 ± 0.9	3.9 ± 1.6	5.2 ± 1.9	6.9 ± 2.0	8.9 ± 2.7	5.2 ± 2.0	0.4 ± 0.4	4.3 ± 1.8
124	0.9 ± 0.6	4.2 ± 1.7	5.6 ± 2.1	3.7 ± 1.4	5.2 ± 1.9	0.4 ± 0.4	0.5 ± 0.5	1.4 ± 0.8
127	1.0 ± 0.7	2.3 ± 1.2	1.2 ± 0.8	1.8 ± 0.9	2.6 ± 1.2	—	—	1.1 ± 0.8
130	—	0.5 ± 0.5	—	0.5 ± 0.5	0.5 ± 0.5	—	—	0.4 ± 0.4
133	—	—	—	—	—	1.1 ± 0.8	—	—

E.2 $d^3\sigma/dE_{\pi^0}\, d\Omega_{\pi^0}\, d\Omega_p$ Spectra

The tables in this section list all data in the coincidence cross section spectra of Figs. 4.15 – 4.26 (measurements on oxygen) and Figs. 4.32 – 4.34 (iron, tin, and lead). Data for all eight proton telescopes are presented in each table. The first column of cross sections always corresponds to the lowest telescope (at out-of-plane angle $\phi_p = -51°$, cf. Sec. 2.2.3). This is usually telescope 1, but it may also be telescope 7 (cf. Sec. 2.2.5). The table heading clarifies this in each case.

Table E.3. Data of Fig. 4.16. Complete spectra for O at $\theta_{\pi^0} = 70.0°$.

T_{π^0}	$\frac{d^3\sigma}{dE_{\pi^0}\, d\Omega_{\pi^0}\, d\Omega_p}$ $\left[\frac{\mu b}{\text{MeV sr}^2}\right]$							
[MeV]	telescope 7	telescope 6	telescope 5	telescope 4	telescope 3	telescope 2	telescope 1	telescope 8
52	4.6 ± 3.4	6.7 ± 3.7	11.0 ± 4.7	12.0 ± 4.8	10.1 ± 4.4	10.0 ± 5.0	3.4 ± 2.6	19.9 ± 6.7
55	3.0 ± 2.2	9.8 ± 3.9	6.1 ± 2.8	17.8 ± 4.9	15.2 ± 4.7	6.4 ± 3.2	3.3 ± 2.2	29.7 ± 7.9
58	2.2 ± 1.6	4.7 ± 2.2	11.0 ± 3.6	20.7 ± 4.8	13.2 ± 3.8	3.8 ± 2.0	4.0 ± 2.2	24.8 ± 6.4
61	4.5 ± 2.5	6.1 ± 2.4	12.7 ± 3.7	27.6 ± 5.4	17.8 ± 4.3	4.2 ± 2.0	3.1 ± 1.7	25.7 ± 6.3
64	1.9 ± 1.3	6.7 ± 2.4	9.2 ± 2.8	21.7 ± 4.3	9.8 ± 2.7	6.6 ± 2.6	3.7 ± 1.8	24.9 ± 5.9
67	2.9 ± 1.6	7.5 ± 2.5	17.1 ± 4.3	20.4 ± 3.9	16.8 ± 3.8	8.8 ± 3.2	2.7 ± 1.4	26.2 ± 6.0
70	2.9 ± 1.6	7.7 ± 2.4	15.3 ± 3.8	23.0 ± 4.1	16.3 ± 3.5	11.5 ± 3.9	3.1 ± 1.5	30.7 ± 6.8
73	2.5 ± 1.4	13.1 ± 3.6	19.4 ± 4.6	26.5 ± 4.4	15.9 ± 3.4	11.6 ± 3.8	2.1 ± 1.1	32.3 ± 7.0
76	3.8 ± 1.9	8.2 ± 2.4	14.2 ± 3.5	24.1 ± 4.0	16.3 ± 3.4	9.6 ± 3.2	3.2 ± 1.4	30.0 ± 6.5
79	4.5 ± 2.3	11.6 ± 3.2	20.4 ± 4.7	25.8 ± 4.2	18.0 ± 3.6	12.3 ± 4.0	4.4 ± 1.8	32.1 ± 6.9
82	3.0 ± 1.5	8.5 ± 2.4	19.8 ± 4.5	24.0 ± 3.9	21.3 ± 4.1	10.3 ± 3.4	3.3 ± 1.4	30.3 ± 6.5
85	1.6 ± 0.9	7.2 ± 2.1	23.1 ± 5.1	34.8 ± 5.2	19.4 ± 3.7	11.4 ± 3.6	4.7 ± 1.8	27.7 ± 5.9
88	3.2 ± 1.6	9.0 ± 2.5	23.9 ± 5.3	41.6 ± 6.0	25.0 ± 4.6	9.9 ± 3.2	1.5 ± 0.8	31.4 ± 6.7
91	1.5 ± 0.9	11.3 ± 3.0	17.4 ± 3.9	32.8 ± 4.9	26.0 ± 4.7	10.7 ± 3.4	1.9 ± 0.9	21.8 ± 4.8
94	1.4 ± 0.8	8.5 ± 2.4	20.6 ± 4.6	38.2 ± 5.6	27.4 ± 5.0	11.1 ± 3.5	1.8 ± 0.9	28.3 ± 6.1
97	2.8 ± 1.5	9.9 ± 2.7	22.0 ± 4.9	34.8 ± 5.2	27.2 ± 4.9	7.8 ± 2.6	2.6 ± 1.1	26.4 ± 5.7
100	3.1 ± 1.6	11.4 ± 3.1	22.7 ± 5.0	36.7 ± 5.4	26.2 ± 4.8	11.3 ± 3.6	2.9 ± 1.3	27.9 ± 6.0
103	4.1 ± 2.0	10.5 ± 2.9	22.9 ± 5.1	30.6 ± 4.7	24.4 ± 4.6	12.6 ± 4.0	2.3 ± 1.1	19.7 ± 4.4
106	2.7 ± 1.4	9.8 ± 2.8	20.1 ± 4.6	23.7 ± 3.9	27.8 ± 5.1	11.2 ± 3.6	1.8 ± 0.9	19.2 ± 4.4
109	3.1 ± 1.6	9.6 ± 2.7	17.2 ± 4.0	25.2 ± 4.1	18.0 ± 3.6	14.0 ± 4.5	0.9 ± 0.6	18.6 ± 4.3
112	2.6 ± 1.4	8.2 ± 2.4	23.2 ± 5.3	21.0 ± 3.7	16.1 ± 3.4	8.8 ± 3.0	1.9 ± 1.0	13.5 ± 3.3
115	1.9 ± 1.1	8.4 ± 2.5	11.3 ± 2.9	14.1 ± 2.8	15.7 ± 3.3	7.3 ± 2.6	1.0 ± 0.7	10.4 ± 2.7
118	1.0 ± 0.7	5.4 ± 1.8	7.7 ± 2.2	11.0 ± 2.4	10.0 ± 2.4	6.0 ± 2.2	—	6.8 ± 2.0
121	1.8 ± 1.1	3.8 ± 1.5	5.4 ± 1.7	7.0 ± 1.9	9.2 ± 2.3	4.9 ± 1.9	0.4 ± 0.4	4.5 ± 1.5
124	0.8 ± 0.6	4.1 ± 1.6	5.8 ± 1.9	3.8 ± 1.3	5.3 ± 1.7	0.4 ± 0.4	0.4 ± 0.4	1.5 ± 0.8
127	0.8 ± 0.7	2.2 ± 1.1	1.2 ± 0.8	1.8 ± 0.9	2.7 ± 1.2	—	—	1.2 ± 0.7
130	—	0.5 ± 0.5	—	0.5 ± 0.5	0.5 ± 0.5	—	—	0.4 ± 0.4
133	—	—	—	—	—	1.0 ± 0.8	—	—

Table E.4. Data of Fig. 4.17. "s-shell" cut for O at $\theta_{\pi^0} = 70.0°$.

T_{π^0}	$\frac{d^3\sigma}{dE_{\pi^0}\, d\Omega_{\pi^0}\, d\Omega_p}$ $\left[\frac{\mu b}{\text{MeV sr}^2}\right]$							
[MeV]	telescope 7	telescope 6	telescope 5	telescope 4	telescope 3	telescope 2	telescope 1	telescope 8
52	4.3 ± 3.6	6.6 ± 3.8	10.1 ± 4.6	7.2 ± 3.8	8.9 ± 4.2	9.7 ± 5.6	3.3 ± 2.7	14.6 ± 5.7
55	2.8 ± 2.3	8.6 ± 3.9	5.5 ± 2.7	15.2 ± 4.7	12.6 ± 4.2	4.2 ± 2.7	3.2 ± 2.3	29.5 ± 8.1
58	2.0 ± 1.7	3.1 ± 1.8	11.0 ± 3.7	17.5 ± 4.6	11.5 ± 3.5	3.7 ± 2.3	3.8 ± 2.3	21.1 ± 5.8
61	3.7 ± 2.6	6.0 ± 2.6	9.3 ± 3.1	16.5 ± 4.1	11.0 ± 3.1	3.0 ± 1.8	3.0 ± 1.8	19.0 ± 5.1
64	1.8 ± 1.4	5.6 ± 2.4	5.7 ± 2.1	12.7 ± 3.2	8.7 ± 2.5	6.0 ± 3.0	3.0 ± 1.8	19.5 ± 5.0
67	2.7 ± 1.9	5.7 ± 2.3	11.6 ± 3.3	12.8 ± 3.1	13.1 ± 3.1	7.7 ± 3.6	2.2 ± 1.3	20.6 ± 5.1
70	2.6 ± 1.9	6.9 ± 2.6	10.1 ± 2.9	13.3 ± 3.0	10.6 ± 2.6	10.1 ± 4.5	3.0 ± 1.7	19.9 ± 4.8
73	2.4 ± 1.7	8.8 ± 3.1	10.4 ± 2.9	15.5 ± 3.3	10.6 ± 2.5	8.3 ± 3.7	0.7 ± 0.6	21.7 ± 5.1
76	2.7 ± 1.8	6.8 ± 2.5	7.6 ± 2.2	10.8 ± 2.5	10.3 ± 2.4	6.9 ± 3.1	2.1 ± 1.2	18.2 ± 4.3
79	3.2 ± 2.2	8.6 ± 3.0	11.9 ± 3.1	12.1 ± 2.6	9.2 ± 2.1	10.0 ± 4.4	3.7 ± 1.9	18.2 ± 4.3
82	2.7 ± 1.8	6.3 ± 2.3	9.9 ± 2.6	11.7 ± 2.5	11.5 ± 2.5	8.2 ± 3.6	1.3 ± 0.8	16.5 ± 3.9
85	0.9 ± 0.7	5.3 ± 1.9	10.3 ± 2.7	13.4 ± 2.7	9.7 ± 2.2	6.4 ± 2.9	2.7 ± 1.4	14.8 ± 3.5
88	1.9 ± 1.3	6.4 ± 2.3	9.0 ± 2.4	18.2 ± 3.4	12.1 ± 2.5	6.2 ± 2.8	0.7 ± 0.5	14.3 ± 3.4
91	1.2 ± 0.9	6.9 ± 2.4	8.7 ± 2.3	13.3 ± 2.7	9.2 ± 2.0	7.0 ± 3.1	1.1 ± 0.7	9.5 ± 2.4
94	0.9 ± 0.7	3.7 ± 1.4	6.2 ± 1.8	11.7 ± 2.5	12.3 ± 2.5	5.3 ± 2.4	0.7 ± 0.5	9.6 ± 2.4
97	1.7 ± 1.2	4.5 ± 1.7	6.9 ± 2.0	8.2 ± 1.9	9.7 ± 2.1	4.9 ± 2.3	1.0 ± 0.7	8.4 ± 2.2
100	1.1 ± 0.8	5.6 ± 2.0	6.8 ± 1.9	8.9 ± 2.0	8.2 ± 1.9	4.0 ± 1.9	1.0 ± 0.7	11.3 ± 2.8
103	1.7 ± 1.2	3.8 ± 1.5	3.6 ± 1.3	7.4 ± 1.8	6.7 ± 1.7	6.1 ± 2.8	1.1 ± 0.7	6.2 ± 1.8
106	1.2 ± 0.9	3.7 ± 1.5	2.9 ± 1.1	3.4 ± 1.1	6.1 ± 1.6	3.9 ± 1.9	0.3 ± 0.3	3.1 ± 1.1
109	1.0 ± 0.8	1.8 ± 0.9	0.6 ± 0.4	3.2 ± 1.1	3.2 ± 1.1	5.5 ± 2.5	0.3 ± 0.3	3.2 ± 1.2
112	0.5 ± 0.5	1.6 ± 0.8	—	0.7 ± 0.5	1.3 ± 0.7	3.0 ± 1.6	—	0.9 ± 0.6
115	—	0.7 ± 0.5	—	0.4 ± 0.4	0.7 ± 0.5	0.6 ± 0.5	—	—

Table E.5. Data of Fig. 4.18. p-shell cut for O at $\theta_{\pi^0} = 80.0°$.

T_{π^0} [MeV]	$\frac{d^3\sigma}{dE_{\pi^0}\, d\Omega_{\pi^0}\, d\Omega_p}$ $\left[\frac{\mu b}{MeV\ sr^2}\right]$							
	telescope 1	telescope 2	telescope 3	telescope 4	telescope 5	telescope 6	telescope 7	telescope 8
46	—	—	—	3.3 ± 3.3	3.3 ± 3.3	—	—	—
49	—	1.6 ± 1.6	—	9.8 ± 4.1	1.6 ± 1.6	1.5 ± 1.5	—	7.9 ± 3.7
52	—	1.0 ± 1.0	2.2 ± 1.5	7.5 ± 2.9	5.3 ± 2.4	1.0 ± 1.0	—	4.1 ± 2.1
55	0.8 ± 0.8	2.2 ± 1.4	4.8 ± 2.0	6.3 ± 2.3	5.4 ± 2.1	0.7 ± 0.7	—	0.7 ± 0.8
58	0.6 ± 0.6	2.9 ± 1.5	4.3 ± 1.7	8.5 ± 2.4	7.2 ± 2.2	3.9 ± 1.9	—	1.8 ± 1.0
61	—	1.0 ± 0.7	8.2 ± 2.1	11.5 ± 2.6	6.5 ± 1.9	0.9 ± 0.7	—	6.3 ± 2.0
64	—	2.1 ± 1.0	7.4 ± 1.9	16.7 ± 3.1	7.2 ± 1.9	1.9 ± 1.0	0.9 ± 0.6	1.6 ± 0.9
67	0.4 ± 0.4	2.5 ± 1.1	9.9 ± 2.1	15.8 ± 2.8	9.0 ± 2.0	2.4 ± 1.1	1.2 ± 0.7	5.1 ± 1.6
70	0.6 ± 0.5	1.6 ± 0.8	9.9 ± 2.0	19.2 ± 3.0	11.7 ± 2.3	3.4 ± 1.4	0.3 ± 0.3	4.8 ± 1.5
73	0.6 ± 0.5	2.6 ± 1.1	15.2 ± 2.5	23.9 ± 3.4	13.4 ± 2.4	3.1 ± 1.3	0.6 ± 0.4	6.5 ± 1.7
76	0.3 ± 0.3	2.7 ± 1.1	12.4 ± 2.2	25.3 ± 3.5	12.1 ± 2.2	3.4 ± 1.4	0.6 ± 0.4	7.9 ± 1.9
79	0.5 ± 0.4	4.1 ± 1.4	19.4 ± 2.8	26.8 ± 3.6	17.6 ± 2.8	3.4 ± 1.3	1.4 ± 0.6	7.4 ± 1.8
82	0.7 ± 0.5	4.3 ± 1.4	17.8 ± 2.6	28.8 ± 3.7	16.9 ± 2.6	5.6 ± 2.0	0.3 ± 0.3	7.3 ± 1.7
85	1.1 ± 0.6	4.7 ± 1.5	21.1 ± 2.8	30.6 ± 3.8	18.8 ± 2.8	4.2 ± 1.6	1.7 ± 0.6	10.5 ± 2.2
88	0.6 ± 0.4	4.6 ± 1.4	20.5 ± 2.8	27.9 ± 3.5	21.4 ± 3.0	5.2 ± 1.8	0.9 ± 0.5	13.5 ± 2.7
91	0.6 ± 0.4	4.5 ± 1.4	21.9 ± 2.9	26.9 ± 3.4	22.1 ± 3.1	4.5 ± 1.6	2.1 ± 0.7	13.8 ± 2.7
94	1.3 ± 0.7	6.1 ± 1.8	22.7 ± 3.0	26.6 ± 3.4	25.6 ± 3.5	6.4 ± 2.2	1.2 ± 0.5	15.0 ± 2.9
97	0.9 ± 0.5	5.3 ± 1.6	22.3 ± 2.9	23.8 ± 3.1	22.5 ± 3.2	6.9 ± 2.4	1.4 ± 0.6	13.5 ± 2.7
100	1.6 ± 0.8	4.1 ± 1.4	22.2 ± 3.0	23.0 ± 3.1	24.5 ± 3.4	7.2 ± 2.5	1.5 ± 0.6	13.8 ± 2.8
103	1.9 ± 0.9	5.9 ± 1.8	18.3 ± 2.6	16.8 ± 2.5	27.0 ± 3.7	5.6 ± 2.0	1.0 ± 0.5	13.7 ± 2.8
106	0.7 ± 0.5	6.4 ± 1.9	19.5 ± 2.8	13.3 ± 2.2	23.5 ± 3.4	5.1 ± 1.9	2.4 ± 0.8	10.6 ± 2.3
109	0.8 ± 0.5	3.6 ± 1.3	13.3 ± 2.2	14.1 ± 2.3	17.0 ± 2.7	5.3 ± 1.9	1.7 ± 0.7	8.2 ± 1.9
112	—	3.4 ± 1.2	12.0 ± 2.1	9.3 ± 1.8	13.1 ± 2.3	4.0 ± 1.5	0.9 ± 0.5	9.0 ± 2.1
115	—	3.8 ± 1.4	10.2 ± 1.9	6.9 ± 1.5	7.4 ± 1.6	4.2 ± 1.6	0.9 ± 0.5	5.5 ± 1.5
118	0.9 ± 0.6	3.8 ± 1.4	6.5 ± 1.5	4.0 ± 1.2	1.5 ± 0.7	1.9 ± 0.9	0.6 ± 0.4	2.9 ± 1.0
121	0.3 ± 0.3	1.9 ± 0.9	3.6 ± 1.1	2.0 ± 0.8	0.7 ± 0.5	1.2 ± 0.7	—	1.3 ± 0.7
124	—	1.0 ± 0.6	1.4 ± 0.7	1.0 ± 0.6	—	—	—	0.3 ± 0.3
127	—	—	0.4 ± 0.4	—	—	—	0.8 ± 0.6	0.4 ± 0.4
130	0.4 ± 0.4	—	0.4 ± 0.4	0.4 ± 0.4	—	0.4 ± 0.4	—	—

Table E.6. Data of Fig. 4.19. Complete spectra for O at $\theta_{\pi^0} = 80.0°$.

T_{π^0}	$\frac{d^3\sigma}{dE_{\pi^0}\, d\Omega_{\pi^0}\, d\Omega_p}$ $\left[\frac{\mu b}{MeV\ sr^2}\right]$							
[MeV]	telescope 1	telescope 2	telescope 3	telescope 4	telescope 5	telescope 6	telescope 7	telescope 8
46	5.8 ± 4.3	17.7 ± 7.9	23.4 ± 8.9	18.2 ± 7.5	17.9 ± 7.5	14.9 ± 6.9	5.8 ± 4.3	8.8 ± 5.3
49	1.4 ± 1.5	11.8 ± 4.7	14.7 ± 5.1	37.9 ± 8.0	15.0 ± 4.9	12.0 ± 4.5	4.4 ± 2.7	11.8 ± 4.6
52	2.8 ± 1.8	8.7 ± 3.3	15.4 ± 4.4	30.8 ± 5.9	29.5 ± 6.0	12.7 ± 3.9	3.8 ± 2.1	13.6 ± 4.2
55	2.1 ± 1.3	12.1 ± 3.6	19.8 ± 4.6	24.2 ± 4.5	26.8 ± 5.0	7.2 ± 2.5	6.3 ± 2.5	12.1 ± 3.5
58	3.3 ± 1.5	10.0 ± 2.9	13.8 ± 3.4	28.6 ± 4.5	27.7 ± 4.6	12.9 ± 3.2	3.8 ± 1.6	13.9 ± 3.6
61	2.2 ± 1.1	13.8 ± 3.5	27.4 ± 5.2	32.5 ± 4.5	27.0 ± 4.3	10.7 ± 2.6	4.5 ± 1.7	18.8 ± 4.2
64	3.5 ± 1.4	9.9 ± 2.6	22.7 ± 4.3	39.7 ± 4.9	28.4 ± 4.2	10.0 ± 2.4	2.3 ± 1.1	11.0 ± 2.8
67	2.7 ± 1.2	10.4 ± 2.6	26.9 ± 4.8	37.0 ± 4.5	27.5 ± 3.9	13.3 ± 2.8	6.5 ± 2.0	14.6 ± 3.3
70	1.8 ± 0.9	11.8 ± 2.8	28.8 ± 5.0	42.2 ± 4.7	34.5 ± 4.5	14.2 ± 2.8	4.3 ± 1.4	17.8 ± 3.7
73	3.1 ± 1.2	13.4 ± 3.0	37.0 ± 6.0	38.0 ± 4.3	32.6 ± 4.2	11.5 ± 2.4	5.0 ± 1.6	22.8 ± 4.5
76	2.8 ± 1.1	14.3 ± 3.2	25.5 ± 4.4	47.6 ± 4.9	31.7 ± 4.0	12.1 ± 2.4	1.8 ± 0.8	25.2 ± 4.8
79	2.7 ± 1.0	13.4 ± 3.0	36.7 ± 5.9	47.3 ± 4.8	32.7 ± 4.1	9.8 ± 2.0	5.1 ± 1.5	19.6 ± 3.9
82	3.4 ± 1.2	9.7 ± 2.3	36.5 ± 5.8	49.9 ± 4.9	33.6 ± 4.1	13.1 ± 2.5	3.9 ± 1.2	22.2 ± 4.3
85	2.6 ± 1.0	14.7 ± 3.1	35.8 ± 5.7	48.9 ± 4.8	31.0 ± 3.8	13.1 ± 2.4	4.3 ± 1.3	24.2 ± 4.5
88	2.5 ± 0.9	13.1 ± 2.8	33.9 ± 5.4	49.1 ± 4.7	32.0 ± 3.8	14.5 ± 2.6	3.4 ± 1.1	31.7 ± 5.8
91	3.1 ± 1.1	11.3 ± 2.5	35.3 ± 5.6	42.5 ± 4.3	33.2 ± 4.0	14.0 ± 2.5	4.0 ± 1.2	30.2 ± 5.5
94	1.9 ± 0.8	12.0 ± 2.6	33.3 ± 5.3	36.8 ± 3.8	36.8 ± 4.3	13.7 ± 2.5	3.4 ± 1.1	31.8 ± 5.8
97	1.9 ± 0.8	12.1 ± 2.7	31.3 ± 5.0	32.8 ± 3.6	27.9 ± 3.5	14.0 ± 2.5	3.5 ± 1.1	30.2 ± 5.5
100	2.5 ± 0.9	10.5 ± 2.4	30.3 ± 4.9	32.4 ± 3.6	27.0 ± 3.4	12.5 ± 2.4	3.1 ± 1.1	22.5 ± 4.3
103	2.1 ± 0.8	11.4 ± 2.6	25.1 ± 4.2	23.1 ± 2.9	27.8 ± 3.5	9.3 ± 1.9	1.6 ± 0.7	22.2 ± 4.3
106	0.7 ± 0.5	8.9 ± 2.1	23.8 ± 4.1	17.7 ± 2.5	23.0 ± 3.1	8.0 ± 1.8	3.6 ± 1.2	15.6 ± 3.2
109	1.3 ± 0.6	4.9 ± 1.4	15.1 ± 2.9	19.0 ± 2.6	16.7 ± 2.5	8.1 ± 1.8	1.8 ± 0.8	9.3 ± 2.2
112	—	3.7 ± 1.2	12.1 ± 2.4	10.3 ± 1.8	12.9 ± 2.2	4.3 ± 1.2	0.8 ± 0.5	9.0 ± 2.1
115	—	3.9 ± 1.2	9.7 ± 2.1	6.8 ± 1.5	7.3 ± 1.6	4.5 ± 1.3	0.8 ± 0.5	5.6 ± 1.5
118	0.9 ± 0.5	3.8 ± 1.3	6.2 ± 1.6	3.9 ± 1.1	1.5 ± 0.7	2.1 ± 0.8	0.6 ± 0.4	3.0 ± 1.1
121	0.3 ± 0.3	1.9 ± 0.8	3.5 ± 1.2	2.0 ± 0.8	0.6 ± 0.5	1.3 ± 0.7	—	1.3 ± 0.7
124	—	1.0 ± 0.6	1.4 ± 0.7	1.1 ± 0.6	—	—	—	0.3 ± 0.3
127	—	—	0.4 ± 0.4	—	—	—	0.7 ± 0.5	0.4 ± 0.4
130	0.4 ± 0.4	—	0.4 ± 0.4	0.4 ± 0.4	—	0.4 ± 0.4	—	—

Table E.7. Data of Fig. 4.20. "s-shell" cut for O at $\theta_{\pi^0} = 80.0°$.

T_{π^0}	$\frac{d^3\sigma}{dE_{\pi^0}\, d\Omega_{\pi^0}\, d\Omega_p}$ $\left[\frac{\mu b}{MeV\ sr^2}\right]$							
[MeV]	telescope 1	telescope 2	telescope 3	telescope 4	telescope 5	telescope 6	telescope 7	telescope 8
46	5.8 ± 4.3	17.9 ± 8.2	22.6 ± 9.7	15.3 ± 7.0	14.9 ± 6.9	15.6 ± 7.1	5.7 ± 4.3	9.0 ± 5.6
49	1.4 ± 1.5	10.5 ± 4.5	14.1 ± 5.7	29.2 ± 7.3	13.5 ± 4.8	11.0 ± 4.3	4.3 ± 2.7	4.5 ± 2.8
52	2.8 ± 1.8	7.9 ± 3.2	13.0 ± 4.7	24.1 ± 5.5	24.5 ± 5.8	12.3 ± 3.7	3.7 ± 2.1	9.9 ± 3.9
55	1.4 ± 1.0	10.1 ± 3.4	15.0 ± 4.9	18.5 ± 4.1	21.6 ± 4.8	6.8 ± 2.3	6.2 ± 2.6	11.6 ± 4.0
58	2.7 ± 1.4	7.3 ± 2.5	9.6 ± 3.3	20.8 ± 4.0	20.8 ± 4.3	9.4 ± 2.5	3.7 ± 1.7	12.5 ± 4.0
61	2.2 ± 1.1	13.0 ± 3.6	19.3 ± 5.6	21.9 ± 3.9	20.9 ± 4.0	10.2 ± 2.4	4.4 ± 1.8	13.1 ± 4.0
64	3.5 ± 1.4	8.0 ± 2.4	15.5 ± 4.5	24.2 ± 4.0	21.5 ± 4.0	8.3 ± 2.0	1.5 ± 0.9	9.6 ± 3.0
67	2.4 ± 1.1	8.1 ± 2.4	17.3 ± 4.9	22.3 ± 3.6	19.0 ± 3.5	11.4 ± 2.3	5.3 ± 1.9	9.9 ± 3.0
70	1.2 ± 0.7	10.4 ± 2.8	19.1 ± 5.3	24.3 ± 3.7	23.3 ± 3.9	11.2 ± 2.2	3.9 ± 1.5	13.3 ± 3.8
73	2.5 ± 1.0	11.0 ± 2.9	22.3 ± 6.0	15.4 ± 2.6	19.9 ± 3.4	8.7 ± 1.8	4.4 ± 1.6	16.8 ± 4.6
76	2.6 ± 1.0	11.8 ± 3.0	13.7 ± 3.9	23.7 ± 3.4	20.1 ± 3.4	9.0 ± 1.8	1.3 ± 0.7	17.8 ± 4.8
79	2.2 ± 0.9	9.6 ± 2.5	18.3 ± 5.0	21.9 ± 3.2	15.8 ± 2.8	6.6 ± 1.4	3.8 ± 1.4	12.6 ± 3.5
82	2.7 ± 1.0	5.6 ± 1.6	19.5 ± 5.3	22.3 ± 3.2	17.3 ± 2.9	7.6 ± 1.5	3.6 ± 1.3	15.3 ± 4.1
85	1.5 ± 0.7	10.2 ± 2.6	15.8 ± 4.3	19.6 ± 2.9	12.9 ± 2.3	9.1 ± 1.7	2.7 ± 1.0	14.1 ± 3.8
88	1.9 ± 0.8	8.7 ± 2.2	14.4 ± 3.9	22.3 ± 3.1	11.3 ± 2.1	9.5 ± 1.7	2.5 ± 1.0	18.8 ± 4.9
91	2.5 ± 1.0	6.9 ± 1.9	14.4 ± 4.0	16.6 ± 2.5	11.8 ± 2.2	9.7 ± 1.7	2.0 ± 0.8	16.9 ± 4.5
94	0.6 ± 0.4	6.1 ± 1.7	11.7 ± 3.3	10.9 ± 1.9	11.9 ± 2.2	7.3 ± 1.4	2.3 ± 0.9	17.3 ± 4.6
97	1.1 ± 0.6	6.9 ± 1.9	10.1 ± 2.9	9.6 ± 1.8	6.0 ± 1.4	7.0 ± 1.4	2.1 ± 0.9	17.0 ± 4.5
100	0.9 ± 0.5	6.5 ± 1.8	9.2 ± 2.7	10.0 ± 1.8	3.0 ± 0.9	5.1 ± 1.2	1.8 ± 0.8	8.9 ± 2.6
103	0.2 ± 0.2	5.5 ± 1.6	7.7 ± 2.3	6.6 ± 1.4	1.4 ± 0.6	3.5 ± 1.0	0.7 ± 0.4	8.7 ± 2.5
106	—	2.5 ± 0.9	5.2 ± 1.7	4.6 ± 1.2	—	2.6 ± 0.9	1.4 ± 0.7	5.0 ± 1.6
109	0.5 ± 0.4	1.3 ± 0.6	2.5 ± 1.0	5.1 ± 1.3	—	2.4 ± 0.8	0.2 ± 0.3	1.0 ± 0.6
112	—	0.3 ± 0.3	0.8 ± 0.5	1.1 ± 0.6	—	—	—	—

Table E.8. Data of Fig. 4.21. p-shell cut for O at $\theta_{\pi^0} = 110.0°$.

T_{π^0}	$\frac{d^3\sigma}{dE_{\pi^0}\, d\Omega_{\pi^0}\, d\Omega_p}$ $\left[\frac{\mu b}{\text{MeV sr}^2}\right]$							
[MeV]	telescope 1	telescope 2	telescope 3	telescope 4	telescope 5	telescope 6	telescope 7	telescope 8
40	3.2 ± 3.3	6.4 ± 4.7	16.6 ± 7.5	32.5 ± 10.5	23.1 ± 8.9	2.9 ± 3.0	—	3.2 ± 3.2
43	—	2.0 ± 2.0	18.7 ± 6.3	42.4 ± 9.6	26.8 ± 7.6	3.7 ± 2.8	—	5.9 ± 3.5
46	1.4 ± 1.5	1.5 ± 1.5	18.2 ± 5.4	49.0 ± 9.1	28.8 ± 6.8	1.3 ± 1.4	1.5 ± 1.5	11.6 ± 4.2
49	—	4.6 ± 2.4	31.9 ± 6.4	49.8 ± 8.3	33.0 ± 6.6	4.2 ± 2.4	1.2 ± 1.2	9.1 ± 3.3
52	0.9 ± 0.9	4.7 ± 2.2	28.0 ± 5.4	52.0 ± 7.8	41.5 ± 6.8	6.9 ± 3.1	0.9 ± 0.9	15.8 ± 4.1
55	0.8 ± 0.8	6.4 ± 2.5	34.7 ± 5.7	65.3 ± 8.4	32.9 ± 5.6	3.7 ± 1.9	0.8 ± 0.8	13.4 ± 3.5
58	0.7 ± 0.7	4.9 ± 2.0	41.3 ± 5.9	61.7 ± 7.7	43.3 ± 6.2	5.8 ± 2.5	1.4 ± 1.0	22.2 ± 4.4
61	1.9 ± 1.2	4.4 ± 1.8	49.8 ± 6.4	64.6 ± 7.7	43.0 ± 5.9	4.7 ± 2.1	—	26.3 ± 4.7
64	1.1 ± 0.9	8.3 ± 2.6	47.8 ± 6.1	68.7 ± 7.8	53.6 ± 6.6	4.4 ± 1.9	—	24.0 ± 4.4
67	2.1 ± 1.2	3.3 ± 1.4	42.4 ± 5.4	76.7 ± 8.2	58.0 ± 6.7	7.0 ± 2.6	—	36.1 ± 5.4
70	2.0 ± 1.1	8.7 ± 2.5	63.6 ± 6.8	69.9 ± 7.5	57.5 ± 6.5	5.1 ± 2.1	—	37.3 ± 5.5
73	2.9 ± 1.4	9.0 ± 2.5	53.9 ± 6.1	64.7 ± 7.1	57.7 ± 6.5	9.1 ± 3.2	—	32.4 ± 5.0
76	0.5 ± 0.5	7.1 ± 2.2	52.3 ± 6.0	60.7 ± 6.8	69.0 ± 7.3	7.8 ± 2.8	1.5 ± 0.9	45.6 ± 6.3
79	2.0 ± 1.1	5.2 ± 1.8	56.3 ± 6.3	60.7 ± 6.8	50.7 ± 6.0	5.7 ± 2.2	2.6 ± 1.2	43.7 ± 6.2
82	0.5 ± 0.5	8.1 ± 2.4	52.5 ± 6.1	47.6 ± 5.9	50.0 ± 6.1	11.8 ± 3.9	0.5 ± 0.5	43.5 ± 6.2
85	2.7 ± 1.4	10.6 ± 2.9	42.9 ± 5.5	48.6 ± 6.1	45.0 ± 5.8	8.6 ± 3.1	2.8 ± 1.3	31.3 ± 5.0
88	2.8 ± 1.4	10.6 ± 3.0	49.5 ± 6.1	46.0 ± 6.0	46.8 ± 6.0	5.4 ± 2.2	1.8 ± 1.0	41.1 ± 6.2
91	1.2 ± 0.9	6.2 ± 2.2	35.2 ± 5.1	41.9 ± 5.8	45.2 ± 6.0	7.4 ± 2.8	0.6 ± 0.6	24.5 ± 4.5
94	1.9 ± 1.2	7.8 ± 2.6	33.6 ± 5.1	35.5 ± 5.3	40.8 ± 5.8	5.4 ± 2.3	1.3 ± 0.9	21.3 ± 4.2
97	3.4 ± 1.7	8.3 ± 2.7	30.5 ± 5.0	28.4 ± 4.8	30.3 ± 5.0	6.9 ± 2.8	1.4 ± 1.0	25.8 ± 4.8
100	1.4 ± 1.1	5.9 ± 2.3	30.2 ± 5.1	38.4 ± 5.9	33.0 ± 5.4	11.4 ± 4.1	1.5 ± 1.0	17.4 ± 3.9
103	1.5 ± 1.1	7.1 ± 2.6	21.9 ± 4.4	31.0 ± 5.3	28.2 ± 5.1	4.3 ± 2.1	1.6 ± 1.1	17.1 ± 4.0
106	1.7 ± 1.2	4.3 ± 2.0	25.5 ± 5.0	23.2 ± 4.7	18.4 ± 4.2	4.7 ± 2.3	1.7 ± 1.2	10.9 ± 3.2
109	1.8 ± 1.4	1.9 ± 1.3	7.6 ± 2.7	15.9 ± 4.0	13.3 ± 3.6	4.3 ± 2.2	1.9 ± 1.3	10.1 ± 3.2
112	2.0 ± 1.5	6.1 ± 2.6	6.2 ± 2.6	18.3 ± 4.5	13.5 ± 3.8	1.8 ± 1.4	—	4.0 ± 2.0
115	—	2.2 ± 1.6	2.3 ± 1.6	7.8 ± 3.0	4.5 ± 2.3	—	—	3.3 ± 1.9
118	—	2.4 ± 1.8	2.5 ± 1.8	1.2 ± 1.2	1.2 ± 1.3	2.2 ± 1.7	—	1.2 ± 1.2
121	1.3 ± 1.4	—	2.8 ± 2.0	—	—	—	—	—
124	—	—	—	1.6 ± 1.6	—	—	—	—

Table E.9. Data of Fig. 4.22. Complete spectra for O at $\theta_{\pi^0} = 110.0°$.

T_{π^0}	$\frac{d^3\sigma}{dE_{\pi^0}\, d\Omega_{\pi^0}\, d\Omega_p}$ $\left[\frac{\mu b}{\text{MeV sr}^2}\right]$							
[MeV]	telescope 1	telescope 2	telescope 3	telescope 4	telescope 5	telescope 6	telescope 7	telescope 8
40	16.8 ± 7.3	28.8 ± 9.7	52.5 ± 12.8	82.4 ± 16.0	47.2 ± 12.1	16.5 ± 7.2	14.3 ± 6.6	38.3 ± 10.8
43	8.8 ± 4.1	27.0 ± 7.6	54.8 ± 10.6	90.2 ± 13.6	66.4 ± 11.6	20.6 ± 6.7	12.5 ± 5.0	33.2 ± 8.0
46	15.5 ± 5.1	20.0 ± 5.6	55.3 ± 9.3	115.5 ± 13.7	66.8 ± 10.2	24.1 ± 6.6	2.6 ± 1.9	43.6 ± 8.1
49	5.1 ± 2.4	20.8 ± 5.2	72.8 ± 9.9	102.0 ± 11.5	66.1 ± 9.1	18.9 ± 5.2	7.2 ± 2.9	43.7 ± 7.2
52	4.2 ± 2.0	27.3 ± 5.7	65.0 ± 8.5	128.4 ± 12.1	88.4 ± 9.9	20.4 ± 5.1	4.2 ± 2.0	41.1 ± 6.4
55	3.6 ± 1.7	26.3 ± 5.3	64.5 ± 8.0	134.6 ± 11.8	71.2 ± 8.2	23.8 ± 5.4	8.7 ± 2.7	37.5 ± 5.7
58	6.9 ± 2.3	17.4 ± 3.9	95.4 ± 9.8	130.5 ± 11.0	77.3 ± 8.2	21.5 ± 4.9	8.3 ± 2.5	66.0 ± 7.5
61	7.4 ± 2.4	21.6 ± 4.3	87.7 ± 9.0	121.8 ± 10.2	86.8 ± 8.5	21.8 ± 4.8	10.4 ± 2.8	59.8 ± 6.8
64	5.9 ± 2.0	26.3 ± 4.8	96.7 ± 9.5	133.3 ± 10.7	85.9 ± 8.3	18.3 ± 4.1	8.7 ± 2.4	70.1 ± 7.4
67	6.9 ± 2.1	21.8 ± 4.1	85.5 ± 8.4	135.4 ± 10.4	84.8 ± 8.0	28.6 ± 5.7	8.0 ± 2.3	78.0 ± 7.7
70	6.9 ± 2.1	28.5 ± 4.8	88.5 ± 8.5	111.5 ± 9.0	89.9 ± 8.1	21.7 ± 4.5	5.2 ± 1.7	78.7 ± 7.5
73	8.6 ± 2.4	25.6 ± 4.5	84.4 ± 8.2	113.1 ± 9.0	97.6 ± 8.5	19.5 ± 4.1	3.7 ± 1.4	75.7 ± 7.3
76	4.1 ± 1.5	20.7 ± 3.9	84.0 ± 8.1	103.9 ± 8.5	101.8 ± 8.8	19.3 ± 4.1	5.1 ± 1.7	85.3 ± 7.9
79	6.1 ± 1.9	16.9 ± 3.4	85.3 ± 8.3	98.3 ± 8.3	71.8 ± 7.1	17.5 ± 3.9	7.2 ± 2.1	84.2 ± 7.9
82	3.9 ± 1.5	24.8 ± 4.5	75.4 ± 7.7	83.8 ± 7.6	79.3 ± 7.6	24.6 ± 5.0	7.0 ± 2.1	75.6 ± 7.5
85	4.1 ± 1.6	20.0 ± 3.9	60.7 ± 6.8	71.9 ± 7.0	65.1 ± 6.8	17.6 ± 4.0	6.2 ± 2.0	67.8 ± 7.1
88	5.9 ± 2.0	20.0 ± 4.0	74.9 ± 7.9	69.8 ± 7.1	66.6 ± 7.1	12.2 ± 3.1	6.0 ± 2.0	60.3 ± 6.7
91	6.3 ± 2.1	14.8 ± 3.4	52.7 ± 6.5	63.4 ± 6.8	70.2 ± 7.5	14.7 ± 3.6	5.3 ± 1.9	47.8 ± 6.0
94	4.2 ± 1.7	18.7 ± 4.0	43.6 ± 5.9	54.1 ± 6.4	52.3 ± 6.4	9.5 ± 2.8	3.1 ± 1.4	37.6 ± 5.3
97	3.2 ± 1.5	15.2 ± 3.6	36.8 ± 5.4	49.9 ± 6.2	45.9 ± 6.1	15.1 ± 3.8	2.0 ± 1.2	36.4 ± 5.3
100	2.7 ± 1.4	9.9 ± 2.9	38.5 ± 5.7	48.2 ± 6.3	44.0 ± 6.1	15.5 ± 4.0	2.1 ± 1.2	27.4 ± 4.7
103	1.5 ± 1.1	10.6 ± 3.1	31.6 ± 5.3	39.6 ± 5.8	36.6 ± 5.7	8.7 ± 2.8	2.3 ± 1.3	24.1 ± 4.5
106	1.6 ± 1.2	7.4 ± 2.6	31.8 ± 5.5	25.3 ± 4.8	21.2 ± 4.4	7.1 ± 2.6	2.5 ± 1.5	16.1 ± 3.8
109	1.7 ± 1.3	4.5 ± 2.1	8.2 ± 2.8	18.4 ± 4.2	12.9 ± 3.5	4.3 ± 2.0	2.7 ± 1.6	10.1 ± 3.1
112	1.9 ± 1.4	5.9 ± 2.5	6.0 ± 2.5	18.1 ± 4.3	13.1 ± 3.7	1.9 ± 1.4	—	4.0 ± 2.0
115	—	2.1 ± 1.5	2.2 ± 1.5	7.7 ± 2.9	4.4 ± 2.2	—	—	3.3 ± 1.9
118	—	2.4 ± 1.7	2.4 ± 1.7	1.2 ± 1.2	1.2 ± 1.2	2.3 ± 1.6	—	1.2 ± 1.2
121	1.3 ± 1.3	—	2.7 ± 1.9	—	—	—	—	—
124	—	—	—	1.5 ± 1.5	—	—	—	—

Table E.10. Data of Fig. 4.23. "s-shell" cut for O at $\theta_{\pi^0} = 110.0°$.

T_{π^0} [MeV]	$\frac{d^3\sigma}{dE_{\pi^0}\, d\Omega_{\pi^0}\, d\Omega_p}$ $\left[\frac{\mu b}{\text{MeV sr}^2}\right]$							
	telescope 1	telescope 2	telescope 3	telescope 4	telescope 5	telescope 6	telescope 7	telescope 8
40	13.9 ± 6.7	22.9 ± 8.7	36.7 ± 11.0	53.2 ± 12.9	26.1 ± 9.0	14.0 ± 6.6	14.2 ± 6.6	36.0 ± 10.6
43	8.7 ± 4.2	25.1 ± 7.5	37.1 ± 9.1	51.8 ± 10.3	41.8 ± 9.4	17.5 ± 6.2	12.4 ± 5.0	28.2 ± 7.5
46	14.1 ± 4.9	18.5 ± 5.5	37.9 ± 8.2	71.0 ± 10.7	40.3 ± 8.1	23.2 ± 6.7	1.3 ± 1.3	33.3 ± 7.1
49	5.0 ± 2.4	16.5 ± 4.7	42.9 ± 8.1	56.6 ± 8.5	35.7 ± 6.8	15.1 ± 4.6	6.1 ± 2.6	35.8 ± 6.6
52	3.3 ± 1.7	22.9 ± 5.4	38.6 ± 7.1	80.7 ± 9.6	50.0 ± 7.8	14.1 ± 4.1	3.4 ± 1.7	26.7 ± 5.1
55	2.8 ± 1.5	20.4 ± 4.7	32.3 ± 6.0	74.4 ± 8.7	40.6 ± 6.5	20.6 ± 5.1	7.9 ± 2.6	25.2 ± 4.6
58	6.2 ± 2.2	12.8 ± 3.3	56.3 ± 8.6	73.5 ± 8.2	37.1 ± 5.8	16.3 ± 4.1	7.0 ± 2.3	45.7 ± 6.1
61	5.6 ± 2.0	17.4 ± 4.0	41.3 ± 6.6	61.8 ± 7.1	46.6 ± 6.6	17.6 ± 4.3	10.4 ± 2.8	35.4 ± 5.1
64	4.8 ± 1.8	18.5 ± 4.0	51.6 ± 7.7	69.2 ± 7.5	35.9 ± 5.4	14.3 ± 3.6	8.6 ± 2.5	48.0 ± 5.9
67	4.9 ± 1.8	18.7 ± 4.0	45.4 ± 6.9	63.6 ± 6.9	30.7 ± 4.7	22.2 ± 4.9	8.0 ± 2.3	45.0 ± 5.5
70	5.0 ± 1.7	20.3 ± 4.1	29.3 ± 4.9	45.8 ± 5.4	35.9 ± 5.1	17.0 ± 3.9	5.1 ± 1.7	43.5 ± 5.2
73	5.8 ± 1.9	17.1 ± 3.6	33.8 ± 5.4	52.0 ± 5.8	43.2 ± 5.8	10.8 ± 2.8	3.7 ± 1.4	45.1 ± 5.3
76	3.6 ± 1.4	14.0 ± 3.2	34.7 ± 5.5	46.4 ± 5.5	36.6 ± 5.2	11.9 ± 3.0	3.7 ± 1.4	41.7 ± 5.1
79	4.2 ± 1.6	12.0 ± 2.9	32.3 ± 5.3	40.7 ± 5.1	23.9 ± 4.0	12.2 ± 3.1	4.8 ± 1.6	42.4 ± 5.2
82	3.4 ± 1.4	17.1 ± 3.7	25.8 ± 4.6	38.5 ± 5.0	31.6 ± 4.8	13.2 ± 3.3	6.5 ± 2.0	33.8 ± 4.6
85	1.5 ± 0.9	9.9 ± 2.6	20.1 ± 3.9	25.4 ± 4.0	22.3 ± 3.9	9.2 ± 2.6	3.6 ± 1.5	37.8 ± 5.0
88	3.2 ± 1.4	9.9 ± 2.7	27.8 ± 4.9	25.7 ± 4.1	21.8 ± 4.0	7.0 ± 2.3	4.4 ± 1.7	20.3 ± 3.6
91	5.1 ± 1.9	8.8 ± 2.6	19.1 ± 3.9	23.1 ± 4.0	26.8 ± 4.6	7.4 ± 2.4	4.7 ± 1.8	24.0 ± 4.1
94	2.4 ± 1.3	11.1 ± 3.0	11.6 ± 3.0	19.8 ± 3.7	13.2 ± 3.1	4.2 ± 1.7	1.8 ± 1.1	16.9 ± 3.4
97	—	7.2 ± 2.4	7.8 ± 2.4	22.3 ± 4.1	16.6 ± 3.6	8.3 ± 2.7	0.6 ± 0.7	11.0 ± 2.8
100	1.4 ± 1.0	4.2 ± 1.8	9.7 ± 2.8	10.8 ± 2.9	12.1 ± 3.1	4.1 ± 1.8	0.7 ± 0.7	10.3 ± 2.8
103	—	3.8 ± 1.8	10.4 ± 3.0	9.4 ± 2.8	9.2 ± 2.8	4.4 ± 1.9	0.7 ± 0.8	7.1 ± 2.4
106	—	3.3 ± 1.7	7.3 ± 2.6	2.5 ± 1.5	3.3 ± 1.7	2.4 ± 1.4	0.8 ± 0.8	5.2 ± 2.1
109	—	2.7 ± 1.6	0.9 ± 0.9	2.8 ± 1.6	—	—	0.9 ± 0.9	—

Table E.11. Data of Fig. 4.24. p-shell cut for O at $\theta_{\pi^0} = 129.7°$.

T_{π^0} [MeV]	$\frac{d^3\sigma}{dE_{\pi^0}\, d\Omega_{\pi^0}\, d\Omega_p}$ $\left[\frac{\mu b}{\text{MeV sr}^2}\right]$							
	telescope 1	telescope 2	telescope 3	telescope 4	telescope 5	telescope 6	telescope 7	telescope 8
40	—	—	30.8 ± 8.4	44.2 ± 10.1	13.2 ± 5.4	—	—	10.6 ± 4.8
43	1.4 ± 1.4	2.7 ± 2.0	30.4 ± 6.9	56.7 ± 9.5	32.0 ± 7.0	2.7 ± 2.0	—	12.6 ± 4.4
46	—	—	42.9 ± 7.2	61.2 ± 8.5	28.4 ± 5.7	4.0 ± 2.1	—	19.3 ± 4.7
49	0.8 ± 0.8	1.5 ± 1.1	41.4 ± 6.4	69.9 ± 8.3	34.9 ± 5.7	0.8 ± 0.8	—	20.1 ± 4.4
52	—	1.3 ± 1.0	39.5 ± 5.8	80.8 ± 8.4	51.6 ± 6.7	2.7 ± 1.4	0.6 ± 0.8	23.3 ± 4.5
55	1.7 ± 1.1	6.9 ± 2.4	40.8 ± 5.6	80.2 ± 8.0	47.8 ± 6.0	2.4 ± 1.2	0.5 ± 0.7	28.8 ± 4.9
58	2.1 ± 1.2	6.7 ± 2.3	66.0 ± 7.2	79.1 ± 7.6	47.8 ± 5.8	4.2 ± 1.7	0.5 ± 0.6	30.1 ± 4.8
61	0.9 ± 0.7	5.1 ± 1.9	62.6 ± 6.8	78.5 ± 7.3	47.2 ± 5.5	3.3 ± 1.4	0.9 ± 0.9	38.4 ± 5.5
64	1.7 ± 1.0	7.7 ± 2.4	67.4 ± 6.9	81.2 ± 7.2	63.9 ± 6.5	7.9 ± 2.3	1.2 ± 1.1	42.2 ± 5.7
67	0.8 ± 0.6	4.9 ± 1.7	64.9 ± 6.6	84.3 ± 7.2	65.1 ± 6.4	6.3 ± 2.0	—	43.3 ± 5.7
70	2.1 ± 1.1	5.0 ± 1.8	53.6 ± 5.9	66.1 ± 6.3	62.8 ± 6.3	6.4 ± 2.0	0.8 ± 0.8	49.5 ± 6.3
73	2.1 ± 1.1	6.4 ± 2.1	55.6 ± 6.0	66.0 ± 6.3	58.9 ± 6.1	5.3 ± 1.8	0.4 ± 0.5	48.7 ± 6.3
76	0.9 ± 0.7	5.4 ± 1.9	69.1 ± 7.1	69.0 ± 6.6	55.1 ± 6.0	5.6 ± 1.9	0.4 ± 0.5	44.4 ± 6.0
79	0.5 ± 0.5	5.2 ± 1.9	65.7 ± 7.0	58.2 ± 6.1	48.3 ± 5.6	6.8 ± 2.2	—	39.3 ± 5.6
82	2.1 ± 1.2	6.7 ± 2.3	55.8 ± 6.5	51.1 ± 5.8	40.4 ± 5.2	7.9 ± 2.5	0.9 ± 1.0	41.9 ± 6.0
85	0.6 ± 0.6	4.4 ± 1.8	43.1 ± 5.7	61.3 ± 6.7	54.6 ± 6.4	4.6 ± 1.8	0.5 ± 0.6	31.9 ± 5.1
88	3.0 ± 1.6	8.3 ± 2.8	51.5 ± 6.5	59.6 ± 6.8	43.9 ± 5.8	5.5 ± 2.1	0.6 ± 0.7	29.4 ± 5.0
91	2.0 ± 1.2	7.8 ± 2.7	39.2 ± 5.7	57.6 ± 6.9	36.5 ± 5.4	6.7 ± 2.4	—	23.7 ± 4.5
94	1.4 ± 1.1	2.1 ± 1.3	30.6 ± 5.2	41.6 ± 6.0	29.2 ± 5.0	5.8 ± 2.3	0.7 ± 0.8	20.8 ± 4.3
97	—	3.2 ± 1.7	24.9 ± 4.9	44.8 ± 6.5	25.8 ± 4.9	5.7 ± 2.4	—	20.8 ± 4.5
100	1.8 ± 1.4	4.5 ± 2.2	24.0 ± 5.0	41.6 ± 6.6	23.1 ± 4.9	5.5 ± 2.4	0.8 ± 1.0	15.9 ± 4.1
103	—	—	18.2 ± 4.5	28.0 ± 5.6	23.7 ± 5.2	4.1 ± 2.2	0.9 ± 1.1	17.7 ± 4.6
106	1.1 ± 1.2	3.3 ± 2.0	19.2 ± 4.9	18.1 ± 4.7	16.8 ± 4.6	5.7 ± 2.7	—	9.3 ± 3.4
109	—	2.5 ± 1.9	6.8 ± 3.1	16.4 ± 4.8	8.2 ± 3.4	2.6 ± 1.9	—	10.6 ± 3.9
112	—	—	6.3 ± 3.2	4.8 ± 2.8	6.4 ± 3.2	1.5 ± 1.5	—	3.1 ± 2.2
115	—	—	—	5.8 ± 3.4	5.8 ± 3.4	—	—	—
118	—	—	—	4.9 ± 3.4	—	—	—	—

Table E.12. Data of Fig. 4.25. Complete spectra for O at $\theta_{\pi^0} = 129.7°$.

T_{π^0} [MeV]	$\frac{d^3\sigma}{dE_{\pi^0}\, d\Omega_{\pi^0}\, d\Omega_p}$ $\left[\frac{\mu b}{\text{MeV sr}^2}\right]$							
	telescope 1	telescope 2	telescope 3	telescope 4	telescope 5	telescope 6	telescope 7	telescope 8
40	7.6 ± 3.9	26.3 ± 7.5	93.9 ± 14.3	139.1 ± 17.6	85.7 ± 13.5	26.7 ± 7.6	11.4 ± 4.9	47.0 ± 9.9
43	11.3 ± 4.0	24.9 ± 6.1	103.1 ± 12.4	146.5 ± 15.2	106.8 ± 12.6	20.2 ± 5.4	7.5 ± 3.2	59.6 ± 9.3
46	4.6 ± 2.1	23.6 ± 5.2	105.8 ± 11.0	152.8 ± 13.7	90.2 ± 10.0	28.4 ± 5.8	9.1 ± 3.1	63.2 ± 8.4
49	13.0 ± 3.4	17.9 ± 4.0	98.3 ± 9.5	174.1 ± 13.7	103.3 ± 9.8	19.6 ± 4.2	10.1 ± 3.0	74.0 ± 8.4
52	6.8 ± 2.2	19.6 ± 4.0	111.4 ± 9.6	160.5 ± 12.3	116.4 ± 9.9	24.8 ± 4.6	10.5 ± 2.9	76.7 ± 8.1
55	10.3 ± 2.7	33.0 ± 5.4	96.4 ± 8.4	169.4 ± 12.2	107.0 ± 8.9	29.0 ± 4.9	8.2 ± 2.4	79.9 ± 7.9
58	6.4 ± 1.9	27.7 ± 4.6	120.3 ± 9.3	173.7 ± 12.0	114.8 ± 9.0	32.0 ± 5.1	11.8 ± 2.9	85.1 ± 7.9
61	7.5 ± 2.0	22.9 ± 3.9	116.1 ± 8.8	161.6 ± 11.2	120.5 ± 9.0	22.3 ± 3.8	11.1 ± 2.7	93.7 ± 8.2
64	8.2 ± 2.1	22.0 ± 3.7	117.8 ± 8.7	145.3 ± 10.1	133.1 ± 9.4	25.6 ± 4.1	3.2 ± 2.1	96.1 ± 8.2
67	4.3 ± 1.4	27.4 ± 4.3	114.3 ± 8.3	144.7 ± 9.9	124.4 ± 8.8	25.0 ± 4.0	5.1 ± 1.6	99.5 ± 8.2
70	4.0 ± 1.4	26.9 ± 4.3	99.6 ± 7.7	121.5 ± 8.8	121.4 ± 8.7	23.5 ± 3.8	4.4 ± 1.5	108.1 ± 8.8
73	9.9 ± 2.4	21.7 ± 3.7	102.8 ± 7.9	124.3 ± 9.0	107.7 ± 8.1	18.7 ± 3.3	4.6 ± 1.5	99.1 ± 8.3
76	3.9 ± 1.4	20.5 ± 3.6	113.4 ± 8.6	106.7 ± 8.3	95.5 ± 7.7	19.8 ± 3.5	4.3 ± 1.6	84.4 ± 7.6
79	4.6 ± 1.6	17.5 ± 3.3	90.5 ± 7.6	95.0 ± 7.9	91.3 ± 7.6	25.2 ± 4.2	7.0 ± 2.0	79.2 ± 7.4
82	7.5 ± 2.1	16.0 ± 3.2	80.4 ± 7.3	84.6 ± 7.5	76.5 ± 7.0	19.7 ± 3.7	3.5 ± 1.4	77.4 ± 7.5
85	4.3 ± 1.6	14.1 ± 3.1	67.8 ± 6.8	85.6 ± 7.9	90.5 ± 8.1	15.9 ± 3.3	3.3 ± 1.4	64.8 ± 6.9
88	7.0 ± 2.2	16.4 ± 3.5	75.1 ± 7.5	79.7 ± 7.8	73.0 ± 7.3	11.2 ± 2.8	1.8 ± 1.0	51.7 ± 6.2
91	2.6 ± 1.3	15.3 ± 3.5	56.8 ± 6.6	79.5 ± 8.0	59.3 ± 6.8	14.8 ± 3.4	3.9 ± 1.7	47.1 ± 6.1
94	4.9 ± 2.0	10.5 ± 2.9	43.0 ± 5.9	56.8 ± 6.9	53.3 ± 6.6	7.1 ± 2.3	3.5 ± 1.6	37.8 ± 5.6
97	0.8 ± 0.8	10.2 ± 3.0	42.6 ± 6.2	56.5 ± 7.2	40.8 ± 6.1	8.0 ± 2.6	2.4 ± 1.4	34.4 ± 5.6
100	2.7 ± 1.6	8.8 ± 2.9	40.3 ± 6.4	53.4 ± 7.4	32.7 ± 5.7	8.0 ± 2.8	0.9 ± 0.9	33.1 ± 5.8
103	1.0 ± 1.0	2.0 ± 1.4	23.1 ± 5.0	35.0 ± 6.2	33.5 ± 6.1	5.0 ± 2.3	2.0 ± 1.4	21.6 ± 4.9
106	2.2 ± 1.6	3.3 ± 2.0	22.4 ± 5.2	22.0 ± 5.1	18.8 ± 4.8	5.6 ± 2.6	—	10.4 ± 3.5
109	—	2.5 ± 1.8	8.1 ± 3.3	15.8 ± 4.6	8.0 ± 3.3	2.6 ± 1.8	—	10.5 ± 3.8
112	—	—	6.3 ± 3.1	4.6 ± 2.7	6.3 ± 3.1	1.5 ± 1.5	—	3.1 ± 2.2
115	—	—	—	5.6 ± 3.2	5.7 ± 3.3	—	—	—
118	—	—	—	4.7 ± 3.3	—	—	—	—

Table E.13. Data of Fig. 4.26. "s-shell" cut for O at $\theta_{\pi^0} = 129.7°$.

T_{π^0}	$\frac{d^3\sigma}{dE_{\pi^0}\, d\Omega_{\pi^0}\, d\Omega_p}$ $\left[\frac{\mu b}{MeV\ sr^2}\right]$							
[MeV]	telescope 1	telescope 2	telescope 3	telescope 4	telescope 5	telescope 6	telescope 7	telescope 8
40	7.6 ± 3.9	26.5 ± 7.6	66.2 ± 12.0	98.0 ± 15.2	73.6 ± 12.8	26.7 ± 7.6	11.5 ± 4.9	37.6 ± 8.9
43	10.0 ± 3.8	22.5 ± 5.8	75.7 ± 10.7	94.0 ± 12.5	77.7 ± 10.9	17.7 ± 5.1	7.6 ± 3.2	48.4 ± 8.5
46	4.6 ± 2.1	23.7 ± 5.3	66.7 ± 8.7	96.2 ± 11.3	64.2 ± 8.6	24.8 ± 5.4	9.2 ± 3.1	45.7 ± 7.1
49	12.3 ± 3.3	16.6 ± 3.9	60.5 ± 7.4	109.2 ± 11.4	71.4 ± 8.3	18.9 ± 4.2	10.2 ± 3.0	55.9 ± 7.3
52	6.8 ± 2.2	18.5 ± 3.9	75.3 ± 7.9	85.9 ± 9.2	68.8 ± 7.6	22.4 ± 4.4	10.0 ± 2.8	55.5 ± 6.8
55	8.7 ± 2.4	26.6 ± 4.7	58.8 ± 6.5	94.9 ± 9.5	62.9 ± 6.9	26.8 ± 4.7	7.7 ± 2.3	53.4 ± 6.3
58	4.4 ± 1.6	21.5 ± 4.0	59.1 ± 6.3	99.8 ± 9.6	70.5 ± 7.1	28.1 ± 4.7	11.4 ± 2.7	57.3 ± 6.4
61	6.7 ± 1.9	18.2 ± 3.4	57.8 ± 6.0	88.3 ± 8.5	76.5 ± 7.3	19.2 ± 3.5	10.3 ± 2.5	58.0 ± 6.2
64	6.6 ± 1.8	14.8 ± 2.9	54.8 ± 5.6	69.6 ± 7.1	73.4 ± 6.9	18.2 ± 3.3	7.1 ± 1.9	56.6 ± 6.0
67	3.6 ± 1.3	22.8 ± 3.8	53.4 ± 5.4	66.0 ± 6.7	63.4 ± 6.1	19.0 ± 3.4	5.2 ± 1.6	58.9 ± 6.0
70	2.0 ± 0.9	22.2 ± 3.8	49.2 ± 5.2	59.4 ± 6.2	62.3 ± 6.1	17.5 ± 3.2	3.7 ± 1.3	61.6 ± 6.3
73	7.9 ± 2.0	15.7 ± 3.0	50.3 ± 5.3	62.0 ± 6.5	52.1 ± 5.5	13.7 ± 2.8	4.2 ± 1.4	53.1 ± 5.7
76	3.1 ± 1.2	15.3 ± 3.1	47.9 ± 5.3	41.8 ± 5.1	43.3 ± 5.0	14.6 ± 2.9	4.4 ± 1.5	42.2 ± 5.0
79	4.2 ± 1.5	12.5 ± 2.7	28.0 ± 4.0	40.0 ± 5.1	45.3 ± 5.3	18.7 ± 3.5	7.0 ± 2.0	41.7 ± 5.1
82	5.5 ± 1.8	9.5 ± 2.4	27.1 ± 4.0	36.1 ± 4.9	38.0 ± 4.9	12.1 ± 2.8	2.5 ± 1.2	37.2 ± 4.9
85	3.8 ± 1.5	9.8 ± 2.5	26.5 ± 4.1	27.6 ± 4.3	38.3 ± 5.1	11.5 ± 2.8	2.7 ± 1.3	34.1 ± 4.8
88	4.1 ± 1.6	8.2 ± 2.4	25.6 ± 4.2	23.3 ± 4.0	30.9 ± 4.7	5.9 ± 2.0	1.2 ± 0.9	23.4 ± 4.0
91	0.6 ± 0.6	7.7 ± 2.4	19.0 ± 3.7	24.7 ± 4.3	24.2 ± 4.2	8.4 ± 2.5	3.9 ± 1.7	24.1 ± 4.3
94	3.5 ± 1.6	8.4 ± 2.6	13.4 ± 3.2	17.1 ± 3.7	25.1 ± 4.5	1.4 ± 1.0	2.8 ± 1.5	17.6 ± 3.7
97	0.8 ± 0.8	7.1 ± 2.5	18.4 ± 4.0	13.6 ± 3.4	15.8 ± 3.7	2.4 ± 1.4	2.4 ± 1.4	14.1 ± 3.5
100	0.9 ± 0.9	4.4 ± 2.0	17.0 ± 4.1	13.5 ± 3.6	10.3 ± 3.1	2.7 ± 1.6	—	17.7 ± 4.2
103	1.0 ± 1.0	2.0 ± 1.4	5.3 ± 2.4	8.1 ± 2.9	10.4 ± 3.4	1.0 ± 1.0	1.0 ± 1.0	4.2 ± 2.1
106	1.1 ± 1.1	—	3.6 ± 2.1	4.5 ± 2.3	2.3 ± 1.7	—	—	1.2 ± 1.2
109	—	—	1.3 ± 1.4	—	—	—	—	—

Table E.14. Data of Fig. 4.32. Complete spectra for Fe at $\theta_{\pi^0} = 110.0°$.

T_{π^0} [MeV]	$\frac{d^3\sigma}{dE_{\pi^0}\, d\Omega_{\pi^0}\, d\Omega_p}$ $\left[\frac{\mu b}{\text{MeV sr}^2}\right]$							
	telescope 1	telescope 2	telescope 3	telescope 4	telescope 5	telescope 6	telescope 7	telescope 8
40	4.7 ± 4.8	27.2 ± 12.4	63.9 ± 19.3	99.3 ± 23.7	64.5 ± 19.1	8.5 ± 6.4	9.4 ± 6.9	56.7 ± 17.9
43	6.1 ± 4.5	20.7 ± 8.9	53.6 ± 14.7	80.2 ± 17.6	39.2 ± 16.9	25.0 ± 10.6	3.1 ± 3.1	61.6 ± 15.8
46	6.8 ± 4.3	26.6 ± 9.5	78.3 ± 17.3	115.9 ± 19.9	74.6 ± 16.1	18.8 ± 8.0	13.9 ± 6.2	34.7 ± 10.0
49	17.9 ± 7.0	26.1 ± 8.6	54.3 ± 12.4	125.3 ± 19.4	60.2 ± 12.8	21.3 ± 8.1	1.8 ± 1.8	54.4 ± 12.1
52	16.0 ± 6.1	22.7 ± 7.4	61.4 ± 12.8	82.8 ± 13.7	76.4 ± 14.2	41.3 ± 13.2	10.3 ± 4.4	47.3 ± 10.3
55	12.3 ± 4.8	46.6 ± 12.2	91.6 ± 16.7	124.9 ± 17.4	71.8 ± 13.0	22.5 ± 7.8	11.2 ± 4.3	57.4 ± 11.2
58	5.4 ± 2.7	26.4 ± 7.6	91.5 ± 16.3	101.4 ± 14.4	73.1 ± 12.8	20.9 ± 7.1	9.9 ± 3.8	63.8 ± 11.6
61	7.9 ± 3.3	19.2 ± 5.8	70.5 ± 12.9	100.1 ± 14.0	80.0 ± 13.4	26.2 ± 8.4	13.0 ± 4.3	52.0 ± 9.8
64	10.0 ± 3.8	23.0 ± 6.6	55.2 ± 10.5	80.2 ± 11.6	65.6 ± 11.3	28.3 ± 8.9	8.3 ± 3.2	67.2 ± 11.6
67	10.2 ± 3.8	19.1 ± 5.6	59.3 ± 10.9	109.0 ± 14.4	63.2 ± 10.8	21.8 ± 7.1	11.2 ± 3.8	51.8 ± 9.4
70	8.1 ± 3.2	26.0 ± 7.0	56.3 ± 10.4	88.7 ± 12.1	65.7 ± 11.0	15.6 ± 5.3	9.0 ± 3.2	55.8 ± 9.8
73	7.7 ± 3.0	22.6 ± 6.2	60.0 ± 10.8	102.3 ± 13.4	61.4 ± 10.3	22.0 ± 7.0	6.3 ± 2.5	52.6 ± 9.3
76	7.8 ± 3.1	21.4 ± 6.0	61.5 ± 11.1	91.6 ± 12.3	51.3 ± 9.0	23.7 ± 7.5	5.6 ± 2.3	56.5 ± 9.8
79	7.4 ± 3.0	19.1 ± 5.6	60.2 ± 11.0	79.1 ± 11.2	53.5 ± 9.4	25.5 ± 8.0	9.9 ± 3.4	47.4 ± 8.7
82	5.0 ± 2.4	18.0 ± 5.3	53.4 ± 10.1	81.0 ± 11.4	47.3 ± 8.7	22.3 ± 7.2	9.3 ± 3.3	42.5 ± 8.1
85	5.5 ± 2.6	22.1 ± 6.4	51.6 ± 10.0	61.8 ± 9.6	45.9 ± 8.6	16.6 ± 5.7	9.2 ± 3.4	41.5 ± 8.1
88	3.8 ± 2.1	12.1 ± 4.2	44.1 ± 9.0	60.3 ± 9.6	27.5 ± 6.2	17.5 ± 6.1	2.9 ± 1.8	34.0 ± 7.2
91	4.0 ± 2.2	14.7 ± 4.9	27.6 ± 6.5	55.1 ± 9.2	59.7 ± 10.8	7.4 ± 3.2	9.1 ± 3.5	31.6 ± 6.9
94	8.5 ± 3.6	9.3 ± 3.7	34.5 ± 7.7	46.6 ± 8.4	27.5 ± 6.4	8.8 ± 3.7	6.5 ± 2.9	32.4 ± 7.2
97	2.3 ± 1.7	10.0 ± 3.9	26.8 ± 6.7	34.7 ± 7.2	20.3 ± 5.4	9.4 ± 4.0	4.6 ± 2.5	11.6 ± 3.9
100	4.9 ± 2.7	10.7 ± 4.2	31.2 ± 7.5	27.3 ± 6.4	24.2 ± 6.2	5.6 ± 2.9	—	26.1 ± 6.6
103	4.0 ± 2.5	3.9 ± 2.4	20.7 ± 6.0	16.1 ± 4.9	13.1 ± 4.5	6.0 ± 3.1	5.3 ± 2.9	12.1 ± 4.3
106	2.9 ± 2.1	4.2 ± 2.6	11.2 ± 4.3	21.9 ± 6.0	8.5 ± 3.6	5.3 ± 3.0	—	23.3 ± 6.5
109	3.1 ± 2.3	7.6 ± 3.7	9.2 ± 4.0	19.0 ± 5.8	12.3 ± 4.6	5.7 ± 3.2	6.3 ± 3.4	12.7 ± 4.8
112	1.7 ± 1.7	5.0 ± 3.0	10.0 ± 4.3	17.3 ± 5.7	3.4 ± 2.4	1.6 ± 1.6	—	12.1 ± 4.8
115	—	—	3.6 ± 2.6	5.6 ± 3.3	1.8 ± 1.8	3.4 ± 2.6	—	1.9 ± 1.9
118	—	—	4.0 ± 2.9	6.2 ± 3.7	8.1 ± 4.2	1.9 ± 1.9	—	4.2 ± 3.0
121	—	2.2 ± 2.3	2.2 ± 2.3	2.3 ± 2.3	2.3 ± 2.3	—	—	4.6 ± 3.3
124	—	—	—	2.6 ± 2.6	—	2.4 ± 2.5	—	—

Table E.15. Data of Fig. 4.33. Complete spectra for Sn at $\theta_{\pi^0} = 110.0°$.

T_{π^0}	$\frac{d^3\sigma}{dE_{\pi^0}\, d\Omega_{\pi^0}\, d\Omega_p}$ $\left[\frac{\mu b}{\text{MeV sr}^2}\right]$							
[MeV]	telescope 1	telescope 2	telescope 3	telescope 4	telescope 5	telescope 6	telescope 7	telescope 8
40	6.8 ± 7.1	47.5 ± 20.8	65.8 ± 23.7	97.7 ± 28.2	88.6 ± 27.7	30.0 ± 16.6	28.6 ± 15.1	48.6 ± 19.7
43	13.0 ± 8.2	30.0 ± 13.2	37.4 ± 14.0	127.8 ± 27.5	60.3 ± 18.3	18.9 ± 10.5	13.6 ± 8.2	48.3 ± 16.1
46	—	31.3 ± 12.1	115.1 ± 27.3	144.7 ± 26.8	113.1 ± 25.0	35.9 ± 15.4	13.2 ± 7.0	60.8 ± 16.5
49	2.4 ± 2.5	36.0 ± 12.3	99.9 ± 23.0	118.3 ± 21.4	72.2 ± 16.8	29.6 ± 12.5	12.6 ± 6.0	58.9 ± 14.7
52	15.5 ± 6.9	34.6 ± 11.2	93.3 ± 20.8	97.0 ± 17.4	90.9 ± 18.7	30.6 ± 12.3	14.2 ± 5.9	67.0 ± 15.0
55	11.4 ± 5.2	30.6 ± 9.8	98.2 ± 21.0	97.6 ± 16.5	88.9 ± 17.6	27.0 ± 10.8	18.7 ± 6.5	61.0 ± 13.3
58	12.9 ± 5.5	22.7 ± 7.6	49.5 ± 11.9	94.8 ± 15.6	84.1 ± 16.3	22.6 ± 9.1	19.4 ± 6.3	65.3 ± 13.5
61	10.4 ± 4.6	33.4 ± 9.9	67.2 ± 14.8	137.4 ± 20.1	63.3 ± 12.9	40.9 ± 14.9	20.3 ± 6.3	61.8 ± 12.7
64	9.4 ± 4.2	45.7 ± 12.5	82.8 ± 17.3	108.3 ± 16.4	74.1 ± 14.2	26.9 ± 10.2	14.8 ± 5.0	61.1 ± 12.3
67	14.4 ± 5.5	22.0 ± 6.9	74.5 ± 15.6	129.8 ± 18.6	72.8 ± 13.8	17.5 ± 7.0	9.3 ± 3.6	60.7 ± 12.0
70	11.6 ± 4.6	31.3 ± 9.0	67.7 ± 14.3	141.5 ± 19.7	65.0 ± 12.5	21.2 ± 8.2	7.7 ± 3.2	73.7 ± 13.8
73	13.9 ± 5.2	35.5 ± 9.9	55.3 ± 12.0	124.5 ± 17.6	67.3 ± 12.7	25.2 ± 9.5	8.3 ± 3.3	63.5 ± 12.1
76	5.1 ± 2.6	20.0 ± 6.3	54.4 ± 11.9	83.5 ± 13.0	71.5 ± 13.4	16.8 ± 6.7	9.5 ± 3.6	56.4 ± 11.1
79	12.4 ± 4.9	25.7 ± 7.7	58.7 ± 12.7	91.8 ± 14.0	56.7 ± 11.2	21.8 ± 8.4	16.2 ± 5.0	70.4 ± 13.3
82	8.6 ± 3.8	18.2 ± 6.0	47.6 ± 10.8	117.5 ± 17.1	67.6 ± 13.0	18.9 ± 7.5	11.3 ± 4.0	55.8 ± 11.2
85	8.0 ± 3.7	26.1 ± 8.0	54.9 ± 12.3	86.3 ± 13.7	47.9 ± 10.1	22.0 ± 8.6	4.8 ± 2.5	48.8 ± 10.3
88	6.0 ± 3.1	20.3 ± 6.7	52.1 ± 11.9	78.6 ± 13.0	44.4 ± 9.7	7.4 ± 3.7	8.8 ± 3.7	55.1 ± 11.4
91	8.9 ± 4.1	16.4 ± 5.8	32.9 ± 8.5	66.0 ± 11.7	54.4 ± 11.4	21.1 ± 8.4	6.6 ± 3.2	37.4 ± 8.8
94	4.0 ± 2.6	13.3 ± 5.2	28.4 ± 7.8	67.1 ± 12.0	34.8 ± 8.5	8.2 ± 4.1	8.4 ± 3.7	34.1 ± 8.4
97	4.3 ± 2.7	9.9 ± 4.4	23.4 ± 7.0	49.6 ± 10.1	34.2 ± 8.6	10.0 ± 4.8	4.5 ± 2.7	29.1 ± 7.7
100	6.1 ± 3.5	7.6 ± 3.8	22.1 ± 6.9	32.8 ± 8.0	27.5 ± 7.6	5.4 ± 3.2	—	23.4 ± 6.9
103	3.3 ± 2.5	9.9 ± 4.6	17.5 ± 6.1	20.3 ± 6.2	23.1 ± 7.0	5.8 ± 3.5	3.5 ± 2.5	21.9 ± 6.8
106	1.8 ± 1.9	12.5 ± 5.5	10.4 ± 4.6	31.2 ± 8.3	16.1 ± 5.9	7.9 ± 4.4	—	18.3 ± 6.3
109	3.9 ± 3.0	7.8 ± 4.2	7.5 ± 4.0	17.9 ± 6.3	19.5 ± 6.8	1.7 ± 1.8	2.0 ± 2.1	9.9 ± 4.7
112	2.1 ± 2.2	8.4 ± 4.6	8.2 ± 4.3	6.5 ± 3.8	12.7 ± 5.5	—	—	13.0 ± 5.6
115	2.3 ± 2.4	4.6 ± 3.4	4.5 ± 3.3	7.1 ± 4.2	2.3 ± 2.3	—	7.3 ± 4.4	2.4 ± 2.4
118	—	—	—	—	2.6 ± 2.6	—	2.7 ± 2.7	10.4 ± 5.4
121	—	—	5.5 ± 4.0	2.9 ± 2.9	5.7 ± 4.1	—	—	5.8 ± 4.2
124	—	—	—	3.3 ± 3.3	—	—	—	—

Table E.16. Data of Fig. 4.34. Complete spectra for Pb at $\theta_{\pi^0} = 110.0°$.

T_{π^0}	$\frac{d^3\sigma}{dE_{\pi^0}\, d\Omega_{\pi^0}\, d\Omega_p}$ $\left[\frac{\mu b}{MeV\ sr^2}\right]$							
[MeV]	telescope 1	telescope 2	telescope 3	telescope 4	telescope 5	telescope 6	telescope 7	telescope 8
40	—	16.5 ± 13.9	69.5 ± 34.0	60.0 ± 26.0	48.4 ± 24.6	34.1 ± 27.0	57.3 ± 27.3	52.0 ± 25.4
43	5.7 ± 6.2	21.5 ± 14.6	35.3 ± 18.4	134.3 ± 39.6	42.1 ± 19.6	22.2 ± 17.6	12.5 ± 9.3	45.3 ± 20.1
46	21.5 ± 13.3	36.4 ± 20.6	83.5 ± 34.7	122.1 ± 34.5	118.8 ± 42.1	23.4 ± 17.7	18.8 ± 10.5	42.6 ± 17.7
49	16.9 ± 10.4	34.9 ± 19.1	80.3 ± 32.6	148.5 ± 38.7	105.6 ± 36.8	47.2 ± 32.9	22.1 ± 10.5	50.1 ± 18.6
52	13.8 ± 8.5	41.4 ± 21.5	63.1 ± 25.7	115.8 ± 30.3	88.7 ± 30.8	34.2 ± 24.0	21.0 ± 9.5	76.2 ± 25.0
55	16.3 ± 9.3	43.8 ± 22.2	51.3 ± 21.0	170.7 ± 41.3	55.7 ± 20.1	21.7 ± 15.5	30.4 ± 11.6	62.1 ± 20.5
58	14.4 ± 8.2	38.6 ± 19.6	74.2 ± 28.9	120.5 ± 30.0	68.0 ± 23.5	22.4 ± 15.8	17.9 ± 7.7	69.1 ± 22.0
61	14.9 ± 8.3	26.3 ± 13.8	83.9 ± 32.2	162.4 ± 38.6	77.3 ± 26.1	30.5 ± 21.0	14.2 ± 6.4	73.8 ± 23.0
64	8.6 ± 5.3	39.0 ± 19.5	92.9 ± 35.2	160.5 ± 38.0	87.4 ± 29.0	25.5 ± 17.7	11.3 ± 5.4	63.2 ± 19.9
67	19.4 ± 10.0	22.8 ± 12.0	88.5 ± 33.5	118.7 ± 28.8	86.4 ± 28.5	18.9 ± 13.3	15.9 ± 6.6	84.9 ± 25.5
70	16.9 ± 8.8	34.6 ± 17.3	81.1 ± 30.8	133.5 ± 31.7	77.6 ± 25.7	25.0 ± 17.3	8.3 ± 4.3	88.0 ± 26.2
73	19.1 ± 9.7	30.4 ± 15.3	67.4 ± 25.8	115.0 ± 27.7	77.1 ± 25.5	22.9 ± 15.8	14.4 ± 6.0	72.7 ± 22.0
76	19.4 ± 9.9	33.7 ± 16.8	74.9 ± 28.5	113.8 ± 27.4	59.0 ± 20.0	32.5 ± 22.1	19.5 ± 7.4	61.9 ± 19.1
79	10.9 ± 6.2	17.6 ± 9.5	71.5 ± 27.4	94.6 ± 23.5	64.6 ± 21.8	20.6 ± 14.4	11.9 ± 5.4	80.3 ± 24.2
82	6.4 ± 4.2	24.1 ± 12.5	64.8 ± 25.0	78.2 ± 20.0	57.4 ± 19.7	23.6 ± 16.4	8.7 ± 4.4	99.6 ± 29.5
85	3.5 ± 2.9	17.9 ± 9.8	59.5 ± 23.3	81.3 ± 20.9	52.6 ± 18.4	13.5 ± 9.8	5.7 ± 3.6	70.2 ± 21.8
88	5.5 ± 3.9	20.6 ± 11.1	48.3 ± 19.3	85.7 ± 22.0	53.8 ± 18.9	14.2 ± 10.3	17.9 ± 7.4	59.6 ± 19.0
91	9.6 ± 5.9	21.6 ± 11.6	43.8 ± 17.8	50.5 ± 14.5	42.2 ± 15.4	19.3 ± 13.8	8.3 ± 4.6	47.3 ± 15.8
94	6.1 ± 4.4	9.6 ± 6.1	48.3 ± 19.6	59.6 ± 16.7	33.6 ± 12.9	19.0 ± 13.6	4.4 ± 3.3	36.2 ± 12.9
97	2.2 ± 2.4	18.4 ± 10.4	38.3 ± 16.1	53.1 ± 15.5	28.0 ± 11.3	13.5 ± 10.1	2.4 ± 2.4	38.7 ± 13.8
100	4.7 ± 3.9	11.0 ± 7.0	18.5 ± 9.0	20.5 ± 8.1	19.3 ± 8.7	3.6 ± 3.5	—	25.4 ± 10.2
103	2.5 ± 2.7	11.9 ± 7.6	33.3 ± 14.7	39.4 ± 13.0	20.9 ± 9.4	11.8 ± 9.1	5.5 ± 4.1	24.9 ± 10.3
106	5.5 ± 4.5	7.7 ± 5.7	14.5 ± 7.9	21.4 ± 8.8	22.7 ± 10.2	6.4 ± 5.6	3.0 ± 3.1	16.3 ± 7.9
109	—	8.4 ± 6.2	15.7 ± 8.5	11.6 ± 6.3	21.9 ± 10.2	4.6 ± 4.5	—	29.5 ± 12.2
112	3.3 ± 3.5	6.1 ± 5.1	20.0 ± 10.4	9.5 ± 5.9	9.0 ± 5.8	5.1 ± 4.9	—	25.7 ± 11.4
115	—	3.3 ± 3.7	9.4 ± 6.4	13.9 ± 7.5	9.8 ± 6.4	—	—	3.5 ± 3.6
118	—	—	6.9 ± 5.5	—	3.6 ± 3.8	—	—	—
121	—	—	—	4.3 ± 4.4	—	—	—	—
124	—	—	—	4.8 ± 5.0	4.6 ± 4.8	—	—	—
127	—	—	—	—	—	—	—	5.6 ± 5.8

E.3 Single Arm $d^2\sigma/dE_{\pi^0}\, d\Omega_{\pi^0}$ Spectra

The tables below list all data in the single arm (π^+, π^0) cross section spectra of Figs. 4.36 – 4.40.

Table E.17. Data of Fig. 4.36. Energy spectra for $O(\pi^+,\pi^0)$.

T_{π^0} [MeV]	$\frac{d^2\sigma}{dE_{\pi^0}\,d\Omega_{\pi^0}}$ $\left[\frac{\mu b}{MeV\,sr}\right]$			
	$\theta_{\pi^0} = 70.0°$	$\theta_{\pi^0} = 80.0°$	$\theta_{\pi^0} = 110.0°$	$\theta_{\pi^0} = 129.7°$
38	—	—	89.1 ± 28.5	142.2 ± 29.2
39	—	—	102.0 ± 23.9	145.0 ± 27.6
40	—	—	154.7 ± 25.1	170.1 ± 26.7
41	—	—	125.6 ± 20.6	142.1 ± 23.8
42	—	—	102.0 ± 19.9	152.4 ± 22.4
43	—	—	145.0 ± 21.9	166.4 ± 22.2
44	—	—	141.9 ± 19.5	160.9 ± 20.1
45	—	39.5 ± 22.9	140.6 ± 17.5	135.2 ± 17.8
46	—	81.2 ± 32.9	123.4 ± 15.7	146.0 ± 17.8
47	—	32.1 ± 20.2	138.2 ± 16.1	153.3 ± 17.5
48	—	86.2 ± 24.2	136.2 ± 15.3	148.9 ± 16.9
49	—	75.2 ± 20.4	139.8 ± 15.3	127.8 ± 14.9
50	101.8 ± 25.6	75.9 ± 19.8	135.1 ± 13.1	149.4 ± 15.9
51	47.6 ± 17.5	75.7 ± 17.7	149.6 ± 13.8	176.7 ± 17.0
52	57.4 ± 20.1	77.7 ± 17.7	130.1 ± 13.7	150.8 ± 15.6
53	65.3 ± 17.7	65.7 ± 16.0	160.7 ± 13.5	183.8 ± 16.9
54	86.0 ± 18.6	63.6 ± 15.4	156.0 ± 14.0	181.6 ± 16.5
55	75.5 ± 16.7	84.1 ± 16.0	131.6 ± 12.8	161.3 ± 15.0
56	74.5 ± 16.7	105.2 ± 16.4	142.1 ± 13.2	194.2 ± 16.5
57	64.3 ± 14.2	107.2 ± 16.1	136.8 ± 12.0	191.1 ± 16.3
58	69.9 ± 14.9	56.8 ± 12.4	153.0 ± 12.3	176.9 ± 15.3
59	57.3 ± 13.5	70.7 ± 12.3	140.8 ± 12.2	191.4 ± 15.8
60	43.5 ± 11.7	63.1 ± 11.4	159.8 ± 11.8	176.2 ± 15.0
61	55.2 ± 13.7	55.0 ± 10.4	167.5 ± 12.9	193.4 ± 15.5
62	42.5 ± 12.3	66.8 ± 11.8	153.1 ± 11.7	178.0 ± 15.0
63	81.8 ± 12.1	76.0 ± 11.4	139.8 ± 11.4	186.1 ± 15.0
64	70.5 ± 11.5	75.5 ± 11.5	151.9 ± 12.0	177.9 ± 14.6
65	57.5 ± 11.5	63.3 ± 10.3	157.9 ± 12.0	188.4 ± 14.8
66	48.6 ± 11.1	91.2 ± 12.0	155.9 ± 11.5	159.8 ± 13.2
67	74.7 ± 11.5	83.9 ± 11.2	173.5 ± 11.9	147.1 ± 12.5
68	76.6 ± 11.7	70.9 ± 10.3	148.0 ± 11.5	159.2 ± 13.4
69	63.8 ± 10.7	60.6 ± 9.3	155.2 ± 11.2	165.3 ± 13.8
70	50.3 ± 9.6	74.9 ± 10.1	160.3 ± 11.0	171.4 ± 13.8
71	60.0 ± 9.4	86.9 ± 10.7	161.3 ± 11.1	174.6 ± 14.1
72	44.2 ± 9.0	69.7 ± 9.7	146.9 ± 10.5	161.4 ± 13.6
73	66.0 ± 9.2	75.0 ± 9.8	170.5 ± 11.2	154.9 ± 13.2
74	40.3 ± 8.3	79.7 ± 9.7	173.7 ± 11.6	143.7 ± 12.6
75	68.4 ± 9.5	86.5 ± 10.1	160.4 ± 11.2	140.1 ± 12.4
76	70.8 ± 9.3	74.9 ± 9.6	163.4 ± 11.3	135.9 ± 12.5
77	57.1 ± 9.5	85.9 ± 10.0	153.9 ± 11.1	137.6 ± 12.9
78	70.3 ± 9.5	66.2 ± 8.5	146.2 ± 10.9	142.5 ± 12.8
79	53.3 ± 8.9	77.3 ± 9.5	160.0 ± 11.0	139.7 ± 12.9
80	57.5 ± 8.6	78.5 ± 9.2	139.7 ± 10.5	147.6 ± 13.4
81	61.4 ± 9.1	92.9 ± 9.9	127.9 ± 10.3	149.7 ± 13.7
82	49.3 ± 7.8	91.8 ± 9.6	126.4 ± 10.3	147.4 ± 13.8
83	79.0 ± 9.2	76.8 ± 8.8	124.8 ± 10.3	139.8 ± 13.5
84	70.5 ± 9.1	85.1 ± 9.3	140.4 ± 10.6	127.8 ± 12.8
85	58.5 ± 8.5	75.4 ± 8.7	128.7 ± 10.5	137.6 ± 13.3
86	53.4 ± 8.1	88.2 ± 9.2	139.6 ± 10.6	133.0 ± 13.6
87	62.5 ± 8.8	78.2 ± 8.8	125.5 ± 10.1	128.5 ± 13.3
88	60.1 ± 7.9	90.0 ± 9.2	127.9 ± 10.7	113.1 ± 12.7

(continued)

Table E.17 (continued)

T_{π^0} [MeV]	$\frac{d^2\sigma}{dE_{\pi^0}\,d\Omega_{\pi^0}}$ $\left[\frac{\mu b}{MeV\,sr}\right]$			
	$\theta_{\pi^0} = 70.0°$	$\theta_{\pi^0} = 80.0°$	$\theta_{\pi^0} = 110.0°$	$\theta_{\pi^0} = 129.7°$
89	58.0 ± 8.1	66.4 ± 7.9	109.9 ± 9.6	101.4 ± 12.1
90	74.3 ± 8.8	87.7 ± 9.0	126.4 ± 10.3	109.4 ± 12.4
91	63.0 ± 8.3	78.8 ± 8.5	107.8 ± 9.7	92.7 ± 11.7
92	61.0 ± 7.7	73.0 ± 8.4	109.6 ± 10.1	102.0 ± 12.4
93	59.9 ± 8.3	84.7 ± 9.0	106.2 ± 9.8	113.6 ± 13.0
94	66.2 ± 8.6	81.2 ± 8.9	106.6 ± 9.9	94.4 ± 12.3
95	76.3 ± 8.9	80.5 ± 8.9	115.9 ± 10.5	83.9 ± 11.8
96	76.2 ± 8.9	84.7 ± 8.9	84.1 ± 8.9	105.3 ± 13.5
97	58.3 ± 8.6	74.9 ± 8.2	96.1 ± 10.0	68.8 ± 10.9
98	77.5 ± 8.9	71.4 ± 8.3	103.9 ± 9.7	102.0 ± 13.8
99	81.0 ± 9.6	75.5 ± 8.9	84.4 ± 8.8	67.1 ± 11.1
100	65.2 ± 8.6	72.1 ± 8.4	88.2 ± 9.3	56.6 ± 10.6
101	62.1 ± 8.8	61.3 ± 8.1	67.5 ± 8.3	76.0 ± 12.5
102	63.2 ± 8.7	56.4 ± 7.8	83.4 ± 10.0	63.5 ± 11.6
103	55.1 ± 8.2	77.8 ± 8.7	73.4 ± 8.7	77.6 ± 12.7
104	62.5 ± 8.5	72.4 ± 8.7	76.0 ± 9.4	59.4 ± 11.3
105	72.7 ± 9.0	69.8 ± 8.4	75.4 ± 9.5	57.4 ± 11.9
106	70.5 ± 9.3	56.1 ± 7.8	61.4 ± 8.6	47.2 ± 10.3
107	68.0 ± 9.4	75.3 ± 9.0	69.0 ± 9.2	52.6 ± 11.2
108	70.2 ± 9.5	72.5 ± 8.9	69.0 ± 9.3	33.5 ± 9.4
109	73.8 ± 9.5	75.8 ± 8.8	61.1 ± 9.3	44.3 ± 10.6
110	72.9 ± 9.7	47.7 ± 7.4	70.1 ± 8.8	41.8 ± 10.9
111	53.8 ± 8.8	63.4 ± 8.3	47.2 ± 8.4	13.9 ± 7.4
112	64.7 ± 9.1	59.9 ± 8.0	51.7 ± 8.5	36.6 ± 10.7
113	60.5 ± 8.9	52.7 ± 7.8	49.1 ± 7.6	46.0 ± 12.0
114	73.4 ± 9.0	62.8 ± 8.3	48.0 ± 8.9	26.9 ± 9.6
115	64.9 ± 8.9	64.9 ± 8.5	41.9 ± 8.2	33.6 ± 10.7
116	70.1 ± 9.2	62.3 ± 8.4	47.0 ± 8.8	7.7 ± 6.7
117	60.3 ± 8.9	67.4 ± 8.7	36.6 ± 7.6	8.4 ± 7.2
118	63.4 ± 9.3	65.6 ± 8.8	48.7 ± 8.8	23.6 ± 10.6
119	58.4 ± 8.7	47.7 ± 7.5	32.4 ± 7.4	11.9 ± 8.3
120	42.7 ± 8.3	60.3 ± 8.5	23.9 ± 7.4	15.3 ± 8.9
121	67.9 ± 10.0	52.4 ± 8.2	30.0 ± 6.8	—
122	65.5 ± 9.7	46.1 ± 7.8	34.8 ± 8.2	—
123	44.7 ± 8.6	45.5 ± 7.9	32.6 ± 7.4	—
124	57.5 ± 8.7	47.7 ± 8.2	22.6 ± 7.2	—
125	57.4 ± 9.3	55.8 ± 8.9	40.8 ± 8.6	—
126	40.0 ± 8.7	57.1 ± 8.7	24.1 ± 6.7	—
127	43.3 ± 8.1	48.0 ± 8.2	17.5 ± 5.9	—
128	48.8 ± 8.8	41.7 ± 8.1	24.4 ± 7.1	—
129	53.0 ± 8.8	28.1 ± 6.4	19.2 ± 6.4	—
130	41.9 ± 7.7	44.0 ± 7.8	11.2 ± 5.0	—
131	60.4 ± 9.6	24.0 ± 6.3	10.0 ± 7.0	—
132	37.7 ± 8.7	33.7 ± 7.2	19.7 ± 7.0	—
133	43.3 ± 8.9	25.3 ± 6.1	—	—
134	36.7 ± 8.1	42.5 ± 7.9	—	—
135	43.9 ± 8.7	24.4 ± 6.4	—	—
136	29.1 ± 7.0	35.0 ± 7.6	—	—
137	21.2 ± 7.7	16.4 ± 5.3	—	—
138	33.7 ± 8.1	10.7 ± 4.4	—	—
139	31.5 ± 7.6	34.3 ± 7.6	—	—
140	33.8 ± 8.2	24.8 ± 6.5	—	—

Table E.18. Data of Fig. 4.37. *A*-dependence of the (π^+, π^0) reaction.

T_{π^0} [MeV]	$\frac{d^2\sigma}{dE_{\pi^0}\, d\Omega_{\pi^0}}$ $\left[\frac{\mu b}{\text{MeV sr}}\right]$			
	O	Fe	Sn	Pb
38	89.1 ± 28.5	147.9 ± 42.3	279.4 ± 69.9	333.0 ± 113.5
39	102.0 ± 23.9	169.6 ± 33.7	357.9 ± 57.9	399.1 ± 86.5
40	154.7 ± 25.1	193.3 ± 30.9	331.6 ± 49.1	369.5 ± 73.4
41	125.6 ± 20.6	200.7 ± 28.2	313.6 ± 42.9	434.0 ± 68.1
42	102.0 ± 19.9	155.8 ± 29.3	270.6 ± 45.1	297.5 ± 76.5
43	145.0 ± 21.9	132.8 ± 28.4	211.6 ± 42.2	315.2 ± 78.6
44	141.9 ± 19.5	174.2 ± 26.1	321.0 ± 40.6	348.8 ± 66.5
45	140.6 ± 17.5	186.8 ± 23.2	305.0 ± 34.8	412.0 ± 57.5
46	123.4 ± 15.7	198.9 ± 22.5	357.5 ± 35.2	413.8 ± 54.2
47	138.2 ± 16.1	172.0 ± 20.9	285.9 ± 31.3	433.5 ± 54.7
48	136.2 ± 15.3	215.6 ± 21.8	327.6 ± 31.5	425.6 ± 51.4
49	139.8 ± 15.3	173.1 ± 20.2	304.2 ± 30.5	384.9 ± 51.4
50	135.1 ± 13.1	189.2 ± 16.6	312.2 ± 25.2	448.7 ± 38.9
51	149.6 ± 13.8	200.7 ± 17.6	297.0 ± 24.9	397.2 ± 39.4
52	130.1 ± 13.7	160.2 ± 18.4	242.0 ± 25.9	365.4 ± 48.2
53	160.7 ± 13.5	215.5 ± 17.0	332.7 ± 24.6	450.5 ± 38.6
54	156.0 ± 14.0	183.2 ± 17.9	241.7 ± 23.9	380.9 ± 44.6
55	131.6 ± 12.8	187.3 ± 17.8	255.6 ± 24.0	369.8 ± 43.9
56	142.1 ± 13.2	167.9 ± 17.2	248.7 ± 23.9	353.9 ± 44.1
57	136.8 ± 12.0	176.7 ± 15.6	269.0 ± 22.0	419.7 ± 39.5
58	153.0 ± 12.3	217.7 ± 16.5	290.8 ± 22.0	417.2 ± 37.4
59	140.8 ± 12.2	188.4 ± 16.5	271.1 ± 22.7	415.9 ± 41.5
60	159.8 ± 11.8	214.3 ± 14.8	277.6 ± 19.4	469.4 ± 33.9
61	167.5 ± 12.9	180.9 ± 15.9	264.1 ± 21.9	367.9 ± 39.2
62	153.1 ± 11.7	187.3 ± 14.6	288.8 ± 20.8	409.1 ± 35.4
63	139.8 ± 11.4	188.0 ± 15.2	225.4 ± 19.2	355.2 ± 35.8
64	151.9 ± 12.0	172.5 ± 14.7	273.0 ± 21.0	379.7 ± 37.0
65	157.9 ± 12.0	181.5 ± 14.7	276.5 ± 20.6	409.5 ± 36.6
66	155.9 ± 11.5	186.4 ± 14.2	289.6 ± 20.2	411.8 ± 34.5
67	173.5 ± 11.9	170.1 ± 13.1	297.1 ± 19.8	467.0 ± 34.9
68	148.0 ± 11.5	179.2 ± 15.1	244.9 ± 20.2	380.1 ± 38.2
69	155.2 ± 11.2	184.4 ± 14.1	276.2 ± 19.6	394.8 ± 34.2
70	160.3 ± 11.0	181.7 ± 13.0	293.7 ± 19.0	385.2 ± 30.5
71	161.3 ± 11.1	166.5 ± 12.9	278.5 ± 18.9	428.1 ± 33.6
72	146.9 ± 10.5	165.5 ± 12.6	240.6 ± 17.3	367.2 ± 30.8
73	170.5 ± 11.2	182.8 ± 12.4	267.0 ± 17.2	439.4 ± 30.3
74	173.7 ± 11.6	167.9 ± 12.7	263.3 ± 18.0	362.1 ± 30.5
75	160.4 ± 11.2	181.3 ± 13.4	269.6 ± 18.5	380.9 ± 32.4
76	163.4 ± 11.3	159.4 ± 12.8	232.4 ± 17.4	398.1 ± 33.1
77	153.9 ± 11.1	153.2 ± 12.8	269.9 ± 19.0	387.2 ± 33.8
78	146.2 ± 10.9	143.6 ± 12.8	228.4 ± 17.9	356.0 ± 33.9
79	160.0 ± 11.0	172.9 ± 12.6	270.8 ± 17.8	395.5 ± 30.4
80	139.7 ± 10.5	133.5 ± 12.0	242.3 ± 17.8	404.8 ± 33.7
81	127.9 ± 10.3	141.0 ± 12.5	220.2 ± 17.5	335.4 ± 32.3
82	126.4 ± 10.3	128.4 ± 12.2	219.1 ± 17.6	327.2 ± 32.4
83	124.8 ± 10.3	131.1 ± 12.5	205.6 ± 17.4	300.7 ± 32.2
84	140.4 ± 10.6	159.1 ± 12.8	220.1 ± 16.9	354.2 ± 31.2
85	128.7 ± 10.5	133.0 ± 12.7	222.2 ± 18.1	299.4 ± 32.5
86	139.6 ± 10.6	121.5 ± 11.1	196.3 ± 15.8	305.5 ± 28.4
87	125.5 ± 10.1	155.0 ± 12.6	189.6 ± 15.7	369.6 ± 31.1
88	127.9 ± 10.7	140.3 ± 13.4	215.0 ± 18.4	273.9 ± 32.9

(continued)

Table E.18 (continued)

T_{π^0} [MeV]	$\frac{d^2\sigma}{dE_{\pi^0}\,d\Omega_{\pi^0}}$ $\left[\frac{\mu b}{\text{MeV sr}}\right]$			
	O	Fe	Sn	Pb
89	109.9 ± 9.6	135.9 ± 12.0	200.2 ± 16.3	306.8 ± 29.2
90	126.4 ± 10.3	130.1 ± 11.5	203.0 ± 16.2	294.9 ± 28.0
91	107.8 ± 9.7	108.0 ± 11.1	188.3 ± 16.2	301.8 ± 29.7
92	109.6 ± 10.1	117.3 ± 12.2	162.7 ± 16.2	234.3 ± 29.9
93	106.2 ± 9.8	110.1 ± 11.4	177.6 ± 16.1	271.4 ± 29.3
94	106.6 ± 9.9	114.7 ± 11.7	162.8 ± 15.7	262.9 ± 29.4
95	115.9 ± 10.5	94.5 ± 11.4	182.7 ± 17.1	290.4 ± 32.1
96	84.1 ± 8.9	100.9 ± 11.1	185.0 ± 16.6	251.0 ± 28.4
97	96.1 ± 10.0	90.0 ± 12.0	126.8 ± 15.8	208.3 ± 31.5
98	103.9 ± 9.7	93.3 ± 10.1	138.1 ± 13.9	295.3 ± 28.0
99	84.4 ± 8.8	119.3 ± 11.5	163.9 ± 15.3	227.0 ± 25.4
100	88.2 ± 9.3	94.2 ± 10.9	140.1 ± 14.9	214.6 ± 27.1
101	67.5 ± 8.3	87.1 ± 10.8	136.7 ± 15.0	187.9 ± 26.4
102	83.4 ± 10.0	83.9 ± 12.7	131.1 ± 17.3	136.6 ± 32.1
103	73.4 ± 8.7	84.8 ± 10.4	158.6 ± 15.8	159.9 ± 23.8
104	76.0 ± 9.4	72.6 ± 11.1	132.0 ± 16.1	206.3 ± 30.7
105	75.4 ± 9.5	73.7 ± 11.4	109.3 ± 15.4	180.5 ± 30.2
106	61.4 ± 8.6	75.0 ± 11.1	138.4 ± 16.3	167.8 ± 28.1
107	69.0 ± 9.2	67.0 ± 10.8	82.7 ± 13.8	154.8 ± 28.0
108	69.0 ± 9.3	59.5 ± 10.6	101.3 ± 15.0	145.4 ± 28.2
109	61.1 ± 9.3	69.4 ± 12.1	98.3 ± 16.0	145.4 ± 31.4
110	70.1 ± 8.8	76.0 ± 9.5	98.0 ± 12.2	178.8 ± 21.6
111	47.2 ± 8.4	63.7 ± 11.5	64.3 ± 13.8	141.0 ± 29.9
112	51.7 ± 8.5	67.1 ± 11.1	83.3 ± 14.1	119.0 ± 26.2
113	49.1 ± 7.6	64.8 ± 9.1	89.5 ± 12.2	94.8 ± 16.1
114	48.0 ± 8.9	42.2 ± 11.0	83.1 ± 15.8	96.8 ± 29.8
115	41.9 ± 8.2	54.0 ± 10.9	92.7 ± 15.6	82.3 ± 26.0
116	47.0 ± 8.8	53.1 ± 11.1	40.6 ± 12.4	111.0 ± 28.3
117	36.6 ± 7.6	59.4 ± 10.6	76.1 ± 13.6	102.1 ± 23.8
118	48.7 ± 8.8	53.0 ± 10.3	56.6 ± 12.4	124.2 ± 25.9
119	32.4 ± 7.4	34.6 ± 9.1	64.4 ± 13.3	87.2 ± 23.9
120	23.9 ± 7.4	20.3 ± 9.8	64.3 ± 15.4	44.7 ± 27.6
121	30.0 ± 6.8	34.6 ± 7.5	51.3 ± 10.4	72.5 ± 16.0
122	34.8 ± 8.2	35.6 ± 9.9	55.0 ± 13.5	83.5 ± 25.8
123	32.6 ± 7.4	30.7 ± 7.3	57.7 ± 11.4	71.2 ± 16.5
124	22.6 ± 7.2	36.9 ± 10.6	52.7 ± 14.0	59.5 ± 25.7
125	40.8 ± 8.6	39.1 ± 8.6	60.3 ± 12.2	118.4 ± 22.3
126	24.1 ± 6.7	33.1 ± 8.1	50.4 ± 11.4	76.9 ± 18.3
127	17.5 ± 5.9	32.6 ± 8.2	52.7 ± 11.9	67.1 ± 17.5
128	24.4 ± 7.1	49.2 ± 10.4	44.2 ± 11.1	79.8 ± 19.5
129	19.2 ± 6.4	26.9 ± 7.8	37.7 ± 10.5	49.3 ± 15.7
130	11.2 ± 5.0	18.9 ± 6.7	48.7 ± 12.3	72.5 ± 19.5
131	10.0 ± 7.0	6.7 ± 10.2	18.5 ± 14.1	6.7 ± 29.3
132	19.7 ± 7.0	18.3 ± 6.9	30.4 ± 10.2	57.5 ± 18.3

Table E.19. Data of Fig. 4.38. Narrow bin energy spectra for $O(\pi^+,\pi^0)$.

T_{π^0} [MeV]	$\frac{d^2\sigma}{dE_{\pi^0}\,d\Omega_{\pi^0}}$ $\left[\frac{\mu b}{\text{MeV sr}}\right]$			
	$\theta_{\pi^0} = 62.0°$	$\theta_{\pi^0} = 70.0°$	$\theta_{\pi^0} = 72.0°$	$\theta_{\pi^0} = 78.0°$
45	—	—	44.2 ± 44.3	—
46	—	—	100.6 ± 58.3	—
47	—	—	−35.7 ± 20.8	—
48	—	—	135.7 ± 56.0	—
49	—	—	76.7 ± 38.7	—
50	116.0 ± 47.9	78.2 ± 36.2	77.7 ± 35.1	111.2 ± 50.1
51	111.9 ± 47.4	22.8 ± 21.4	97.8 ± 34.8	38.0 ± 35.7
52	40.5 ± 28.9	88.0 ± 38.5	91.9 ± 32.8	30.2 ± 21.4
53	56.2 ± 29.1	91.3 ± 31.7	28.6 ± 16.6	63.8 ± 28.7
54	76.4 ± 30.0	101.1 ± 29.0	43.4 ± 21.7	48.7 ± 39.9
55	66.3 ± 26.0	96.5 ± 28.0	51.1 ± 22.7	76.7 ± 30.0
56	60.1 ± 28.5	58.4 ± 22.7	81.4 ± 26.1	111.3 ± 38.1
57	28.4 ± 23.5	57.4 ± 19.9	87.9 ± 26.7	111.7 ± 30.8
58	63.8 ± 20.9	35.6 ± 21.1	37.0 ± 19.0	83.5 ± 32.4
59	49.4 ± 22.6	87.8 ± 24.4	61.3 ± 20.6	50.6 ± 23.9
60	49.3 ± 19.2	29.4 ± 16.0	36.3 ± 14.9	58.5 ± 25.7
61	47.0 ± 20.0	52.2 ± 22.4	50.9 ± 17.1	82.1 ± 28.9
62	35.8 ± 17.8	58.3 ± 19.8	68.4 ± 19.3	44.3 ± 26.5
63	88.6 ± 20.2	71.2 ± 19.7	43.9 ± 16.3	88.7 ± 21.7
64	58.0 ± 17.6	64.1 ± 18.3	58.4 ± 18.3	84.3 ± 21.4
65	44.9 ± 16.9	44.1 ± 17.6	38.2 ± 15.0	109.8 ± 24.8
66	0.1 ± 16.0	56.1 ± 18.5	53.5 ± 16.2	84.5 ± 21.6
67	63.6 ± 17.3	89.8 ± 19.5	46.1 ± 14.7	70.1 ± 21.3
68	66.9 ± 16.7	80.6 ± 18.2	76.2 ± 17.9	110.2 ± 24.7
69	44.9 ± 17.6	72.1 ± 16.9	60.4 ± 15.8	70.3 ± 19.5
70	67.2 ± 15.4	8.6 ± 14.4	62.1 ± 15.8	70.2 ± 18.3
71	82.4 ± 17.9	45.6 ± 12.7	67.5 ± 16.2	61.6 ± 18.0
72	58.1 ± 15.7	51.0 ± 14.1	48.4 ± 13.6	56.4 ± 17.5
73	27.7 ± 12.7	69.6 ± 15.1	41.8 ± 14.1	73.4 ± 16.9
74	7.4 ± 12.1	63.3 ± 14.0	62.0 ± 16.0	33.0 ± 14.9
75	69.2 ± 15.4	69.4 ± 14.5	76.6 ± 17.3	88.2 ± 19.0
76	43.3 ± 12.2	92.5 ± 15.9	49.2 ± 13.3	60.0 ± 17.4
77	45.2 ± 14.0	58.4 ± 14.9	62.3 ± 15.5	73.9 ± 18.8
78	58.8 ± 13.9	74.7 ± 15.3	48.8 ± 12.4	92.7 ± 18.3
79	37.8 ± 12.0	56.1 ± 14.7	68.6 ± 14.6	78.2 ± 16.8
80	31.7 ± 13.5	56.0 ± 13.6	58.3 ± 13.9	105.6 ± 17.5
81	37.8 ± 12.7	48.6 ± 13.5	85.1 ± 16.3	83.2 ± 17.8
82	39.7 ± 11.1	57.0 ± 13.2	57.3 ± 13.1	71.2 ± 14.9
83	54.8 ± 13.5	83.4 ± 14.6	38.3 ± 11.4	75.5 ± 16.8
84	46.7 ± 12.7	83.2 ± 14.2	80.6 ± 14.9	91.9 ± 17.8
85	50.5 ± 13.4	60.4 ± 13.3	60.2 ± 12.6	80.2 ± 16.1
86	48.3 ± 12.5	68.2 ± 13.3	77.4 ± 15.0	45.0 ± 14.2
87	44.9 ± 13.4	60.5 ± 13.4	58.2 ± 12.4	86.5 ± 17.0
88	39.1 ± 10.3	73.2 ± 13.7	71.6 ± 13.9	83.3 ± 15.2
89	40.8 ± 11.7	67.8 ± 13.8	59.7 ± 13.0	53.8 ± 13.4
90	63.9 ± 13.2	85.5 ± 14.9	77.8 ± 14.6	79.1 ± 15.4
91	51.6 ± 13.1	72.0 ± 13.2	62.7 ± 13.1	73.1 ± 15.0
92	58.0 ± 12.2	52.1 ± 11.6	89.4 ± 15.6	77.5 ± 15.3
93	45.1 ± 11.2	55.9 ± 13.5	36.9 ± 10.6	88.3 ± 16.2
94	56.7 ± 12.1	74.2 ± 13.9	64.4 ± 13.4	73.3 ± 16.3
95	83.2 ± 14.9	62.8 ± 12.8	81.5 ± 14.4	85.1 ± 16.0

(continued)

Table E.19 (continued)

T_{π^0} [MeV]	$\frac{d^2\sigma}{dE_{\pi^0}\,d\Omega_{\pi^0}}$ $\left[\frac{\mu b}{\text{MeV sr}}\right]$			
	$\theta_{\pi^0} = 62.0°$	$\theta_{\pi^0} = 70.0°$	$\theta_{\pi^0} = 72.0°$	$\theta_{\pi^0} = 78.0°$
96	52.4 ± 12.5	79.7 ± 14.4	67.7 ± 13.3	90.8 ± 16.4
97	58.8 ± 13.9	50.4 ± 12.7	59.1 ± 12.3	78.5 ± 15.9
98	56.9 ± 13.6	83.0 ± 13.4	86.1 ± 15.2	103.8 ± 17.4
99	81.9 ± 15.6	81.7 ± 14.7	64.0 ± 14.5	94.3 ± 16.3
100	48.5 ± 11.7	73.5 ± 14.9	65.3 ± 13.9	72.7 ± 15.6
101	68.3 ± 13.4	60.3 ± 14.3	88.8 ± 16.1	72.2 ± 15.8
102	38.9 ± 13.5	88.3 ± 15.2	44.9 ± 11.4	55.9 ± 15.0
103	43.2 ± 13.3	67.4 ± 14.2	47.6 ± 11.7	60.1 ± 13.5
104	49.7 ± 13.4	46.7 ± 12.3	71.0 ± 15.3	79.4 ± 15.3
105	46.5 ± 13.3	83.4 ± 14.4	57.3 ± 12.8	104.6 ± 18.6
106	57.1 ± 13.8	85.1 ± 15.5	69.0 ± 13.5	53.6 ± 14.9
107	68.7 ± 15.4	79.0 ± 15.7	61.4 ± 13.3	67.8 ± 15.5
108	44.6 ± 14.2	73.9 ± 14.7	78.1 ± 15.4	109.2 ± 19.2
109	51.6 ± 14.6	80.6 ± 14.9	69.9 ± 14.3	73.7 ± 15.9
110	68.4 ± 13.7	81.1 ± 16.5	42.2 ± 12.2	61.1 ± 16.7
111	69.0 ± 16.7	60.4 ± 14.9	44.7 ± 12.5	53.3 ± 13.9
112	75.9 ± 15.9	77.4 ± 15.6	53.3 ± 14.3	44.3 ± 13.6
113	51.5 ± 13.2	49.9 ± 13.9	54.1 ± 13.8	70.8 ± 16.3
114	87.1 ± 15.9	75.5 ± 14.5	41.6 ± 11.8	63.3 ± 14.1
115	56.4 ± 15.1	75.2 ± 14.9	66.8 ± 15.4	62.4 ± 15.0
116	85.4 ± 16.1	81.2 ± 15.3	39.1 ± 12.5	53.0 ± 14.7
117	61.2 ± 16.2	55.9 ± 13.6	59.9 ± 14.9	51.3 ± 14.8
118	73.8 ± 15.7	83.0 ± 16.2	73.7 ± 16.5	40.8 ± 13.3
119	59.7 ± 14.1	58.7 ± 14.2	39.3 ± 12.6	53.0 ± 14.3
120	54.4 ± 16.3	45.8 ± 14.0	60.8 ± 14.5	48.5 ± 14.5
121	62.8 ± 16.0	89.7 ± 17.8	41.9 ± 12.8	38.1 ± 14.7
122	53.5 ± 15.8	60.7 ± 15.1	37.6 ± 12.6	69.1 ± 16.6
123	59.7 ± 15.7	57.3 ± 15.4	75.4 ± 16.8	14.5 ± 12.4
124	54.8 ± 14.4	68.8 ± 15.0	23.3 ± 11.1	52.4 ± 13.9
125	48.3 ± 16.0	68.1 ± 15.7	42.9 ± 13.7	47.3 ± 14.2
126	49.1 ± 15.8	44.8 ± 15.0	73.6 ± 16.7	41.9 ± 14.4
127	73.5 ± 16.4	39.6 ± 13.6	48.1 ± 14.6	25.8 ± 13.4
128	53.7 ± 15.1	43.5 ± 13.7	32.7 ± 13.7	43.7 ± 14.4
129	57.8 ± 15.1	60.1 ± 15.3	25.1 ± 11.2	37.5 ± 13.7
130	49.4 ± 14.3	42.5 ± 13.4	52.2 ± 14.6	37.7 ± 12.0
131	73.8 ± 17.3	50.7 ± 15.3	33.5 ± 12.0	50.6 ± 15.1
132	41.8 ± 14.5	38.8 ± 14.8	34.5 ± 13.1	48.3 ± 15.9
133	32.6 ± 14.3	43.1 ± 14.9	24.4 ± 10.0	53.3 ± 15.9
134	29.5 ± 13.3	50.9 ± 14.6	33.1 ± 11.8	30.0 ± 13.7
135	55.8 ± 16.9	37.8 ± 13.9	50.6 ± 14.8	21.4 ± 9.6
136	30.3 ± 11.9	46.2 ± 14.4	49.5 ± 15.2	9.2 ± 8.6
137	43.5 ± 16.7	16.4 ± 10.9	4.7 ± 6.8	14.3 ± 11.6
138	39.6 ± 13.7	36.8 ± 13.4	22.2 ± 9.9	14.7 ± 11.9
139	25.2 ± 13.8	17.0 ± 10.1	42.9 ± 14.5	33.1 ± 12.6
140	50.5 ± 17.5	34.6 ± 13.5	36.5 ± 13.0	38.7 ± 13.8

Table E.20. Data of Fig. 4.39. Narrow bin energy spectra for $O(\pi^+, \pi^0)$.

T_{π^0} [MeV]	$\frac{d^2\sigma}{dE_{\pi^0}\, d\Omega_{\pi^0}}$ $\left[\frac{\mu b}{\text{MeV sr}}\right]$			
	$\theta_{\pi^0} = 80.0°$	$\theta_{\pi^0} = 88.0°$	$\theta_{\pi^0} = 102.0°$	$\theta_{\pi^0} = 110.0°$
38	—	—	45.7 ± 62.6	95.3 ± 32.0
39	—	—	120.9 ± 40.5	72.5 ± 31.8
40	—	—	88.8 ± 38.9	161.8 ± 38.2
41	—	—	148.6 ± 37.4	97.2 ± 27.6
42	—	—	57.3 ± 41.5	113.7 ± 28.9
43	—	—	187.7 ± 36.6	110.8 ± 30.5
44	—	—	105.2 ± 39.2	110.6 ± 23.8
45	28.1 ± 28.2	55.3 ± 55.4	128.9 ± 26.8	146.0 ± 28.5
46	66.6 ± 45.6	102.1 ± 71.9	74.9 ± 24.3	140.5 ± 25.5
47	52.6 ± 35.9	60.0 ± 42.5	111.9 ± 26.4	141.1 ± 22.2
48	76.3 ± 34.5	46.4 ± 32.9	117.2 ± 28.4	128.5 ± 21.5
49	51.7 ± 26.1	110.8 ± 45.5	125.5 ± 25.0	139.2 ± 21.4
50	73.4 ± 30.0	61.9 ± 35.3	108.7 ± 19.9	137.1 ± 19.6
51	39.0 ± 19.7	153.4 ± 46.8	153.3 ± 24.2	136.4 ± 19.7
52	62.5 ± 23.9	79.4 ± 37.5	110.5 ± 23.5	120.7 ± 20.0
53	75.5 ± 27.8	91.0 ± 34.5	153.3 ± 23.1	142.1 ± 18.8
54	68.3 ± 24.1	45.9 ± 39.3	110.4 ± 20.5	150.9 ± 20.9
55	94.4 ± 25.7	147.6 ± 38.8	132.8 ± 19.8	143.9 ± 20.4
56	83.7 ± 21.9	161.8 ± 37.9	121.4 ± 21.2	122.5 ± 18.7
57	107.8 ± 24.6	97.5 ± 27.4	125.9 ± 20.1	116.6 ± 16.9
58	80.1 ± 21.7	44.9 ± 21.2	147.0 ± 19.4	144.0 ± 18.2
59	74.6 ± 19.6	63.0 ± 22.3	132.0 ± 19.4	112.2 ± 17.3
60	68.2 ± 18.5	105.1 ± 26.7	161.5 ± 19.7	147.6 ± 17.4
61	38.4 ± 15.7	109.7 ± 25.6	147.1 ± 20.2	179.3 ± 18.8
62	50.1 ± 17.4	68.2 ± 20.8	135.6 ± 18.0	171.0 ± 18.1
63	97.5 ± 19.3	84.4 ± 22.2	134.1 ± 20.1	124.8 ± 15.4
64	74.9 ± 17.2	99.5 ± 24.0	151.6 ± 18.5	145.9 ± 17.5
65	57.5 ± 15.6	95.0 ± 22.9	119.5 ± 19.4	148.6 ± 16.8
66	114.8 ± 20.2	87.0 ± 22.1	149.7 ± 18.9	147.6 ± 16.1
67	72.3 ± 16.9	131.8 ± 24.9	165.9 ± 20.3	146.8 ± 15.5
68	64.9 ± 15.6	85.9 ± 20.6	115.8 ± 19.5	159.3 ± 16.6
69	39.1 ± 12.2	86.2 ± 19.7	141.6 ± 18.9	147.0 ± 16.2
70	76.0 ± 16.2	104.8 ± 20.7	131.2 ± 18.0	150.8 ± 15.1
71	93.2 ± 17.2	103.4 ± 20.8	155.6 ± 18.6	146.3 ± 14.8
72	57.4 ± 14.2	109.3 ± 21.6	138.9 ± 16.8	148.2 ± 15.5
73	69.5 ± 14.8	114.0 ± 21.1	157.4 ± 17.4	159.9 ± 15.4
74	65.8 ± 13.3	112.3 ± 20.1	165.2 ± 18.7	155.2 ± 16.1
75	85.4 ± 14.7	97.7 ± 19.3	137.6 ± 17.1	142.1 ± 15.8
76	68.3 ± 14.0	89.2 ± 19.0	156.4 ± 19.1	153.7 ± 15.9
77	90.6 ± 15.2	121.9 ± 21.9	143.9 ± 17.3	141.1 ± 15.9
78	64.9 ± 13.5	89.4 ± 17.4	138.9 ± 17.8	132.6 ± 15.8
79	78.0 ± 15.4	76.2 ± 16.6	148.9 ± 17.2	161.5 ± 16.3
80	91.6 ± 14.8	91.8 ± 18.1	134.4 ± 16.9	113.8 ± 14.7
81	92.3 ± 15.4	113.9 ± 19.0	129.0 ± 17.2	130.2 ± 15.4
82	117.7 ± 16.8	108.1 ± 18.3	126.8 ± 17.8	119.4 ± 15.3
83	98.3 ± 15.3	67.8 ± 14.6	116.5 ± 17.9	117.7 ± 14.5
84	74.3 ± 13.6	115.7 ± 19.3	108.0 ± 16.5	134.7 ± 15.9
85	83.6 ± 14.1	79.7 ± 16.0	124.3 ± 18.3	118.9 ± 15.1
86	85.3 ± 14.0	83.6 ± 16.5	127.0 ± 17.0	121.3 ± 14.7
87	79.3 ± 13.5	98.2 ± 17.6	121.0 ± 16.7	105.9 ± 14.3
88	94.3 ± 14.5	118.8 ± 18.6	97.2 ± 16.5	128.7 ± 16.1

(continued)

Table E.20 (continued)

T_{π^0} [MeV]	$\frac{d^2\sigma}{dE_{\pi^0}\,d\Omega_{\pi^0}}$ $\left[\frac{\mu b}{\text{MeV sr}}\right]$			
	$\theta_{\pi^0} = 80.0°$	$\theta_{\pi^0} = 88.0°$	$\theta_{\pi^0} = 102.0°$	$\theta_{\pi^0} = 110.0°$
89	59.4 ± 11.9	105.7 ± 17.1	114.6 ± 16.5	89.8 ± 12.7
90	76.6 ± 13.2	79.5 ± 15.2	143.0 ± 19.2	99.5 ± 13.0
91	80.5 ± 13.2	90.3 ± 16.0	90.4 ± 17.9	100.2 ± 13.2
92	54.5 ± 11.4	100.0 ± 17.7	101.3 ± 16.8	103.9 ± 15.1
93	102.3 ± 15.2	91.7 ± 16.4	99.0 ± 17.5	111.0 ± 15.2
94	97.1 ± 15.3	75.0 ± 15.1	102.3 ± 17.2	114.9 ± 15.2
95	76.8 ± 13.6	91.5 ± 17.4	115.1 ± 17.5	96.4 ± 14.7
96	97.7 ± 14.8	89.7 ± 16.3	103.0 ± 16.8	60.0 ± 12.1
97	75.4 ± 12.8	87.6 ± 15.9	113.0 ± 18.5	86.5 ± 15.0
98	64.8 ± 12.0	77.7 ± 16.2	107.3 ± 17.5	119.9 ± 15.7
99	76.1 ± 13.5	73.1 ± 15.6	119.8 ± 18.7	55.5 ± 10.6
100	67.1 ± 12.6	82.6 ± 15.7	83.7 ± 16.0	78.3 ± 14.3
101	41.7 ± 10.5	61.1 ± 14.3	79.7 ± 14.8	47.5 ± 12.8
102	66.6 ± 13.8	63.3 ± 14.8	62.1 ± 16.7	93.1 ± 15.9
103	75.4 ± 13.5	88.3 ± 16.5	73.7 ± 15.8	51.1 ± 11.7
104	63.2 ± 12.7	96.4 ± 17.5	73.0 ± 16.0	77.2 ± 14.3
105	64.2 ± 12.7	91.8 ± 17.2	67.0 ± 17.0	77.0 ± 14.5
106	36.2 ± 10.7	64.4 ± 15.0	50.6 ± 15.7	50.6 ± 12.3
107	77.1 ± 14.2	94.7 ± 18.0	79.5 ± 17.4	66.8 ± 14.1
108	53.7 ± 12.8	87.7 ± 17.0	68.0 ± 15.0	45.0 ± 14.4
109	70.5 ± 13.9	88.4 ± 17.2	70.8 ± 17.1	60.5 ± 13.9
110	65.4 ± 13.1	48.6 ± 13.1	93.5 ± 19.6	53.7 ± 12.1
111	51.5 ± 11.8	80.6 ± 16.2	36.2 ± 13.7	38.8 ± 10.4
112	59.2 ± 12.7	70.1 ± 15.0	54.5 ± 14.2	50.2 ± 15.0
113	50.4 ± 12.2	53.3 ± 13.2	52.6 ± 14.2	49.7 ± 12.2
114	76.8 ± 14.8	56.8 ± 13.7	25.4 ± 15.6	54.1 ± 12.9
115	59.1 ± 13.0	82.3 ± 16.0	37.2 ± 15.1	55.8 ± 13.4
116	67.7 ± 14.0	60.2 ± 13.7	49.6 ± 14.5	32.9 ± 12.5
117	66.1 ± 13.6	74.5 ± 16.0	60.9 ± 18.8	36.7 ± 11.2
118	43.7 ± 11.1	81.8 ± 17.1	52.9 ± 15.4	53.1 ± 15.8
119	48.7 ± 12.0	49.8 ± 13.5	54.6 ± 15.9	25.5 ± 9.7
120	60.8 ± 13.5	59.9 ± 14.8	42.3 ± 14.2	19.1 ± 8.6
121	60.9 ± 13.9	44.0 ± 14.6	29.1 ± 11.9	24.0 ± 9.8
122	40.6 ± 11.4	67.3 ± 16.6	16.4 ± 14.2	46.3 ± 14.1
123	33.3 ± 11.7	36.7 ± 12.4	37.8 ± 18.0	17.7 ± 8.9
124	62.5 ± 14.6	47.7 ± 14.6	32.3 ± 13.2	28.0 ± 11.5
125	70.4 ± 15.7	50.8 ± 15.5	44.8 ± 15.9	29.5 ± 12.1
126	61.0 ± 14.6	44.9 ± 13.7	11.6 ± 8.2	31.1 ± 12.8
127	49.2 ± 12.8	47.8 ± 14.6	36.4 ± 14.9	—
128	33.7 ± 10.7	44.9 ± 15.8	38.0 ± 15.6	22.9 ± 11.5
129	20.8 ± 8.5	36.0 ± 12.8	13.3 ± 9.4	18.0 ± 10.4
130	30.4 ± 10.9	36.2 ± 12.9	34.9 ± 15.6	18.9 ± 10.9
131	33.2 ± 11.9	32.2 ± 12.3	9.3 ± 18.0	6.6 ± 6.6
132	20.8 ± 9.4	41.0 ± 13.8	31.0 ± 15.6	20.5 ± 11.9
133	34.7 ± 11.7	19.7 ± 9.9	—	—
134	49.7 ± 14.6	43.8 ± 14.0	—	—
135	12.6 ± 8.6	4.9 ± 6.9	—	—
136	46.0 ± 14.0	18.6 ± 10.6	—	—
137	19.5 ± 9.8	18.6 ± 9.3	—	—
138	11.2 ± 7.9	7.4 ± 7.1	—	—
139	18.0 ± 9.1	29.7 ± 12.2	—	—
140	32.4 ± 12.3	13.2 ± 9.3	—	—

Table E.21. Data of Fig. 4.40. Narrow bin energy spectra for $O(\pi^+, \pi^0)$.

T_{π^0} [MeV]	$\frac{d^2\sigma}{dE_{\pi^0}\, d\Omega_{\pi^0}}$ $\left[\frac{\mu b}{\text{MeV sr}}\right]$			
	$\theta_{\pi^0} = 118.0°$	$\theta_{\pi^0} = 121.7°$	$\theta_{\pi^0} = 129.7°$	$\theta_{\pi^0} = 137.7°$
38	116.7 ± 61.7	103.1 ± 49.9	199.7 ± 51.0	65.3 ± 32.8
39	95.2 ± 50.3	119.9 ± 47.8	189.5 ± 46.8	125.1 ± 44.3
40	184.3 ± 48.2	102.6 ± 36.6	161.2 ± 39.9	159.2 ± 43.3
41	177.3 ± 42.3	149.2 ± 43.3	119.1 ± 35.0	118.3 ± 34.6
42	116.1 ± 35.7	203.0 ± 45.1	140.2 ± 32.8	126.9 ± 34.4
43	154.3 ± 46.8	181.8 ± 42.2	174.9 ± 34.1	148.3 ± 33.9
44	183.8 ± 35.6	149.4 ± 34.8	155.2 ± 29.2	104.5 ± 27.4
45	162.1 ± 34.4	128.5 ± 31.5	190.2 ± 31.7	98.1 ± 24.3
46	129.4 ± 27.1	109.8 ± 28.3	159.8 ± 28.8	146.8 ± 28.1
47	145.6 ± 31.5	110.0 ± 26.8	196.3 ± 29.7	114.1 ± 23.9
48	177.2 ± 31.0	147.9 ± 28.1	160.6 ± 26.8	129.0 ± 25.5
49	132.3 ± 28.8	96.1 ± 22.9	137.3 ± 23.2	143.9 ± 25.3
50	158.5 ± 26.9	135.0 ± 26.1	122.5 ± 22.1	164.5 ± 25.6
51	147.3 ± 24.9	177.2 ± 28.2	172.3 ± 25.6	162.2 ± 25.6
52	169.4 ± 27.7	122.9 ± 22.6	163.0 ± 24.7	131.9 ± 23.7
53	205.1 ± 26.3	195.3 ± 28.7	192.7 ± 25.9	155.3 ± 23.8
54	184.7 ± 27.5	205.9 ± 29.3	186.9 ± 25.0	118.3 ± 21.5
55	116.2 ± 21.3	138.6 ± 23.2	167.7 ± 23.2	156.0 ± 22.6
56	172.0 ± 24.5	184.9 ± 26.7	170.7 ± 23.1	195.7 ± 25.5
57	189.1 ± 25.7	188.6 ± 26.4	185.1 ± 23.8	171.3 ± 23.5
58	150.2 ± 22.1	127.5 ± 21.9	229.0 ± 26.1	156.3 ± 21.8
59	167.4 ± 22.9	194.5 ± 26.0	162.6 ± 21.0	182.8 ± 24.0
60	200.8 ± 23.0	193.3 ± 25.2	169.1 ± 22.2	153.8 ± 21.6
61	136.2 ± 22.2	137.7 ± 21.4	215.9 ± 23.8	192.9 ± 23.6
62	135.5 ± 21.8	135.2 ± 21.6	199.7 ± 23.2	155.6 ± 21.5
63	166.5 ± 22.6	157.1 ± 22.6	204.8 ± 23.1	186.1 ± 22.9
64	152.8 ± 21.7	155.6 ± 22.6	187.0 ± 22.0	160.4 ± 20.6
65	211.6 ± 24.1	155.2 ± 21.1	190.8 ± 21.8	173.1 ± 21.4
66	166.7 ± 21.3	126.9 ± 19.4	192.1 ± 21.6	143.9 ± 19.1
67	235.2 ± 23.3	170.2 ± 21.8	132.1 ± 17.7	123.3 ± 17.6
68	152.8 ± 20.5	158.1 ± 21.7	166.9 ± 20.1	139.4 ± 18.7
69	178.0 ± 20.4	185.0 ± 24.4	156.2 ± 19.7	124.9 ± 17.8
70	198.1 ± 20.7	193.7 ± 24.1	153.3 ± 19.2	142.4 ± 18.9
71	173.1 ± 19.8	170.6 ± 22.4	179.6 ± 21.2	158.5 ± 19.9
72	149.2 ± 18.8	142.9 ± 20.7	172.9 ± 21.4	121.1 ± 17.9
73	224.2 ± 23.5	193.8 ± 23.9	149.3 ± 19.5	126.1 ± 18.1
74	190.2 ± 21.1	136.0 ± 20.3	140.1 ± 18.8	135.4 ± 18.7
75	183.1 ± 20.5	122.6 ± 19.3	155.6 ± 20.1	115.5 ± 16.9
76	189.7 ± 21.1	122.4 ± 19.9	141.2 ± 19.7	125.2 ± 18.0
77	165.1 ± 20.7	128.4 ± 20.5	133.6 ± 19.4	128.8 ± 18.7
78	177.9 ± 19.5	129.0 ± 20.4	160.4 ± 20.7	117.3 ± 17.8
79	166.8 ± 19.9	130.8 ± 20.9	154.9 ± 20.6	132.2 ± 19.0
80	174.3 ± 20.3	152.9 ± 23.4	146.2 ± 20.0	134.1 ± 19.4
81	127.3 ± 17.7	171.3 ± 24.7	132.4 ± 19.5	137.6 ± 19.9
82	141.5 ± 18.2	130.7 ± 22.1	143.3 ± 20.6	141.9 ± 20.1
83	127.3 ± 18.9	139.4 ± 23.0	125.9 ± 19.6	102.7 ± 17.5
84	169.3 ± 19.6	156.0 ± 24.0	133.6 ± 20.7	117.5 ± 18.5
85	150.1 ± 18.6	183.2 ± 26.7	133.6 ± 20.2	94.9 ± 16.6
86	161.2 ± 20.0	158.3 ± 25.8	128.6 ± 20.3	89.3 ± 16.8
87	155.4 ± 19.2	163.4 ± 26.3	129.7 ± 20.4	85.2 ± 16.3
88	154.8 ± 21.0	111.0 ± 21.8	131.1 ± 21.9	91.2 ± 16.9

(continued)

Table E.21 (continued)

T_{π^0} [MeV]	$\frac{d^2\sigma}{dE_{\pi^0}\,d\Omega_{\pi^0}}$ $\left[\frac{\mu b}{\text{MeV sr}}\right]$			
	$\theta_{\pi^0} = 118.0°$	$\theta_{\pi^0} = 121.7°$	$\theta_{\pi^0} = 129.7°$	$\theta_{\pi^0} = 137.7°$
89	126.6 ± 17.7	74.1 ± 18.6	141.6 ± 22.1	78.4 ± 16.7
90	136.4 ± 19.2	65.4 ± 17.1	127.4 ± 21.2	95.3 ± 17.4
91	140.6 ± 19.0	104.0 ± 22.1	100.8 ± 19.3	69.4 ± 15.5
92	118.3 ± 17.7	89.8 ± 20.4	87.3 ± 18.3	99.2 ± 18.4
93	105.7 ± 16.8	101.0 ± 21.9	117.9 ± 21.2	92.4 ± 18.0
94	120.6 ± 18.0	82.2 ± 20.2	122.6 ± 22.4	57.1 ± 14.5
95	130.5 ± 20.2	123.1 ± 24.6	77.0 ± 18.9	74.2 ± 16.5
96	79.5 ± 15.8	103.1 ± 23.4	107.3 ± 22.0	82.9 ± 18.1
97	106.6 ± 17.3	64.4 ± 18.1	50.4 ± 15.9	60.2 ± 15.8
98	79.0 ± 15.2	104.7 ± 25.0	131.7 ± 25.7	79.8 ± 18.2
99	88.0 ± 16.1	86.6 ± 22.7	47.0 ± 15.0	52.3 ± 14.7
100	96.7 ± 16.1	43.7 ± 18.5	70.0 ± 19.0	65.0 ± 17.1
101	72.8 ± 14.0	70.0 ± 21.3	63.9 ± 19.4	74.2 ± 18.9
102	91.9 ± 18.0	65.6 ± 20.0	70.8 ± 19.9	52.0 ± 15.9
103	95.7 ± 16.5	43.2 ± 16.4	70.8 ± 19.9	69.2 ± 20.1
104	74.8 ± 17.1	80.2 ± 23.4	46.6 ± 16.6	48.3 ± 15.4
105	70.2 ± 15.8	81.2 ± 25.6	48.7 ± 17.4	53.7 ± 18.0
106	84.1 ± 17.4	51.8 ± 19.7	41.6 ± 15.9	67.8 ± 19.0
107	62.0 ± 15.5	43.6 ± 19.4	53.5 ± 19.1	16.3 ± 9.4
108	77.1 ± 18.6	70.6 ± 23.7	16.9 ± 11.7	20.2 ± 11.6
109	52.5 ± 14.9	69.1 ± 23.2	41.5 ± 17.0	18.6 ± 12.4
110	72.9 ± 15.8	52.7 ± 21.6	51.2 ± 19.5	19.4 ± 13.0
111	55.5 ± 15.7	26.4 ± 17.6	12.2 ± 11.5	13.0 ± 9.2
112	56.0 ± 14.2	17.7 ± 12.5	54.4 ± 22.3	20.5 ± 11.9
113	43.2 ± 12.6	42.7 ± 21.3	44.3 ± 19.9	33.0 ± 16.5
114	62.9 ± 15.5	49.5 ± 22.2	24.5 ± 17.0	30.6 ± 15.3
115	24.0 ± 12.7	31.6 ± 18.3	20.6 ± 14.6	40.6 ± 18.3
116	56.1 ± 17.3	6.5 ± 12.3	11.2 ± 11.2	13.6 ± 12.8
117	28.3 ± 10.8	1.8 ± 14.3	—	9.3 ± 9.3
118	33.4 ± 11.9	26.4 ± 18.7	26.7 ± 19.0	25.7 ± 17.9
119	14.2 ± 12.2	14.4 ± 14.4	14.8 ± 14.8	−4.7 ± 4.7
120	16.0 ± 16.1	15.9 ± 15.9	16.4 ± 16.5	11.8 ± 11.8
121	41.5 ± 13.9	—	—	—
122	33.5 ± 12.7	—	—	—
123	29.8 ± 12.2	—	—	—
124	15.5 ± 9.0	—	—	—
125	43.0 ± 15.3	—	—	—
126	44.8 ± 15.9	—	—	—
127	11.7 ± 8.3	—	—	—
128	18.3 ± 10.6	—	—	—
129	12.8 ± 9.1	—	—	—
130	—	—	—	—
131	7.0 ± 7.0	—	—	—
132	22.2 ± 12.9	—	—	—

Appendix F

Beam Time for Empty Target Measurements

The aim of this appendix is to find an expression for how the available beam time is best shared between full target measurements and empty target measurements.

The experimentally measured quantity is a cross section σ. In the case of coincidence measurements, this notation is shorthand for

$$\sigma \equiv \frac{d^4\sigma}{dE_{\pi^0}\, dE_p\, d\Omega_{\pi^0}\, d\Omega_p}\,. \tag{F.1}$$

For a given experimental situation we obtain two cross sections: σ_f for the full target measurements and σ_e for the empty target measurements, each of which is calculated according to

$$\sigma_i = \frac{N_i}{(N_b)_i\, n_t\, \Delta E_{\pi^0}\, \Delta E_p\, \Delta\Omega_{\pi^0}\, \Delta\Omega_p\, \epsilon}\,. \tag{F.2}$$

In this equation the index i indicates either full (f) or empty (e) target. N_i is the number of "good" events, $(N_b)_i$ is the number of beam particles, n_t is the number of target nuclei per area (adjusted for target angle), and ϵ is a general efficiency factor.

The same (full target) value n_t is used to calculate both σ_f and σ_e. Assuming that the efficiencies also are the same, then N_i and $(N_b)_i$ are the only quantities in Eq. (F.2)

that are different for the two measurements. The number of incident particles must be proportional to the effective beam time t_i (measured in clock time, toroid counts, or any other suitable unit). It then follows that

$$\sigma_i = A\frac{N_i}{t_i} = Ar_i\,, \tag{F.3}$$

where A is a constant, and r_i is the rate of good events per unit time.

In the analysis of the experiment the empty target contribution is subtracted from the full target data. The final experimental cross section is thus

$$\sigma = \sigma_f - \sigma_e = A\left(r_f - r_e\right) \tag{F.4}$$

with uncertainty

$$(\Delta\sigma)^2 = A^2\left[(\Delta r_f)^2 + (\Delta r_e)^2\right]\,. \tag{F.5}$$

The number of good events should follow a Poisson distribution. Assuming that the uncertainty in the time measurement can be ignored, one then has

$$(\Delta r_i)^2 = \left(\Delta\frac{N_i}{t_i}\right)^2 = \frac{N_i}{t_i^2} = \frac{r_i}{t_i}\,. \tag{F.6}$$

(It is important to remember that r_i is a *physical property* of the reaction being studied. It is obtained by measuring the *experimental quantities* N_i and t_i. Therefore all manipulation of uncertainties has to take place through N_i and t_i.) Finally, inserting Eq. (F.6) in Eq. (F.5) gives a useful expression for the total uncertainty:

$$(\Delta\sigma)^2 = A^2\left[\frac{r_f}{t_f} + \frac{r_e}{t_e}\right]\,. \tag{F.7}$$

The total uncertainty must be minimized under the constraint that the total beam time T is fixed. This is equivalent to solving

$$\left.\frac{\partial(\Delta\sigma)^2}{\partial t_e}\right|_{t_f+t_e=T} = 0\,. \tag{F.8}$$

Using $t_f(t_e) = T - t_e$, Eq. (F.8) becomes

$$-\frac{r_f}{t_f^2}\frac{\partial t_f}{\partial t_e} - \frac{r_e}{t_e^2} = \frac{r_f}{t_f^2} - \frac{r_e}{t_e^2} = 0 \tag{F.9}$$

or

$$t_e = t_f\sqrt{\frac{r_e}{r_f}}, \tag{F.10}$$

as quoted in Sec. 4.1.5. That is, the available beam time should be divided between full target measurements and empty target measurements according to the ratio between the square roots of the event rates for the two measurements.

References

1 S. Høibråten *et al.*, in G. M. Bunce, ed., *Proceedings of the Third Conference on the Intersections Between Particle and Nuclear Physics*, AIP Conference Proceedings **176**, American Institute of Physics, New York, New York, 1988, p. 614.

2 Particle Data Group, Phys. Lett. **204B**, 1 (1988).

3 H. Yukawa, Proc. Phys.-Math. Soc. Jpn. **17**, 48 (1935).

4 L. M. Brown, Physics Today **39**, No. 12, 55 (1986).

5 C. M. G. Lattes, H. Muirhead, C. F. Powell, and G. P. S. Occhialini, Nature **159**, 694 (1947).

6 D. H. Perkins, Nature **159**, 126 (1947).

7 G. P. S. Occhialini and C. F. Powell, Nature **159**, 186 (1947).

8 R. Bjorklund, W. E. Crandall, B. J. Moyer, and H. F. York, Phys. Rev. **77**, 213 (1950).

9 A. G. Carlson, J. E. Hooper, D. T. King, Phil. Mag. Ser. 7 **41**, 701 (1950).

10 M. A. Preston and R. K. Bhaduri, *Structure of the Nucleus*, Addison-Wesley Publishing Company, Reading, Massachusetts, 1975.

11 D. E. Nagle, M. B. Johnson, and D. F. Measday, Physics Today **40**, No. 4, 56 (1987).

12 L. Rosen, *The Los Alamos Clinton P. Anderson Meson Physics Facility (LAMPF) — Fifteen Years Later*, Report No. LA-UR-84-2031, Los Alamos National Laboratory, Los Alamos, New Mexico, 1984.

13 S. R. Amendolia *et al.*, Phys. Lett. **146B**, 116 (1984).

14 R. A. Arndt and L. D. Roper, *Scattering Analysis Interactive Dial-in*, Report No. CAPS–80–3 (rev), Center for Analysis of Particle Scattering, Virginia Polytechnic Institute and State University, Blacksburg, Virginia, 1983.

15 R. A. Arndt, J. M. Ford, and L. D. Roper, Phys. Rev. D **32**, 1085 (1985).

16 We used solution FA86. This contains more recent Los Alamos pion–nucleon data not included in the published solution FP84 (Ref. 15).
R. A. Arndt, private communication.

17 H. L. Anderson *et al.*, Phys. Rev. **85**, 934 (1952).

18 H. L. Anderson, E. Fermi, E. A. Long, and D. E. Nagle, Phys. Rev. **85**, 936 (1952).

19 D. H. Perkins, *Introduction to High Energy Physics*, 2nd Ed., Addison-Wesley Publishing Company, Reading, Massachusetts, 1982.

20 E. Piasetzky *et al.*, Phys. Rev. Lett. **46**, 1271 (1981); Phys. Rev. C **25**, 2687 (1982).

21 D. Ashery *et al.*, Phys. Rev. C **23**, 2173 (1981).

22 D. Ashery *et al.*, Phys. Rev. C **30**, 946 (1984).

23 D. S. Koltun, Adv. Nucl. Phys. **3**, 71 (1969).

24 J. Alster and J. Warszawski, Phys. Rep. **52**, 87 (1979).

25 M. S. Kozodaev *et al.*, Sov. Phys. JETP **11**, 300 (1960) (J. Exptl. Theoret. Phys. (U.S.S.R.) **38**, 409 (1960)).

26 P. L. Reeder and S. S. Markowitz, Phys. Rev. **133**, B639 (1964).

27 A. M. Poskanzer and L. P. Remsberg, Phys. Rev. **134**, B779, (1964).

28 C. O. Hower and S. B. Kaufman, Phys. Rev. **144**, 917 (1966).

29 D. T. Chivers *et al.*, Phys. Lett. **26B**, 573 (1968); Nucl. Phys. **A126**, 129 (1969).

30 D. H. Wilkinson, Comm. Nucl. Part. Phys. **1**, 169 (1967).

31 A. O. Aganyants *et al.*, Phys. Lett. **27B**, 590 (1968); Nucl. Phys. **B11**, 79 (1969).

32 Yu. R. Gismatullin and V. I. Ostroumov, Sov. J. Nucl. Phys. **11**, 159 (1970) (Yad. Fiz. **11**, 285 (1970)).

33 E. Bellotti, S. Bonetti, D. Cavalli, and C. Matteuzzi, Nuovo Cimento Ser. 2 **14A**, 567 (1973).

34 B. J. Dropesky *et al.*, Phys. Rev. Lett. **34**, 821 (1975); Phys. Rev. C **20**, 1844 (1979).

35 C. L. Morris *et al.*, Phys. Rev. C **17**, 227 (1978).

36 L. W. Swenson *et al.*, Phys. Rev. Lett. **40**, 10 (1978).

37 H. J. Ziock *et al.*, Phys. Rev. Lett. **43**, 1919 (1979).

38 E. Piasetzky *et al.*, Phys. Lett. **114B**, 414 (1982).

39 E. Piasetzky *et al.*, Phys. Rev. C **26**, 2702 (1982).

40 G. S. Kyle *et al.*, Phys. Rev. Lett. **52**, 974 (1984).

41 G. S. Kyle *et al.*, to be published.

42 J. A. Faucett *et al.*, Phys. Rev. C **30**, 1622 (1984).

43 S. Gilad *et al.*, Phys. Rev. Lett. **57**, 2637 (1986).

44 E. Fermi *et al.*, Phys. Rev. **85**, 935 (1952).

45 J. H. Tinlot, in H. P. Noyes, M. Camac, and W. D. Walker, ed., *Proceedings of the Third Annual Rochester Conference on High Energy Nuclear Physics*, Interscience Publishers, New York, New York, 1952, p. 32;
A. Roberts and J. Tinlot, Phys. Rev. **90**, 951 (1953).

46 H. Hilscher, W.-D. Krebs, G. Sepp, and V. Soergel, Nucl. Phys. **A158**, 602 (1970).

47 T. J. Bowles *et al.*, Phys. Rev. Lett. **40**, 97 (1978); Phys. Rev. C **23**, 439 (1981).

48 D. Ashery *et al.*, Phys. Rev. Lett. **50**, 482 (1983).

49 D. Ashery, private communication.

50 M. M. Sternheim and R. R. Silbar, Phys. Rev. Lett. **34**, 824 (1975).

51 L. S. Kisslinger and W. L. Wang, Phys. Rev. Lett. **30**, 1071 (1973).

52 T. Takaki and M. Thies, Phys. Rev. C **38**, 2230 (1988).

53 D. Ashery and J. P. Schiffer, Ann. Rev. Nucl. Part. Sci. **36**, 207 (1986).

54 M. Hirata, F. Lenz, and M. Thies, Phys. Rev. C **28**, 785 (1983).

55 M. Thies, Nucl. Phys. **A382**, 434 (1982).

56 G. S. Kyle, private communication.

57 *LAMPF Users Handbook*, Report No. MP-DO-3-UHB (Rev.), Los Alamos National Laboratory, Los Alamos, New Mexico, 1984.

58 R. L. Burman, R. L. Fulton, and M. Jakobson, Nucl. Instr. and Meth. **131**, 29 (1975).

59 Mylar® is a registered trademark of E. I. du Pont de Nemours & Co. Inc., Wilmington, Delaware.

60 The value 0.1 mm per week was determined by D. Mack. Several measurements at PSI have confirmed that water diffuses through Mylar windows. G. S. Kyle, private communication.

61 H. W. Baer *et al.*, Nucl. Instr. and Meth. **180**, 445 (1981).

62 S. Gilad, Ph. D. thesis, Tel Aviv University, 1979 (unpublished).

63 It is somewhat unclear which diodes were used for this purpose. Most likely it was 3 mm diameter Stanley ESBG3401 diodes which emit green light. U. Sennhauser and D. R. Tieger, private communication.

64 Program PIANG1 modified from PIANG by S. Gilad.

65 C. M. Lederer and V. S. Shirley, ed., *Table of Isotopes*, 7th Ed., John Wiley & Sons, New York, New York, 1978.

66 M. Bernheim *et al.*, Nucl. Phys. **A375**, 381 (1982).

67 J. Mougey, in H. Arenhövel and D. Drechsel, ed., *Proceedings of the International Conference on Nuclear Physics with Electromagnetic Probes*, Lecture Notes in Physics **108**, Springer-Verlag, Berlin, 1979, p 124.

68 G. S. Kyle *et al.*, in T.-S. H. Lee, D. F. Geesaman, and J. P. Schiffer, ed., *Proceedings of the Symposium on Δ-Nucleon Dynamics*, Report No. ANL-PHY-83-1, Argonne National Laboratory, Argonne, Illinois, 1983, p. 505.

69 S. Frullani and J. Mougey, Adv. Nucl. Phys. **14**, 1 (1984).

70 Program KINREL by M. Oothoudt, Los Alamos National Laboratory, Los Alamos, New Mexico, 1976 (unpublished).

71 *Q Programmer's Information Manual*, Document No. MP-1-3401-5, Los Alamos National Laboratory, Los Alamos, New Mexico, 1986.

72 A general discussion of the CAMAC standard (Computer Automated Measurement And Control) is found in P. N. Clout, *A CAMAC Primer*, Report No. LA-UR-82-2718, Los Alamos National Laboratory, Los Alamos, New Mexico, 1982.

73 There are a number of manuals covering the various aspects and features of the Q system. For a listing consult the manual *Read This First*, Document No. MP-1-3414-2, Los Alamos National Laboratory, Los Alamos, New Mexico, 1986.

74 J. H. Hubbell, H. A. Gimm, and I. Øverbø, J. Phys. Chem. Ref. Data 9, 1023 (1980).

75 J. H. Hubbell, Int. J. Appl. Radiat. Isot. **33**, 1269 (1982).

76 Particle Data Group, Rev. Mod. Phys. **56**, S1 (1984).

77 The exact time of the calibration is uncertain because the old log books are difficult to get at. The quoted year is from memory.
H. W. Baer, private communication.

78 R. D. Bolton, H. W. Baer, J. D. Bowman, and L. Gordon, Nucl. Instr. and Meth. **174**, 411 (1980).

79 S. H. Rokni, Ph. D. thesis, Report No. LA–11004–T, Los Alamos National Laboratory, Los Alamos, New Mexico, 1987.

80 The converter planes in the π^0 spectrometer were changed after publication of Ref. 61. Updated information is found in Ref. 79.
H. W. Baer, private communication.

81 The program MINUIT originates from CERN. See for instance *MINUIT — A Package of Programs to Minimize a Function of* n *Variables, Compute the Covariance Matrix, and Find the True Errors*, Document No. D 506/D 516, Long Write-up, CERN Computer 7600 Interim Program Library, 1971.

82 See for example the section on scintillation counters in D. H. Perkins, *Introduction to High Energy Physics*, 2nd Ed., Addison-Wesley Publishing Company, Reading, Massachusetts, 1982.

83 L. Holm, H. W. Fielding, and G. C. Neilson, Nucl. Instr. and Meth. **A234**, 517 (1985).

84 W. L. Reiter and G. Stengl, Nucl. Instr. and Meth. **169**, 469 (1980).

85 Used in Experiment 84–25 at Bates Linear Accelerator Center, Middleton, Massachusetts, 1988.
F. J. Federspiel and L. D. Pham, private communication.

86 M. de Palma *et al.*, Nucl. Instr. and Meth. **190**, 41 (1981).

87 J. Mougey *et al.*, Nucl. Phys. **A262**, 461 (1976).

88 D. F. Measday and C. Richard-Serre, Nucl. Instr. and Meth. **76**, 45 (1969).

89 A. M. Sourkes *et al.*, Nucl. Instr. and Meth. **143**, 589 (1977).

90 J. W. Negele and K. Yazaki, Phys. Rev. Lett. **47**, 71 (1981).

91 Gilad *et al.* have not published energy spectra for telescope 8, but they were used to calculate the ratios presented in Ref. 43 and reproduced in our Fig. 1.13. These spectra have been made available to us.
S. Gilad, private communication.

92 The reanalysis was done by G. S. Kyle, S. Høibråten, and C. H. Q. Ingram in 1985.

93 T. Takaki, private communication.

94 W. J. Burger *et al.*, Phys. Rev. Lett. **57**, 58 (1986).

95 G. Garino *et al.*, contributed paper at the Annual Meeting of the Division of Nuclear Physics of the American Physical Society, Santa Fe, New Mexico, 1988; Bull. Am. Phys. Soc. **33**, 1594 (1988).

96 C. H. Q. Ingram *et al.*, Phys. Rev. C **27**, 1578 (1983).

97 J. D. Bowman, in R. J. Peterson and D. D. Strottman, ed., *Proceedings of the Conference on Pion-Nucleus Physics: Future Directions and New Facilities at LAMPF*, AIP Conference Proceedings **163**, American Institute of Physics, New York, New York, 1988, p. 119.

98 S. Gilad and E. Piasetzky, spokesmen, *Study of the* ^{3}He$(\pi^-, \pi^0 p)$ *Reaction by Detecting Neutral Pions and Protons in Coincidence*, LAMPF Proposal No. 920, Los Alamos National Laboratory, Los Alamos, New Mexico.

99 S. Gilad and E. Piasetzky, spokesmen, *Study of the* ^{3}He, ^{3}H$(\pi^+, \pi^0 p)$ *Reactions by Detecting Neutral Pions and Protons in Coincidence*, LAMPF Proposal No. 921, Los Alamos National Laboratory, Los Alamos, New Mexico.

100 S. Gilad and R. P. Redwine, spokesmen, *Study of the* ^{16}O$(\gamma, \pi^- p)$ *Reaction*, Proposal No. 84–25, Bates Linear Accelerator Center, Middleton, Massachusetts.

101 The original author of the program ACT is unknown. The program was put in its present form by M. J. Leitch in 1983.

102 W. C. Davidon, Computer J. **10**, 406 (1968).